# GEOCHEMICAL CYCLING OF 210PO AND 210PB IN MARINE ENVIRONMENTS

EDITED BY: Weifeng Yang, Jinzhou Du and Laodong Guo

PUBLISHED IN: Frontiers in Marine Science

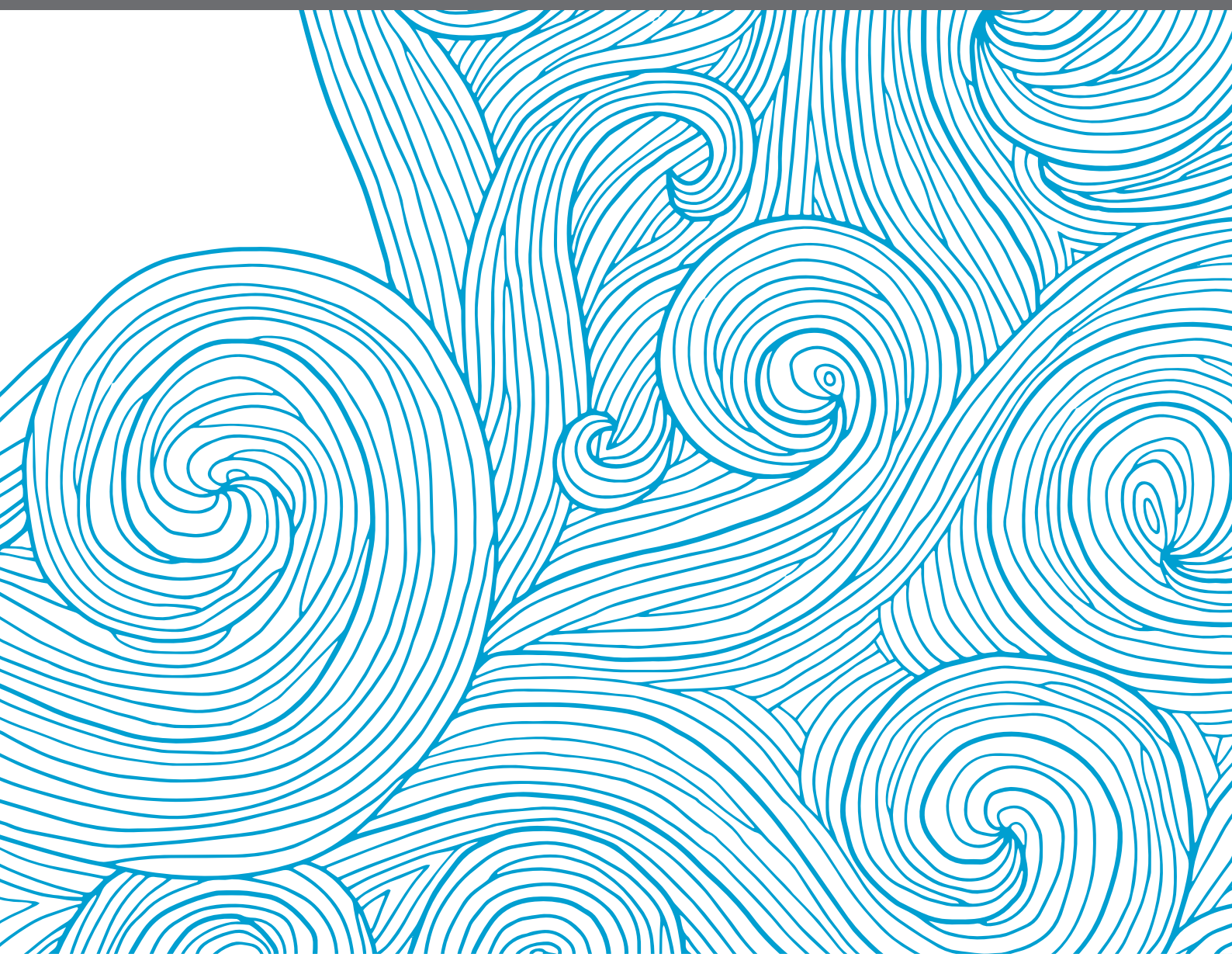

frontiers Research Topics

**Frontiers eBook Copyright Statement**

The copyright in the text of individual articles in this eBook is the property of their respective authors or their respective institutions or funders. The copyright in graphics and images within each article may be subject to copyright of other parties. In both cases this is subject to a license granted to Frontiers.

The compilation of articles constituting this eBook is the property of Frontiers.

Each article within this eBook, and the eBook itself, are published under the most recent version of the Creative Commons CC-BY licence. The version current at the date of publication of this eBook is CC-BY 4.0. If the CC-BY licence is updated, the licence granted by Frontiers is automatically updated to the new version.

When exercising any right under the CC-BY licence, Frontiers must be attributed as the original publisher of the article or eBook, as applicable.

Authors have the responsibility of ensuring that any graphics or other materials which are the property of others may be included in the CC-BY licence, but this should be checked before relying on the CC-BY licence to reproduce those materials. Any copyright notices relating to those materials must be complied with.

Copyright and source acknowledgement notices may not be removed and must be displayed in any copy, derivative work or partial copy which includes the elements in question.

All copyright, and all rights therein, are protected by national and international copyright laws. The above represents a summary only. For further information please read Frontiers' Conditions for Website Use and Copyright Statement, and the applicable CC-BY licence.

ISSN 1664-8714
ISBN 978-2-88974-664-4
DOI 10.3389/978-2-88974-664-4

## About Frontiers

Frontiers is more than just an open-access publisher of scholarly articles: it is a pioneering approach to the world of academia, radically improving the way scholarly research is managed. The grand vision of Frontiers is a world where all people have an equal opportunity to seek, share and generate knowledge. Frontiers provides immediate and permanent online open access to all its publications, but this alone is not enough to realize our grand goals.

## Frontiers Journal Series

The Frontiers Journal Series is a multi-tier and interdisciplinary set of open-access, online journals, promising a paradigm shift from the current review, selection and dissemination processes in academic publishing. All Frontiers journals are driven by researchers for researchers; therefore, they constitute a service to the scholarly community. At the same time, the Frontiers Journal Series operates on a revolutionary invention, the tiered publishing system, initially addressing specific communities of scholars, and gradually climbing up to broader public understanding, thus serving the interests of the lay society, too.

## Dedication to Quality

Each Frontiers article is a landmark of the highest quality, thanks to genuinely collaborative interactions between authors and review editors, who include some of the world's best academicians. Research must be certified by peers before entering a stream of knowledge that may eventually reach the public - and shape society; therefore, Frontiers only applies the most rigorous and unbiased reviews.
Frontiers revolutionizes research publishing by freely delivering the most outstanding research, evaluated with no bias from both the academic and social point of view. By applying the most advanced information technologies, Frontiers is catapulting scholarly publishing into a new generation.

## What are Frontiers Research Topics?

Frontiers Research Topics are very popular trademarks of the Frontiers Journals Series: they are collections of at least ten articles, all centered on a particular subject. With their unique mix of varied contributions from Original Research to Review Articles, Frontiers Research Topics unify the most influential researchers, the latest key findings and historical advances in a hot research area! Find out more on how to host your own Frontiers Research Topic or contribute to one as an author by contacting the Frontiers Editorial Office: frontiersin.org/about/contact

# GEOCHEMICAL CYCLING OF 210PO AND 210PB IN MARINE ENVIRONMENTS

Topic Editors:
**Weifeng Yang,** Xiamen University, China
**Jinzhou Du,** East China Normal University, China
**Laodong Guo,** University of Wisconsin–Milwaukee, United States

**Citation:** Yang, W., Du, J., Guo, L., eds. (2022). Geochemical Cycling of 210Po and 210Pb in Marine Environments. Lausanne: Frontiers Media SA.
doi: 10.3389/978-2-88974-664-4

# Table of Contents

frontiers in Marine Science

EDITORIAL
published: 17 February 2022
doi: 10.3389/fmars.2022.852558

# Editorial: Geochemical Cycling of $^{210}$Po and $^{210}$Pb in Marine Environments

*Weifeng Yang*[1]*, *Jinzhou Du*[2]* and *Laodong Guo*[3]*

[1] State Key Laboratory of Marine Environmental Science, College of Ocean and Earth Sciences, Xiamen University, Xiamen, China, [2] State Key Laboratory of Estuarine and Coastal Research, East China Normal University, Shanghai, China, [3] School of Freshwater Sciences, University of Wisconsin-Milwaukee, Milwaukee, WI, United States

**Keywords: polonium-210, lead-210, biological pump, radiochronology, particulate organic carbon (POC)**

**Editorial on the Research Topic**

**Geochemical Cycling of $^{210}$Po and $^{210}$Pb in Marine Environments**

OPEN ACCESS

***Edited and reviewed by:***
*Pere Masque,*
*IAEA International Atomic Energy Agency, Monaco*

***Correspondence:**
*Weifeng Yang*
*wyang@xmu.edu.cn*
*Jinzhou Du*
*jzdu@sklec.ecnu.edu.cn*
*Laodong Guo*
*guol@uwm.edu*

***Specialty section:***
*This article was submitted to Marine Biogeochemistry, a section of the journal Frontiers in Marine Science*

***Received:*** *11 January 2022*
***Accepted:*** *27 January 2022*
***Published:*** *17 February 2022*

***Citation:***
*Yang W, Du J and Guo L (2022) Editorial: Geochemical Cycling of $^{210}$Po and $^{210}$Pb in Marine Environments. Front. Mar. Sci. 9:852558. doi: 10.3389/fmars.2022.852558*

## INTRODUCTION

The radioactive isotope $^{210}$Po ($T_{1/2}$ = 138.4 days) and its grandparent $^{210}$Pb ($T_{1/2}$ = 22.3 years) have been increasingly used to trace particle dynamics and the biogeochemical cycling of chemical species in aquatic environments over recent decades (Verdeny et al., 2009). This Research Topic provides a set of new studies focusing on the biogeochemical cycling of both $^{210}$Po and $^{210}$Pb in the marine environments. A total of 11 articles were published on this Research Topic, covering the biogeochemical behaviors of $^{210}$Po and $^{210}$Pb in various oceanic settings, their ability to bind with diatom- and coccolithophore-associated biopolymers, the utilization of $^{210}$Po/$^{210}$Pb to quantify the sinking flux of particulate organic carbon and the residence times (or ages) of particulate matter in a variety of environmental settings, and the coupled application with other radionuclides and soot to expand their utilities as biogeochemical proxies.

## GEOCHEMICAL BEHAVIORS OF $^{210}$Po AND $^{210}$Pb

An understanding of the geochemical behaviors of $^{210}$Po and $^{210}$Pb is the foundation for their applications in constraining particle dynamics. In studying this Research Topic, Seo et al. observed contrasting behaviors of $^{210}$Po and $^{210}$Pb over the productive East China Sea Shelf, showing a net addition of $^{210}$Po and a net removal of $^{210}$Pb from the water column. The regeneration of $^{210}$Po from organic matter in the sinking particles and sediments was suggested to explain the difference in behavior, which is also supported by the observation that $^{210}$Po was mainly bound to more hydrophobic (high protein to carbohydrate ratio) nitrogen/sulfur-enriched organic moieties, whereas the strongest $^{210}$Pb binding agents were phosphate-containing molecules based on coccolithophore (*Emiliania huxleyi*)- and diatom (*Phaeodactylum tricornutum*)-associated biopolymers (Lin P. et al.). These results highlight the role of marine organisms in affecting the disequilibrium between $^{210}$Po and $^{210}$Pb

and lend support for the potential application of $^{210}$Po as a proxy for sulfur group elements (S, Se, and Te) (Seo et al.) and nitrogen cycling. Based on a direct assessment of $^{210}$Po and $^{210}$Pb in marine organisms, Sun et al. reported bioconcentration factors (BCFs) up to 3–4 orders of magnitude higher for $^{210}$Po than for $^{210}$Pb, indicating that bioconcentration might, particularly in productive waters, affect the disequilibrium between $^{210}$Po and $^{210}$Pb. The close relationship between the $^{210}$Po deficit and the dissolved silicate concentration in the upper 200 m of the water column also highlights the influence of organisms (i.e., phytoplankton growth) on the disequilibria between $^{210}$Po and $^{210}$Pb (Ma et al.). All these results confirm the important roles of marine organisms in affecting the deficit of $^{210}$Po in the upper ocean.

## TRACE PARTICLE CYCLING USING $^{210}$Po AND $^{210}$Pb

One of the applications of $^{210}$Po and $^{210}$Pb is the quantification of the sinking fluxes of various particulate components such as particulate organic carbon (POC; Stewart et al., 2007; Verdeny et al., 2009), particulate nitrogen (PN; Yang et al., 2011), and biogenic silica (BSi; Friedrich and Rutgers van der Loeff, 2002). In studying this Research Topic, Bam et al. reported the highest fluxes of POC and PN in rarely studied ice-covered areas near the North Pole compared with other non-permanent ice-covered areas, based on $^{210}$Po-$^{210}$Pb disequilibria. In addition, extremely low BSi and particulate inorganic carbon (PIC) fluxes were observed, suggesting the absence of ballast effects in the Arctic Ocean. Such a high POC flux scenario, independent of the ballast effect, indicates differences in the biological carbon pump below the sea ice compared with other oceanic environments. Hu et al. found a significant positive correlation between POC and the partitioning of $^{210}$Po between particles and seawater, lending support for the application of $^{210}$Po-$^{210}$Pb disequilibrium in evaluating the POC fluxes in Prydz Bay, Antarctica. A similar investigation was conducted in the western North Pacific Ocean (Zhong et al.), which showed enhanced POC export fluxes near the continental shelf corresponding to a moderate biological carbon pump efficiency, compared with the high-latitudinal Arctic and Southern Ocean (Bam et al.; Hu et al.). In addition, Lin F. et al. evaluated organic carbon transport from the surface to deeper sediment by benthos using excess $^{210}$Pb relative to supported $^{210}$Pb ($^{226}$Ra; i.e., the difference between total $^{210}$Pb and supported $^{210}$Pb from $^{226}$Ra) in the sediment of the Tropical Northwest Pacific, highlighting the driving relation between POC flux and the benthic ecosystem.

## NOVEL APPLICATION OF THE $^{210}$Po/$^{210}$Pb PAIR

The expansion of $^{210}$Po and $^{210}$Pb in constraining geochemical processes is of great importance to the field of isotopic marine chemistry. In studying this Research Topic, Baskaran and Krupp proposed a novel application of the $^{210}$Po-$^{210}$Pb pair as a chronometer to date the age of snow, the formation time of ice cores and melt ponds, and the residence time of ice-rafted sediment in the Arctic Ocean. These timescales constrained a series of crucial parameters for certain geochemical processes, e.g., the age of snow and the elapsed time of ice-rafted sediment after incorporation into ice. Yang et al. quantified the laterally contributed sinking flux of soot (the refractory fraction of black carbon) using $^{210}$Po-$^{210}$Pb disequilibria and discriminated locally settled POC fluxes from those contributed by sediment resuspension coupled with lateral transport over the slope region of the northern South China Sea, which enables the $^{210}$Po-$^{210}$Pb disequilibrium method to quantify the efficiency of the biological carbon pump in marginal seas with intensive cross-shelf material exchange. In combination with $^{7}$Be, Schmidt et al. used excess $^{210}$Pb to estimate the residence times of total suspended sediment (TSS) in Galveston Bay, thus constraining the cycling of TSS within shallow, dynamic marine environments.

## CONCLUSION

This Research Topic expands our knowledge of the biogeochemical cycling of $^{210}$Po and $^{210}$Pb and their applications to understanding different biogeochemical processes in the marine environments. Overall, the collected articles enhance the understanding of the behaviors of $^{210}$Po and $^{210}$Pb and the potential roles of various organic components and marine organisms in affecting the scavenging and phase partitioning of $^{210}$Po and $^{210}$Pb, validate the applicability of $^{210}$Po/$^{210}$Pb disequilibrium in quantifying POC fluxes in various oceanic settings, and apply the pair in the dating of snow, ice, and ice-rafted sediment. Still, future studies are needed to improve our understanding of the biogeochemical behaviors of $^{210}$Po and $^{210}$Pb and to expand their applications.

## AUTHOR CONTRIBUTIONS

All authors listed have made intellectual contributions to this Research Topic and approved it for publication.

## FUNDING

This work was supported by the National Natural Science Foundation of China (42076030 and 41476061).

## ACKNOWLEDGMENTS

We thank all the authors, reviewers, and editors for their contributions to this Research Topic.

## REFERENCES

Friedrich, J., and Rutgers van der Loeff, M. M. (2002). A two-tracer ($^{210}$Po-$^{234}$Th) approach to distinguish organic carbon and biogenic silica export flux in the Antarctic Circumpolar Current. *Deep-Sea Res. I* 49, 101–120. doi: 10.1016/S0967-0637(01)00045-0

Stewart, G., Cochran, J. K., Miquel, J. C., Masqué, P., Szlosek, J., Baena, A. M. R., et al. (2007). Comparing POC export from $^{234}$Th/$^{238}$U and $^{210}$Po/$^{210}$Pb disequilibria with estimates from sediment traps in the northwest Mediterranean. *Deep-Sea Res. I* 54, 1549–1570. doi: 10.1016/j.dsr.2007.06.005

Verdeny, E., Masqué, P., Garcia-Orellana, J., Hanfland, C., Cochran, J. K., and Stewart, G. M. (2009). POC export from ocean surface waters by means of $^{234}$Th/$^{238}$U and $^{210}$Po/$^{210}$Pb disequilibria: a review of the use of two radiotracer pairs. *Deep-Sea Res. II* 56, 1502–1518. doi: 10.1016/j.dsr2.2008.12.018

Yang, W., Huang, Y., Chen, M., Qiu, Y., Li, H., and Zhang, L. (2011). Carbon and nitrogen cycling in the Zhubi coral reef lagoon of the South China Sea as revealed by $^{210}$Po and $^{210}$Pb. *Mar. Poll. Bull.* 62, 905–911. doi: 10.1016/j.marpolbul.2011.02.058

**Conflict of Interest:** The authors declare that the research was conducted in the absence of any commercial or financial relationships that could be construed as a potential conflict of interest.

**Publisher's Note:** All claims expressed in this article are solely those of the authors and do not necessarily represent those of their affiliated organizations, or those of the publisher, the editors and the reviewers. Any product that may be evaluated in this article, or claim that may be made by its manufacturer, is not guaranteed or endorsed by the publisher.

*Copyright © 2022 Yang, Du and Guo. This is an open-access article distributed under the terms of the Creative Commons Attribution License (CC BY). The use, distribution or reproduction in other forums is permitted, provided the original author(s) and the copyright owner(s) are credited and that the original publication in this journal is cited, in accordance with accepted academic practice. No use, distribution or reproduction is permitted which does not comply with these terms.*

frontiers in Marine Science

ORIGINAL RESEARCH
published: 18 June 2021
doi: 10.3389/fmars.2021.703503

# Molecular Level Characterization of Diatom and Coccolithophore-Associated Biopolymers That Are Binding $^{210}$Pb and $^{210}$Po in Seawater

*Peng Lin[1]*, Chen Xu[1], Wei Xing[1] and Peter H. Santschi[1,2]*

*[1] Department of Marine and Coastal Environmental Science, Texas A&M University at Galveston, Galveston, TX, United States, [2] Department of Oceanography, Texas A&M University, College Station, TX, United States*

Through a combination of selective extractions and molecular characterization techniques including Isoelectric Focusing Chromatography and Electrospray Ionization Fourier-Transform Ion Cyclotron Resonance Mass spectrometry, molecular structures of diatom (*Phaeodactylum tricornutum*) and coccolithophore (*Emiliania huxleyi*)-associated biopolymers that are responsible for the distinct partitioning behavior between $^{210}$Pb and $^{210}$Po were determined. Our results show that diatom-derived biopolymers have distinctive elemental grouping distributions as compared to those excreted by the coccolithophore, with the former consisting of more heterogeneous elements (i.e., nitrogen, sulfur and phosphorus-containing organic compounds). For the coccolithophore culture, two $^{210}$Pb-enriched biopolymers (non-attached exopolymeric substances and coccosphere shell-associated biopolymers) have a higher abundance of CHO-type compounds, suggesting CHO-only-type compounds as the main binding moieties for $^{210}$Pb. In contrast, such association was not evident in the diatom culture. Different with $^{210}$Pb, $^{210}$Po enrichment in coccolithophore-derived attached exopolymeric substances and Fe-Mn-associated metabolites coincided with the higher abundance of nitrogen/sulfur-containing organic compounds in these two biopolymer fractions, suggesting the strong parallel of Po with the production of nitrogen-rich organic matter as well as sulfur-containing amino acids. These different associations between $^{210}$Pb/$^{210}$Po and organic functional groups were further explored by separating $^{210}$Pb or $^{210}$Po-labeled coccolithophore-derived biopolymers *via* isoelectric focusing. This technique suggests that phosphate group-containing molecules but not the other molecules that contain heterogeneous elements (e.g., CHONS, CHON, and CHOS) as the strongest binding agents for $^{210}$Pb, while the more hydrophobic (high protein to carbohydrate ratio) nitrogen/sulfur-enriched organic moieties acted as the main $^{210}$Po-binding ligands. It is concluded that the deficiency of $^{210}$Po with respect to $^{210}$Pb can be influenced by the relative abundance of nitrogen/sulfur-enriched organic moieties to the nitrogen/sulfur-depleted organic compounds in the water column. This behavior constrains the application of $^{210}$Po-$^{210}$Pb approach to quantify the particulate organic

OPEN ACCESS

**Edited by:**
*Weifeng Yang,*
*Xiamen University, China*

**Reviewed by:**
*Jinlong Wang,*
*East China Normal University, China*
*Wokil Bam,*
*Louisiana State University, United States*

***Correspondence:**
*Peng Lin*
*pengL1104@tamug.edu*

**Specialty section:**
*This article was submitted to Marine Biogeochemistry, a section of the journal Frontiers in Marine Science*

**Received:** *30 April 2021*
**Accepted:** *28 May 2021*
**Published:** *18 June 2021*

**Citation:**
*Lin P, Xu C, Xing W and Santschi PH (2021) Molecular Level Characterization of Diatom and Coccolithophore-Associated Biopolymers That Are Binding $^{210}$Pb and $^{210}$Po in Seawater. Front. Mar. Sci. 8:703503. doi: 10.3389/fmars.2021.703503*

carbon (POC) export flux in the ocean. It also explains that differences in chemical binding of the $^{210}$Po as compared to those of other radionuclides (e.g., thorium-234) as the main factor. That suggests that differences in decay half-lives or physical factors are less important when these nuclides are applied to estimate the POC flux in the ocean.

**Keywords: polonium-210, lead-210, organic moieties, diatom, coccolithophore, FTICR mass spectrometry**

## INTRODUCTION

Naturally occurring radionuclides with strong particle-reactivity, such as lead (Pb), polonium (Po), and thorium (Th), are widely used in estimating various biogeochemical and physical processes associated with marine particles in the ocean, mostly based on their strong particle reactivity and making use of disequilibria between parent and daughter radionuclides (e.g., Santschi et al., 1980; Anderson et al., 1983; Kumar et al., 1995; Murray et al., 2005; Stewart et al., 2010; Yang et al., 2011). Although most of these tracer applications are generally resting on inferences from correlations of isotopic ratios with bulk particle properties, experimental evidence reveals organic compound-specific scavenging and partitioning for different radionuclides, either in particulate or in colloidal phases (Hayes et al., 2015a,b; Lam et al., 2015; Lin et al., 2015). Furthermore, while previous focus was on inorganic matter as the main binding agents (e.g., opal, carbonate, and lithogenic; Chase et al., 2002; Guo et al., 2002; Roy-Barman et al., 2009; Lin et al., 2014), more recent experimental studies reveal the role of specific organic matter compounds in the scavenging of different radionuclides in marine environments (Roberts et al., 2009; Xu et al., 2011a; Chuang et al., 2014, 2015a,b; Lin et al., 2017).

In the global oceans, diatom and coccolithophores serve as the most important contributors to global oceanic primary production and to carbon flux (Nelson et al., 1995; Armbrust, 2009), whereby in-situ production and excretion of biogenic materials account for the majority of natural organic matter in the water column. During phytoplankton growth, secretion of fresh biopolymers (Chin et al., 1998; Santschi et al., 1998; Quigg et al., 2016) was shown to provide the strongest binding agents for different radionuclides compared with the naked diatom frustule (Chuang et al., 2014) or coccosphere (Lin et al., 2017, 2020). Furthermore, particle-reactive radionuclides can partition differently between diatom- and coccolithophore-predominated systems or among different biopolymer fractions of diatom or coccolithophore cells, which were attributed to different organic composition between different biopolymer fractions, and thus, to different affinities of the radionuclides to these fractions (Chuang et al., 2015b; Lin et al., 2017). However, the chemical composition of radionuclide-carrying biopolymer compounds derived from diatoms and coccolithophores are typically only quantified and characterized in terms of few groups of organic components, such as proteins, uronic acids, and carbohydrates. To fill this knowledge gap, the diatom *P. tricornutum* and coccolithophore *Emiliania huxleyi* were incubated for later separation of different biopolymer fractions, including extracellular fractions (non-attached and attached exopolymeric substances), frustule/coccosphere-associated biopolymers and intracellular biopolymers from cell lysis (Chuang et al., 2015b; Lin et al., 2017). In order to characterize the diatom/coccolithophore-derived biopolymers, specific organic compounds likely responsible for the scavenging and partitioning of $^{210}$Pb and $^{210}$Po in the water column, and examine their differences at the molecular level, Electrospray Ionization Fourier-Transform Ion Cyclotron Resonance Mass Spectrometry (ESI-FTICRMS) (Xu et al., 2020) was applied in the present study. In addition, different biopolymer fractions from coccolithophore were further labeled with $^{210}$Pb and $^{210}$Po, followed by the isoelectric focusing (IEF) gel electrophoresis and organic characterization of biopolymers enriched in the tracer radionuclides $^{210}$Pb and $^{210}$Po.

Considering the significant contribution of diatoms and coccolithophores to the carbon flux in the ocean, a better understanding on the association between radionuclides and organic components of diatom and coccolithophore-associated biopolymers can provide molecular level insights into the processes that control the oceanographic applications of natural radionuclides, such as the $^{210}$Po-$^{210}$Pb pair, in predicting the organic carbon flux.

## MATERIALS AND METHODS

### *Emiliania huxleyi* and *Phaeodactylum tricornutum* Culturing

As described in Lin et al. (2017), natural seawater (pH = 8.0), collected from the Gulf of Mexico (Salinity = 35), was first filtered through a 0.2 μm polycarbonate cartridge to remove all particles, followed by cross-flow ultrafiltration using a 1 kDa cutoff membrane to remove colloidal organic matter (COM). Thus, the ultra-filterpassing fraction that contained only low-molecular-weight organic matter (<1 kDa), was then used as the culturing medium for the diatom *P. tricornutum* and coccolithophore *Emiliania huxleyi* species. After enrichment with f/2 medium nutrients, trace metals and vitamins, and sterilization, laboratory axenic *P. tricornutum* and *E. huxleyi* cultures were added to 100 mL of medium. All the incubations were conducted induplicates at 19 ± 1°C with a light:dark cycle of 14 h:10 h under an irradiation condition of 100 μmol-quanta/m$^2$/s. Additionally, a control cultures for each species were also set up to monitor the pH and growth status, measured as the change in optical density at 750 nm wavelength ($OD_{750}$) with a UV-Visspectrometer. Once the $OD_{750}$ value was constant, i.e., when the stationary phase for growth was reached, all cultures were harvested. Biopolymers were also sequentially extracted from the culture for the analysis of the biopolymer components (see details below).

## Extracellular Biopolymer Extraction

The sequential chemical extraction scheme for obtaining individual fractions from *P. tricornutum* (**Supplementary Figure 1**) and *E. huxleyi* (**Supplementary Figure 2**) followed the procedures described in Chuang et al. (2015b) and Lin et al. (2017), with some modification. For the extracellular biopolymers excreted by the phytoplankton, non-attached exopolymeric substances (NAEPS) in the surrounding seawater and attached EPS (AEPS) associated with the cellular surface, were harvested. Laboratory cultures were centrifuged at 3,000 × *g* for 30 min, followed by filtration of the supernatant which was further concentrated and desalted with nanopure water (18.2 Ω) in 3 kDa Microsep centrifugal filter tubes (Milipore) to obtain the NAEPS fraction, while the resultant pellet from the centrifugation was resuspended by 50 mL 3% NaCl solution and stirred gently overnight at 4°C to extract EPS from the cellular surface. The solution was also centrifuged, and the supernatant containing the AEPS was then filtered to remove residual cells before further desalting *via* the 3 kDa ultrafiltration centrifugation tubes. The final volume of concentrated solution of each biopolymer fraction (>3 kDa) was 2 mL.

## Extraction of *Phaeodactylum tricornutum* Intracellular Biopolymers and Its Frustule-Related Biopolymers

Given the different shells for these two phytoplankton species (silica frustule for the diatom *P. tricornutum* and biogenic calcite for the coccolithophore *E. huxleyi*), sequential extraction procedures were applied to access the intracellular and frustule/coccosphere associated biopolymers in *P. tricornutum* and *E. huxleyi* cells, respectively (**Supplementary Figures 1, 2**). For the *P. tricornutum* cultures, 10 mL of 100 mM EDTA (pH 8.0) solution was added to the diatom cells from the previous AEPS extraction step. The diatom cells were resuspended at 4°C overnight to extract the intracellular material after diatom cell lysis and the supernatant was collected after centrifugation to obtain the EDTA-extractable intracellular biopolymers (EDTA-intracellular, **Supplementary Figure 1**). Then, the resultant pellet was further resuspended in 10 mL of 1% SDS/10 mM Tris (pH 6.8) solution and heated at 95°C for 1 h. The centrifuged supernatant was also collected and defined as SDS-extractable intracellular biopolymer (SDS-intracellular, **Supplementary Figure 1**) in *P. tricornutum* cells.

To access the diatom frustule-associated biopolymers (Frustule-BP, **Supplementary Figure 1**), 5 mL of 52% HF was then added to the frustules and incubated on ice for 1 h. After the separation of the HF-insoluble pellet, the HF-soluble fraction was evaporated under $N_2$ stream and neutralized, followed by 3 kDa centrifugal filtration to collect the digested frustule silica fraction (<3 kDa) and HF-soluble frustule-associated biopolymer (>3 kDa). Lastly, the residual biopolymer in the HF-insoluble pellet was collected by resuspension in a 2 mL of 100 mM ammonium acetate solution and sonication. Similar to NAEPS and AEPS, all the *P. tricornutum* cellular biopolymers were concentrated and desalted with nanopure water in 3 kDa Microsep centrifugal filter tubes (Milipore).

## *Emiliania huxleyi* Coccosphere (Biogenic Calcite) and Biopolymer Extraction

The coccosphere of the *E. huxleyi* cells was first dissolved before the extraction of intracellular biopolymers. In brief, the pellet from the previous AEPS extraction step was digested in 0.44 M acetic acid (HAc) (weak acidity and non-oxidizing nature to avoid the breakage of cells) plus 0.1 M NaCl solution at 4°C for 8 h. After the digestion, the mixed solution was centrifuged and filtered, followed by ultrafiltration of the supernatant with 3 kDa Microsep centrifugal filter tubes. The retentate (>3 kDa) was defined as coccosphere-associated biopolymers (Shell-BP, **Supplementary Figure 2**).

The *E. huxleyi* cells after the removal of shells were further heated in 20 mL of 1% SDS/10 mM Tris mixed solution (pH 6.8) at 95°C for 1 h. The supernatant was also collected by centrifugation and filtration, followed by desalting with 3 kDa Microsep centrifugal filter tubes. Subsequently, the remaining pellet was further digested by 0.04 M $NH_2OH{\cdot}HCl$/4.35 M HAc mixture at 96°C for 6 h to obtain the intracellular metabolitic biopolymer. These two fractions (Intracellular and Fe, Mn-BP, **Supplementary Figure 2**) can represent the intracellular biopolymers in *E. huxleyi* cells.

Lastly, it should be noted that the parallel $^{210}$Pb/$^{210}$Po-labeled diatom and coccolithophore incubation experiments have been described in Chuang et al. (2015b) and Lin et al. (2017), whose data (**Supplementary Figures 3, 4**) were used in the present study to examine the association between $^{210}$Pb/$^{210}$Po partitioning and organic characterization in various biopolymer fractions.

## Isoelectric Focusing of Radionuclide-Labeled Biopolymer

Different fractions of purified *E. huxleyi*-derived biopolymers were incubated individually with $^{210}$Pb and $^{210}$Po (total activity at 250 Bq, respectively, equivalent to 50 fMoles, considerably lower than ambient Pb/Po concentration), respectively, in nanopure water (18.2 Ω), followed by subsequent isoelectric focusing (IEF) gel electrophoresis to determine the $pH_{IEF}$ of potential binding ligands for each radionuclide (Alvarado Quiroz et al., 2006; Chuang et al., 2014). This was to further examine the organic compounds binding the majority of each radionuclide in each biopolymeric fraction. After IEF separation, the strip was then cut into 11 1-cm pieces and measured for the radionuclide activities in each pH section, through gamma spectrometry ($^{210}$Pb at 46.3 kev) and liquid scintillation counting ($^{210}$Po). The samples were counted for enough time to obtain the activity error < 10%, with the detection limit of 0.05 Bq for $^{210}$Pb (based on at least 1-day counting) and 0.5 Bq for $^{210}$Po, respectively. The pH section, which contained the highest activity of radionuclide was cut from the IEF gel of the non-radiolabeled biopolymers and extracted with 1% sodium dodecyl sulfate (SDS) solution for 2 days, and is called here the "IEF extract." Similar to the bulk biopolymer fraction, these radionuclide-enriched "IEF extracted" biopolymer fractions were diafiltered with nanopure water through 3 kDa Microsep centrifugal filter tubes, to remove all electrophoresis reagents and SDS that would otherwise interfere with later ESI-FTICRMS analysis.

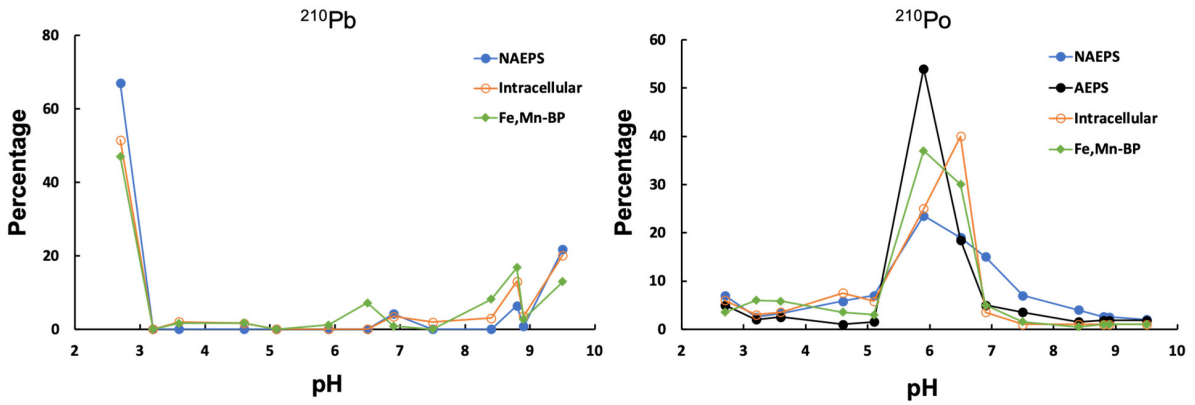


**FIGURE 1 |** Isoelectric focusing (IEF) electrophoresis of $^{210}$Pb- and $^{210}$Po-labeled biopolymers extracted from *Emiliania huxleyi* coccolithophore in seawater.

## ESI-FTICRMS Analysis

All the *E. huxleyi*-derived biopolymers, including the bulk and IEF-fractionated fractions, were freeze-dried, re-dissolved in nanopure water, mixed with methanol at a 1:1 ratio, and analyzed by electrospray ionization Fourier-transform ion cyclotron resonance mass spectrometry (ESI-FTIRCMS) in the negative mode (Xu et al., 2015, 2020), at the College of Sciences Major Instrumentation Cluster, Old Dominion University, Virginia. The procedural blank, which went through all isotope incubation and IEF gel electrophoresis experiment steps, was analyzed at the same time. Samples were injected using a Hamilton syringe at a flow rate of 2 μL/min into the Apollo II ESI ion source of a Bruker Daltonics 12 Tesla Apex Qe FTICRMS. The coated glass capillary temperature was set to 200°C and the electrospray voltages were optimized to keep the ion current constant. The ion accumulation time was set to 2.0 s and 200 scan averages were co-added between 100 and 1,000 m/z.

Mass spectra were internally calibrated using a series of reference organic acids. Formula calculation was accomplished using a molecular formula calculator (Molecular Formula Calc. v. 1.1 NHMFL) developed at the national High Magnetic Field Laboratory in Tallahassee, FL, using peaks with a signal-to-noise (S/N) ratio of ≥ 4, a m/z range between 200 and 900, and a mass error less than 1.0 ppm. The following criteria were used for formula assignment: $C_{6-75}$, $H_{2-100}$, $N_{0-8}$, $O_{0-35}$, $S_{0-4}$, and $P_{0-1}$. All formulas were screened to eliminate those that are unlikely to occur in NOM, according to a list of selection criteria (Stubbins et al., 2010). Procedure blanks peaks were removed from the final formula list. Peaks with multiple possible formulas (usually those peaks with m/z values > 400 Da) were assigned formulas through the detection of homologous series ($CH_2$, COO, $O_2$, $C_2H_4O$, $H_2$, etc.). Molecular formulas were lastly screened by searching chemical structures in the Pubchem database[1]. Formulas with no chemical structures identified in the Pubchem database were excluded from the final formula assignment.

Aromatic compounds and condensed aromatic compounds were assigned to formulas with aromaticity indices [AI, calculated by (1+C-0.5O-S-0.5H)/(C-0.5O-S-N-P)] greater than 0.5 and 0.67, respectively. The double bond equivalent (DBE) was calculated as DBE = 1+ 0.5 (2C-H+N+P). Aliphatic compounds were assigned to formulas DBE: C < 0.3 and H:C = 1.0–3.0. The carboxyl-containing aliphatic (number of COO-R functionality ≥ 1) and/or alicyclic molecules (CCAM) were assigned to formulas with H:C of 0.85–2.00 and O:C of 0–0.40.

[1]https://pubchem.ncbi,nlm.nih.gov/search

# RESULTS AND DISCUSSION

## pH Gradient of Radionuclides in Isoelectric Focusing

Distributions of $^{210}$Pb and $^{210}$Po bound by coccolithophore-derived biopolymers, along the IEF-pH gradient, are shown in **Figure 1**. The results clearly indicate that Po and Pb radionuclides selectively bind with coccolithophore biopolymers of distinctly different IEF points ($pH_{IEF}$) where a compound class has a zero net surface charge. This compound class contains specific functional groups for binding the $^{210}$Pb and $^{210}$Po. For $^{210}$Pb, about 50% of labeled SDS-extractable intracellular biopolymers and intracellular Fe-Mn-associated metabolites was found below pH of 3, with a minor fraction concentrated above pH of 8. For labeled NAEPS, more than 60% of $^{210}$Pb was detected below pH of 3. Such $^{210}$Pb-IEF pH profiles are the opposite of the observed patterns for the $^{210}$Pb-labeled diatom-derived biopolymers showing the majority of $^{210}$Pb distributing above pH of 9 (Chuang et al., 2014), probably due to different compositions and specific functional groups between diatom- and coccolithophore-derived biopolymers (see sections below).

In contrast, results from the pH gradient of $^{210}$Po-labeled coccolithophore-derived biopolymers demonstrated similar profiles as the observation in diatom-derived biopolymers (Chuang et al., 2014), as discussed below. As shown in **Figure 1**, all the $^{210}$Po-labeled biopolymers showed a main $pH_{IEF}$ peak between pH 6–7. Overall, it is evident that $^{210}$Pb and $^{210}$Po showed different patterns in their IEF profiles (**Figure 1**), demonstrating that these two radionuclides are bound to different types of organic functional groups in

individual biopolymers from the coccolithophore. $^{210}$Pb seemed to be complexed mainly by negatively charged organic macromolecules, while neutral organic functional groups are responsible for the binding of $^{210}$Po.

## Different Molecular Compositions of Diatom- and Coccolithophore-Derived Biopolymers Associated With Radionuclide Partitioning

Distribution of various molecular formula types among different biopolymer fractions in diatom and coccolithophore cultures were identified through the generation of a van Krevelen diagram of all formulas (**Figure 2**), and their elemental groupings for bulk organic matter from the two species are displayed in **Figure 3**. It is evident that diatom-derived biopolymers have different distinct elemental grouping distributions compared to those excreted by coccolithophore, with the former consisting of more heterogeneous elements (i.e., nitrogen, sulfur and phosphorus-containing groups). For example, coccolithophore-derived NAEPS consisted primarily of CHO formulas (68% by number and 58% by intensity) and had minor abundance of CHONS-only and phosphorus-containing compounds (both $<$ 10%), while CHONS-type (31% by number and 28% by intensity) and phosphorus-containing compounds (20% by number and 30% by intensity) were both predominant formula types in diatom-derived NAEPS. Additionally, individual diatom-derived biopolymer fractions had a relatively more homogeneous distributions in elemental grouping (e.g., 15–25% for all molecular formula type in AEPS), compared to coccolithophore, showing a higher concentration in specific molecular formula types for an individual biopolymer fraction (e.g., $>$80% as CHOS in intracellular Fe-Mn-associated metabolites, **Figure 3**).

Such significant differences in the molecular composition of these biopolymers of the two phytoplankton species can explain our previously observed different partitioning of $^{210}$Pb or $^{210}$Po in biopolymers derived from diatom and coccolithophore (**Supplementary Figures 3, 4**, also reported in Chuang et al., 2015b; Lin et al., 2017). In coccolithophore cultures, $^{210}$Pb was mostly concentrated in the coccosphere shell (∼65%), with a minor abundance in shell-associated biopolymers and moderate abundance in NAEPS (∼30%). None of $^{210}$Pb can pass through the coccosphere shell to the intracellular fraction (**Supplementary Figure 3**). In contrast, $^{210}$Pb can be detected in all diatom-derived biopolymers. It showed relatively even amounts of $^{210}$Pb in three main diatom-derived biopolymer fractions (i.e., exopolymeric substances (NAEPS+AEPS) vs. frustule-associated biopolymer vs. intracellular biopolymer, **Supplementary Figure 4**), ranging from 20 to 35% (**Supplementary Figure 4**). Together, $^{210}$Pb distribution patterns seemed to coincide with the distribution pattern of elemental groupings as mentioned above for coccolithophores and diatoms. Specifically, for the coccolithophore, higher enrichment in CHO-type compounds in NAEPS and coccosphere shell-associated biopolymers coincided with their higher enrichment in $^{210}$Pb (**Supplementary Figure 3**), suggesting that CHO-only-type compounds are the main moieties binding $^{210}$Pb in the coccolithophore. However, substituting of $^{210}$Pb for $Ca^{2+}$ during coccolith formation seemed to prevent the uptake of $^{210}$Pb by intracellular biopolymers that were also enriched in CHO-type moieties, as reflected in a CHO-only compound-dominant in the intracellular biopolymer (**Figure 3**), yet ∼0% of the amended $^{210}$Pb was found (**Supplementary Figure 3**; Lin et al., 2017). In contrast, the diatom frustule (i.e., biogenic silica) does not have such a "shielding" effect for the intracellular uptake of $^{210}$Pb. Therefore, considerable and relatively even activity of $^{210}$Pb can be detected among exopolymeric substances, frustule-associated biopolymer and intracellular biopolymer (**Supplementary Figure 4**). The apparent "non-specific" binding of $^{210}$Pb in diatom-associated biopolymer fractions as well as the diatom frustule suggests that the responsible $^{210}$Pb binding moieties have a more homogeneous distribution in diatom species.

Different from $^{210}$Pb, $^{210}$Po can be detected in various coccolithophore-derived biopolymers, especially in the AEPS and intracellular Fe-Mn-associated metabolites (**Supplementary Figure 3**). Together with the distribution of molecular formula types (**Figure 3**), we can easily find that the $^{210}$Po-enriched APES and Fe-Mn-associated metabolites both have higher abundance of nitrogen/sulfur-containing organic compounds (e.g., $>$40% as CHONS for AEPS and $>$80% as CHOS for Fe-Mn-associated metabolites), in agreement with the binding properties of Po, i.e., being preferentially related to the production and distribution of nitrogen-rich organic matter as well as sulfur-containing amino acids (Stewart et al., 2007b). Although the Po partitioning among different diatom-derived biopolymers was not investigated in the present study, we may expect stronger association of Po with diatom-derived biopolymers considering the more heterogeneous organic compounds produced by the diatom (i.e., N and S-containing compounds).

Overall, distinct molecular compositions between diatom- and coccolithophore-derived biopolymers not only result in considerable differences in radionuclide partitioning [e.g., $^{210}$Pb, Lin et al. (2017) vs. Chuang et al. (2015b)] between diatoms and coccolithophores, but also contribute to the possible fractionation between radionuclides in diatom- vs. coccolithophore-dominated marine environments (see sections below).

## Radionuclide-Carrying Moieties in Coccolithophore-Derived Biopolymers

Since the isoelectric points are unique for the different radionuclides as shown in **Figure 1**, it suggests that specific organic carrier moieties are responsible for the binding of individual radionuclides in the coccolithophore. Thus, the molecular compositions of the Pb/Po-enriched macromolecules were further explored through IEF separation of different coccolithophore-derived biopolymers and characterization by ESI-FTICRMS.

Among five biopolymers, only two fractions of biopolymers, including NAEPS and coccosphere shell-associated biopolymers, have the capability to strongly bind the $^{210}$Pb (**Supplementary Figure 3**; Lin et al., 2017). Nevertheless, IEF sections of

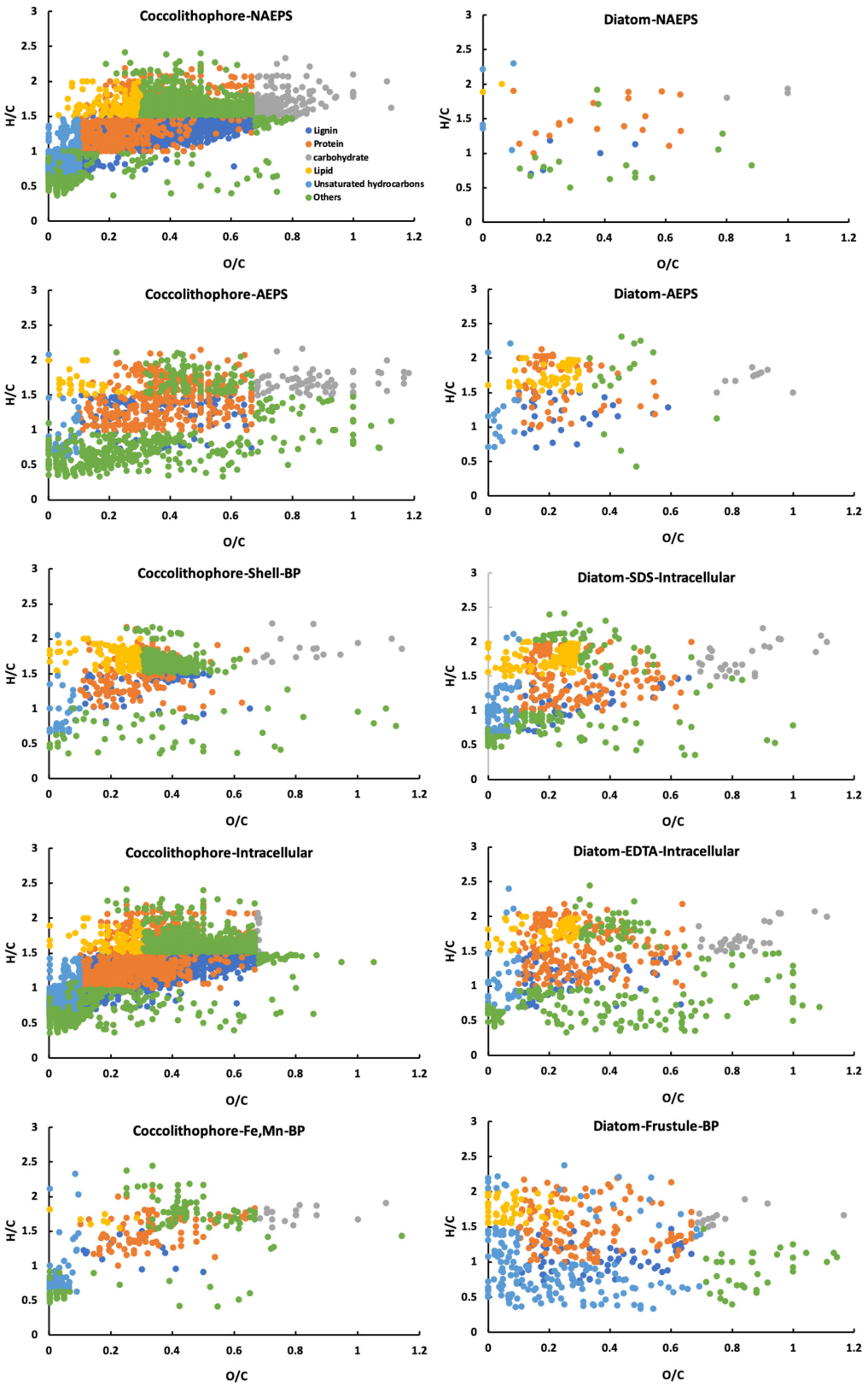


**FIGURE 2 |** van Krevelen diagram showing all formulas and molecular classes for various biopolymers (BP) excreted by *Emiliania huxleyi* coccolithophore and *Phaeodactylum tricornutum* diatom in seawater.

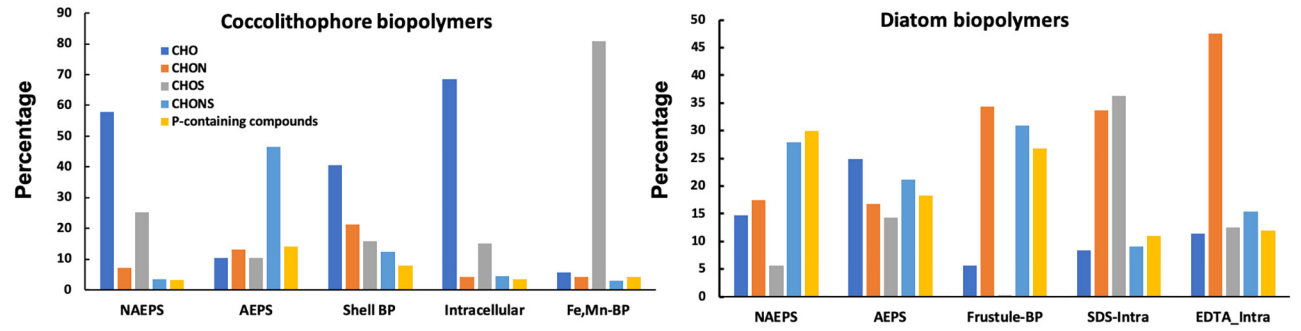


**FIGURE 3 |** Distribution of different molecular formula types, by peak intersity, for the bulk organic matter pool in various biopolymers (BP) harvested from *Phaeodactylum tricornutum* diatom and *Emiliania huxleyi* coccolithophore in seawater.

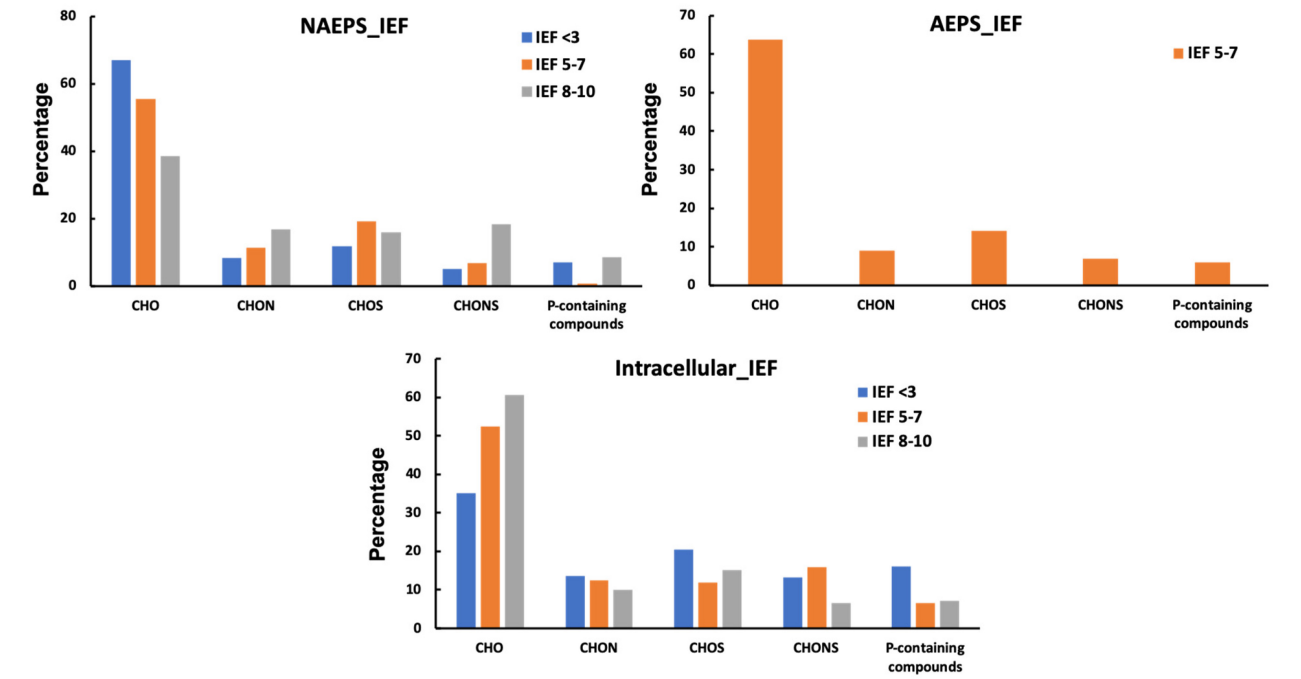


**FIGURE 4 |** Distribution of different molecular formula types, by peak intersity, for the IEF extract $^{210}$Pb (IEF < 3 section)/$^{210}$Po (IEF 5-7 section)-enriched organic matter in various biopolymers harvested from *Emiliania huxleyi* coccolithophore in seawater.

coccosphere shell-associated biopolymers are not presented here due to limitations in sample availability for FTICR-MS analysis and relatively minor partitioning of $^{210}$Pb in this biopolymer fraction (<5%). For NAEPS, the CHO-only functional group consistently decreased from 67 to 39% along the IEF pH gradient from anode (NAEPS IEF < 3) to the cathode (NAEPS IEF 8–10), whereas nitrogen- or sulfur-containing organic compounds (i.e., CHON+CHONS or CHOS+CHONS) increased from low to high pH sections (**Figure 4**). Furthermore, it is notable that phosphorus enrichment can be seen along with the $^{210}$Pb augmentation of NAEPS-"IEF extracts" (i.e., IEF < 3, **Figure 4**) based on our elemental ratio results, showing a 2–3 fold increase in phosphorus to carbon ratio for $^{210}$Pb-enriched IEF < 3 sub-fraction of NAEPS compared with that in the bulk NAEPS (**Supplementary Table 1** phosphorus% and phosphorus:carbon ratio in the bulk NAEPS as 0.21% and $1.50*10^{-3}$ vs. those as $0 \times 54\%$ and $3.97 \times 10^{-3}$ in the IEF < 3 sub-fraction, respectively). Together, these phosphorus-containing molecules but not the other molecules that contain heterogeneous elements (e.g., CHONS, CHON, and CHOS) stand out as the main binding moieties for $^{210}$Pb in the coccolithophore-dominated systems. Considering the majority of $^{210}$Pb complexed by negatively charged organic macromolecules (**Figure 1**), our IEF observational results may allow us to consider that these phosphorus-containing molecules can be composed of abundant phosphate functional groups (e.g., Karl, 2014; Albi and Serrano, 2016), consequently serving as the main $^{210}$Pb-binding ligands in the coccolithophore-dominated marine environments.

For the $^{210}$Po, its major peak along the IEF sections was identified at pH 6 (i.e., pH between 5 and 7, **Figures 1, 4**) for the coccolithophore-derived biopolymers. All the biopolymer fractions, excluding coccosphere shell-associated biopolymer, have the capability to bind $^{210}$Po in seawater (**Supplementary Figure 3**). The IEF 5-7 section were then further processed for the molecular compositional analysis, except for Fe-Mn-associated metabolites due to the limitation of sample availability. Notably, N enrichment can be seen with the Po enriched fraction of both "IEF extract" for NAEPS (11–18%) and intracellular biopolymers (9–28%), while the sulfur enrichment can be only found in the "IEF extract" of intracellular biopolymers (20–27%) of the coccolithophore. However, neither N nor sulfur enrichment was seen for the "IEF extract" of the AEPS. Instead, the abundance of nitrogen/sulfur-containing groups evidently decreased in AEPS-"IEF extract" (60–16% for N and 57–28% for sulfur). This is likely due to the fact that the only portion of nitrogen/sulfur-rich organic compounds in the bulk AEPS contain specific ligands that can strongly bind Po from the seawater, e.g., neutrally charged amphiphilic protein-containing compounds. Other nitrogen/sulfur-rich organic compounds in the bulk AEPS were concentrated in other IEF sections, e.g., the negatively charged acid polysaccharide containing the sulfate functional groups. This can be further confirmed by the difference in the molecular class information between the "IEF extract" and the bulk biopolymers (**Table 1**). For example, strong enrichment in protein-containing compounds can be seen along with the $^{210}$Po augmentation of intracellular biopolymer-"IEF extracts," coincidence with the intensified relative hydrophobicity of Po-carrying macromolecules based on the ratio of protein to carbohydrate (Xu et al., 2011b). Although the protein abundance in "IEF extract" of both extracellular biopolymers (i.e., NAEPS and AEPS) decreased compared with the bulk extracellular biopolymers, the nature of their Po-carrying moieties became relatively more hydrophobic along the pH gradient in the IEF gel (e.g., four times increase in protein/carbohydrate ratio for NAEPS IEF anode as 3.56 to IEF pH 5-7 as 11.35, **Table 1**). Therefore, these results provide direct evidence supporting the hydrophobic nitrogen/sulfur-enriched organic moieties, either within colloidal extracellular pool or within particulate intracellular pool, serving as the strongest binding agents for Po scavenging in the coccolithophore-dominated marine environments. Higher protein/carbohydrate ratios of EPS are indicators of their "stickiness" or propensity for aggregate formation (Santschi et al., 2020). Furthermore, this further confirmed the distinct organic-binding nature of the $^{210}$Po carrier compounds, as compared with to its parent nuclide, $^{210}$Pb, which could strongly affect their scavenging and their tracing application in the ocean.

## Implications for the Application of $^{210}$Pb and $^{210}$Po

Based on the $^{210}$Po deficiency with respect to $^{210}$Pb, they have been widely used as radionuclide tracer pair to quantify the particulate organic carbon (POC) export from the upper water column to deeper ocean. Nevertheless, as mentioned above, $^{210}$Pb in coccolithophore dominated algae culture would be not only preferentially scavenged by coccoliths (**Supplementary Figure 3**), but also have distinct affinity

**TABLE 1 |** Molecular class information and its individual distribution percentage for the bulk biopolymers (BP) and corresponding "IEF extract" Pb-enriched- (IEF < 3) or Po-enriched- (IEF 5-7) organic matter in the coccolithophore culture, as well as for the bulk biopolymers in the diatom culture, as revealed by ESI-FTICRMS.

| | Lignin | Protein | Carbohydrate | Lipids | Unsaturated hydrocarbon | Others | Carboxyl-rich alicyclic molecules (CRAM) | Protein-C/Carbohydrate-C ratio* |
|---|---|---|---|---|---|---|---|---|
| **Coccolithophore (*Emiliania huxleyi*)** | | | | | | | | |
| NAEPS | 20.79 | 10.46 | 4.92 | 1.80 | 24.15 | 37.87 | 10.50 | 2.82 |
| AEPS | 5.38 | 22.61 | 4.97 | 0.65 | 1.99 | 64.38 | 15.49 | 6.02 |
| Shell-BP | 8.91 | 27.95 | 2.37 | 14.70 | 6.74 | 39.33 | 16.79 | 15.61 |
| Intracellular | 18.95 | 9.02 | 7.98 | 1.34 | 34.85 | 27.86 | 10.00 | 1.50 |
| Fe, Mn-BP | 0.99 | 9.70 | 1.03 | 11.20 | 4.73 | 72.35 | 4.63 | 12.43 |
| **Coccolithophore (*Emiliania huxleyi*)-IEF** | | | | | | | | |
| NAEPS-IEF < 3 | 49.76 | 9.33 | 3.47 | 11.21 | 3.67 | 22.57 | 10.29 | 3.56 |
| NAEPS-IEF 5-7 | 52.71 | 10.49 | 1.22 | 3.69 | 2.73 | 29.16 | 16.25 | 11.35 |
| AEPS-IEF 5-7 | 58.58 | 9.48 | 1.67 | 8.13 | 2.60 | 19.55 | 9.74 | 7.54 |
| Intracellular-IEF 5-7 | 52.94 | 19.64 | 1.35 | 6.11 | 2.88 | 17.08 | 14.62 | 19.23 |
| **Diatom (*Phaeodactylum tricornutum*)** | | | | | | | | |
| NAEPS | 10.52 | 45.59 | 5.40 | 2.11 | 5.31 | 31.08 | 26.63 | 11.19 |
| AEPS | 11.97 | 25.86 | 13.73 | 33.16 | 5.67 | 9.60 | 8.99 | 2.50 |
| SDS-intracellular | 4.62 | 36.10 | 2.29 | 10.50 | 7.52 | 38.97 | 30.79 | 20.88 |
| EDTA-intracellular | 10.23 | 58.36 | 3.65 | 5.49 | 1.90 | 20.36 | 51.40 | 21.16 |
| Frustule-BP | 10.42 | 48.93 | 9.02 | 8.61 | 19.59 | 3.42 | 13.58 | 7.18 |

**Protein to carbohydrate ratio, using the value in "Protein" column multiplied by 0.53 (the average carbon content in protein) divided by the product of the value in "Carbohydrate" column and 0.4 (the average carbon content in carbohydrate).*

and selectivity to the organic functional groups, compared with $^{210}$Po. Thus, the deficiency of $^{210}$Po with respect to $^{210}$Pb may limit the quantification of the POC export fluxes under certain situations (Friedrich and Rutgers van der Loeff, 2002; Stewart et al., 2005; Lin et al., 2017), specifically when more hydrophobic nitrogen/sulfur-enriched organic moieties are enriched (preferentially scavenge $^{210}$Po) or where biogenic carbonate particles (i.e., incorporation of $^{210}$Pb into coccosphere shell) are abundant. Instead, when biogenic carbonate is not abundant (e.g., diatom-dominated environments), the deficiency of $^{210}$Po with respect to $^{210}$Pb may actually reflect the relative abundance of nitrogen/sulfur-enriched organic moieties (e.g., protein for $^{210}$Po) to the nitrogen/sulfur-depleted organic compounds (e.g., polysaccharides for $^{210}$Pb) in the water column. Thus, the investigation on the particle composition, including inorganic (e.g., abundance of biogenic carbonate) and organic compound characterization, may help us distinguish if the $^{210}$Pb/$^{210}$Po disequilibrium can be applied or not for the POC export estimation. Specific correction of the $^{210}$Pb/$^{210}$Po disequilibrium based on the variation in the particle composition in the water column (e.g., vertical profile of particulate protein to polysaccharide ratio) may increase the accuracy of this radionuclide pair for the POC export estimation.

Similarly, this may also explain the different estimated POC export fluxes in the same oceanic regions between several radionuclide-pair tracing approaches, such as $^{234}$Th/$^{238}$U vs. $^{210}$Po/$^{210}$Pb (Verdeny et al., 2009; Stewart et al., 2011; Le Moigne et al., 2013). Different selectivity to the organic matter between $^{234}$Th (e.g., selectivity to negatively charged functional groups, like acid polysaccharide; Guo et al., 2002; Quigley et al., 2002; Lin et al., 2015) and $^{210}$Po may be biasing the corresponding POC export flux estimates. For example, a higher $^{234}$Th-derived POC flux than $^{210}$Po-derived POC flux may potentially resulting from the higher abundance of acid polysaccharide-like compounds relative to more amphiphilic nitrogen/sulfur-rich organic compounds (e.g., proteins) in the bulk organic matter pool. Therefore, a combination of the organic compound characterization with the application of radionuclides may help us better understand biases in the estimates of the export fluxes of the particulate organic matter in the ocean by providing a firmer confirmation of earlier suggestions of the preference of $^{210}$Po for binding to compounds in the cytoplasm (Friedrich and Rutgers van der Loeff, 2002). In particular, it provides a better foundation to the earlier suggestion by Friedrich and Rutgers van der Loeff (2002) of strong $^{210}$Po binding to diatoms. Our study also provides primary evidence that distinct organic matter compounds are responsible when the $^{210}$Po/$^{210}$Pb approach in field-based POC flux estimations significantly differ from estimates by other approaches, e.g., using $^{234}$Th/$^{238}$U disequilibria (Shimmield et al., 1995; Friedrich and Rutgers van der Loeff, 2002; Stewart et al., 2007a, 2011; Verdeny et al., 2009; Wei et al., 2011; Anand et al., 2018). Field studies at best provide correlations, but intrinsically suffer from hiding unequivocal causal relationships. Thus, when different approaches to POC flux estimations were carried out, significant differences in the results usually could not distinguish between different causes, e.g., time scales (half-lives of tracers, 24 days for $^{234}$Th and 138 days for $^{210}$Po), physical factors (Moran et al., 2003), and differences in organic matter ligand moieties.

## DATA AVAILABILITY STATEMENT

The original contributions presented in the study are included in the article/**Supplementary Material**, further inquiries can be directed to the corresponding author/s.

## AUTHOR CONTRIBUTIONS

PL, CX, and PS conceived and designed the experiment and wrote the manuscript. PL and WX performed the incubation and partitioning experiment. PL performed the organic matter extraction. PL, CX, and WX performed the data processing. All authors contributed to the article and approved the submitted version.

## FUNDING

This study benefited from the previous support by NSF-OCE 1356453.

## ACKNOWLEDGMENTS

We appreciate the FTICR-MS sample analysis and service, provided by Deepti Varma and Hongmei Chen at the College of Sciences Major Instrumentation Cluster, Old Dominion University, Virginia.

## SUPPLEMENTARY MATERIAL

The Supplementary Material for this article can be found online at: https://www.frontiersin.org/articles/10.3389/fmars.2021.703503/full#supplementary-material

## REFERENCES

Albi, T., and Serrano, A. (2016). Inorganic polyphosphate in the microbial world. Emerging roles for a multifaceted biopolymer. *World J. Microbiol. Biotechnol.* 32:27.

Alvarado Quiroz, N. G., Hung, C.-C., and Santshi, P. H. (2006). Binding of thorium(IV) to carboxylate, phosphate and sulfate functional groups from marine exopolymeric substances (EPS). *Mar. Chem.* 100, 337–353. doi: 10.1016/j.marchem.2005.10.023

Anand, S. S., Rengarajan, R., Shenoy, D., Gauns, M., and Naqvi, S. W. A. (2018). POC export fluxes in the Arabian Sea and the Bay of Bengal: a simultaneous $^{234}$Th/$^{238}$U and $^{210}$Po/$^{210}$Pb study. *Mar. Chem.* 198, 70–87.

Anderson, R. F., Bacon, M. P., and Brewer, P. G. (1983). Removal of $^{230}$Th and $^{231}$Pa at ocean margins. *Earth Planet. Sci. Lett.* 66, 73–90.

Armbrust, E. V. (2009). The life of diatoms in the world's oceans. *Nature* 459, 185–192. doi: 10.1038/nature08057

Chase, Z., Anderson, R. F., Fleisher, M. Q., and Kubik, P. W. (2002). The influence of particle composition and particle flux on scavenging of Th, Pa and Be in the ocean. *Earth Planet. Sci. Lett.* 204, 215–229. doi: 10.1016/s0012-821x(02)00984-6

Chin, W. C., Orellana, M. V., and Verdugo, P. (1998). Spontaneous assembly of marine dissolved organic matter into polymer gels. *Nature* 391, 567–571.

Chuang, C.-Y., Santschi, P. H., Jiang, Y., Ho, Y.-F., Quigg, A., Guo, L., et al. (2014). Important role of biomolecules from diatoms in the scavenging of particle-reactive radionuclides of thorium, protactinium, lead, polonium and beryllium in the ocean: a case study with *Phaeodactylum tricornutum*. *Limnol. Oceanogr.* 59, 1256–1266. doi: 10.4319/lo.2014.59.4.1256

Chuang, C.-Y., Santschi, P. H., Wen, L.-S., Guo, L., Xu, C., Zhang, S., et al. (2015a). Binding of Th, Pa, Pb, Po and Be radionuclides to marine colloidal macromolecular organic matter. *Mar. Chem.* 173, 320–329. doi: 10.1016/j.marchem.2014.10.014

Chuang, C.-Y., Santschi, P. H., Xu, C., Jiang, Y., Ho, Y.-F., Quigg, A., et al. (2015b). Molecular level characterization of diatom-associated biopolymers that bind $^{234}$Th, $^{233}$Pa, $^{210}$Pb, and $^{7}$Be in seawater: a case study with *Phaeodactylum tricornutum*. *J. Geophys. Res. Biogeosci.* 120, 1858–1869. doi: 10.1002/2015jg002970

Friedrich, J., and Rutgers van der Loeff, M. M. (2002). A two-tracer ($^{210}$Po-$^{234}$Th) approach to distinguish organic carbon and biogenic silica export flux in the Antarctic circumpolar current. *Deep Sea Res. I* 49, 101–120. doi: 10.1016/s0967-0637(01)00045-0

Guo, L., Chen, M., and Gueguen, C. (2002). Control of Pa/Th ratio by particulate chemical composition in the ocean. *Geophys. Res. Lett.* 29:1961.

Hayes, C. T., Anderson, R. F., Fleisher, M. Q., Huang, K.-F., Robinson, L. F., Lu, Y., et al. (2015a). $^{230}$Th and $^{231}$Pa on GEOTRACES GA03, the U.S. GEOTRACES North Atlantic transect, and implications for modern and paleoceanographic chemical fluxes. *Deep Sea Res. I Top. Stud. Oceanogr.* 116, 29–41. doi: 10.1016/j.dsr2.2014.07.007

Hayes, C. T., Anderson, R. F., Fleisher, M. Q., Vivancos, S. M., Lam, P. J., Ohnemus, D. C., et al. (2015b). Intensity of Th and Pa scavenging partitioned by particle chemistry in the North Atlantic Ocean. *Mar. Chem.* 170, 49–60. doi: 10.1016/j.marchem.2015.01.006

Karl, D. M. (2014). Microbially mediated transformations of phosphorus in the sea: new views of an old cycle. *Annu. Rev. Mar. Sci.* 6, 279–337. doi: 10.1146/annurev-marine-010213-135046

Kumar, N., Anderson, R. F., Mortlock, R. A., Froelich, P. N., Kubik, P., Dittrich-Hannen, B., et al. (1995). Increased biological productivity and export production in the glacial Southern Ocean. *Nature* 378, 675–680. doi: 10.1038/378675a0

Lam, P. J., Ohnemus, D. C., and Auro, M. E. (2015). Size-fractionated major particle composition and concentrations from the US GEOTRACES North Atlantic Zonal Transect. *Deep Sea Res. II Top. Stud. Oceanogr.* 116, 303–320. doi: 10.1016/j.dsr2.2014.11.020

Le Moigne, F. A. C., Villa-Alfageme, M., Sanders, R. J., Marsay, C., Henson, S., and Garcia-Tenorio, R. (2013). Export of organic carbon and biominerals derived from $^{234}$Th and $^{210}$Po at the Porcupine Abyssal Plain. *Deep Sea Res. I Oceanogr. Res. Papers* 72, 88–101. doi: 10.1016/j.dsr.2012.10.010

Lin, P., Chen, M., and Guo, L. (2015). Effect of natural organic matter on the adsorption and fractionation of thorium and protactinium on nanoparticles in seawater. *Mar. Chem.* 173, 291–301. doi: 10.1016/j.marchem.2014.08.006

Lin, P., Guo, L., and Chen, M. (2014). Adsorption and fractionation of thorium and protactinium on nanoparticles in seawater. *Mar. Chem.* 162, 50–59. doi: 10.1016/j.marchem.2014.03.004

Lin, P., Xu, C., Xing, W., Sun, L., Schwehr, K. A., Quigg, A., et al. (2020). Partitioning of iron and plutonium to exopolymeric substances and intracellular biopolymers: a comparison study between the coccolithophore *Emiliania huxleyi* and the diatom *Skeletonema costatum*. *Mar. Chem.* 218:103735. doi: 10.1016/j.marchem.2019.103735

Lin, P., Xu, C., Zhang, S., Sun, L., Schwehr, K. A., Bretherton, L., et al. (2017). Importanceof coccolithophore-associated organic biopolymers for fractionating particle-reactive radionuclides ($^{234}$Th, $^{233}$Pa, $^{210}$Pb, $^{210}$Po, and $^{7}$Be) in the ocean. *J. Geophys. Res. Biogeosci.* 122, 2033–2045. doi: 10.1002/2017jg003779

Moran, S. B., Weinstein, S. E., Edmonds, H. N., Smith, J. N., Kelly, R. P., Pilson, M. E. Q., et al. (2003). Does $^{234}$Th/$^{238}$U and disequilibrium provide an accurate record of the export flux of and particulate organic carbon from the upper ocean. *Limnol. Oceanogr.* 48, 1018–1029. doi: 10.4319/lo.2003.48.3.1018

Murray, J. W., Paul, B., Dunne, J. P., and Chapin, T. (2005). $^{234}$Th, $^{210}$Pb, $^{210}$Po and stable Pb in the central equatorial Pacific: tracers for particle cycling. *Deep Sea Res. I Oceanogr. Res. Papers* 52, 2109–2139. doi: 10.1016/j.dsr.2005.06.016

Nelson, D. M., Treguer, P., Brzezinski, M. A., Leynaert, A., and Queguiner, B. (1995). Production and dissolution of biogenic silica in the ocean-revised global estimates, comparison with regional data and relationship to biogenic sedimentation. *Glob. Biogeochem. Cycles* 9, 359–372. doi: 10.1029/95gb01070

Quigg, A., Passow, U., Chin, W.-C., Bretherton, L., Kamalanathan, M., Xu, C., et al. (2016). The role of microbial exopolymers in determining the fate of oil and chemical dispersants in the ocean. *Limnol. Oceanogr. Lett.* 1, 3–26. doi: 10.1002/lol2.10030

Quigley, M. S., Santschi, P. H., Hung, C.-C., Guo, L., and Honeyman, B. D. (2002). Importance of acid polysaccharides for $^{234}$Th complexation to marine organic matter. *Limnol. Oceanogr.* 47, 367–377. doi: 10.4319/lo.2002.47.2.0367

Roberts, K. A., Xu, C., Hung, C.-C., Conte, M. H., and Santschi, P. H. (2009). Scavenging and fractionation of thorium vs. protactinium in the ocean, as determined from particle-water partitioning experiments with sediment trap material from the Gulf of Mexico and Sargasso Sea. *Earth Planet. Sci. Lett.* 286, 131–138. doi: 10.1016/j.epsl.2009.06.029

Roy-Barman, M., Lemaître, C., Ayrault, S., Jeandel, C., Souhaut, M., and Miquel, J.-C. (2009). The influence of particle composition on Thorium scavenging in the Mediterranean Sea. *Earth Planet. Sci. Lett.* 286, 526–534. doi: 10.1016/j.epsl.2009.07.018

Santschi, P. H., Adler, D., Amdurer, V. M., Li, Y.-H., and Bell, J. J. (1980). Thorium isotopes as analogs for particle-reactive pollutants in coastal marine environments. *Earth Planet. Sci. Lett.* 47, 327–335. doi: 10.1016/0012-821x(80)90019-9

Santschi, P. H., Balnois, E., Wilkinson, K. J., Zhang, J., and Buffle, J. (1998). Fibrillar polysaccharides in marine macromolecular organic matter as imaged by atomic force microscopy and transmission electron microscopy. *Limnol. Oceanogr.* 43, 896–908. doi: 10.4319/lo.1998.43.5.0896

Santschi, P. H., Xu, C., Schwehr, K. A., Lin, P., Sun, L., Chin, W.-C., et al. (2020). Can the protein/carbohydrate (P/C) ratio of exopolymeric substances (EPS) be used as a proxy for their 'stickiness' and aggregation propensity? *Mar. Chem.* 218:103734. doi: 10.1016/j.marchem.2019.103734

Shimmield, G. M., Ritchie, G. D., and Fileman, T. W. (1995). The impact of marginal ice zone processes on the distribution of 210Pb, 210Po and 234Th and implications for new production in the Bellingshausen Sea, Antarctica. *Deep Sea Res. II* 42, 1313–1335. doi: 10.1016/0967-0645(95)00071-w

Stewart, G. M., Cochran, J. K., Miquel, J. C., Masque, P., Szlosek, J., Rodriguez y Baena, A. M., et al. (2007a). Comparing POC export from $^{234}$Th/$^{238}$U and $^{210}$Po/$^{210}$Pb disequilibria with estimates from sediment traps in the northwest Mediterranean. *Deep-Sea Res. I* 54, 1549–1570. doi: 10.1016/j.dsr.2007.06.005

Stewart, G. M., Cochran, J. K., Xue, J., Lee, C., Wakeham, S. G., Armstrong, R. A., et al. (2007b). Exploring the connection between $^{210}$Po and organic matter in the northwestern Mediterranean. *Deep Sea Res. I Oceangr. Res. Papers* 54, 415–427. doi: 10.1016/j.dsr.2006.12.006

Stewart, G. M., Fowler, S. W., Teyssle, J. L., Cotret, O., Cochran, J. K., and Fisher, N. S. (2005). Contrasting transfer of polonium-210 and lead-210 across three trophic levels in marine plankton. *Mar. Ecol. Prog. Series* 290, 27–33. doi: 10.3354/meps290027

Stewart, G. M., Moran, S. B., and Lomas, M. W. (2010). Seasonal POC fluxes at BATS estimated from $^{210}$Po deficits. *Deep Sea Res. I* 57, 113–124. doi: 10.1016/j.dsr.2009.09.007

Stewart, G. M., Moran, S. B., Lomas, M. W., and Kelly, R. P. (2011). Direct comparison of $^{210}$Po, $^{234}$Th and POC particle-size distributions and export fluxes at the Bermuda Atlantic Time-series Study (BATS) site. *J. Environ. Radioact.* 102, 479–489. doi: 10.1016/j.jenvrad.2010.09.011

Stubbins, A., Spencer, R. G. M., Chen, H., Hatcher, P. G., Mopper, K., Hernes, P. J., et al. (2010). Illuminated darkness: molecular signatures of Congo River dissolved organic matter and its photochemical alteration as revealed by ultrahigh precision mass spectrometry. *Limnol. Oceanogr.* 55, 1467–1477. doi: 10.4319/lo.2010.55.4.1467

Verdeny, E., Masque, P., Garcia-Orellana, J., Hanfland, C., Cochran, J. K., and Stewart, G. M. (2009). POC export from ocean surface waters by means of $^{234}$Th/$^{238}$U and $^{210}$Po/$^{210}$Pb disequilibria: a review of the use of two radiotracer pairs. *Deep Sea Res. II Top. Stud. Oceangr.* 56, 1502–1518. doi: 10.1016/j.dsr2.2008.12.018

Wei, C.-L., Lin, S.-Y., Sheu, D. D.-D., Chou, W.-C., Yi, M.-C., Santschi, P. H., et al. (2011). Particle-reactive radionuclides ($^{234}$Th, $^{210}$Pb, $^{210}$Po) as tracers for the estimation of export production in the South China Sea. *Biogeosciences* 8, 3793–3808. doi: 10.5194/bg-8-3793-2011

Xu, C., Lin, P., Sun, L., Chen, H., Hatcher, P. G., Conte, M. H., et al. (2020). Molecular nature of marine particulate organic iron-carrying moieties revealed by Fourier-Transform Ion Cyclotron Resonance Mass Spectrometry (ESI-FTICRMS). *Front. Earth Sci.* 8:266. doi: 10.3389/feart.2020.00266

Xu, C., Santschi, P. H., Hung, C.-C., Zhang, S., Schwehr, K. A., Roberts, K. A., et al. (2011a). Controls of $^{234}$Th removal from the oligotrophic ocean by polyuronic acids and modification by microbial activity. *Mar. Chem.* 123, 111–126. doi: 10.1016/j.marchem.2010.10.005

Xu, C., Zhang, S., Chuang, C.-Y., Miller, E. J., Schwehr, K. A., and Santschi, P. H. (2011b). Chemical composition and relative hydrophobicity of microbial exopolymeric substances (EPS) isolated by anion exchange chromatography and their actinide-binding affinities. *Mar. Chem.* 126, 27–36. doi: 10.1016/j.marchem.2011.03.004

Xu, C., Zhang, S. J., Kaplan, D. I., Ho, Y. F., Schwehr, K. A., Roberts, K. A., et al. (2015). Evidence for hydroxamate siderophores and other n-containing organic compounds controlling (Pu)-239,240 immobilization and remobilization in a wetland sediment. *Environ. Sci. Technol.* 49, 11458–11467. doi: 10.1021/acs.est.5b02310

Yang, W., Huang, Y., Chen, M., Qiu, Y., Li, H., and Zhang, L. (2011). Carbon and nitrogen cycling in the Zhubi coral reef lagoon of the South China Sea as revealed by $^{210}$Po and$^{210}$Pb. *Mar. Pollut. Bull.* 62, 905–911. doi: 10.1016/j.marpolbul.2011.02.058

**Conflict of Interest:** The authors declare that the research was conducted in the absence of any commercial or financial relationships that could be construed as a potential conflict of interest.

*Copyright © 2021 Lin, Xu, Xing and Santschi. This is an open-access article distributed under the terms of the Creative Commons Attribution License (CC BY). The use, distribution or reproduction in other forums is permitted, provided the original author(s) and the copyright owner(s) are credited and that the original publication in this journal is cited, in accordance with accepted academic practice. No use, distribution or reproduction is permitted which does not comply with these terms.*

frontiers in Marine Science

ORIGINAL RESEARCH
published: 02 July 2021
doi: 10.3389/fmars.2021.701441

# Contrasting Behaviors of $^{210}$Pb and $^{210}$Po in the Productive Shelf Water Versus the Oligotrophic Water

*Hojong Seo, DongJoo Joung† and Guebuem Kim**

*Research Institute of Oceanography, School of Earth and Environmental Sciences, Seoul National University, Seoul, South Korea*

We measured the total, truly dissolved (<10 kDa), colloidal (10 kDa–0.2 μm), and particulate phases (>0.2 μm) of $^{210}$Pb and $^{210}$Po in the East China Sea (ECS) shelf water and the East Sea (Japan Sea). In order to examine the behaviors of $^{210}$Pb and $^{210}$Po in different marine environments, we compiled our results with previously reported data in the same region and in the northwestern Pacific Ocean (NWPO). The proportions of the truly dissolved, colloidal, and particulate phases in the shelf water were 32, 27, and 41% for $^{210}$Pb and 49, 32, and 19% for $^{210}$Po, respectively. Based on a steady-state scavenging model, $^{210}$Pb and $^{210}$Po showed higher (3.0 ± 0.6 year$^{-1}$) and lower (0.3 ± 0.2 year$^{-1}$) scavenging rates, respectively, in the shelf water than those in the NWPO and the East Sea. A non-steady-state model, accounting for the residence time of the shelf water, also showed twice more efficient removal rate of $^{210}$Pb in the shelf water than that in the NWPO and the East Sea. In contrast, there was the net input of $^{210}$Po in the shelf water relative to the large removal in the NWPO and the East Sea. The large proportions of total dissolved (truly dissolved + colloidal) $^{210}$Po (>80%) in the shelf water indicate active regeneration of $^{210}$Po from the sinking particles and the surface sediments. Our results suggest that the ECS shelf is the source for Po in the northwestern Pacific marginal seas, a proxy for sulfur group elements (S, Se, and Te), whereas it is the efficient sink for Pb, together with other particle-reactive trace elements.

**Keywords: $^{210}$Pb, $^{210}$Po, shelf water, scavenging, colloid**

OPEN ACCESS

***Edited by:***
*Laodong Guo, University of Wisconsin–Milwaukee, United States*

***Reviewed by:***
*Jinlong Wang, East China Normal University, China*
*Leonardo Langone, National Research Council (CNR), Italy*

****Correspondence:***
*Guebuem Kim*
*gkim@snu.ac.kr*

***†Present address:***
*DongJoo Joung, Department of Earth and Environmental Sciences, University of Rochester, Rochester, NY, United States*

***Specialty section:***
*This article was submitted to Marine Biogeochemistry, a section of the journal Frontiers in Marine Science*

***Received:*** *28 April 2021*
***Accepted:*** *31 May 2021*
***Published:*** *02 July 2021*

***Citation:***
*Seo H, Joung D and Kim G (2021) Contrasting Behaviors of $^{210}$Pb and $^{210}$Po in the Productive Shelf Water Versus the Oligotrophic Water. Front. Mar. Sci. 8:701441. doi: 10.3389/fmars.2021.701441*

## INTRODUCTION

Naturally occurring $^{210}$Pb (half-life = 22.3 years) is produced from $^{222}$Rn (half-life = 3.8 days), belonging to the $^{238}$U decay series, and it produces $^{210}$Po (half-life = 138.4 days). In oceanic environments, $^{210}$Pb originates mainly from the atmospheric deposition in the upper ocean and *in situ* production from $^{226}$Ra (half-life = 1,600 years) decay, *via* $^{222}$Rn, in the deep ocean. Since the production of $^{210}$Po from $^{210}$Pb is negligible in the atmosphere, most $^{210}$Po in the ocean is assumed to be produced from $^{210}$Pb decay. Both $^{210}$Pb and $^{210}$Po are known to be particle reactive in aqueous systems, but $^{210}$Po tends to be preferentially assimilated by marine biota (Fisher et al., 1983; Wei and Murray, 1994; Hung and Chung, 1998; Stewart and Fisher, 2003; Carvalho, 2011). This efficient biological removal of $^{210}$Po results in disequilibria between $^{210}$Pb and $^{210}$Po in the upper ocean,

and this principle has been used to determine particulate organic carbon export (Bacon et al., 1976; Friedrich and van der Loeff, 2002; Stewart et al., 2007; Tang and Stewart, 2019).

Although the removal of $^{210}$Po is known to be related to marine productivity, previous studies have reported a large deficiency of $^{210}$Po in oligotrophic oceans (Nozaki et al., 1990a; Kim, 2001; Chung and Wu, 2005). Nozaki et al. (1990a) attributed such a distinct deficiency to the significant atmospheric input of $^{210}$Pb. However, Kim (2001) suggested that an unusually large deficiency in the oligotrophic ocean could be due to the efficient uptake of $^{210}$Po by cyanobacteria and then transfer to higher trophic levels along marine food chains rather than downward settling. On the contrary, in the eutrophic ocean, $^{210}$Po may reside for a much longer time in the non-settling organic pool as it is taken up by free-living bacteria (Kim, 2001). This hypothesis was further supported by Chung and Wu (2005) in the South China Sea.

The East China Sea (ECS) shelf, including the Yellow Sea and the southern sea of Korea, is one of the largest continental shelves in the world. It has a total area of $3.6 \times 10^5$ km$^2$ with a mean depth of 70 m (Fang et al., 2009; Dong et al., 2011). This sea receives great amounts of nutrients from the Changjiang (e.g., $1.1 \times 10^{11}$ mol year$^{-1}$ for dissolved inorganic nitrogen; Dai et al., 2011) and also shows high primary productivity (510–580 mg C m$^{-2}$ day$^{-1}$), which is 2.7 times higher than that in the adjacent Kuroshio water (Hama et al., 1997; Gong et al., 2000). As very oligotrophic Kuroshio water in the northwestern Pacific Ocean (NWPO) flows into the East Sea (Japan Sea) through this ECS shelf, significant biogeochemical alterations occur in the shelf water (Kim et al., 2018; Cho et al., 2019). The East Sea is a semi-enclosed marginal sea that has a total area of $1.0 \times 10^6$ km$^2$ with a maximum depth of over 3,500 m. This interconnected system (the NWPO–the ECS shelf water–the East Sea) may provide an ideal opportunity to study how chemical species behave in different biogeochemical conditions. However, only a few studies have examined the behaviors of $^{210}$Pb and $^{210}$Po according to the change in environmental conditions in this region. Thus, in this study, we aim to (1) investigate the behaviors of $^{210}$Pb and $^{210}$Po in different oceanic settings (productive shelf water versus oligotrophic water) and (2) understand the scavenging mechanisms of both radionuclides in association with colloids.

# MATERIALS AND METHODS

## Sampling

Sampling was conducted over two periods in the southern sea of Korea and the East Sea: from May 8 to 22, 2005, on the R/V *Tamgu* (Stn. C-1, C-2, C-3, and C-4), and from January 26 to February 2, 2018, on the R/V *ISABU* (Stn. S1, S4, E1, E5, and E8; **Figure 1**). Seawater samples for total (∼10–20 L) and size fractionation (∼40 L) were collected directly from Niskin bottles. To collect the size-fractionated samples, seawater was filtered through the 0.2-μm cartridge filter using a peristaltic pump. The pre-filtered (<0.2 μm) samples were separated into the truly dissolved (<10 kDa) and colloidal phases (10 kDa–0.2 μm) using a tangential flow filtration system (PLCGC, Pellicon, Millipore, Burlington, MA, United States), which was pre-cleaned with 1 M HCl, 10 L deionized water, and 0.5 M NaOH (Guéguen et al., 2002; Baskaran et al., 2003; Kim and Kim, 2012, 2014). This filtration procedure was completed within 10 h after collection to avoid adsorption of particles onto the bottles. The filtered samples were acidified with 8 M nitric acid (pH ∼1) and transferred into 40-L plastic buckets.

## $^{210}$Pb and $^{210}$Po Analysis

The analytical methods for $^{210}$Pb and $^{210}$Po were adapted from Kim and Kim (2012). Briefly, the $^{209}$Po spike (1 dpm), $Pb^{2+}$ carrier (20 mg), and $Fe^{3+}$ carrier (50 mg) were added to the seawater samples. After the equilibration, the pH was raised to 8 using $NH_4OH$ to precipitate $Fe(OH)_3$, together with $^{210}$Pb and $^{210}$Po. The precipitates were allowed to settle for 4 h. After the supernatants were siphoned off, the precipitates were filtered using Whatman 41 grade paper. The precipitates and any organic matters in the sample were fully digested with the mixed solution of concentrated $HNO_3$, HCl, and HF and then converted to 0.5 M HCl. The samples were heated to 80°C after adding ascorbic acid (0.5 *g*) to reduce $Fe^{3+}$ to $Fe^{2+}$. Po from the heated samples was simultaneously plated onto a silver disk while rotating the disk for 3 h using a magnetic stirrer. The $^{210}$Po sources were counted using alpha spectrometry with a passivated implanted planar silicon detector (Alpha Analyst, Canberra, Australia). The remaining solution was further purified for $^{210}$Pb analysis. Concentrated $HNO_3$ was added to the solution and heated to oxidize the ascorbic acid. After the solution was converted to 9 M HCl, it was loaded onto the pre-conditioned anion exchange column (AG 1 × 8 resin, Bio-Rad Laboratories, Hercules, CA, United States) to separate Pb. The eluents (Pb) were stored for more than 6 months for the ingrowth of $^{210}$Po. The $^{210}$Pb activity was determined *via* the ingrown $^{210}$Po activity using the same Po plating and alpha counting procedures. The recovery of $^{210}$Pb was obtained by measuring stable Pb in $^{210}$Pb solutions using a magnetic sector field inductively coupled plasma mass spectrometer (ICP-MS; Element 2, Thermo Scientific, Waltham, MA, United States).

# RESULTS

In order to examine the behaviors of $^{210}$Pb and $^{210}$Po in different oceanic settings, our results are compared with previously published data in the northwestern Pacific seas. The data are sorted into three regions: the NWPO (Tsunogai and Nozaki, 1971; Nozaki and Tsunogai, 1976; Nozaki et al., 1990a), the ECS shelf water (Lee et al., 1996; Hong et al., 1999; Su et al., 2017; this study), and the East Sea (Kim and Kim, 2012; this study; **Figure 1**). Data on the truly dissolved and colloidal phases of $^{210}$Pb and $^{210}$Po are only available in this study (ECS shelf water) and in Kim and Kim (2012; East Sea). Although the stations of Lee et al. (1996) and stations E1, S1, and S4 in this study are located in the southwestern part of the East Sea, they are included in the ECS shelf water data because they are located downstream of the ECS shelf water flows (Morimoto and Yanagi, 2001; Chang et al., 2004, 2016). Some data near the Changjiang (Hong et al., 1999;

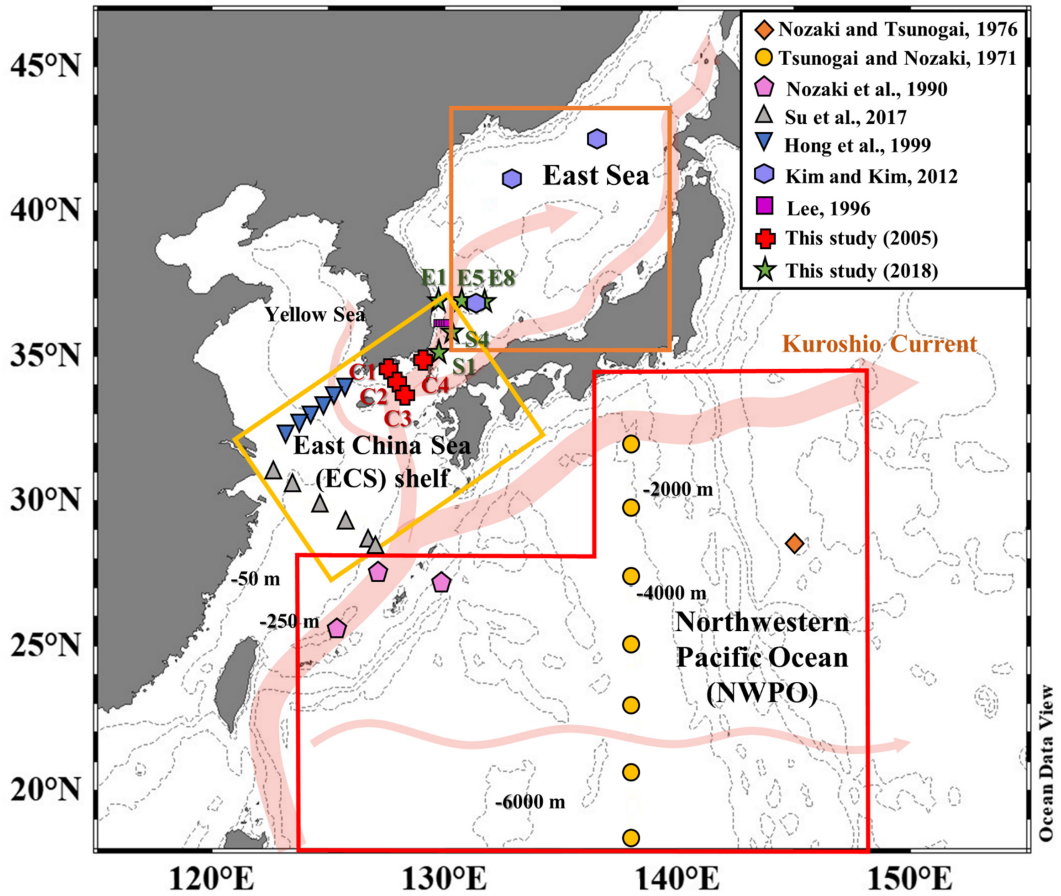


**FIGURE 1 |** Locations of the sampling stations in this study and previous studies in the northwestern Pacific Ocean (NWPO) and its adjacent marginal seas.

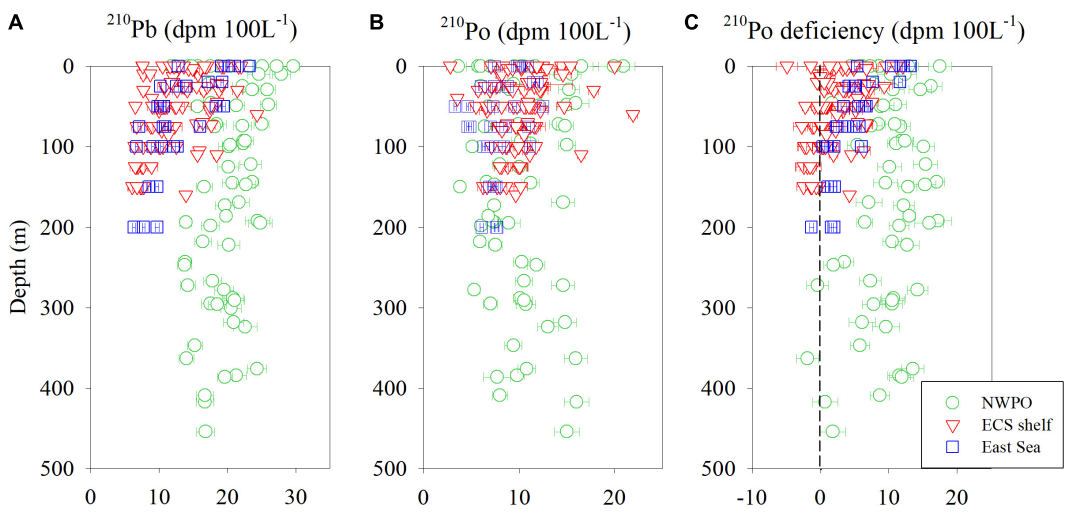


**FIGURE 2 |** Vertical distributions of $^{210}$Pb **(A)**, $^{210}$Po **(B)**, and $^{210}$Po deficiency (**C**; $^{210}$Pb-$^{210}$Po) in the northwestern Pacific Ocean (NWPO; Tsunogai and Nozaki, 1971; Nozaki and Tsunogai, 1976; Nozaki et al., 1990a), the East China Sea (ECS) shelf water (Lee et al., 1996; Hong et al., 1999; Su et al., 2017; this study), and the East Sea (Kim and Kim, 2012; this study).

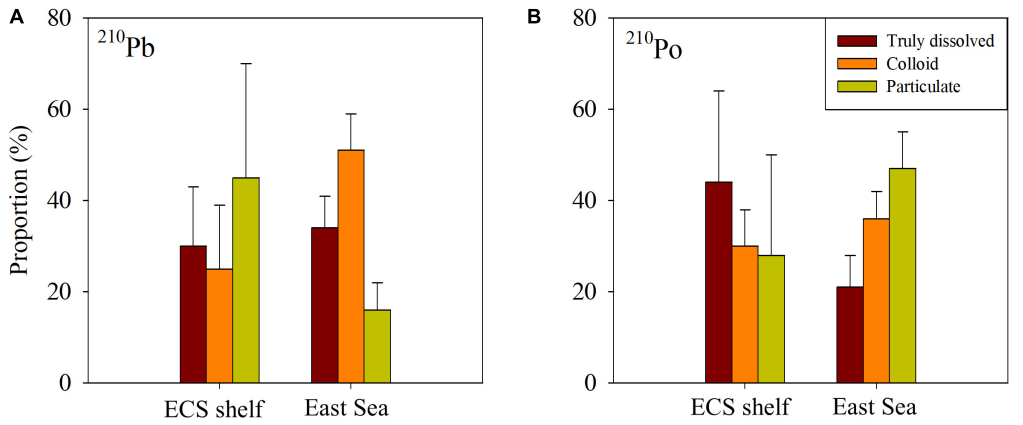


**FIGURE 3 |** Proportions of $^{210}$Pb **(A)** and $^{210}$Po **(B)** in truly dissolved (<10 kDa), colloidal (10 kDa–0.2 μm), and particulate (>0.2 μm) phases in the East China Sea (ECS) shelf water and the East Sea.

Su et al., 2017) and the southern Yellow Sea (Hong et al., 1999), which show unusually high activities ($^{210}$Po/$^{210}$Pb ratios > 1), are excluded since they are considered to be significantly influenced by terrestrial sources. All the analytical results of our experiments are given in **Supplementary Table 1**.

In the surface layer (0–25 m), the activities of total $^{210}$Pb were lower in the ECS shelf water (14 ± 3 dpm 100 L$^{-1}$) relative to the NWPO (20 ± 6 dpm 100 L$^{-1}$) and the East Sea (17 ± 4 dpm 100 L$^{-1}$; **Figure 2A**). The distributions of total $^{210}$Pb generally showed maximum values in the surface layer and decreased with depth in the three regions, as observed in other major oceans (e.g., Nozaki et al., 1980; Kim, 2001; Rigaud et al., 2015; Horowitz et al., 2020). For example, the activities of total $^{210}$Pb decreased by approximately 50, 20, and 50% from 0 to 150 m in the ECS shelf water, the NWPO, and the East Sea, respectively. In the ECS shelf water, several stations showed maximum $^{210}$Pb activities near the bottom sediments, which were 1.5–2.0 times higher than those in the surface layer. Of the total activities, the proportions of truly dissolved, colloidal, and particulate $^{210}$Pb in the ECS shelf water were about 32 ± 13%, 27 ± 14%, and 41 ± 24%, whereas those in the East Sea were about 34 ± 7%, 51 ± 8%, and 16 ± 6%, respectively (**Figure 3A**). There was no significant difference in the activities of truly dissolved and colloidal phases between the ECS shelf water and the East Sea. However, the activities of particulate $^{210}$Pb in the ECS shelf water were about four times higher than those in the East Sea (**Supplementary Table 1**).

For total $^{210}$Po activities, there was no distinct difference in the surface layer (0–25 m) among the ECS shelf water (11 ± 3 dpm 100 L$^{-1}$), the NWPO (11 ± 5 dpm 100 L$^{-1}$), and the East Sea (10 ± 2 dpm 100 L$^{-1}$; **Figure 2B**). As such, there was no clear trend with depth. However, there was a significant difference in the deficiency of $^{210}$Po ($^{210}$Pb-$^{210}$Po) in the three regions (**Figure 2C**). The most oligotrophic NWPO showed a relatively larger deficiency (9 ± 4 dpm 100 L$^{-1}$) in the upper ocean (0–25 m) compared with those in the East Sea (7 ± 3 dpm 100 L$^{-1}$) and the ECS shelf water (3 ± 3 dpm 100 L$^{-1}$). The largest deficiency of $^{210}$Po in the NWPO was observed at 200 m, while it was observed in the surface layer and decreased with depth in the ECS shelf water and the East Sea. Of the total activities, the proportions of truly dissolved, colloidal, and particulate $^{210}$Po in the ECS shelf water were about 48 ± 19%, 31 ± 8%, and 24 ± 21%, whereas those in the East Sea were about 21 ± 7%, 36 ± 6%, and 47 ± 8%, respectively (**Figure 3B**). The activities of $^{210}$Po in the ECS shelf water were approximately 3.8, 1.7, and 1.8 times higher than those in the East Sea for the truly dissolved, colloidal, and particulate phases, respectively (**Supplementary Table 1**).

# DISCUSSION

## Steady-State and Non-steady-State Scavenging Models for $^{210}$Pb and $^{210}$Po

A steady-state (SS) scavenging model is used to estimate the scavenging rates of $^{210}$Pb and $^{210}$Po in this study, as utilized by previous studies in open ocean (e.g., Bacon et al., 1976; Obata et al., 2004; Murray et al., 2005). At steady state ($\partial A/\partial t$ = 0), if advection and diffusion are neglected, the scavenging rate constants of $^{210}$Pb and $^{210}$Po can be calculated using the following equations:

For $^{210}$Pb:

$$\frac{\partial A^{t}_{Pb}}{\partial t} = \lambda_{Pb} \times \left(A_{Ra} - A^{t}_{Pb}\right) + F_{Atm} - A^{t}_{Pb}k^{t}_{Pb} = 0 \quad (1)$$

$$\frac{\partial A^{td}_{Pb}}{\partial t} = \lambda_{Pb} \times \left(A_{Ra} - A^{td}_{Pb}\right) + F_{Atm} - A^{td}_{Pb}k^{td}_{Pb} = 0 \quad (2)$$

$$\frac{\partial A^{c}_{Pb}}{\partial t} = \lambda_{Pb} \times \left(-A^{c}_{Pb}\right) + A^{td}_{Pb}k^{td}_{Pb} - A^{c}_{Pb}k^{c}_{Pb} = 0 \quad (3)$$

$$\frac{\partial A^{p}_{Pb}}{\partial t} = \lambda_{Pb} \times \left(-A^{p}_{Pb}\right) + A^{c}_{Pb}k^{c}_{Pb} - A^{p}_{Pb}k^{p}_{Pb} = 0 \quad (4)$$

For $^{210}$Po:

$$\frac{\partial A^{t}_{Po}}{\partial t} = \lambda_{Po} \times \left(A^{t}_{Pb} - A^{t}_{Po}\right) - A^{t}_{Po}k^{t}_{Po} = 0 \quad (5)$$

$$\frac{\partial A_{Po}^{td}}{\partial t} = \lambda_{Po} \times \left(A_{Pb}^{td} - A_{Pb}^{td}\right) - A_{Po}^{td} k_{Po}^{td} = 0 \quad (6)$$

$$\frac{\partial A_{Po}^{c}}{\partial t} = \lambda_{Po} \times \left(A_{Pb}^{c} - A_{Pb}^{c}\right) + A_{Po}^{td} k_{Po}^{td} - A_{Po}^{c} k_{Po}^{c} = 0 \quad (7)$$

$$\frac{\partial A_{Po}^{p}}{\partial t} = \lambda_{Po} \times \left(A_{Pb}^{p} - A_{Pb}^{p}\right) + A_{Po}^{c} k_{Po}^{c} - A_{Po}^{p} k_{Po}^{p} = 0 \quad (8)$$

where $\lambda$, $A$, $F_{Atm}$, and $k$ are the decay constant (day$^{-1}$), inventory of element (dpm m$^{-2}$), atmospheric depositional flux of $^{210}$Pb (55 dpm m$^{-2}$ day$^{-1}$; Nozaki et al., 1973; Turekian et al., 1977), and the scavenging rate constant (year$^{-1}$), respectively. t, td, c, and p represent the total, truly dissolved, colloidal, and particulate phases, respectively. To obtain the activities of $^{226}$Ra in the ECS shelf water, the empirical relationship with salinity is used for the southern sea of Korea (Stn. C-1, C-2, C-3, and C-4; Yang et al., 1992, 1996), and the data from Wang et al. (2018c) are used for the other ECS shelf regions. The activities of $^{226}$Ra in the NWPO and the East Sea are from previously published results (Nozaki and Tsunogai, 1976; Chung and Craig, 1980; Harada and Tsunogai, 1986; Nozaki et al., 1990b). The riverine inputs are neglected because $^{210}$Pb is almost completely trapped in the Changjiang estuary (Wang et al., 2018b). The atmospheric input of $^{210}$Po is also neglected since the $^{210}$Po/$^{210}$Pb ratios in precipitation in this study region are lower than 0.2 (Kim et al., 2005a; Yan et al., 2012).

The hydrological conditions and biogeochemical processes in the ECS shelf water are significantly affected by the intrusion of the NWPO (Wang et al., 2018a; Zuo et al., 2019; Liu et al., 2021). The chemical properties of the intruded water undergo rapid changes during the water residence times in the ECS shelf. Therefore, the removal fluxes of $^{210}$Pb and $^{210}$Po in the ECS shelf water can be calculated using the non-steady-state (NSS) model, accounting for the residence times of the shelf water. The removal fluxes of $^{210}$Pb and $^{210}$Po in the ECS shelf water are expressed by the following equations:

$$\frac{\partial A_{Pb}^{ECS}}{\partial t} = \lambda_{Pb} \times \left(A_{Ra}^{ECS} - A_{Pb}^{ECS}\right) + F_{Atm} - R_{Pb}^{ECS} + F_{lateral,\ Pb} \quad (9)$$

$$\frac{\partial A_{Po}^{ECS}}{\partial t} = \lambda_{Po} \times \left(A_{Pb}^{ECS} - A_{Po}^{ECS}\right) - R_{Po}^{ECS} + F_{lateral,\ Po} \quad (10)$$

where $R$ and $F_{lateral}$ are the removal flux (in disintegrations per minute per square meter per day) and the lateral transport of the radionuclide by current, respectively. Assuming that $A_{Ra}$, $F_{Atm}$, $R$, and $F_{lateral}$ are constant during a given time interval, the solutions for Eqs 9, 10 are expressed as follows (based on the work by Friedrich and van der Loeff, 2002):

$$R_{Pb}^{ECS} = F_{atm} + F_{lateral,\ Pb} + \lambda_{Pb} A_{Ra}^{ECS} + \frac{\lambda_{Pb}}{1 - e^{-\lambda_{Pb}\Delta t}} \left(A_{Pb,t1} e^{-\lambda_{Pb}\Delta t} - A_{Pb,t2}\right) \quad (11)$$

$$R_{Po}^{ECS} = F_{lateral,\ Po} + \frac{\lambda_{Po}}{1 - e^{-\lambda_{Po}\Delta t}} \left[ \frac{\lambda_{Pb} A_{Ra}^{ECS} + F_{atm} + F_{lateral,\ Pb} - R_{Pb}^{ECS}}{\lambda_{Pb}} \left\{ \frac{\lambda_{Po}}{\lambda_{Po} - \lambda_{Pb}} \left(e^{-\lambda_{Po}\Delta t} - e^{-\lambda_{Pb}\Delta t}\right) + \left(1 - e^{-\lambda_{Po}\Delta t}\right) \right\} + A_{Pb,t1} \frac{\lambda_{Po}}{\lambda_{Po} - \lambda_{Pb}} \left(e^{-\lambda_{Pb}\Delta t} - e^{-\lambda_{Po}\Delta t}\right) + A_{Po,t1} e^{-\lambda_{Po}\Delta t} - A_{Po,t2} \right] \quad (12)$$

In this calculation, we assume that the water of the NWPO enters the ECS shelf at time $t_1$ and stays for an amount of time $\Delta t$ ($t_2$–$t_1$). Therefore, $\Delta t$ is the residence time of the ECS shelf water. $A_{t1}$

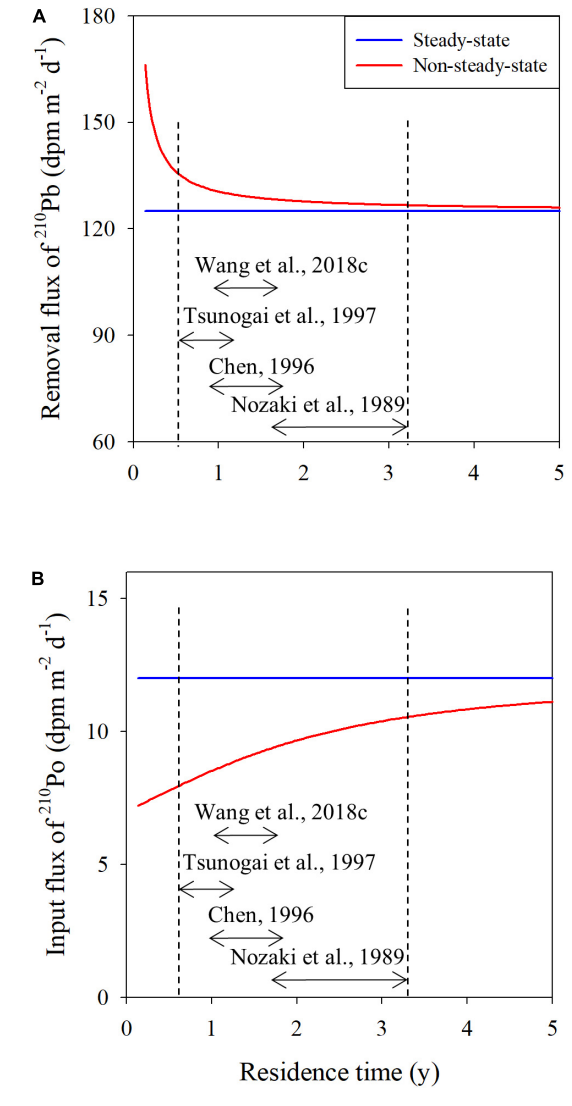


**FIGURE 4 |** Net removal flux of total $^{210}$Pb (in disintegrations per minute per square meter per day; **A**) and net input flux of total $^{210}$Po (in disintegrations per minute per square meter per day; **B**) from the upper 0–50 m in the East China Sea (ECS) shelf water, calculated based on the steady-state and non-steady-state models accounting for the advection of water. The *dotted lines* represent the range of the previously reported residence times in the ECS shelf water.

and $A_{t2}$ are the activities of radionuclides in the NWPO and the ECS shelf water, respectively. The lateral transport term ($F_{lateral}$) is calculated by multiplying the current velocity of ~20 cm $s^{-1}$ (Ichikawa and Beardsley, 2002; Lee et al., 2014) by the activity gradient between the NWPO and the ECS shelf water along the 400-km distance (Yangtze River mouth–Jeju Island). The calculated results using Eqs 11, 12 according to the change in residence times of the ECS shelf water are shown in **Figure 4**. The SS model, which accounts for the advection of water, is given for comparison.

## Behaviors of $^{210}$Pb and $^{210}$Po

The scavenging rate constant of total $^{210}$Pb in the ECS shelf water (3.0 ± 0.6 $year^{-1}$) was relatively higher than that in the NWPO (2.2 ± 0.4 $year^{-1}$) and the East Sea (2.6 ± 0.4 $year^{-1}$) based on the SS model (**Table 1**). The corresponding values of truly dissolved and colloidal $^{210}$Pb in the ECS shelf water were also 1.2–2.0 times higher than those in the East Sea. However, the scavenging rate constant of particulate $^{210}$Pb in the ECS shelf water was approximately 3.8 times lower than that in the East Sea, perhaps associated with the higher activities of particulate $^{210}$Pb in the ECS shelf water. Given that the maximum activities of particulate $^{210}$Pb were observed in the surface layer at C3 and the bottom layer at C4, respectively, such high activities of particulate $^{210}$Pb might be attributed to the lateral input from land or the resuspension from the bottom sediments. This could occur due to the shallow water depth and by episodic storm events (Choi et al., 2004, 2010). In both cases, the SS model is not appropriate for calculating the scavenging rate constant and removal flux in the ECS shelf water.

Based on the NSS model, total $^{210}$Pb was more effectively removed in the ECS shelf water (128–137 dpm $m^{-2}$ $day^{-1}$) relative to the NWPO (55 dpm $m^{-2}$ $day^{-1}$) and the East Sea (55 dpm $m^{-2}$ $day^{-1}$; **Figure 5**). The removal flux of total $^{210}$Pb showed differences from 1 to 9% between the NSS and SS models within the previously reported residence times of the ECS shelf water (0.5–3.1 years; **Figure 4A**; Nozaki et al., 1989; Chen, 1996; Tsunogai et al., 1997; Wang et al., 2018c). These high scavenging rate and removal flux of $^{210}$Pb in the ECS shelf water might be due to the higher concentrations of the suspended particulate matters in the ECS shelf water (6.8–15.0 mg $L^{-1}$; Bi et al., 2020) compared with those in the NWPO (0.1–0.3 mg $L^{-1}$; Hung and Chan, 1998) and the East Sea (0.2–0.6 mg $L^{-1}$; Chen et al., 1996; Hong et al., 2008).

For $^{210}$Po, the scavenging rate constant of total $^{210}$Po in the ECS shelf water (0.3 ± 0.2 $year^{-1}$) was much lower than that in

**TABLE 1 |** Scavenging rate constants (per year) of total, truly dissolved (<10 kDa), colloidal (10 kDa–0.2 μm), and particulate (>0.2 μm) $^{210}$Pb and $^{210}$Po in the upper 0–50 m of the northwestern Pacific Ocean (NWPO), the East China Sea (ECS) shelf water, and the East Sea.

| Location | Total | | Truly dissolved (<10 kDa) | | Colloidal (10 kDa–0.2 or 0.45 μm) | | Particulate (>0.2 or 0.45 μm) | |
|---|---|---|---|---|---|---|---|---|
| | $^{210}$Pb | $^{210}$Po | $^{210}$Pb | $^{210}$Po | $^{210}$Pb | $^{210}$Po | $^{210}$Pb | $^{210}$Po |
| NWPO | 2.2 ± 0.4 | 1.3 ± 0.5 | – | – | – | – | – | – |
| ECS shelf water | 3.0 ± 0.6 | 0.3 ± 0.2 | 8.6 ± 0.3 | 0.2[a] | 11.3 ± 1.7 | 0.3[a] | 6.1 ± 0.2 | 4.5 ± 3 |
| East Sea | 2.6 ± 0.4 | 1.8 ± 0.3 | 7.4 ± 1.1 | 5.9 ± 3.2 | 5.8 ± 1.3 | 6.5 ± 2.1 | 23.6 ± 7.6 | 3.8 ± 1.1 |

[a] *The C4 station showed a negative scavenging constant due to the equilibrium state between $^{210}$Pb and $^{210}$Po.*

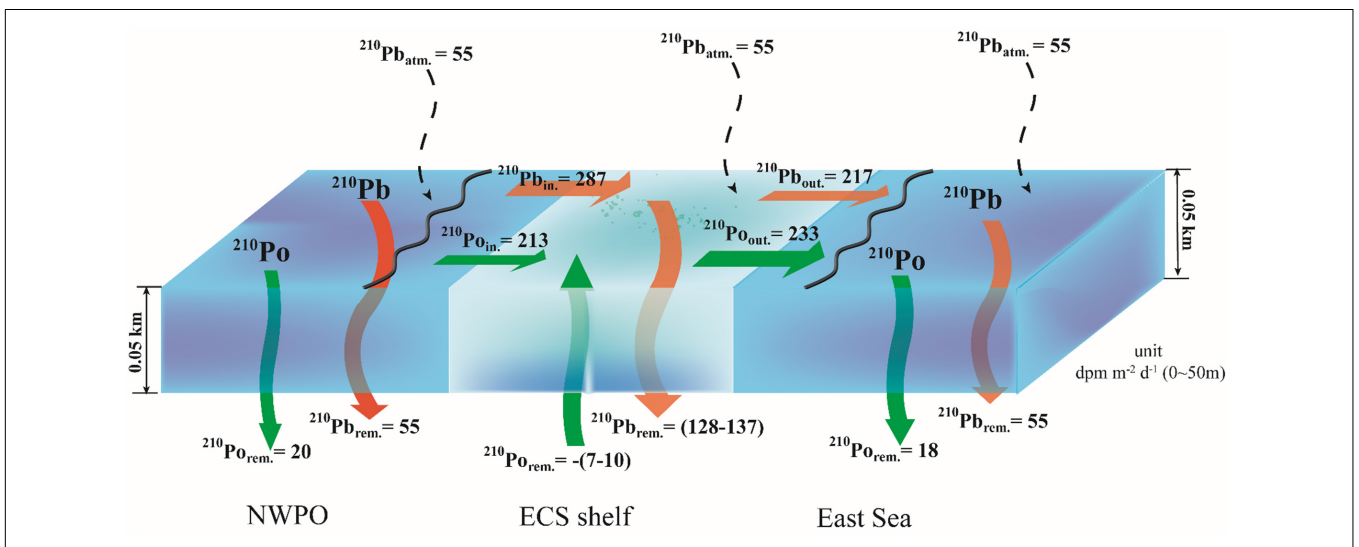


**FIGURE 5 |** A schematic box model (non-steady-state) of total $^{210}$Pb and $^{210}$Po accounting for the lateral transport of water from the northwestern Pacific Ocean (NWPO) to the East Sea through the East China Sea (ECS) shelf. The uncertainty of each source and sink term accounting for variations in the current velocity and atmospheric input of $^{210}$Pb is below 15%, except for the net input of $^{210}$Po in the ECS shelf water (28%).

the NWPO ($1.3 \pm 0.5$ year$^{-1}$) and the East Sea ($1.8 \pm 0.3$ year$^{-1}$), which is opposite to the $^{210}$Pb trend (**Table 1**). Especially, the truly dissolved and colloidal $^{210}$Po in the ECS shelf water approached equilibrium with $^{210}$Pb. The calculated results of the NSS model showed the net input of $^{210}$Po in the ECS shelf water (7–10 dpm m$^{-2}$ day$^{-1}$), opposite to the net removal in the NWPO (20 dpm m$^{-2}$ day$^{-1}$) and the East Sea (18 dpm m$^{-2}$ day$^{-1}$; **Figure 5**). The net input flux of $^{210}$Po increased with the residence times of the ECS shelf water and showed a difference from 13 to 35% between the NSS and SS models (**Figure 4B**).

These distinctively low scavenging rate constant and net input flux of $^{210}$Po have been reported in the ECS (Nozaki et al., 1991), Gulf of Lion (Radakovitch et al., 1998), and northwestern Mediterranean Sea (Masqué et al., 2002). Nozaki et al. (1991) and Radakovitch et al. (1998) argued that this trend might be due to the extensive inputs of suspended particulate matters from river discharges with $^{210}$Po/$^{210}$Pb ratios of ∼1. On the other hand, Masqué et al. (2002) suggested that the incorporation of $^{210}$Po into the organic matter following the uptake by buoyant particles resulted in the low scavenging rate constant of $^{210}$Po. In this study, we discount the riverine sources as the main reason for the low scavenging rate constant of $^{210}$Po because the influence of river discharge with high $^{210}$Po/$^{210}$Pb ratios was excluded in the comparison. In addition, the $^{210}$Po/$^{210}$Pb ratios were ∼0.5 for the particulate phase and ∼1 for the total dissolved (truly dissolved + colloidal) phases in the ECS shelf water.

In general, low contents of organic carbon (0.2–1.0%) were observed in the sinking particles and the bottom sediments in the ECS shelf, associated with rapid organic carbon remineralization (Lin et al., 2000, 2002; Iseki et al., 2003). The results of sediment core incubation also showed that the organic carbon remineralization rate in the bottom sediments accounted for 12–24% of the primary productivity in this highly eutrophic ECS shelf water (Song et al., 2016), indicating the efficient regeneration of organic matter in the bottom sediments. In addition, hypoxia occurred intermittently in the bottom of ECS shelf water (dissolved oxygen concentrations <2–3 mg L$^{-1}$; Chen et al., 2007), which can also increase the net input flux of $^{210}$Po as insoluble Po(IV) can be reduced to soluble Po(II) (Balistrieri et al., 1995; Kim et al., 2005b; Kim and Kim, 2014). Considering the relatively higher proportions of the total dissolved (truly dissolved + colloidal) $^{210}$Po in the ECS shelf water (>80%), the colloidal matter might be associated with the net input of $^{210}$Po due to regeneration from the sinking particles and in the bottom sediments.

Thus, our results suggest that $^{210}$Po, a proxy for sulfur group elements (S, Se, and Te), may reside longer in the water column because of active regeneration, while $^{210}$Pb and other particle-reactive elements would be removed in association with the large population of the sinking particles in the shelf water.

## CONCLUSION

The scavenging rate constant and removal flux of $^{210}$Pb and $^{210}$Po were estimated using a geochemical scavenging model in the productive shelf system connected to the oligotrophic NWPO. The scavenging rate constant of $^{210}$Pb was relatively higher ($3.0 \pm 0.6$ year$^{-1}$) in the ECS shelf water, whereas that of $^{210}$Po was lower ($0.3 \pm 0.2$ year$^{-1}$) than that in the NWPO and the East Sea. In addition, a NSS model accounting for the ocean currents showed the effective removal of $^{210}$Pb in the ECS shelf water (128–137 dpm m$^{-2}$ day$^{-1}$), whereas $^{210}$Po showed the net input from the sinking particles and the bottom sediments (7–10 dpm m$^{-2}$ day$^{-1}$). Given that the largest proportions of $^{210}$Pb and $^{210}$Po were particulate and total dissolved (truly dissolved + colloidal) phases, respectively, these opposite behaviors could be due to the efficient scavenging of $^{210}$Pb versus the efficient regeneration of $^{210}$Po from organic matter in the ECS shelf water. Thus, our results suggest that particle-reactive elements would be effectively removed in the shelf water, whereas sulfur group elements (S, Se, and Te) might be supplied from the sinking particles and the bottom sediments by efficient regeneration.

## DATA AVAILABILITY STATEMENT

The original contributions presented in the study are included in the article/**Supplementary Material**, further inquiries can be directed to the corresponding author/s.

## AUTHOR CONTRIBUTIONS

GK contributed to the conceptualization of the study. HS and DJ performed field sampling and analyses. HS and GK were involved in the data interpretation and writing of the manuscript. All authors contributed to the final version of the manuscript.

## FUNDING

This research was a part of the project titled "Deep Water Circulation and Material Cycling in the East Sea (20160040)," funded by the Ministry of Oceans and Fisheries, South Korea, and the National Research Foundation of Korea (NRF) grant funded by the Korean government (MSIT; 2018R1A2B3001147).

## ACKNOWLEDGMENTS

We thank the crew members of the R/V *Tamgu* and R/V *Isabu* for their help with field sampling. We also thank all lab members for their assistance with sampling and analyses.

## SUPPLEMENTARY MATERIAL

The Supplementary Material for this article can be found online at: https://www.frontiersin.org/articles/10.3389/fmars.2021.701441/full#supplementary-material

## REFERENCES


Bacon, M., Spencer, D., and Brewer, P. (1976). $^{210}$Pb/$^{226}$Ra and $^{210}$Po/$^{210}$Pb disequilibria in seawater and suspended particulate matter. *Earth Planet. Sci. Lett.* 32, 277–296.

Balistrieri, L. S., Murray, J. W., and Paul, B. (1995). The geochemical cycling of stable Pb, $^{210}$Pb, and $^{210}$Po in seasonally anoxic Lake Sammamish, Washington, USA. *Geochim. Cosmochim. Acta* 59, 4845–4861. doi: 10.1016/0016-7037(95)00334-7

Baskaran, M., Swarzenski, P., and Porcelli, D. (2003). Role of colloidal material in the removal of $^{234}$Th in the Canada basin of the Arctic Ocean. *Deep Sea Res. 1 Oceanogr. Res. Pap.* 50, 1353–1373. doi: 10.1016/s0967-0637(03)00140-7

Bi, Q., Zhang, F., Deng, B., and Du, J. (2020). SPM control on the partitioning and balance of $^{210}$Po and $^{210}$Pb in high-turbidity surface waters of the East China Sea. *J. Environ. Radioact.* 222:106367. doi: 10.1016/j.jenvrad.2020.106367

Carvalho, F. P. (2011). Polonium ($^{210}$Po) and lead ($^{210}$Pb) in marine organisms and their transfer in marine food chains. *J. Environ. Radioact.* 102, 462–472. doi: 10.1016/j.jenvrad.2010.10.011

Chang, K.-I., Teague, W., Lyu, S., Perkins, H., Lee, D.-K., Watts, D., et al. (2004). Circulation and currents in the southwestern East/Japan Sea: overview and review. *Prog. Oceanogr.* 61, 105–156. doi: 10.1016/j.pocean.2004.06.005

Chang, K.-I., Zhang, C.-I., Park, C., Kang, D.-J., Ju, S.-J., Lee, S.-H., et al. (2016). *Oceanography of the East Sea (Japan Sea)*. Berlin: Springer.

Chen, C. (1996). The Kuroshio intermediate water is the major source of nutrients on the East China Sea continental shelf. *Oceanol. Acta* 19, 523–527.

Chen, C.-C., Gong, G.-C., and Shiah, F.-K. (2007). Hypoxia in the east China sea: one of the largest coastal low-oxygen areas in the world. *Mar. Environ. Res.* 64, 399–408. doi: 10.1016/j.marenvres.2007.01.007

Chen, C.-T. A., Lin, C.-M., Huang, B.-T., and Chang, L.-F. (1996). Stoichiometry of carbon, hydrogen, nitrogen, sulfur and oxygen in the particulate matter of the western North Pacific marginal seas. *Mar. Chem.* 54, 179–190. doi: 10.1016/0304-4203(96)00021-7

Cho, H. M., Kim, G., Kwon, E. Y., and Han, Y. (2019). Radium tracing cross-shelf fluxes of nutrients in the northwest Pacific Ocean. *Geophys. Res. Lett.* 46, 11321–11328. doi: 10.1029/2019gl084594

Choi, J.-Y., Kim, S.-Y., and Kang, H.-J. (2004). Distribution of suspended particulate matters in the east China sea, southern yellow sea and south sea of Korea during the winter season. *J. Korea Soc. Oceanogr.* 39, 212–221.

Choi, K.-H., Lee, S.-M., Lim, S.-M., Walton, M., and Park, G.-S. (2010). Benthic habitat quality change as measured by macroinfauna community in a tidal flat on the west coast of Korea. *J. Oceanogr.* 66, 307–317. doi: 10.1007/s10872-010-0027-7

Chung, Y., and Craig, H. (1980). $^{226}$Ra in the Pacific Ocean. *Earth Planet. Sci. Lett.* 49, 267–292.

Chung, Y., and Wu, T. (2005). Large $^{210}$Po deficiency in the northern South China sea. *Cont. Shelf Res.* 25, 1209–1224. doi: 10.1016/j.csr.2004.12.016

Dai, Z., Du, J., Zhang, X., Su, N., and Li, J. (2011). Variation of riverine material loads and environmental consequences on the Changjiang (Yangtze) Estuary in recent decades (1955- 2008). *Environ. Sci. Technol.* 45, 223–227. doi: 10.1021/es103026a

Dong, L., Guan, W., Chen, Q., Li, X., Liu, X., and Zeng, X. (2011). Sediment transport in the Yellow Sea and East China Sea. *Estuar. Coast. Shelf Sci.* 93, 248–258. doi: 10.1016/j.ecss.2011.04.003

Fang, T.-H., Li, J.-Y., Feng, H.-M., and Chen, H.-Y. (2009). Distribution and contamination of trace metals in surface sediments of the East China Sea. *Mar. Environ. Res.* 68, 178–187. doi: 10.1016/j.marenvres.2009.06.005

Fisher, N. S., Burns, K. A., Cherry, R., and Heyraud, M. (1983). Accumulation and cellular distribution of $^{241}$Am, $^{210}$Po, and $^{210}$Pb in two marine algae. *Mar. Ecol. Prog. Ser.* 11, 233–237. doi: 10.3354/meps011233

Friedrich, J., and van der Loeff, M. M. R. (2002). A two-tracer ($^{210}$Po–$^{234}$Th) approach to distinguish organic carbon and biogenic silica export flux in the Antarctic circumpolar current. *Deep Sea Res. 1 Oceanogr. Res. Pap.* 49, 101–120. doi: 10.1016/s0967-0637(01)00045-0

Gong, G.-C., Shiah, F.-K., Liu, K.-K., Wen, Y.-H., and Liang, M.-H. (2000). Spatial and temporal variation of chlorophyll a, primary productivity and chemical hydrography in the southern East China Sea. *Cont. Shelf Res.* 20, 411–436. doi: 10.1016/s0278-4343(99)00079-5

Guéguen, C., Belin, C., and Dominik, J. (2002). Organic colloid separation in contrasting aquatic environments with tangential flow filtration. *Water Res.* 36, 1677–1684. doi: 10.1016/s0043-1354(01)00374-8

Hama, T., Shin, K., and Handa, N. (1997). Spatial variability in the primary productivity in the East China Sea and its adjacent waters. *J. Oceanogr.* 53, 41–51. doi: 10.1007/bf02700748

Harada, K., and Tsunogai, S. (1986). $^{226}$Ra in the Japan Sea and the residence time of the Japan Sea water. *Earth Planet. Sci. Lett.* 77, 236–244. doi: 10.1016/0012-821x(86)90164-0

Hong, G.-H., Kim, Y.-I., Baskaran, M., Kim, S.-H., and Chung, C.-S. (2008). Distribution of $^{210}$Po and export of organic carbon from the euphotic zone in the southwestern East Sea (Sea of Japan). *J. Oceanogr.* 64, 277–292. doi: 10.1007/s10872-008-0022-4

Hong, G.-H., Park, S.-K., Baskaran, M., Kim, S.-H., Chung, C.-S., and Lee, S.-H. (1999). Lead-210 and polonium-210 in the winter well-mixed turbid waters in the mouth of the Yellow Sea. *Cont. Shelf Res.* 19, 1049–1064. doi: 10.1016/s0278-4343(99)00011-4

Horowitz, E. J., Cochran, J. K., Bacon, M. P., and Hirschberg, D. J. (2020). $^{210}$Po and $^{210}$Pb distributions during a phytoplankton bloom in the North Atlantic: implications for POC export. *Deep Sea Res. I. Oceanogr. Res. Pap.* 164:103339. doi: 10.1016/j.dsr.2020.103339

Hung, G. W., and Chung, Y.-C. (1998). Particulate fluxes, $^{210}$Pb and $^{210}$Po measured from sediment trap samples in a canyon off northeastern Taiwan. *Cont. Shelf Res.* 18, 1475–1491. doi: 10.1016/s0278-4343(98)00032-6

Hung, J.-J., and Chan, C.-L. (1998). Distribution and enrichment of particulate trace metals in the southern East China Sea. *Geochem. J.* 32, 189–203. doi: 10.2343/geochemj.32.189

Ichikawa, H., and Beardsley, R. C. (2002). The current system in the Yellow and East China Seas. *J. Oceanogr.* 58, 77–92.

Iseki, K., Okamura, K., and Kiyomoto, Y. (2003). Seasonality and composition of downward particulate fluxes at the continental shelf and Okinawa Trough in the East China Sea. *Deep Sea Res. 2 Top. Stud. Oceanogr.* 50, 457–473. doi: 10.1016/s0967-0645(02)00468-x

Kim, G. (2001). Large deficiency of polonium in the oligotrophic ocean's interior. *Earth Planet. Sci. Lett.* 192, 15–21. doi: 10.1016/s0012-821x(01)00431-9

Kim, G., Hong, Y.-L., Jang, J., Lee, I., Hwang, D.-W., and Yang, H.-S. (2005a). Evidence for anthropogenic $^{210}$Po in the urban atmosphere of Seoul, Korea. *Environ. Sci. Technol.* 39, 1519–1522. doi: 10.1021/es049023u

Kim, G., Kim, S.-J., Harada, K., Schultz, M. K., and Burnett, W. C. (2005b). Enrichment of excess $^{210}$Po in anoxic ponds. *Environ. Sci. Technol.* 39, 4894–4899. doi: 10.1021/es0482334

Kim, J., Cho, H.-M., and Kim, G. (2018). Significant production of humic fluorescent dissolved organic matter in the continental shelf waters of the northwestern Pacific Ocean. *Sci. Rep.* 8:4887.

Kim, T.-H., and Kim, G. (2012). Important role of colloids in the cycling of $^{210}$Po and $^{210}$Pb in the ocean: results from the East/Japan Sea. *Geochim. Cosmochim. Acta* 95, 134–142. doi: 10.1016/j.gca.2012.07.029

Kim, T.-H., and Kim, G. (2014). Estimating benthic fluxes of trace elements to hypoxic coastal waters using $^{210}$Po. *Estuar. Coast. Shelf Sci.* 151, 324–330. doi: 10.1016/j.ecss.2014.05.008

Lee, H., Kim, G., Kim, J., Park, G., and Song, K. H. (2014). Tracing the flow rate and mixing ratio of the Changjiang diluted water in the northwestern Pacific marginal seas using radium isotopes. *Geophys. Res. Lett.* 41, 4637–4645. doi: 10.1002/2014gl060230

Lee, H.-P., Yang, H.-S., and Kim, K.-H. (1996). Removal of $^{210}$Po and $^{234}$Th from seawater at the East-southern Coastal Region of Korea Peninsula in spring. *Bull. Korean Fish. Soc.* 29, 332–344.

Lin, S., Hsieh, I.-J., Huang, K.-M., and Wang, C.-H. (2002). Influence of the Yangtze River and grain size on the spatial variations of heavy metals and organic carbon in the east China Sea continental shelf sediments. *Chem. Geol.* 182, 377–394. doi: 10.1016/s0009-2541(01)00331-x

Lin, S., Huang, K.-M., and Chen, S.-K. (2000). Organic carbon deposition and its control on iron sulfide formation of the southern East China sea continental shelf sediments. *Cont. Shelf Res.* 20, 619–635. doi: 10.1016/s0278-4343(99)00088-6

Liu, Z., Gan, J., Hu, J., Wu, H., Cai, Z., and Deng, Y. (2021). Progress of studies on circulation dynamics in the east China sea: the kuroshio exchanges with the shelf currents. *Front. Mar. Sci.* 8:620910. doi: 10.3389/fmars.2021.620910

Masqué, P., Sanchez-Cabeza, J., Bruach, J., Palacios, E., and Canals, M. (2002). Balance and residence times of $^{210}$Pb and $^{210}$Po in surface waters of the northwestern Mediterranean Sea. *Cont. Shelf Res.* 22, 2127–2146. doi: 10.1016/s0278-4343(02)00074-2

Morimoto, A., and Yanagi, T. (2001). Variability of sea surface circulation in the Japan Sea. *J. Oceanogr.* 57, 1–13.

Murray, J. W., Paul, B., Dunne, J. P., and Chapin, T. (2005). $^{234}$Th, $^{210}$Pb, $^{210}$Po and stable Pb in the central equatorial Pacific: tracers for particle cycling. *Deep Sea Res. 1 Oceanogr. Res. Pap.* 52, 2109–2139. doi: 10.1016/j.dsr.2005.06.016

Nozaki, Y., Ikuta, N., and Yashima, M. (1990a). Unusually large $^{210}$Po deficiencies relative to $^{210}$Pb in the Kuroshio Current of the East China and Philippine Seas. *J. Geophys. Res. Oceans* 95, 5321–5329. doi: 10.1029/jc095ic04p05321

Nozaki, Y., Kasemsupaya, V., and Tsubota, H. (1989). Mean residence time of the shelf water in the East China and the Yellow Seas determined by $^{228}$Ra/$^{226}$Ra measurements. *Geophys. Res. Lett.* 16, 1297–1300. doi: 10.1029/gl016i011p01297

Nozaki, Y., Kasemsupaya, V., and Tsubota, H. (1990b). The distribution of $^{228}$Ra and $^{226}$Ra in the surface waters of the northern North Pacific. *Geochem. J.* 24, 1–6.

Nozaki, Y., Tsubota, H., Kasemsupaya, V., Yashima, M., and Naoko, I. (1991). Residence times of surface water and particle-reactive $^{210}$Pb and $^{210}$Po in the East China and Yellow seas. *Geochim. Cosmochim. Acta* 55, 1265–1272. doi: 10.1016/0016-7037(91)90305-o

Nozaki, Y., and Tsunogai, S. (1976). $^{226}$Ra, $^{210}$Pb and $^{210}$Po disequilibria in the western North Pacific. *Earth Planet. Sci. Lett.* 32, 313–321.

Nozaki, Y., Tsunogai, S., and Nishimura, M. (1973). Lead-210 in the Japan Sea. *J. Oceanogr.* 29, 251–256. doi: 10.1007/bf02108844

Nozaki, Y., Turekian, K., and Von Damm, K. (1980). $^{210}$Pb in GEOSECS water profiles from the North Pacific. *Earth Planet. Sci. Lett.* 49, 393–400. doi: 10.1016/0012-821x(80)90081-3

Obata, H., Nozaki, Y., Alibo, D. S., and Yamamoto, Y. (2004). Dissolved Al, In, and Ce in the eastern Indian Ocean and the Southeast Asian seas in comparison with the radionuclides $^{210}$Pb and $^{210}$Po. *Geochim. Cosmochim. Acta* 68, 1035–1048. doi: 10.1016/j.gca.2003.07.021

Radakovitch, O., Cherry, R. D., Heyraud, M., and Heussner, S. (1998). Unusual $^{210}$Po/$^{210}$Pb ratios in the surface water of the Gulf of Lions. *Oceanol. Acta* 21, 459–468. doi: 10.1016/s0399-1784(98)80030-3

Rigaud, S., Stewart, G., Baskaran, M., Marsan, D., and Church, T. (2015). $^{210}$Po and $^{210}$Pb distribution, dissolved-particulate exchange rates, and particulate export along the North Atlantic US GEOTRACES GA03 section. *Deep Sea Res. 2 Top. Stud. Oceanogr.* 116, 60–78. doi: 10.1016/j.dsr2.2014.11.003

Song, G., Liu, S., Zhu, Z., Zhai, W., Zhu, C., and Zhang, J. (2016). Sediment oxygen consumption and benthic organic carbon mineralization on the continental shelves of the East China sea and the Yellow sea. *Deep Sea Res. 2 Top. Stud. Oceanogr.* 124, 53–63. doi: 10.1016/j.dsr2.2015.04.012

Stewart, G., Cochran, J., Miquel, J., Masqué, P., Szlosek, J., Rodriguez y Baena, A. M., et al. (2007). Comparing POC export from $^{234}$Th/$^{238}$U and $^{210}$Po/$^{210}$Pb disequilibria with estimates from sediment traps in the northwest Mediterranean. *Deep Sea Res. 1 Oceanogr. Res. Pap.* 54, 1549–1570. doi: 10.1016/j.dsr.2007.06.005

Stewart, G. M., and Fisher, N. S. (2003). Bioaccumulation of polonium-210 in marine copepods. *Limnol. Oceanogr.* 48, 2011–2019. doi: 10.4319/lo.2003.48.5.2011

Su, K., Du, J., Baskaran, M., and Zhang, J. (2017). $^{210}$Po and $^{210}$Pb disequilibrium at the PN section in the East China Sea. *J. Environ. Radioact.* 174, 54–65. doi: 10.1016/j.jenvrad.2016.07.031

Tang, Y., and Stewart, G. (2019). The $^{210}$Po/$^{210}$Pb method to calculate particle export: lessons learned from the results of three GEOTRACES transects. *Mar. Chem.* 217:103692. doi: 10.1016/j.marchem.2019.103692

Tsunogai, S., and Nozaki, Y. (1971). Lead-210 and polonium-210 in the surface water of the Pacific. *Geochem. J.* 5, 165–173. doi: 10.2343/geochemj.5.165

Tsunogai, S., Watanabe, S., Nakamura, J., Ono, T., and Sato, T. (1997). A preliminary study of carbon system in the East China sea. *J. Oceanogr.* 53, 9–17. doi: 10.1007/bf02700744

Turekian, K. K., Nozaki, Y., and Benninger, L. K. (1977). Geochemistry of atmospheric radon and radon products. *Annu. Rev. Earth Planet. Sci.* 5, 227–255. doi: 10.1146/annurev.ea.05.050177.001303

Wang, C., Zou, X., Feng, Z., Hao, Z., and Gao, J. (2018a). Distribution and transport of heavy metals in estuarine–inner shelf regions of the East China sea. *Sci. Total Environ.* 644, 298–305. doi: 10.1016/j.scitotenv.2018.06.383

Wang, J., Zhang, W., Baskaran, M., Du, J., Zhou, F., and Wu, H. (2018b). Fingerprinting sediment transport in river-dominated margins using combined mineral magnetic and radionuclide methods. *J. Geophys. Res. Oceans* 123, 5360–5374. doi: 10.1029/2018jc014174

Wang, X., Baskaran, M., Su, K., and Du, J. (2018c). The important role of submarine groundwater discharge (SGD) to derive nutrient fluxes into river dominated ocean margins–the East China sea. *Mar. Chem.* 204, 121–132. doi: 10.1016/j.marchem.2018.05.010

Wei, C.-L., and Murray, J. W. (1994). The behavior of scavenged isotopes in marine anoxic environments: $^{210}$Pb and $^{210}$Po in the water column of the Black sea. *Geochim. Cosmochim. Acta* 58, 1795–1811. doi: 10.1016/0016-7037(94)90537-1

Yan, G., Cho, H.-M., Lee, I., and Kim, G. (2012). Significant emissions of $^{210}$Po by coal burning into the urban atmosphere of Seoul. *Korea. Atmos. Environ.* 54, 80–85. doi: 10.1016/j.atmosenv.2012.02.090

Yang, H.-S., Kim, S.-S., and Lee, J.-C. (1996). Distribution characteristics of $^{210}$Po and $^{210}$Pb in the seawater from the Korean East sea in spring. *Bull. Korean Fish. Soc.* 29, 238–245.

Yang, H.-S., Kwon, Y.-A., Kim, G.-B., and Kim, S.-S. (1992). Distributions of $^{226}$Ra and $^{228}$Ra in the surface Waters of East sea of Korea. *Bull. Korean Fish. Soc.* 25, 399–405.

Zuo, J., Song, J., Yuan, H., Li, X., Li, N., and Duan, L. (2019). Impact of Kuroshio on the dissolved oxygen in the East China sea region. *J. Oceanol. Limnol.* 37, 513–524. doi: 10.1007/s00343-019-7389-5

**Conflict of Interest:** The authors declare that the research was conducted in the absence of any commercial or financial relationships that could be construed as a potential conflict of interest.

*Copyright © 2021 Seo, Joung and Kim. This is an open-access article distributed under the terms of the Creative Commons Attribution License (CC BY). The use, distribution or reproduction in other forums is permitted, provided the original author(s) and the copyright owner(s) are credited and that the original publication in this journal is cited, in accordance with accepted academic practice. No use, distribution or reproduction is permitted which does not comply with these terms.*

frontiers in Marine Science

ORIGINAL RESEARCH
published: 15 July 2021
doi: 10.3389/fmars.2021.701014

# $^{210}$Po/$^{210}$Pb Disequilibria and Its Estimate of Particulate Organic Carbon Export Around Prydz Bay, Antarctica

*Huina Hu[1,2], Xiao Liu[1], Chunyan Ren[1], Renming Jia[1], Yusheng Qiu[1], Minfang Zheng[1] and Min Chen[1]**

[1] College of Ocean and Earth Sciences, Xiamen University, Xiamen, China, [2] South China Sea Environmental Monitoring Center, South China Sea Bureau, Ministry of Natural Resources, Guangzhou, China

Due to the remoteness and difficulty of sampling, the $^{210}$Po and $^{210}$Pb data are scarce in the Southern Ocean. Here, the activity concentrations of $^{210}$Po and $^{210}$Pb around Prydz Bay in austral summer were determined to understand their spatial variation and evaluate the dynamics of particle organic matter (POM). The activity concentrations of dissolved $^{210}$Po (D$^{210}$Po) and $^{210}$Pb (D$^{210}$Pb) range from 0.47 to 3.20 Bq·m$^{-3}$ and from 1.15 to 2.97 Bq·m$^{-3}$, respectively, with the lower values in the shelf. The particulate $^{210}$Po (P$^{210}$Po) and $^{210}$Pb (P$^{210}$Pb) are lower in the open ocean and increase to the coastal waters, among which the circumpolar deep water (CDW) is the lowest. The activity concentration of total $^{210}$Pb (T$^{210}$Pb) ranges from 1.26 Bq·m$^{-3}$ to 3.16 Bq·m$^{-3}$, with a higher value in CDW, which is ascribed to radiogenic production from $^{226}$Ra and subsequent lateral transport. Occasionally a high value of T$^{210}$Po occurs in deep water (>3.00 Bq·m$^{-3}$), which may be caused by the remineralization of POM. The disequilibria between T$^{210}$Po and T$^{210}$Pb appears throughout the water column at most stations. The average T$^{210}$Po/T$^{210}$Pb)$_{A.R.}$ in the euphotic zone is 0.66, reflecting the effect of strong particle scavenging. There is a good positive correlation between the solid-liquid ratio of $^{210}$Po and POC, while $^{210}$Pb does not, indicating that particulate organic matter regulates the biogeochemical cycle of $^{210}$Po around Prydz Bay. Based on the $^{210}$Po/$^{210}$Pb disequilibria, the export flux of POC in the water column is estimated to be 0.8–31.9 mmol m$^{-2}$ d$^{-1}$, with the higher values in the shelf.

**Keywords: $^{210}$Po, $^{210}$Pb, POC export flux, Prydz Bay, biogeochemical behavior**

OPEN ACCESS

***Edited by:***
*Laodong Guo, University of Wisconsin–Milwaukee, United States*

***Reviewed by:***
*Ravi Bhushan, Physical Research Laboratory, India*
*Peng Lin, Texas A&M University at Galveston, United States*

***Correspondence:**
*Min Chen*
*mchen@xmu.edu.cn*

***Specialty section:***
*This article was submitted to Marine Biogeochemistry, a section of the journal Frontiers in Marine Science*

***Received:*** *27 April 2021*
***Accepted:*** *22 June 2021*
***Published:*** *15 July 2021*

***Citation:***
*Hu H, Liu X, Ren C, Jia R, Qiu Y, Zheng M and Chen M (2021) $^{210}$Po/$^{210}$Pb Disequilibria and Its Estimate of Particulate Organic Carbon Export Around Prydz Bay, Antarctica. Front. Mar. Sci. 8:701014. doi: 10.3389/fmars.2021.701014*

## INTRODUCTION

$^{210}$Po ($T_{1/2}$ = 138.4 days) and $^{210}$Pb ($T_{1/2}$ = 22.3 years) are radionuclides in $^{238}$U decay chain. Naturally occurring $^{210}$Po is a $\beta^-$-decay product of $^{210}$Pb via short-lived $^{210}$Bi ($T_{1/2}$ = 5.0 days), and $^{210}$Pb is produced throughout $^{226}$Ra decay via several short-lived isotopes ($^{222}$Rn, $^{218}$Po, $^{214}$Pb, etc.). $^{210}$Po mainly comes from *in-situ* decay of $^{210}$Pb in seawater, and $^{210}$Pb has three sources: atmospheric deposition, terrestrial runoff, and *in situ* production via $^{226}$Ra decay (Bacon et al., 1976; Moore and Smith, 1986; Nozaki et al., 1997; Wei et al., 2011; Kaste and Baskaran, 2012).

Unlike $^{210}$Pb mainly being adsorbed to particle surfaces, $^{210}$Po is additionally assimilated by phytoplankton (Nozaki et al., 1976; Cochran, 1992; Verdeny et al., 2009). The behavior difference results in a depletion of $^{210}$Po as compared to $^{210}$Pb in water column, which provides a tool for quantifying the adsorption rate by particles, and export flux on a seasonal-to-decadal timescale (Fisher et al., 1983; Cherrier et al., 1995; Stewart et al., 2005; Rigaud et al., 2014; Tang et al., 2019).

The Southern Ocean divides the polar parts from the warm tropical ocean, including the southern part of the Pacific, Atlantic, and Indian Oceans. Although it represents only 10% of the ocean surface area, it accounts for approximately 25% of the oceanic uptake of atmospheric $CO_2$ (Takahashi et al., 2002; Arrigo et al., 2008). The Prydz Bay, located in the Indian sector of the Southern Ocean, is the third largest bay in the Antarctica, following the Weddell Sea and the Ross Sea. Previous studies on $^{210}$Po and $^{210}$Pb in the Southern Ocean mainly focused on the Antarctic Circumpolar Current (ACC) (Shimmield et al., 1995; Friedrich and Rutgers van der Loeff, 2002), there is still very little research on Prydz Bay. $^{210}$Po/$^{210}$Pb and $^{234}$Th/$^{238}$U disequilibria have been used to estimate POC export flux in the Southern Ocean, but the results obtained by the two methods are sometimes different. The POC export fluxes estimated by $^{210}$Po/$^{210}$Pb disequilibria were significantly lower than those by $^{234}$Th/$^{238}$U disequilibria in the Bellingshausen Sea (Shimmield et al., 1995). In contrast, the POC export fluxes estimated by the two methods were similar in the ACC (Rutgers van der Loeff et al., 1997). Therefore, comparing the two methods not only helps to deepen the understanding of their applicability, but also helps to more accurately understand the temporal and spatial variability of the POC export flux.

Here, we report the activity concentrations of $^{210}$Po and $^{210}$Pb around Prydz Bay, including dissolved $^{210}$Po ($D^{210}Po$), particulate $^{210}$Po ($P^{210}Po$), dissolved $^{210}$Pb ($D^{210}Pb$), and particulate $^{210}$Pb ($P^{210}Pb$). The main objectives include: (1) revealing the distribution of $^{210}$Po and $^{210}$Pb around Prydz Bay; (2) assessing the factors affecting the disequilibria between$^{210}$Po and $^{210}$Pb; and (3) quantifying the export flux of POC via $^{210}$Po/$^{210}$Pb disequilibria, and compared with the result by $^{234}$Th/$^{238}$U disequilibria.

# MATERIALS AND METHODS

## Sampling

Seawater sample was collected using a Teflon-coated Niskin bottle assembled on a Sea-Bird SBE-911 rosette system (Sea-Bird Electronics Inc., United States) from January 31 to February 3, 2013 onboard R/V *XUELONG*. A total of 104 water samples (about 5 L each) was collected at different depths at six stations on the transect P7, covering the continental shelf (water depth from 200 to 400 m), continental slope (water depth of about 1,000 m), and the open ocean (water depth of about 3,500 m) (**Figure 1**). The water sample was filtered through a 0.4 μm polycarbonate membrane to separate the dissolved and particulate phases. The filtrate was acidified to pH <2 with approximately 20 mL concentrated HCl immediately. The particulate matter was frozen and stored at −20°C for further processing in the onshore laboratory.

## Measurements

Temperature and conductivity were measured by SBE-911 CTD, the accuracy of which was 0.001°C and 0.0003 S/m, respectively. The water sample used for nutrient determination was filtered through a 0.45 μm cellulose acetate membrane and stored in a 100 mL acid-cleaned HDPE bottle by adding saturated $HgCl_2$ solution. The nitrate ($NO_3$-N), phosphate ($PO_4$-P), and silicate ($SiO_3$-Si) was determined by the zinc-cadmium reduction method, molybdenum-blue method, and molybdate-blue method, respectively (Grasshoff et al., 1983).

The particulate matter in the water sample (5–10 L) was filtered on a pre-combusted 47 mm GF/F membrane (450°C, 4 h) for POC measurement. After the sample was dried at 60°C, it was stored frozen at −20°C. In the laboratory, the filter was fumigated with concentrated HCl for 48 h to remove inorganic carbonate. The sub-sample was encapsulated in a tin boat, and sent to the elemental analyzer (NC2500, Carlo Erba) for POC determination. The detection limit of POC is 0.1 μmolC, and the precision is 0.2% (Ren, 2015).

The dissolved sample was enriched with $^{210}$Po by co-precipitating with $Fe(OH)_3$, and purified by spontaneous deposition on a silver disk (4 h at 85°C). The mixed acid of $HNO_3$, $HClO_4$, and HCl was used to digest the particulate sample, and the subsequent procedure was the same as that of the dissolved sample. The radioactivity of $^{210}$Po was counted by an alpha spectrometer (Octête® Plus, EG&G) in Xiamen University. After the first self-deposition of $^{210}$Po, the sample solution was left for more than 9 months, and the second spontaneous deposition of $^{210}$Po was performed to determine the radioactivity of $^{210}$Po produced by the decay of $^{210}$Pb (Yang, 2005).

The radioactivity of $^{210}$Po in the sample was calculated by correcting the $^{210}$Po activity measured from the first self-deposition to the sampling time point. The calculation formula is as follows:

$$A_2^0 = \frac{A_2^1 - A_2^2 e^{\lambda_1 t_1}(e^{-\lambda_1 t_0} - e^{-\lambda_2 t_0})/(e^{-\lambda_1 t_2} - e^{-\lambda_2 t_2})R_1}{e^{-\lambda_2 t_0} R_2} - B$$

where $A_2^0$ is the activity concentration of $^{210}$Po at the time of sampling (Bq·m$^{-3}$); $A_2^1$ is the activity concentration of $^{210}$Po at the time of first self-deposition (Bq·m$^{-3}$); $t_0$ represents the time interval from sampling to the first self-deposition; $R_2$ represents the chemical recovery of $^{210}$Po, as determined by the $^{209}$Po tracer; $B$ denotes the blank in the analysis process.

In the calculation of $^{210}$Pb activity, considering that $^{210}$Pb has a long half-life (22.3 years) and the time interval from sampling to co-precipitation is short, the effects of $^{210}$Pb decay and ingrowth from sampling to co-precipitation could be ignored. Therefore, the $^{210}$Pb activity was corrected back to the time point of co-precipitation. The calculation formula is as follows:

$$A_1^0 = \frac{A_2^2(\lambda_2 - \lambda_1)}{\lambda_2 e^{-\lambda_1 t_1}(e^{-\lambda_1 t_2} - e^{-\lambda_2 t_2})R_1} - B$$

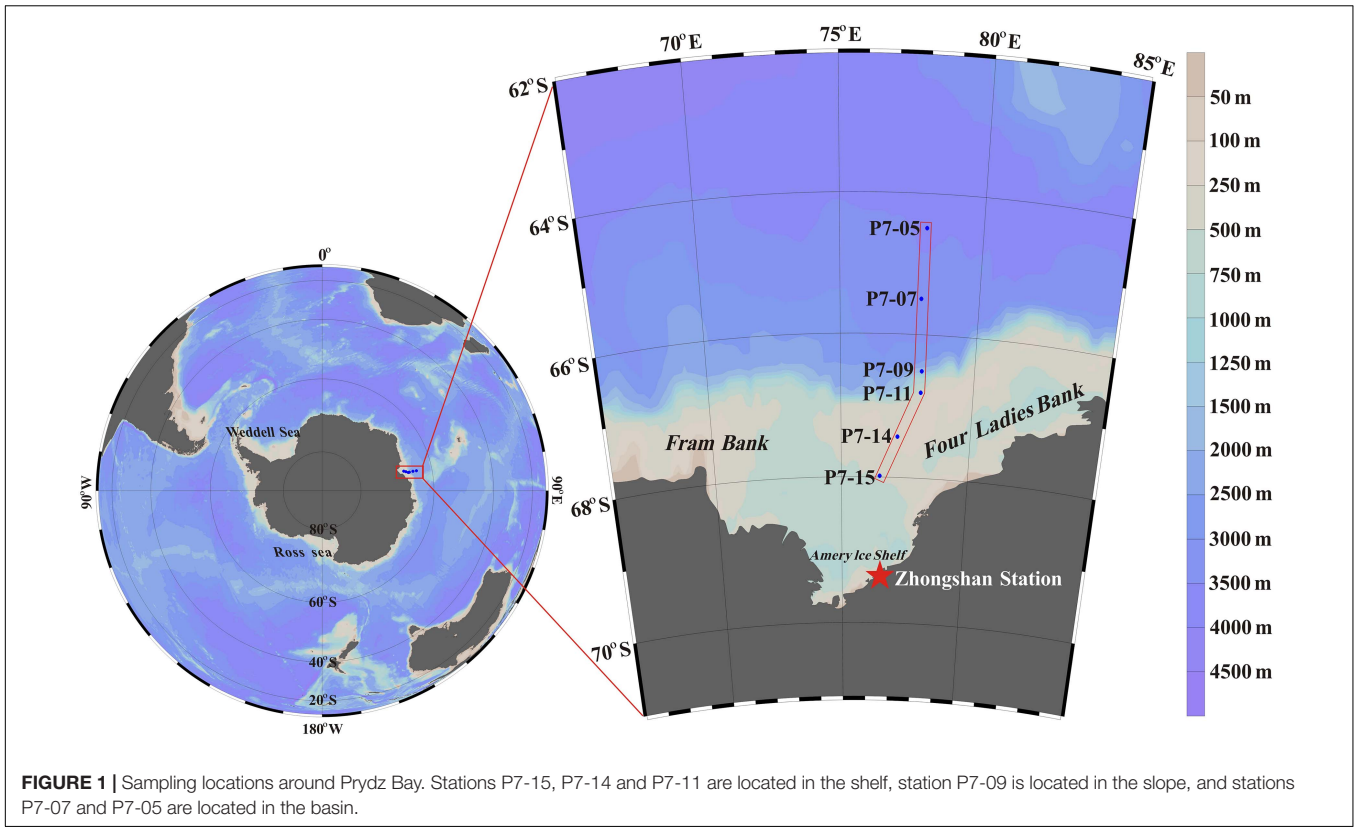


**FIGURE 1 |** Sampling locations around Prydz Bay. Stations P7-15, P7-14 and P7-11 are located in the shelf, station P7-09 is located in the slope, and stations P7-07 and P7-05 are located in the basin.

where $A_1^0$ is the activity of $^{210}$Pb at the time point of co-precipitation (that is, the activity of $^{210}$Pb in the sample, Bq·m$^{-3}$); $A_2^2$ is the $^{210}$Po activity measured from the second self-deposition sample (Bq·m$^{-3}$); $\lambda_1$ and $\lambda_2$ are the decay constants of $^{210}$Pb (0.031 a$^{-1}$) and $^{210}$Po (1.828 a$^{-1}$), respectively; $t_1$ and $t_2$ represent the time interval from co-precipitation to the first self-deposition and the time interval from the first to second self-deposition, respectively; $R_1$ represents the chemical recovery of $^{210}$Pb, which was determined by the stable Pb content measured by an atomic absorption spectroscopy; $B$ represents the blank in the analysis process.

The error of $^{210}$Po and $^{210}$Pb activity reported here is $\pm 1\sigma$ counting uncertainty.

## Estimation of POC Export Flux

Friedrich and Rutgers van der Loeff (2002) found that $^{210}$Po activity has a stronger correlation with POC and biogenic silica in the Southern Ocean, indicating that $^{210}$Po/$^{210}$Pb disequilibria is a reliable method for estimating the export flux of POC in the Southern Ocean. Similar to the $^{234}$Th approach (Buesseler et al., 1992, 2006; Stewart et al., 2007), the export flux of POC is calculated by multiplying the export flux of P$^{210}$Po (i.e., the removal flux of $^{210}$Po) by the POC/P$^{210}$Po ratio at the export interface (Shimmield et al., 1995). This is an empirical approach. It is not necessary to assume that POC and P$^{210}$Po have the same residence time. The calculation equation is as follows:

$$F_{POC} = F_{P^{210}Po} \cdot \frac{POC}{P^{210}Po}$$

where $F_{\mathrm{POC}}$ and $F_{P^{210}Po}$ represent the export flux of POC and P$^{210}$Po, respectively; $\frac{POC}{P^{210}Po}$ is the ratio of POC to P$^{210}$Po at the export interface.

The $F_{P^{210}Po}$ was calculated by a classical steady-state irreversible scavenging model after ignoring the atmospheric deposition flux of $^{210}$Po (Bacon et al., 1976; Friedrich and Rutgers van der Loeff, 2002; Masqué et al., 2002; Yang et al., 2006).

Here, the integration depth interval of P$^{210}$Po export is delineated according to the physical properties of water masses, namely, from 0 to 25 m (the mixed layer), from 50 to 200 m (the thermocline water), from 300 to 1,000 m (the CDW), and from 2,000 m to the bottom (the AABW), respectively. As the water depth of the continent shelf is relative shallow, it is divided into surface (from 0 to 25 m), subsurface (from 50 to 100 m), and deep layer (from 200 m to the bottom).

# RESULTS

## Hydrological Characteristics

The temperature in the upper water increased to the north outside Prydz Bay (**Figure 2A**). The summer surface water in the top 50 m layer has a salinity of about 33.8 and a maximum temperature of 0.8°C. Below the surface water, extremely low temperature and higher salinity appear, which are characteristics of the Winter Water (WW, $T < -1.5$°C, $34.2 < S < 34.56$). The formation of the WW is due to the weak mixing in the upper waters in summer, which causes the water to retain the

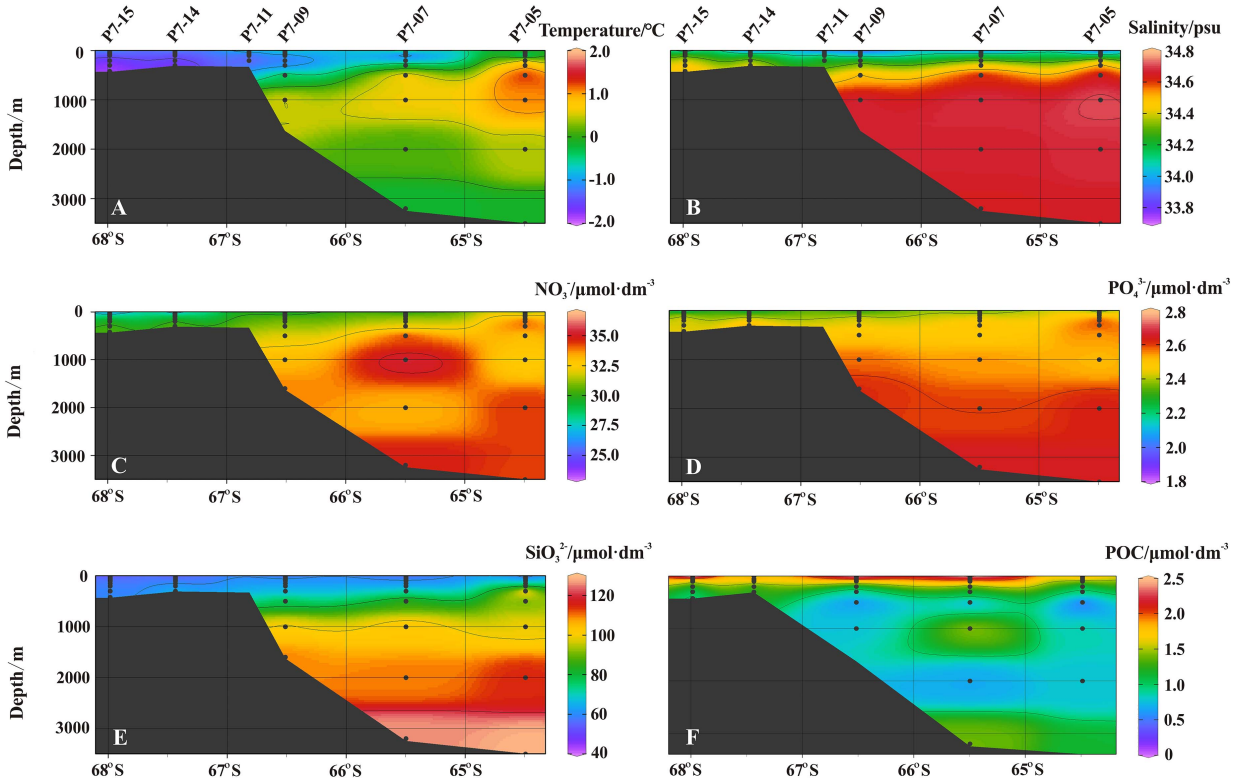


**FIGURE 2 |** The sectional distribution of **(A)** temperature (°C), **(B)** salinity (psu), **(C)** nitrate (μmol dm$^{-3}$), **(D)** phosphate (μmol dm$^{-3}$), **(E)** silicate (μmol dm$^{-3}$), and **(F)** POC (μmol dm$^{-3}$).

winter characteristics for a long time (Pu et al., 2002a). The water with a depth of 500–2,000 m shows the characteristics of high temperature and high salinity of Circumpolar Deep Water (CDW) ($T$ > 1.0°C, 34.5 < S < 34.75, **Figures 2A,B**). It is widely distributed in a large area around the continental shelf and is also one of the main water masses of Antarctic Circumpolar Current (ACC) (Pu et al., 2002b). Below the CDW (>2,000 m), the water mass with the highest salinity and the low temperature is called Antarctic Bottom Water (AABW), and its average temperature and salinity are −0.153 ± 0.022°C and 34.651 ± 0.001, respectively.

## Nutrients

Nitrate gradually increases from the shelf to the open ocean, while nitrite shows an increasing trend from north to south. Although the concentration of nitrate in surface water is low, it is still detectable. The concentration of nitrate in the bottom water increases, which may be due to the nitrification of ammonia released from the sediments (**Figure 2C**). The concentration of phosphate in the upper ocean is low, but it remains abundant at depths deeper than the mixed layer (**Figure 2D**). The vertical change of silicate in the shelf (Stns. P7-15, P7-14, and P7-11) is not obvious, but the profiles in the slope and the open ocean are different, in which the silicate increases as the depth increases. The highest silicate concentration appears near the bottom, which is attributed to the dissolution of biogenic silica in the sediments and subsequent transport to the overlying water (**Figure 2E**).

## POC

The POC concentration varies from 0.35 to 5.37 μmol/dm$^3$, with an average of 1.51 μmol/dm$^3$. The POC concentration in surface water falls in a range of 1.77–5.37 μmol/dm$^3$, with an average of 3.83 μmol/dm$^3$. In the upper 100 m water column, POC decreases significantly as the depth increases, which is resulted from the photosynthesis of phytoplankton and the degradation of organic matter. In addition, the POC concentration in the shelf is higher than those in the slope and the open ocean, reflecting the spatial variation of primary productivity. Note that the POC concentration in near-bottom water tends to increase, especially at stations P7-05, P7-07, and P7-09, which may reflect the effect of sediment resuspension (**Figure 2F**).

## $^{210}$Po and $^{210}$Pb

The activity concentrations of $^{210}$Po and $^{210}$Pb are shown in **Table 1**, and the sectional distribution along ∼78.0 °E is shown in **Figure 3**.

The activity concentration of D$^{210}$Po ranges from 0.47 to 3.20 Bq·m$^{-3}$, with an average of 1.44 ± 0.15 Bq·m$^{-3}$. The D$^{210}$Po in the shelf water (avg. 1.04 ± 0.11 Bq·m$^{-3}$) is lower than those in the slope (avg. 1.51 ± 0.15 Bq·m$^{-3}$) and open ocean (avg. 2.08 ± 0.20 Bq·m$^{-3}$). Compared with other water

**TABLE 1 |** The activity concentration of dissolved and particulate $^{210}$Po and $^{210}$Pb, and the activity ratio of $T^{210}Po/T^{210}Pb$.

| Depth (m) | $D^{210}Po$ | $P^{210}Po$ | $T^{210}Po$ | $D^{210}Pb$ | $P^{210}Pb$ | $T^{210}Pb$ | $T^{210}Po/T^{210}Pb)_{A.R.}$ |
|---|---|---|---|---|---|---|---|
| | | | | ($Bq \cdot m^{-3}$) | | | |
| **P7-05 (78.030 °E, 64.494 °S, 3,547 m)** | | | | | | | |
| 0 | 1.02 ± 0.11 | 0.29 ± 0.06 | 1.31 ± 0.13 | 2.12 ± 0.19 | 0.29 ± 0.04 | 2.40 ± 0.19 | 0.55 ± 0.07 |
| 25 | 1.24 ± 0.15 | 0.23 ± 0.05 | 1.47 ± 0.16 | 2.48 ± 0.22 | 0.20 ± 0.03 | 2.68 ± 0.22 | 0.55 ± 0.07 |
| 50 | 1.91 ± 0.14 | 0.29 ± 0.06 | 2.20 ± 0.15 | 2.62 ± 0.23 | 0.19 ± 0.02 | 2.82 ± 0.23 | 0.78 ± 0.08 |
| 75 | 2.15 ± 0.14 | 0.09 ± 0.03 | 2.24 ± 0.14 | 2.61 ± 0.25 | 0.15 ± 0.02 | 2.76 ± 0.25 | 0.81 ± 0.09 |
| 100 | 1.10 ± 0.14 | 0.16 ± 0.03 | 1.26 ± 0.14 | 2.70 ± 0.20 | 0.08 ± 0.01 | 2.78 ± 0.20 | 0.45 ± 0.06 |
| 200 | 2.38 ± 0.25 | 0.10 ± 0.03 | 2.48 ± 0.26 | 2.97 ± 0.25 | 0.19 ± 0.03 | 3.16 ± 0.25 | 0.78 ± 0.10 |
| 300 | 2.83 ± 0.28 | 0.18 ± 0.04 | 3.00 ± 0.29 | 2.88 ± 0.24 | 0.12 ± 0.02 | 2.99 ± 0.24 | 1.00 ± 0.12 |
| 500 | 3.20 ± 0.30 | 0.14 ± 0.03 | 3.34 ± 0.31 | 2.55 ± 0.21 | 0.10 ± 0.01 | 2.65 ± 0.21 | 1.26 ± 0.15 |
| 1,000 | 2.19 ± 0.23 | 0.16 ± 0.03 | 2.35 ± 0.24 | 2.46 ± 0.18 | 0.09 ± 0.01 | 2.55 ± 0.18 | 0.92 ± 0.11 |
| 2,000 | 2.64 ± 0.25 | 0.14 ± 0.03 | 2.78 ± 0.25 | 2.82 ± 0.21 | 0.11 ± 0.01 | 2.92 ± 0.21 | 0.95 ± 0.11 |
| 3,493 | 2.24 ± 0.23 | 0.16 ± 0.03 | 2.40 ± 0.23 | 2.17 ± 0.16 | 0.15 ± 0.02 | 2.32 ± 0.17 | 1.03 ± 0.12 |
| **P7-07 (77.919 °E, 65.497 °S, 3250 m)** | | | | | | | |
| 0 | 1.05 ± 0.13 | 0.36 ± 0.05 | 1.41 ± 0.14 | 2.08 ± 0.16 | 0.23 ± 0.03 | 2.31 ± 0.16 | 0.61 ± 0.08 |
| 25 | 1.18 ± 0.15 | 0.24 ± 0.06 | 1.43 ± 0.16 | 2.32 ± 0.18 | 0.48 ± 0.06 | 2.80 ± 0.19 | 0.51 ± 0.07 |
| 50 | 1.28 ± 0.15 | 0.31 ± 0.05 | 1.58 ± 0.15 | 2.19 ± 0.17 | 0.18 ± 0.02 | 2.37 ± 0.17 | 0.67 ± 0.08 |
| 75 | 0.98 ± 0.09 | 0.23 ± 0.04 | 1.21 ± 0.10 | 1.78 ± 0.16 | 0.11 ± 0.01 | 1.89 ± 0.16 | 0.64 ± 0.08 |
| 100 | 1.54 ± 0.18 | 0.13 ± 0.03 | 1.67 ± 0.18 | 2.52 ± 0.24 | 0.10 ± 0.01 | 2.62 ± 0.24 | 0.64 ± 0.09 |
| 200 | 1.21 ± 0.14 | 0.13 ± 0.03 | 1.34 ± 0.14 | 2.02 ± 0.18 | 0.13 ± 0.01 | 2.15 ± 0.18 | 0.62 ± 0.08 |
| 300 | 1.62 ± 0.19 | 0.17 ± 0.03 | 1.79 ± 0.19 | 2.35 ± 0.18 | 0.12 ± 0.01 | 2.46 ± 0.18 | 0.73 ± 0.09 |
| 500 | 2.47 ± 0.27 | 0.20 ± 0.04 | 2.68 ± 0.27 | 2.47 ± 0.22 | 0.13 ± 0.02 | 2.60 ± 0.23 | 1.03 ± 0.14 |
| 1,000 | 2.62 ± 0.20 | 0.17 ± 0.05 | 2.79 ± 0.21 | 2.67 ± 0.24 | 0.35 ± 0.04 | 3.02 ± 0.24 | 0.92 ± 0.10 |
| 2,000 | 2.65 ± 0.24 | 0.66 ± 0.09 | 3.31 ± 0.26 | 2.32 ± 0.20 | 0.16 ± 0.02 | 2.49 ± 0.20 | 1.33 ± 0.15 |
| 3,200 | 0.73 ± 0.10 | 0.25 ± 0.05 | 0.98 ± 0.11 | 1.89 ± 0.18 | 0.21 ± 0.03 | 2.09 ± 0.18 | 0.47 ± 0.07 |
| **P7-09 (78.029 °E, 66.511 °S, 1,628 m)** | | | | | | | |
| 0 | 1.21 ± 0.14 | 0.18 ± 0.06 | 1.39 ± 0.15 | 2.11 ± 0.16 | 0.37 ± 0.04 | 2.48 ± 0.16 | 0.56 ± 0.07 |
| 25 | 1.14 ± 0.13 | 0.18 ± 0.06 | 1.33 ± 0.15 | 1.89 ± 0.17 | 0.37 ± 0.04 | 2.26 ± 0.18 | 0.59 ± 0.08 |
| 50 | 0.95 ± 0.12 | 0.17 ± 0.05 | 1.12 ± 0.13 | 2.01 ± 0.16 | 0.15 ± 0.04 | 2.16 ± 0.17 | 0.52 ± 0.07 |
| 75 | 1.05 ± 0.10 | 0.09 ± 0.03 | 1.14 ± 0.10 | 1.96 ± 0.15 | 0.14 ± 0.02 | 2.10 ± 0.15 | 0.55 ± 0.06 |
| 100 | 1.20 ± 0.10 | 0.03 ± 0.02 | 1.23 ± 0.10 | 1.86 ± 0.15 | 0.14 ± 0.02 | 2.00 ± 0.15 | 0.62 ± 0.07 |
| 200 | 1.56 ± 0.13 | 0.12 ± 0.02 | 1.69 ± 0.13 | 1.82 ± 0.15 | 0.08 ± 0.01 | 1.90 ± 0.15 | 0.89 ± 0.10 |
| 300 | 1.23 ± 0.13 | 0.11 ± 0.03 | 1.35 ± 0.14 | 1.83 ± 0.15 | 0.13 ± 0.02 | 1.96 ± 0.15 | 0.69 ± 0.09 |
| 500 | 1.55 ± 0.13 | 0.15 ± 0.04 | 1.70 ± 0.14 | 1.77 ± 0.15 | 0.22 ± 0.03 | 1.99 ± 0.15 | 0.86 ± 0.10 |
| 1,000 | 2.98 ± 0.22 | 0.15 ± 0.04 | 3.13 ± 0.22 | 2.56 ± 0.18 | 0.16 ± 0.02 | 2.72 ± 0.18 | 1.15 ± 0.11 |
| **P7-11 (78.019 °E, 66.813 °S, 334 m)** | | | | | | | |
| 0 | 1.10 ± 0.12 | 0.51 ± 0.11 | 1.62 ± 0.16 | 1.50 ± 0.12 | 0.59 ± 0.06 | 2.09 ± 0.13 | 0.77 ± 0.09 |
| 25 | 1.26 ± 0.15 | 0.27 ± 0.06 | 1.52 ± 0.16 | 2.02 ± 0.17 | 0.15 ± 0.02 | 2.17 ± 0.17 | 0.70 ± 0.09 |
| 50 | 1.14 ± 0.11 | 0.30 ± 0.06 | 1.44 ± 0.12 | 2.06 ± 0.17 | 0.18 ± 0.02 | 2.24 ± 0.17 | 0.64 ± 0.07 |
| 75 | 1.18 ± 0.11 | 0.12 ± 0.02 | 1.29 ± 0.11 | 2.04 ± 0.17 | 0.09 ± 0.01 | 2.12 ± 0.18 | 0.61 ± 0.07 |
| 100 | 1.40 ± 0.12 | 0.12 ± 0.03 | 1.52 ± 0.13 | 2.31 ± 0.19 | 0.07 ± 0.01 | 2.38 ± 0.19 | 0.64 ± 0.07 |
| 200 | 1.68 ± 0.15 | 0.16 ± 0.03 | 1.85 ± 0.15 | 1.60 ± 0.13 | 0.09 ± 0.01 | 1.68 ± 0.13 | 1.10 ± 0.12 |
| **P7-14 (77.187 °E, 67.436 °S, 312 m)** | | | | | | | |
| 0 | 1.06 ± 0.12 | 0.21 ± 0.04 | 1.26 ± 0.12 | 1.77 ± 0.15 | 0.18 ± 0.02 | 1.95 ± 0.15 | 0.65 ± 0.08 |
| 25 | 1.11 ± 0.14 | 0.29 ± 0.07 | 1.39 ± 0.15 | 1.74 ± 0.15 | 0.24 ± 0.03 | 1.97 ± 0.15 | 0.71 ± 0.10 |
| 50 | 0.84 ± 0.09 | 0.13 ± 0.03 | 0.96 ± 0.10 | 1.64 ± 0.13 | 0.08 ± 0.01 | 1.72 ± 0.13 | 0.56 ± 0.07 |
| 75 | 0.86 ± 0.10 | 0.08 ± 0.03 | 0.94 ± 0.11 | 1.70 ± 0.14 | 0.10 ± 0.01 | 1.80 ± 0.14 | 0.52 ± 0.07 |
| 100 | 0.90 ± 0.10 | 0.04 ± 0.02 | 0.94 ± 0.10 | 1.81 ± 0.14 | 0.08 ± 0.01 | 1.89 ± 0.14 | 0.50 ± 0.06 |
| 200 | 0.73 ± 0.08 | 0.09 ± 0.03 | 0.81 ± 0.09 | 1.49 ± 0.11 | 0.08 ± 0.01 | 1.57 ± 0.11 | 0.52 ± 0.07 |
| 303 | 0.47 ± 0.08 | 0.03 ± 0.03 | 0.49 ± 0.09 | 1.26 ± 0.09 | 0.12 ± 0.02 | 1.38 ± 0.10 | 0.36 ± 0.07 |
| **P7-15 (76.517 °E, 67.984 °S, 436 m)** | | | | | | | |
| 0 | 1.11 ± 0.11 | 0.47 ± 0.07 | 1.58 ± 0.13 | 1.29 ± 0.10 | 0.26 ± 0.03 | 1.56 ± 0.10 | 1.01 ± 0.11 |
| 25 | 1.43 ± 0.14 | 0.43 ± 0.07 | 1.85 ± 0.15 | 1.43 ± 0.11 | 0.11 ± 0.01 | 1.55 ± 0.11 | 1.20 ± 0.13 |

*(Continued)*

**TABLE 1** | Continued

| Depth (m) | $D^{210}Po$ | $P^{210}Po$ | $T^{210}Po$ | $D^{210}Pb$ | $P^{210}Pb$ | $T^{210}Pb$ | $T^{210}Po/T^{210}Pb)_{A.R.}$ |
|---|---|---|---|---|---|---|---|
| | | | (Bq·m$^{-3}$) | | | | |
| 50 | 0.77 ± 0.09 | 0.07 ± 0.03 | 0.83 ± 0.10 | 2.16 ± 0.17 | 0.07 ± 0.01 | 2.23 ± 0.17 | 0.37 ± 0.05 |
| 75 | 1.08 ± 0.12 | 0.08 ± 0.03 | 1.16 ± 0.12 | 1.70 ± 0.12 | 0.07 ± 0.01 | 1.77 ± 0.12 | 0.66 ± 0.08 |
| 100 | 0.62 ± 0.08 | 0.03 ± 0.03 | 0.66 ± 0.08 | 1.76 ± 0.12 | 0.07 ± 0.01 | 1.83 ± 0.13 | 0.36 ± 0.05 |
| 200 | 1.02 ± 0.09 | 0.05 ± 0.03 | 1.07 ± 0.10 | 1.43 ± 0.10 | 0.10 ± 0.01 | 1.53 ± 0.11 | 0.70 ± 0.08 |
| 300 | 1.26 ± 0.10 | 0.08 ± 0.03 | 1.34 ± 0.11 | 1.15 ± 0.11 | 0.11 ± 0.01 | 1.26 ± 0.11 | 1.06 ± 0.13 |
| 425 | 0.87 ± 0.09 | 0.09 ± 0.03 | 0.96 ± 0.09 | 1.39 ± 0.10 | 0.11 ± 0.01 | 1.51 ± 0.10 | 0.64 ± 0.08 |

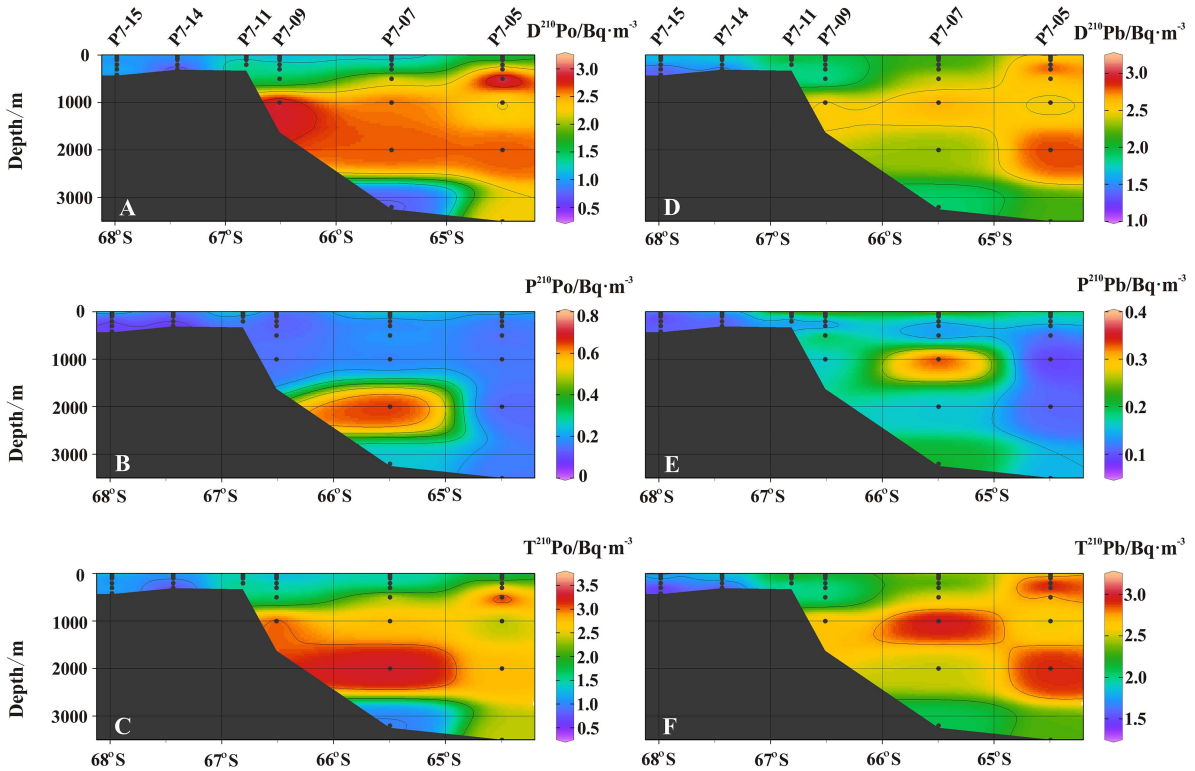


**FIGURE 3 |** The sectional distribution of **(A)** dissolved $^{210}$Po (Bq/m$^3$), **(B)** particulate $^{210}$Po (Bq·m$^{-3}$), **(C)** total $^{210}$Po (Bq·m$^{-3}$), **(D)** dissolved $^{210}$Pb (Bq·m$^{-3}$), **(E)** particulate $^{210}$Pb (Bq·m$^{-3}$), and **(F)** total $^{210}$Pb (Bq·m$^{-3}$).

masses, the $D^{210}Po$ in CDW is higher ($p < 0.0001$, one-way ANOVA, **Figure 3A**). The activity concentration of $P^{210}Po$ varies in a wide range from 0.03 to 0.66 Bq·m$^{-3}$, with an average of 0.18 ± 0.04 Bq·m$^{-3}$. The vertical variation of $P^{210}Po$ in the shelf decreases as the depth increases. The activity concentration of $P^{210}Po$ in the slope is mostly stable at about 0.13 Bq·m$^{-3}$, but an abnormally high value appears at a depth of 2,000 m at station P7-07. The activity concentration of $P^{210}Po$ in surface water (upper 50 m) of the open ocean is higher than that in the shelf and slope, with an average of 0.27 ± 0.06 Bq·m$^{-3}$ (**Figure 3B**). The activity concentration of $T^{210}Po$ is mainly contributed by $D^{210}Po$, and its value is between 0.49 and 3.34 Bq·m$^{-3}$ (avg. 1.63 ± 0.15 Bq·m$^{-3}$). The $T^{210}Po$ in the surface and the bottom layer is lower than that in the CDW. In general, the $T^{210}Po$ shows a decreasing trend from open ocean (avg. 2.26 ± 0.21 Bq·m$^{-3}$) to the slope (avg. 1.71 ± 0.16 Bq·m$^{-3}$) and the shelf (avg. 1.21 ± 0.12 Bq·m$^{-3}$) (**Figure 3C**). This spatial variation is attributed to the high biological productivity and the active sediment resuspension in the shelf, resulting in the rapid scavenging of particle-reactive radionuclides (Chen et al., 2012). The vertical change of $T^{210}Po$ in the shelf is small, which indicates that the particle scavenging is strong in the entire water column.

The distribution pattern of $D^{210}Pb$ is generally similar to that of $D^{210}Po$ (**Figures 3A,D**). The variation range of $D^{210}Pb$ is from 1.15 to 2.97 Bq·m$^{-3}$, with the lowest in the shelf and the highest in the open ocean ($p < 0.001$, one-way ANOVA, **Figure 3D**). The $D^{210}Pb$ is lower in surface water due to more effective particle scavenging, while the $D^{210}Pb$ increases in the subsurface and deep water. The higher $D^{210}Pb$ in CDW is affected by the remineralization of particulate organic matter (Bacon et al., 1976;

Somayajulu and Craig, 1976; Thomson and Turekian, 1976; Wei et al., 2011). The activity concentration of $P^{210}Pb$ ranges from 0.07 to 0.59 Bq·m$^{-3}$. In the shelf, the $P^{210}Pb$ is higher in surface water, and lower in deep water (0.07–0.11 Bq·m$^{-3}$) (**Figure 3E**). The activity concentration of $T^{210}Pb$ ranges from 1.26 to 3.16 Bq·m$^{-3}$, with an average of 2.20 ± 0.17 Bq·m$^{-3}$ (**Table 1**). The $T^{210}Pb$ in the surface water is the lowest, especially in the shelf (**Figure 3F**), indicating that $^{210}$Pb is effective scavenged by particles. The activity concentration of $T^{210}Pb$ in CDW (2.49–3.02 Bq·m$^{-3}$) is higher than that in other water masses ($p < 0.002$, one-way ANOVA), which is consistent with the highest $T^{210}Pb$ (~3 Bq·m$^{-3}$) in ACC reported previously (Rama et al., 1961; Somayajulu and Craig, 1976; Chung and Applequist, 1980; Chung, 1981).

# DISCUSSION

## $^{210}$Po/$^{210}$Pb Disequilibria

The activity ratio of $T^{210}Po/T^{210}Pb$ ranges from 0.36 to 1.33, and shows a widespread deficiency of $^{210}$Po with respect to $^{210}$Pb around Prydz Bay (**Figure 4**). The average value of $(T^{210}Po/T^{210}Pb)_{A.R.}$ in the upper 100 m water column is 0.66, reflecting the influence of biological activity and particle scavenging. Compared with $^{210}$Pb, organisms preferentially absorb $^{210}$Po, and organic tissues have a stronger affinity for $^{210}$Po (Bacon et al., 1976; Cochran et al., 1983; Stewart and Fisher, 2003; Stewart et al., 2007; Yang et al., 2009), which leads to more effective removal of $^{210}$Po from the euphotic zone. Under the combined action of biological absorption and particle adsorption, the $T^{210}Po/T^{210}Pb$ ratio in the shelf is lower than those in the slope and open ocean (compare the right and left panels in **Figure 4**), which is consistent with the observed low nutrients and high POC in the shelf (**Figure 2**).

Some previous studies have shown a secular equilibrium is reached between $^{210}$Pb and $^{210}$Po in water deeper than 1000 m, such as the North Atlantic (Bacon et al., 1976), the South Pacific (Turekian and Nozaki, 1980), and the Indian Ocean (Chung and Finkel, 1988). However, a large deficiency of $^{210}$Po has been found in deep waters of some seas, such as the East China Sea and the Philippine Sea (Nozaki et al., 1990), the equatorial Pacific and the Bering Sea (Nozaki et al., 1997), the Sargasso Sea (Kim and Church, 2001), and the South China Sea (Chung and Wu, 2005; Hong et al., 2013). In this study, most of the $^{210}$Po in deep water around Prydz Bay are in equilibrium with $^{210}$Pb, but there is an excess or deficiency of $^{210}$Po at certain depths at some sites (**Figure 4**). These disequilibria may be caused by differences in particle composition. Hong et al. (2013) found a positive correlation between the flux of $P^{210}Po$ and the flux of calcium carbonate, while no correlation between $P^{210}Pb$ and calcium carbonate. However, Niedermiller and Baskaran (2019) found a significant negative correlation between the inventories of $T^{210}Pb$ and particulate Al, but no correlation between $^{210}$Po and particulate Al, suggesting much less removal of $^{210}$Po by lithogenic material compared to $^{210}$Pb. Therefore, detailed mineralogical and chemical composition of particles play an important role in deep water scavenging.

The activity ratios of $T^{210}Po/T^{210}Pb$ are less than 1.0 in the bottom water of some sites, such as Stns. P7-15, P7-14, and P7-07 (**Figure 4**), indicating that boundary scavenging results in preferential removal of $^{210}$Po over $^{210}$Pb. The resuspension of sediments may increase the concentration of particles in near-bottom water, thereby enhancing the scavenging and removal of $^{210}$Po in the benthic boundary layer, similar to what happens in

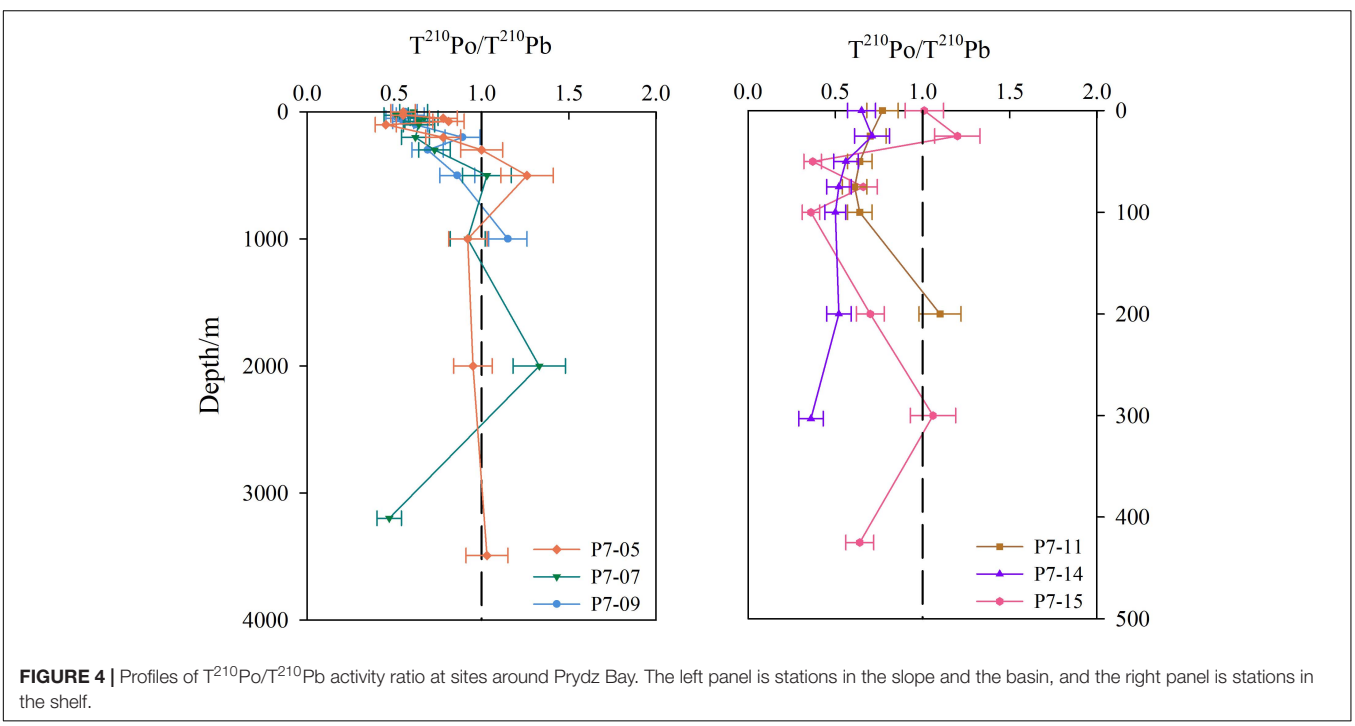


**FIGURE 4 |** Profiles of $T^{210}Po/T^{210}Pb$ activity ratio at sites around Prydz Bay. The left panel is stations in the slope and the basin, and the right panel is stations in the shelf.

the euphotic zone. Ma (2006) found that $^{210}$Po in the bottom water of the Northeast Pacific was depleted relative to $^{210}$Pb (the average ratio of T$^{210}$Po/T$^{210}$Pb was 0.64), which was attributed to the effect of benthic boundary scavenging.

## High Activity Concentrations of $^{210}$Po and $^{210}$Pb in CDW

The CDW around Prydz Bay mainly exists in a depth range of 200–2,000 m, and it upwells during southward movement due to the effect of the seabed topography (Smith et al., 1984; Pu and Dong, 2003; Pu et al., 2007). Our results show that CDW has the highest activity concentrations of $^{210}$Po and $^{210}$Pb compared with other water masses ($p < 0.01$, one-way ANOVA, **Figure 5**). The reason is worthy of in-depth study.

The half-life of$^{210}$Pb is relatively long (22.3 years), so lateral transport is one of the important factors affecting its redistribution in seawater (Smoak et al., 1996; Moran et al., 1997). Ku and Lin (1976) measured $^{226}$Ra in deep water south of the Antarctic Convergence Zone, and found that the distribution of $^{226}$Ra is related to the latitudinal transport of the circumpolar current from the Pacific sector to the Atlantic sector. Hanfland (2002) found that the highest activity concentration of $^{226}$Ra (about 3.08 Bq·m$^{-3}$) was stable in the ACC. $^{226}$Ra is a soluble radionuclide with a half-life of 1602 years. The movement of ACC around the Antarctic continent causes $^{226}$Ra to accumulate in the CDW and present a uniform characteristics. Therefore, the high activity concentration of $^{210}$Pb in CDW is attributed to the *in situ* decay of $^{226}$Ra.

However, for the $^{210}$Po in CDW, only considering the *in situ* production by $^{210}$Pb decay cannot explain the $^{210}$Po excess we observed (**Figure 5**). Due to the short half-life of $^{210}$Po (138.4 days), the horizontal transport of the water mass cannot retain the excess signal of $^{210}$Po for a long time. Therefore, the $^{210}$Po in CDW is more likely to be supplied by local source. In the process of remineralization of POM, both $^{210}$Po and $^{210}$Pb are released into the dissolved phase, but the priority of $^{210}$Po can lead to an excess of $^{210}$Po over $^{210}$Pb, because more $^{210}$Po is bound to organic matter (Shimmield et al., 1995; Nozaki et al., 1997; Wei et al., 2011). Therefore, the remineralization of particulate organic matter is most likely to be responsible for the high $^{210}$Po and its excess in the CDW. A similar situation was observed in the 100–300 m layer in the eastern North Atlantic and the intermediate layer in the northwestern North Pacific, which was attributed to the remineralization of biogenic particles or measurement errors (Bacon et al., 1976; Kawakami et al., 2008).

## Estimates of POC Export Flux

Our results show that there is a good positive correlation between the solid to liquid ratio of $^{210}$Po (i.e., P$^{210}$Po/D$^{210}$Po) and POC, while $^{210}$Pb does not (**Figure 6**). This confirms that particulate organic matter regulates the biogeochemical cycle of $^{210}$Po, and it is feasible to use $^{210}$Po/$^{210}$Pb disequilibria to estimate POC export flux around Prydz Bay.

Based on the $^{210}$Po/$^{210}$Pb disequilibria, the POC export flux in the entire water column varies from 0.8–31.9 mmol·m$^{-2}$·d$^{-1}$, among which the variation ranges in the open ocean, the slope and the shelf are 0.8–20.2, 1.5–4.8, and 4.8–31.9 mmol·m$^{-2}$·d$^{-1}$, respectively (**Table 2**). Note that the calculated $F_{POC}$ at station P7-15 is negative, which is caused by a slight excess of $^{210}$Po over $^{210}$Pb. In this case, the removal flux of $^{210}$Po calculated by the model may not represent the real situation and will not be considered in the subsequent discussion. As shown in **Figure 7**, the POC export flux in the upper water column in the shelf is higher than that in the slope and the open ocean ($p < 0.05$, one-way ANOVA). The high POC export is consistent with active biological activities in the shelf. Previous studies have shown that

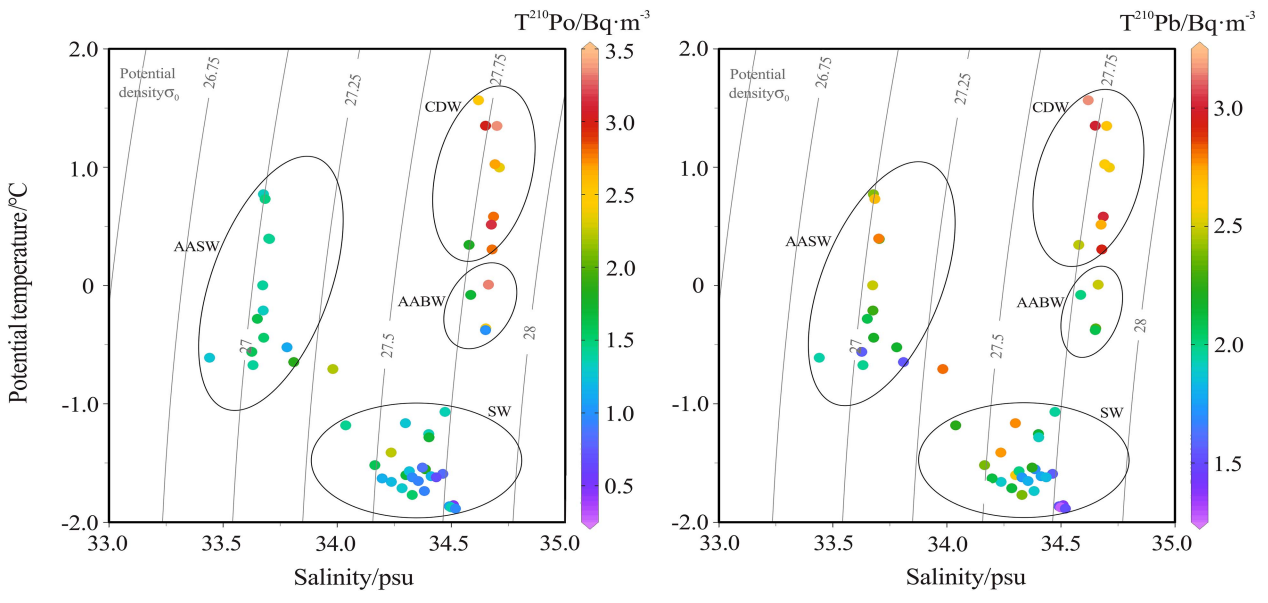


**FIGURE 5 |** Scatter plots of T$^{210}$Po (left panel) and T$^{210}$Pb activity concentration (right panel) versus potential temperature and salinity.

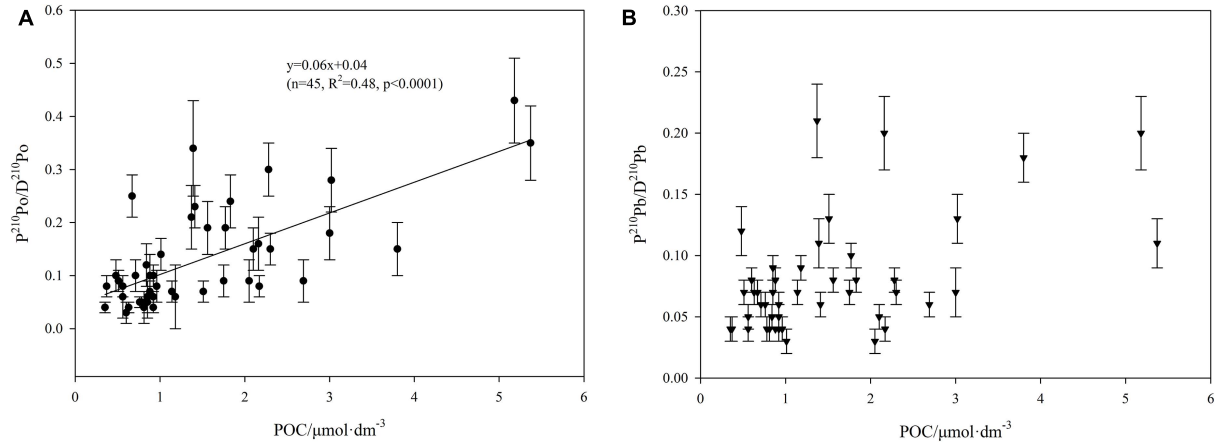


**FIGURE 6 |** The relationship between $P^{210}Po/D^{210}Po$ ratio, $P^{210}Pb/D^{210}Pb$ ratio, and POC concentration (**A**: $P^{210}Po/D^{210}Po$ ratio vs POC, **B**: $P^{210}Po/D^{210}Po$ ratio vs POC).

the Chl-*a* concentration and primary productivity in Prydz Bay are significantly higher than those outside the bay, and there is a positive correlation between the Chl-*a* and POC in the euphotic zone (Liu et al., 2002; Qiu et al., 2004; Cai et al., 2005; Han et al., 2011; Yu et al., 2011; Sun et al., 2012). The active photosynthesis in the upper water enhances the export of POC to the deep sea in Prydz Bay. In fact, the POC export flux in deep water in the shelf (such as Stn. P7-14 and P7-15) is also higher than that in the slope and the open ocean.

In addition to $^{210}$Po/$^{210}$Pb disequilibria,$^{234}$Th/$^{238}$U disequilibria have also been widely used to estimate the POC export flux in the euphotic zone (Murray et al., 1989, 2005; Shimmield et al., 1995; Kim and Church, 2001; Friedrich and Rutgers van der Loeff, 2002; Stewart et al., 2007; Buesseler et al., 2008; Wei et al., 2011). However, the different half-lives of $^{234}$Th and $^{210}$Po and their different affinities for particulate matter (Po >> Pb ≈ Th >> Ra > U) may cause differences in the POC export fluxes estimated by the two methods (Kharkar et al., 1976; Murray et al., 2005). It is of great significance to compare the POC export flux obtained by the two methods. Since most of the reports based on $^{234}$Th/$^{238}$U disequilibria are concerned with the POC export at a depth of 100 m, here we focus on comparing the POC export at this interface. Based on $^{210}$Po/$^{210}$Pb disequilibria, POC export flux at 100 m depth interface around Prydz Bay is estimated to be in a range of 4.2–9.0 mmol $m^{-2}$ $d^{-1}$, with an average of 6.9 mmol $m^{-2}$ $d^{-1}$, which is comparable to most previously reported values in Antarctica seas, whether based on $^{234}$Th/$^{238}$U or $^{210}$Po/$^{210}$Pb disequilibria (**Table 3**). Yang et al. (2009) estimated by $^{210}$Po/$^{210}$Pb disequilibria that the POC export flux at a site (64.00 °S, 73.00 °E) outside Prydz Bay is 2.3 mmol $m^{-2}$ $d^{-1}$, which is slightly lower than this study. Note that its site is located in the northern part of our sites and is more affected by the ACC upwelling, its lower POC export is reasonable. In contrast, the reported POC export fluxes at the 100 m interface in Prydz Bay via $^{234}$Th/$^{238}$U disequilibria (17.1−117.2 mmol $m^{-2}$ $d^{-1}$, avg. 63.5 mmol $m^{-2}$ $d^{-1}$, He et al., 2007) were 9.2 times of our estimates on average, even though the sampling season and locations are close. We found that the POC concentration in the He et al. (2007) (avg. 17.5 μmol/$dm^3$) was on average 8.3 times that of this study (avg. 2.1 μmol/$dm^3$), which resulted in a significant increase in their POC export flux. Considering that biological activities in the Antarctic seas often show large interannual and temporal variability, it cannot be ruled out that the changes in phytoplankton growth have led to such large differences.

The difference in the POC export flux obtained between the $^{234}$Th method and the $^{210}$Po method has also been found in the study of the equatorial Pacific Ocean (Murray et al., 1989),

**TABLE 2 |** POC export flux at different depth interfaces estimated from $^{210}$Po/$^{210}$Pb disequilibria.

| Station | Depth interface | $F_{PPo}$ | $POC/P^{210}Po$ | $F_{POC}$ |
|---|---|---|---|---|
| | (m) | (Bq·$m^{-2}$ $d^{-1}$) | (mmol $Bq^{-1}$) | (mmol $m^{-2}$ $d^{-1}$) |
| P7-05 | 25 | 0.14 ± 0.02 | 6.8 ± 1.4 | 1.0 ± 0.3 |
| | 200 | 0.63 ± 0.17 | 6.3 ± 2.0 | 4.0 ± 1.6 |
| | 1,000 | 0.97 ± 0.83 | 5.5 ± 1.1 | 5.3 ± 4.7 |
| | 3,493 | 1.19 ± 1.62 | 7.1 ± 1.4 | 8.4 ± 11.6 |
| P7-07 | 25 | 0.14 ± 0.02 | 5.6 ± 1.3 | 0.8 ± 0.2 |
| | 200 | 0.74 ± 0.12 | 5.6 ± 1.3 | 4.2 ± 1.2 |
| | 1,000 | 2.32 ± 0.72 | 8.7 ± 2.4 | 20.2 ± 8.4 |
| | 3,200 | 3.19 ± 1.18 | 5.6 ± 1.2 | 17.9 ± 7.6 |
| P7-09 | 25 | 0.13 ± 0.02 | 11.9 ± 3.8 | 1.5 ± 0.5 |
| | 200 | 0.60 ± 0.11 | 3.0 ± 0.6 | 1.8 ± 0.5 |
| | 1,000 | 0.95 ± 0.62 | 5.0 ± 1.2 | 4.8 ± 3.3 |
| P7-14 | 25 | 0.08 ± 0.02 | nd[a] | nd |
| | 100 | 0.29 ± 0.03 | 21.8 ± 13.2 | 6.4 ± 3.9 |
| | 303 | 0.71 ± 0.05 | 44.7 ± 50.2 | 31.9 ± 35.9 |
| P7-15 | 25 | −0.02 ± 0.02 | 5.4 ± 0.8 | −0.1 ± 0.1 |
| | 100 | 0.30 ± 0.03 | 16.0 ± 11.8 | 4.8 ± 3.6 |
| | 425 | 0.87 ± 0.11 | 9.6 ± 3.4 | 8.4 ± 3.2 |

[a]*nd means no data.*

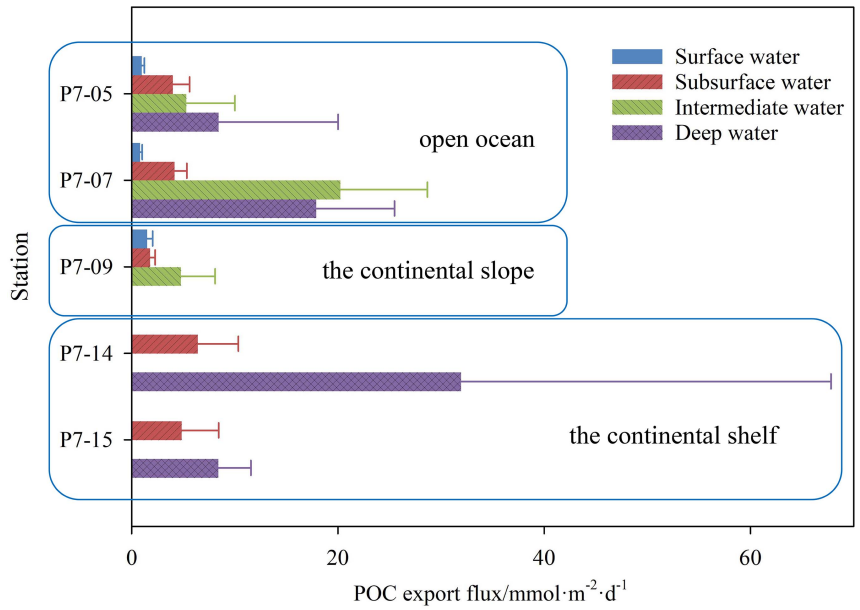


**FIGURE 7 |** The export flux of POC at different depth interface in the shelf, slope, and basin.

**TABLE 3 |** The POC export flux at a depth of 100 m in the Southern Ocean estimated from $^{234}$Th/$^{238}$U to $^{210}$Po/$^{210}$Pb disequilibria.

| Method | Sampling month | Region | $F_{POC}$ (mmol m$^{-2}$ d$^{-1}$) | References |
|---|---|---|---|---|
| $^{234}$Th | December | Bellingshausen Sea | 21 | Shimmield et al., 1995 |
| $^{234}$Th[a] | October–December | Polar Front (49 °S) | 13–26 | Rutgers van der Loeff et al., 1997 |
| | | Southern ACC (57 °S) | 3–5 | |
| | | Marginal Ice Zone (51 °S) | 11–20 | |
| $^{234}$Th | October–November | Ross Sea | 0–4 | Cochran et al., 2000 |
| | January–February | | 7–91 | |
| | March–May | | 2–22 | |
| $^{234}$Th | October–March | Southern Ocean[b] | 5–45 | Buesseler et al., 2001 |
| $^{234}$Th | October–November | Polar Front | 14.1–84.1 | Friedrich and Rutgers van der Loeff, 2002 |
| | | Southern ACC | 17.4–38.7 | |
| $^{234}$Th | January–February | Prydz Bay | 29.5–262.4 | He et al., 2007 |
| $^{210}$Po | December | Bellingshausen Sea | 0.03–2.2 | Shimmield et al., 1995 |
| $^{210}$Po | October–November | Southern ACC | 14.1–84.1 | Friedrich and Rutgers van der Loeff, 2002 |
| $^{210}$Po | February | Prydz Bay | 2.3 | Yang et al., 2009 |
| $^{210}$Po | January–February | Prydz Bay | 4.2–9.0 | This study |

[a] *A latitudinal transect along 6 °W.*
[b] *A latitudinal transect along 170 °W.*

the Mediterranean Sea (Stewart et al., 2007), the Bellingshausen Sea (Shimmield et al., 1995), and the Antarctic Circumpolar Current (Friedrich and Rutgers van der Loeff, 2002; Verdeny et al., 2009). The difference in the time scale and biogeochemical behavior between $^{234}$Th and $^{210}$Po is proposed to be responsible for this. The half-life of $^{234}$Th is relatively short (24.1 days), it records the export of particulate matter in a short time scale, including occasional blooms in productive sea areas, while $^{210}$Po has a longer half-life (138.4 days), and its record is more likely to be smoothed and homogenized. In addition, in the one-dimensional steady-state model for calculating the export flux of nuclides, the physical processes such as advection, upwelling, and horizontal transport are ignored. This may have different effects on different nuclides, leading to deviations in the calculated export flux. For example, the upwelling brings deep water with a high activity concentration of $^{210}$Po or $^{234}$Th to the surface, which underestimates the POC export flux. The underestimation of the $^{210}$Po method may be greater because $^{210}$Po has a longer half-life. The difference in biogeochemical behavior between $^{234}$Th and $^{210}$Po is another possibility (Fisher et al., 1983; Murray et al., 2005). In the Bellingshausen Sea, the POC export flux estimated by the $^{234}$Th method is higher than that by the $^{210}$Po method, which is attributed to the fact that $^{234}$Th tends to be adsorbed by lithogenic materials (Shimmield et al., 1995). Friedrich and Rutgers van der Loeff (2002) found that in the ACC, $^{234}$Th is easier to bind with biogenic silica, while $^{210}$Po has a stronger

affinity for POC. Murray et al. (2005) pointed out that $^{210}$Po can be absorbed into cells by organisms, while $^{234}$Th is only adsorbed on particle surface, thereby $^{210}$Po may be more conducive to tracking the export of POC. As the phytoplankton around Prydz Bay grows rapidly in summer (Liu et al., 2002; Qiu et al., 2004; Cai et al., 2005), $^{210}$Po/$^{210}$Pb disequilibria is an ideal method to estimate the POC export flux in this case.

Although the values of POC export flux estimated by the two methods are different, their spatial distributions are similar around Prydz Bay, showing that the POC export flux at the 100 m interface in the shelf is higher than those in the slope and open ocean (**Figure 7**). It is worth noting that He et al. (2007) observed an extremely high POC export flux at 50 m in the slope, which was attributed to the rising CDW transporting nutrients to the surface, stimulating the primary productivity and the removal of $^{234}$Th. However, judging from our $^{210}$Po/$^{210}$Pb results, the upwelling of CDW may lead to an underestimation of $^{210}$Po export flux due to the impact of organic matter remineralization. In addition, we noticed that the POC/P$^{210}$Po ratios in the slope are closer to those in the shelf. Therefore, horizontal transport across the shelf may partially compensate for the underestimated $^{210}$Po export's impact on the POC export flux.

## CONCLUSION

In this study, dissolved and particulate $^{210}$Po and $^{210}$Pb were measured in the entire water column around Prydz Bay. Our results show that the D$^{210}$Po and D$^{210}$Pb in the shelf are lower than those in the slope and the open ocean, indicating an enhanced particle scavenging in the shelf. Among the various water masses, the CDW has the highest activity concentrations of T$^{210}$Pb and T$^{210}$Po, reflecting the effects of $^{210}$Pb decay and POM remineralization. Our results show that there is a good positive correlation between the solid-liquid ratio of $^{210}$Po and POC, while $^{210}$Pb does not. This indicates that particulate organic matter regulates the biogeochemical cycle of $^{210}$Po, and $^{210}$Po/$^{210}$Pb disequilibria is a reliable method for estimating the POC export flux around Prydz Bay. The estimated POC export flux based on $^{210}$Po/$^{210}$Pb disequilibria ranges from 0.8 to 31.9 mmol $m^{-2}$ $d^{-1}$. The higher POC export at the 100 m interface in the slope is attributed to the horizontal transport across the shelf. Although the difference in biogeochemical behavior and time scale between $^{210}$Po and $^{234}$Th may affect the estimated POC export flux, the spatial variation of POC export flux estimated by these two methods is consistent, which shows that $^{210}$Po/$^{210}$Pb disequilibria is a reliable method for POC export.

## DATA AVAILABILITY STATEMENT

The original contributions presented in the study are included in the article/supplementary material, further inquiries can be directed to the corresponding author.

## AUTHOR CONTRIBUTIONS

HH and MC designed the study and wrote the manuscript. XL sampled onboard and measured $^{210}$Po. CR determined POC. RJ sampled and revised the manuscript. YQ and MZ contributed the experimental tools. All authors contributed to the article and approved the submitted version.

## FUNDING

This work was supported by Impact and Response of Antarctic Seas to Climate Change (IRASCC 01-01-02C and 02-01-01) and funded by Ministry of Natural Resources of the People's Republic of China and Chinese Arctic and Antarctic Administration, National Natural Science Foundation of China (41721005), and Program funded by China Ocean Mineral Resources R&D Association (No. DY135-13-E2-03).

## ACKNOWLEDGMENTS

As with most endeavors, we owe thank to a number of people: Jianming Pan and Zhengbing Han for providing nutrient data, the captains and crews of R/V *XUELONG* for their assistance in sampling, and colleagues in the SCSEMC for supporting efforts.

## REFERENCES

Arrigo, K. R., Van Dijken, G. L., and Bushinsky, S. (2008). Primary production in the Southern Ocean, 1997–2006. *J. Geophys. Res.* 113:C08004. doi: 10.1029/2007JC004551

Bacon, M. P., Spencer, D. W., and Brewer, P. G. (1976). $^{210}$Pb/$^{226}$Ra and $^{210}$Po/$^{210}$Pb disequilibria in seawater and suspended particulate matter. *Earth Planet. Sci. Lett.* 32, 277–296. doi: 10.1016/0012-821X(76)90068-6

Buesseler, K. O., Bacon, M. P., Cochran, J. K., and Livingston, H. D. (1992). Carbon and nitrogen export during the JGOFS North Atlantic Bloom experiment estimated from $^{234}$Th: $^{238}$U disequilibria. *Deep Sea Res. I* 39, 1115–1137. doi: 10.1016/0198-0149(92)90060-7

Buesseler, K. O., Ball, L., Andrews, J., Cochran, J. K., Hirschberg, D. J., Bacon, M. P., et al. (2001). Upper ocean export of particulate organic carbon and biogenic silica in the Southern Ocean along 170°W. *Deep Sea Res. II* 48, 4275–4297. doi: 10.1016/S0967-0645(01)00089-3

Buesseler, K. O., Benitez-Nelson, C. R., Moran, S. B., Burd, A., Charette, M., Cochran, J. K., et al. (2006). An assessment of particulate organic carbon to thorium-234 ratios in the ocean and their impact on the application of $^{234}$Th as a POC flux proxy. *Mar. Chem.* 100, 213–233. doi: 10.1016/j.marchem.2005.10.013

Buesseler, K. O., Lamborg, C., Cai, P., Escoube, R., Johnson, R., Pike, S., et al. (2008). Particle fluxes associated with mesoscale eddies in the Sargasso Sea. *Deep Sea Res. II* 55, 1426–1444. doi: 10.1016/j.dsr2.2008.02.007

Cai, Y. M., Ning, X. R., Zhu, G. H., and Shi, J. X. (2005). Size fractionated biomass and productivity of phytoplankton and new production in the Prydz Bay and the adjacent Indian sector of the Southern Ocean during the austral summer of 1998/1999. *Acta Oceanol. Sin.* 27, 135–147. doi: 10.1029/2002JC001507

Chen, M., Ma, Q., Guo, L. D., Qiu, Y. S., Li, Y. P., and Yang, W. F. (2012). Importance of lateral transport processes to $^{210}$Pb budget in the eastern Chukchi Sea during summer 2003. *Deep Sea Res. II* 81, 53–62. doi: 10.1016/j.dsr2.2012.03.011

Cherrier, J., Burnett, W. C., and LaRock, P. A. (1995). Uptake of polonium and sulfur by bacteria. *Geomicrobiol. J.* 13, 103–115. doi: 10.1080/01490459509378009

Chung, Y. (1981). $^{210}$Pb and $^{226}$Ra distributions in the circumpolar waters. *Earth Planet. Sci. Lett.* 55, 205–216. doi: 10.1016/0012-821X(81)90100-X

Chung, Y., and Applequist, M. D. (1980). $^{226}$Ra and $^{210}$Pb in the Weddell Sea. *Earth Planet. Sci. Lett.* 55, 401–410. doi: 10.1016/0012-821X(80)90082-5

Chung, Y., and Finkel, R. (1988). $^{210}$Po in the western Indian Ocean: distributions, disequilibria and partitioning between the dissolved and particulate phases. *Earth Planet. Sci. Lett.* 88, 232–240. doi: 10.1016/0012-821X(88)90080-5

Chung, Y., and Wu, T. (2005). Large $^{210}$Po deficiency in the northern South China Sea. *Cont. Shelf Res.* 25, 1209–1224. doi: 10.1016/j.csr.2004.12.016

Cochran, J. K. (1992). "The oceanic chemistry of the uranium- and thorium-series nuclides," in *Uranium-Series Disequilibrium–Applications to Earth, Marine, and Environmental Sciences*, 2nd Edn, eds M. Ivanovich and R. S. Harmon (Oxford: Clarendon Press), 334–395.

Cochran, J. K., Bacon, M. P., Krishnaswami, S., and Turekian, K. K. (1983). $^{210}$Po and $^{210}$Pb distributions in the central and eastern Indian Ocean. *Earth Planet. Sci. Lett.* 65, 433–452. doi: 10.1016/0012-821X(83)90180-2

Cochran, J. K., Buesseler, K. O., Bacon, M. P., Wang, H. W., Hirschberg, D. J., Ball, L., et al. (2000). Short-lived thorium isotopes ($^{234}$Th, $^{228}$Th) as indicators of POC export and particle cycling in the Ross Sea, Southern Ocean. *Deep Sea Res. II* 47, 3451–3490. doi: 10.1016/S0967-0645(00)00075-8

Fisher, N. S., Burns, K. A., and Heyraud, M. (1983). Accumulation and cellular distribution of $^{241}$Am, $^{210}$Po and $^{210}$Pb in two marine algae. *Mar. Ecol. Prog. Ser.* 11, 233–237. doi: 10.3354/meps011233

Friedrich, J., and Rutgers van der Loeff, M. M. (2002). A two-tracer ($^{210}$Po-$^{234}$Th) approach to distinguish organic carbon and biogenic silica export flux in the Antarctic Circumpolar Current. *Deep Sea Res. I* 49, 101–120. doi: 10.1016/S0967-0637(01)00045-0

Grasshoff, K., Kremling, K., and Ehrhardt, M. (1983). *Methods of Seawater Analysis*. Weinheim: Verlag Chemie.

Han, Z. B., Hu, C. Y., Xue, B., Pan, J. M., and Zhang, H. S. (2011). Particulate organic carbon in the surface water of South Ocean and Prydz Bay during the austral summer of 2007/2008 and 2008/2009. *Chin. J. Polar Res.* 23, 11–18. doi: 10.1007/s11589-011-0776-4

Hanfland, C. (2002). Radium-226 and Radium-228 in the Atlantic sector of the Southern Ocean. *Polar Mar. Res.* 431:135.

He, J. H., Ma, H., Chen, L. Q., Xiang, B. Q., Zeng, X. Z., Yin, M. D., et al. (2007). The estimates of the particulate organic carbon export fluxes in Prydz Bay, Southern Ocean using $^{234}$Th/$^{238}$U disequilibria. *Acta Oceanol. Sin.* 29, 69–76. doi: 10.3321/j.issn:0253-4193.2007.04.008

Hong, G. H., Baskaran, M., Church, T. M., and Conte, M. (2013). Scavenging, cycling and removal fluxes of $^{210}$Po and $^{210}$Pb at the Bermuda time-series study site. *Deep Sea Res. II* 93, 108–118. doi: 10.1016/j.dsr2.2013.01.005

Kaste, J. M., and Baskaran, M. (2012). "Meteoric $^{7}$Be and $^{10}$Be as process tracers in the environment," in *Handbook of Environmental Isotope Geochemistry*, ed. M. Baskaran (Berlin: Springer-Verlag), doi: 10.1007/978-3-642-10637-8_5

Kawakami, H., Yang, Y., and Kusakabe, M. (2008). Distributions of $^{210}$Po and $^{210}$Pb radioactivity in the intermediate layer of the northwestern North Pacific. *J. Radioanal. Nucl. Chem.* 279, 561–566. doi: 10.1007/s10967-008-7324-2

Kharkar, D. P., Thomson, J., Turekian, K. K., and Forster, W. O. (1976). Uranium and thorium decay series nuclides in plankton from the Caribbean. *Limnol. Oceanogr.* 21, 294–299. doi: 10.4319/lo.1976.21.2.0294

Kim, G., and Church, T. M. (2001). Seasonal biogeochemical fluxes of $^{234}$Th and $^{210}$Po in the upper Sargasso Sea: influence from atmospheric iron deposition. *Global Biogeochem. Cycles.* 15, 651–661. doi: 10.1029/2000GB001313

Ku, T. L., and Lin, M. C. (1976). $^{226}$Ra distribution in the Antarctic Ocean. *Earth Planet. Sci. Lett.* 32, 236–248. doi: 10.1016/0012-821X(76)90064-9

Liu, Z. L., Cai, Y. M., Chen, Z. Y., Liu, C. G., Zhu, G. H., and Wang, X. G. (2002). The distribution feature of chlorophyll a and primary productivity in Prydz Bay and its north sea area during the austral summer of 1998/1999. *Chin. J. Polar Res.* 14, 12–21.

Ma, Q. (2006). *Particle Transport and Export in the North Pacific and the Western Arctic Ocean as Revealed by Radionuclides*. Ph.D thesis. Xiamen: Xiamen University.

Masqué, P., Sanchez-Cabeza, J. A., Bruach, J. M., Palacios, E., and Canals, M. (2002). Balance and residence times of $^{210}$Pb and $^{210}$Po in surface waters of the northwestern Mediterranean Sea. *Cont. Shelf Res.* 22, 2127–2146. doi: 10.1016/S0278-4343(02)00074-2

Moore, R. M., and Smith, J. N. (1986). Disequilibria between $^{226}$Ra, $^{210}$Pb and $^{210}$Po in the Arctic Ocean and the implications for chemical modification of the Pacific water inflow. *Earth Planet. Sci. Lett.* 77, 285–292. doi: 10.1016/0012-821X(86)90140-8

Moran, S. B., Charette, M. A., Hoff, J. A., Edwards, R. L., and Landing, W. M. (1997). Distribution of $^{230}$Th in the Labrador Sea and its relation to ventilation. *Earth Planet. Sci. Lett.* 150, 151–160. doi: 10.1016/S0012-821X(97)00081-2

Murray, J. W., Downs, J. N., Strom, S., Wei, C. L., and Jannasch, H. W. (1989). Nutrient assimilation, export production and $^{234}$Th scavenging in the eastern equatorial Pacific. *Deep Sea Res. A* 36, 1471–1489. doi: 10.1016/0198-0149(89)90052-6

Murray, J. W., Paul, B., Dunne, J. P., and Thomas, C. (2005). $^{234}$Th, $^{210}$Pb, $^{210}$Po and stable Pb in the central equatorial Pacific: tracers for particle cycling. *Deep Sea Res. I* 52, 2109–2139. doi: 10.1016/j.dsr.2005.06.016

Niedermiller, J., and Baskaran, M. (2019). Comparison of the scavenging intensity, remineralization and residence time of $^{210}$Po and $^{210}$Pb at key zones (biotic, sediment-water and hydrothermal) along the East Pacific GEOTRACES transect. *J. Environ. Radioactiv.* 198, 165–188. doi: 10.1016/j.jenvrad.2018.12.016

Nozaki, Y., Ikuta, N., and Yashima, M. (1990). Unusually large $^{210}$Po deficiencies relative to $^{210}$Pb in the Kuroshio Current of the East China and Philippine Seas. *J. Geophys. Res.* 95, 5321–5329. doi: 10.1029/JC095iC04p05321

Nozaki, Y., Thomson, J., and Turekian, K. K. (1976). The distribution of $^{210}$Pb and $^{210}$Po in the surface waters of the Pacific Ocean. *Earth Planet. Sci. Lett.* 32, 304–312. doi: 10.1016/0012-821X(76)90070-4

Nozaki, Y., Zhang, J., and Takeda, A. (1997). $^{210}$Pb and $^{210}$Po in the equatorial Pacific and the Bering Sea: the effects of biological productivity and boundary scavenging. *Deep Sea Res. II* 44, 2203–2220. doi: 10.1016/S0967-0645(97)00024-6

Pu, S. Z., and Dong, Z. Q. (2003). Progress in physical oceanographic studies of Prydz Bay and its adjacent oceanic area. *Chin. J. Polar Res.* 15, 53–64. doi: 10.1016/S0955-2219(02)00073-0

Pu, S. Z., Dong, Z. Q., Hu, X. M., Yu, F., and Zhao, X. (2002a). Variability of the continental water boundary near the Prydz Bay. *Mar. Sci. Bull.* 4, 1–10.

Pu, S. Z., Dong, Z. Q., Yu, W. D., Lu, Y., and Xiang, B. Q. (2007). Features and spatial distributions of circumpolar deep water in the Southern Indian Ocean and effect of Antarctic Circumpolar Current. *Adv. Mar. Sci.* 25, 1–8. doi: 10.3969/j.issn.1671-6647.2007.01.001

Pu, S. Z., Hu, X. M., Dong, Z. Q., Yu, F., and Chen, X. R. (2002b). Features of circumpolar deep water, Antarctic Bottom Water and their movement near the Prydz Bay. *Acta Oceanol. Sin.* 24, 1–8. doi: 10.3321/j.issn:0253-4193.2002.03.001

Qiu, Y. S., Huang, Y. P., Liu, G. S., and Chen, M. (2004). Spatial and temporal variations of primary productivity in Prydz Bay and its Adjacent Sea Area, Antarctica. *J. Xiamen Uni. (Nat. Sci.)* 43, 676–681.

Rama, Koide, M., and Goldberg, E. D. (1961). Lead-210 in natural waters. *Science* 134, 98–99. doi: 10.1126/science.134.3472.98

Ren, C. Y. (2015). *Stable Carbon and Nitrogen Isotopic Composition in Particulate organic Matter in the Prydz Bay and the Antarctic Peninsula*. PhD thesis. Xiamen: Xiamen University.

Rigaud, S., Stewart, G., Baskaran, M., Marsan, D., and Church, T. (2014). $^{210}$Po and $^{210}$Pb distribution, dissolved-particulate exchange rates, and particulate export along the North Atlantic US GEOTRACES GA03 section. *Deep Sea Res. II* 116, 60–78. doi: 10.1016/j.dsr2.2014.11.003

Rutgers van der Loeff, M. M., Friedrich, J., and Bathmann, U. V. (1997). Carbon export during the Spring Bloom at the Antarctic Polar Front, determined with the natural tracer $^{234}$Th. *Deep Sea Res. II* 44, 457–478. doi: 10.1016/S0967-0645(96)00067-7

Shimmield, G. B., Ritchie, G. D., and Fileman, T. W. (1995). The impact of marginal ice zone processes on the distribution of $^{210}$Pb, $^{210}$Po and $^{234}$Th and implications for new production in the Bellingshausen Sea, Antarctica. *Deep Sea Res. II* 42, 1313–1335. doi: 10.1016/0967-0645(95)00071-W

Smith, N. R., Dong, Z. Q., Kerry, K. R., and Wright, S. (1984). Water masses and circulation in the region of Prydz Bay, Antarctica. *Deep Sea Res. I* 31, 1121–1147. doi: 10.1016/0198-0149(84)90016-5

Smoak, J. M., Demaster, D. J., Kuehl, S. A., Pope, R. H., and Mckee, B. A. (1996). The behavior of particle-reactive tracers in a high turbidity environment: $^{234}$Th and $^{210}$Pb on the Amazon continental shelf. *Geochim. Cosmochim. Acta.* 60, 2123–2137. doi: 10.1016/0016-7037(96)00092-0

Somayajulu, B. L. K., and Craig, H. (1976). Particulate and soluble $^{210}$Pb activities in the deep sea. *Earth Planet. Sci. Lett.* 32, 268–276. doi: 10.1016/0012-821X(76)90067-4

Stewart, G., Cochran, J. K., Miquel, J. C., Masqué, P., Szlosek, J., Rodriguez y Baena, A. M., et al. (2007). Comparing POC export from $^{234}$Th/$^{238}$U and $^{210}$Po/$^{210}$Pb disequilibria with estimates from sediment traps in the northwest Mediterranean. *Deep Sea Res. I* 54, 1549–1570. doi: 10.1016/j.dsr.2007.06.005

Stewart, G. M., and Fisher, N. S. (2003). Experimental studies on the accumulation of polonium-210 by marine phytoplankton. *Limnol. Oceanogr.* 48, 1193–1201. doi: 10.4319/lo.2003.48.3.1193

Stewart, G. M., Fowler, S. W., Teyssié, J. L., Cotret, O., Cochran, J. K., and Fisher, N. S. (2005). Contrasting transfer of polonium-210 and lead-210 across three trophic levels in marine plankton. *Mar. Ecol. Prog. Ser.* 290, 27–33. doi: 10.3354/meps290027

Sun, W. P., Hu, C. Y., Han, Z. B., Pan, J. M., and Weng, H. X. (2012). Distribution of nutrients and Chl a in Prydz Bay during the austral summer of 2011. *Chin. J. Polar Res.* 24, 178–186. doi: 10.3724/SP.J.1084.2012.00178

Takahashi, T., Sutherland, S. C., Sweeney, C., Poisson, A., Metzl, N., Tibrook, B., et al. (2002). Global sea-air $CO_2$ flux based on climatological surface ocean $pCO_2$, and seasonal biological and temperature effects. *Deep Sea Res. II* 49, 1601–1622.

Tang, Y., Lemaitre, N., Castrillejo, M., Roca-Martí, M., and Masqué, P. (2019). The export flux of particulate organic carbon derived from $^{210}$Po/$^{210}$Pb disequilibria along the North Atlantic GEOTRACES GA01 transect: GEOVIDE cruise. *Biogeosciences* 16, 309–327. doi: 10.5194/bg-16-309-2019

Thomson, J., and Turekian, K. K. (1976). $^{210}$Po and $^{210}$Pb distributions in ocean water profiles from the Eastern South Pacific. *Earth Planet. Sci. Lett.* 32, 297–303. doi: 10.1016/0012-821X(76)90069-8

Turekian, K. K., and Nozaki, Y. (1980). "$^{210}$Po and $^{210}$Pb in the Eastern South Pacific: the role of upwelling on their distributions in the water column," in *Isotope Marine Chemistry*, eds E. D. Goldberg, Y. Horibe, and K. Saruhashi (Tokyo: Uchida Rokakuho Publ Co), 157–164.

Verdeny, E., Masqué, P., Garcia-Orellana, J., Hanfland, C., Cochran, J. K., and Stewart, G. M. (2009). POC export from ocean surface waters by means of $^{234}$Th/$^{238}$U and $^{210}$Po/$^{210}$Pb disequilibria: a review of the use of two radiotracer pairs. *Deep Sea Res. II* 56, 1502–1518. doi: 10.1016/j.dsr2.2008.12.018

Wei, C. L., Lin, S. Y., Sheu, D. D. D., Chou, W. C., Yi, M. C., Santschi, P. H., et al. (2011). Particle-reactive radionuclides ($^{234}$Th, $^{210}$Pb, $^{210}$Po) as tracers for the estimation of export production in the South China Sea. *Biogeosciences* 8, 3793–3808. doi: 10.5194/bg-8-3793-2011

Yang, W. F. (2005). *Marine Biogeochemistry of $^{210}$Po and $^{210}$Pb and Their Implications Regarding the Cycling and Export of Particles*. PhD thesis. Xiamen: Xiamen University.

Yang, W. F., Huang, Y. P., Chen, M., Qiu, Y. S., Peng, A. G., and Zhang, L. (2009). Export and remineralization of POM in the Southern Ocean and the South China Sea estimated from $^{210}$Po/$^{210}$Pb disequilibria. *Chin. Sci. Bull.* 54, 2118–2123. doi: 10.1007/s11434-009-0043-4

Yang, W. F., Huang, Y. P., Chen, M., Zhang, L., Li, H. B., Liu, G. S., et al. (2006). Disequilibria between $^{210}$Po and $^{210}$Pb in surface waters of the southern South China Sea and their implications. *Sci. China Ser. D.* 49, 103–112. doi: 10.1007/s11430-004-5233-y

Yu, P. S., Hu, C. Y., Zhu, G. H., Pan, J. M., and Zhang, H. S. (2011). Characteristics of particulate organic carbon in the Prydz Bay of Antarctica. *Acta Oceanol. Sin.* 33, 181–186.

**Conflict of Interest:** The authors declare that the research was conducted in the absence of any commercial or financial relationships that could be construed as a potential conflict of interest.

*Copyright © 2021 Hu, Liu, Ren, Jia, Qiu, Zheng and Chen. This is an open-access article distributed under the terms of the Creative Commons Attribution License (CC BY). The use, distribution or reproduction in other forums is permitted, provided the original author(s) and the copyright owner(s) are credited and that the original publication in this journal is cited, in accordance with accepted academic practice. No use, distribution or reproduction is permitted which does not comply with these terms.*

frontiers in Marine Science

ORIGINAL RESEARCH
published: 20 July 2021
doi: 10.3389/fmars.2021.703945

# $^{7}Be/^{210}Pb_{xs}$ Ratio-Derived Age and Residence Time of Suspended Sediments in Galveston Bay

*Nicole Schmidt[1], Timothy Dellapenna[1,2]* and Peng Lin[2]**

[1] Coastal Geology Laboratory, Department of Oceanography, Texas A&M University at Galveston, Galveston, TX, United States, [2] Department of Marine and Coastal Environmental Science, Texas A&M University at Galveston, Galveston, TX, United States

OPEN ACCESS

**Edited by:**
Weifeng Yang,
Xiamen University, China

**Reviewed by:**
Huan Feng,
Montclair State University, United States
Ziming Fang,
Hong Kong University of Science and Technology, Hong Kong, SAR China

***Correspondence:**
Timothy Dellapenna
dellapet@tamug.edu
Peng Lin
pengl1104@tamug.edu

**Specialty section:**
This article was submitted to Marine Biogeochemistry, a section of the journal Frontiers in Marine Science

**Received:** 01 May 2021
**Accepted:** 28 June 2021
**Published:** 20 July 2021

**Citation:**
Schmidt N, Dellapenna T and Lin P (2021) $^{7}Be/^{210}Pb_{xs}$ Ratio-Derived Age and Residence Time of Suspended Sediments in Galveston Bay. Front. Mar. Sci. 8:703945. doi: 10.3389/fmars.2021.703945

The winds associated with the passage of meteorological fronts cause waves that induce sediment remobilization/resuspension, especially within shallow estuaries such as Galveston Bay. The passage of cold fronts, collectively, on an annual to decadal basis, generate more sediment resuspension than most hurricanes and tropical storms. With a warming climate, the intensity of all meteorological events is shifting toward having greater impacts on these biologically productive environments. To better understand sediment resuspension within the bay, water samples were collected during frontal passages at two locations in Galveston Bay, including one location in the middle portion of the bay and another closer to the mouth of the bay. By collecting precipitation, water samples in both the middle and lower bay, and measuring the ratio of $^{7}Be/^{210}Pb_{xs}$ in these samples; we quantified the residence times of total suspended sediment (TSS) in middle and lower Galveston Bay. Our results showed that suspended sediment age increased and percent of new suspended sediment decreased along the axis from the middle bay to the lower bay. This results from the initial introduction of newly labeled isotopes and suspended load coming from fluvial discharges which enter at the top of the bay and travel through the bay. The age of suspended sediment from the first sampling event was 70 ± 10 days, whereas the age in the second event was 16 ± 3 days greater. In the last sampling event, the age of suspended sediment event was 35 ± 7.4 days younger than the second, suggesting that the majority of suspended sediments was likely transported entirely out of the bay by the second cold front, prior to the final sampling event. This indicates that there are longer suspended sediment residence times when the water is trapped within the bay. Our estimated residence time of suspended sediments (51–105 days) suggest the particle-bound contaminants adsorb to suspended sediment may spend months suspended in the bay before exiting the bay or being accreted into the bay sediment column, increasing the exposure time of living organisms to various particle-bound contaminants.

**Keywords: sediment resuspension, lead-210, residence times, beryllium-7, Galveston Bay**

## INTRODUCTION

Sediment remobilization/resuspension plays a role in many estuarine processes; especially associated with the cycling of nutrients and pollutants in and out of an estuary (Baskaran and Santschi, 1993). Wind-induced currents and wave resuspension are important sources of energy for sediment transport within an ecosystem and can be dominant in shallow, microtidal estuaries, affecting a large portion, if not all of the water column (Booth et al., 2000). Sediment resuspension associated with strong weather events can reintroduce trace elements and pollutants back into the water column, which can have significant environmental impacts in an estuary (e.g., Dellapenna et al., 2006, 2020). These constituents can be stored in the sediment during periods of sediment deposition and are resuspended during wind-induced wave resuspension, in addition to any other resuspension events (Dellapenna et al., 2006). Particle reactive contaminants generally move slowly through an estuarine system, transported through the innumerous cycles of deposition and resuspension during various hydrological stages (Saari et al., 2010). Therefore, evaluating how long such innumerous cycles last will help us better monitor the transport of suspended sediments and their associated pollutants and trace elements, such as examining the residence time of suspended sediment, defined as the average length of time during which the sediment resides within the bay as suspended sediment.

Two naturally occurring radionuclides, i.e., beryllium-7 ($^{7}Be$) and lead-210 ($^{210}Pb$) can be paired and used to quantify the time that the particles surfaces sorbed the isotopes from the water column, which occurs when the particle became suspended in the water column (Matisoff et al., 2005). $^{7}Be$ is a cosmogenic radionuclide produced in both the stratosphere and troposphere as a result of cosmic ray spallation of nitrogen and oxygen (Brost et al., 1991). Following atmospheric fallout, $^{7}Be$ rapidly adsorbs to fine sediment particles (Taylor et al., 2013). Similar to $^{7}Be$, atmospherically derived $^{210}Pb$ ($^{210}Pb_{xs}$), produced from the decay of its parent nuclide, radon-222, are also delivered to the waters *via* wet and dry fallout. Fallout patterns of $^{7}Be$ and $^{210}Pb$ are tightly correlated leading to these nuclides being useful for dependent tracers (Baskaran et al., 1993). Once radionuclides adsorb to sediment particles, they are strongly and nearly irreversibly bound to these particles, making it possible to study the movement and obtain the age of suspended sediment (Taylor et al., 2013). Short half-lives for $^{7}Be$ ($t_{1/2}$ = 53 days) relative to 22.3 years for $^{210}Pb$ not only provide an advantage when considering recent events (e.g., winter cold front) that cause sediment redistribution (Taylor et al., 2013), but also allow us to use the ratio of $^{7}Be$ /$^{210}Pb_{xs}$ to quantify the proportion of resuspended bottom material in the water column, e.g., higher values indicating younger particles (Olsen et al., 1989).

Galveston Bay, the second largest estuarine system in Texas, United States, is a shallow and microtidal estuary, with an average depth of 2.1 m and water residence time of ∼40 days (Solis and Powell, 1999). The surrounding area of Galveston Bay are heavily industrialized, dominated by petroleum, petrochemical, and chemical industries, collectively hosting nearly 50% of total United States chemical production and oil refineries (Santschi et al., 2001). This makes Galveston Bay an important area to investigate sediment dynamics. The purpose of the present study is to understand the relationship between meteorological fronts, sediment resuspension and suspended sediment residence times. In the context of this study, we operationally define suspended sediment residence time as the amount of time a short-lived radio-isotope labeled sediment particle is actively involved within the water column sediment load prior to either being incorporated into the seabed or exported from the bay. These particles may be resuspended from the bay bottom and newly radio-isotope labeled or it may have been advected into the bay either from offshore or from the drainage basin.

Along the northern Gulf of Mexico, most meteorologically driven sediment resuspension occurs during the passage of northern cold fronts which mainly occur during winter months (Henry, 1979; Hardy and Henderson, 2003). Besides, meteorological events are necessary to collect precipitation along with suspended sediments as cold fronts are accompanied by precipitation and greater wind speeds, which allow us accessible to the near-bottom suspended sediments and their associated $^{7}Be/^{210}Pb_{xs}$. Therefore, together with rainwater samples, water samples in the middle and lower Galveston Bay during each weather event were collected at early 2020 for the measurement of $^{7}Be$ and $^{210}Pb_{xs}$ to test and apply $^{7}Be/^{210}Pb$ pair to quantify the residence times of suspended sediment in the bay. We hypothesize that the age of the sediment should be younger in mid-Galveston Bay and older toward the mouth of Galveston Bay. Additionally, with the abundance of clay dominated mud in the middle bay and coarser mud (e.g., higher silt content, with sand) in the lower bay, total suspended sediment (TSS) concentrations will be higher in middle Galveston Bay versus closer to the mouth, allowing for deposition of coarser mud to occur at a faster rate than finer muds. Understanding physical processes, such as sediment resuspension and residence times, allows for proper management strategies to be developed to ensure a stable and productive ecosystem in the estuary (Walker and Hammack, 2000).

## MATERIALS AND METHODS

### Background

Galveston Bay is a shallow, microtidal estuary and is the second largest estuarine system in Texas with a surface area of approximately 1,360 $km^2$ (Dellapenna et al., 2006). The average depth of the bay is 2.1 m and contains a ship channel with dimensions of 150 m in width and 10–15 m deep, oriented along the main axis of the bay (50 km long) (Du and Park, 2019). The exchange of tidal water flows through Bolivar Roads, which is the tidal inlet between Bolivar Peninsula and Galveston Island. An additional inlet exists 47 km to the west and provides gulf flow into Christmas Bay and the western half of West Galveston Bay. Average water residence time within Galveston Bay is approximately 40 days (Solis and Powell, 1999). Trinity Bay comprises the northeastern portion of Galveston Bay (**Figure 1**), has depths generally ranging between 3 and 4 m (Dellapenna et al., 2006) and the Trinity River flows into the head northeastern

end of the bay, The Trinity River accounts for approximately 90% of the freshwater input and is the largest sediment source into Galveston Bay [United States Geological Survey [USGS], 2005]. Another significant sediment load within the bay is the ongoing maintenance of the Houston Ship Channel. In waters deeper than 1.5 m, Trinity Bay bottom sediment is mud dominated (approx. 40% of total bay area) (Dellapenna et al., 2006). Mud is the dominant sediment composition of the majority of the Galveston Bay system (**Figure 1**).

The watershed of Galveston Bay contains both metropolitan Houston as well as the Clear Lake-Texas City-Galveston area and the Port of Houston. Houston, Texas, is the fifth-largest metropolitan area (population of 7 million), is the fourth-largest city in the United States, and hosts the second-largest petrochemical complex in the world (Morse et al., 1993; Santschi et al., 2001). The Port of Houston is the second-largest seaport in the United States in terms of total shipping tonnage (Chambers et al., 2018) and services the 80 km long Houston Ship Channel, which extends up the axis of Galveston Bay from Bolivar Roads at its entrance to the San Jacinto Estuary and Buffalo Bayou. Further south of Houston is the Clear Lake-Texas City-Galveston area which is also heavily industrialized, dominated by petroleum, petrochemical, and chemical industries as well as shipyards in Galveston. Collectively, the shores and watershed of Galveston Bay host nearly 50% of total United States chemical production and oil refineries (Santschi et al., 2001). Galveston Bay also receives a significant amount of wastewater discharges for the state from surrounding facilities. Galveston Bay provides nursing habitat for multiple valuable fisheries, including white and brown shrimp (Stunz et al., 2010) and provides approximately 14% of the United States wild catch of oysters (Haby et al., 2009). A key process in shallow estuaries is the frequency of sediment resuspension. An increased amount of sediment resuspension and deposition in an estuary may cause smothering of benthic aquatic organisms and the clogging of water intakes (Winterwerp and Van Kesteren, 2004).

## Sample Collection

Sampling occurred during three meteorological fronts from January 2020 to February 2020. 60–80 L of bay waters in two sites of the Galveston Bay (**Figure 1**), depending upon the turbidity of bay waters, were sampled within 1–2 days after each storm event, conducted by attaching a bilge pump to a 4 m long, 3.81 cm diameter aluminum pole, with the bilge pump being mounted 30 cm above the bottom of the pole to prevent penetration into the sediment while still collecting suspended sediment from the bottom-water. The pump rate of the bilge pump is about 1.5 L/min, which is slow enough that additional bottom sediment was not eroded during sample collection. This flow rate calculation was based upon information provided by the bilge pump company; therefore, the rate may be slower with the hose being attached to the pump and the distance required to pump water into the carboys.

Aliquots of the samples were filtered in the lab through a 0.45 μm polycarbonate filter for the measurement of total suspended particle (TSS) concentrations. The remaining samples were placed on the bench for a few days until the water is visibly clear of particles to allow the suspended particles sinking to the bottom of the containers, followed by the centrifugation to separate water from suspended sediments. Collected particulate matter from the centrifugation were dried in an oven at 50°C. The dried particles were grounded and transferred into the gamma counting tubes for the measurement of $^{7}Be$ and $^{210}Pb$.

Precipitation was collected on the roof of the Ocean and Coastal Studies Building (OCSB) at Texas A&M Galveston Campus, where was close to the lower bay water sampling site (**Figure 1**). Although there is a distance of 30 km between middle bay water sampling site and precipitation sampling location, the $^{7}Be/^{210}Pb$ ratios in precipitation vary little in one study area (Baskaran et al., 1993; Koch et al., 1996), regardless of variable precipitation amounts between sites. The rainwater was collected using a 20 L jug with a large funnel attached to the opening along with a 2 L bucket of water next to it for more collection. This was deployed before each rain event (**Supplementary Table 1**). At the end of each storm event, the collected rainwater in all containers will be combined for the extraction and analysis of $^{7}Be$ and $^{210}Pb$ (Section "Measurements of $^{7}Be$ and $^{210}Pb$"). Activity measurements of $^{210}Pb$ and $^{7}Be$ from rainwater is necessary to perform the Matisoff method, to determine the "initial" age of the two radionuclides for each frontal passage event.

## Measurements of $^{7}Be$ and $^{210}Pb$

For the rainwater samples, $^{7}Be$ and $^{210}Pb$ were be extracted from the collected precipitation based on the published method from Olsen et al. (1985) and Wang et al. (2013). After the adjustment of pH to $< 2$, a certain amount of $Fe^{3+}$ carrier solution ($FeCl_3$, 5 mg Fe per L of sample) is added under stirring. After homogenization and equilibration for overnight, pH is adjusted to 9 with ammonia solution to precipitate the iron, and $Fe(OH)_3$ containing $^{7}Be$ and $^{210}Pb$ are left to stand overnight. The $Fe(OH)_3$ precipitate will be collected through centrifugation and dissolved by 3M HCl solution. Extracted sample from precipitation and the ground sediments from bay waters will be placed into gamma counting tubes for analysis by a Canberra ultrahigh-purity germanium well gamma detector at the decay energies of 46.5 kev for $^{210}Pb$ and 477.6 kev for $^{7}Be$. The sediment samples will be counted again after 3 weeks to allow secular equilibrium ingrowth of gaseous $^{222}Rn$ from the decay of $^{226}Ra$, the parent nuclide of $^{210}Pb$. The supported $^{210}Pb$ will be determined from the activity of the $^{214}Bi$ from the $^{222}Rn$, at the decay energy of 609.3 kev. The atmospherically derived $^{210}Pb$ in suspended sediments ($^{210}Pb_{xs}$) will be determined based on the difference between total activity of $^{210}Pb$ and the supported $^{210}Pb$.

All samples will be counted for enough time to obtain the counting errors $< 10\%$. Counting efficiencies will be determined, using the standards that are prepared with the same geometries as the samples. Activities concentrations of $^{7}Be$ and $^{210}Pb_{xs}$ will be decay-corrected to the date of collection before the calculation of residence times of suspended sediments or the percentage of newly labeled sediments/particles.

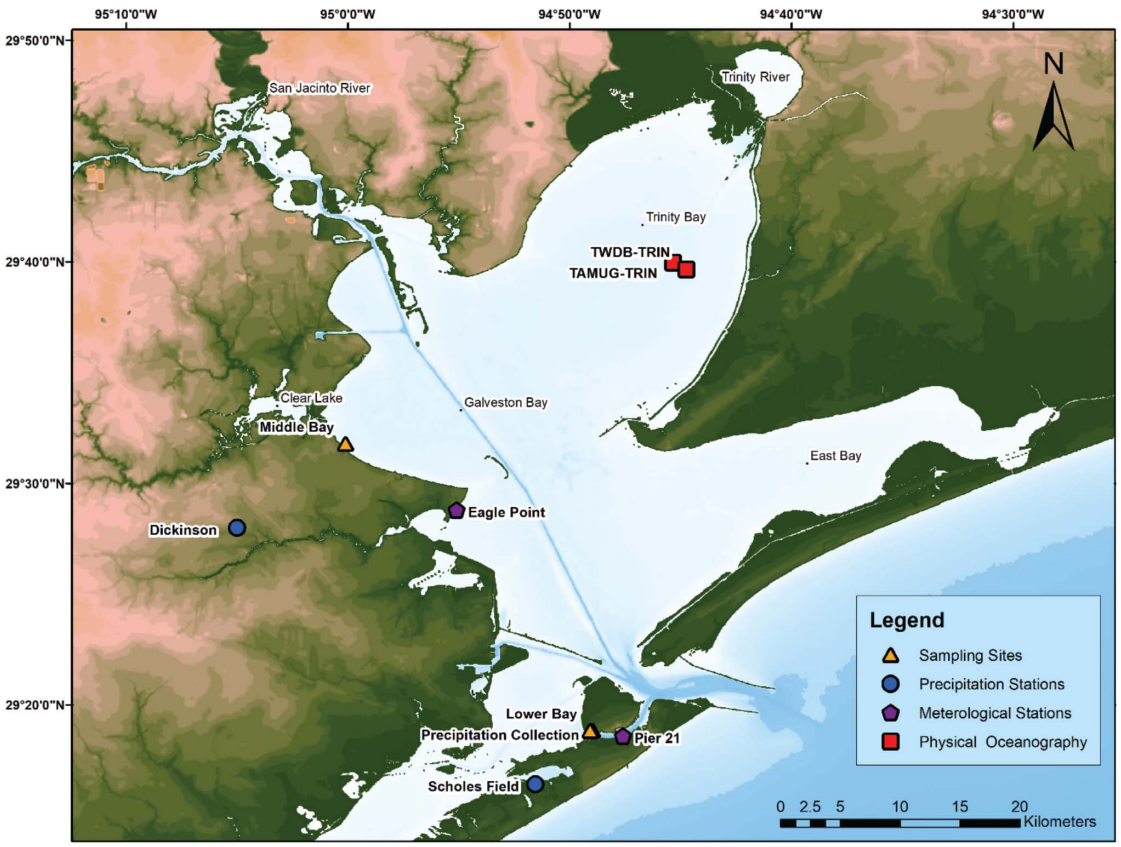


**FIGURE 1 |** Map of Study Area and Sampling Stations, including Meteorological Stations (pentagon), Precipitation stations (circle), suspended sediment/precipitation sampling sites (triangle), and physical oceanography sites (square).

## Estimate of Residence Time and Percentage of Newly Labeled Sediments/Particles of Suspended Sediments

Due to the significant difference in half-life between two radionuclides (53.3 days for $^{7}$Be vs. 22.3 years for $^{210}$Pb) and their strong binding to particles after their delivery from the atmosphere to the surface, the ratio of $^{7}$Be over the atmospherically derived $^{210}$Pb ($^{210}$Pb$_{xs}$) can be an indicator of the extent of mixing of freshly derived ($^{7}$Be enriched) suspended sediment with old ($^{7}$Be deficient) sediment resuspended from the bed of the Galveston Bay. Therefore, the $^{7}$Be/$^{210}$Pb$_{xs}$ ratio in the atmospheric deposition during the storm events is defined as the atmospheric tag received by the "newly tagged sediment" in the Galveston Bay (Matisoff et al., 2005). Based on the variability of $^{7}$Be/$^{210}$Pb$_{xs}$ ratio in suspended sediments relative to the atmospheric $^{7}$Be/$^{210}$Pb$_{xs}$ ratio, the residence time or the age of suspended sediments can be estimated, across the middle Galveston Bay to the lower bay, based on the following equation:

$$\mathbf{T} = \frac{-\mathbf{1}}{(\lambda_{^{7}Be} - \lambda_{^{210}Pb})} \ln\left(\frac{\mathbf{A}}{\mathbf{B}}\right) + \frac{\mathbf{1}}{(\lambda_{^{7}Be} - \lambda_{^{210}Pb})} \ln\left(\frac{\mathbf{A_o}}{\mathbf{B_o}}\right) \quad (1)$$

where T is the age of suspended sediment; A and B is the activity concentration of $^{7}$Be and $^{210}$Pb in the suspended sediments, respectively; $A_o$ and $B_o$ is the activity concentration of $^{7}$Be and $^{210}$Pb in the precipitation, respectively.

On the other hand, the $^{7}$Be/$^{210}$Pb$_{xs}$ ratio can be alternatively used to estimate the percentage "new" particles in suspended sediments, which is defined as the sediment particles that have a $^{7}$Be/$^{210}$Pb$_{xs}$ ratio equal to precipitation, as following shown:

$$\%'\,\boldsymbol{new'\,sediment} = \boldsymbol{100\,x}\frac{(\boldsymbol{A/B})}{(\boldsymbol{A_o/B_o})} \quad (2)$$

Errors are provided throughout the manuscript for residence times and percentage of "new" particles. These are based on errors associated with the radioisotope counting method, addressed in Section "Measurements of $^{7}$Be and $^{210}$Pb."

# RESULTS AND DISCUSSION

## $^{7}$Be/$^{210}$Pb$_{xs}$ Ratios in Precipitation and Suspended Sediments

Activities of $^{210}$Pb$_{xs}$ and $^{7}$Be, shown in **Table 1**, were obtained for suspended sediment samples in both middle and lower bay along with precipitation samples during three sampling events.

**TABLE 1 |** $^{210}Pb_{xs}$ and $^{7}Be$ Activities (Bq/kg) in Suspended Sediment and Precipitation samples.

| | | Middle bay | | Lower bay | | Precipitation | |
|---|---|---|---|---|---|---|---|
| Dates | Tide | $^{210}Pb_{xs}$ (Bq/kg) | $^{7}Be$ (Bq/kg) | $^{210}Pb_{xs}$ (Bq/kg) | $^{7}Be$ (Bq/kg) | $^{210}Pb_{xs}$ (Bq/kg) | $^{7}Be$ (Bq/kg) |
| 1/29/2020 | in | 26 ± 2.7 | 98 ± 3.4 | 78 ± 8.0 | 186 ± 8.7 | 22 ± 1.9 | 205 ± 5.4 |
| 2/13/2020 | out | 58 ± 5.0 | 204 ± 6.0 | Not Collected | Not Collected | 44 ± 5.2 | 482 ± 7.4 |
| 2/21/2020 | in | 60 ± 6.0 | 117 ± 6.6 | 50 ± 5.2 | 79 ± 5.2 | 17 ± 1.5 | 63 ± 2.5 |

**TABLE 2 |** $^{7}Be/^{210}Pb_{xs}$ ratios ± standard error calculated from activities of precipitation, suspended sediment samples with calculated suspended sediment age and percentage new sediment.

| Date/Tidal phase | January 29, 2020 (in) | | | February 13, 2020 (out) | | | February 21, 2020 (in) | | |
|---|---|---|---|---|---|---|---|---|---|
| | $^{7}Be/^{210}Pb_{xs}$ | Age (d) | % New | $^{7}Be/^{210}Pb_{xs}$ | Age (d) | % New | $^{7}Be/^{210}Pb_{xs}$ | Age (d) | % New |
| Precipitation | 9.4 ± 0.8 | 0 | 100 ± 9.0 | 11 ± 1.2 | 0 | 100 ± 12 | 3.7 ± 0.4 | 0 | 100 ± 9.5 |
| Middle Bay | 3.8 ± 0.5 | 70 ± 10 | 40 ± 5.6 | 3.5 ± 0.5 | 86 ± 13 | 32 ± 5.0 | 2.0 ± 0.3 | 51 ± 8.0 | 52 ± 8.0 |
| Lower Bay | 2.4 ± 0.4 | 105 ± 15 | 25 ± 3.6 | | Not collected | | 1.6 ± 0.2 | 67 ± 10 | 42 ± 7.0 |

Generally, $^{7}Be$ activities in all samples were higher than $^{210}Pb$. During January sampling, activities of $^{7}Be$ and $^{210}Pb_{xs}$ were both higher in the lower bay than those in the middle bay, whereas, during late February sampling, the opposite occurred. The highest activities of $^{7}Be$ for both bay waters and precipitation can be seen during middle February sampling (**Table 1**), which also coincides with an ebb tide. The ebb tide water mass is derived from upper Galveston Bay within estuarine tributaries, where this water is in more direct contact with drainage basin derived water. Therefore, newly deposited radioisotopes are rich, especially enriched in $^{7}Be$ within this water mass. In contrast, the flood tide water mass is marine derived, only receiving drainage basin water after mixing with the ebb tidal water mass. For $^{210}Pb_{xs}$, compared to the bay water samples, precipitation samples had lower $^{210}Pb_{xs}$ activities for all sampling events, ranging from 17 ± 1.5 Bq/kg for late February to 44 ± 5.2 Bq/kg for early February (**Table 1**). This could be due to the entirety of $^{210}Pb$ flux in rainfall being solely from wet fallout, whereas in suspended sediment samples $^{210}Pb$ becomes remobilized from bottom sediment (Baskaran et al., 1993). Overall, activities of both radionuclides fluctuated throughout sampling events at all locations.

For the $^{7}Be/^{210}Pb$ ratios of precipitation, the maximum value (11 ± 1.2) was detected at middle February 2020 (**Table 2**), where the greatest amount of rainfall was collected, but not recorded at Scholes Field (**Supplementary Table 2**). January samples had a close ratio (9.4 ± 0.8) to that collected in middle February 2020, but there was less rain collected and higher rainfall measurement from Scholes Field. The lowest $^{7}Be/^{210}Pb$ ratio in precipitation samples was found in late February 2020 (3.7 ± 0.4, **Table 2**), which had the least amount of rainfall collected for sampling. When looking at the activities in precipitation of all three events, the lowest $^{7}Be/^{210}Pb$ ratio in precipitation samples at late February were mostly caused by its low $^{7}Be$ activity, showing more than 5 times decreasing activity concentrations compared with first two storms (**Figure 2** and **Table 1**). This may be due to the relatively low precipitation amounts and probably weak stratosphere/troposphere exchange (Duenas et al., 2002) during our late February sampling period. Nevertheless, our reported $^{7}Be/^{210}Pb$ ratios of precipitation and its temporal change in the short period were comparable to and consistent with some previous observation in other study area (2–16, Caillet et al., 2001) or in the Galveston Bay, reported by Baskaran et al. (1993), which $^{7}Be/^{210}Pb$ ratios in precipitation ranged from 8.6 to 15.4 on average between Jan and March (1990−1992).

When considering the variations in the $^{7}Be/^{210}Pb_{xs}$ ratios in suspended sediment (**Table 2**), the January sample had a ratio of 3.8 ± 0.5 for the middle bay, higher than that (2.4 ± 0.4) in the lower bay. In contrast, for the late February samples, the middle and lower bay had relatively closer $^{7}Be/^{210}Pb_{xs}$ ratios in suspended sediments (2.0 ± 0.4 vs. 1.6 ± 0.2). In comparison, the ratios of suspended sediment previously recorded in the Gironde estuary had comparable activity ratios of bottom sediment (averaging at 1.5, Saari et al., 2010) with our reported values, especially for the lower Galveston Bay site (**Table 2**). Both the Gironde (**Supplementary Figure 1**) and the lower Galveston Bay sites (**Figure 1**) were proximal to the respective bay mouths and the ocean. Lower ratios in suspended sediment can be from the reintroduction of $^{7}Be$-dead sediment, which is more commonly found below 2 cm into sediment column. During times of strong sediment resuspension, this can be reintroduced into the water column along with older $^{210}Pb$. This can be possible when measuring suspended sediment. For the middle and lower bay, this is not as likely even during frontal events, unless measurements were taken from where scouring may occur (i.e., wooden pilings). It is expected that the highest ratios would be found in rainfall followed by suspended sediment in "upstream" areas, like the middle bay, followed by suspended sediment in "downstream" areas (e.g., lower bay). All three-sampling events follow this trend throughout the Galveston Bay system (**Table 2**).

## Age or Freshness of Suspended Sediments

Based on the $^{7}Be/^{210}Pb_{xs}$ ratios in suspended sediments, our results show that age of suspended sediments during our sampling events increased along the axis from the upper/middle

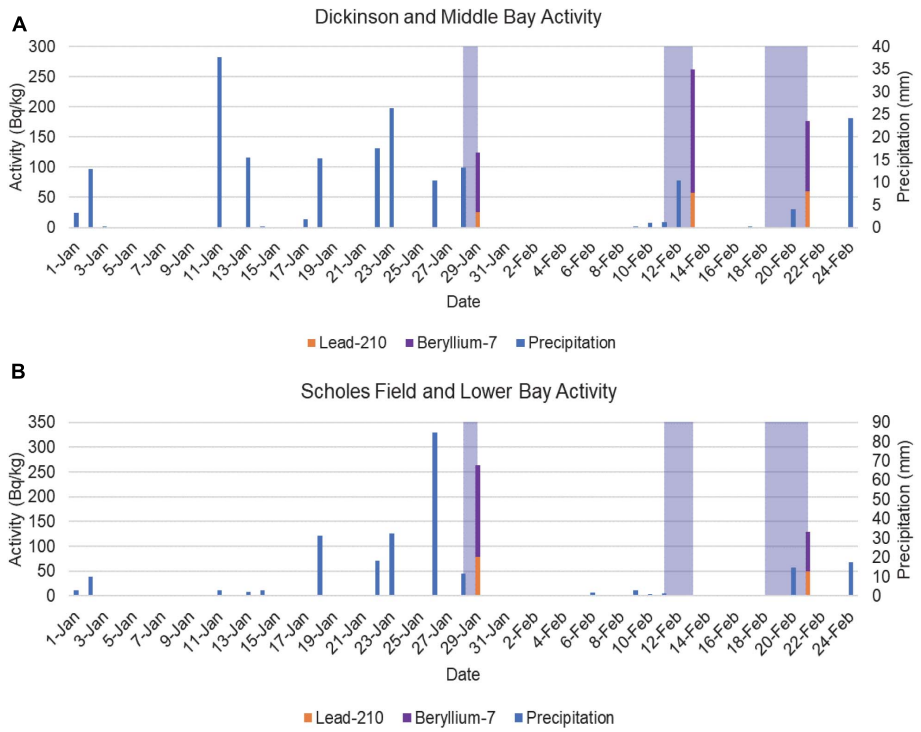


**FIGURE 2 |** Rainfall vs. Isotope Activity. Rainfall data (blue) from Dickinson **(A)** and Scholes Field **(B)** Station (NWS) and Isotopic Activity of $^{210}Pb$ (orange) and $^{7}Be$ (purple) collected at the middle and lower bay site. Shading represents our precipitation sampling period.

bay to the lower bay (**Figure 3**), corresponding to the decreasing abundance of newly labeled suspended sediments/particles, which were also derived from $^{7}Be/^{210}Pb_{xs}$ ratios (**Table 2**). Throughout the three events, the age of the suspended sediment from the middle bay in middle February 2020 was the highest at 86 ± 13 days, followed by late January 2020 at 70 ± 10 days, and then late February 2020 at 50 ± 8.0 days. The abundance or percentage of newly labeled particles in the total suspended sedimentary pool were correspondingly to this, with the lowest percent new occurring with the middle February sample was 32 ± 5.0%, followed by late January 2020 (40 ± 5.6%), and the highest abundance was found to be 52 ± 8.0% at late February 2020, out of the three samples.

Matisoff et al. (2005) measured the ages of suspended sediment or the percent new for three catchments (**Table 3**), all within the United States National Estuarine Research Reserves, they are: (1) Weeks Bay which is small bay embayed into the eastern shore of Mobile Bay; (2) South Slough, a small estuary off of Coos Bay in OR, United States; and (3) Old Woman Creek, a lake/fluvial system (lacustrine equivalent to an estuary) that empties into Lake Erie along its southern shore, in Ohio, United States. Among them, Weeks Bay is most comparable to Galveston Bay in terms of environments, both are shallow estuaries along the northern Gulf of Mexico. In addition to bay characteristics, water residence time in Galveston Bay has been measured to be about 40 days (Du et al., 2019), much longer than the water residence time in Weeks Bay (13 days, Solis and Powell, 1999; Novoveská and MacIntyre, 2019) and in Old Woman Creek (8.5 days, Matisoff et al., 2005). Therefore, it would be expected that the sediment would be older. However, the age of suspended sediments from both bays (i.e., Weeks Bay and Old Woman Creek) are actually falling within our reported range in the Galveston Bay (51–105 days, **Table 3**), with the age of the suspended sediment in Weeks Bay estimated to be 79 days; in Old Woman Creek, 104 days; South Slough, 93 days (Matisoff et al., 2005). It should be noted that the age of the suspended sediment is not the duration of time that the sediment has remained suspended in the water column, but rather the duration of time that the sediment remains an active component of the suspended sediment load. Being active within the sediment load means it is either suspended or sitting at or very near the seabed surface and maintaining a $^{7}Be$ label comparable to the suspended sediment. An example of this is sediment that settles out during slack tide, when the tidal currents are below the critical shear stress velocity, but which is resuspended as the tidal current increase and exceed the critical shear stress. This would be an example of ephemeral deposition. If the water column residence time is longer than the age of the suspended sediment, then the suspended sediment is either buried to a depth for which it is no longer ephemerally resuspended or it is exported out of the bay within a single residence time. If, in contrast, the suspended sediment age is longer than the residence time of the bay water, then that means that the sediment would be trapped within the bay, maintained as part of the suspended sediment load for multiple water column residence time cycles. This trend was found to be the case in all samples throughout the sampling period at both locations in our study area (**Table 2**).

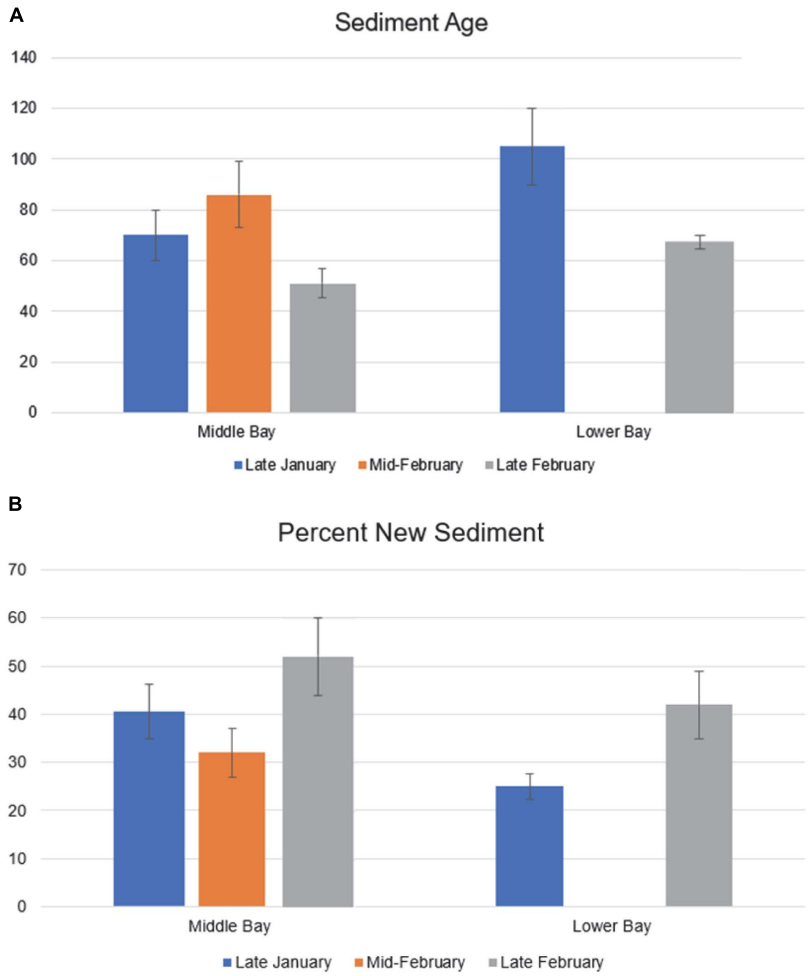


**FIGURE 3 |** Age of suspended sediments **(A)** and Percent "New" sediments **(B)** in middle and lower Galveston Bay during three weather events at 2020.

If we divide the age of the suspended sediment by the water column residence time, the ratio produced is an estimate of the retention/export efficiency of the suspended sediment within the estuary. A higher value indicates that the suspended sediment is retained and available for sediment resuspension for a longer time. Whereas, a lower value indicates either more rapid burial to below a depth of resuspension or a more rapid export from the bay. The ratio of suspended sediment age over water residence time ranged from 1.28 to 2.15 in the middle bay and from 1.68 to 2.63 in the lower bay.

Among three estuarine systems (Galveston Bay vs. Weeks Bay vs. Old Woman Creek) the suspended sediment of Galveston Bay was available for resuspension for 1.28–2.63 water column residence times (**Table 3**), whereas, the suspended sediment within Weeks Bay was available for 6.1 water column residence times. If we divide the number of residence times needed to trap or export sediment for Weeks Bay by the same parameter for Galveston Bay, we can see that Galveston Bay is 2.3 to 4.7 times more efficient in trapping its sediment than Weeks Bay. At this point, we could not find any additional published literature where this method has been used to estimate suspended sediment residence within estuaries, so it is difficult to say whether the results so far for Galveston Bay are typical of other large, shallow, coastal plain estuaries. Additionally, this study is of only three events in a single year, so it is difficult to say whether these results are typical for Galveston Bay. However, the results show, for the period of time for which this study was conducted, that residence times for suspended sediment within Galveston Bay were much longer than the residence time of the water within the bay and suggest that this is a line of research that is both in its infancy and also warrants further investigation, both seasonally and also of other bay systems.

## Sediment Transport in the Galveston Bay

Following precipitation and fluvial runoff, younger isotopes are introduced into the bay where the suspended load of sediment becomes isotopically labeled with a younger age. In contrast, precipitation in the bay resides within the fresher surface water while the bottom waters are isotopically older and have a higher salinity. As a result, resuspended sediment within the bay will, in

general, have an older age than newly introduced suspended load from the fluvial systems. Because the head of the bay is where the largest fluvial systems discharge, the $^{7}Be/^{210}Pb_{xs}$ ratio is expected to decrease as isotopes travel through a system (middle bay to lower bay). This statement assumes that suspended sediment is being advected through the bay along the salinity gradient. This is true for late January and late-February 2020, during each of these time periods there was a decreasing $^{7}Be/^{210}Pb_{xs}$ ratio (**Table 2**) but increasing sediment age (**Figure 3A**) from middle to lower bay. These observations confirm the hypothesis that sediment age should increase as suspended sediment moves through an estuarine system. Alternatively, from the prospective of the percentage of newly labeled sediments/particles, an increase in the abundance of old particles in the suspended sediments pool can be observed from the middle bay to the bay mouth (**Figure 3B**) for both the late January and February sampling events. An older age in the lower bay versus the middle bay is likely due to the distal location of freshly labeled sediment along with the mixing with older resuspended bay sediment when they travel through the system. With the variability of water mass transport and trapping within Galveston Bay, the values obtained can only be used to observe the bigger picture of the overall sediment transport. It should be noted that the time of year and characteristics of meteorological events could potentially produce much different results than those observed here.

In order to understand what these trends mean in Galveston Bay, water levels and salinities were examined during the weeks preceding the sampling (**Figure 4**). It should be noted that the salinity data was collected from the Trinity Bay, part of the Galveston Bay (**Figure 1**). Although the data collected in Trinity bay may not completely reflect the salinity for the entirety of the bay but can provide inside on average salinity within the bay and how rainfall has an effect on changes in salinity in a shallow estuary. Based on the analyses of the water levels when compared to the predicted tides, we found that there was a large influx of flood water trapped within the bay during much of January 2020 before our sampling during late January 2020 (**Figure 4**). When we considered the variation in salinity (monitored in Trinity Bay, part of the Galveston Bay, **Figure 1**), for the month of January 2020, it ranged between 19 and 10 PSU. Nevertheless, combined with the total amount of rainfall for the month of January 2020 being 200 mm, it would imply that the salinity would be much lower than this range (10–19 of salinity). Therefore, such a phenomenon indicates that there was a greater mass of high-salinity marine-derived water trapped within the bay.

During our sampling on late January 2020 (**Figure 4**), salinity was observed to be between 13 and 14 PSU and progressively decreased to below 10 PSU following the cold front in late January 2020. After this rain event, the salinity does not rise above 11 PSU for the remainder of sampling period. This indicates that high salinity water mass was flushed following the weather event in late January 2020 toward the mouth of the bay. By the time of the water sampling on middle February 2020, the age of sediment was older than late January samples (**Figure 3** and **Table 2**), implying that the high salinity water mass had yet to exit the bay but had moved further toward the mouth of the bay. Additionally, it is possible that the water pass may have passed the mouth of the bay, where suspended sediments had yet to arrive in middle February due to the longer transport time of suspended sediments (51–105 days, **Table 3**) than water masses (40 days, **Table 3**) within the bay. According to a 3D modeling study of the hydrodynamic circulation showing the weak tidal currents in the bay (Du et al., 2020), water masses can be trapped within the bay for prolonged periods of time, which appeared to be the case for much of January 2020 and middle February 2020. Based on this observation, there are longer residence times of unflushed water, leading to longer residence times of suspended sediment within these water masses. Older suspended sediment from January 2020 was still present in middle February 2020 where the age was $16 \pm 3$ days greater than late January 2020 (**Figure 3** and **Table 2**). Whereas, in late February 2020, it appears that the majority of the sediment measured in middle February 2020 was transported entirely out of the bay from this cold front, as a result, the age in late February 2020 was $35 \pm 7.4$ days younger (**Figure 3**). Correspondingly, sediment dynamics with bay water masses can also be observed based on the variation in $^{7}Be/^{210}Pb_{xs}$-derived abundance of newly labeled particles in suspended sedimentary pool. For example, the percentage of new sediment in middle bay from middle February was about $8 \pm 0.6\%$ lower than that from late January 2020 (**Figure 3**), demonstrating the weather event in middle February 2020 resulted in more $^{7}Be$-depleted particles resuspended from deeper bay sediments to the water column. In comparison, more newly labeled suspended particles were found for both sampling sites from late February 2020 (e.g.,

**TABLE 3 |** Summary of areas, water residence times, age and % new suspended sediment.

| System | Area of estuary | Water residence time | Age of suspended sediment | % New suspended sediment | Water column residence time/age of suspended sediment |
|---|---|---|---|---|---|
| Galveston bay | 1,397 $km^2$ | 40 days[2] | 51–105 days | 25–52% | 1.28–2.63 |
| Weeks bay[1] | 24 $km^2$ | 13 days[3] | $79 \pm 8$ days | $36 \pm 4\%$ | 6.1 |
| South slough[1] | 19 $km^2$ | n/a | $93 \pm 9$ days | $30 \pm 4\%$ | n/a |
| Old woman creek[1] | 2.3 $km^2$ | 8.5 days[1] | $26 \pm 3$ days | $26 \pm 3\%$ | 3.1 |

[1] *Matisoff et al. (2005)*
[2] *Du et al. (2019)*
[3] *Herdendorf et al. (2004)*

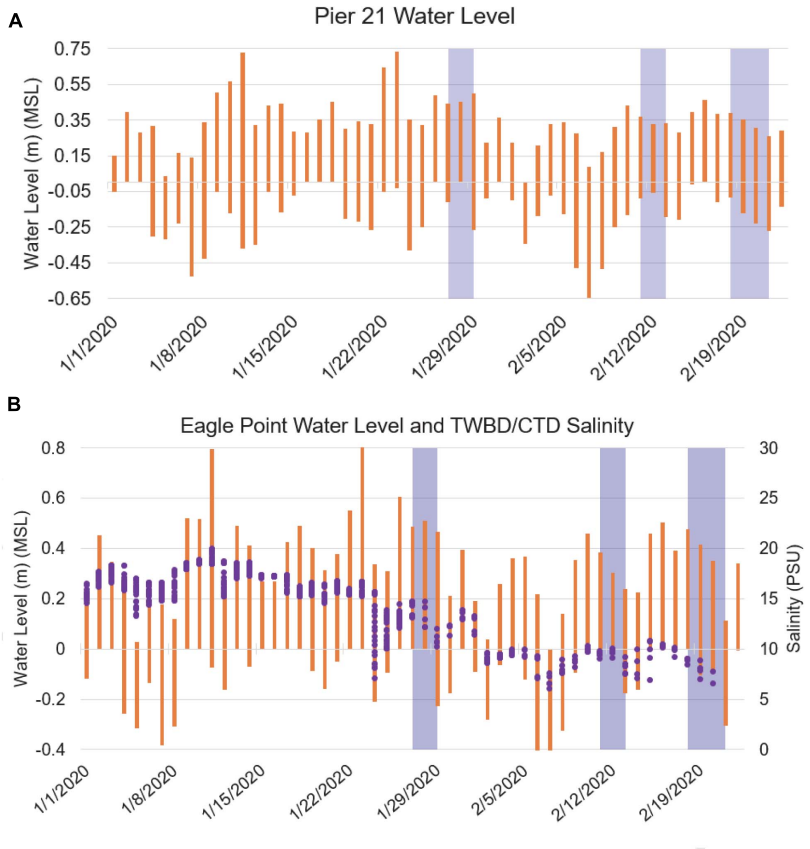


**FIGURE 4 |** Water levels from NOAA Pier 21 **(A)** and Eagle Point Stations **(B)** for the months of January and February 2020, as well as the salinity (PSU) obtained from Texas Water Development Board (TWBD-TRIN) station (1/1/2020-2/5/2020) and from the TAMUG-TRIN CTD station (2/6/2020-2/20/2020). Shading represents our precipitation sampling period.

20% increase in middle bay compared with middle February 2020, **Figure 3**). This also suggests that the majority of $^{7}Be$-depleted old sediments may have been flushed out of the bay during the meteorological front in middle February 2020. The majority of suspended sediments during late February 2020 was thus mainly composed by newly $^{7}Be$-labeled particles. Thus, our results generally displayed that meteorological fronts have the ability to resuspend and transport sediments, but with the hydrodynamic trapping of water masses within the bay (e.g., Trinity River), the length of time sediment reside within the bay may vary significantly.

## Implications to the Galveston Bay Environment

Estuaries and coasts are known to be the primary filter between the land-sea margin, where rivers and estuaries serve as sources of particulate contaminants to coastal environments (Huang et al., 2011). With Galveston Bay being a microtidal environment, residence times can be longer due to less water mass transport from tides, especially during low flow/water discharge periods. The heavy metals and different organic pollutants that quickly sorb to settling particles become the "sink" within an estuary. With much of the western shore of Galveston Bay and the watershed of many of its smaller tributaries heavily industrialized, there is an abundance of pollutants/chemical constituents which reside within the bottom sediment. For example, surface sediment was measured in Galveston Bay, and it was found that various particle reactive metals (e.g., lead, barium, mercury, copper, manganese, zinc, etc.) and polycyclic aromatic hydrocarbons (PAHs) sorbet onto the sediment, meaning that they have a great chance of resuspending during resuspension events (Santschi et al., 2001; Dellapenna et al., 2020; Camargo et al., 2021). Therefore, our estimated residence time of suspended sediments (51–105 days, **Table 2**) suggest these pollutants that adsorb to suspended sediment may spend months before they leave the Galveston Bay. The long residence times of sediments in Galveston Bay will increase the exposure time of living organisms to various pollutants. Along with the trapping of water masses that potentially allow for the accumulation in organisms will affect the health of Galveston Bay. Additionally, although cold fronts or other storm events can enhance sediment transport (i.e., reduce the residence time of suspended sediment), their induced sediment resuspension will result in the continuous interaction of the sedimentary pollutants with the water column of Galveston Bay, which loosely adsorbed pollutants in sediments may be released back to the Galveston

Bay waters. In contrast to the potential negative impact from long resident time and resuspension of bay sediments, some positive feedback may be beneficial to the bay environments, such as the nutrients release from the sediment resuspension (e.g., phosphate, Lin et al., 2013; Chao et al., 2017; Guo et al., 2020), which can promote the phytoplankton growth and accelerate the ecosystem function in Galveston Bay. Thus, $^{7}Be/^{210}Pb$-assisted investigation of sediment dynamics and age will help us better monitor the environmental quality in estuarine systems. Another factor this study brings to light is the ratio of the residence time of the water column to the residence time of the suspended sediment. The residence time of suspended sediment is an estimate of the duration of time that the sediment available for resuspension before either exiting the bay or being buried to a depth below which it can be resuspended. The more water column residence times that particle reactive contaminant labeled sediment resides within the estuary, the greater the opportunity that pelagic organisms have to be exposed to these particle reactive contaminants. It is not just the long residence time of the suspended sediment that is a factor, but also the amount of water column the particle reactive suspended sediment is exposed that is the risk to the environment.

## DATA AVAILABILITY STATEMENT

The original contributions presented in the study are included in the article/**Supplementary Material**, further inquiries can be directed to the corresponding author/s.

## AUTHOR CONTRIBUTIONS

TD provided the funding, designed and planned the project, and experimental process. NS carried out the experiments and data collection. PL performed the isotopic methods and analysis. NS, TD, and PL wrote the manuscript. All authors contributed to the article and approved the submitted version.

## FUNDING

This work was also made possible in part by National Oceanic and Atmospheric Administration (NOAA) and the Texas General Land Office Texas Coastal Management Program under Grant Number NA18NOS4190153.

## ACKNOWLEDGMENTS

We appreciate the assistance from undergraduate volunteers including Gregory Grimm, Ryland Lewis, Ryan Gage and Oscar Cavazos who assisted in collecting sample during frontal passages. All in-lab processing work conducted for this study was completed independently, with assistance from Josh Alarcon.

## SUPPLEMENTARY MATERIAL

The Supplementary Material for this article can be found online at: https://www.frontiersin.org/articles/10.3389/fmars.2021.703945/full#supplementary-material

## REFERENCES

Baskaran, M., Coleman, C. H., and Santschi, P. H. (1993). Atmospheric depositional fluxes of 7Be and 210Pb at Galveston and College Station, Texas. *J. Geophys. Res.* 98, 20555–20571. doi: 10.1029/93jd02182

Baskaran, M., and Santschi, P. H. (1993). The role of particles and colloids in the transport of radionuclides in coastal environments of Texas. *Mar. Chem.* 43, 95–114. doi: 10.1016/0304-4203(93)90218-d

Booth, J. G., Miller, R. L., McKee, B. A., and Leathers, R. A. (2000). Wind-induced bottom sediment resuspension in a microtidal coastal environment. *Cont. Shelf Res.* 20, 785–806. doi: 10.1016/s0278-4343(00)00002-9

Brost, R. A., Feichter, J., and Heimann, M. (1991). Three-dimensional simulation of 7Be in a global climate model. *J. Geophys. Res.* 96, 22423–22445. doi: 10.1029/91jd02283

Camargo, K., Sericano, J. L., Bhandari, S., *Hoelscher, C., McDonald, T. J., Chiu, W. A., et al. (2021). Polycyclic aromatic hydrocarbon status in post-hurricane Harvey sediments: considerations for environmental sampling in the Galveston Bay / Houston Ship Channel region. *Mar. Pollut. Bull.* 162:111872. doi: 10.1016/j.marpolbul.2020.111872

Caillet, S., Arpagaus, P., Monna, F., and Dominik, J. (2001). Factors controlling 7Be and 210Pb atmospheric deposition as revealed by sampling individual rain events in the region of Geneva. *Switzerland. J. Environ. Radio* 53, 241–256. doi: 10.1016/s0265-931x(00)00130-2

Chambers, M., Mitchell, A., Fine, A., Mulder, K., Rainville, L., Hackett, D., et al. (2018). *Port Performance Freight Statistics Program: Annual Report to Congress 2017*. (Washington, DC: Department of Transportation. Bureau of Transportation Statistics).

Chao, J. Y., Zhang, Y. M., Kong, M., Zhuang, W., Wang, L. M., Shao, K. Q., et al. (2017). Long-term moderate wind induced sediment resuspension meeting phosphorus demand of phytoplankton in the large shallow eutrophic Lake Taihu. *PLoS One* 12:e0173477. doi: 10.1371/journal.pone.0173477

Dellapenna, T., Allison, M., Gill, G., Lehman, R., and Warnken, K. (2006). The impact of shrimp trawling and associated sediment resuspension in mud dominated, shallow estuaries. *Estuar. Coast. Shelf Sci.* 69, 519–530. doi: 10.1016/j.ecss.2006.04.024

Dellapenna, T. M., Hoelscher, C., Hill, L., Al Mukaimi, M. E., and Knap, A. (2020). How tropical cyclone flooding caused erosion and dispersal of mercury-contaminated sediment in an urban estuary: the impact of Hurricane Harvey on Buffalo Bayou and the San Jacinto Estuary, Galveston Bay, USA. *Sci. Total Environ.* 748:141226. doi: 10.1016/j.scitotenv.2020.141226

Du, J., and Park, K. (2019). Estuarine salinity recovery from an extreme precipitation event: hurricane Harvey in Galveston Bay. *Sci. Total Environ.* 670, 1049–1059. doi: 10.1016/j.scitotenv.2019.03.265

Du, J., Park, K., Shen, J., Zhang, Y. J., Yu, X., Ye, F., et al. (2019). A hydrodynamic model for Galveston Bay and the shelf in the northern Gulf of Mexico. *Ocean Sci.* 15, 951–966. doi: 10.5194/os-15-951-2019

Du, J., Park, K., Yu, X., Zhang, Y. J., and Ye, F. (2020). Massive pollutants released to Galveston Bay during Hurricane Harvey: understanding their retention and pathway using Lagrangian numerical simulations. *Sci. Total Environ.* 704:135364. doi: 10.1016/j.scitotenv.2019.135364

Duenas, C., Fernandez, M. C., Carretero, J., Liger, E., and Canete, S. (2002). Atmospheric deposition of 7Be at a coastal Mediterranean station. *J. Geophy. Res.* 106, 34059–34065. doi: 10.1029/2001jd000771

Guo, M., Li, X., Song, C., Liu, G., and Zhou, Y. (2020). Photo-induced phosphate release during sediment resuspension in shallow lakes: a potential positive feedback mechanism of eutrophication. *Environ. Pollut.* 258:113679. doi: 10.1016/j.envpol.2019.113679

Haby, M. G., Miget, R. J., and Falconer, L. L. (2009). *Hurricane Damage Sustained by the Oyster Industry and the Oyster Reefs Across the Galveston Bay System With Recovery Recommendations. A Texas AgriLife Extension Service/Sea Grant Extension Program Staff Paper*. Galveston, TX: The Texas A&M University System.

Hardy, J. W., and Henderson, K. G. (2003). Cold front variability in the southern United States and the influence of atmospheric teleconnection patterns. *Phys. Geogr.* 24, 120–137. doi: 10.2747/0272-3646.24.2.120

Henry, W. K. (1979). Some aspects of the fate of cold fronts in the Gulf of Mexico. *Monthly Weather Rev.* 107, 1078–1082. doi: 10.1175/1520-0493(1979)107<1078:saotfo>2.0.co;2

Herdendorf, C., Klarer, D. M., and Herdendorf, R. C. (2004). *The Ecology of Old Woman Creek, Ohio: An Esturine and Watershed Profile*. Columbus OH: Ohio Department of Natural Resources.

Huang, D., Du, J., and Zhang, J. (2011). Particle dynamics of 7Be, 210Pb and the implications of sedimentation of heavy metals in the Wenjiao/Wenchang and Wanquan River estuaries, Hainan, China. *Estuar. Coast. Shelf Sci.* 93, 431–437. doi: 10.1016/j.ecss.2011.05.013

Koch, D. M., Jacob, D. J., and Graustein, W. C. (1996). Vertical transport of troposheric aerosols as indicated by $^{7}Be$ and $^{210}Pb$ in a chemical tracer model. *J. Geophy. Res.* 101, 18651–18666. doi: 10.1029/96JD01176

Lin, P., Guo, L., Chen, M., and Cai, Y. (2013). Distribution, partitioning and mixing behavior of phosphorus species in the Jiulong River estuary. *Mar. Chem.* 157, 93–105. doi: 10.1016/j.marchem.2013.09.002

Matisoff, G., Wilson, C., and Whiting, P. (2005). The 7Be/210PbXS ratio as an indicator of suspended sediment age or fraction new sediment in suspension. *Earth Surf. Process. Landf.* 30, 1191–1201. doi: 10.1002/esp.1270

Morse, J. W., Presley, B. J., Taylor, R. J., Benoit, G., and Santschi, P. (1993). Trace metal chemistry of Galveston Bay: water, sediments and biota. *Mar. Environ. Res.* 36, 1–37. doi: 10.1016/0141-1136(93)90087-g

Novoveská, L., and MacIntyre, H. L. (2019). Study of the seasonality and hydrology as drivers of phytoplankton abundance and composition in a shallow estuary. Weeks Bay, Alabama (USA). *J. Aquac. Mar. Biol.* 8, 69–80.

Olsen, C. R., Larsen, I. L., Lowry, P. D., Cutshall, N. H., Todd, J. F., Wong, G. T. F., et al. (1985). Atmospheric fluxes and marsh-soil inventories of 7Be and 210Pb. *J. Geophys. Res.* 90, 10487–10495.

Olsen, C. R., Thein, M., Larsen, I. L., Lowry, P. D., Mulholland, P. J., Cutshall, N. H., et al. (1989). Plutonium, lead-210, and carbon isotopes in the Savannah estuary: riverborne versus marine sources. *Environ. Sci. Technol.* 23, 1475–1481. doi: 10.1021/es00070a004

Saari, H., Schmidt, S., Castaing, P., Blanc, G., Sautour, B., Masson, O., et al. (2010). The particulate 7Be/210Pbxs and 234Th/210Pbxs activity ratios as tracers for tidal-to-seasonal particle dynamics in the Gironde estuary (France): implications for the budget of particle-associated contaminants. *Sci. Total Environ.* 408, 4784–4794. doi: 10.1016/j.scitotenv.2010.07.017

Santschi, P. H., Presley, B. J., Wade, T. L., Garcia-Romero, B., and Baskaran, M. (2001). Historical contamination of PAHs, PCBs, DDTs, and heavy metals in Mississippi river Delta, Galveston bay and Tampa bay sediment cores. *Mar. Environ. Res.* 52, 51–79. doi: 10.1016/s0141-1136(00)00260-9

Solis, R. S., and Powell, G. (1999). *Hydrography, Residence Times, and Physical Processes. Biogeochemistry of Gulf of Mexico Estuaries*. New York NY: John Wiley, 29–61.

Stunz, G. W., Minello, T. J., and Rozas, L. P. (2010). Relative value of oyster reef as habitat for estuarine nekton in Galveston Bay, Texas. *Mar. Ecol. Prog. Ser.* 406:159.

Taylor, A., Blake, W. H., Smith, H. G., Mabit, L., and Keith-Roach, M. J. (2013). Assumptions\and challenges in the use of fallout beryllium-7 as a soil and sediment tracer in river basins. *Earth Sci. Rev.* 126, 85–95. doi: 10.1016/j.earscirev.2013.08.002

United States Geological Survey [USGS] (2005). *US Geological Survey Suspended-Sediment Database, Daily Values of suspended Sediment And Ancillary Data*. Reston, VA: USGS.

Walker, N. D., and Hammack, A. B. (2000). Impacts of winter storms on circulation and sediment transport: atchafalaya-Vermilion Bay region, Louisiana, USA. *J. Coastal Res.* 16, 996–1010.

Wang, Z., Yang, W., Chen, M., Lin, P., and Qiu, Y. (2013). Intra-annual deposition of atmospheric 210Pb, 210Po and the residence times of aerosol in Xiamen, China. *Aerosol Air Qual. Res.* 14, 1402–1410. doi: 10.4209/aaqr.2013.05.0170

Winterwerp, J. C., and Van Kesteren, W. G. (2004). *Introduction to the Physics of Cohesive Sediment Dynamics in the Marine Environment*. Amsterdam: Elsevier.

**Conflict of Interest:** The authors declare that the research was conducted in the absence of any commercial or financial relationships that could be construed as a potential conflict of interest.

*Copyright © 2021 Schmidt, Dellapenna and Lin. This is an open-access article distributed under the terms of the Creative Commons Attribution License (CC BY). The use, distribution or reproduction in other forums is permitted, provided the original author(s) and the copyright owner(s) are credited and that the original publication in this journal is cited, in accordance with accepted academic practice. No use, distribution or reproduction is permitted which does not comply with these terms.*

frontiers in Marine Science

ORIGINAL RESEARCH
published: 29 July 2021
doi: 10.3389/fmars.2021.697444

# $^{210}$Po and $^{210}$Pb as Tracers of Particle Cycling and Export in the Western Arctic Ocean

*Wokil Bam[1]*, Kanchan Maiti[1]* and Mark Baskaran[2]*

[1] *Department Oceanography and Coastal Sciences, Louisiana State University, Baton Rouge, LA, United States,*
[2] *Department of Environmental Science and Geology, Wayne State University, Detroit, MI, United States*

The distribution and vertical fluxes of particulate organic carbon and other key elements in the Arctic Ocean are primarily governed by the spatial and seasonal changes in primary productivity, areal extent of ice cover, and lateral exchange between the shelves and interior basins. The Arctic Ocean has undergone rapid increase in primary productivity and drastic decrease in the areal extent of seasonal sea ice in the last two decades. These changes can greatly influence the biological pump as well as associated carbon export and key element fluxes. Here, we report the export of particulate organic and inorganic carbon, particulate nitrogen and biogenic silica using $^{210}$Po and $^{210}$Pb as tracers for the seasonal vertical fluxes. Samples were collected as a part of US GEOTRACES Arctic transect from western Arctic Basin in 2015. The total activities of $^{210}$Po and $^{210}$Pb in the upper 300 m water column ranged from 0.46 to 16.6 dpm 100L$^{-1}$ and 1.17 to 32.5 dpm 100L$^{-1}$, respectively. The $^{210}$Pb and $^{210}$Po fluxes varied between 5.04–6.20 dpm m$^{-2}$ d$^{-1}$ and 8.26–21.02 dpm m$^{-2}$ d$^{-1}$, respectively. The corresponding particulate organic carbon (POC) and particulate nitrogen (PN) fluxes ranged between 0.75–7.43 mg C m$^{-2}$ d$^{-1}$ and 0.08–0.78 mg N m$^{-2}$ d$^{-1}$, respectively, with highest fluxes observed in the northern ice-covered stations. The particulate inorganic carbon (PIC) and biogenic silica (bSi) fluxes were extremely low ranging from 0 to 0.14 mg C m$^{-2}$ d$^{-1}$ and 0.14 to 2.88 mg Si m$^{-2}$ d$^{-1}$, respectively, at all stations suggesting absence of ballast elements in facilitating the biological pump. The variability in POC fluxes with depth suggest prominent influence of lateral transport to downward fluxes across the region. The results provide a better understanding of the spatial variability in the vertical fluxes POC, PN, bSi, and PIC in the western Arctic which is currently undergoing dramatic changes.

**Keywords: export production, POC flux, particle export, Arctic Ocean, organic matter export**

OPEN ACCESS

***Edited by:***
*Laodong Guo,*
*University of Wisconsin–Milwaukee, United States*

***Reviewed by:***
*J. Kirk Cochran,*
*Stony Brook University, United States*
*Anne-Marie Wefing,*
*ETH Zürich, Switzerland*

****Correspondence:***
*Wokil Bam*
*wbam1@lsu.edu;*
*bamwokil1@gmail.com*
*Kanchan Maiti*
*kmaiti@lsu.edu*

***Specialty section:***
*This article was submitted to Marine Biogeochemistry, a section of the journal Frontiers in Marine Science*

***Received:*** *19 April 2021*
***Accepted:*** *09 July 2021*
***Published:*** *29 July 2021*

***Citation:***
*Bam W, Maiti K and Baskaran M (2021) $^{210}$Po and $^{210}$Pb as Tracers of Particle Cycling and Export in the Western Arctic Ocean. Front. Mar. Sci. 8:697444. doi: 10.3389/fmars.2021.697444*

## INTRODUCTION

The Arctic Ocean covers an area of 9.6 × 10$^6$ km$^2$ (Serreze et al., 2006), which corresponds to 5% of the world oceans by surface area, with 1.5% by volume (Meybeck and Ragu, 1997; Guay and Falkner, 1998) indicating that it is a relatively shallow ocean with about 50% of the total Arctic Ocean surface area as continental shelf area (Jakobsson et al., 2004). Approximately 10% of the world's rivers discharge flow into the Arctic Ocean making it one of the most dynamic systems, similar

to estuarine systems (Aagaard and Carmack, 1989; Meybeck and Ragu, 1997; Guay and Falkner, 1998; Dickson et al., 2007). The catchment area of these rivers is estimated to store about 30% of the world's soil carbon (Hugelius et al., 2014; Schuur et al., 2015). Thus, recent climate changes can have profound impacts on the Arctic region resulting in increased export of organic carbon, and associated trace elements and sediments to the Arctic Ocean (Rachold et al., 2000; Moran et al., 2005; Jorgenson et al., 2006; Schuur et al., 2008; Lannuzel et al., 2020; and reference therein).

The input of freshwater from Arctic rivers into the Arctic Ocean has increased significantly during recent decades (Peterson et al., 2002; Ahmed et al., 2020). This increase in freshwater discharge, coupled with increased coastal erosion, permafrost thaw and sea ice melting suggest that the riverine input of carbon, nutrients, and metals will continue to increase in the future. The highly productive shallow shelf serves as a source of organic carbon and nutrients to the central Arctic Ocean through the two major currents systems, Transpolar Drift (TPD), and Beaufort Gyre (e.g., Wheeler et al., 1997; Krishnamurthy et al., 2001; Klunder et al., 2012; Charette et al., 2020). The Arctic Ocean has also undergone more than 20% increase in primary productivity in the last two decades due to decrease in the areal extent of sea ice cover (Arrigo and van Dijken, 2011). The sea ice in this region serves as a platform for retaining atmospherically delivered particle-reactive species, as well as a vehicle for transport of organic and inorganic species incorporated into sea ice formed in the coastal areas (e.g., Krishnamurthy et al., 2001; Tovar-Sánchez et al., 2010). Thus, changes in freshwater input and extent of sea-ice melting can greatly influence the biological pump and particle scavenging in this region.

The present research focuses on the Western Arctic Canada Basin where the vertical fluxes of biogenic materials are reported to be lowest compared to the global ocean, with only 1–2% of the new production reaching the deep basin (Honjo et al., 2010; Hwang et al., 2015). However, expected changes in freshwater discharge will affect the lateral transport of particles into the interior basin (Fahl and Nöthig, 2007; Hwang et al., 2008; Honjo et al., 2010). Water mass exchange between the highly productive shelf and interior basin has been reflected in the observed shelf scavenging signal into the interior basin (Moore and Smith, 1986; Smith et al., 2003). The biogeochemistry in the western Arctic Basin can thus be significantly altered by the influx of shelf-derived materials, and their subsequent transport by TPD (Kipp et al., 2018).

A better understanding of particle cycling and their export to deeper ocean is crucial considering the rapid changes occurring on multiple fronts in this region. The naturally occurring radioisotope pairs from $^{238}$U decay series such as $^{234}$Th – $^{238}$U, $^{210}$Pb – $^{226}$Ra, and $^{210}$Po – $^{210}$Pb have been widely used as tracers of particulate matter in the water column, especially in the estimation of the export flux and cycling of particulate matter. Most of the $^{226}$Ra ($t_{1/2}$ = 1602 y) in the oceanic water column in deep ocean basins are derived from bottom sediment via diffusion (Cochran, 1992). $^{210}$Pb ($T_{1/2}$ = 22 y) is produced from *in situ* decay of its grandparent $^{226}$Ra (which has highest concentration near bottom water) present in the water column as well as direct atmospheric deposition (highest concentration at air-sea interface). $^{210}$Po is derived from decay of $^{210}$Pb in the water column. The $^{210}$Po/$^{210}$Pb activity ratio in atmospheric deposition is generally $< 0.1$ (Baskaran, 2011), and thus acts as a minor source of $^{210}$Po in the surface ocean. Both the $^{210}$Pb and $^{210}$Po are highly particle reactive, with partition coefficient ($K_d$) values of $10^4$–$10^6$ and $10^5$–$10^9$, respectively (Baskaran and Santschi, 2002; Su et al., 2017; Tang et al., 2017; Bam et al., 2020) and hence are scavenged by both suspended and sinking particulate matter. Higher partition coefficient values represent higher affinity of elements to be adsorb/attach to particles. A deficiency of $^{210}$Po relative to $^{210}$Pb is often observed in the upper few hundred meters of the water column due to higher scavenging efficiency of Po (Bacon et al., 1976; Nozaki et al., 1976). Po has stronger affinity for biogenic particulate matter and thus preferential removal of $^{210}$Po takes place in the upper water column. While $^{210}$Pb is only adsorbed onto particle surfaces, $^{210}$Po is also assimilated into phytoplankton cells (Bacon et al., 1976; Nozaki et al., 1976; Fisher et al., 1983). The preferential adsorption and accumulation of $^{210}$Po in organic matter is well documented in both lab culture and field studies (Fisher et al., 1983; Stewart and Fisher, 2003a,b). Similarly, preferential adsorption of $^{210}$Pb compared to $^{210}$Po onto silicious frustules had been previously reported (Friedrich and Rugters van der Loeff, 2002; Lin et al., 2021). The $^{226}$Ra – $^{210}$Pb and $^{210}$Pb – $^{210}$Po pairs can thus be used to trace particle transport processes and quantify chemical scavenging and particle removal rates in the upper ocean for time scales of months to years.

In this article, we utilize these two isotope pairs to investigate the spatial variability in fluxes of particulate organic carbon (POC), particulate inorganic carbon (PIC), particulate nitrogen (PN), and biogenic silica (bSi) across the open water to permanently ice-covered region of the western Arctic Ocean. The spatial and seasonal changes in sea-ice cover, primary productivity, riverine input of freshwater, sediment resuspension, physical processes, and strong halocline play important roles in the distribution of particles, nutrients, and trace elements in the Arctic Ocean (Rachold et al., 2004; Lepore et al., 2009; Chen et al., 2012; Jeandel et al., 2015). Here, we report export fluxes of POC (using POC/$^{210}$Po ratio), PN (using PN/$^{210}$Po ratio), bSi (using bSi/$^{210}$Pb ratio), and PIC (using PIC/$^{210}$Pb ratio) from upper 250 m of the water column.

# MATERIALS AND METHODS

## Study Area

Arctic water comprises of several distinct water masses which include the high salinity and low temperature Pacific water coming through the Bering Strait, freshwater from river discharge, and high salinity and high temperature Atlantic water coming through Fram Strait (Moore and Smith, 1986; Rutgers Van Der Loeff et al., 1995; Hu et al., 2014). The largest freshwater inventory is found in the upper 300 m of the Canadian Basin (Yamamoto-Kawai et al., 2008; Rabe et al., 2011). Pacific water contributes to the surface and halocline waters of the Canadian Basin (Bauch et al., 1995). Pacific water of winter origin tends to enter the interior Arctic below the upper mixed layer because of

their higher salinity and creating the lower halocline water masses (Weingartner et al., 1998; Zhong et al., 2019). Warmer Pacific and colder Atlantic water masses make the system highly stratified and lead to formation of two distinct halocline; the upper and the lower halocline (Smith et al., 2003; Lepore et al., 2009; Zhong et al., 2019). Halocline waters from the shelf seas are the key source of high nutrients in the Arctic basin (Aagaard et al., 1981; Moore and Smith, 1986; Fripiat et al., 2018; Granger et al., 2018).

The upper halocline is mainly confined to the Canadian Basin and is characterized by high nutrients and low dissolved oxygen, whereas the lower halocline is characterized by lower nutrients and higher dissolved oxygen (Jensen et al., 2019, 2020). The compositions of these water masses are greatly altered during their residence on the shelves due to ice formation and melting, primary production, and exchanges with the atmosphere and the seafloor (Rutgers Van Der Loeff et al., 1995).

## Sample Collection

Samples were collected during the US Arctic GEOTRACES (GN01) cruise onboard US Coast Guard Cutter *Healy* (HLY1502) from August 9th to October 11th, 2015. Water samples for dissolved and particulate $^{210}$Po and $^{210}$Pb, particulate organic carbon (POC), particulate inorganic carbon (PIC), particulate nitrogen (PN), and biogenic silica (bSi) were collected at Station 30, Station 43, Station 48, and Station 56 (**Figure 1**). Station 30 and 43 are permanently ice covered, station 48 is seasonally ice covered and station 56 is predominantly open water located on the continental slope (**Figure 1**). The station 30, 43, and 48 are within the area of TPD and Beaufort Gyre whereas the station 56 is influenced by Pacific Water inflow and Beaufort Gyre. About 20-L water samples were collected at various depths using a 30-L Niskin bottles. For dissolved $^{210}$Po and $^{210}$Pb, water samples were filtered through a 0.45 μm cartridge filter within 1–2 h after collection and transferred to acid-cleaned cubitainers. The dissolved samples were adjusted to pH 1–2 by adding 6 M HCl within less than 2–3 h after collection and stored onboard. Particulate samples were collected using battery-operated submersible pumps (McLane Research Laboratories, Inc., Falmouth, MA, United States). The pump deployment consisted of a vertical array of pumps at depths coinciding with dissolved samples. For the particulate matter, large-volume water samples (400–600 L) were filtered at a flow rate of ∼6 L min$^{-1}$ through acid-washed 150 mm pre-filters (51 μm polycarbonate screen) and then onto pre-acid-washed, pre-combusted 1 μm nominal, 150 mm diameter Quartz Microfiber Filter (QMA) (Whatman, Kent, United Kingdom) to capture suspended particles. The particles captured on 1 and 51 μm filters are referred to as small and large particles, respectively.

Dissolved and particulate $^{210}$Po and $^{210}$Pb analysis were carried out in the lab following procedures outlined in Bam et al. (2020). Plating of Po was done by spontaneous electro-deposition onto silver planchets, following methods described in Geotraces Cookbook (2017) and Bam et al. (2020). The average time between sample collection and initial plating of $^{210}$Po for dissolved and particulate samples was approximately 1.5–2 months. The final Po-Pb data was appropriately corrected for decay and ingrowth between the sampling and first plating along with other radiometric decay correction (Baskaran et al., 2013; Bam and Maiti, 2021). Data on POC, PN, PIC, bSi, and $\delta^{13}C_{POC}$ data were obtained from BCO-DMO website and details on sampling and analytical methods are reported in Xiang and Lam, 2020 and (Lam, 2020)[1]. The $\delta^{13}$C-DIC data were also obtained from BCO-DMO website (Quay, 2019)[2] and sampling and analytical methods are reported in Ko and Quay (2020). $^{226}$Ra activities were also obtained from BCO-DMO website (Charette and Moore, 2020)[3] and the details for sampling and analytical methods were reported in Kipp et al. (2019). Temperature, fluorescence, dissolved oxygen, and salinity in-situ data were collected using the shipboard CTD at each station and are reported in BCO-DMO website (Cutter et al., 2019)[4].

## Pb and Po Export Models

The major source of $^{210}$Pb in seawater is from *in-situ* decay of $^{226}$Ra and atmospheric deposition. The rate of change of $^{210}$Pb activity can be expressed as follows (Moore and Smith, 1986; Friedrich and Rugters van der Loeff, 2002; Smith et al., 2003):

$$\frac{\partial A_{Pb}}{\partial t} = (A_{Ra} - A_{Pb})\lambda_{Pb} + I_{Pb} - F_{Pb} - V \quad (1)$$

where, $A_{Ra}$ and $A_{Pb}$ are the activities of dissolved $^{226}$Ra (dpm L$^{-1}$) and total $^{210}$Pb (dpm L$^{-1}$), $\lambda_{Pb}$ is decay constant (d$^{-1}$) of $^{210}$Pb, $I_{Pb}$ is the atmospheric depositional input flux of $^{210}$Pb assumed to be 0.17 dpm cm$^{-1}$ y$^{-1}$, based on the mean value (range 0.12–0.22 dpm cm$^{-1}$ y$^{-1}$) of previous estimates by Baskaran (2011), $F_{Po}$ is the export flux of $^{210}$Pb (dpm m$^{-2}$ d$^{-1}$) on to sinking particles and V is the sum of advective and diffusive fluxes of $^{210}$Pb activities (dpm m$^{-2}$ d$^{-1}$).

Similarly, the major source of $^{210}$Po in the water column is from the in-situ decay of its longer-lived grandparent $^{210}$Pb. $^{210}$Po can also be added via atmospheric deposition from the decay of $^{210}$Pb within the atmosphere, but this activity usually represents < 10% of the $^{210}$Pb activity because of the short atmospheric residence time of $^{210}$Pb-containing aerosols (Harada et al., 1989; Kim et al., 2005; Baskaran, 2011). The rate of change of $^{210}$Po due to export can be expressed as follows: (e.g., Bacon et al., 1976; Moore and Smith, 1986):

$$\frac{\partial APo}{\partial t} = (A_{Pb} - A_{Po})\lambda_{Po} + I_{Po} - F_{Po} - V \quad (2)$$

where, $I_{Po}$ is the atmospheric depositional input flux of $^{210}$Po (dpm cm$^{-1}$ y$^{-1}$) which is extremely low for this region (Baskaran, 2011), $A_{Pb}$ is the total $^{210}$Pb activity in the water column (dpm L$^{-1}$), $A_{Po}$ is the total $^{210}$Po activity (dpm L$^{-1}$), $\lambda_{Po}$ is the decay constant (d$^{-1}$), $F_{Po}$ is the export flux of $^{210}$Po (dpm cm$^{-1}$ y$^{-1}$) on sinking (large) particle, and V is the sum of advective and diffusive fluxes of $^{210}$Po activities (dpm cm$^{-1}$ y$^{-1}$).

The export fluxes of $^{210}$Pb can be estimated using a 1-D steady state model (i.e., $\partial$APb/ $\partial$t = 0 total $^{210}$Pb remain constant),

[1]https://www.bco-dmo.org/dataset/807340
[2]https://www.bco-dmo.org/dataset/751211
[3]https://www.bco-dmo.org/dataset/718440
[4]https://www.bco-dmo.org/dataset/651599/data

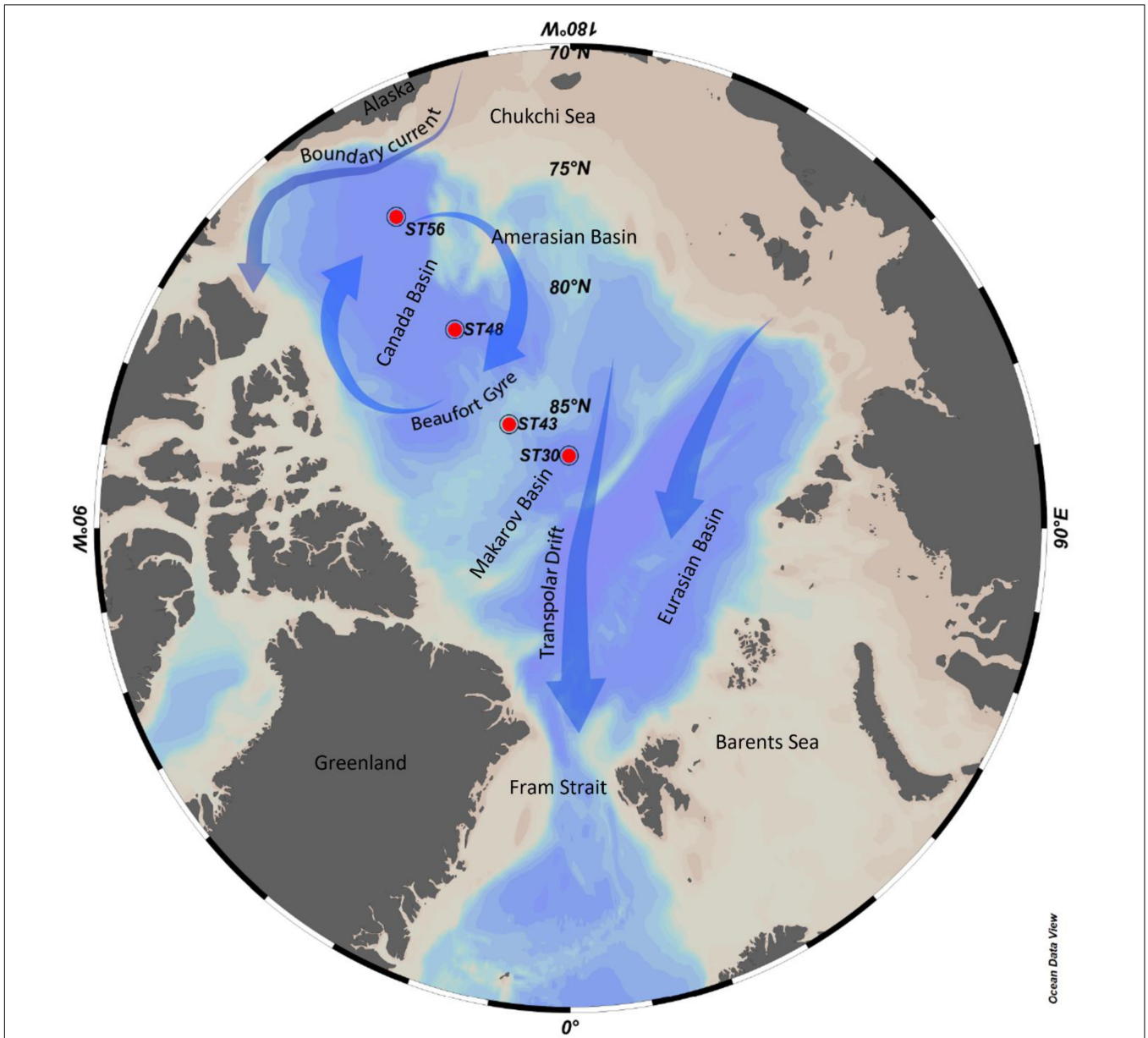


**FIGURE 1 |** Map showing the sampling stations 30, 43, 48, and 56 in the US Arctic GEOTRACES (GN01) section. Water samples for dissolved and particulate $^{210}$Po and $^{210}$Pb were collected onboard US Coast Guard Cutter *Healy* (HLY1502) from August 9th to October 11th, 2015. The arrows represent the major circulation pattern of the surface layer water mass. The map was created using Ocean Data View 5.2.0.

which assumes negligible advective and diffusive fluxes ($V = 0$) as follows:

$$F_{Pb} = \int_0^z \lambda_{Pb} \left(A_{Ra} - A_{Pb}\right) dz + I_{Pb} \tag{3}$$

where, $F_{Pb}$ is the $^{210}$Pb flux, $A_{Ra}$ is the total activity of $^{226}$Ra in the water column, $A_{Pb}$ is the total activity of $^{210}$Pb in the water column, $\lambda_{Pb}$ is the $^{210}$Pb decay constant, $I_{Pb}$ is the atmospheric depositional input flux of $^{210}$Pb, and $z$ is the integrated thickness of the water column layer.

Similarly, the export fluxes of $^{210}$Po can be estimated using a 1-D steady state model (i.e., $\partial$APo/ $\partial$t = 0, total $^{210}$Po remain constant), which assumes negligible advective and diffusive fluxes ($V = 0$) and negligible $^{210}$Po atmospheric flux (considering the fact that $^{210}$Po/$^{210}$Pb activity in atmospheric deposition is $< 0.1$) as follows:

$$F_{Po} = \int_0^z \lambda_{Po} \left(A_{Pb} - A_{Po}\right) dz \tag{4}$$

where, $F_{Po}$ is the $^{210}$Po flux, $A_{Pb}$ is the total activity of $^{210}$Pb in the water column, $A_{Po}$ is the total activity of $^{210}$Po in

the water column, $\lambda_{Po}$ is the $^{210}$Po decay constant, and $z$ is the integrated thickness of the water column layer. However, western Arctic Ocean can be influenced by shelf interaction which could overestimate the $^{210}$Po and $^{210}$Pb flux due to $^{210}$Po and $^{210}$Pb deficit in shelf water. Previous studies have shown lateral input and transport of materials in the western Arctic from the continental shelf areas (Lepore et al., 2009; Kipp et al., 2018; Rutgers Van Der Loeff et al., 2018). The melting ice can also contribute to water column $^{210}$Pb and $^{210}$Po inventory, but previous studies have suggested melting of all sea-ice present in the Arctic will only contribute to 10% of the $^{210}$Pb inventory (Masqué et al., 2007; Roca-Martí et al., 2016). Moreover, such contribution from ice is likely to have $^{210}$Po-$^{210}$Pb in equilibrium and will have negligible impact on $^{210}$Po flux estimates in the Arctic.

The $^{210}$Po has higher particle affinity for biogenic material such as POC and PN whereas the $^{210}$Pb has higher affinity for species such as PIC and bSi (Fisher et al., 1983; Friedrich and Rugters van der Loeff, 2002). Thus, $^{210}$Po fluxes can be used to estimate the sinking fluxes of POC and PN and $^{210}$Pb fluxes can be used to estimate the sinking fluxes of PIC and bSi. The POC flux can be calculated as follows.

$$F_{POC} = F_{210Po}\left[\frac{POC}{APo}\right]_{particles} \quad (5)$$

where, $F_{POC}$ is the flux of POC, $F_{210Po}$ is the flux of $^{210}$Po, and $A_{Po}$ is the activity of $^{210}$Po in the particulate phase and POC is the POC concentration in the particles. The PN, PIC, and bSi fluxes were also calculated in a similar method as the POC flux using equation 5.

Estimation of export of particulate phases in the water column, using equations 3 and 4 involve the following assumptions: (i) the atmospheric input of $^{210}$Pb and $^{210}$Po in the surface ocean is at steady state on time scale that we integrate for the estimation of POC fluxes. Previous studies from this region have shown the atmospheric input in the Arctic (60–80 °N), to be extremely low ranging between 0.12 and 0.22 dpm cm$^{-2}$ y$^{-1}$ (Baskaran, 2011); (ii) the elemental to radionuclide ratios measured in particles collected by *in situ* pumps are representative of sinking particles. In this study, the elemental ratios in both the small (1–51 um) and large (>51um) particles were measured, we used both the ratios in large and small particles to estimate the export fluxes. However, we primarily focused on the larger particle export similar to earlier studies (Stewart et al., 2007; Maiti et al., 2016; Roca-Martí et al., 2016); (iii) the one-time sampling in the summer is representative for much longer time scales of months to years over which $^{210}$Po and $^{210}$Pb fluxes integrates. This region is characterized by phytoplankton bloom at the onset of summer which could result in non-steady condition. However, our sampling was carried out in late summer and the longer half-life of $^{210}$Po ($t_{1/2}$ = 138 d) results in flux integrated over timescales of months, making it less sensitive to short-term non-steady state events.

# RESULTS

## Hydrological Parameters

The national snow and ice data center sea ice index suggests that permanent sea ice (multi-year) is present throughout the year at stations 30 and 43, station 48 is covered with sea ice most of the time during the year whereas station 56 is rarely covered with ice. The mixed layer, defined as the depth where density increased from its surface value by 20% of the difference surface and 100 m, varied between 40 and 50 m in all four stations (Shaw et al., 2009). The top 50–75 m water column is strongly stratified as shown by the temperature and salinity transect (**Figures 2A,B**). The stations 30 and 43 had maximum chlorophyll-a concentration in the upper 10 m of the water column, whereas stations 48 and 56 had maximum chlorophyll-a concentrations at 50–60 m (**Figure 2C**). The presence of surface maximum chlorophyll concentration in stations 30 and station 43 could be attributed to melting of sea ice (sea ice present during the sampling) with high concentrations of algae in sea ice. The dissolved oxygen (DO) varied between 7.02 and 12.2 mg L$^{-1}$, with station 30 having higher DO in the mixed layer (**Supplementary Figure 1**). In the upper 500 m water column, the silicate, nitrate, and phosphate concentrations varied between 0 and 50 μmol kg$^{-1}$, 0 and 20 μmol kg$^{-1}$ and 0 to 2.5 μmol kg$^{-1}$, respectively, with significantly higher concentrations between 100 and 250 m (**Figure 3**). The station 30 had the lowest nutrient concentration which increased from North to Southward. The nutrient maximum layer showed a similar pattern to temperature and salinity profiles corresponding to the distinct water masses. The spatial distribution of nutrient in the Arctic water column is mainly influenced by the water masses specially the warm Pacific Water (Jensen et al., 2019, 2020).

## Distribution of $^{226}$Ra, $^{210}$Pb, and $^{210}$Po in the Water Column

The $^{226}$Ra activity in the upper 300 m water column ranged from 7.53 ± 0.28 to 14.5 ± 0.5 dpm 100L$^{-1}$ with lower $^{226}$Ra activities at stations 30 and 43 compared to stations 48 and 56 (**Figure 4**). Elevated $^{226}$Ra activities were observed at depths of 75-100 m (station 43), 65–190 m (station 48), and 82–237 m (station 56) (**Figure 4**). The total $^{210}$Po and $^{210}$Pb activities (dissolved and particulate) in the upper 300 m water column varied between 0.47 ± 0.06 to 8.2 ± 1.2 dpm 100L$^{-1}$ and 1.18 ± 0.09 to 11.0 ± 1.0 dpm 100L$^{-1}$, respectively (**Figure 4**). There is deficiency of $^{210}$Po with respect to $^{210}$Pb throughout most of the upper 500 m water column, with exceptions at 225 m for station 43 and at 56 m for station 56, where $^{210}$Po activities and $^{210}$Pb were similar within uncertainties. The particulate $^{210}$Po and $^{210}$Pb activities in the large particles varied between 0.016 ± 0.001 to 2.32 ± 0.04 dpm 100L$^{-1}$ and 0.054 ± 0.004 to 2.50 ± 0.06 dpm 100L$^{-1}$, respectively, with stations 30 and 43 having lower particulate $^{210}$Po activities (**Figure 5**). The total particulate (large + small) activities of $^{210}$Po and $^{210}$Pb followed a similar trend (**Supplementary Figure 2**) with an exception at station 56 where the $^{210}$Po activities were higher at 25 and 56 m depth and similar at 86 m depth. The $^{210}$Pb and $^{210}$Po data for dissolved and

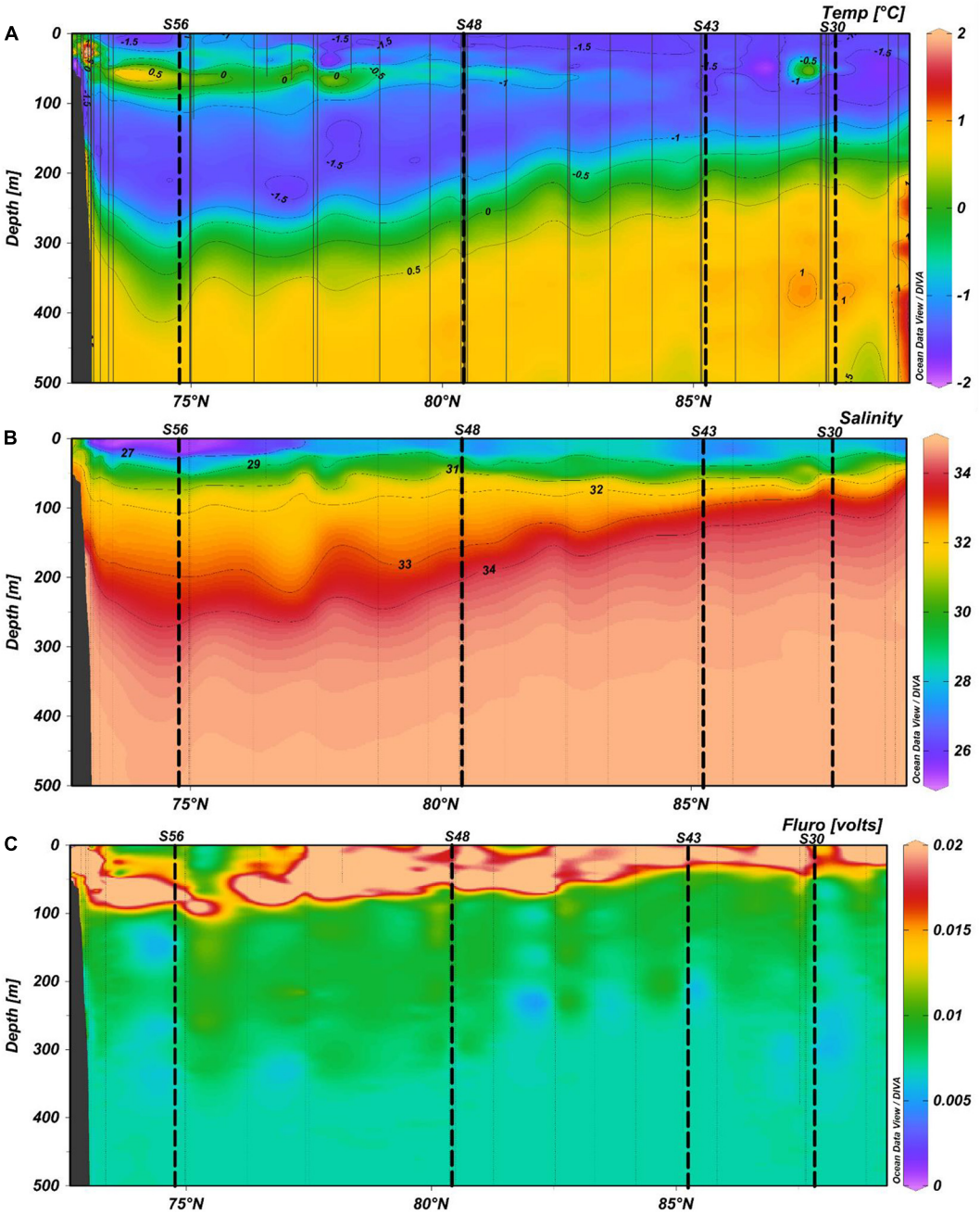


**FIGURE 2 |** Northbound section plots of **(A)** water temperature (°C), **(B)** salinity (sal) and **(C)** fluorescence (volts -relative units) in the upper 500 m water column. The vertical dashed lines represent the sampling stations along the transect. The transect images were created using Ocean Data View 5.2.0.

particulate samples are archived on BCO-DMO website[5], [6] and [7] (Baskaran and Krupp, 2020; Maiti and Bam, 2020a,b).

The total $^{210}Pb/^{226}Ra$ activity ratio in the mixed layer (50 m) varied from 0.12 to 1.1 showing a progressively decreasing trend toward north. The total activity ratio of $^{210}Po/^{210}Pb$ ranged from 0.19 to 1.11 and was <0.75 for 90% of the sample in the upper 300 m water column, indicating high particle scavenging intensity and low remineralization rate of organic matter.

## Distribution of Particulate C, N, and bSi in the Water Column

The POC and PN concentrations ranged from 0.002 ± 0.001 to 0.158 ± 0.002 μmol $L^{-1}$ and below detection limit to 43.9 ± 0.2

[5]https://www.bco-dmo.org/dataset/808151

[6]https://www.bco-dmo.org/dataset/808502

[7]https://www.bco-dmo.org/dataset/794064

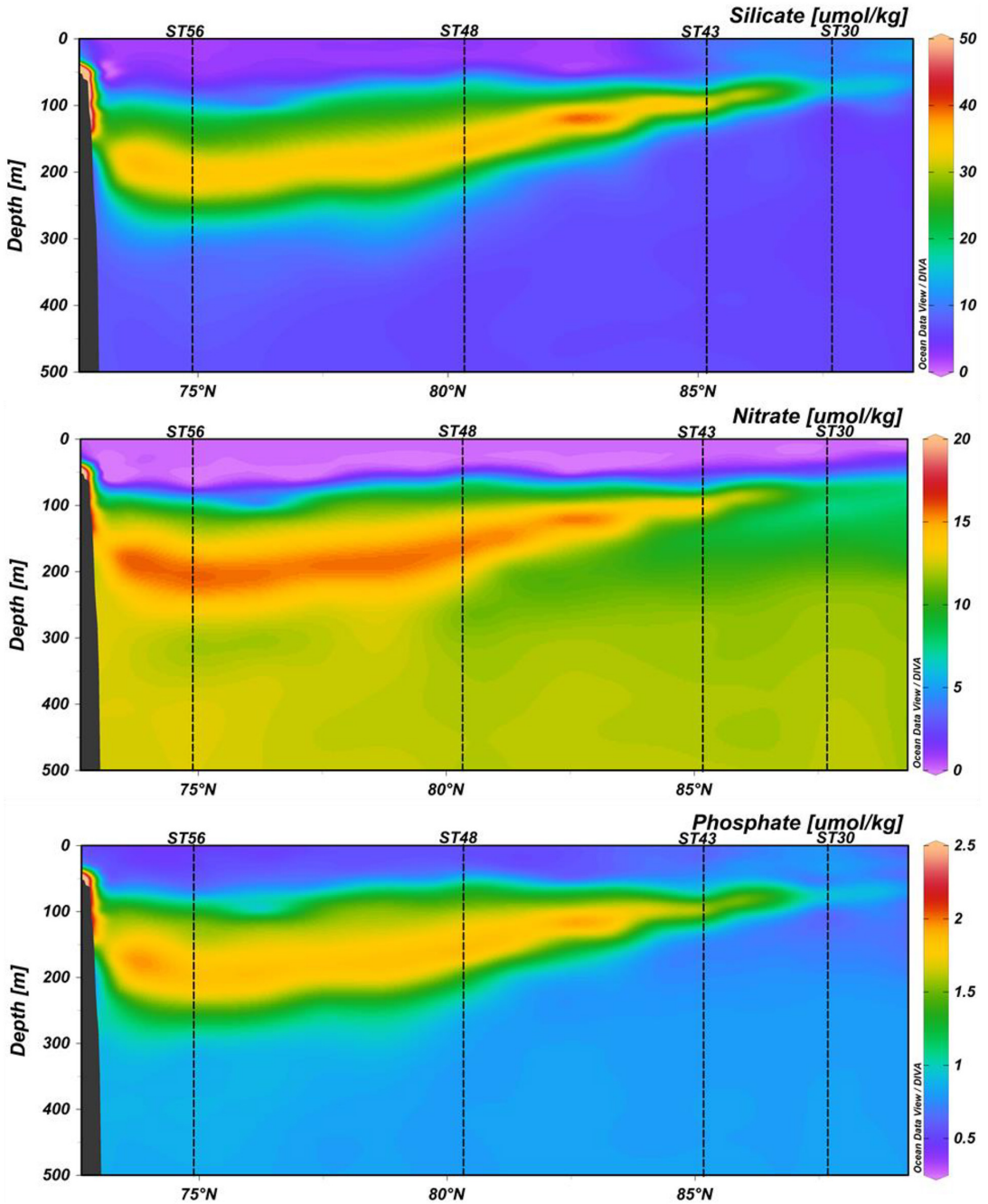


**FIGURE 3 |** Distribution of silicate (μmol/kg) nitrate (μmol/kg) and phosphate (μmol/kg) in the upper 500 m water column of the sampling transect. The transect images were created using Ocean Data View 5.2.0.

nmol $L^{-1}$, respectively (**Supplementary Figure 3**). The PIC and bSi concentration ranged from below detection limit to 0.005 ± 0.001 μmol $L^{-1}$and 0.78 ± 0.29 to 85.5 ± 0.3 nmol $L^{-1}$, respectively (**Supplementary Figure 3**). The POC content was higher for station 30 compared to other stations, whereas PIC content was higher for station 43 and 48 compared to station 30. The PN and bSi concentrations were lowest for station 56, which also had lower PIC concentrations. In general, POC, PIC, PN, and bSi concentration decreased significantly with depth in the upper 100 m.

## Radionuclide and Elemental Fluxes

Water column $^{210}$Pb and $^{210}$Po fluxes were calculated according to eqn 3 and 4, respectively, at the base of the euphotic zone (100 m) as well as at 50 m and 100 m below the base of the euphotic zone (150 and 200 m water depth). The $^{210}$Pb fluxes ranged

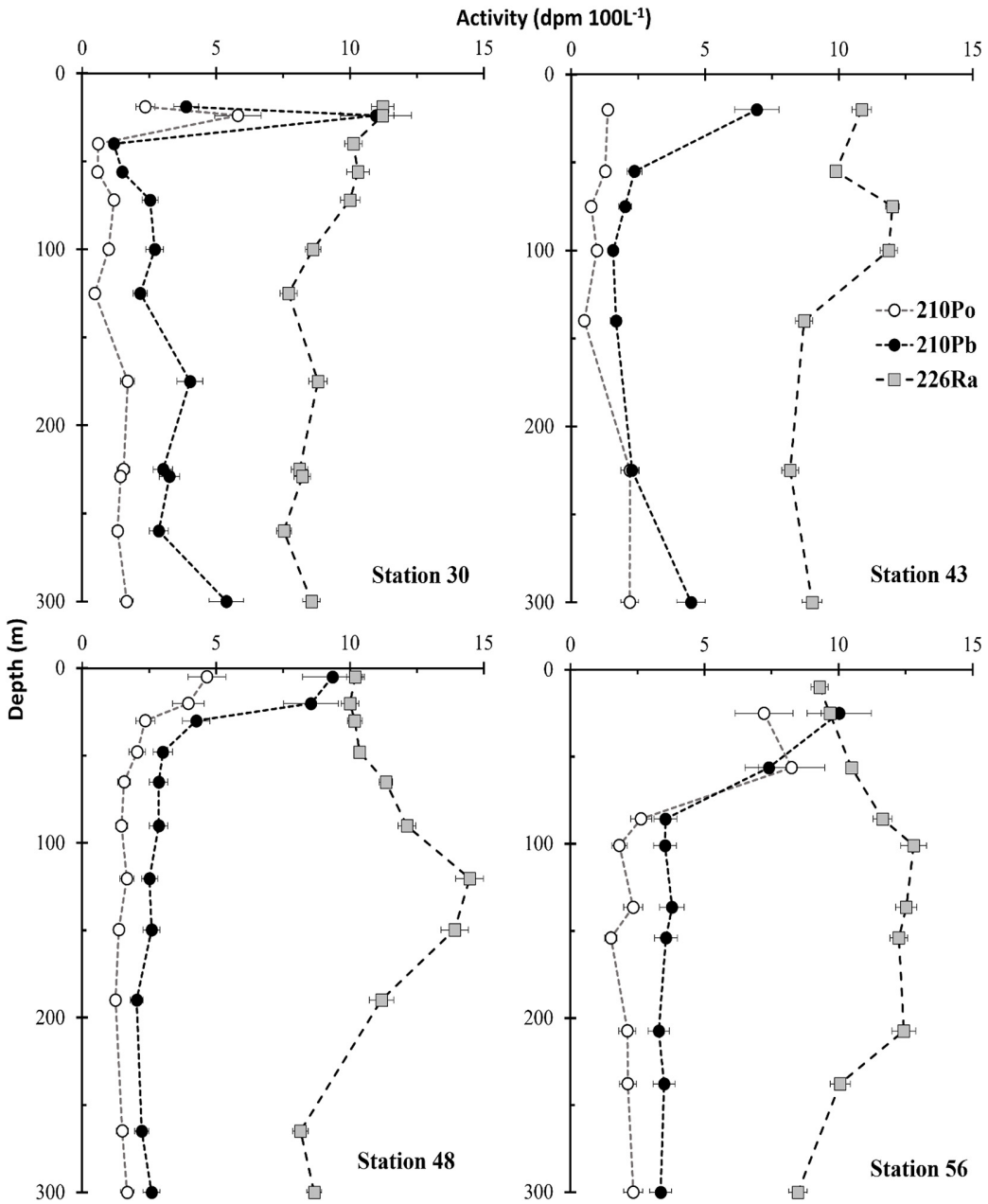


**FIGURE 4 |** The water column profiles of total $^{210}$Po (open circle), $^{210}$Pb (filled circle), and $^{226}$Ra (filled square) at each station.

between 5.04 ± 0.92 and 6.20 ± 0.92 dpm $m^{-2}$, $d^{-1}$ with highest $^{210}$Pb flux at station 48 and lowest at station 56 (**Figure 6A**). The $^{210}$Pb fluxes for all the stations were similar within uncertainties. The $^{210}$Po flux ranged between 8.26 ± 0.89 and 21.0 ± 1.9 dpm $m^{-2}$ $d^{-1}$ with highest $^{210}$Po flux observed at station 56 and lowest at station 30 (**Figure 6B**).

In order to translate these water column fluxes of $^{210}$Po and $^{210}$Pb to elemental fluxes, corresponding depth distribution of POC/$^{210}$Po, PN/$^{210}$Po, PIC/$^{210}$Pb, and bSi/$^{210}$Pb ratio at each station is needed (**Figure 7**). The POC/$^{210}$Po ratio ranged between 1.04 ± 0.41 and 257 ± 11 μmol $dpm^{-1}$ (**Figure 7A**), PN/$^{210}$Po ranged from 0.11 ± 0.06 to 35.2 ± 1.5 μmol $dpm^{-1}$ (**Figure 7B**). PIC/$^{210}$Pb ranged from 0.13 ± 0.03 to 2.12 ± 0.63 μmol $dpm^{-1}$ (**Figure 7C**) and bSi/$^{210}$Pb ranged from 0.19 ± 0.07 to 18.1 ± 0.9 μmol $dpm^{-1}$ (**Figure 7D**). On average, station 30 had higher ratio of POC/$^{210}$Po and PN/$^{210}$Po and station 43 had higher bSi/$^{210}$Pb ratio than other stations. These values are comparable to the previously reported water column activities from the region (He et al., 2015; Roca-Martí et al., 2016).

The POC, PN, PIC, and bSi export fluxes were calculated according to eqn 5 at the base of euphotic zone (100 m) as well as at 150 and 200 m depth horizons to estimate the production

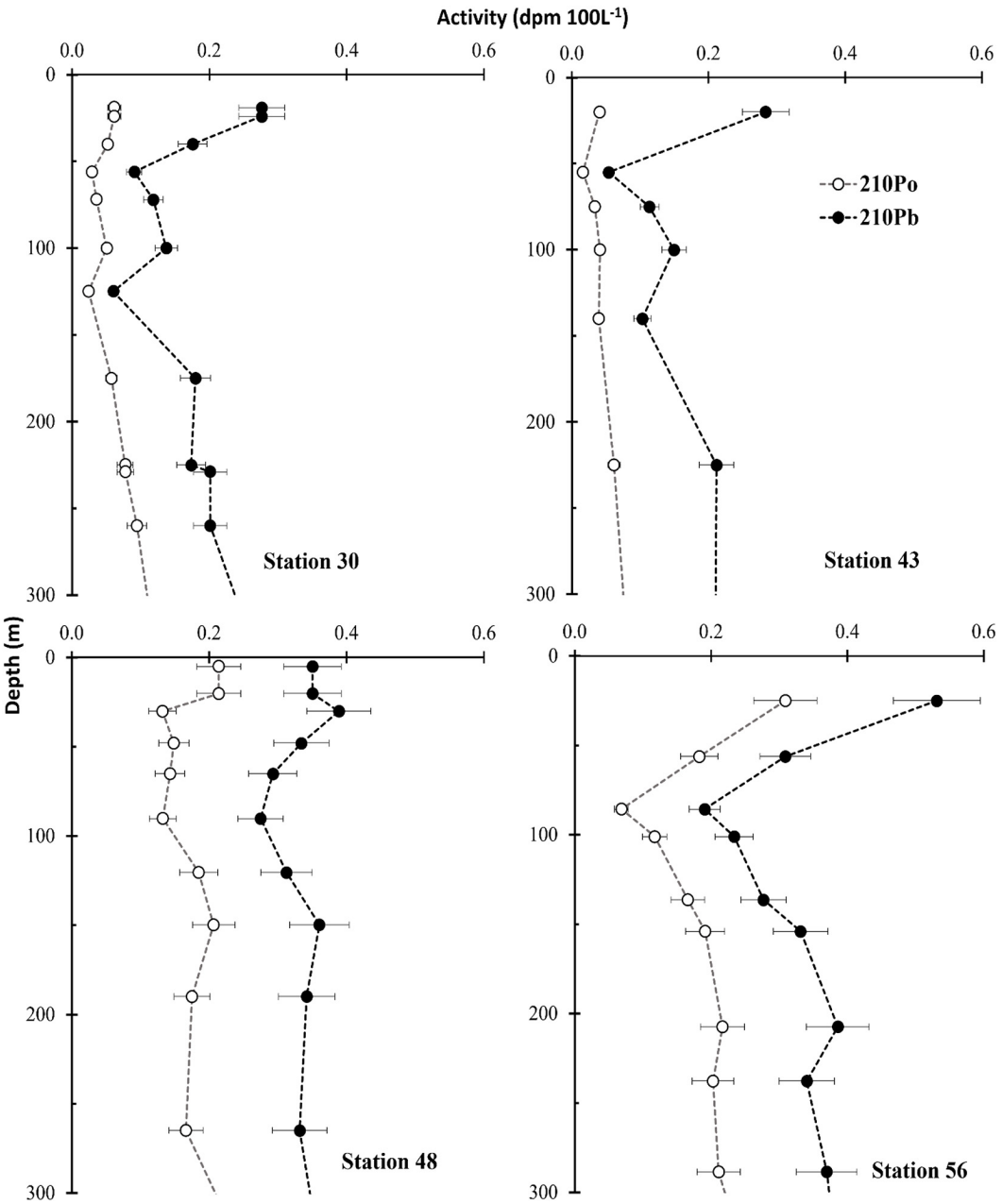


**FIGURE 5 |** The water column profile of large particulate $^{210}$Po (open circle) and $^{210}$Pb (filled circle) at each station.

export and flux attenuation with depth. The POC flux varied between 1.59 ± 0.16 and 7.43 ± 0.41 mg C $m^{-2}$ $d^{-1}$ at 100 m (**Figure 8A**). Similarly, it varied between 0.75 ± 0.07 and 7.23 ± 0.41 mg C $m^{-2}$ $d^{-1}$ at 150 m and 1.1 ± 0.10 to 4.86 ± 0.40 mg C $m^{-2}$ $d^{-1}$ at 200 m (**Figure 8A**). The POC flux was highest at station 43 and lowest at station 56. The PN flux ranged from 0.18 ± 0.02 to 0.78 ± 0.04 mg N $m^{-2}$ $d^{-1}$ at 100 and 200 m, ranged from 0.08 ± 0.008 to 0.65 ± 0.04 mg N $m^{-2}$ $d^{-1}$ at 150 m and 0.11 ± 0.01 to 0.48 ± 0.04 mg N $m^{-2}$ $d^{-1}$ (**Figure 8B**). The flux was higher at the ice stations compared to open water stations with decreasing trend from North to South. The spatial distribution trend of POC and PN fluxes were similar. The POC and PN fluxes estimated using POC/Po and PN/Po ratio in 1–51 um size fraction were in general found higher by up to a factor 2 compared to those estimated using the POC/$^{210}$Po ratio in the >51 um size fraction (**Supplementary Tables 1, 2**). This observation is similar to what other studies have reported and can be attributed to the fact that not all suspended particles in 1–51 μm sink fast enough to contribute to the net sinking fluxes (Buesseler et al., 2006; Tang and Stewart, 2019; Bam and Maiti, 2021). The flux estimates using POC/$^{210}$Po ratio on smaller size fraction particles tend to overestimate when

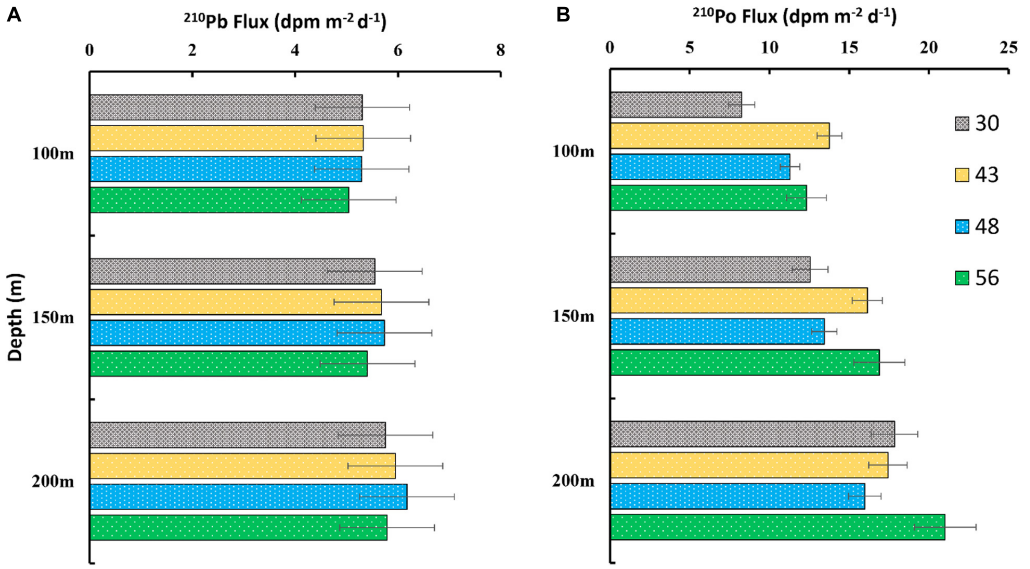


**FIGURE 6 | (A)** $^{210}$Po and **(B)** $^{210}$Pb fluxes calculated at 100 m, 150 m and 200 m depth.

compared with sediment traps, as a significant portion of this pool can be slow sinking particles whose contribution to net flux is reduced by remineralization in the water column. Thus, we suggest that the flux estimate is probably lower bound by the estimates from large particle ratio and upper bound by estimates from small particle ratio.

The PIC fluxes in all stations were low and varied from below detection limit to 0.042 ± 0.007 mg C m$^{-2}$ d$^{-1}$ at 100 m, 0.010 ± 0.001 to 0.145 ± 0.023 at 150 m, and 0 to 0.059 ± 0.009 mg C m$^{-2}$ d$^{-1}$ at 200 m depth (**Figure 8C**). Overall, station 48 had the highest and station 56 had the lowest PIC flux (**Figure 8C**). The bSi flux ranged from 0.67 ± 0.12 to 1.54 ± 0.26 mg Si m$^{-2}$ d$^{-1}$ at the euphotic zone (**Figure 8D**). The bSi flux ranged from 0.14 ± 0.02 to 2.88 ± 0.46 and 0.14 ± 0.02 to 1.25 ± 0.19 at 150 m and 200 m depths, respectively (**Figure 8D**). Station 43 had the highest bSi flux, followed by stations 30, 48, and 56. The spatial distribution trend of bSi and PIC fluxes were similar expect for station 56, where extremely low PIC fluxes were observed at 100 m and 200 m. PIC and bSi fluxes were also estimated by utilizing Po fluxes (**Supplementary Tables 3, 4**) which were higher than $^{210}$Pb estimates. The $^{210}$Po based fluxes represent the fluxes integrated over shorter time scale whereas the $^{210}$Pb based fluxes represent the fluxes integrated over a longer time scale. The major reasons for difference in PIC and bSi fluxed based on $^{210}$Pb and $^{210}$Po is discussed in the section below.

# DISCUSSION

## Water Mass Structure and $^{226}$Ra, $^{210}$Pb, and $^{210}$Po Distribution

The hydrological characters and elemental distribution in the Western Arctic are mainly determined by water masses with unique thermohaline macronutrient distribution (Aagaard et al., 1985; Aagaard and Carmack, 1989; Rudels, 2015; Carmack et al., 2016). The basin wide water column section of temperature and salinity showed the mixed layer was limited to upper ∼50 m. During the sampling transect, four major water masses were encountered – the surface polar mixed layer (PML) (0–50 m), upper halocline layer (UHL) (50–150 m), lower halocline layer (LHL) (150–400 m), and Makarov/Amundsen basin single halocline (50–300 m) (Jensen et al., 2019).

The $^{226}$Ra activities are similar in the mixed layers across all the sampling stations and showed a general decrease in activities with depth, similar to earlier results (Moore and Smith, 1986; and other articles). At certain discrete depths, $^{226}$Ra activities were elevated and these depths also correspond to nutrient maximum in the halocline (**Figures 3**, **4**). The general pattern of increase in $^{226}$Ra activities as a function of increase in the silicate concentration were found to be similar to the previously reported relationship showing – $\Delta^{226}$Ra/ΔSi = 0.1 dpm/ 100 μ mol (Broecker et al., 1976; Moore and Smith, 1986). Previous studies have also reported such concurrent increase in phosphate, silicate, and $^{226}$Ra in the Arctic basin which were attributed to the halocline water (Kinney et al., 1970; Moore et al., 1983; Moore and Smith, 1986). The elevated $^{226}$Ra activities observed between 100 and 200 m at station 56 is likely related to the shelf-modified Pacific inflow of water, whereas the elevated $^{226}$Ra activities observed between 100–200 m and 75–125 m at station 43 and station 48, respectively, are probably associated with Chukchi winter water (CWW), remnant winter water (RWW), and meteoric cold water (MCW) associated with ice melt that has been carried by the TPD (Kipp et al., 2018). The higher nutrients concentrations and $^{226}$Ra activities at this depth likely represent the different water masses and circulation pattern compared to the surface and below the halocline. $^{226}$Ra activities in the upper 100 m were found to be consistently higher than that of total $^{210}$Pb activities ($^{210}$Pb/$^{226}$Ra < 1) which is due to the low $^{210}$Pb

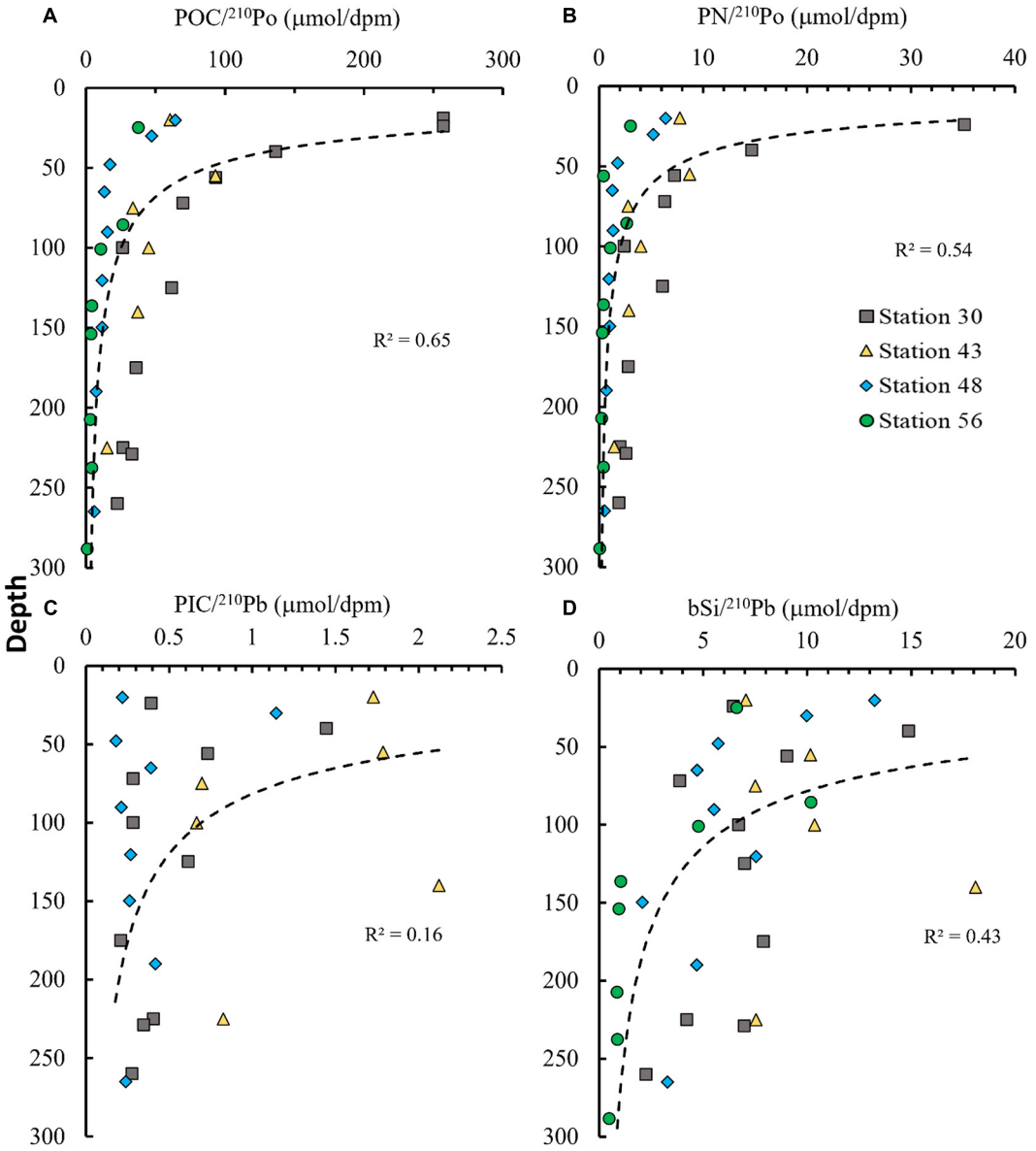


**FIGURE 7 |** The ratios of **(A)** POC/$^{210}$Po, **(B)** PN/$^{210}$Po, **(C)** PIC/$^{210}$Pb and **(D)** bSi/$^{210}$Pb in the large particulate samples for upper 300 m water column depth. The dashed black line represents the power function fitted using the samples collected in upper 300 m depth.

atmospheric input of 0.12–0.22 dpm cm$^{-2}$ y$^{-1}$ in the Arctic (Baskaran, 2011). In most oceans, the contribution of $^{210}$Pb from atmospheric fallout to the upper ∼500 m is higher and thus, the $^{210}$Pb/$^{226}$Ra activity ratio is usually > 1.0 in surface waters (Bacon et al., 1976; Cochran et al., 1983; Rigaud et al., 2015; Niedermiller and Baskaran, 2019).

The total activities of $^{210}$Po and $^{210}$Pb in the water column showed a general decrease in activity with depth (**Figure 4**). In the Arctic Ocean beside atmospheric deposition, additional surface input of $^{210}$Pb is possible during the melting of sea ice which can trap atmospheric flux of $^{210}$Pb (Masqué et al., 2007; Chen et al., 2012). The $^{210}$Pb input from sea-ice melting is probably not significant, as previous estimates indicate that melting all of sea ice in the Arctic can only contribute up to 10% of the $^{210}$Pb inventory in the region (Smith et al., 2003; Masqué et al., 2007; Roca-Martí et al., 2016). However, release of ice-rafted sediment (IRS) from sea ice melt can release a large amount of $^{210}$Pb, as its concentration in IRS has been reported to be 1–2 orders of magnitude higher than those in the Arctic benthic sediments (Baskaran, 2005). The largest $^{210}$Po – $^{210}$Pb disequilibria were observed in the surface layers of most stations, which is expected due to increased biological scavenging of $^{210}$Po with respect to $^{210}$Pb in the euphotic layer as well the atmospheric deposition which has $^{210}$Po/$^{210}$Pb AR of < 0.1. However, permanently sea ice covered station 30 was an exception where we did not observe a $^{210}$Po-$^{210}$Pb disequilibrium in the surface layer (**Figure 4**). The

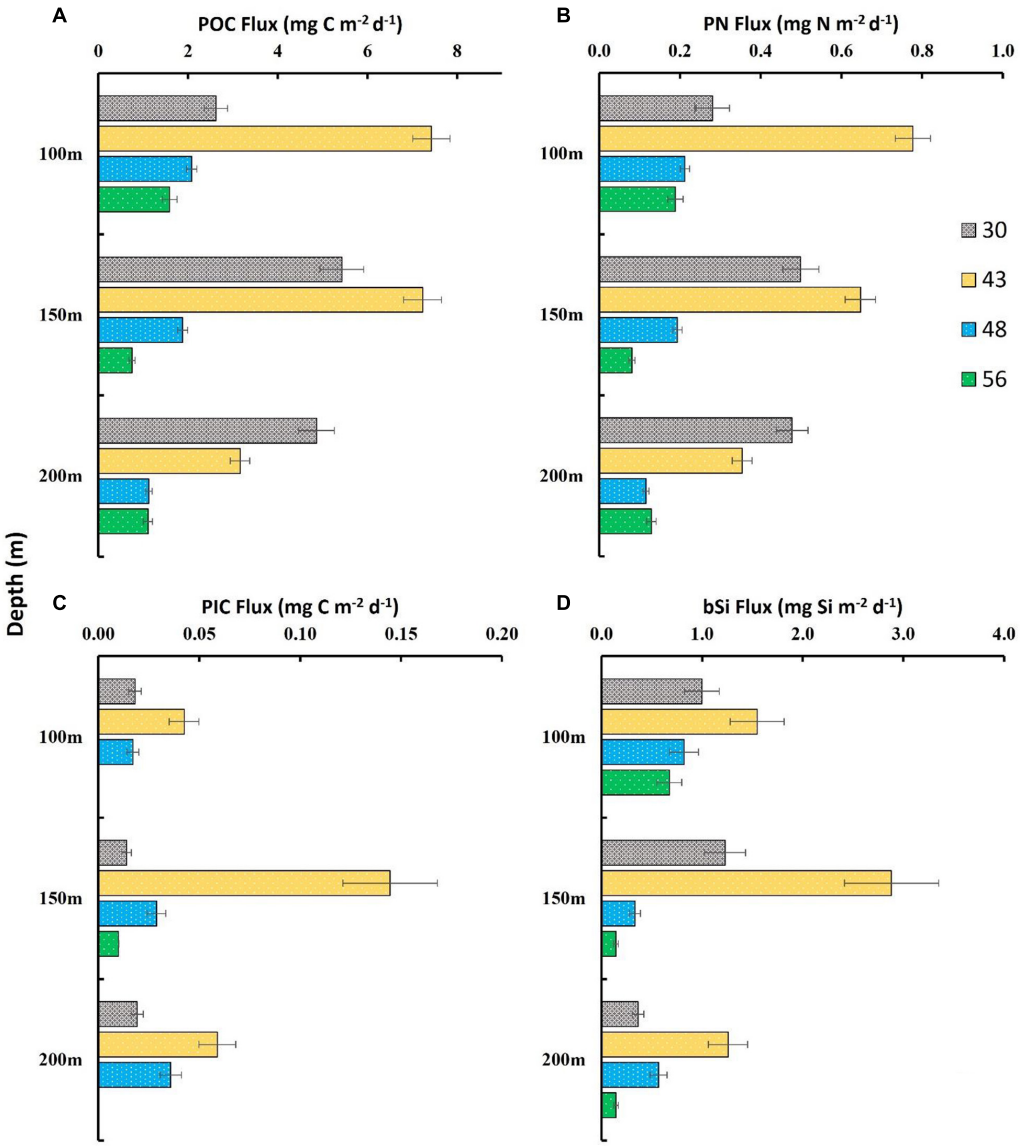


**FIGURE 8 |** Export fluxes of **(A)** POC, **(B)** PIC, **(C)** PN, and **(D)** bSi in the water column.

particulate $^{210}$Pb activities were also higher in the surface layer which could be attributed to release of particles from melting of sea ice at partially ice-covered stations 43 and 48 and lateral input from the adjacent area for station 56. In the Arctic, particle Po/Pb ratio are mostly $< 1$ in this study which is consistent with other results from the Arctic but contrast with ratios $> 1$ reported in other oceanic settings. This is probably due to (i) lower atmospheric input of $^{210}$Pb in the Arctic and (ii) release of the lithogenic particulate materials during the melting of sea-ice, which contributes higher proportion of $^{210}$Pb in the water column resulting in Po/Pb ratio $< 1$. Thus sea-ice dynamics plays an important role in the distribution of particulate $^{210}$Po-$^{210}$Pb in the Arctic Ocean.

The low activities of $^{210}$Pb and $^{210}$Po and high activities of $^{226}$Ra observed in the nutrient rich water mass indicate scavenging of $^{210}$Po and $^{210}$Pb by particles and lateral transport of shelf-derived $^{226}$Ra (Baskaran et al., 2021). The relative increase in the $^{210}$Po and $^{210}$Pb activities below 150 m depth compared to halocline at stations 30 and 43 likely indicate lateral transport of particulate material by the Transpolar drift and Beaufort Gyre. The $^{210}$Pb and $^{226}$Ra distribution appear to be predominantly regulated by the shelf-basin interactions and the halocline water circulation in this region. The particulate and total $^{210}$Po and $^{210}$Pb activities in this study were similar to previously reported activities in this region (Smith et al., 2003; He et al., 2015; Roca-Martí et al., 2018). The activity ratios of $^{210}$Po/$^{210}$Pb and $^{210}$Pb/$^{226}$Ra showed the preferential scavenging of $^{210}$Po and $^{210}$Pb, respectively, throughout the upper 300 m of the water column for all the stations. Further, the spatial pattern in $^{210}$Po/$^{210}$Pb and $^{210}$Pb/$^{226}$Ra

ratios demonstrate low scavenging rates at higher latitudes in the Arctic basin.

## $^{210}$Pb and $^{210}$Po Fluxes

The export fluxes of $^{210}$Pb at the base of the euphotic zone, were found to be similar for stations 30, 43 and 48 whereas station 56 had lower $^{210}$Pb flux (**Figure 6A**). The $^{210}$Pb fluxes increased with depth at all stations. The sharp increase in the $^{210}$Pb fluxes between 100 and 250 m at stations 48 and 56 can be attributed to the lateral input of particulate matter from the inflow of Pacific water and the Beaufort Gyre. Previous sediment trap studies in the interior Canadian Basin have reported significant contribution of lateral input to the vertical flux (Honjo et al., 2010). We utilized previously reported water column activities of $^{226}$Ra and $^{210}$Pb (Smith et al., 2003) to estimate $^{210}$Pb fluxes for three stations in proximity of station 48 and 56. The estimated fluxes for these three stations ranged from 5.32 to 5.48 dpm $m^{-2}$ $d^{-1}$ and 5.94 to 6.38 dpm $m^{-2}$ $d^{-1}$ at 100 m and 200 m, respectively, which is similar to our current estimates (4.99–6.18 dpm $m^{-2}$ $d^{-1}$).

There are spatial differences in $^{210}$Po fluxes at the four stations, which did not follow any latitudinal trend (**Figure 6B**). Station 56 in the Canadian basin had the highest $^{210}$Po flux which is expected due to higher particle scavenging in the slope area compared to interior stations. The $^{210}$Po fluxes varied between 8.26–13.76 7.23 dpm $m^{-2}$ $d^{-1}$ and 12.54–16.89 dpm $m^{-2}$ $d^{-1}$ at 100 and 150 m, respectively (**Figure 6B**), which are higher than previously reported $^{210}$Po fluxes in the Arctic Ocean. Roca-Martí et al. (2016) reported $^{210}$Po fluxes of 7.2 dpm $m^{-2}$ $d^{-1}$ and 3.7 dpm $m^{-2}$ $d^{-1}$ at 150 m for two stations in the central Arctic which are in proximity of our stations 30 and 43. The higher observed fluxes at stations 30 and 43 is likely due to the sea ice dynamics. Roca-Martí et al. (2016) sampled during the record sea-ice minimum with mostly single year ice whereas during our sampling in 2015 multi-year sea-ice was observed. The particulate $^{210}$Po and $^{210}$Pb were found to be orders of magnitude higher during our sampling, pointing to the possible increased input of sediment from melting of multi-year sea-ice which could result in higher $^{210}$Po fluxes. The $^{210}$Po fluxes estimated using previously reported data (Smith et al., 2003) ranged between 3.95–6.69 dpm $m^{-2}$ $d^{-1}$ and 5.29–7.42 dpm $m^{-2}$ $d^{-1}$ at 100 m and 200 m depth, respectively. These stations were in proximity to our stations 48 and 56 and the fluxes are lower than our current estimates (8.26–21.0 dpm $m^{-2}$ $d^{-1}$). $^{210}$Po fluxes in this region is overall lower compared to other regions of the world ocean (Murray et al., 2005; Wei et al., 2011; Anand et al., 2018; Bam and Maiti, 2021). In the future, the $^{210}$Po and $^{210}$Pb fluxes in the Arctic might change with changing Arctic climatic conditions such as rapid ice melting, increased ice algae growth and enhanced transport of shelf sediments but our current comparison of fluxes with data collected over two decades back (Smith et al., 2003) showed no significant differences. However, it must be noted that large spatiotemporal variability in this region can result in export fluxes varying by a factor of 7 (Roca-Martí et al., 2016). Thus, it will be difficult to identify any recent changes unequivocally in a single study, unless time series measurements are carried out at a particular site for several years.

## Distribution of Elemental and Radionuclide Ratios

The higher concentration of POC and PN in surface water at station 30 (**Supplementary Figure 3**) could be attributed to the supply of POC and PN from melting of the ice (Yu et al., 2012). In the central Arctic, there is no direct external input of POC (Xiang and Lam, 2020) even though the TPD influences the distribution of trace metal and dissolve organic matter (Kipp et al., 2018; Charette et al., 2020). Overall, the surface water in the top 20 m had the highest concentration of POC, PIC, PN and bSi. PIC concentrations were low throughout this region and was below detection limit at station 56 (**Supplementary Figure 3**). The coccolithophores are the major source of PIC in the ocean and the lower concentration of PIC indicates the absence of coccolithophores in the Arctic waters (Honjo et al., 2010, Xiang and Lam, 2020 and references therein). The total bSi concentration were relatively higher in the shelf/slope region (station 48 and 56) compared to interior station (30 and 43) (**Supplementary Figure 3**), which is attributed to the diatoms. In the Arctic Ocean, diatoms are major phytoplankton community responsible for > 45% of the total primary production (Coupel et al., 2012; Balch et al., 2014).

The ratios of POC/$^{210}$Po, PN/$^{210}$Po in the water column decreased with depth following a general power law (**Figures 7A,B**) as previously observed by number of studies (Maiti et al., 2008; Tang and Stewart, 2019; Bam and Maiti, 2021). This is expected because of the remineralization of particulate organic matter during settling through the water column and preferential association of $^{210}$Po with POC ($R^2$ = 0.65) and PN ($R^2$ = 0.54). The PIC/$^{210}$Pb and bSi/$^{210}$Pb ratios did not show such well-defined power law attenuation with depth (**Figures 7C,D**). This is because both bSi and PIC will solubilize with depth, with the solubility of bSi being much faster than PIC in the water column (Cappellen et al., 2002; Rickert et al., 2002). For all four ratios, maximum variability is observed in the upper 100 m layer, which is due to high biological activity in the euphotic zone. The shelf station 56 had the lowest POC/$^{210}$Po ratio while station 30 had the highest POC/$^{210}$Po ratios. This gradual poleward increase in POC/$^{210}$Po ratio could be due to change in the phytoplankton communities as the station transited from open ocean to permanently sea-ice covered. In the western Arctic Ocean, the coccolithophores and foraminifera are nearly absent thus resulting in low PIC/$^{210}$Pb ratio (Coupel et al., 2012, 2015; Xiang and Lam, 2020). On the other hand, the bSi/$^{210}$Pb ratios in the water column were relatively high compared to other oceans due to the abundance of diatoms in the western Arctic (Lalande et al., 2009; Boetius, 2013).

## Elemental Fluxes From the Euphotic Zone

In the Arctic, the export production is high during the early summer. The sampling for this study was carried out from August – October which represents the end of high productive season. The 138 days half-life of $^{210}$Po results in fluxes integrated over seasonal timescales. Thus, the $^{210}$Po flux reported here probably reflects average export for the entire summer season.

In the central Arctic, the export fluxes are highest during June-August and ice algae contributes significantly to the export fluxes (Fahl and Nöthig, 2007; Lalande et al., 2009). The $^{210}$Po based POC flux estimates at 100 m depth varied widely with higher values in the northern ice-covered stations and lowest in the Canada basin (station 56) (**Figure 8A**). A previous study showed that the POC exports are greater in areas with sea-ice coverage than in open water (Roca-Martí et al., 2016). Similarly, the studies from the central Arctic using different method ($^{234}$Th-$^{238}$U) showed POC fluxes to be less than 60 mg C m$^{-2}$ d$^{-1}$ (Moran et al., 1997; Baskaran et al., 2003; Roca-Martí et al., 2016). In contrast, He et al. (2015) reported $^{210}$Po based POC export fluxes to vary between 2.7 and 31 mg C m$^{-2}$ d$^{-1}$ with fluxes decreasing northward. A comprehensive analysis of reported POC flux in the published literature from the Arctic Ocean shows that POC export fluxes vary between 0.23 and 216 mg C m$^{-2}$ d$^{-1}$ (**Table 1**) which are difficult to compare given the inherent differences in various flux estimation methods (Maiti et al., 2016; Anand et al., 2018). For example, the POC flux estimated using $^{234}$Th-$^{238}$U methods are higher than $^{210}$Po-$^{210}$Pb and traps in the compiled literature (**Table 1**). The highest fluxes are reported from the marginal seas where biological productivity is expected to be higher while the lowest fluxes are in the central Arctic. Our study indicates that the POC export at the pole is higher than other parts of the deep basin pointing to the importance of sea-ice algae in driving POC fluxes in ice covered region. Ice algae and diatoms are the major component influencing the export fluxes of production in the Arctic Ocean (Lalande et al., 2009; Boetius, 2013).

With increasing freshwater input and associated terrestrial organic matter in the Arctic, it is crucial to understand the source of the POC contributing to this downward flux. The $\delta^{13}$C composition of POC indicate predominantly marine origin of POC and PN at all the four stations (**Figure 9A**; Xiang and Lam, 2020). The $\delta^{13}$C-DIC in the water column can provide relative estimate of primary productivity (Ko and Quay, 2020) while $\delta^{13}$C POC in large particle can help understand the source of POC contributing to fluxes (Griffith et al., 2012; Tolosa et al., 2013; Xiang and Lam, 2020). The higher $\delta^{13}$C-DIC values are associated with enhanced biological productivity in the water column (Ko and Quay, 2020). The value of $\delta^{13}$C-DIC values ranged from −0.04 to 1.47%, with station 48 having higher values (**Figure 9B**) indicating higher productivity. The difference in the $\delta^{13}$C-DIC for the stations suggest the difference in the magnitude of primary productivity among stations. $\delta^{13}$C-DIC in the top 100 m is usually depleted compared to the surface due to uptake of $CO_2$ and incorporation of lighter $^{12}$C by the phytoplankton into organic matter (Bauch et al., 2015). The top 100 m is biological active as reflected by the higher fluorescence content (**Figure 2C**). Thus, $\delta^{13}$C-DIC water column distribution suggests that station 48 might have higher primary productivity followed by station 43 and then station 30. The $\delta^{13}$C $POC_{large}$ values were greatly depleted (-30.8 ± 5.7% to −24.45 ± 0.4%), indicating the POC is predominately supplied by marine sources (Xiang and Lam, 2020; **Figure 9A**). The $\delta^{13}$C POC values are similar to values reported by Brown et al. (2014) in the central Canada Basin. In general, the phytoplankton in open ocean show $\delta^{13}$C values ranging −25 to −18%, however, the $\delta^{13}$C POC in polar systems pelagic and sea ice can exhibit −20 to −34.7% (Sallon et al., 2011; Pineault et al., 2013; Brown et al., 2014). Further, the highly depleted $\delta^{13}$C $POC_{large}$ might also reflect the slow growth rates of the phytoplankton (Fry, 1996; Griffith et al., 2012; Tolosa et al., 2013), and temperature effect (Rau et al., 1989). This suggests that POC in the upper water column is

**TABLE 1 |** Published data on POC fluxes in the Arctic Ocean.

| Sampling | Sampling | POC flux | Export | Method | References | Note |
|---|---|---|---|---|---|---|
| Location | Year | mg C m$^{-2}$ d$^{-1}$ | Depth (m) | | | |
| Amundsen Gulf Shelf | 1988 | 14.4 | 118 | Trap | O'Brien et al., 2006 | Sea-ice |
| Mackenzie Est. | 1988 | 23.8 | 145 | Trap | O'Brien et al., 2006 | Near Estuary |
| Tuktoyaktuk Shelf | 1988 | 4.2 | 125 | Trap | O'Brien et al., 2006 | Shelf Edge |
| Laptev Sea | 1995–1996 | 6–30 | 150 | Trap | Lalande et al., 2009 | |
| Lomansov Ridge | 1996 | 3.2 | 150 | Trap | Fahl and Nöthig, 2007 | Sea-ice |
| Bering Sea | 1999 | 118–164 | 100 | Th-U | Chen et al., 2003 | |
| Fram Strait | 2012 | 21.6–216 | 100 | Th-U | Le Moigne et al., 2015 | |
| Chukchi Rasie | 1996 | 1.61 | 120 | Trap | Honjo et al., 2010 | Sea-ice |
| Chukchi Shelf | 2010 | 2.7–31 | 150 | Po-Pb | He et al., 2015 | |
| Chukchi Sea | 2002 | 0.37–34.8 | 150–200 | Th-U | Moran et al., 2005 | Shelf-slope |
| Canada Basin | 1996 | 0.23 | 200 | Trap | Honjo et al., 2010 | Sea-ice |
| Canada Basin | 1998 | 67–78 | 100 | Th-U | Baskaran et al., 2003 | |
| Canada Basin | 1999 | 12 | 100 | Th-U | Chen et al., 2003 | |
| Canada Basin | 2000 | 31.2 | 100 | Th-U | Trimble and Baskaran, 2005 | |
| Central Arctic | 2012 | 1.2–57.6 | 150 | Po-Pb | Roca-Martí et al., 2016 | |
| Central Arctic | 1994 | 3.6–84 | 30 | Th-U | Moran et al., 1997 | |
| Central Arctic | 2012 | 24–84 | 150 | Th-U | Roca-Martí et al., 2016 | |
| Western Arctic | 2003 | 28.8–243 | 50 | Th-U | Yu et al., 2010 | |
| Western Arctic | 2015 | 0.75–7.4 | 150 | Po-Pb | This study | Basin Wide |

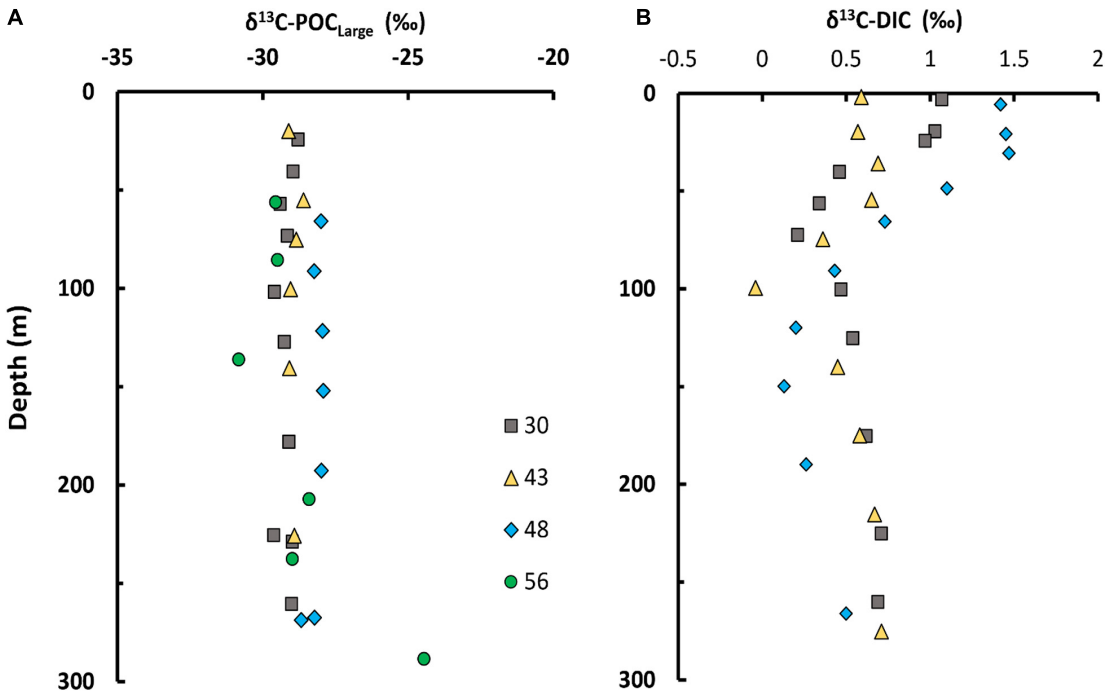


**FIGURE 9 | (A)** $\delta^{13}C_{POC}$ and **(B)** $\delta^{13}C_{DIC}$ distribution in the water column and large (>51um) particles.

supported by sea ice and not from terrestrial sources, despite the strong riverine input of POC at the coastal and shelf region, which continues to increase due to increasing river discharge and coastal erosion (Rachold et al., 2000, 2004; Krishnamurthy et al., 2001).

The $^{210}$Po and $^{210}$Pb fluxes can both be used to estimate the bSi and PIC fluxes. However, there are some fundamental differences on which tracer better represents the fluxes of inorganic material such as bSi and PIC. The key differences are due to (i) the bioaccumulation and adsorption of $^{210}$Po and $^{210}$Pb in the phytoplankton and particles and (ii) the flux integration timescale. Previous studies have reported differences in the bioaccumulation of $^{210}$Po and $^{210}$Pb in phytoplankton (Fisher et al., 1983; Stewart and Fisher, 2003a,b). $^{210}$Po is incorporated inside the cells of phytoplankton while the $^{210}$Pb is mostly bound to cell walls (Fisher et al., 1983; Friedrich and Rugters van der Loeff, 2002). A recent study by Lin et al. (2021) showed the difference in binding capacity of $^{210}$Po and $^{210}$Pb in diatoms and coccolithophore. Therefore, it is expected that $^{210}$Pb would be a better tracer for inorganic components whereas $^{210}$Po would better reflect the organic component. Using the $^{210}$Po, $^{210}$Pb and $^{234}$Th, Friedrich and Rugters van der Loeff (2002) showed that $^{210}$Po and $^{234}$Th fluxes were more useful to estimate POC and $^{210}$Pb to estimate bSi. For this study, bSi and PIC fluxes are estimated from $^{210}$Pb fluxes although bSi and PIC fluxes based on $^{210}$Po fluxes are also included in supplementary data (**Supplementary Tables 3, 4**). $^{210}$Pb fluxes represent longer time scale for the export compared to $^{210}$Po based fluxes which represent much shorter seasonal scale. Thus, a direct comparison of $^{210}$Pb based and $^{210}$Po based fluxes is not appropriate but in general $^{210}$Po based fluxes tend to be higher than $^{210}$Pb fluxes. The bSi and PIC fluxes showed a similar trend with highest fluxes at station 43 followed by stations 30, 48 and 56 (**Figures 8C,D**). Based on the low PIC and bSi fluxes at station 30, we attribute the POC flux at station 30 is mostly contributed by the sea algae. The PIC fluxes were extremely low because the primary productivity in this region is currently driven by picoplankton, diatoms, and green algae such as prasinophytes (Lalande et al., 2009; Boetius, 2013; Metfies et al., 2016). However, the eco-regime shifts to coccolithophore, and diatoms blooms are expected (Forest et al., 2008; Honjo et al., 2008) which could increase the PIC and bSi fluxes in future. Due to the ballast effect, the increase in the PIC and bSi fluxes could potentially result in increase of POC and PN fluxes. Biominerals or lithogenic particles increase the density of sinking, particles because of their high density and higher specific gravity, thus increasing the sinking rates and POC export fluxes known as ballast effect.

The primary productivity in the Arctic has been increasing over the last couple of decades (Arrigo and van Dijken, 2011), however, this enhanced productivity might not necessarily translate to larger POC exports fluxes due to changing Arctic environmental conditions as new conditions favor phytoplankton community structure which is based on the smaller cells (Li et al., 2009). With the changes in the phytoplankton community structure due to the changes in environmental conditions such as ice melting, nutrient input and temperature, the magnitude of export flux will be impacted. If the smaller cell phytoplankton community is favored, the export flux might decrease while the larger phytoplankton community

could lead to increase in flux. Thus, the changing climatic and environmental conditions could directly or indirectly impact not only the marine carbon cycle but also the trace elements and nutrients distribution in the Arctic Ocean.

## Particle Flux Attenuation and Lateral Input in Mesopelagic Zone

The POC fluxes at 150 m and 200 m depth were estimated to understand the particle attenuation and the remineralization below the euphotic zone. At station 30, the POC and PN fluxes increased by factor of 2 at 150 m and subsequently decreased to 15% at 200 m depth with respect to the fluxes measured at 100 m (**Figure 8A**). This increase in the POC and PN fluxes at 150 m could be attributed to lateral transport by the RWW and MCW. The particle attenuation and remineralization were higher at station 43, 48 and 56 which is expected due to high nutrient rich water. At station 56, POC and PN fluxes were 50% lower at 150 m than at 100 m (**Figures 8A,B**). However, there was 45% increase in POC and PN fluxes between 150 and 200 m which suggests contribution from lateral transport by inflow of Pacific water. The lower halocline layer with Pacific nutrient rich water is located between 150 and 400 m depth which contributed to the lateral transport of organic matter. The bSi flux at 150 m increase at station 30 and 43 whereas it decreased for stations 48 and 56 compared to the flux estimates at 100 m depth (**Figure 8D**). High concentration of bSi were observed at station 43 and other nearby stations which could possibly be due to sporadic sinking of ice diatoms such as *Melsoria arctica* (Fahl and Nöthig, 2007; Lalande et al., 2014). Station 43 is covered with the sea ice during most of the time. The RWW and MCW cold water from TPD and the edge of the high nutrient water with sea ice on the top makes this station one of the most dynamics and interesting in terms of biogeochemical interaction. These combined physical and hydrological characteristics probably enhanced the export fluxes.

## Export Efficiency

The export efficiency or *e-ratio* is defined as the ratio of export flux and net primary productivity (NPP). The mean NPP reported were 265 mg C $m^{-2}$ $d^{-1}$ in the Beaufort Basin, 195 mg C $m^{-2}$ $d^{-1}$ in Chukchi Basin (Arrigo and van Dijken, 2011) and 12–84 mg C $m^{-2}$ $d^{-1}$ in the central Arctic Ocean (Fernandez-Mendez et al., 2015). The average annual export efficiency (>30%) is high in the Arctic Waters (Henson et al., 2015). Since the NPP data during our sampling time was not available, the export efficiency was estimated using the average NPP values for sea-ice covered and open water areas from Fernandez-Mendez et al. (2015),. The export efficiency ranged from 5 to >50% with lowest export efficiency in the slope (5–15%) and highest in the sea-ice covered stations (12–50%). Previous studies have reported export efficiency > 30% in the Eurasian Basin (Gustafsson and Andersson, 2012), 26% in the Canada Basin (Chen et al., 2003), and >30% in the central Arctic (Roca-Martí et al., 2016) which are within the range of this study. The export efficiencies estimated in the Arctic Ocean are higher compared to other oceans (Buesseler et al., 1992, 1995, 1998; Bacon et al., 1996; Murray et al., 1996; Buesseler and Boyd, 2009; Haskell et al., 2013; Anand et al., 2018; Laws and Maiti, 2019; Bam and Maiti, 2021) probably due to lower metabolic rates associated with colder temperature. The lower export efficiency in the slope (station 56) and central Canada basin (station 48) compared to ice-covered interior stations 43 and 30 suggest higher recycling of the particles in the slope and central Canada basin which could be related to relatively higher microbial respiration at these stations compared to colder ice-covered stations.

# CONCLUSION

We estimated the export flux of POC, PN, PIC, and bSi based on the $^{210}$Po and $^{210}$Pb fluxes obtained during the 2015 US Arctic GEOTRACES cruise in the western Arctic Ocean. Overall, the vertical fluxes of the four key elements remain extremely low throughout the upper 200 m of the ocean. The low fluxes of bSi and PIC indicate that ballast particle fluxes which represent an important mechanism of POC transport to deep ocean are orders of magnitude lower than other regions of the global ocean, similar to what has been shown using deep sediment trap studies (Honjo et al., 2010). The overall low vertical fluxes of POC and prominent influence of lateral transport presented in this study concurs with previous work which suggested that the biological pump is currently inefficient in the cryopelagic Canada Basin. Thus, in this region a lateral POC pump from the shelf/slope region might be playing a more dominant role in transporting POC to the deeper basin.

Our study showed that the particulate organic matter in the western Arctic basin is predominantly the result of in-situ biological activities supported by biological pump. Thus, any changes to the in-situ primary production in the western region will influence the export efficiency and overall carbon cycling. In this study, the production export showed an increasing tend toward north with station 43 having the highest export fluxes. The projected melting of sea ice in future can result in large changes to the top Polar Mixed layer which can potentially transform the biological pump in this region (Macdonald et al., 2002). Thus, it is pertinent that carbon cycling and accompanying biogeochemical responses in the rapidly changing Arctic be closely monitored as it can have far reaching global impact in the future.

# DATA AVAILABILITY STATEMENT

The original contributions presented in the study are included in the article/**Supplementary Material**, further inquiries can be directed to the corresponding authors.

# AUTHOR CONTRIBUTIONS

WB: data curation, formal analysis, methodology, validation, writing-original daft, review, and editing. KM: conceptualization, funding acquisition, methodology, supervision, validation, writing-review, and editing. MB: conceptualization, funding acquisition, methodology, writing-review, and editing.

All authors contributed to the article and approved the submitted version.

## FUNDING

Funding for ship time, sampling operations, and hydrographic data was supported by the US National Science Foundation to the US GEOTRACES Western Arctic Management team. This research was funded by the US National Science Foundation grant NSF-OPP-1435376 to KM and NSF-PLR-1434578 to MB. Partial funding for open access publication was provided by Louisiana State University Library Open Access Fund.

## ACKNOWLEDGMENTS

We would like to thank the captain and crew of the USCGC Healy. Special thanks to Tim Kenna and Martin Fleisher for collecting dissolved water samples and the pumping group led by Phoebe Lam for the particulate samples. We would also like to thank two reviewers whose comments improved this manuscript, and the chief scientists and Arctic GEOTRACES cruise coordinators, David Kadko and Greg Cutter.

## SUPPLEMENTARY MATERIAL

The Supplementary Material for this article can be found online at: https://www.frontiersin.org/articles/10.3389/fmars.2021.697444/full#supplementary-material

**Supplementary Figure 1 |** Water column CTD profiles showing Salinity [%], Fluorescence (0- 5 VDC volts), and Dissolved Oxygen [mg $L^{-1}$] for all the sampling station. The fluorescence has been magnified 100 times to show on the same x-scale. The top *X*-axis represents the salinity and fluorescence, and the bottom *X*-axis represents the dissolved oxygen.

**Supplementary Figure 2 |** The activity depth profile of particulate (large and small) $^{210}$Po (open circle) and $^{210}$Pb (filled circle) for the sampling station in the upper 300 m.

**Supplementary Figure 3 |** POC, PIC, PN, and bSi concentration on the large particle samples for upper 300 m water column depth.

**Supplementary Table 1 |** POC fluxes in large and small particle fraction sizes using $^{210}$Po flux.

**Supplementary Table 2 |** PN fluxes in large and small particles fraction sizes using $^{210}$Po flux.

**Supplementary Table 3 |** PIC flux estimated based on the $^{210}$Pb and $^{210}$Po fluxes in large particles.

**Supplementary Table 4 |** bSi flux estimated based on the $^{210}$Pb and $^{210}$Po fluxes in large particles.

## REFERENCES

Aagaard, K., and Carmack, E. C. (1989). The role of sea ice and other fresh water in the Arctic circulation. *J. Geophys. Res. Oceans* 94, 14485–14498.

Aagaard, K., Coachman, L. K., and Carmack, E. (1981). On the halocline of the Arctic Ocean. *Deep Sea Res. A* 28, 529–545. doi: 10.1016/0198-0149(81)90115-1

Aagaard, K., Swift, J. H., and Carmack, E. C. (1985). Thermohaline circulation in the Arctic Mediterranean Seas. *J. Geophys. Res. Oceans* 90, 4833–4846. doi: 10.1029/JC090iC03p04833

Ahmed, R., Prowse, T., Dibike, Y., Bonsal, B., and O'Neil, H. (2020). Recent trends in freshwater influx to the Arctic Ocean from four major Arctic-draining rivers. *Waters* 12:1189. doi: 10.3390/w12041189

Anand, S. S., Rengarajan, R., Shenoy, D., Gauns, M., and Naqvi, S. W. A. (2018). POC export fluxes in the Arabian Sea and the Bay of Bengal: a simultaneous 234Th/238U and 210Po/210Pb study. *Mar. Chem.* 198, 70–87. doi: 10.1016/j.marchem.2017.11.005

Arrigo, K. R., and van Dijken, G. L. (2011). Secular trends in Arctic Ocean net primary production. *J. Geophys. Res.* 116:C09011. doi: 10.1029/2011JC007151

Bacon, M. P., Cochran, J. K., Hirschberg, D., Hammar, T. R., and Fleer, A. P. (1996). Export flux of carbon at the equator during the EqPac time-series cruises estimated from 234Th measurements. *Deep Sea Res. II Top. Stud. Oceanogr.* 43, 1133–1153. doi: 10.1016/0967-0645(96)00016-1

Bacon, M. P., Spencer, D. W., and Brewer, P. G. (1976). 210Pb/226Ra and 210Po/210Pb disequilibria in seawater and suspended particulate matter. *Earth Planet. Sci. Lett.* 32, 277–296.

Balch, W. M., Bowler, B. C., Lubelczyk, L. C., and Stevens, M. W. (2014). Aerial extent, composition, bio−optics and biogeochemistry of a massive under−ice algal bloom in the Arctic. *Deep Sea Res. II Top. Stud. Oceanogr.* 105, 42–58. doi: 10.1016/j.dsr2.2014.04.001

Bam, W., and Maiti, K. (2021). 210Po-210Pb distribution and carbon export in the northern Gulf of Mexico continental slope. *Deep Sea Res. I* 172:103535. doi: 10.1016/j.dsr.2021.103535

Bam, W., Maiti, K., Baskaran, M., Krupp, K., Lam, P. J., and Xiang, Y. (2020). Variability in 210Pb and 210Po partition coefficients (Kd) along US GEOTRACES Arctic transect. *Mar. Chem.* 219:103749. doi: 10.1016/j.marchem.2020.103749

Baskaran, M. (2005). Interaction of sea ice sediments and surface sea water in the Arctic Ocean: evidence from excess 210Pb. *Geophys. Res. Lett.* 32:L12601. doi: 10.1029/2004GL022191

Baskaran, M. (2011). Po-210 and Pb-210 as atmospheric tracers and global atmospheric Pb-210 fallout: a review. *J. Environ. Radioact.* 102, 500–513. doi: 10.1016/j.jenvrad.2010.10.007

Baskaran, M., Church, T., Hong, G., Kumar, A., Qiang, M., Choi, H., et al. (2013). Effects of flow rates and composition of the filter, and decay/in-growth correction factors involved with the determination of in-situ particulate 210Po and 210Pb in seawater. *Limnol. Oceanogr. Methods* 11, 126–128. doi: 10.4319/lom.2013.11.126

Baskaran, M., and Krupp, K. (2020). *Particulate & Dissolved Po-210 & Pb-210 in Seawater, Snow, Melt Ponds, Ice Core, Ice-Rafted Sediments, and Aerosols from the US GEOTRACES Arctic Cruise (HLY1502) on USCGC Healy from August to October 2015*. Woods Hole, MA: Biological and Chemical Oceanography Data Management Office (BCO-DMO). doi: 10.1575/1912/bco-dmo.794064.1

Baskaran, M., Krupp, K., Bam, W., and Maiti, K. (2021). Recent biogeochemical changes in the Arctic Ocean using $^{210}$Po-$^{210}$Pb-$^{226}$Ra disequilibria: evidence from 2015 GEOTRACES Arctic cruise. (Submitted)

Baskaran, M., and Santschi, P. H. (2002). Particulate and dissolved 210Pb activities in the shelf and slope regions of the Gulf of Mexico waters. *Cont. Shelf Res.* 22, 1493–1510. doi: 10.1016/S0278-4343(02)00017-1

Baskaran, M., Swarzenski, P. W., and Porcelli, D. (2003). Role of colloidal material in the removal of 234Th in the Canada basin of the Arctic Ocean. *Deep Sea Res. Part* 1, 1353–1373.

Bauch, D., Polyak, L., and Ortiz, J. D. (2015). A baseline for the vertical distribution of the stable carbon isotopes of dissolved inorganic carbon ($\delta 13C_{DIC}$) in the Arctic Ocean. *Arktos* 1:15. doi: 10.1007/s41063-015-0001-0

Bauch, D., Schlosser, P., and Fairbanks, R. G. (1995). Freshwater balance and the sources of deep and bottom waters in the Arctic Ocean inferred from the distribution of $H_2{}^{18}O$. *Prog. Oceanogr.* 35, 53–80. doi: 10.1016/0079-6611(95)00005-2

Boetius, A. (2013). *The Expedition of the Research Vessel "Polarstern" to the Arctic in 2012 (ARK−XXVII/3), in Reports on Polar and Marine Research, Report 663*. Bremerhaven: Alfred Wegener Inst. for Polar and Mar. Res., 166.

Broecker, W. S., Goddard, J., and Sarmiento, J. L. (1976). The distribution of $^{226}$Ra in the Atlantic Ocean. *Earth Planet. Sci. Lett.* 32, 220–235. doi: 10.1016/0012-821X(76)90063-7

Brown, K. A., McLaughlin, F. A., Tortell, P. D., Varela, D. E., Yamamoto−Kawai, M., Hunt, B., et al. (2014). Determination of particulate organic carbon sources to the surface mixed layer of the Canada Basin, Arctic Ocean. *J. Geophys. Res. Oceans* 119, 1084–1102. doi: 10.1002/2013JC009197

Buesseler, K., Ball, L., Andrews, J., Benitez-Nelson, C., Belastock, R., Chai, F., et al. (1998). Upper ocean export of particulate organic carbon in the Arabian Sea derived from thorium-234. *Deep Sea Res. II Top. Stud. Oceanogr.* 45, 2461–2487. doi: 10.1016/S0967-0645(98)80022-2

Buesseler, K. O., Andrews, J. A., Hartman, M. C., Belastock, R., and Chai, F. (1995). Regional estimates of the export flux of particulate organic carbon derived from thorium-234 during the JGOFS EqPac program. *Deep Sea Res. II Top. Stud. Oceanogr.* 42, 777–791. doi: 10.1016/0967-0645(95)00043-P

Buesseler, K. O., Bacon, M. P., Cochran, J. K., and Livingston, H. D. (1992). Carbon and nitrogen export during the JGOFS North Atlantic bloom experiment estimated from 234Th: 238U disequilibria. *Deep Sea Res. A* 39, 1115–1137. doi: 10.1016/0198-0149(92)90060-7

Buesseler, K. O., Benitez-Nelson, C. R., Moran, S. B., Burd, A. B., Charette, M. A., Cochran, J. K., et al. (2006). An assessment of particulate organic carbon to thorium-234 ratios in the ocean and their impact on the application of $^{234}$Th as a POC flux proxy. *Mar. Chem.* 100, 213–233. doi: 10.1016/j.marchem.2005.10.013

Buesseler, K. O., and Boyd, P. W. (2009). Shedding light on processes that control particle export and flux attenuation in the twilight zone of the open ocean. *Limnol. Oceanogr.* 54, 1210–1232. doi: 10.4319/lo.2009.54.4.1210

Cappellen, P. V., Dixit, S., and Beusekom, J. V. (2002). Biogenic silica dissolution in the oceans: reconciling experimental and field−based dissolution rates. *Glob. Biogeochem. Cycle* 16, 23-1–23-10. doi: 10.1029/2001GB001431

Carmack, E. C., Yamamoto-Kawai, M., Haine, T. W. N., Bacon, S., Bluhm, B. A., Lique, C., et al. (2016). Fresh water and its role in the Arctic marine system: sources, disposition, storage, export, and physical and biogeochemical consequences in the Arctic and global oceans. *J. Geophys. Res. Biogeosci.* 121, 675–717. doi: 10.1002/2015JG003140

Charette, M., Kipp, L. E., Jensen, L. T., Dabrowski, J. S., Whitmore, L. M., Fitzsimmons, J. N., et al. (2020). The transpolar drift as a source of riverine and shelf−derived trace elements to the central Arctic Ocean. *J. Geophys. Res. Oceans* 125:e2019JC015920. doi: 10.1029/2019JC015920

Charette, M., and Moore, W. (2020). *Radium and Thorium Isotopes Measured in the Western Arctic as Part of the 2015 US GEOTRACES Arctic Cruise on the USCGC Healy (HLY1502) from August to October 2015.* Woods Hole, MA: Biological and Chemical Oceanography Data Management Office (BCO-DMO). doi: 10.26008/1912/bco-dmo.718440.3

Chen, M., Huang, Y., Cai, P., and Guo, L. (2003). Particulate organic carbon export fluxes in the Canada Basin and Bering Sea as derived from 234Th/238U disequilibria. *Arctic* 56, 32–44. doi: 10.14430/arctic600

Chen, M., Ma, Q., Guo, L., Qiu, Y., Li, Y., and Yang, W. (2012). Importance of lateral transport processes to 210Pb budget in the eastern Chukchi Sea during summer 2003. *Deep Sea Res. II Top. Stud. Oceanogr.* 81-84, 53–62. doi: 10.1016/j.dsr2.2012.03.011

Cochran, J. K. (1992). "The oceanic chemistry of the uranium and thorium series nuclides," in *Uranium-Series Disequilibrium; Applications to Earth, Marine, and Environmental Sciences*, eds M. Ivanovich, and R. S. Harmon (Oxford: OUP), 334–395.

Cochran, J. K., Bacon, M. P., Krishnaswami, S., and Turekian, K. K. (1983). 210Po and210Pb distributions in the central and eastern Indian Ocean. *Earth Planet. Sci. Lett.* 65, 433–452. doi: 10.1016/0012-821X(83)90180-2

Coupel, P., Jin, H. Y., Joo, M., Horner, R., Bouvet, H. A., Sicre, M. A., et al. (2012). Phytoplankton distribution in unusually low sea ice cover over the Pacific Arctic. *Biogeosciences* 9, 4835–4850. doi: 10.5194/bg-9-4835-2012

Coupel, P., Matsuoka, A., Ruiz-Pino, D., Gosselin, M., Marie, D., Tremblay, J. E., et al. (2015). Pigment signatures of phytoplankton communities in the Beaufort Sea. *Biogeosciences* 12, 991–1006.

Cutter, G., Kadko, D., and Landing, W. M. (2019). *Bottle Data from the CTD−ODF Carousel on the GEOTRACES Arctic Section Cruise (HLY1502) from August to October 2015 (U.S. GEOTRACES Arctic Project). Dataset Version 2019−07−29.* Woods Hole, MA: Biological and Chemical Oceanography Data Management Office (BCO−DMO). doi: 10.1575/1912/bco-dmo.646825.4

Dickson, R., Rudels, B., Dye, S., Karcher, M., Meincke, J., and Yashayaev, I. (2007). Current estimates of freshwater flux through Arctic and subarctic seas. *Prog. Oceanogr.* 73, 210–230. doi: 10.1016/j.pocean.2006.12.003

Fahl, K., and Nöthig, E. M. (2007). Lithogenic and biogenic particle fluxes on the Lomonosov Ridge (central Arctic Ocean) and their relevance for sediment accumulation: vertical vs. lateral transport. *Deep Sea Res. I* 54, 1256–1272. doi: 10.1016/j.dsr.2007.04.014

Fernandez-Mendez, M., Katlein, C., Rabe, B., Nicolaus, M., Peeken, I., Bakker, K., et al. (2015). Photosynthetic production in the central Arctic Ocean during the record sea-ice minimum in 2012. *Biogeosciences* 12, 3525–3549. doi: 10.5194/bg-12-3525-2015

Fisher, N. S., Burns, K. A., Cherry, R. D., and Heyraud, M. (1983). Accumulation and cellular distribution of $^{241}$Am, $^{210}$Po, and $^{210}$Pb in two marine algae. *Mar. Ecol.* 11, 233–237.

Forest, A., Sampei, M., Hattori, H., Makabe, R., Sasaki, H., Barber, D. G., et al. (2008). The annual cycle of particulate organic carbon export in Franklin Bay (Canadian Arctic): environmental control and food web implications. *J. Geophys. Res.* 113:CO3SO5. doi: 10.1029/2007JC004262

Friedrich, J., and Rugters van der Loeff, M. M. (2002). A two-tracer (210Po–234Th) approach to distinguish organic carbon and biogenic silica export flux in the Antarctic Circumpolar Current. *Deep Sea Res. I* 49, 101–120. doi: 10.1016/S0967-0637(01)00045-0

Fripiat, F., Declercq, M., Sapart, C. J., Anderson, L. G., Bruechert, V., Deman, F., et al. (2018). Influence of the bordering shelves on nutrient distribution in the Arctic halocline inferred from water column nitrate isotopes. *Limnol. Oceanogr.* 63, 2154–2170. doi: 10.1002/lno.10930

Fry, B. (1996). 13C/12C fractionation by marine diatoms. *Mar. Ecol. Prog. Ser.* 134, 283–294. doi: 10.3354/meps134283

Geotraces Cookbook. (2019). *Sampling and Sample-handling Protocols for GEOTRACES Cruise*. Available online at: https://www.geotraces.org/methods-cookbook/

Granger, J., Sigman, D. M., Gagnon, J., Tremblay, J.-E., and Mucci, A. (2018). On the properties of the Arctic halocline and deep water masses of the Canada Basin from nitrate isotope ratios. *J. Geophys. Res. Oceans* 123, 5443–5458. doi: 10.1029/2018JC014110

Griffith, D. R., McNichol, A. P., Xu, L., McLaughlin, F. A., Macdonald, R. W., Brown, K. A., et al. (2012). Carbon dynamics in the western Arctic Ocean: insights from full−depth carbon isotope profiles of DIC, DOC, and POC. *Biogeosciences* 9, 1217–1224. doi: 10.5194/bg-9-1217-2012

Guay, C. K., and Falkner, K. K. (1998). A survey of dissolved barium in the estuaries of major Arctic rivers and adjacent seas. *Cont. Shelf Res.* 18, 859–882. doi: 10.1016/S0278-4343(98)00023-5

Gustafsson, O., and Andersson, P. S. (2012). $^{234}$Th-derived surface export fluxes of POC from the Northern Barents Sea and the Eurasian sector of the central Arctic Ocean. *Deep Sea Res. I* 68, 1–11. doi: 10.1016/j.dsr.2012.05.014

Harada, K., Burnett, W. C., and LaRock, P. A. (1989). Polonium in Florida groundwater and its possible relationship to the sulfer cycle and bacteria. *Geochim. Cosmochim. Acta* 53, 143–150.

Haskell, W. Z. I. I., Berelson, W. M., Hammond, D. E., and Capone, D. G. (2013). Particle sinking dynamics and POC fluxes in the eastern Tropical South Pacific based on 234Th budgets and sediment trap deployments. *Deep Sea Res. I* 81, 1–13. doi: 10.1016/j.dsr.2013.07.001

He, J., Yu, W., Lin, W., Men, W., and Chen, L. (2015). Particulate organic carbon export fluxes on Chukchi Shelf, western Arctic Ocean, derived from 210Po/210Pb disequilibrium. *Chin. J. Oceanol. Limnol.* 33, 741–747.

Henson, S. A., Yool, A., and Sanders, R. (2015). Variability in efficiency of particulate organic carbon export: a model study. *Glob. Biogeochem. Cycles* 29, 33–45. doi: 10.1002/2014GB004965

Honjo, S., Krishfield, R. A., Eglinton, T. I., Manganini, S. J., Kemp, J. N., Doherty, K., et al. (2010). Biological pump processes in the cryopelagic and hemipelagic Arctic Ocean: Canada Basin and Chukchi Rise. *Prog. Oceanogr.* 85, 137–170. doi: 10.1016/j.pocean.2010.02.009

Honjo, S., Manganini, S. J., Krishfield, R. A., and Francois, R. (2008). Particulate organic carbon fluxes to the ocean interior and factors controlling the biological pump: a synthesis of global sediment trap programs since 1983. *Prog. Oceanogr.* 76, 217–285. doi: 10.1016/j.pocean.2007.11.003

Hu, W., Chen, M., Yang, W., Zhang, R., Qiu, Y., and Zheng, M. (2014). Low 210Pb in the upper thermocline in the Canadian Basin: scavenge process over the Chukchi Sea. *Acta Oceanol. Sin.* 33, 28–39. doi: 10.1007/s13131-014-0486-6

Hugelius, G., Strauss, J., Zubrzycki, S., Harden, J. W., Schuur, E. A. G., Ping, C.-L., et al. (2014). Estimated stocks of circumpolar permafrost carbon with quantified uncertainty ranges and identified data gaps. *Biogeosciences* 11, 6573–6593. doi: 10.5194/bg-11-6573-2014

Hwang, J., Eglinton, T. I., Krishfield, R. A., Manganini, S. J., and Honjo, S. (2008). Lateral organic carbon supply to the deep Canada Basin. *Geophys. Res. Lett.* 325:L11607. doi: 10.1029/2008GL034271

Hwang, J., Kim, M., Manganini, S. J., McIntyre, C. P., Haghipour, N., Park, J., et al. (2015). Temporal and spatial variability of particle transport in the deep Arctic Canada Basin. *J. Geophys. Res. Oceans* 120, 2784–2799. doi: 10.1002/2014JC010643

Jakobsson, M., Grantz, A., Kristoffersen, Y., and Macnab, M. (2004). "Bathymetry and physiography of the Arctic Ocean and its constituent seas," in *The Organic Carbon Cycle in the Arctic Ocean*, eds R. Stein, and R. W. MacDonald (Heidelberg: Springer), 1–6.

Jeandel, C., Rutgers van der Loeff, M., Lam, P. J., Roy-Barman, M., Sherrell, R. M., Kretschmer, S., et al. (2015). What did we learn about ocean particle dynamics in the GEOSECS-JGOFS era? *Prog. Oceanogr.* 133, 6–16.

Jensen, L. T., Morton, P., Twining, B. S., Heller, M. I., Hatta, M., Measures, C. I., et al. (2020). A comparison of marine Fe and Mn cycling: U.S. GEOTRACES GN01 Western Arctic case study. *Geochim. Cosmochim. Acta* 299, 138–160. doi: 10.1016/j.gca.2020.08.006

Jensen, L. T., Wyatt, N. J., Twining, B. S., Rauschenberg, S., Landing, W. M., Sherrell, R. M., et al. (2019). Biogeochemical cycling of dissolved zinc in the Western Arctic (Arctic GEOTRACES GN01). *Glob. Biogeochem. Cycles* 33, 343–369. doi: 10.1029/2018GB005975

Jorgenson, T. M., SHur, Y. L., and Pullman, E. R. (2006). Abrupt increase in permafrost degradation in Arctic Alaska. *Geophys. Res. Lett.* 33:L02503. doi: 10.1029/2005GL024960

Kim, G., Kim, S.-J., Harada, K., Schultz, M. K., and Burnett, W. C. (2005). Enrichment of excess 210Po in anoxic ponds. *Environ. Sci. Technol.* 39, 4894–4899.

Kinney, P., Arhelger, M. E., and Burrell, D. C. (1970). Chemical characteristics of water masses in the Amerasian Basin of the Arctic Ocean. *J. Geophys. Res.* 75, 4097–4104. doi: 10.1029/JC075i021p04097

Kipp, L. E., Charette, M. A., Moore, W. S., Henderson, P. B., and Rigor, G. I. (2018). Increased fluxes of shelf-derived materials to the central Arctic Ocean. *Sci. Adv.* 4:eaao1302.

Kipp, L. E., Kadko, D. C., Pickart, R. S., Henderson, P. B., Moore, W. S., and Charette, M. A. (2019). Shelf—basin interactions and water mass residence times in the Western Arctic Ocean: insights provided by radium isotopes. *JGR Oceans* 124, 3279–3297. doi: 10.1029/2019JC014988

Klunder, M. B., Bauch, D., Laan, P., Baar, H. J. W. D., Heuven, S.v., and Ober, S. (2012). Dissolved iron in the Arctic shelf seas and surface waters of the central Arctic Ocean: impact of Arctic river water and ice—melt. *J. Geophys. Res.* 117:C01027. doi: 10.01029/02011JC007133

Ko, Y. H., and Quay, P. D. (2020). Origin and accumulation of an anthropogenic CO2 and 13C Suess effect in the Arctic Ocean. *Glob. Biogeochem. Cycles* 34:e2019GB006423. doi: 10.1029/2019GB006423

Krishnamurthy, R. V., Machavaram, M., Baskaran, M., Champ, M., and Brooks, J. M. (2001). Organic carbon flow in the Ob, Yenisey Rivers and Kara Sea of the Arctic Region. *Mar. Pollut. Bull.* 42, 726–732.

Lalande, C., Forest, A., Barber, D. G., Gratton, Y., and Fortier, L. (2009). Variability in the annual cycle of vertical particulate organic carbon export on Arctic shelves: contrasting the Laptev Sea, Northern Baffin Bay and the Beaufort Sea. *Cont. Shelf Res.* 29, 2157–2165. doi: 10.1016/j.csr.2009.08.009

Lalande, C., Nöthig, E. M., Somavilla, R., Bauerfeind, E., Shevchenko, V., and Okolodkov, Y. (2014). Variability in under—ice export fluxes of biogenic matter in the Arctic Ocean. *Glob. Biogeochem. Cycles* 28, 571–583. doi: 10.1002/2013GB004735

Lam, P. (2020). *Size-Fractionated Major and Minor Particle Composition and Concentration from the US GEOTRACES Arctic Cruise (HLY1502) on USCGC Healy from August to October 2015. (Version 1)*. Woods Hole, MA: Biological and Chemical Oceanography Data Management Office (BCO-DMO). doi: 10.26008/1912/bco-dmo.807340.1

Lannuzel, D., Tedesco, L., Leeuwe, M. V., Campbell, K., Flores, H., Delille, B., et al. (2020). The future of Arctic sea-ice biogeochemistry and ice-associated ecosystems. *Nat. Clim. Change* 10, 983–992. doi: 10.1038/s41558-020-00940-4

Laws, E. A., and Maiti, K. (2019). The relationship between primary production and export production in the ocean: effects of time lags and temporal variability. *Deep Sea Res. Part I* 148, 100–107. doi: 10.1016/j.dsr.2019.05.006

Le Moigne, F. A. C., Poulton, A. J., Henson, S. A., Daniels, C. J., Fragoso, G. M., et al. (2015). Carbon export efficiency and phytoplankton community composition in the Atlantic sector of the Arctic Ocean. *J. Geophys. Res. Oceans* 120, 3896–3912. doi: 10.1002/2015JC010700

Lepore, K., Moore, R. M., and Smith, J. N. (2009). 210Pb as a tracer of shelf–basin transport and sediment focusing in the Chukchi Sea. *Deep Sea Res. II Top. Stud. Oceanogr.* 56, 1305–1315.

Li, W. K. W., McLaughlin, F. A., Lovejoy, C., and Carmack, E. C. (2009). Smallest algae thrive as the Arctic Ocean freshens. *Science* 326:539. doi: 10.1126/science.1179798

Lin, P., Xu, C., Xing, W., and Santschi, P. H. (2021). Molecular level characterization of diatom and coccolithophore-associated biopolymers that are binding 210Pb and 210Po in seawater. *Front. Mar. Sci.* 8:703503. doi: 10.3389/fmars.2021.703503

Macdonald, R. W., McLaughlin, F. A., and Carmack, E. C. (2002). Freshwater and its sources during the SHEBA drift in the Canada Basin of the Arctic Ocean. *Deep Sea Res. I* 49, 1769–1785. doi: 10.1016/S0967-0637(02)00097-3

Maiti, K., and Bam, W. (2020a). *Dissolved and Large Particulate Polonium 210 and Lead 210 Measurements from the Western Arctic Ocean, Which Were Sampled as Part of the 2015 US GEOTRACES Cruise, HLY1502 (GN01), on USCGC Healy. (Version 1) Version Date 2020-04-01*. Woods Hole, MA: Biological and Chemical Oceanography Data Management Office (BCO-DMO). doi: 10.26008/1912/bco-dmo.808151.1

Maiti, K., and Bam, W. (2020b). *Small Particulate Polonium 210 and Lead 210 Measurements from the Western Arctic Ocean, Which Were Sampled as Part of the 2015 US GEOTRACES Cruise, HLY1502 (GN01), on USCGC Healy. (Version 1) Version Date 2020-04-07*. Woods Hole, MA: Biological and Chemical Oceanography Data Management Office (BCO-DMO). doi: 10.26008/1912/bco-dmo.808502.1

Maiti, K., Benitez-Nelson, C. R., Rii, Y., and Bidigare, R. (2008). The influence of a mature cyclonic eddy on particle export in the lee of Hawaii. *Deep Sea Res. II* 55, 1445–1460. doi: 10.1016/j.dsr2.2008.02.008

Maiti, K., Bosu, S., D'Sa, E. J., Adhikari, P. L., Sutor, M., and Longnecker, K. (2016). Export fluxes in northern Gulf of Mexico-comparative evaluation of direct, indirect and satellite-based estimates. *Mar. Chem.* 184, 60–77. doi: 10.1016/j.marchem.2016.06.001

Masqué, P., Cochran, J. K., Hirschberg, D. J., Dethleff, D., Hebbeln, D., Winkler, A., et al. (2007). Radionuclides in Arctic sea ice: tracers of sources, fates and ice transit time scales. *Deep Sea Res. I* 54, 1289–1310. doi: 10.1016/j.dsr.2007.04.016

Metfies, K., von Appen, W. J., Kilias, E., Nicolaus, A., and Nöthig, E. M. (2016). Biogeography and photosynthetic biomass of arctic marine pico-eukaroytes during summer of the record sea ice minimum 2012. *PLoS One* 11:e0148512. doi: 10.1371/journal.pone.0148512

Meybeck, M., and Ragu, A. (1997). *River Discharges to the Oceans: an Assessment of Suspended Solids, Major Ions and Nutrients*. Geneva: UNEP.

Moore, R. M., Lowings, M. G., and Tan, F. C. (1983). Geochemical profiles in the central Arctic Ocean: their relation to freezing and shallow circulation. *J. Geophys. Res. Oceans* 88, 2667–2674. doi: 10.1029/JC088iC04p02667

Moore, R. M., and Smith, J. N. (1986). Disequilibria between226Ra, 210Pb and 210Po in the Arctic Ocean and the implications for chemical modification of the Pacific water inflow. *Earth Planet. Sci. Lett.* 77, 285–292.

Moran, S. B., Ellis, K. M., and Smith, J. N. (1997). 234Th/238U disequilibrium in the central Arctic Ocean: implications for particulate organic carbon export. *Deep Sea Res. II Top. Stud. Oceanogr.* 44, 1593–1606. doi: 10.1016/S0967-0645(97)00049-0

Moran, S. B., Kelly, R. P., Hagstrom, K., Smith, J. N., Grebmeier, J. M., Cooper, L. W., et al. (2005). Seasonal changes in POC export flux in the Chukchi Sea and implications for water column—benthic coupling in Arctic shelves. *Deep Sea Res. II Top. Stud. Oceanogr.* 52, 3427–3451. doi: 10.1016/j.dsr2.2005.09.011

Murray, J. W., Paul, B., Dunne, J. P., and Chapin, T. (2005). 234Th, 210Pb, 210Po and stable Pb in the central equatorial Pacific: tracers for particle cycling. *Deep Sea Res. I Oceanogr. Res. Pap.* 52, 2109–2139.

Murray, J. W., Young, J., Netwon, J., Dunne, J., Chapin, T., Paul, B., et al. (1996). Export flux of particulate organic carbon from the central equatorial Pacific determined using a combined drifting trap-234Th approach. *Deep Sea Res. II Top. Stud. Oceanogr.* 43, 1095–1132. doi: 10.1016/0967-0645(96)00036-7

Niedermiller, J., and Baskaran, M. (2019). Comparison of the scavenging intensity, remineralization and residence time of 210Po and 210Pb at ley zones (biotic, sediment-water and hydrothermal) along the East Pacific GEOTRACES transect. *J. Environ. Radioact.* 198, 165–188. doi: 10.1016/j.jenvrad.2018.12.016

Nozaki, Y., Thompson, J., and Turekian, K. K. (1976). The distribution of210Pb and210Po in the surface water of the Pacific Ocean. *Earth Planet. Sci. Lett.* 32, 304–312. doi: 10.1016/0012-821X(76)90070-4

O'Brien, M. C., Macdonald, R. W., Melling, H., and Iseki, K. (2006). Particle fluxes and geochemistry on the Canadian Beaufort Shelf: Implications for sediment transport and deposition. *Cont. Shelf Res.* 26, 41–81. doi: 10.1016/j.csr.2005.09.007

Peterson, B. J., Holmes, R. M., McClelland, J. W., Vörösmarty, C. J., Lammers, R. B., Shiklomanov, A. I., et al. (2002). Increasing river discharge to the Arctic Ocean. *Science* 298, 2171–2173.

Pineault, S., Tremblay, J. E., Gosselin, M., Thomas, H., and Shadwick, E. H. (2013). The isotopic signature of particulate organic C and N in bot-tom ice: key influencing factors and applications for tracing the fate of ice-algae in the Arctic Ocean. *J. Geophys. Res.* 118, 287–300. doi: 10.1029/2012JC008331

Quay, P. (2019). *The Ratio of 13C to 12C of Dissolved Inorganic Carbon (DIC) Measured During the GEOTRACES Arctic Cruise (HLY 1502, ARC01) During FALL 2015. (Version 1)*. Woods Hole, MA: Biological and Chemical Oceanography Data Management Office (BCO-DMO).

Rabe, B., Karcher, M., Schauer, U., Toole, J. M., Krishfield, R. A., Pisarev, S., et al. (2011). An assessment of Arctic Ocean freshwater content changes from the 1990s to 2006–2008 period. *Deep Sea Res. I* 58, 173–185. doi: 10.1016/j.dsr.2010.12.002

Rachold, V., Eicken, H., Gordeev, V., and Schirrmeister, L. (2004). "Modern terrigenous organic carbon input to the Arctic Ocean," in *The Organic Carbon Cycle in the Arctic Ocean*, eds R. S. Stein, and R. W. Macdonald (New York, NY: Springer), 33–55.

Rachold, V., Grigoriev, M. N., Are, F. E., Solomon, S., Reimnitz, E., Kassens, H., et al. (2000). Coastal erosion vs riverine sediment discharge in the Arctic Shelf seas. *Int. J. Earth Sci.* 89, 450–460. doi: 10.1007/s005310000113

Rau, G. H., Takahashi, T., and Des Marais, D. J. (1989). Latitudinal variations in plankton δ13C: implications for CO2 and productivity in past oceans. *Nature* 341, 516–518. doi: 10.1038/341516a0

Rickert, D., Schluter, M., and Wallmann, K. (2002). Dissolution kinetics of biogenic silica from the water column to the sediments. *Geochim. Cosmochim. Acta* 66, 439–455. doi: 10.1016/S0016-7037(01)00757-8

Rigaud, S., Stewart, G., Baskaran, M., Marsan, D., and Church, T. (2015). 210Po and 210Pb distribution, dissolved-particulate exchange rates, and particulate export along the North Atlantic US GEOTRACES GA03section. *Deep Sea Res. II* 116, 60–78. doi: 10.1016/j.dsr2.2014.11.003

Roca-Martí, M., Puigcorbéc, V., Friedrich, J., Rutgers van der Loeff, M., Rabe, B., Korhonen, M., et al. (2018). Distribution of 210Pb and 210Po in the Arctic water column during the 2007 sea-ice minimum: particle export in the ice-covered basins. *Deep Sea Res. I* 142, 94–106. doi: 10.1016/j.dsr.2018.09.011

Roca-Martí, M., Puigcorbé, V., Rutgers van der Loeff, M. M., Katlein, C., Fernandez-Mendez, M., Peeken, I., et al. (2016). Carbon export fluxes and export efficiency in the central Arctic during the record sea-ice minimum in 2012: a joint 234Th/238U and 210Po/210Pb study. *J. Geophys. Res. Oceans* 121, 5030–5049. doi: 10.1002/2016JC011816

Rudels, B. (2015). Arctic Ocean circulation, processes and water masses: a description of observations and ideas with focus on the period prior to the International Polar Year 2007–2009. *Prog. Oceanogr.* 132, 22–67. doi: 10.1016/j.pocean.2013.11.006

Rutgers Van Der Loeff, M., Key, R. M., Scholten, J., Bauch, D., and Michel, A. (1995). 228Ra as a tracer for shelf water in the Arctic Ocean. *Deep Sea Res. II Top. Stud. Oceanogr.* 42, 1533–1553. doi: 10.1016/0967-0645(95)00053-4

Rutgers Van Der Loeff, M., Kipp, L., Charette, M. A., Moore, W. S., Black, E., Stimac, I., et al. (2018). Radium isotopes across the arctic ocean show time scales of water mass ventilation and increasing shelf inputs. *J. Geophys. Res. Oceans* 123, 4853–4873. doi: 10.1029/2018JC013888

Sallon, A., Michel, C., and Gosselin, M. (2011). Summertime primary production and carbon export in the southeastern Beaufort Sea during the low ice year of 2008. *Polar Biol.* 34, 1989–2005. doi: 10.1007/s00300-011-1055-5

Schuur, E. A., McGuire, A. D., Schädel, C., Grosse, G., Harden, J. W., Hayes, D. J., et al. (2015). Climate change and the permafrost carbon feedback. *Nature* 520, 171–179. doi: 10.1038/nature14338

Schuur, E. A. G., Bockheim, J., Canadell, J. G., Euskirchen, E., Field, C. B., Goryachkin, S. V., et al. (2008). Vulnerability of permafrost carbon to climate change: implications for the global carbon cycle. *Bioscience* 58, 701–714. doi: 10.1641/B580807

Serreze, M. C., Barrett, A. P., Slater, A. G., Woodgate, R. A., Aagaard, K., Lammers, R. B., et al. (2006). The large−scale freshwater cycle of the Arctic. *J. Geophys. Res. Oceans* 111:C11010. doi: 10.1029/2005JC003424

Shaw, W. J., Stanton, T. P., McPhee, M. G., Morison, J. H., and Martinson, D. G. (2009). Role of the upper ocean in the energy budget of Arctic sea ice during SHEBA. *J. Geophys. Res.* 114:C06012. doi: 10.1029/2008JC004991

Smith, J. N., Moran, S. B., and Macdonald, R. W. (2003). Shelf–basin interactions in the Arctic Ocean based on 210Pb and Ra isotope tracer distributions. *Deep Sea Res. I* 50, 397–416.

Stewart, G., Cochran, J. K., Miquel, J. C., Masqué, P., Szlosek, J., Rodriguez y Baena, A. M., et al. (2007). Comparing POC export from 234Th/238U and 210Po/210Pb disequilibria with estimates from sediment traps in the northwest Mediterranean. *Deep Sea Res. I* 54, 1549–1570. doi: 10.1016/j.dsr.2007.06.005

Stewart, G. M., and Fisher, N. S. (2003a). Bioaccumulation of polonium-210 in marine copepods. *Limnol. Oceanogr.* 48, 2011–2019. doi: 10.4319/lo.2003.48.5.2011

Stewart, G. M., and Fisher, N. S. (2003b). Experimental studies on the accumulation of polonium-210 by marine phytoplankton. *Limnol. Oceanogr.* 48, 1193–1201. doi: 10.4319/lo.2003.48.3.1193

Su, K., Du, J., Baskaran, M., and Zhang, J. (2017). 210Po and 210Pb disequilibrium at the PN section in the East China Sea. *J. Environ. Radioact.* 174, 54–65. doi: 10.1016/j.jenvrad.2016.07.031

Tang, Y., and Stewart, G. (2019). The 210Po/210Pb method to calculate particle export: lessons learned from the results of three GEOTRACES transects. *Mar. Chem.* 217:103692. doi: 10.1016/j.marchem.2019.103692

Tang, Y., Stewart, G., Lam, P. J., Riguad, S., and Church, T. (2017). The influence of particle concentration and composition on the fractionation of 210 Po and 210 Pb along the North Atlantic GEOTRACES transect GA03. *Deep Sea Res. I* 128, 42–54. doi: 10.1016/j.dsr.2017.09.001

Tolosa, I., Fiorini, S., Gasser, B., Martín, J., and Miquel, J. C. (2013). Carbon sources in suspended particles and surface sediments from the Beaufort Sea revealed by molecular lipid biomarkers and compound−specific isotope analysis. *Biogeosciences* 10, 2061–2087. doi: 10.5194/bg-10-2061-2013

Tovar-Sánchez, A., Duarte, C. M., Alonso, J. C., Lacorte, S., Tauler, R., Galbán-Malagón, C. (2010). Impacts of metals and nutrients released from melting multiyear Arctic sea ice. *J. Geophys. Res.* 115, 1–7. doi: 10.1029/2009JC005685

Trimble, S. M., and Baskaran, M. (2005). The role of suspended particulate matter in 234Th scavenging and 234Th-derived export fluxes of POC in the Canada Basin of the Arctic Ocean. *Marine Chemistry* 96, 1–19. doi: 10.1016/j.marchem.2004.10.003

Wei, C. L., Lin, S. Y., Sheu, D. D. D., Chou, W.-C., Yi, M.-C., Santschi, P. H., et al. (2011). Particle-reactive radionuclides (234Th, 210Pb, 210Po) as tracers for the estimation of export production in the South China Sea. *Biogeosciences* 8, 3793–3808. doi: 10.5194/bg-8-3793-2011

Weingartner, T. J., Cavalieri, D. J., Aagaard, K., and Sasaki, Y. (1998). Circulation, dense water formation, and outflow on the northeast Chukchi shelf. *J. Geophys. Res.* 103, 7647–7661. doi: 10.1029/98JC00374

Wheeler, P. A., Watkins, J. W., and Hansing, R. L. (1997). Nutrients, organic carbon and organic nitrogen in the upper water column of the Arctic Ocean: implications for the sources of dissolved organic carbon. *Deep Sea Res. II Top. Stud. Oceanogr.* 44, 1571–1592.

Xiang, Y., and Lam, P. J. (2020). Size−fractionated compositions of marine suspended particles in the Western Arctic Ocean: lateral and vertical

sources. *J. Geophys. Res. Oceans* 125:e2020JC016144. doi: 10.1029/2020JC016144

Yamamoto-Kawai, M., McLaughlin, F. A., Carmack, E. C., Nishino, S., and Shimada, K. (2008). Freshwater budget of the Canada Basin, Arctic Ocean, from salinity, δ18O, and nutrients. *J. Geophys. Res. Oceans* 113:C01007. doi: 10.1029/2006JC003858

Yu, W., Chen, L., Cheng, J., He, J., Yin, M., and Zeng, Z. (2010). 234Th-derived particulate organic carbon export fluxes in the western Arctic Ocean Chin. *J. Oceanol. Limnol.* 28, 1146–1151. doi: 10.1007/s00343-010-9933-1

Yu, W., He, J., Li, Y., Lin, W., and Chen, L. (2012). Particulate organic carbon export fluxes and validation of steady state model of 234Th export in the Chukchi Sea. *Deep Sea Res. II Top. Stud. Oceanogr.* 8, 63–71. doi: 10.1016/j.dsr2.2012.03.003

Zhong, W., Steele, M., Zhang, J., and Cole, S. T. (2019). Circulation of Pacific winter water in the Western Arctic Ocean. *J. Geophys. Res. Oceans* 124, 863–881. doi: 10.1029/2018jc014604

**Conflict of Interest:** The authors declare that the research was conducted in the absence of any commercial or financial relationships that could be construed as a potential conflict of interest.

**Publisher's Note:** All claims expressed in this article are solely those of the authors and do not necessarily represent those of their affiliated organizations, or those of the publisher, the editors and the reviewers. Any product that may be evaluated in this article, or claim that may be made by its manufacturer, is not guaranteed or endorsed by the publisher.

*Copyright © 2021 Bam, Maiti and Baskaran. This is an open-access article distributed under the terms of the Creative Commons Attribution License (CC BY). The use, distribution or reproduction in other forums is permitted, provided the original author(s) and the copyright owner(s) are credited and that the original publication in this journal is cited, in accordance with accepted academic practice. No use, distribution or reproduction is permitted which does not comply with these terms.*

frontiers in Marine Science

ORIGINAL RESEARCH
published: 30 July 2021
doi: 10.3389/fmars.2021.692631

# Novel Application of $^{210}$Po-$^{210}$Pb Disequilibria to Date Snow, Melt Pond, Ice Core, and Ice-Rafted Sediments in the Arctic Ocean

*Mark Baskaran* and Katherine Krupp*

*Department of Environmental Science and Geology, Wayne State University, Detroit, MI, United States*

We collected surface ocean water, snow, grab ice, ice core, melt pond and ice-rafted sediment (IRS) from 5 ice stations during the Western Arctic US GEOTRACES cruise (USGCG Healy; August 10 – October 7, 2015) and analyzed for $^{210}$Po ($T_{1/2}$ = 138.4 days) and $^{210}$Pb ($T_{1/2}$ = 22.3 years) in dissolved and particulate phases (snow, grab ice, ice core, surface seawater) to investigate the $^{210}$Po:$^{210}$Pb disequilibria in these matrices. Thirteen aerosol samples, using a large-volume aerosol sampler (PM10), from Dutch Harbor, AK to North Pole, were also collected and analyzed for $^{210}$Po/$^{210}$Pb to quantify the atmospheric depositional input to the snow and surface waters. Falling snowfall is tagged with $^{210}$Po/$^{210}$Pb ratio (AR) similar to that in the air column from the cloud condensation height to air-sea interface. From the measured AR in aerosol and snow, modeling the sources of $^{210}$Po and $^{210}$Pb input to the melt pond, and measured disequilibrium in ice core and ice-rafted sediment, we show $^{210}$Po/$^{210}$Pb AR is a novel chronometer to date snow, ice core, melt pond, and IRS. The calculated mean ages of aerosol, snow, melt pond and IRS are 12 ± 7 ($n$ = 13), 13 ± 11 ($n$ = 6), 60 ± 14 ($n$ = 4), and 87 ± 23 ($n$ = 6) days, respectively. The average IRS age corresponds to an average drift velocity of sediment-laden ice of 0.18 ± 0.06 ($n$ = 6) m s$^{-1}$. We report highly elevated levels of $^{210}$Po and $^{210}$Pb in snow and melt pond compared to those in Arctic surface seawater and enrichment of $^{210}$Po compared to $^{210}$Pb onto particles extracted from snow, ice and melt ponds. The observed disequilibrium between $^{210}$Po and $^{210}$Pb in ice could serve as a quantitative tool in delineating multiple-year ice from seasonal ice as well as a metric in quantifying the speed of ice/snow melting and delay in autumn freeze.

**Keywords: Po-210/Pb-210 dating, Arctic pollutant transport, dating ice-rafted sediment, dating of snow and melt pond, Po-210 enrichment in particulate matter, environmental changes in the Arctic**

OPEN ACCESS

***Edited by:***
*Laodong Guo,*
*University of Wisconsin–Milwaukee, United States*

***Reviewed by:***
*Guebuem Kim,*
*Seoul National University, South Korea*
*Xilong Wang,*
*Beibu Gulf University, China*

****Correspondence:***
*Mark Baskaran*
*Baskaran@wayne.edu*
*orcid.org/0000-0002-2218-4328*

***Specialty section:***
*This article was submitted to Marine Biogeochemistry, a section of the journal Frontiers in Marine Science*

***Received:*** *08 April 2021*
***Accepted:*** *18 June 2021*
***Published:*** *30 July 2021*

***Citation:***
*Baskaran M and Krupp K (2021) Novel Application of $^{210}$Po-$^{210}$Pb Disequilibria to Date Snow, Melt Pond, Ice Core, and Ice-Rafted Sediments in the Arctic Ocean. Front. Mar. Sci. 8:692631. doi: 10.3389/fmars.2021.692631*

## INTRODUCTION

The Arctic is undergoing drastic environmental change which has manifested in decrease in the areal extent of sea ice cover, from 6.95 million km$^2$ in 1980 to 3.95 million km$^2$ in 2015, ∼45% decrease which is attributed to increase in sea surface as well as surface air temperature. Earlier melt of sea ice and later freeze in the Arctic shelves lead to a longer open-water season which has

impacted the biogeochemical cycling of key trace elements and isotopes due to wind-driven vertical mixing (Kipp et al., 2018; Rutgers van der Loeff et al., 2018; Grenier et al., 2019). In addition, early retreat of sea ice edge is expected to result in higher wave action which in turn, expected to affect the amount of energy transferred from wind to surface water. Ice-free shelf waters are anticipated to result in higher wind-driven upwelling which in turn is expected to increase the amount of deeper waters onto the shelf (Carmack and Chapman, 2003). Thus, the residence time of snow, ice, and melt ponds is of great interest and has bearing on the changes in the biogeochemical cycling. The age of snow, melt pond, ice and ice-rafted sediment (IRS) in the Arctic Ocean has direct relevance to the total heat energy absorbed by surface water due to differences in their albedo and heat transfer during phase change (e.g., heat absorbed by snow/ice to become liquid water) (Uttal et al., 2002).

Polonium-210 ($^{210}$Po, $T_{1/2}$ = 138.4 days) and lead-210 ($^{210}$Pb, $T_{1/2}$ = 22.3 years), progeny of radon-222 [$^{222}$Rn, half-life ($T_{1/2}$) = 3.82 days], the heaviest and longest-lived noble gas in the U-Th series, are particle-reactive and thus have been utilized as tracers and chronometers in environmental studies (Robbins, 1978; Turekian et al., 1977; Cochran and Masque, 2003; Rutgers van der Loeff and Geibert, 2008; Baskaran, 2016). A major fraction of $^{210}$Pb in surface ocean waters is derived from direct atmospheric deposition, which is derived from the decay of atmospheric Radon (e.g., Bacon et al., 1976). A small fraction of $^{222}$Rn, daughter of $^{226}$Ra, produced in rocks and mineral grains on the Earth's upper crust escapes through cracks and crevices to the atmosphere. From there, it embarks on its journey in the atmosphere via advection and diffusion and produces 12 different isotopes, including $^{210}$Po and $^{210}$Pb (Turekian et al., 1977). The radon emanation rates from continents decrease with increasing latitude by a factor of 5, from 1 atom cm$^{-2}$ s$^{-1}$ at 30°N to 0.2 atom cm$^{-2}$ s$^{-1}$ at 70°N (Conan and Robertson, 2002; Baskaran, 2011). In addition, the average $^{222}$Rn emanation rate from the continental area (including land area covered by glaciers and permafrost with negligible $^{222}$Rn release) of 0.75 atom cm$^{-2}$ s$^{-1}$ is ∼1-2 orders of magnitude higher compared to surface waters (rivers, lakes, and ocean) (e.g., Wilkening and Clements, 1975). In the absence of $^{210}$Po from sources other than the radioactive decay of atmospheric $^{222}$Rn-derived $^{210}$Pb (such as volcanic, industrial release, etc.), the $^{210}$Po/$^{210}$Pb activity ratio (AR) in aerosols has been utilized to determine the 'age' of aerosols (Moore et al., 1973; Robbins, 1978; Marley et al., 2000) and is generally reported to be <0.1 in the lower and middle troposphere (Turekian et al., 1977; Baskaran, 2011).

The upper end of the dating range of a radioactive daughter-parent pair, where the parent half-life is much longer than the daughter half-life, is typically about 5-6 half-lives of the daughter isotope and hence $^{210}$Po:$^{210}$Pb disequilibrium is useful from a few days up to 2 years. From simultaneous measurements of $^{210}$Po and $^{210}$Pb in aerosols and precipitation, it was shown that the initial $^{210}$Po/$^{210}$Pb AR was similar in rain/snow and aerosols (McNeary and Baskaran, 2007). During precipitation in the Arctic (and elsewhere), the falling snow underneath the cloud cover is tagged with the $^{210}$Po/$^{210}$Pb AR of aerosols generally with values of <0.1 (Baskaran, 2011); as time elapses, this ratio in snow increases due to $^{210}$Po ingrowth from the decay of $^{210}$Pb. With time, the accumulated snow becomes ice or undergoes melting. During the beginning of the melt season, generally in June, meltwater from snow and ice, mostly freshwater, begins to form a pond at the surface and grow, both in areal extent and depth (Polashenski et al., 2012). From the estimated initial and measured $^{210}$Po/$^{210}$Pb AR of the melt pond, its age can be determined. During storm events in early autumn, atmospherically delivered $^{210}$Po and $^{210}$Pb, with $^{210}$Po/$^{210}$Pb AR of <0.1, are scavenged by resuspended sediments and eventually incorporated into coastal sea ice which are subsequently transported to the interior Arctic (Nürnberg et al., 1994). The in-growth of $^{210}$Po from the decay of $^{210}$Pb provides the time elapsed since incorporation of these radionuclides. Here, we report a novel application of disequilibrium between $^{210}$Po and $^{210}$Pb in dating snow, melt pond, ice core and IRS collected from the Arctic Ocean.

The primary goal of the present study, is to test the following hypotheses: (i) The in-growth of $^{210}$Po from the decay of $^{210}$Pb in snowfall provides a tool to determine the age of snow; (ii) From quantifying the fractional input of the sources of water to the melt pond and knowing the end-member activities of $^{210}$Po and $^{210}$Pb, the age of the melt ponds can be determined; (iii) Since the time range for daughter-deficient $^{210}$Po:$^{210}$Pb dating is up to ∼ 2 years (or $^{210}$Po/$^{210}$Pb ∼0.97), multi-year ice in ice-pack can be recognized; and (iv) Most of the atmospherically delivered $^{210}$Pb, with $^{210}$Po/$^{210}$Pb AR similar to that in aerosol, is scavenged by resuspended sediment which gets incorporated into sea ice in the coastal areas and thus, we can date the IRS using $^{210}$Po/$^{210}$Pb pair. The ages of snow, melt pond and ice core are relevant to the exchange of latent heat with the surrounding, changes in the albedo while ages of IRS are relevant to the transport velocity of coastal sediments and sediment-laden contaminants. In addition, transport of nutrients from coastal zone to the deep Arctic through sea ice makes a coupling between coastal and deep arctic benthic community.

# MATERIALS AND METHODS

## Sample Collection

During US GEOTRACES Arctic cruise (HLY1502; R/V Icebreaker USCGC *Healy;* August 10 – October 7, 2015), the following samples were collected from 6 ice stations (ST-31, -33, -39, -42, -43, and -46, **Figure 1**): snow, melt pond (only 5 stations) and ice core; IRS, often are sporadically distributed in the ice, from two ice stations (E-6195 and -6244); and 13 aerosol samples (**Figure 1**), using a large-volume aerosol sampler ($PM_{10}$), from Dutch Harbor, AK to North Pole, where each deployment averaged ∼30 h of run time (**Figure 1** and **Table 1**). Aliquots of GFF aerosol filters, corresponding to filtered air volume, 72 to 463 m$^3$ (**Table 1**), were provided for analysis from the aerosol group of the U.S. GEOTRACES program. Details on aerosol collection were published in Morton et al. (2013).

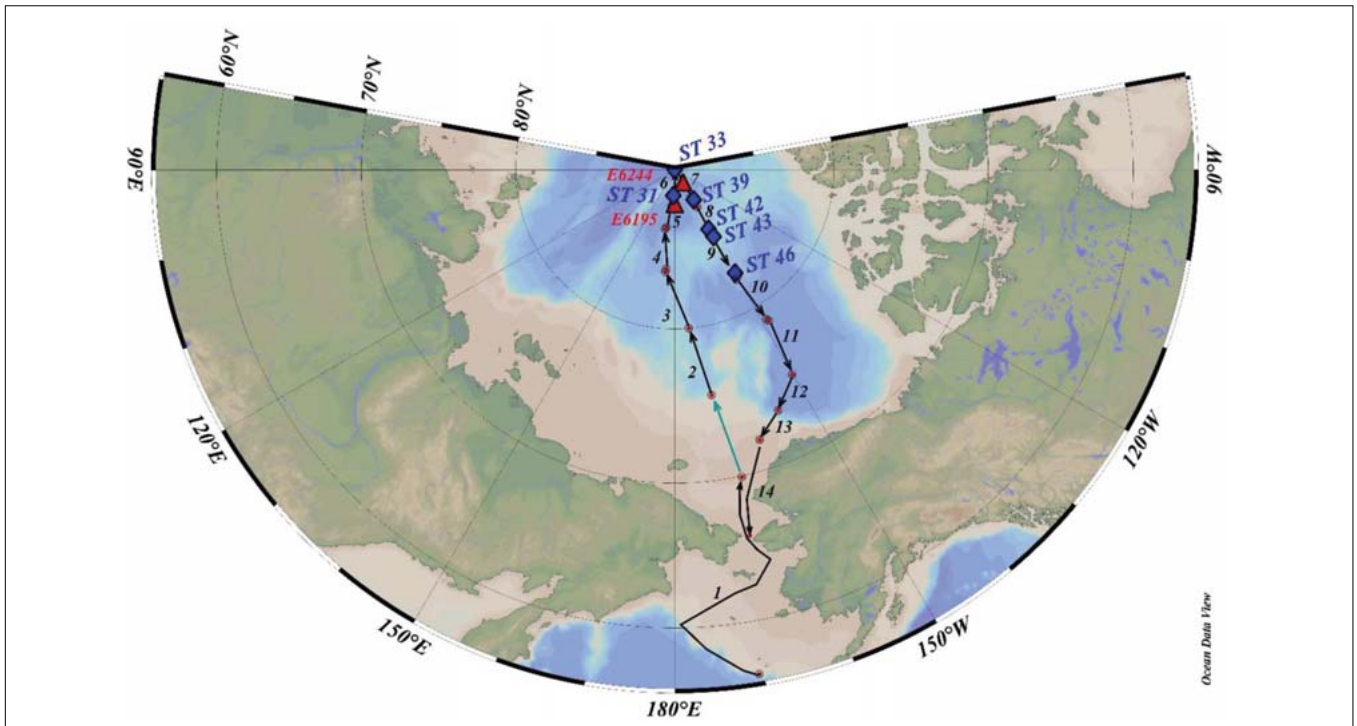


**FIGURE 1 |** Sampling stations for aerosols, ice-rafted sediment and ice stations. Green arrow shows transit with no sampling; distance between successive red dots denote aerosol sampling (starting and ending of location) for that particular sample; pumps didn't work for ST-5 and no sample. Two red lettered stations (E6244 and E6195 in red triangle) denote the dirty sea ice sample collection; Blue lettered stations 31, 33, 39, 42, 43, and 46 denote ice stations (US GEOTRACES Arctic cruise, HLY1502, R/V Icebreaker USCGC *Healy*).

Appropriate care was taken in preventing plume discharged from the ship's chimney when sailing. Since a large number of trace metals were also analyzed in the same aerosol filters, extreme caution was exercised in sample collection. At ice stations, bulk snow deposited on sea ice were collected into precleaned plastic bags and melted onboard to a volume of 20 L and filtered. For melt pond water samples, a hole was drilled in the frozen closed melt ponds using a TM-clean corer. A battery-powered peristaltic pump with silicone tube was used to fill a carboy with unfiltered water (Kadko and Landing, 2015; depth of the melt pond not known) and was filtered onboard. In each of the 6 ice stations, 2 ice cores next to each other, from surface to all the way down to the seawater, were collected with the Kovaks corer (9 cm ID), evenly divided into 5-6 segments approximately 20-40 cm each and same segments were combined, and melted in the onboard laboratory. The melt water from snow, ice core, and melt pond water were filtered using 0.4 μm Whatman Nuclepore track-etched membrane filter in a vacuum filtration system and the material retained in the filter were considered particulate matter. All filters were retained for particulate analysis, and filtered water samples were acidified to a pH of 2 with 6M HCl and the preconcentration was done following $Fe(OH)_3$ method (details in Methodology). The IRS was collected by shoveling sediment-laden ice (sediment found both at the surface and inside of the ice fragments), into pre-cleaned 20 L buckets, melted, sediments were allowed to settle, and the 'supernatant' meltwater was poured off to concentrate the sample. The sediment solution was then dried in an oven at 100°C and used for further analysis.

## Development of Chemical Leaching Method for Aerosol Filter and Ice-Rafted Sediment for $^{210}$Po and $^{210}$Pb

The general procedure for measuring $^{210}$Po and $^{210}$Pb in aerosol and involves complete digestion using concentrated hydrochloric acid, nitric acid, and hydrofluoric acid, followed by drying, and then taken in dilute HCl solution for electroplating. Since the *in situ* $^{210}$Po/$^{210}$Pb AR in aerosol is generally less than 0.1 (Baskaran, 2011), it is a prerequisite that *in situ* $^{210}$Po is separated from *in situ* $^{210}$Pb soon after the sample collection (note: in 30 days from sample collection to Po plating, 14% in-growth $^{210}$Po would take place). In order to avoid usage of concentrated hydrofluoric acid on the ship, prior to the cruise we tested a series of different leaching procedures in one aerosol filter (aerosol sample collected at Wayne State University campus, Detroit, MI, United States) by both leaching and total digestion, and compared the amount of $^{210}$Po extracted by each method performed on separate aliquots of the same filter. The aerosol sample was filtered through one 8″ × 10″ QFF filter at a flow rate of 1.4 $m^3$/min for approximately 24 h, similar to the arctic aerosol samples collection (**Table 1**). The filter was cut into 4 quarters and were weighed. Visual observation of the filter and the weights indicated uniform aerosol mass distribution. The

**TABLE 1 |** Aerosol collection time, location, volume, activities and depositional fluxes of $^{210}$Po and $^{210}$Pb and $^{210}$Po/$^{210}$Pb AR.

| #: Event, Deployment | Start-end Date | Latitude (N) | Longitude (W) | Volume | $^{210}$Po | $^{210}$Pb | $^{210}$Po/$^{210}$Pb | $^{210}$Po flux | $^{210}$Pb flux |
|---|---|---|---|---|---|---|---|---|---|
| | [dd/mm/yyyy] | Start-End | Start-End | m$^3$ | dpm/100 m$^3$ | dpm/100 m$^3$ | AR | dpm cm$^{-2}$ y$^{-1}$ | dpm cm$^{-2}$ y$^{-1}$ |
| 6060-1 | 10-17/8/2015 | 56.074-69.926 | 170.509 to 167.688 | 463 | 0.0042 ± 0.0003 | 0.056 ± 0.003 | 0.074 ± 0.007 | 0.0013 ± 0.0001 | 0.018 ± 0.001 |
| 6123-2 | 20-23/8/2015 | 75.566-79.997 | 170.75-174.953 | 174 | 0.023 ± 0.001 | 0.42 ± 0.01 | 0.054 ± 0.004 | 0.0071 ± 0.0004 | 0.133 ± 0.004 |
| 6149-3 | 23-27/8/2015 | 80.001-83.572 | 174.96 to −174.731 | 275 | 0.033 ± 0.002 | 0.63 ± 0.03 | 0.052 ± 0.004 | 0.0103 ± 0.0006 | 0.20 ± 0.01 |
| 6168-4 | 27-30/8/2015 | 83.757-86.244 | −175.043 to −170.654 | 118 | 0.049 ± 0.004 | 0.64 ± 0.02 | 0.077 ± 0.007 | 0.0156 ± 0.0012 | 0.20 ± 0.01 |
| 6236-6 | 4-8/9/2015 | 88.408-89.945 | −176.752 to 97.848 | 272 | 0.029 ± 0.002 | 0.63 ± 0.02 | 0.046 ± 0.004 | 0.0090 ± 0.0006 | 0.20 ± 0.01 |
| 6267-7 | 8-12/9/2015 | 89.941-87.352 | 104.19 to 149.43 | 116 | 0.012 ± 0.001 | 0.63 ± 0.02 | 0.019 ± 0.002 | 0.0037 ± 0.0003 | 0.20 ± 0.01 |
| 6304-8 | 12-16/9/2015 | 87.2785.145 | 149.044 to 149.855 | 72 | 0.0010 ± 0.0001 | 0.34 ± 0.02 | 0.0030 ± 0.0003 | 0.0003 ± 0.0000 | 0.11 ± 0.01 |
| 6347-9 | 17-20/09/2015 | 85.163-82.259 | 150.395 to 149.377 | 108 | 0.00039 ± 0.0003 | 0.43 ± 0.02 | 0.0090 ± 0.0009 | 0.0012 ± 0.0001 | 0.14 ± 0.01 |
| 6387-10 | 21-26/09/2015 | 82.101-78.974 | 150.811 to 148.501 | 320 | 0.0085 ± 0.0006 | 0.60 ± 0.02 | 0.014 ± 0.001 | 0.0027 ± 0.0002 | O.lfttO.01 |
| 6424-11 | 26-29/09/2015 | 78.804-75.047 | 148.093 to 150.176 | 116 | 0.035 ± 0.003 | 2.15 ± 0.18 | 0.016 ± 0.001 | 0.0110 ± 0.0008 | 0.68 ± 0.03 |
| 6444-12 | 29/09-3/10/2015 | 75.06-73.426 | 150.215 to 156.793 | 211 | 0.028 ± 0.002 | 0.75 ± 0.03 | 0.037 ± 0.003 | 0.0088 ± 0.0006 | 0.24 ± 0.01 |
| 6487-13 | 3-7/10/2015 | 73.397-71.998 | 156.766 to 162.562 | 151 | 0.031 ± 0.002 | 0.95 ± 0.04 | 0.033 ± 0.003 | 0.0098 ± 0.0007 | 0.30 ± 0.01 |
| 6495-14 | 7-9/10/2015 | 72.004-65.95 | 162.56 to 168.449 | 90 | 0.055 ± 0.004 | 0.76 ± 0.05 | 0.073 ± 0.007 | 0.0175 ± 0.0011 | 0.24 ± 0.02 |
| | | | | | | Average: | 0.039 ± 0.026 | 0.0076 ± 0.005 | 0.22 ± 0.15 |

aerosol collection occurred from May 23 to May 24, 2015 and $^{210}$Po plating was performed on the same day of retrieval. To each aliquot, varying concentrations of hydrochloric and nitric acid were used (**Table 2**). For leaching, an aliquot of the filter along with the acids (**Table 2**) was taken in a centrifuge tube and placed in an ultrasonic bath at 70°C. The filtrate was then separated from filter by vacuum filtration and the process was repeated once more. The solutions were combined and processed further for $^{210}$Po plating (Krupp, 2017). The typical time involved are: leaching (2 h total), digestion (12 h), and drying (∼6-8 h). Additional details are given in Krupp (2017).

The calculated $^{210}$Po activities are given in **Table 2**. We report that leaching of the filter with 6M hydrochloric acid + 8M nitric acid, followed by drying (necessary to prevent dissolution of planchet in nitric acid medium) and dilution, provided results consistent with total digestion with HF ($^{210}$Po = 0.329 ± 0.013 dpm 100 m$^{-3}$ vs. 0.315 ± 0.013 dpm 100 m$^{-3}$ for leaching and HF digestion, respectively). The results show that 6M hydrochloric acid leaching alone is not sufficient ($^{210}$Po = 0.250 ± 0.009 dpm 100 m$^{-3}$), suggesting that nitric acid is necessary as an oxidizing agent to quantitatively extract $^{210}$Po from the aerosol filter due to possible presence of $^{210}$Po-laden organic aerosol particles. These results also suggest that the complete destruction of the quartz fiber by hydrofluoric acid is not necessary to extract $^{210}$Po from the filter media, implying that sorbed $^{210}$Po onto lithogenic particles can be quantitatively removed by a mixture of 6M HCl + 8M $HNO_3$ alone. This leaching method was used in place of total digestion on the cruise in order to eliminate the need for hydrofluoric acid and concentrated nitric and hydrochloric acid, as well as reduce the time usually needed to digest the aerosol filters, which is important when considering the time-sensitivity of the $^{210}$Po isotope and the volume of work involved onboard the ship.

In most of the enriched $^{210}$Po and $^{210}$Pb are sorbed onto sediment surface, we tested a set of leaching methods. Approximately 12 L of dirty lake ice using a 20 L plastic bucket was collected on March 14-15, 2015 near the mouth of the Clinton River which discharges into Lake St. Clair in southeast Michigan. After melting (melt volume = 8.7 L), settling (after 48 h), decanting, and drying the concentrated solution in an oven (48-72 h), the total amount of dried silty-clay sediment collected was 3.617 g. To ensure fine clays were collected, the decanted ice solution was subsequently allowed to settle (48 h) and then dried in the same manner, providing a total amount of clay sediment of 0.242 g. This was combined with the other aliquot of 3.617 g. The collected sediments overall were fine-textured and grayish-brown, and included a small amount of macro-organic material (grass and hairs) which was removed before leaching. About 0.2 g of the homogenized sediment sample was leached for 1 h at ∼90°C with 10 mL of 6M HCl twice and the leachate were combined. The combined solution was dried and taken in 5 mL 1 M HCl and gamma counted. To minimize time, acid consumption and waste generation onboard, results from a leaching experiment showed that 6M HCl leaching of

**TABLE 2 |** Activities for aerosol filter aliquots processed by total digestion or two leaching methods.

| Method | $^{210}$Po (dpm/100 m$^3$ air) |
|---|---|
| Digestion (10 mL of HCl, $HNO_3$, HF, dry and dilute) | 0.315 ± 0.013 |
| Leaching (10 mL of 6M HCl, 10 mL of 8M $HNO_3$, dry and dilute) | 0.329 ± 0.013 |
| Leaching (20 mL of 6M HCl dilute only) | 0.250 ± 0.009 |

ice-rafted sediment collected from Lake St. Clair quantitatively extracts $^{210}$Po and $^{210}$Pb from IRS (Krupp, 2017).

## Analytical Procedure for $^{210}$Po and $^{210}$Pb

Polonium-210 and $^{210}$Pb activities of snow, ice, melt pond, seawater and aerosol were measured on the same sample. IRS samples were divided into two fractions, one for gamma spectrometry to measure $^{210}$Pb and the other for $^{210}$Po by alpha spectrometer. Precise determination of *in situ* $^{210}$Po requires that the sample be analyzed soon after the collection to minimize in-growth of $^{210}$Po. The dissolved phase (filtrate of melt water of snow, ice core and melt pond) was acidified with 5 ml/L of 6M HCl (Trace-Metal grade) to prevent the loss of $^{210}$Po and $^{210}$Pb by sorption on to the container wall. Each acidified sample was spiked with: (i) a known amount of $^{209}$Po US-NIST Standard Reference Material as an internal yield tracer; (ii) 20 mg stable lead via a stable lead carrier of $PbCl_2$ in order to determine chemical efficiency of $^{210}$Pb recovery; and (iii) iron carrier ($FeCl_3$; 5 mg Fe/L of water) to co-precipitate $^{210}$Po and $^{210}$Pb with $Fe(OH)_3$ precipitate. After 12-24 h equilibration period and periodic vigorous shaking of the sample, ammonium hydroxide was added to samples to increase the pH from 2 to 4, and then, 1 mL of 10% sodium chromate was added to samples to increase the lead yield by the co-precipitation of lead chromate. Then, the pH was increased to ∼8. This rise in pH causes the iron to flocculate to co-precipitate $^{210}$Po and $^{210}$Pb with $Fe(OH)_3$. Details on separation of precipitate and solution, chemical processing and plating of Po are given in Niedermiller and Baskaran (2019). After Po plating, each solution was transferred to a precleaned 60 ml Nalgene bottle and stored for further onshore $^{210}$Pb analysis. After polonium plating, any residual $^{210}$Po (and $^{209}$Po) must be removed from sample solution for the future measurement of *in situ* $^{210}$Pb, which is measured by in-growth of $^{210}$Po from the decay of $^{210}$Pb. Details on the quantitative removal of $^{210}$Po using a column separation technique, chemical efficiency determination for $^{210}$Pb are given in Niedermiller and Baskaran (2019). Details on decay and in-growth corrections for $^{210}$Po and $^{210}$Pb are given in Baskaran et al. (2013), Rigaud et al. (2013), Cookbook (2014).

All particulate samples (from snow, ice, melt pond samples) processing was performed using leaching methods. The particulate sample was taken in a 50-ml centrifuge tube and was leached with 10 mL 6M Omni-trace HCl and 10 mL 8M $HNO_3$ mixture with agitation for 1 h at 70°C in an ultrasonic bath. Subsequently, the solution was filtered, spiked, with a known amount of $^{209}$Po and stable Pb, and dried. To the residue, 2 mL of HCl was added and warmed it to bring the residue to solution and then diluted to 40 ml with deionized water. This solution was used for electroplating.

The $^{210}$Po-plated discs were assayed in an Octete PC-8 input alpha spectrometer. The background subtraction in most of the samples was less than 0.1% of the net counts for both $^{210}$Po and $^{210}$Pb. The activities of $^{210}$Pb in IRS samples were measured directly in a high-resolution, high-purity Ge well detector coupled to DSA multi-channel analyzer. The gamma-ray spectrometer was calibrated with RGU-1, RGU-Th, both IAEA Certified Reference Materials, periodically. Details on the chemical procedures, counting methods and reagent blanks subtracted, QA/QC and intercalibration results are given below.

## Blanks and QA/QC

We ran a total of 17 blanks (6 blank aerosol filters with reagent blanks, 2 reagent blanks for IRS, and 9 reagent blanks for snow, ice core, and melt ponds) for both $^{210}$Po and $^{210}$Pb. Due to very low activities of $^{210}$Po in aerosols (generally ∼5% as that of $^{210}$Pb), the blank levels are relatively high, as expected. The average blank activity accounted for 43-83% (mean: 60%, $n$ = 6) for $^{210}$Po and 10.4-60.9% (mean: 28.2%, $n$ = 6) for $^{210}$Pb. For snow samples, the reagent blank for particulate $^{210}$Po ($^{210}Po_p$) and $^{210}Pb_p$ accounted for 0.2-12.5% (mean: 5.5%), and 0.5-14.0% (mean: 4.3%, $n$ = 6), respectively. The corresponding values for dissolved $^{210}$Po ($^{210}Po_d$) and $^{210}Pb_d$ accounted for 0.3-5.3% (mean: 2.0%, $n$ = 6) and 0.2-0.8% (mean: 0.4%, $n$ = 6), respectively. The $^{210}$Po blank in ice-rafted sediment varied from 0.3 to 3.2% (mean: 1.1%, $n$ = 6). For melt pond samples, the reagent blank values for particulate $^{210}Po_p$ and $^{210}Pb_p$ are higher due to lower activities, accounting for 16.8-48.7% (mean: 24.8%, $n$ = 5), and 8.8-66.0% (mean: 28.3%, $n$ = 5), respectively. The corresponding values for $^{210}Po_d$ and $^{210}Pb_d$ accounted for 0.6-3.9% (mean: 2.0%, $n$ = 5) and 0.9-9.4% (mean: 3.5%, $n$ = 6), respectively. The melt volume of segment of ice core sample was small with lower $^{210}$Po and $^{210}$Pb activities compared to snow and hence the reagent blanks are higher, accounting for 2.8-89.7% (mean: 48.9%, $n$ = 31) for $^{210}Po_p$, and 3.5-96.3% (mean: 49.3%, $n$ = 31) for $^{210}Pb_p$ and 2.0-68.9% (mean: 33.3%, $n$ = 31) for $^{210}Po_d$, and 4.9-82.9% (mean: 28.2%, $n$ = 31)$^{210}Pb_d$.

We analyzed Certified Reference Material (CRM) RGU-1 ($^{238}$U concentration 400 ± 2 ppm, with all the progeny of $^{238}$U in secular equilibrium, including $^{210}$Pb and $^{210}$Po; IAEA CRM) eight different times as blind samples following the same procedure as the samples determined by alpha spectrometry to assess the accuracy. About 30 mg (weighed to a precision of ±0.1 mg) of the standard (∼9 dpm) was taken each time and about 5.5 dpm of $^{209}$Po spike was added. The same chemical procedure was followed as was outlined in Baskaran et al. (2013). Agreement between the measured and certified value is excellent. The ratio of measured activity to certified value of RGU-1 varied between 0.96 ± 0.01 and 1.02 ± 0.00, with a mean value of 1.00 ± 0.01.

The intercalibration exercise between Wayne State University and Louisiana State University (LSU) showed that the $^{210}$Po and $^{210}$Pb activities on four water samples (two from GEOTRACES station in the Arctic and two collected from Gulf of Mexico

collected by Dr. Kanchan Maiti, LSU) agreed within 1 standard deviation from each other and hence our $^{210}$Po and $^{210}$Pb data are of high quality. The results from the intercalibration was submitted to BCO-DMO data center along with all of our $^{210}$Po and $^{210}$Pb data obtained during 2015 GEOTRACES cruise.

# RESULTS AND DISCUSSION

## Residence Time and Depositional Velocity of Aerosol Using $^{210}$Po and $^{210}$Pb and Their Fluxes

The mean specific activity of $^{210}$Po and $^{210}$Pb in aerosols, 0.023 ± 0.018 (range: 0.0004-0.055, $n$ = 13) dpm 100 m$^{-3}$ (1 dpm = 1 disintegration per minute = 1 atom decaying per minute; 60 dpm = 1 Bq) and 0.69 ± 0.18 (range: 0.06-2.15, $n$ = 13) dpm 100 m$^{-3}$, respectively (**Table 1**), are significantly lower than those reported in sub-Arctic latitudes (e.g., $^{210}$Po: 0.43 (range: 0.11-0.71, $n$ = 30) dpm 100 m$^{-3}$; $^{210}$Pb: 6.9 range: 1.8-25.3, $n$ = 30) dpm 100 m$^{-3}$ in Detroit, MI, United States (42°25′N, McNeary and Baskaran, 2003). Land-derived air masses have significantly higher $^{210}$Pb activity compared to maritime air masses due to differences in the $^{222}$Rn emanation rates between ocean surface, 0.102 dpm cm$^{-2}$ day$^{-1}$, and land surface, 7.8-10.8 dpm cm$^{-2}$ day$^{-1}$ (Baskaran, 2011). Long-term global $^{222}$Rn fluxes were found to decrease with increasing latitude, from 0.57 ± 0.38 atom cm$^{-2}$ s$^{-1}$ ($n$ = 46) at 30-40°N latitudinal belt to ≤0.12 ± 0.11 atom cm$^{-2}$ s$^{-1}$ ($n$ = 19) at north of 60-70°N belt (Baskaran, 2011). An order of magnitude variations in $^{210}$Pb activities is mainly attributed to variations in sources of air masses. Since samples were collected during transit covering large distances (**Figure 1** and **Table 1**), it is not possible to quantitatively assess the influence of land-derived vs. maritime air masses.

The calculated depositional flux of $^{210}$Po or $^{210}$Pb ($F_{Po\ or\ Pb}$), using eq. (1), from the measured activity of $^{210}$Po ($C_{Po}$) or $^{210}$Pb ($C_{Pb}$) (**Table 1**), assuming aerosol deposition velocity ($V_d$) of 1 cm s$^{-1}$ (average of 8 global sites, McNeary and Baskaran, 2003), varied from 0.0003 to 0.018 dpm cm$^{-2}$ year$^{-1}$ (mean: 0.0076 ± 0.0055, $n$ = 13 for $^{210}$Po; note: here and elsewhere the error is 1σ on data) and 0.018 to 0.68 dpm cm$^{-2}$ year$^{-1}$ (mean: 0.22 ± 0.05, $n$ = 13 for $^{210}$Pb; **Table 1**).

$$F_{Po\ or\ Pb}(\text{dpm cm}^{-2}\text{year}^{-1}) = C_{Po}(\text{or } C_{Pb}, \text{dpm cm}^{-3}\text{air}) \times V_d(\text{cm y}^{-1}) \quad (1)$$

The calculated depositional fluxes critically depend on the assumed $V_d$ value of 1 cm s$^{-1}$. An independent validation for $V_d$ in the Arctic can be obtained from the published $F_{Pb}$ values. From the summarized sedimentary inventory of $F_{Pb}$ in lakes, coastal regions and glaciers/ice cores, the calculated $V_d$ ranged from 0.3 to 1.6 cm s$^{-1}$ (mean: 0.9 ± 0.4 cm s$^{-1}$ ($n$ = 13)), indicating $V_d$ for Arctic is similar to subarctic (Turekian et al., 1977; McNeary and Baskaran, 2003).

The residence time of aerosols ($\tau_{Po-Pb}$) has been calculated from the measured $^{210}$Po-$^{210}$Pb disequilibrium using the equation (Moore et al., 1973).

$$\tau_{Po-Pb} = [-b + (b^2 - 4ac)^{1/2}]/2a \quad (2)$$

where a = $A_{Pb}$ – $A_{Po}$; b = -$A_{Po}$ ($\tau_{Bi}$ + $\tau_{Po}$) and c = -$A_{Po}$ ($\tau_{Bi}$ $\tau_{Po}$); $A_{Pb}$ and $A_{Po}$ are activities of $^{210}$Po and $^{210}$Pb respectively; $\tau_{Bi}$: $^{210}$Bi mean-life, 7.2 days; $\tau_{Po}$: $^{210}$Po mean-life, 199.7 days. The $^{210}$Po/$^{210}$Pb AR in aerosols varied between 0.003 and 0.077 (mean: 0.039 ± 0.026, $n$ = 13) corresponding to a mean residence time of 12 ± 7 days which is comparable to the mean residence time of water vapor as well as the residence times reported in regions where anthropogenic inputs of $^{210}$Po and $^{210}$Pb were reported to be negligible (Moore et al., 1973; Baskaran and Shaw, 2001; Baskaran, 2011). If there are additional contributions of $^{210}$Po from sources such as volcanic eruption, transport from urban setting, and other anthropogenic sources, the estimated residence time will be an upper estimate (Kim et al., 2000, 2005; Su and Huh, 2002; summarized in Baskaran, 2011).

## Age of Snow Using $^{210}$Po/$^{210}$Pb AR

During the sampling expedition, in each ice station, a composite sample was collected and the snow depth was not measured.

**TABLE 3 |** Activity of particulate (p), dissolved (d) and total (T) $^{210}$Po and $^{210}$Pb (in dpm 100L$^{-1}$), $^{210}$Po/$^{210}$Pb activity ratio, and age of snow.

| Station & Event # | ST-31; 6206 | ST-33; 6230 | ST-39; 6263 | ST42; 6291 | ST-43; 6316 | ST-46; 6338 |
|---|---|---|---|---|---|---|
| Location | 88.42°N;183.33°W | 89.96°N; 3.529°E | 87.78°N 149.61°W | 85.74°N 150.54°W | 85.16°N 150.00 W | 82.49°N 149.93°W |
| $^{210}Po_p$ | 220 ± 7 | 15.2 ± 0.5 | 2.85 ± 0.13 | 8.89 ± 0.35 | 13.1 ± 0.5 | 2.42 ± 0.11 |
| $^{210}Po_d$ | 103 ± 3 | 112 ± 3 | 3.31 ± 0.12 | 21.9 ± 0.8 | 23.4 ± 0.9 | 7.40 ± 0.35 |
| $^{210}Po_T$ | 323 ± 7 | 127 ± 3 | 6.16 ± 0.17 | 30.8 ± 0.9 | 36.6 ± 1.0 | 9.82 ± 0.36 |
| $^{210}Pb_p$ | 265 ± 9 | 78.4 ± 3.0 | 33.9 ± 1.3 | 38.6 ± 1.5 | 27.1 ± 1.0 | 5.64 ± 0.23 |
| $^{210}Pb_d$ | 1394 ± 51 | 872 ± 32 | 158 ± 5 | 238 ± 8 | 553 ± 19 | 469 ± 18 |
| $^{210}Pb_T$ | 1659 ± 52 | 951 ± 32 | 192 ± 5 | 276 ± 8 | 580 ± 19 | 475 ± 17 |
| $(^{210}Po/^{210}Pb)_T$ | 0.20 ± 0.01 | 0.13 ± 0.01 | 0.032 ± 0.001 | 0.11 ± 0.01 | 0.063 ± 0.003 | 0.021 ± 0.001 |
| $(^{210}Po/^{210}Pb)_p$ | 0.83 ± 0.04 | 0.19 ± 0.01 | 0.084 ± 0.005 | 0.23 ± 0.01 | 0.48 ± 0.03 | 0.43 ± 0.03 |
| *Age (d) | 34 ± 2 | 20 ± 1 | 4.0 ± 0.3 | 15 ± 1 | 4.9 ± 0.6 | 1.7 ± 0.2 |

**Age was calculated using eq. (3) with $(^{210}Po/^{210}Pb)_i$ = 0.039 ± 0.026 (for ST-31, 33, 42, and 43) average of 13 aerosol samples (**Table 1**) and for ST-39 and 46 where $(^{210}Po/^{210}Pb)$ is <0.039, the $(^{210}Po/^{210}Pb)_i$ value of 0.0122 ± 0.0005 (average of the lowest 5 values in **Table 1**) was used.*

However, the average snow depth has been reported to vary from 30-40 cm, with up to 150 cm after a snowstorm (Sturm et al., 2002). The total $^{210}$Po ($^{210}Po_T$ = particulate, ≥0.4 μm, $^{210}Po_p$ + dissolved, <0.4 μm, $^{210}Po_d$) and $^{210}Pb_T$ activities varied from 6 to 323 (mean: 89 ± 123, $n$ = 6) and 192 to 1659 (mean: 689 ± 545, $n$ = 6) dpm 100L$^{-1}$ water equivalent, respectively (**Table 3**), about 1-2 orders of magnitude higher than those in Arctic surface ocean waters (Moore and Smith, 1986; Smith et al., 2003; Chen et al., 2012; Roca-Marti et al., 2016; Bam et al., 2020; **Figures 2A,B**). The particulate $^{210}$Po fraction, 12.0 to 68.1% (mean: 36 ± 19%), is significantly higher than that of $^{210}Pb_p$, 1.2 to 17.7% (mean: 10.3 ± 6.6%, **Table 3**). The observed higher fraction of $^{210}Po_p$ in snow (and melt pond and ice cores) is intriguing as it may be due to production of higher amounts of gelatinous exopolymeric substances (EPS) by microorganisms underneath the snow which serve as agents for increased primary productivity (Krembs et al., 2011). Laboratory experiments have shown that Po strongly adsorbed on to biogenic organic matter such as chitin compared to lithogenic elements such as Pb and, with fractionation factor (=$K_d^{Po}/K_d^{Pb}$ ratio; $K_d$, partition coefficient = (particulate activity/dissolved activity)* (1/particulate concentration, μg/L)) of ∼4 compared to 0.2 to 1.0 for commonly occurring clay minerals (Fowler, 2011; Yang et al., 2013; Wang et al., 2019). Since no measurements of POC, macronutrients or pigments were made on collected snow or ice or melt pond samples, we cannot corroborate this hypothesis. Note that the higher fraction of $^{210}Po_p$ has no bearing on the age determination, as age calculation involves only total $^{210}$Po ($^{210}Po_T$) and total $^{210}$Pb ($^{210}Pb_T$) (see below). The $(^{210}Po/^{210}Pb)_p$ ARs varied from 0.08 to 0.83 (mean: 0.38 ± 0.27) which are significantly higher than that in the dissolved phase (range: 0.016 to 0.128, mean: 0.062 ± 0.044; calculated from data in **Figures 3A,B** and **Table 3**).

The age of snow (and ice core, melt pond or IRS) can be obtained from eq. (3). Age of snow refers to time elapsed between the snow fall to the ground and sample collection; age of ice core is the time elapsed between the formation of ice core and sample collection; age of melt pond is the time elapsed between the formation of melt pond and the sample collection; and age of ice-rafted sediment (IRS) is the time elapsed between the incorporation of excess $^{210}$Pb in to the sediment and the time of collection IRS. The age can be obtained from eq. (3):

$$t = (-1/\lambda)[\ln(1-(^{210}Po/^{210}Pb)_T - (^{210}Po/^{210}Pb)_i)] \quad (3)$$

The $(^{210}Po/^{210}Pb)_i$ is initial AR at the time of deposition, taken to be 0.039 ± 0.026, average ($^{210}$Po/$^{210}$Pb) AR of aerosols ($n$ = 13, **Table 1**); λ is $^{210}$Po decay constant (λ = 5.01 × 10$^{-3}$ day$^{-1}$). Instead of taking average of 13 samples, taking a subset (station 4, 6-10), the initial ratio becomes 0.031 ± 0.029 and it made very little difference on the age of snow. Since there is large spatial and temporal variability on the activities of $^{210}$Po and $^{210}$Pb in aerosols, we chose to use the average of all 13 samples.

The age of snow obtained from eq. (3) varied between 1.7 to 34 days (mean: 13 ± 11 days, **Figure 4** and **Tables 1**, **3**).

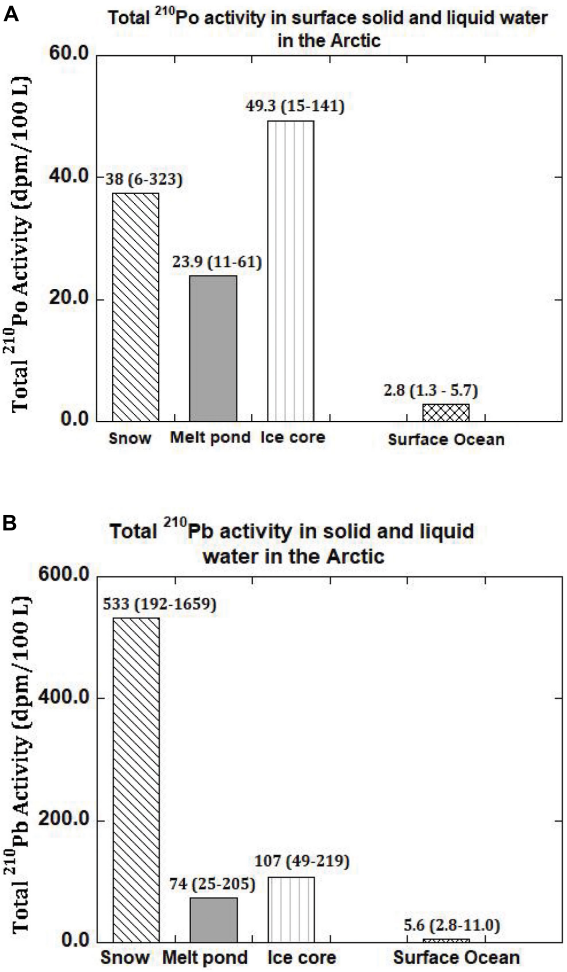


**FIGURE 2 | (A)** Activity of total (= particulate + dissolved) $^{210}$Po and $^{210}$Pb in snow, melt pond, ice core and surface ocean in the Arctic. The mean values are given and numbers in parenthesis denote the range (US GEOTRACES Arctic cruise, HLY 1502, R/V Icebreaker USCGC Healy). **(B)** Activity of total (= particulate + dissolved) $^{210}$Pb and $^{210}$Pb in snow, melt pond, ice core and surface ocean in the Arctic. The mean values are given and numbers in parenthesis denote the range (US GEOTRACES Arctic cruise, HLY 1502, R/V Icebreaker USCGC Healy).

If the analyzed snow is from multiple snow events at different times, then this is a composite age. The snowfall in the Arctic is highly patchy and no weather records are available for individual ice stations. The low-end age likely represents recent snow deposition. It is commonly assumed that once $^{210}$Pb and $^{210}$Po are delivered from the Arctic atmosphere to the air-sea interface through snowfall, they remain as a closed system and the changes in their activities are caused only by their radioactive decay as well as in-growth of $^{210}$Po from the decay of $^{210}$Pb until sample collection. This study shows generally that the age of snow is less than a month, and thus, snow deposited more than a month ago likely has undergone changes to become ice with associated exchange of heat energy with the surroundings. The implication of this study is that the changes in the ages

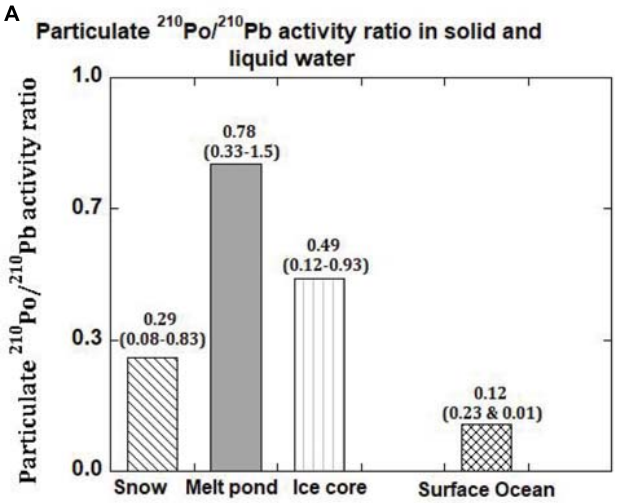


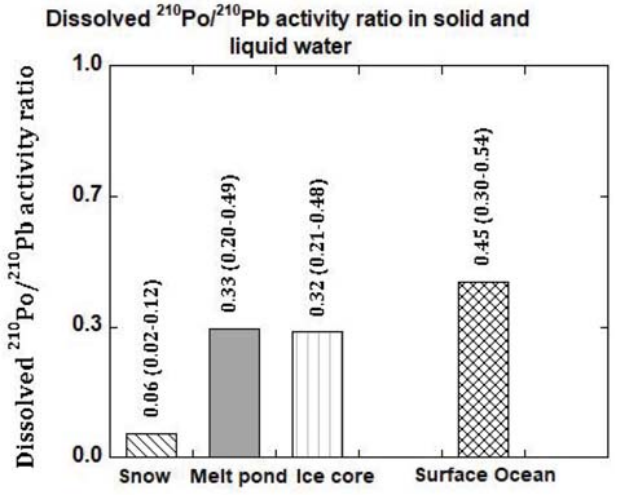


**FIGURE 3 | (A)** $^{210}$Po/$^{210}$Pb activity ratio in the particulate matter in snow, melt pond, ice core and surface ocean in the Arctic. The mean values are given and numbers in parenthesis denote the range (US GEOTRACES Arctic cruise, HLY 1502, R/V Icebreaker USCGC Healy). **(B)** $^{210}$Po/$^{210}$Pb activity ratio in the dissolved phase in snow, melt pond, ice core and surface ocean in the Arctic. The mean values are given and numbers in parenthesis denote the range (US GEOTRACES Arctic cruise, HLY 1502, R/V Icebreaker USCGC Healy).

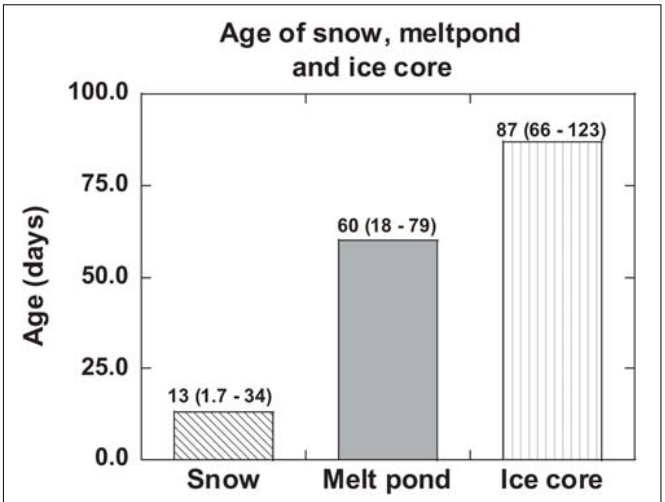


**FIGURE 4 |** $^{210}$Po:$^{210}$Pb-disequilibrium-based age/residence time of snow, melt pond ice core and compared to the residence time of surface ocean water. The mean values are given and numbers in parenthesis denote the range (US GEOTRACES Arctic cruise, HLY 1502, R/V Icebreaker USCGC Healy).

of snow and ice due to global climate change (e.g., earlier melt and later freeze of ice) will affect the latent heat exchanged with the surroundings.

## Age of Ice-Rafted Sediment Using $^{210}Po_{xs}/^{210}Pb_{xs}$ Activity Ratio

Sea ice in the Arctic plays an important role in the biogeochemical cycling of key trace metals, transport and subsequent dispersal of coastal sediments and nutrients to the deep Arctic as well as impacting radiation balance. Three proposed mechanisms for sediment entrainment into sea ice include: (i) incorporation of fine suspended sedimentary particles into frazil-ice crystals in shallow coastal areas; (ii) uplift of sediments by anchor ice; and (iii) discharge of river-borne ice-laden sediments into the sea (Reimnitz et al., 1987; Hebbeln and Weber, 1991; Nürnberg et al., 1994; Eicken et al., 1997). The concentration and composition of IRS, incorporated in coastal sea ice which are subsequently transported to the deep Arctic by the Beaufort Gyre and Transpolar Drift, has direct bearing on the albedo, long-range redistribution of contaminants, and particle flux to the deep sea (Hebbeln and Weber, 1991; Nürnberg et al., 1994; Pfirman et al., 1995; Eicken et al., 1997; Landa et al., 1997; Meese et al., 1997; Cooper et al., 1998; Charette et al., 2020).

The excess $^{210}Pb_{xs}$ activities ($^{210}Pb_{xs}$ = $^{210}Pb_{total}$ – $^{226}Ra$; average measured $^{226}Ra$: 0.95 ± 0.18) in IRS, range between 19 and 186 dpm g$^{-1}$ (mean: 96 ± 76, **Table 4**), similar to earlier published data and is up to 2 orders of magnitude higher than the average total $^{210}Pb$ activity, 1.90 dpm g$^{-1}$ ($n$ = 134) of Russian Arctic surface sediments (Roberts et al., 1997; Baskaran, 2005). The $^{210}Po_{xs}$ ($^{210}Po_{xs}$ = $^{210}Po_{total}$ – $^{226}Ra$) ranged from 5 to 76 dpm g$^{-1}$ (mean: 40 ± 33, **Table 4**). This is the first $^{210}Po$ published data in IRS showing high $^{210}Po$ enrichment as well disequilibrium between $^{210}Po$ and $^{210}Pb$. Note that enrichment of $^{210}Po$ onto particulate matter will not affect the total $^{210}Po$/total $^{210}Pb$ activity ratio (total $^{210}Po$ = particulate $^{210}Po$ + dissolved $^{210}Po$) of the ages calculated based on $^{210}Po/^{210}Pb$ activity ratio. The $^{210}Po_{xs}/^{210}Pb_{xs}$ AR varied from 0.27 to 0.50 (mean: 0.38 ± 0.09, $n$ = 6) and the differences in the AR and enrichment of $^{210}Pb$ are attributed to the differences in their extent of initial interaction with seawater, and the time elapsed since the incorporation of $^{210}Pb$ into IRS.

Assuming the incorporation of atmospherically delivered $^{210}Pb$ into IRS is a one-time event (e.g., $^{210}Pb$-laden sediment

**TABLE 4 |** Activities+ of excess $^{210}$Po, $^{210}$Pb, $^{210}$Po/$^{210}$Pb AR and age of ice-rafted sediment.

| Station | Location | $^{210}$Po (dpm/g) | $^{210}$Pb (dpm/g) | ($^{210}$Po/$^{210}$Pb) AR | "Age" (day) |
|---|---|---|---|---|---|
| E6195 | 87°45.1′ N | 58.5 ± 1.9 | 118 ± 3 | 0.50 ± 0.02 | 122 ± 8 |
| | 179°43.4′W | 76.4 ± 2.5 | 180 ± 6 | 0.42 ± 0.02 | 97 ± 7 |
| | | 75.2 ± 2.8 | 186 ± 5 | 0.40 ± 0.02 | 88 ± 6 |
| E6244 | 88°58.4′ N | 10.5 ± 0.5 | 37.4 ± 1.8 | 0.28 ± 0.02 | 56 ± 4 |
| | 150°24.8′W | 15.0 ± 0.7 | 35.6 ± 1.2 | 0.42 ± 0.03 | 96 ± 9 |
| | | 5.18 ± 0.20 | 18.9 ± 0.7 | 0.27 ± 0.02 | 52 ± 5 |

*+$^{226}$Ra activity of 0.95 ± 0.18 dpm g$^{-1}$ was subtracted from total $^{210}$Po and $^{210}$Pb activities. Errors associated with activity in all Tables are propagated error arising from counting statistics, error associated with the spike and reagent blank.*

incorporation in to sea ice sediment taking place in one freeze over a short period of time), and the $^{210}$Po and $^{210}$Pb in IRS remains a closed system, the calculated age ranged from 52 to 122 days (mean = 85 ± 27 days, $n$ = 6, **Table 4**). Although there is no direct observation from the Arctic for this assumed one-time incorporation of radionuclides, a serendipitous observation from collection and analysis of sediment-laden ice from Lake St. Clair in southeast Michigan showed that the sediment extracted from ice during a snow storm during March 14-15, 2015 had an average $^{210}$Pb$_{xs}$ activity of 555 ± 138 ($n$ = 3) dpm g$^{-1}$ (Krupp, 2017). This is ∼6 times higher than that in the Arctic and about 100 times that of surficial sediments in Lake St. Clair (Robbins et al., 1990; Jweda and Baskaran, 2011). Note that the average atmospheric depositional flux of $^{210}$Pb in 60-80°N belt of 0.18 dpm cm$^{-2}$ year$^{-1}$ is only 13% as that of Detroit, MI (1.41 dpm cm$^{-2}$ year$^{-1}$), a mid-latitude site, and such larges differences are due to low emanation rate of $^{222}$Rn as well as low annual amount of precipitation in the Arctic (McNeary and Baskaran, 2003; Baskaran, 2011). The corresponding transport velocities (transport velocity = shortest distance between sampling site and the nearest coastal site, taking in to consideration the currents in the sampling area and back tracked the trajectory of the ice since its formation/age) varied between 0.12 ± 0.01 and 0.27 ± 0.02 m s$^{-1}$ (mean: 0.18 ± 0.06 m$^{-1}$, **Table 4**). These velocities can be compared to 0.082-0.086 m s$^{-1}$ obtained using buoys in Laptev Sea and 0.09 ± 0.04 m s$^{-1}$ (range: 0.04-0.18 m s$^{-1}$, $n$ = 23, monthly, April 1996 – February 1998) over Eastern Beaufort Sea using Acoustic Doppler Current Profiler (Melling and Riedel, 2003). Note that the calculated velocities are based on $^{210}$Po/$^{210}$Pb initial AR value of 0.039 (**Table 1**) and if AR is higher due to significant contribution of $^{210}$Po from resuspension of superfine sedimentary material with initial AR > 0.039, then, the age will be lower and the transport velocities will be higher.

## Dating of Melt Pond Using $^{210}$Po/$^{210}$Pb AR

During late spring and early summer, melt from snow (meteoric water) and surface ice (ice core salinity range: 0-5.2 ppt, surface to 169 cm, **Supplementary Figure 1**) mixing with a fraction of surface seawater result in the formation of melt ponds. The melt ponds are generally darker compared to ice leading to more absorption of incident radiation (lower albedo) compared to snow and ice. Furthermore, the vertical and horizontal fluxes of melt water from snow and ice play a key role in the evolution of albedo, heat transfer, and mass balance of the Arctic ice pack (Eicken, 1994; Eicken et al., 2002; Perovich et al., 2003). Surface area and depth of the melt ponds were not recorded during the field expedition; however, an average surface area of 30 m$^2$ and depth of 0.2 m have been reported (Eicken et al., 2002). The fractions of these three contributing sources to these melt ponds were estimated using a three end-member mixing model using salinity, $\delta^{18}$O and $^7$Be data (Marsay et al., 2018; **Table 5**).

The activities of $^{210}$Po$_p$ range from 0.4 to 4.0 (mean: 1.7 ± 0.2 dpm 100L$^{-1}$, $n$ = 5) while the corresponding $^{210}$Pb$_p$ range from 0.3 to 5.6 (mean: 2.6 ± 0.4 dpm 100L$^{-1}$, $n$ = 5) which are comparable to values in Arctic surface waters (Moore and Smith, 1986; Smith et al., 2003; Roca-Marti et al., 2016; Bam et al., 2020). However, the $^{210}$Po$_T$ range from 11 to 61 (mean: 28 ± 3, $n$ = 5) dpm 100L$^{-1}$ and $^{210}$Pb$_T$ range from 25 to 205 (mean: 94 ± 8, $n$ = 5) dpm 100L$^{-1}$, which are about 5 to 10 times higher than those found in surface seawater from the same or nearby stations (**Figures 2A,B** and **Table 5**). Such differences between particulate and total activities are attributed to differences in the sources of water to the melt ponds, with differences in the activities between the three source waters (**Figures 2A,B** and **Table 5**). The activities of $^{210}$Po$_T$ and $^{210}$Pb$_T$ at the time of melt pond formation were calculated using three end-member (snow, ice, and surface seawater) mixing model, as given in (eq. 4). The initial ($^{210}$Po$_T$/$^{210}$Pb$_T$) AR varied between 0.071 and 0.143 ($n$ = 4); however, in ST-39, the ratio is >1.0.

$$\text{Activity of } {}^{210}\text{Po}_\text{T} (\text{or } {}^{210}\text{Pb}_\text{T}) \text{ at the beginning of melt pond formation} = (F^*_{\text{snow}}\,{}^{210}\text{Po}_{\text{T-snow}}) + (F^*_{\text{sw}}\,{}^{210}\text{Po}_{\text{T-sw}}) + (F^*_{\text{ice}}\,{}^{210}Po_{T-\text{ice}}) \quad (4)$$

and likely the assumptions are not well constrained; taking the initial AR to be the same as that of the aerosols (**Table 1**), we get an age of 75 ± 9 days, although no other rationale can be given for using this ratio. Assuming the melt pond was formed in a relatively short timescale compared to the age of the pond, its age calculated using eq. (3) varied between 18 ± 3 and 79 ± 6 days (mean: 60 ± 14 days, $n$ = 4, **Table 5**). If this assumption is not strictly valid, then, the calculated age reported in **Table 5** is an overestimate. The ages (**Figure 4** and **Table 5**) indicate that ST-33 pond formed in late spring while ST-42, 43 in early summer and ST-46 in mid-summer.

If the particulate matter present in some of the melt ponds had undergone multiple melt-freeze cycles spanning over more than a year, then, we expect secular equilibrium between $^{210}$Po$_p$ and $^{210}$Pb$_p$ with $^{210}$Po$_p$/$^{210}$Pb$_p$ AR ∼ 1.0, under a closed system for $^{210}$Po and $^{210}$Pb. In two samples where ($^{210}$Po/$^{210}$Pb)$_p$ AR is >1.0, the particulate matter could have undergone multiple melt-freeze cycles although we have no

**TABLE 5 |** *Activities of $^{210}$Po and $^{210}$Pb (dpm/100 L), fractional amounts snow ($F_{snow}$), ice ($F_{ice}$), and seawater ($F_{sw}$), and age** of melt ponds.

| Station | 33 | 39 | 42 | 43 | 46 |
|---|---|---|---|---|---|
| $^{210}Po_p$ | 1.88 ± 0.09 | 0.90 ± 0.06 | 1.46 ± 0.09 | 0.40 ± 0.03 | 4.02 ± 0.16 |
| $^{210}Po_d$ | 9.35 ± 0.41 | 20.3 ± 0.8 | 18.5 ± 0.8 | 61.0 ± 3.1 | 22.6 ± 1.0 |
| $^{210}Po_T$ | 11.2 ± 0.4 | 21.2 ± 0.8 | 20.0 ± 0.9 | 61.4 ± 3.1 | 26.6 ± 1.0 |
| $^{210}Pb_p$ | 5.62 ± 0.24 | 0.92 ± 0.06 | 3.46 ± 0.18 | 0.28 ± 0.03 | 2.70 ± 0.11 |
| $^{210}Pb_d$ | 18.9 ± 0.7 | 60.1 ± 2.5 | 59.7 ± 2.1 | 204 ± 7 | 112 ± 5 |
| $^{210}Pb_T$ | 24.6 ± 0.8 | 61.0 ± 2.5 | 63.2 ± 2.1 | 205 ± 7 | 115 ± 5 |
| $(^{210}Po/^{210}Pb)_p$ AR | 0.33 ± 0.02 | 0.98 ± 0.09 | 0.43 ± 0.03 | 1.40 ± 0.02 | 1.50 ± 0.10 |
| Salinity | 1.4 | 10.6 | 5.92 | 25.76 | 4.49 |
| $F_{snow}$ | 0.94 | 0.21 | 0.24 | 0.21 | 0.2 |
| $F_{sw}$ | 0.04 | 0.25 | 0.09 | 0.79 | 0.03 |
| $F_{ice}$ | 0.02 | 0.54 | 0.67 | 0 | 0.77 |
| $^{210}Po_{T-snow}$ | 127 ± 3 | 61.6 ± 0.2 | 30.8 ± 0.9 | 36.6 ± 1.0 | 9.82 ± 0.36 |
| $^{210}Po_{T-sw}$ | 0.99 ± 0.08 | 0.99 ± 0.08 | 1.34 ± 0.12 | 1.34 ± 0.12 | 1.34 ± 0.12 |
| $^{210}Po_{T-ice}$ | 31.1 ± 1.0 | 141 ± 4 | 15.1 ± 0.7 | 112 ± 4 | 23.8 ± 0.9 |
| $^{210}Pb_{T-snow}$ | 951 ± 32 | 192 ± 5 | 276 ± 8 | 580 ± 19 | 475 ± 17 |
| $^{210}Pb_{T-sw}$ (dpm/100 L) | 3.28 ± 0.28 | 3.28 ± 0.28 | 2.82 ± 0.12 | 2.82 ± 0.12 | 2.82 ± 0.12 |
| $^{210}Pb_{T-ice}$ (dpm/100 L) | 86.9 ± 2.4 | 49 ± 1.7 | 131 ± 5 | 219 ± 6 | 61.5 ± 2.1 |
| Calculated $^{210}Po_T$ | 120 ± 3 | 78 ± 2 | 17.6 ± 0.5 | 8.7 ± 0.2 | 20.3 ± 0.7 |
| Calculated $^{210}Pb_T$ | 896 ± 30 | 68 ± 1 | 154 ± 4 | 124 ± 4 | 142 ± 3.8 |
| $(^{210}Po/^{210}Pb)_i$ AR (calculated)+ | 0.134 ± 0.005 | 1.15 ± 0.04 | 0.114 ± 0.004 | 0.071 ± 0.003 | 0.143 ± 0.006 |
| $(^{210}Po/^{210}Pb)_T$ AR (measured) | 0.46 ± 0.02 | 0.35 ± 0.02 | 0.32 ± 0.02 | 0.30 ± 0.02 | 0.23 ± 0.01 |
| AR-measured-initial | 0.326 ± 0.020 | 0.311 ± 0.033 | 0.206 ± 0.020 | 0.229 ± 0.020 | 0.087 ± 0.012 |
| Age** (days) | 79 ± 6 | 75 ± 9 | 46 ± 5 | 52 ± 5 | 18 ± 3 |

*p, particulate; d, dissolved; T, total (=particulate + dissolved), sw: seawater; for sw $^{210}Po_T$ and $^{210}Pb_T$, ST-33 surface water values were used for ST-39; for ice stations 42 and 46, ST-43 surface seawater values were used; data from Krupp (2017).

**Ages for ST-33, 42, 43 and 46 were calculated from calculated initial and measured. $(^{210}Po/^{210}Pb)_T$ AR. In the calculation for ST-39, $(^{210}Po/^{210}Pb)$ AR was assumed to the same as in aerosols (0.039 ± 0.026) and yields an age of 75 ± 9 days, which is a lower estimate (see in the text). Fractional values of $F_{snow}$, $F_{sw}$ and $F_{ice}$ are taken from Marsay et al. (2018). Calculated $^{210}Po$ (or $^{210}Pb$) is the activity at the time of formation of melt pond = $(F_{snow}{}^{*210}Po_{T-snow}) + (F_{sw}{}^{210}Po_{T-sw}) + (F_{ice}{}^{*210}Po_{T-ice})$. + calculated AR value for ST 33, 42, 43 and 46 is assumed to be the initial AR at the time of formation of melt pond using eq. (4). For ST-39, $^{210}Po/^{210}Pb$ AR is 1.15 ± 0.04 and is not well constrained by the 3-end-member mixing model.

other supporting evidence (**Figure 3A** and **Table 5**). Note that average particulate fraction of $^{210}$Po is only 8.8% (range: 0.7-16.7%), and even if some of the particulate matter is derived from multiple melt-freeze cycles that will not affect the $(^{210}Po/^{210}Pb)_T$ AR-based-ages. However, in 3 samples $(^{210}Po/^{210}Pb)_p$ AR is < 1.0 and $(^{210}Po/^{210}Pb)_T$ AR is <1.0 in all 5 samples (**Table 5**).

## Activity of $^{210}$Po and $^{210}$Pb, Their AR and Dating of Ice Core

The $^{210}Po_{p,d}$ and $^{210}Pb_{p,d}$ activities in the upper segment of 6 ice cores varied by more than an order of magnitude, from 4.4 to 75 dpm $100L^{-1}$ for $^{210}Po_p$ and 11 to 120 dpm 100 $L^{-1}$ for $^{210}Pb_p$ and 11 to 96 dpm $100L^{-1}$ for $^{210}Po_d$ and 0.8 to 174 dpm 100 $L^{-1}$ for $^{210}Pb_d$. The activities of particulate, dissolved and total phases varied over two orders of magnitude in all 31 split samples (**Table 6**), similar to an earlier study (Masqué et al., 2007). Although there is no excess $^{210}$Po (i.e., $^{210}Po/^{210}Pb$ AR < 1.0) in the inventory-based particulate or dissolved phases (**Table 7**), excess $^{210}Po_d$ (and $^{210}Po_T$) were observed in three discrete layers: ST-31 (100-130 cm), ST-33 (84-112 cm), and ST-39 (0-38 cm); the $(^{210}Po/^{210}Pb)_T$ AR in those layers ranged between 2.88 and 4.58 (**Table 6**), indicating preferential sorption of $^{210}$Po and/or preferential loss of $^{210}$Pb. This contrasts with observed $^{210}$Po-$^{210}$Pb equilibrium in 87%, (within ± 1σ) of the 38 segments from two ice cores from Fram Strait, although reported associated errors in majority of the samples were high in Masqué et al. (2007).

If the accumulation and ablation of ice takes place uniformly, with accretion from the top and ablation from the bottom, the $(^{210}Po/^{210}Pb)_T$ AR profile is expected to increase with increasing depth; however, when multiple processes such as meltwater deformation, seawater congelation, and false bottom formation takes place, the measured $(^{210}Po/^{210}Pb)_T$ AR will result in a more complicated profile. If a multi-year (≥2 year) ice is present, the $(^{210}Po/^{210}Pb)_T$ AR is expected to be ∼1.0 under the assumption that the $^{210}$Po-$^{210}$Pb has remained a closed system. We contend that ice that are >2 year old should have an $^{210}Po_p/^{210}Pb_p$ AR of ∼1.0, because any disequilibrium broken earlier in the decay chain will adjust to radioactive secular equilibrium in about two years, and thus paving the way to delineate >1 year old ice from more recent ones. The $^{210}Po/^{210}Pb$ AR of 0.95 ± 0.07 in only one sample (ST-30, 60-80 cm, **Table 6**) could be a part of multi-year ice segment; thus, we report the ice samples we collected are mostly first-year ice, with $^{210}Po/^{210}Pb$

**TABLE 6 |** Dissolved, particulate, total activities and activity ratios for ice station samples.

| ST & Event | Ice Core Depth (cm) | $^{210}Po_p$ dpm 100L$^{-1}$ | $^{210}Po_d$ dpm 100L$^{-1}$ | $^{210}Po_T$ dpm 100L$^{-1}$ | $^{210}Pb_p$ dpm 100L$^{-1}$ | $^{210}Pb_d$ dpm 100L$^{-1}$ | $^{210}Pb_T$ dpm 100L$^{-1}$ | $^{210}Po_T/^{210}Pb_T$ AR |
|---|---|---|---|---|---|---|---|---|
| ST-31 6205 | | | | | | | | |
| | 0-20 | 20.9 ± 1.0 | 60.0 ± 2.2 | 80.9 ± 2.4 | 28.0 ± 1.1 | 174 ± 6 | 202 ± 6 | 0.40 ± 0.02 |
| | 20-40 | 5.59 ± 0.39 | 10.9 ± 0.6 | 16.4 ± 0.7 | 13.7 ± 0.6 | 72.1 ± 2.9 | 85.8 ± 3.0 | 0.19 ± 0.01 |
| | 40-60 | 1.36 ± 0.11 | 2.55 ± 0.19 | 3.91 ± 0.22 | 3.23 ± 0.20 | 11.9 ± 0.6 | 15.2 ± 0.6 | 0.26 ± 0.02 |
| | 60-80 | 1.89 ± 0.16 | 5.21 ± 0.34 | 7.10 ± 0.37 | 1.24 ± 0.08 | 6.23 ± 0.41 | 7.47 ± 0.41 | 0.95 ± 0.07 |
| | 80-100 | 1.04 ± 0.10 | 1.72 ± 0.13 | 2.75 ± 0.16 | BDL | 3.52 ± 0.25 | 3.52 ± 0.25 | 0.78 ± 0.07 |
| | 100-130 | 0.94 ± 0.09 | 2.70 ± 0.20 | 3.63 ± 0.22 | 0.031 ± 0.002 | 1.09 ± 0.09 | 1.12 ± 0.09 | 3.25 ± 0.32 |
| ST-33; Event #: 6238 | | | | | | | | |
| | 0-28 | 17.4 ± 0.8 | 13.7 ± 0.6 | 31.1 ± 1.0 | 37.1 ± 1.4 | 49.8 ± 1.9 | 86.9 ± 2.4 | 0.36 ± 0.01 |
| | 28-56 | 3.23 ± 0.22 | 40.2 ± 1.8 | 43.5 ± 1.8 | 2.09 ± 0.14 | 45.3 ± 1.8 | 47.4 ± 1.8 | 0.92 ± 0.05 |
| | 56-84 | 2.33 ± 0.15 | 1.52 ± 0.11 | 3.85 ± 0. 0.19 | 2.15 ± 0.14 | 6.09 ± 0.38 | 8.24 ± 0.41 | 0.47 ± 0.03 |
| | 84-112 | 0.25 ± 0.02 | 1.23 ± 0.10 | 1.48 ± 0.10 | BDL | 0.32 ± 0.03 | 0.32 ± 0.03 | 4.58 ± 0.51 |
| | 112-140 | 0.84 ± 0.07 | 3.60 ± 0.21 | 4.44 ± 0.23 | 1.11 ± 0.08 | 16.7 ± 0.8 | 17.8 ± 0.8 | 0.25 ± 0.02 |
| ST-39; Event #: 6271 | | | | | | | | |
| | 0-38 | 44.8 ± 3.7 | 96.3 ± 3.3 | 141 ± 4 | 48.2 ± 1.7 | 0.78 ± 0.13 | 49.0 ± 1.7 | 2.88 ± 0.12 |
| | 38-76 | 3.67 ± 0.22 | 20.5 ± 0.9 | 24.2 ± 0.9 | 15.7 ± 0.7 | 59.7 ± 2.5 | 75.4 ± 2.6 | 0.32 ± 0.02 |
| | 76-114 | 2.67 ± 0.17 | 9.97 ± 0.47 | 12.6 ± 0.5 | 4.26 ± 0.21 | 72.7 ± 2.8 | 77.0 ± 2.8 | 0.16 ± 0.01 |
| | 114-152 | 2.70 ± 0.23 | 5.10 ± 0.33 | 7.81 ± 0.41 | 7.03 ± 0.43 | 25.1 ± 1.5 | 32.1 ± 1.5 | 0.24 ± 0.02 |
| | 152-190 | 3.99 ± 0.25 | 7.64 ± 0.47 | 11.6 ± 0.5 | 10.7 ± 0.75 | 20.2 ± 0.9 | 31.0 ± 1.2 | 0.38 ± 0.02 |
| ST-42; Event #: 6292 | | | | | | | | |
| | 0-20 | 4.46 ± 0.29 | 10.7 ± 0.6 | 15.1 ± 0.7 | 36.6 ± 1.9 | 94.2 ± 4.1 | 131 ± 5 | 0.12 ± 0.01 |
| | 20-40 | 7.37 ± 0.49 | 6.63 ± 0.44 | 14.0 ± 0.7 | 20.0 ± 1.0 | 30.9 ± 1.5 | 50.9 ± 1.8 | 0.28 ± 0.02 |
| | 40—60 | 14.1 ± 0.8 | 10.8 ± 0.6 | 24.9 ± 0.9 | 24.4 ± 1.1 | 34.7 ± 1.7 | 59.2 ± 2.0 | 0.42 ± 0.02 |
| | 60-80 | 4.51 ± 0.37 | 3.37 ± 0.27 | 7.88 ± 0.46 | 5.28 ± 0.35 | 16.8 ± 1.0 | 22.0 ± 1.1 | 0.36 ± 0.03 |
| | 80-100 | 2.64 ± 0.23 | 4.74 ± 0.33 | 7.38 ± 0.41 | 6.22 ± 0.44 | 28.1 ± 1.8 | 34.3 ± 1.8 | 0.21 ± 0.02 |
| ST-43; Event #: 6323 | | | | | | | | |
| | 0-33 | 74.7 ± 3.2 | 37.2 ± 1.8 | 112 ± 4 | 120 ± 5 | 99.3 ± 3.5 | 219 ± 6 | 0.51 ± 0.02 |
| | 33-66 | 7.43 ± 0.39 | 12.2 ± 0.7 | 19.6 ± 0.8 | 14.3 ± 0.7 | 26.7 ± 1.4 | 41.0 ± 1.5 | 0.48 ± 0.03 |
| | 66-99 | 2.10 ± 0.16 | 8.15 ± 0.41 | 10.2 ± 0.4 | 6.50 ± 0.39 | 46.3 ± 1.7 | 52.8 ± 1.7 | 0.19 ± 0.01 |
| | 99-132 | 0.97 ± 0.08 | 1.37 ± 0.12 | 2.34 ± 0.14 | 0.13 ± 0.01 | 3.52 ± 0.24 | 3.65 ± 0.24 | 0.64 ± 0.06 |
| | 132-165 | 1.58 ± 0.12 | 4.48 ± 0.28 | 6.06 ± 0.30 | 1.64 ± 0.12 | 16.8 ± 1.9 | 18.4 ± 1.9 | 0.33 ± 0.04 |
| ST-46; GT # 11717 | | | | | | | | |
| | 0-34 | 5.71 ± 0.34 | 18.1 ± 0.8 | 23.8 ± 0.9 | 10.7 ± 0.6 | 50.9 ± 2.0 | 61.5 ± 2.1 | 0.39 ± 0.02 |
| | 34-68 | 2.36 ± 0.18 | 5.53 ± 0.37 | 7.89 ± 0.41 | 5.78 ± 0.36 | 15.9 ± 1.7 | 21.6 ± 1.8 | 0.36 ± 0.04 |
| | 68-102 | 0.37 ± 0.03 | 3.21 ± 0.24 | 3.57 ± 0.24 | 1.96 ± 0.15 | 11.9 ± 0.8 | 13.8 ± 0.8 | 0.26 ± 0.02 |
| | 102-136 | 0.26 ± 0.03 | 1.73 ± 0.16 | 1.99 ± 0.16 | 0.011 ± 0.001 | 7.80 ± 0.66 | 7.81 ± 0.66 | 0.25 ± 0.03 |
| | 136-170 | 0.53 ± 0.04 | 2.35 ± 0.18 | 2.88 ± 0.19 | 0.87 ± 0.07 | 7.26 ± 0.45 | 8.13 ± 0.45 | 0.35 ± 0.03 |

*BDL = below detection level; activity of sample was lower than the average blank level.*

ARs ranging between 0.12 ± 0.01 and 0.78 ± 0.07 ($n$ = 25, **Table 6**).

The inventory-based (=Σ activities in each segment of the ice core, dpm/Σ volume of melt water, L) activities of $^{210}Po_p$, $^{210}Pb_p$, $^{210}Po_d$ and $^{210}Pb_d$ varied widely: $^{210}Po_p$, varied about an order of magnitude, from 1.8 to 17.4 (mean: 8.1 ± 5.8, $n$ = 6) dpm 100L$^{-1}$; $^{210}Po_T$ varied within a factor of ∼3, from 7.9 to 26.2 (mean: 18.8 ± 6.4, $n$ = 6, calculated from **Table 7**) dpm 100L$^{-1}$. The range of $^{210}Pb_p$ activities is similar to $^{210}Po_p$, from 3.8 to 28.5 (mean: 14.3 ± 9.2, $n$ = 6) dpm 100L$^{-1}$, while the corresponding values for $^{210}Pb_T$ varied within a factor of ∼3, from 22 to 69 (mean: 49 ± 18, $n$ = 6, dpm 100L$^{-1}$). These values are almost an order of magnitude higher than those for the Arctic surface waters (**Figures 2A,B** and **Tables 6**, **7**), suggesting a significant fraction of the source of water is from snow melt and possibly some recycled component of melt ponds. During spring and summer, melt pond water can percolate through the depth of the ice floe forming a lens of super-cooled freshwater at the interface between the ice floe and surface seawater, which ultimately grows into a horizontal ice sheet known as false-bottom ice (Eicken, 1994; Eicken et al., 1997; Polashenski et al., 2012) and thus the signature of the melt pond could have been be imprinted on bottom ice. It seems this is a novel observation presenting a radioisotope-based evidence that the ice core derived some component of water from snow.

**TABLE 7 |** Calculated inventory-based particulate (p) and total (T = p + d) activity of $^{210}$Po and $^{210}$Pb and their activity ratio in whole ice core collected during US GEOTRACES Arctic cruise (HLY 1502).

| Parameter | ST-31 | ST-33 | ST-39 | ST42 | ST-43 | ST-46 |
|---|---|---|---|---|---|---|
| Core length (cm) | 115 | 126 | 171 | 90 | 149 | 153 |
| Melt volume (L) | 11.6 | 14.5 | 17.5 | 9.8 | 17.5 | 18.25 |
| $^{210}Po_p$ (dpm/100 L)* | 5.44 ± 0.19 | 4.86 ± 0.17 | 12.7 ± 0.8 | 6.66 ± 0.22 | 17.4 ± 0.6 | 1.82 ± 0.08 |
| $^{210}Po_T$ (dpm/100 L)* | 19.7 ± 0.4 | 15.9 ± 0.4 | 23.6 ± 0.9 | 19.4 ± 0.5 | 26.2 ± 0.7 | 7.89 ± 0.20 |
| $^{210}Pb_p$ (dpm/100 L)* | 7.96 ± 0.22 | 8.71 ± 0.29 | 18.2 ± 0.4 | 18.8 ± 0.5 | 28.5 ± 1.0 | 3.81 ± 0.14 |
| $^{210}Pb_T$ (dpm/100 L)* | 54.3 ± 2.2 | 31.6 ± 1.9 | 69.0 ± 1.7 | 61.0 ± 1.7 | 57.4 ± 2.2 | 22.2 ± 0.3 |
| $(^{210}Po/^{210}Pb)_p$ | 0.68 ± 0.02 | 0.56 ± 0.02 | 0.70 ± 0.05 | 0.36 ± 0.01 | 0.61 ± 0.02 | 0.48 ± 0.02 |
| $(^{210}Po/^{210}Pb)_T$ | 0.36 ± 0.01 | 0.50 ± 0.02 | 0.34 ± 0.01 | 0.32 ± 0.01 | 0.46 ± 0.02 | 0.36 ± 0.01 |
| **Age (days) | 77 ± 3 | 123 ± 8 | 72 ± 3 | 66 ± 3 | 109 ± 7 | 77 ± 3 |

*Activities of individual layers are given in **Table 6**. The particulate and total activities were calculated from the summation of the corresponding activity in each layer and divided by total melt volume of water for each core.*

***In the calculation of the age, the average of 13 aerosol initial $(^{210}Po/^{210}Pb)_i$ value of 0.039 ± 0.026 was used.*

The $(^{210}Po/^{210}Pb)_p$ AR for the whole ice core varied between 0.36 and 0.70 (mean: 0.56 ± 0.13, $n$ = 6) which is significantly higher than the range of values and mean for $(^{210}Po/^{210}Pb)_T$ AR, 0.32 to 0.50 (mean: 0.39 ± 0.07, $n$ = 6, **Table 7**). The higher $(^{210}Po/^{210}Pb)_p$ AR compared to $(^{210}Po/^{210}Pb)_d$ and $(^{210}Po/^{210}Pb)_T$ are similar to snow and melt pond, confirming enrichment of $^{210}$Po in particulate matter. The calculated composite ages of the ice core, based on the inventory of $^{210}Po_T$ and $^{210}Pb_T$ and assuming initial $(^{210}Po/^{210}Pb)$ AR = 0.039, ranged between 66 and 123 days (mean: 87 ± 23 days; **Figure 4** and **Table 7**). If the initial ARs are higher, the calculated ages are upper limits.

## CONCLUSION AND FUTURE OUTLOOK

We measured the disequilibrium between $^{210}$Po and $^{210}$Pb in a suite of aerosols and ice-rafted sediment as well in particulate and dissolved phases of snow, water from melt pond and surface seawater. We report, for the first time, highly elevated levels of $^{210}$Po in biogenic particulate matter in snow and melt pond compared to $^{210}$Pb indicating biogeochemical cycling of biogenic elements such as polonium is different in the Arctic. We also report one to two orders of magnitude higher $^{210}$Pb and $^{210}$Po activities in ice-rafted sediments (IRS) compared to benthic source sediments which indicate that the sea ice-sediment (i.e., IRS) is a powerful vector in the transport of land- and atmospherically delivered particle-reactive contaminants from the coastal area to the deep Arctic. Furthermore, transport of ice-rafted sediments through sea ice is one of the major mechanisms by which coastal sediments are transported and dispersed in the deep Arctic (during melt season) and nutrients associated with coastal sediments serve as food resource for deep benthic organisms in the open Artic, thus indicating coupling between coastal and deep arctic benthic ecosystems. The key findings are given below:

(i) From the measured $^{210}$Po/$^{210}$Pb AR in snow and using the mean AR in aerosol as the initial AR in snow, the calculated age of snow collected from 6 different ice stations varied between 1.7 and 34 days (mean: 13 days);
(ii) The ages of 5 different melt ponds, based on the measured $^{210}$Po/$^{210}$Pb AR and three end-member mixing modeling, ranged between 18 and 79 days (mean: 60 days). The activities of $^{210}$Po and $^{210}$Pb in melt-ponds is about 10 times higher compared to the surface seawater in the Arctic Ocean;
(iii) From the measured $^{210}$Po-$^{210}$Pb activities in aerosols, collected from 13 different stations covering the entire 10 weeks of Western Arctic GEOTRACES cruise track from Dutch Harbor, AK to the North Pole, we show that the mean $^{210}$Po/$^{210}$Pb activity ratio (AR) of 0.039 ± 0.026 ($n$ = 13) corresponds to a residence time of 12 ± 7 days;
(iv) The transport velocity of the ice-rafted sediment in the shelf and interior Arctic Ocean, estimated based on the age obtained using $^{210}$Po/$^{210}$Pb AR, 0.12 and 0.27 m/s, (mean: 0.18 ± 0.06 m/s) agree with the data obtained using buoys and Acoustic Doppler current profiler; and
(v) The $^{210}$Po/$^{210}$Pb AR serves as a quantitative tool in delineating multiple-year ice from seasonal ice.

The residence time of snow and melt pond has direct bearing on the energy exchange between surface ocean and atmosphere as well as the heat exchange between Arctic and sub-arctic global oceans. The disequilibrium between $^{210}$Po and $^{210}$Pb provide not only a powerful tool in establishing chronology but also insight on the mechanism(s) of Po enrichment onto biogenic particulate matter. Routine identification of multi-year (those that survived more than one melt cycle) ice is now possible using $^{210}$Po/$^{210}$Pb AR as a metric. Furthermore, long-term longitudinal study on the annual variations in the age of snow and melt pond in a particular region caused by climate change in the Arctic may enable us to quantify the radiation balance changes caused by faster melting of snow and later freeze. Highly enriched $^{210}$Po in particulate matter in snow, ice and melt ponds suggest that the biological organisms play a key role in the enrichment of biogenic elements. The factors and processes that cause high enrichment of polonium in the particulate matter obtained from snow, ice and melt pond remains

unknown. A systematic study on the distribution of $^{210}$Po and $^{210}$Pb in particulate and dissolved phases along with characterization of particulate matter including quantification of acid polysaccharides and other biogenic molecular compounds will yield valuable information to understand the mechanisms of Po enrichment onto particulate matter in the Arctic.

## DATA AVAILABILITY STATEMENT

The original data for this study are presented in the article/**Supplementary Material**. The data also can be obtained from https://www.bco-dmo.org/dataset/794064; and further inquiries can be directed to the corresponding author.

## AUTHOR CONTRIBUTIONS

MB developed the idea, secured the funding, oversaw the project from conception to the end, and wrote most of the manuscript. KK participated in the cruise, collected and analyzed the samples, and interpreted the data. Both authors contributed to the article and approved the submitted version.

## FUNDING

The work presented was a part of a master's thesis of KK. This work was supported by the National Science Foundation grant (NSF-PLR-1434578).

## ACKNOWLEDGMENTS

We thank Captain, crew, and US GEOTRACES Western Arctic Management team for collection of water, snow, ice, and aerosol samples.

## SUPPLEMENTARY MATERIAL

The Supplementary Material for this article can be found online at: https://www.frontiersin.org/articles/10.3389/fmars.2021.692631/full#supplementary-material

**Supplementary Figure 1** | Vertical profiles of salinity in 5 ice cores.

## REFERENCES

Bacon, M. P., Spencer, D. W., and Brewer, P. G. (1976). $^{210}$Pb/$^{226}$Ra and $^{210}$Po/$^{210}$Pb disequilibria in seawater and suspended particulate matter. *Earth Planet. Sci. Lett.* 32, 277–296.

Bam, W., Maiti, K., Baskaran, M., Krupp, K., Lam, P. J., and Xiang, Y. (2020). Variability of $^{210}$Pb and $^{210}$Po partition coefficients ($K_d$) along the US GEOTRACES Arctic Transect. *Mar. Chem.* 219:103749. doi: 10.1016/j.marchem.2020.103749

Baskaran, M. (2005). Interaction of sea ice sediments and surface sea water in the Arctic Ocean: Evidence from excess 210Pb. *Geophys. Res. Lett.* 32:L12601.

Baskaran, M. (2011). Po-210 and Pb-210 as atmospheric tracers and global atmospheric Pb-210 fallout: a Review. *J. Environ. Radioact.* 102, 500–513. doi: 10.1016/j.jenvrad.2010.10.007

Baskaran, M. (2016). *Applications of Radon progeny in atmospheric studies. In: Radon: A Tracer for Geological, Geophysical and Geochemical Studies*. Berlin: Springer.

Baskaran, M., Church, T. M., Hong, G.-H., Kumar, A., Qiang, M., Choi, H., et al. (2013). Effects of flow rates and composition of the filter, and decay-in-growth correction factors involved with the determination of in-situ particulate $^{210}$Po and $^{210}$Pb in seawater. *Limnol. Oceanogr. Methods* 11, 126–138. doi: 10.4319/lom.2013.11.126

Baskaran, M., and Shaw, G. E. (2001). Residence time of arctic haze aerosols using the concentrations and activity ratios of $^{210}$Po, $^{210}$Pb, and $^{7}$Be. *J. Aerosol Sci.* 32, 17–26.

Carmack, E., and Chapman, D. C. (2003). Wind-driven shelf/basin exchange on the Arctic shelf: the joint roles of ice cover extent and shelf-break bathymetry. *Geophys. Res. Lett.* 30:1778.

Charette, M. A., Kipp, L. E., Jensen, L. T., Dabrowski, J. S., Whitmore, L. M., Fitzsimmons, J. N., et al. (2020). The transpolar drift as a source of riverine and shelf-derived trace elements to the Central Arctic Ocean. *J. Geophys. Res.* 125:e2019JC01520.

Chen, M., Ma, Q., Guo, L. D., Qiu, Y., Li, Y., and Yang, W. (2012). Importance of lateral transport processes to $^{210}$Pb budget in the eastern Chukchi Sea during summer 2003. *Deep-Sea Res. II* 81-84, 53–62. doi: 10.1016/j.dsr2.2012.03.011

Cochran, J. K., and Masque, P. (2003). Short-lived U/Th-series radionuclides in the ocean: tracers for scavenging rates, export fluxes and particle dynamics. *Rev. Mineral. Geochem.* 52, 461–492. doi: 10.2113/0520461

Conan, F., and Robertson, L. B. (2002). Latitudinal distribution of radon-222 flux from continents. *Tellus* 54B, 127–133. doi: 10.1034/j.1600-0889.2002.00365.x

Cookbook (2014). *Sampling and Sample-handling Protocols for GEOTRACES Cruises*. Available Online at: http://www.geotraces.org/images/stories/documents/intercalibration/Cookbook_v2.pdf

Cooper, L. W., Larsen, I. L., Beasley, T. M., Dolvin, S. S., Grebmeier, J. M., Kelley, J. M., et al. (1998). The distribution of radiocesium and plutonium in sea ice-entrained Arctic sediments in relation to potential sources and sinks. *J. Environ. Radioact.* 39, 279–303. doi: 10.1016/s0265-931x(97)00058-1

Eicken, H. (1994). Structure of under-ice melt ponds in the Central Arctic and their effect on sea-ice cover. *Limnol. Oceanogr.* 39, 682–694. doi: 10.4319/lo.1994.39.3.0682

Eicken, H., Krouse, H. R., Kadko, D., and Perovich, D. K. (2002). Tracer studies of pathways and rates of meltwater transport through Arctic summer sea ice. *J. Geophys. Res.* 107:8046. doi: 10.1029/2000JC000583

Eicken, H., Reimnitz, E., Alexandrov, V., Martin, T., Kassens, H., and Viehoff, T. (1997). Sea-ice processes in the Laptev Sea and their importance for sediment export. *Cont. Shelf Res.* 17, 205–233. doi: 10.1016/s0278-4343(96)00024-6

Fowler, S. W. (2011). $^{210}$Po in the marine environment with emphasis on its behavior within the biosphere. *J. Environ. Radioact.* 102, 448–461. doi: 10.1016/j.jenvrad.2010.10.008

Grenier, M., Francois, R., Soon, M., van der Loeff, M. R., Yu, X., Valk, O., et al. (2019). Changes in circulation and particle scavenging in the Amerasian Basin of the Arctic Ocean over the last three decades inferred from the water column distribution of geochemical tracers. *J. Geophys. Res.* 124, 9338–9363. doi: 10.1029/2019jc015265

Hebbeln, D., and Weber, G. (1991). Effects of ice coverage and ice-rafted material on sedimentation in the fram strait. *Nature* 350, 409–411. doi: 10.1038/350409a0

Jweda, J., and Baskaran, M. (2011). Interconnected riverine-lacustrine systems as sedimentary repositories: A case study in southeast Michigan using excess $^{210}$Pb- and $^{137}$Cs-based sediment accumulation and mixing models. *J. Great Lakes Res.* 37, 432–446. doi: 10.1016/j.jglr.2011.04.010

Kadko, D., and Landing, W. M. (2015). *U.S. Arctic GEOTRACES Cruise Report*. Available Online at: https://www.bodc.ac.uk/resources/inventories/cruise_inventory/reports/healy1502.pdf

Kim, G., Hong, Y.-L., Jang, J., Lee, I., Hwang, D.-W., and Yang, H.-S. (2005). Evidence for anthropogenic $^{210}$Po in urban atmosphere of Seoul, Korea. *Environ. Sci. Technol.* 39, 1519–1522. doi: 10.1021/es049023u

Kim, G., Hussain, N., and Church, T. M. (2000). Excess $^{210}$Po in the coastal atmosphere. *Tellus B* 52, 74–80. doi: 10.1034/j.1600-0889.2000.00975.x

Kipp, L. E., Charette, M. A., Moore, W. S., Henderson, P. B., and Rigor, I. G. (2018). Increased fluxes of shelf-derived materials to the central Arctic Ocean. *Sci. Adv.* 4:eaao1302. doi: 10.1126/sciadv.aao1302

Krembs, C., Eicken, H., and Deming, J. W. (2011). Exopolymer alteration of physical properties of sea ice and implications for ice habitability and biogeochemistry in a warmer Arctic. *Proc. Natl. Acad. Sci.* 108, 3653–3658. doi: 10.1073/pnas.1100701108

Krupp, K. D. (2017). *Using $^{210}$Po/$^{210}$Pb disequilibria to characterize the biogeochemistry and quantify the dynamics of sea ice in the Arctic. M.S. thesis*. Detroit: Wayne State University.

Landa, E. R., Reimnitz, E., Beals, D. M., Pochkowski, J. M., Winn, W. G., and Rigor, I. (1997). Transport of $^{137}$Cs and $^{239,240}$Pu with ice-rafted debris in the Arctic Ocean. *Arctic* 51, 27–39.

Marley, N. A., Gaffney, J. S., and Drayton, P. J. (2000). Measurement of $^{210}$Pb, $^{210}$Po and $^{210}$Bi in size-fractionated atmospheric aerosols: an estimate of fine-aerosol residence times. *Aerosol. Sci. Technol.* 32, 569–583. doi: 10.1080/027868200303489

Marsay, C. M., Aguilar-Islas, A., Fitzsimmons, J. N., Hatta, M., Jensen, L. T., John, S. G., et al. (2018). Dissolved and particulate trace elements in late summer Arctic melt ponds. *Mar. Chem.* 204, 70–85. doi: 10.1016/j.marchem.2018.06.002

Morton, P. L., Landing, W. M., Hsu, S. C., Milne, A., Aguilar-Islas, A. M., Baker, A. R., et al. (2013). Methods for the sampling and analysis of marine aerosols: results from the 2008 GEOTRACES aerosol intercalibration experiment. *Limnol. Oceanogra. Methods* 11, 62–78. doi: 10.4319/lom.2013.11.62

Masqué, P., Cochran, J. K., Hirschberg, D. J., Dethleff, D., Hebbeln, D., Winkler, A., et al. (2007). Radionuclides in Arctic sea ice: Tracers of sources, fates, and ice transit time scales. *Deep-Sea Res. I* 54, 1289–1310. doi: 10.1016/j.dsr.2007.04.016

McNeary, D., and Baskaran, M. (2003). Depositional characteristics of $^{7}$Be and $^{210}$Pb in Southeastern Michigan. *J. Geophys. Res.* 108:D04210. doi: 10.1029/2002JD003021

McNeary, D., and Baskaran, M. (2007). Residence times and temporal variations of $^{210}$Po in aerosols and precipitation from Southeastern Michigan, USA. *J. Geophys. Res.* 112:D04208. doi: 10.1029/2006JD007639

Meese, D. A., Reimitz, E., Tucker, W. B., Gow, A. J., Bischoff, J., and Darby, D. (1997). Evidence for radionuclide transport by sea ice. *Sci. Total Environ.* 202, 267–278. doi: 10.1016/s0048-9697(97)00121-6

Melling, M., and Riedel, D. A. (2003). *Ice draft and ice velocity data in the Beaufort Sea, 1990-2003, Versions. 1*. Boulder, Colorado: National Snow and Ice Data Center.

Moore, H. E., Poet, S. E., and Martell, E. A. (1973). $^{222}$Rn, $^{210}$Pb, $^{210}$Bi, and $^{210}$Po profiles and aerosol residence times versus altitude. *J. Geophys. Res.* 78, 7065–7075.

Moore, R. M., and Smith, J. N. (1986). Disequilibria between $^{226}$Ra, $^{210}$Pb and $^{210}$Po in the Arctic Ocean and the implications for chemical modification of the Pacific water inflow. *Earth Planet. Sci. Lett.* 77, 285–292. doi: 10.1016/0012-821x(86)90140-8

Niedermiller, J., and Baskaran, M. (2019). Comparison of the scavenging intensity, remineralization and residence time of $^{210}$Po and $^{210}$Pb at key zones (biotic, sediment-water and hydrothermal) along the East Pacific GEOTRACES transect. *J. Environ. Radioact.* 198, 165–188. doi: 10.1016/j.jenvrad.2018.12.016

Nürnberg, D., Wollenburg, I., Dethleff, D., Eicken, H., Kassens, H., Letzig, T., et al. (1994). Sediments in Arctic sea ice – implications for entrainment, transport and release. *Mar. Geol.* 119, 185–214. doi: 10.1016/0025-3227(94)90181-3

Perovich, D. K., Grenfell, T. C., Richter-Menge, J. A., Light, B., Tucker, W. B. III, and Eicken, H. (2003). Thin and thinner: sea ice mass balance measurements during SHEBA. *J. Geophys. Res.* 108:8050.

Pfirman, S. L., Eicken, H., Bauch, D., and Weeks, W. F. (1995). The potential transport of pollutants by Arctic sea ice. *Sci. Total Environ.* 159, 129–146. doi: 10.1016/0048-9697(95)04174-y

Polashenski, C., Perovich, D., and Courville, Z. (2012). The mechanisms of sea ice melt pond formation and evolution. *J. Geophys. Res.* 117:C01001.

Reimnitz, E., Kempema, E. W., and Barnes, P. W. (1987). Anchor ice, seabed freezing, and sediment dynamics in shallow arctic seas. *J. Geophys. Res.* 92, 14671–14678. doi: 10.1029/jc092ic13p14671

Rigaud, S., Puigcorbe, V., Camara-Mor, P., Casacuberta, N., Roca-Marti, M., Garcia-Orellana, J., et al. (2013). A method assessment and recommendations for improving calculations and reducing uncertainties in the determination of $^{210}$Po and $^{210}$Pb activities in seawater. *Limnol. Oceanogr. Methods* 11, 561–571. doi: 10.4319/lom.2013.11.561

Robbins, J. A. (1978). "Geochemical and geophysical applications of radioactive lead," in *The Biogeochemistry of Lead in the Environment*, ed. J. O. Nriagu (Amsterdam: Elsevier/North-Holland Biomedical Press), 285–393.

Robbins, J. A., Murdock, A., and Oliver, B. G. (1990). Transport and storage of $^{137}$Cs and $^{210}$Pb in sediments of Lake St. *Clair. Can. J. Fish. Aquat. Sci.* 47, 572–587.

Roberts, K. A., Cochran, J. K., and Barnes, C. (1997). $^{210}$Pb, $^{239,240}$Pu in the Northeast Water Polynya, Greenland: Particle dynamics and sediment mixing rates. *J. Mar. Syst.* 10, 401–413. doi: 10.1016/s0924-7963(96)00061-9

Roca-Marti, M., Puigcorbe, V., Rutgers van der Loeff, M. M., Katlein, C., Fernandez-Mendez, M., Peeken, I., et al. (2016). Carbon export fluxes and export efficiency in the central Arctic during the record sea-ice minimum in 2012: a joint $^{234}$Th/$^{238}$U and $^{210}$Po/$^{210}$Pb study. *J. Geophys. Res.* 121, 5030–5049. doi: 10.1002/2016jc011816

Rutgers van der Loeff, M., Kipp, L., Charette, M. A., Moore, W. S., Black, E., Stimac, I., et al. (2018). Radium isotopes across the Arctic Ocean show time scales of wáter mass ventilation and increasing shelf inputs. *J. Geophys. Res.* 123, 4853–4873. doi: 10.1029/2018jc013888

Rutgers van der Loeff, M. M., and Geibert, W. (2008). "U/Th series nuclides as tracers of particle dynamics, scavenging and biogeochemical cycles in the ocean," in *U-Th Series radionuclides in aquatic systems*, eds S. Krishnaswami and J. K. Cochran (Amsterdam: Elsevier).

Smith, J. N., Moran, S. B., and Macdonald, R. W. (2003). Shelf-basin interactions in the Arctic Ocean based on $^{210}$Pb and Ra isotope tracer distributions. *Deep-Sea Res. I* 50, 397–416. doi: 10.1016/s0967-0637(02)00166-8

Sturm, M., Holmgren, J., and Perovich, D. K. (2002). Winter snow cover on the sea ice of the Arctic Ocean at the Surface Heat Budget of the Arctic Ocean (SHEBA): Temporal evolution and spatial variability. *J. Geophys. Res.* 107:8047.

Su, C. C., and Huh, C. A. (2002). Atmospheric $^{210}$Po anomaly as a precursor of volcanic eruptions. *Geophys. Res. Lett.* 29:1070. doi: 10.1029/2001GL013856

Turekian, K. K., Nozaki, Y., and Benninger, K. (1977). Geochemistry of atmospheric radon and radon products. *Ann. Rev. Earth Planetary Sci.* 5:227. doi: 10.1146/annurev.ea.05.050177.001303

Uttal, T., Curry, J. A., McPhee, M. G., Perovich, D. K., Moritz, R. E., Maslanik, J. A., et al. (2002). Surface heat budget of the Arctic Ocean. *Bull. Am. Meteo. Soc.* 83, 255–275.

Wang, J., Zhong, Q., Baskaran, M., and Du, J. Z. (2019). Investigations on the time-series partitioning of $^{210}$Pb, $^{207}$Bi and $^{210}$Po between marine particles and solution under different salinity and pH conditions. *Chem. Geol.* 528:119275. doi: 10.1016/j.chemgeo.2019.119275

Wilkening, M. H., and Clements, W. E. (1975). Radon-222 from ocean surface. *J. Geophys. Res.* 80, 3828–3830. doi: 10.1029/jc080i027p03828

Yang, W., Guo, L., Chuang, C., Schumann, D., Ayranov, M., and Santschi, P. H. (2013). Adsorption characteristics of $^{210}$Pb, $^{210}$Po and $^{7}$Be onto micro-particle surfaces and the effects of macromolecular organic compounds. *Geochim. Cosmochim. Acta* 107, 47–64. doi: 10.1016/j.gca.2012.12.039

**Conflict of Interest:** The authors declare that the research was conducted in the absence of any commercial or financial relationships that could be construed as a potential conflict of interest.

**Publisher's Note:** All claims expressed in this article are solely those of the authors and do not necessarily represent those of their affiliated organizations, or those of the publisher, the editors and the reviewers. Any product that may be evaluated in this article, or claim that may be made by its manufacturer, is not guaranteed or endorsed by the publisher.

*Copyright © 2021 Baskaran and Krupp. This is an open-access article distributed under the terms of the Creative Commons Attribution License (CC BY). The use, distribution or reproduction in other forums is permitted, provided the original author(s) and the copyright owner(s) are credited and that the original publication in this journal is cited, in accordance with accepted academic practice. No use, distribution or reproduction is permitted which does not comply with these terms.*

frontiers in Marine Science

ORIGINAL RESEARCH
published: 13 August 2021
doi: 10.3389/fmars.2021.702124

# Activity Levels of $^{210}$Po, $^{210}$Pb and Other Radionuclides ($^{134}$Cs, $^{137}$Cs, $^{90}$Sr, $^{110m}$Ag, $^{238}$U, $^{226}$Ra and $^{40}$K) in Marine Organisms From Coastal Waters Adjacent to Fuqing and Ningde Nuclear Power Plants (China) and Radiation Dose Assessment

*Jiang Sun*[1,2], *Wu Men*[2,3]*, *Fenfen Wang*[2] *and Junwen Wu*[1,4]*

[1] Institute of Marine Sciences, Shantou University, Shantou, China, [2] Laboratory of Marine Isotopic Technology and Environmental Risk Assessment, Third Institute of Oceanography, Ministry of Natural Resources, Xiamen, China, [3] School of Marine Sciences, Nanjing University of Information Science and Technology, Nanjing, China, [4] Southern Marine Science and Engineering Guangdong Laboratory, Guangzhou, China

With the rapid development of nuclear power, the radiation impacts on edible marine organisms, and the potential radiation risks to humans have become of considerable concern to public health. In this study, the activities of $^{210}$Po and $^{210}$Pb as well as those of other radionuclides in fishes (*Mugil cephalus*, *Konosirus punctatus*, *Largehead hairtail*, and *Larimichthys polyactis*), crustaceans (*Mantis shrimp*, *Parapenaeopsis hardwickii*, and *Portunus trituberculatus*), bivalves (*Crassostrea gigas*, *Sinonovacula conzcta*), and macroalgae (*Gracilaria*, *Porphyra*) collected in the coastal area adjacent to the Fuqing and Ningde nuclear power plants (NPPs) were determined. The activity range of $^{210}$Po and $^{210}$Pb was 0.60–48.09 and 0.07–2.76 Bq/kg $_{\text{freshweight}}$, respectively, with $^{210}$Po/$^{210}$Pb activity ratios of 1.1–189.7. The ranking of $^{210}$Po activity levels in marine organisms was bivalve mollusks > crustaceans > fishes > macroalgae. The calculated bioconcentration factors of $^{210}$Po and $^{210}$Pb were 636–44,944 and 3–1,226 L/kg, respectively. These values provide a new supplement to the IAEA reference database. The radiation dose rates for these marine organisms ranged from 0.037 to 1.531 μSv/h, which was much lower than the ERICA ecosystem screening benchmark of 10 μGy/h. The calculated committed effective dose received by humans from ingestion of these marine organisms was 0.06–2.99 mSv. Overall, $^{210}$Po was the dominant radiation dose contributor in marine organisms and humans, whereas the dose contributions from the artificial nuclides $^{90}$Sr and $^{137}$Cs were negligible.

**Keywords: lead, polonium, marine biota, nuclear power plant, dose assessment**

OPEN ACCESS

***Edited by:***
*Weifeng Yang,*
*Xiamen University, China*

***Reviewed by:***
*Martin F. Soto-Jimenez,*
*National Autonomous University of Mexico, Mexico*
*Alberto Sánchez-González,*
*Instituto Politécnico Nacional (IPN), Mexico*

***Correspondence:**
*Wu Men*
*menwu@nuist.edu.cn*
*Junwen Wu*
*wujw@stu.edu.cn*

***Specialty section:***
*This article was submitted to Marine Biogeochemistry, a section of the journal Frontiers in Marine Science*

***Received:*** *29 April 2021*
***Accepted:*** *15 July 2021*
***Published:*** *13 August 2021*

***Citation:***
*Sun J, Men W, Wang F and Wu J (2021) Activity Levels of $^{210}$Po, $^{210}$Pb and Other Radionuclides ($^{134}$Cs, $^{137}$Cs, $^{90}$Sr, $^{110m}$Ag, $^{238}$U, $^{226}$Ra and $^{40}$K) in Marine Organisms From Coastal Waters Adjacent to Fuqing and Ningde Nuclear Power Plants (China) and Radiation Dose Assessment. Front. Mar. Sci. 8:702124. doi: 10.3389/fmars.2021.702124*

## INTRODUCTION

The polonium isotope $^{210}$Po (half-life, $T_{1/2}$ = 138.4 d) and its grandparent $^{210}$Pb ($T_{1/2}$ = 22.26 y) are nonconservative, naturally occurring radionuclides within the uranium $^{238}$U decay chain, which is ubiquitous in the environment of the earth. The isotopes $^{210}$Po and $^{210}$Pb in the atmosphere mainly originated from the release of $^{222}$Rn from the ground and its subsequent decay. Due to their strong particle reactivity, they are firmly attached to the aerosol soon after they are produced. With the dry and wet depositions, they are subsequently discharged into the terrestrial and marine environment *via* dry and wet deposition (Seiler and Wiemels, 2012). Due to their unique geochemical properties, $^{210}$Po and $^{210}$Pb are used as a tracer pair to study the dynamic processes of aerosols in the atmosphere and estimate the residence times of aerosols (Aba et al., 2020). They are also used to study particle scavenging processes in the sea, particularly in assessing the export of particulate organic carbon (POC) fluxes from the euphotic zone (Zhang et al., 2020; Bam and Maiti, 2021), as well as specific marine food chain processes (Strady et al., 2015). Indeed, beyond the oceanographic application of $^{210}$Po and $^{210}$Pb, their accumulation in marine organisms and transfer to human consumers of seafood, and the resulting radiation doses to marine organisms or committed effective doses to humans are also issues of public concern. This is especially true for $^{210}$Po, as it is one of the most radiotoxic nuclides that emit high-energy (∼5.3 MeV) alpha rays and is the main contributor of the radiation dose received by marine organisms and humans (UNSCEAR, 2000; Sivakumar, 2014; Men et al., 2020a,b).

Marine organisms usually concentrate $^{210}$Po and $^{210}$Pb from the marine environment. Although the activity levels of $^{210}$Po and $^{210}$Pb in the marine environment are relatively low compared with those in the terrestrial environment, different marine organisms can concentrate these two radionuclides to relatively high levels with high concentration factors (CFs) (∼$10^2$ to ∼$10^5$) (IAEA, 2004). Therefore, $^{210}$Po and $^{210}$Pb provide the main radiation source for marine organisms. In seawater, there are relatively higher levels of other naturally occurring nuclides, such as uranium $^{238}$U (12.2–215.4 Bq/m$^3$), radium $^{226}$Ra (0.22–7.20 Bq/m$^3$), and potassium $^{40}$K (∼12,000 Bq/m$^3$), and artificial radionuclides, such as cesium $^{137}$Cs (<3.2 Bq/m$^3$) and strontium $^{90}$Sr (<2.2 Bq/m$^3$) (IAEA, 2005; Liu, 2010). Marine organisms also concentrate these nuclides in their body, which thus also produce self-radiation. Since the 1980s, the concept of human-centered environmental protection has gradually evolved into the concept of ecological protection in which the whole ecosystem is the protection target within the field of radiation protection. Many international organizations and government departments have been studying the effects of ionizing radiation on nonhuman species, including the International Commission on Radiation Protection (ICRP), the International Atomic Energy Agency (IAEA), the United Nations Scientific Committee on the Effects of Atomic Radiation (UNSCEAR), and the European Commission (EC). Additionally, after the 2011 Fukushima Dai-ichi Nuclear Power Plant (FDNPP) accident, the rapid development of nuclear power has raised increasing attention to the radiation impacts on marine organisms and the potential radiation risks to public health (Yu et al., 2018; Men et al., 2020a,b).

At present, the Fuqing and Ningde Nuclear Power Plants (NPPs), located on the coast of Fujian province (**Figure 1**), are in operation. The marine organisms living in the area adjacent to these two NPPs provide ideal experimental test subjects to study the concentrations of radionuclides in the marine environment as well as to undertake radiation dose assessment. In this study, data are provided on the activity levels of naturally occurring and artificial radionuclides in marine organisms used as bio-monitors of nuclear power plant operations. Activity levels of $^{210}$Po, $^{210}$Pb, and other naturally occurring or artificial radionuclides were investigated in fish, crustaceans, bivalve mollusks, and macroalgae in the areas surrounding Fuqing and Ningde NPPs, and the resulting radiation doses to both marine organisms and humans were assessed.

## MATERIALS AND METHODS

### Sample Collection

Samples of marine organisms were obtained by hired fishermen in areas adjacent to Fuqing and Ningde NPPs (i.e., within 10 km) in July 2020 (**Figure 1**). Twelve samples with a fresh weight of ∼2.2–10.6 kg each were collected. They were refrigerated and immediately sent to the laboratory (within 24 h). Marine organisms include fishes (the mullet *Mugil cephalus*, *Konosirus punctatus*, *Largehead hairtail*, and *Larimichthys polyactis*), crustaceans (*Mantis shrimp*, *Parapenaeopsis hardwickii*, and crab *Portunus trituberculatus*), bivalves (soft tissues of the Pacific oyster *Crassostrea gigas*, and razor clam *Sinonovacula conzcta*), macroalgae [the red algae *Gracilaria* spp. (*Gracilariaceae*) and *Porphyra* spp. (*Bangiaceae*)] (**Figure 2**). Seawater and sediment samples were also collected at each of 10 stations near Fuqing NPP and Ningde NPP (**Figure 1**).

### Sample Processing and Analysis

The weighed marine organism samples were dried to constant weight for 48–96 h at 60°C in a drum dryer. Dried samples were pulverized, using agate mortar and pestle sets in preparation for the radioactive analysis. About 1 g of these pulverized dry samples was used for the measurement of $^{210}$Po, using α spectrometer (Canberra 7200) (Štrok and Smodiš, 2011). The rest was transferred into crucibles and ashed in a muffle furnace at 450°C for 24–40 h. The ashes were ground and weighed at room temperature, stored in sealed boxes (∼100 g per sample) for 20 days until analysis. Canberra BE6530 and GR4021 HPGe spectrometers were used to determine the activities of $^{210}$Pb, $^{134}$Cs, $^{137}$Cs, $^{110m}$Ag, $^{238}$U, $^{226}$Ra, and $^{40}$K (Men et al., 2017). The di (2-ethylhexyl) phosphoric acid (HDEHP) extraction-β counting method and the Ortec MPC-9604 α/β counter were employed for $^{90}$Sr analysis (Men et al., 2017), using ∼10 g of the ashes. Seawater and sediment samples were also analyzed according to the Technical Specification for Marine Radioactivity Monitoring (State Oceanic Administration of China, 2011). All marine organisms were analyzed whole, except for the bivalves whose shells were removed. Parallel sample analysis was

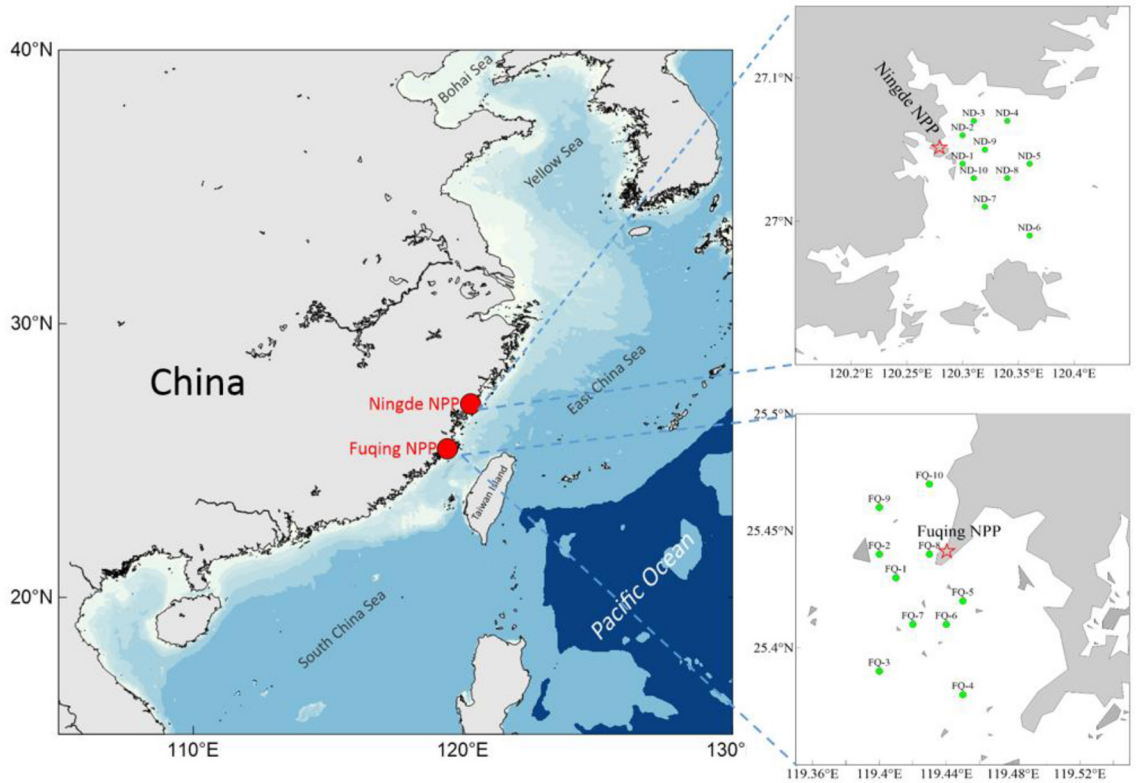


**FIGURE 1 |** Sediment and water sampling stations (green symbols) near the Fuqing and Ningde nuclear power plants along the coast of China.

implemented for *Konosirus punctatus* and *Mantis shrimp*; the results were in good agreement within an error <3%.

Specifically, ca. 1 ml of 0.12848 Bq/ml $^{209}$Po was added to 1 g of a dry biological sample, and then the spiked sample was digested with a mixture of concentrated nitric acid and hydrogen peroxide. After steaming until nearly dry, 2 mL of concentrated hydrochloric acid (HCl) was added and steaming carried out again, and the residue was dissolved with 2-M HCl. After filtration, the filtrate was placed in an α spectrometer for measurement over 24 h. The chemical yield for $^{209}$Po ranged from 52 to 89%, averaging 72 ± 12% (SD, $n = 14$) after adding 1 ml of 0.12848 Bq/ml of $^{209}$Po standard solution.

Seawater (5 L) was taken from each station for analysis. A known amount of $^{209}$Po (∼1 g) was added to the seawater samples to determine the yield. The spiked samples were co-precipitated with ferric hydroxide by adding ∼50 mg of $Fe^{3+}$ and adjusting the pH to ∼8, with the addition of concentrated ammonium hydroxide ($NH_4OH$). The precipitate was then dissolved in concentrated HCl, and auto-deposition was carried out. The analysis of other radionuclides in seawater is described in detail by Men et al. (2017).

## Radiation Dose for Marine Organisms

The ERICA assessment tool (version 1.3, Tier 2) was used to evaluate the dose rates for marine organisms (Beresford et al., 2007; Men et al., 2020a,b). The average biological parameters of the specimens sampled, including length, width, and height, as well as weight, are listed in **Table 1**, and were used to calculate the radiation doses listed (the biological parameters were determined for all individuals of each species in the sample). The average nuclide activities in seawater and sediment were used to estimate the external dose rates. The activity levels of these nuclides in the marine organism were used to estimate the internal dose rates. The low beta, beta/gamma, and alpha weighing factors were taken to be 3, 1, and 10, respectively. The other parameters were set to their default values.

## Committed Effective Dose for Humans Consuming Various Marine Organisms

After ingestion or inhalation by humans, some radionuclides persist in the body and irradiate various tissues for many years. The resulting total effective dose over a lifetime (70 years or number of years up to reaching age, 70 for infants, 50 years for adults) is the committed effective dose (ICRP, 2007; Men et al., 2017). This dose received by a human per unit intake (1 Bq) of a given radionuclide is the radionuclide-specific dose coefficient (DC) for ingestion (Fisher et al., 2013), which converts the energy emitted from the ingested radionuclide into a radionuclide-specific, committed effective dose for human


**FIGURE 2 |** Specimens of the marine organism sampled in this study.

adults (Sv). For calculation of the committed effective dose for ingestion of marine organisms in this study, the ingestion rate was assumed as exact ingestion rates were not available. Here, the mean *per capita* consumption rate of aquatic products in China (50.97 kg/year) in 2018 was used to estimate the committed effective dose (FAOSTAT, 2018). This was calculated by multiplying the radionuclide activity in the marine organism (Bq/kg $_{freshweight}$) by the ingested mass (kg) and the DC (Sv/Bq) (ICRP, 2012).

# RESULTS AND DISCUSSION

## Activity Levels of $^{210}$Po and $^{210}$Pb and Other Radionuclides in Marine Organisms

The activities of $^{210}$Po and $^{210}$Pb as well as other radionuclides in marine organisms from the coastal area adjacent to Fuqing and Ningde NPPs are listed in **Table 2**; $^{210}$Po and $^{210}$Pb activities ranged from 0.60 to 48.09 Bq/kg $_{freshweight}$ and 0.07 to 2.76 Bq/kg $_{freshweight}$, respectively. These values are within

**TABLE 1 |** Average biological parameters of the sampled marine organisms.

| Sea area | Organism | Length (cm) | Width (cm) | Height (cm) | Mass (kg) |
|---|---|---|---|---|---|
| Fuqing NPP | *Mugil cephalus* | 27.00 | 5.00 | 4.00 | 1.100 |
| | *Gracilaria* | 60.00 | 0.10 | 0.10 | 0.006 |
| | *Portunus trituberculatus* | 10.00 | 6.00 | 3.00 | 0.400 |
| | *Konosirus punctatus* | 18.00 | 4.50 | 4.00 | 0.110 |
| | *Porphyra* | 35.00 | 2.00 | 0.10 | 0.009 |
| Ningde NPP | *Sinonovacula constrzcta* | 5.00 | 2.00 | 2.00 | 0.012 |
| | *Largehead hairtail* | 60.00 | 5.00 | 2.00 | 1.000 |
| | *Crassostrea gigas* | 7.00 | 4.00 | 3.00 | 0.056 |
| | *Parapenaeopsis hardwickii* | 8.00 | 1.00 | 1.00 | 0.020 |
| | *Mantis shrimp* | 16.00 | 2.50 | 2.00 | 0.050 |
| | *Larimichthys polyactis* | 15.00 | 6.00 | 2.00 | 0.080 |
| | *Porphyra* | 20.00 | 1.50 | 0.10 | 0.007 |

**TABLE 2 |** Activities of $^{210}$Po and $^{210}$Pb and other radionuclides in marine organisms sampled in this study.

| Sea area | Organisms | $^{210}$Po | $^{210}$Pb | $^{137}$Cs | $^{90}$Sr | $^{238}$U | $^{226}$Ra | $^{40}$K | $^{210}$Po/$^{210}$Pb)$_{A.R.}$ |
|---|---|---|---|---|---|---|---|---|---|
| | | Bq/kg $_{fresh\ weight}$ | | | | | | | |
| Fuqing NPP | *Mugil cephalus* | 2.25 ± 0.24 | 1.33 ± 0.36 | 0.05 ± 0.01 | 0.37 ± 0.03 | 2.66 ± 0.08 | 1.61 ± 0.03 | 121.1 ± 3.3 | 1.7 |
| | *Gracilaria* | 3.06 ± 0.19 | 2.76 ± 0.73 | 0.01 ± 0.01 | 0.03 ± 0.01 | 0.50 ± 0.02 | 0.13 ± 0.01 | 106.6 ± 2.9 | 1.1 |
| | *Portunus trituberculatus* | 41.04 ± 0.67 | / | ND | 0.39 ± 0.04 | 0.69 ± 0.21 | 1.22 ± 0.03 | 81.9 ± 2.4 | / |
| | *Konosirus punctatus* | 2.07 ± 0.27 | 0.32 ± 0.09 | ND | 0.08 ± 0.03 | 0.25 ± 0.02 | 0.24 ± 0.01 | 107.7 ± 2.9 | 6.5 |
| | *Porphyra* | 0.60 ± 0.13 | 0.51 ± 0.14 | ND | 0.09 ± 0.01 | 0.13 ± 0.01 | 0.08 ± 0.01 | 93.4 ± 2.5 | 1.2 |
| Ningde NPP | *Sinonovacula constrzcta* | 33.09 ± 1.09 | 1.42 ± 0.38 | ND | 0.05 ± 0.01 | 1.03 ± 0.04 | 0.36 ± 0.01 | 174.9 ± 4.8 | 23.3 |
| | *Largehead hairtail* | 32.25 ± 0.74 | 0.17 ± 0.05 | 0.08 ± 0.01 | 0.44 ± 0.05 | 0.15 ± 0.01 | 0.09 ± 0.01 | 63.7 ± 1.7 | 189.7 |
| | *Crassostrea gigas* | 48.09 ± 1.06 | 0.65 ± 0.18 | 0.03 ± 0.01 | 0.50 ± 0.05 | 0.33 ± 0.01 | 0.04 ± 0.01 | 76.3 ± 2.1 | 74.0 |
| | *Parapenaeopsis hardwickii* | 13.29 ± 0.59 | 0.14 ± 0.05 | 0.03 ± 0.01 | 0.75 ± 0.08 | 0.71 ± 0.03 | 0.53 ± 0.01 | 56.9 ± 1.6 | 94.9 |
| | *Mantis shrimp* | 21.54 ± 0.7 | 0.30 ± 0.08 | 0.03 ± 0.01 | 0.10 ± 0.02 | 0.65 ± 0.03 | 0.35 ± 0.01 | 55.4 ± 1.5 | 71.8 |
| | *Larimichthys polyactis* | 15.53 ± 0.71 | / | ND | 0.03 ± 0.01 | 0.04 ± 0.01 | 0.11 ± 0.01 | 72.5 ± 2.0 | / |
| | *Porphyra* | 0.68 ± 0.13 | 0.07 ± 0.03 | ND | 0.09 ± 0.01 | 0.07 ± 0.01 | 0.02 ± 0.01 | 51.0 ± 1.4 | 9.7 |

*ND, not detected. $^{134}$Cs and $^{110m}$Ag were also undetectable. The MDA (minimum detectable activity) for $^{137}$Cs, $^{134}$Cs, and $^{110m}$Ag was 0.0014 Bq/kg $_{freshweight}$, (661.7 keV), 0.0014 (604.7 keV) Bq/kg $_{freshweight}$, and 0.0012 Bq/kg $_{freshweight}$ (657.8 keV), respectively, during a counting time of 96,708 s and with 10 kg samples. The MDA for $^{210}$Po was 0.0022 Bq/kg $_{freshweight}$ (5,304.5 keV) during a counting time of 172,800 s and with 5 g samples. The blank for $^{210}$Po was 2.7641 Bq/kg $_{freshweight}$. The blank for $^{90}$Sr was 0.215 cpm. The blank for $^{238}$U, $^{226}$Ra, and $^{40}$K was 0.016 cpm, 0.004 cpm, and 0.005 cpm, respectively. The CRM (certified reference material) was 100-g fish ash (standard values: 5.9815 Bq/kg $_{fishash}$, $^{134}$Cs; 34.2954 Bq/kg $_{fishash}$ $^{137}$Cs; 0.7990 Bq/kg $_{fishash}$ $^{110m}$Ag). The measured values for $^{134}$Cs, $^{137}$Cs, and $^{110m}$Ag in 100-g fish ash dry weight during the counting time of 176,619 s were 0.1405, 0.5023, and 0.0104 Bq/kg $_{fishash}$. /indicates lack of data.*

the reported ranges of $^{210}$Po and $^{210}$Pb in marine organisms in China ($^{210}$Po: 0.117–65.8 Bq/kg $_{freshweight}$; $^{210}$Pb: 0.02–6.88 Bq/kg $_{freshweight}$) (Li et al., 2016, 2018; Lin et al., 2016; Dong et al., 2018; Lin, 2018). The limit of $^{210}$Po activity recommended in fish, meat, and shrimp by the Chinese National Standard on limited concentrations of radioactive materials in foods (GB 14882-94) is 15 Bq/kg $_{freshweight}$ (Ministry of Health of the People's Republic of China, 1994). About 50% of $^{210}$Po activities in marine organisms reported in the present study exceeded this value. Most $^{210}$Po activities were higher than the UNSCEAR representative $^{210}$Po activities in marine fish, crustaceans, and mollusks (2.4, 6, and 15 Bq/kg $_{freshweight}$) (UNSCEAR, 2000). The activity levels of $^{210}$Po varied greatly among the different marine species. For example, the highest and lowest $^{210}$Pb activities were measured in *Crassostrea gigas* and *Porphyra*, respectively. In general, $^{210}$Po activities in marine organisms ranked in the order bivalves > crustaceans > fishes > macroalgae.

**TABLE 3 |** Average activities of $^{210}$Po and $^{210}$Pb and other radionuclides in seawater/sediment.

| Sea area | $^{210}$Po | $^{210}$Pb | $^{137}$Cs | $^{90}$Sr | $^{238}$U | $^{226}$Ra | $^{40}$K |
|---|---|---|---|---|---|---|---|
| | Seawater (Bq/m$^3$)/Sediment (Bq/kg) | | | | | | |
| Fuqing NPP ($n = 10$) | 2.24/87.8 | 2.51/82.5 | 1.31/1.13 | 0.71/0.17 | 33.6/41.5 | 3.36/31.2 | 11,550/687.9 |
| Ningde NPP ($n = 10$) | 1.07/108.6 | 1.28/104.7 | 1.46/2.08 | 0.74/0.20 | 33.5/51.8 | 2.75/31.2 | 11,510/647.4 |

*$^{134}$Cs and $^{110m}$Ag were undetectable in seawater and sediment.*

**TABLE 4 |** Bioconcentration factors of $^{210}$Po and $^{210}$Pb and other radionuclides in marine organisms sampled in this study.

| Organisms | $^{210}$Po | $^{210}$Pb | $^{137}$Cs | $^{90}$Sr | $^{238}$U | $^{226}$Ra | $^{40}$K |
|---|---|---|---|---|---|---|---|
| *Mugil cephalus* | 1,004 | 591 | 38 | 521 | 79 | 479 | 10 |
| *Gracilaria* | 1,366 | 1,226 | 8 | 42 | 15 | 39 | 9 |
| *Portunus trituberculatus* | 18,321 | 18 | / | 549 | 20 | 363 | 7 |
| *Konosirus punctatus* | 924 | 142 | / | 113 | 7 | 71 | 9 |
| *Porphyra* | 268 | 227 | / | 127 | 4 | 24 | 8 |
| *Sinonovacula constrzcta* | 30,925 | 1,109 | / | 68 | 29 | 131 | 15 |
| *Largehead hairtail* | 30,140 | 133 | 55 | 595 | 4 | 33 | 6 |
| *Crassostrea gigas* | 44,944 | 508 | 21 | 676 | 9 | 15 | 7 |
| *Parapenaeopsis hardwickii* | 12,421 | 109 | 21 | 1,014 | 20 | 193 | 5 |
| *Mantis shrimp* | 20,131 | 234 | 21 | 135 | 18 | 127 | 5 |
| *Larimichthys polyactis* | 14,514 | 3 | / | 41 | 1 | 40 | 6 |
| *Porphyra* | 636 | 55 | / | 122 | 2 | 7 | 4 |
| Fish[a] | 2,000 | 200 | 100 | 3 | 1 | 100 | \ |
| Macroalgae[a] | 1,000 | 1,000 | 5 | 1 | 100 | 100 | \ |
| Crustaceas[a] | 20,000 | 90,000 | 50 | 5 | 10 | 100 | \ |
| Molluscs[a] | 20,000 | 50,000 | 60 | 10 | 30 | 100 | \ |

*/Indicates that the value was below the detection limit or was not determined; \indicates lack of data in the database of IAEA recommended values. [a]IAEA recommended value (IAEA, 2004).*

The accumulation of $^{210}$Po in marine organisms is related to food type, life cycle stage, trophic level, and body size (Carvalho, 2018). Firstly, suspension-feeding bivalves are primary consumers that mainly ingest phytoplankton and detrital particulate organic matter. Crustaceans are opportunistic secondary consumers that mainly ingest benthic organisms. Biomagnification can significantly enhance the $^{210}$Po activity level in bivalves (Fowler, 2011; Dong et al., 2018). Secondly, bivalves that usually live on the bottom showed higher $^{210}$Po activities due to rapid bottom deposition and biological adsorption. The higher $^{210}$Po level in their bodies has been attributed to bioconcentration (Sirelkhatim et al., 2008; Lin, 2018). Finally, $^{210}$Po is typically more concentrated in the digestive tract and hepatopancreas or in the gonads (Carvalho, 2018; Dong et al., 2018; Hurtado-Bermudez et al., 2019). The $^{210}$Po/$^{210}$Pb activity ratios in the present study ranged from 1.1 to 189.7 (**Table 2**). It is reported that both $^{210}$Po and $^{210}$Pb bind strongly to organisms, and that $^{210}$Pb is preferably associated with the mineral fractions of bones and shells. Compared with $^{210}$Pb, $^{210}$Po is primarily associated with proteins in organisms and can penetrate the cell cytoplasm. Therefore, $^{210}$Po can be more effectively assimilated in marine organisms than $^{210}$Pb, resulting in $^{210}$Po/$^{210}$Pb activity ratios >1 in most marine organisms (Stewart et al., 2008).

As shown in **Table 2**, the activities of $^{137}$Cs, $^{90}$Sr, $^{238}$U, $^{226}$Ra, and $^{40}$K ranged from undetectable to 0.08,0.03–0.75,0.04–2.66,0.02–1.61, and 51.−174.9 Bq/kg $_{\text{freshweight}}$, respectively. The activity levels ranked in the order $^{40}$K > $^{210}$Po > $^{210}$Pb > $^{238}$U > $^{226}$ Ra > $^{90}$Sr > $^{137}$Cs. The activity levels of $^{90}$Sr and $^{137}$Cs in marine organisms were $\sim10^{-2}$ to $\sim10^{-1}$ Bq/kg $_{\text{freshweight}}$, which is within background levels (Liu and Zhou, 2000; Chen et al., 2003; Zhang, 2015; Lou et al., 2018). Those of $^{90}$Sr and $^{137}$Cs activities in fish, meat, and shrimp established by the Chinese National Standard on limited concentrations of radioactive materials in foods are 290 and 800 Bq/kg $_{\text{freshweight}}$, respectively (Ministry of Health of the People's Republic of China, 1994). The radioisotope $^{210}$Po is the major natural decay product from the uranium series and provides the largest radiation dose to the human body *via* consumption of marine organisms (UNSCEAR, 2000; Carvalho, 2011; Khot et al., 2021; Kong et al., 2021). Indeed, the scavenging rate of $^{210}$Po is higher than that of other radionuclides in the atmospheric environment (Alam and Mohamed, 2011), resulting in high $^{210}$Po deposition in the marine environment. In turn, marine organisms show a stronger

affinity for $^{210}$Po than for other radionuclides (Bogdan, 1997; Lin, 2018), resulting in a higher activity level of $^{210}$Po than that of other radionuclides. The activity levels of $^{90}$Sr and $^{137}$Cs in marine organisms in the present study are far below these values. The average activities of $^{210}$Po and $^{210}$Pb as well as other radionuclides in seawater and sediment in the sea area adjacent to Fuqing and Ningde NPPs are listed in **Table 3**. The data in **Tables 2**, **3** were used to estimate the radiation doses for the corresponding marine organisms.

## Bioaccumulation of $^{210}$Po and $^{210}$Pb and Other Radionuclides in Marine Organisms

The bioconcentration factor is defined as the activity ratio of a radionuclide in the marine organism or biota to that in ambient seawater (L/kg) and is an indicator of the accumulation capacity of a given organism for a particular nuclide (Arnot and Gobas, 2006; Alava and Gobas, 2016; Ishii et al., 2020). Bioconcentration factors in different radionuclides vary widely due to their different biochemical properties, while bioconcentration factors (BCFs) in different marine organisms differ greatly due to their different bioaccumulation capacities. Even within the same species, BCFs vary among individuals due to differences in physiology, microhabitat, etc. For the sake of convenience and standardization, a set of values for different radionuclides and different kinds of marine organisms was recommended by the IAEA (**Table 4**) (IAEA, 2004). Using the data for seawater and marine organism samples in the present study, the BCFs of $^{210}$Po and $^{210}$Pb as well as those of other radionuclides can be estimated (**Table 4**). The BCFs for $^{210}$Po and $^{210}$Pb were in the ranges 636–44,944 and 3–1,226, respectively. BCFs of $^{137}$Cs, $^{90}$Sr, $^{238}$U, $^{226}$Ra, and $^{40}$K were in the range 5–55, 41–1,014, 1–79, 7–479, and 4–15 L/g $_{\text{freshweight}}$, respectively. The BCF data reported in this study provide a useful supplement of information for the IAEA database.

## Radiation Dose Assessment

The radiation doses for nonhuman species have become an issue of increasing public health concern. The ERICA tools downloaded freely from the internet are widely used for radiation assessment (Garnier-Laplace et al., 2011; Johansen et al., 2015; Men et al., 2017, 2020a,b). As shown in **Tables 1**–**4**, the radiation doses received by marine organisms in the studied area were assessed, using the ERICA tools. The internal and external dose rates derived for each radionuclide and the total radiation dose rates are listed in **Table 5**. The total dose rates ranged from 0.037 to 1.531 μSv/h. Around the Ningde NPP, the highest and lowest radiation doses were observed in *Crassostrea gigas* and *Porphyra*, respectively. Overall, these values are markedly lower than the ERICA ecosystem screening benchmark of 10 μGy/h (Beresford et al., 2007) and the most conservative safety benchmark, which is one to two orders of magnitude lower than the International Commission on Radiological Protection (ICRP)-derived reference levels for corresponding reference animals or plants (ICRP, 2008; Fisher et al., 2013; Men et al., 2017). This suggested that there are no irradiation effects on marine organisms in the area adjacent to Fuqing and Ningde NPPs.

**TABLE 5 |** Internal and external radiation dose rates derived for each radionuclide for the different marine species sampled in this study (in μSv/h).

| Orginisms | $^{210}$Po | | $^{210}$Pb | | $^{137}$Cs | | $^{90}$Sr | | $^{238}$U | | $^{226}$Ra | | $^{40}$K | | Total |
|---|---|---|---|---|---|---|---|---|---|---|---|---|---|---|---|
| | Internal | External | Internal | External | Internal | External | Internal | External | Internal | External | Internal | External | Internal | External | |
| *Mugil cephalus* | 68.7 | 0.000000007 | 0.337 | 0.000007 | 0.009 | 0.0004 | 0.23 | 0.00002 | 64.3 | 0.000004 | 223.5 | 0.003 | 36.9 | 1.0 | 394.9 |
| *Graciaria* | 93.5 | 0.000000008 | 0.514 | 0.000121 | 0.001 | 0.0005 | 0.01 | 0.00020 | 12.1 | 0.000021 | 18.0 | 0.004 | 20.3 | 2.3 | 146.7 |
| *Portunus trituberculatus* | 1,253.9 | 0.000199604 | 0.010 | 0.240170 | / | 0.2235 | 0.24 | 0.00240 | 16.7 | 0.002909 | 169.3 | 13.283 | 24.6 | 27.8 | 1,506.3 |
| *Konosirus punctatus* | 63.2 | 0.000000007 | 0.080 | 0.000013 | / | 0.0004 | 0.05 | 0.00003 | 6.0 | 0.000007 | 33.3 | 0.003 | 31.5 | 1.1 | 135.4 |
| *Porphyra (Fuqing NPP)* | 18.3 | 0.000000007 | 0.123 | 0.000027 | / | 0.0004 | 0.05 | 0.00007 | 3.1 | 0.000012 | 11.1 | 0.003 | 25.7 | 1.3 | 59.8 |
| *Sinonovacula constrzcta* | 1,011.0 | 0.000476112 | 0.345 | 1.459055 | / | 0.5396 | 0.03 | 0.01597 | 24.9 | 0.015291 | 49.9 | 32.585 | 48.6 | 75.5 | 1,244.9 |
| *Largehead hairtail* | 985.3 | 0.000000007 | 0.043 | 0.000010 | 0.014 | 0.0004 | 0.27 | 0.00003 | 3.6 | 0.000005 | 12.5 | 0.003 | 18.9 | 1.1 | 1,021.8 |
| *Crassostrea gigas* | 1,469.3 | 0.000116337 | 0.162 | 0.230209 | 0.005 | 0.1313 | 0.30 | 0.00246 | 8.0 | 0.002707 | 5.5 | 7.824 | 22.1 | 17.8 | 1,531.3 |
| *Parapenaeopsis hardwickii* | 406.0 | 0.000285720 | 0.034 | 0.903700 | 0.004 | 0.3241 | 0.43 | 0.00953 | 17.2 | 0.009096 | 73.5 | 19.541 | 15.8 | 46.1 | 579.8 |
| *Mantis shrimp* | 658.1 | 0.000235172 | 0.074 | 0.544626 | 0.005 | 0.2655 | 0.06 | 0.00588 | 15.7 | 0.006198 | 48.5 | 15.889 | 15.8 | 35.9 | 790.9 |
| *Larimichthys polyactis* | 474.5 | 0.000000007 | 0.001 | 0.000017 | / | 0.0004 | 0.02 | 0.00004 | 1.0 | 0.000008 | 15.3 | 0.003 | 20.8 | 1.2 | 512.8 |
| *Porphyra (Ningde NPP)* | 20.8 | 0.000000008 | 0.013 | 0.000126 | / | 0.0005 | 0.03 | 0.00021 | 1.7 | 0.000021 | 2.8 | 0.004 | 9.5 | 2.4 | 37.1 |

*/Lack of data due to the fact that the activities of $^{137}$Cs in marine organisms were below the MDA.*

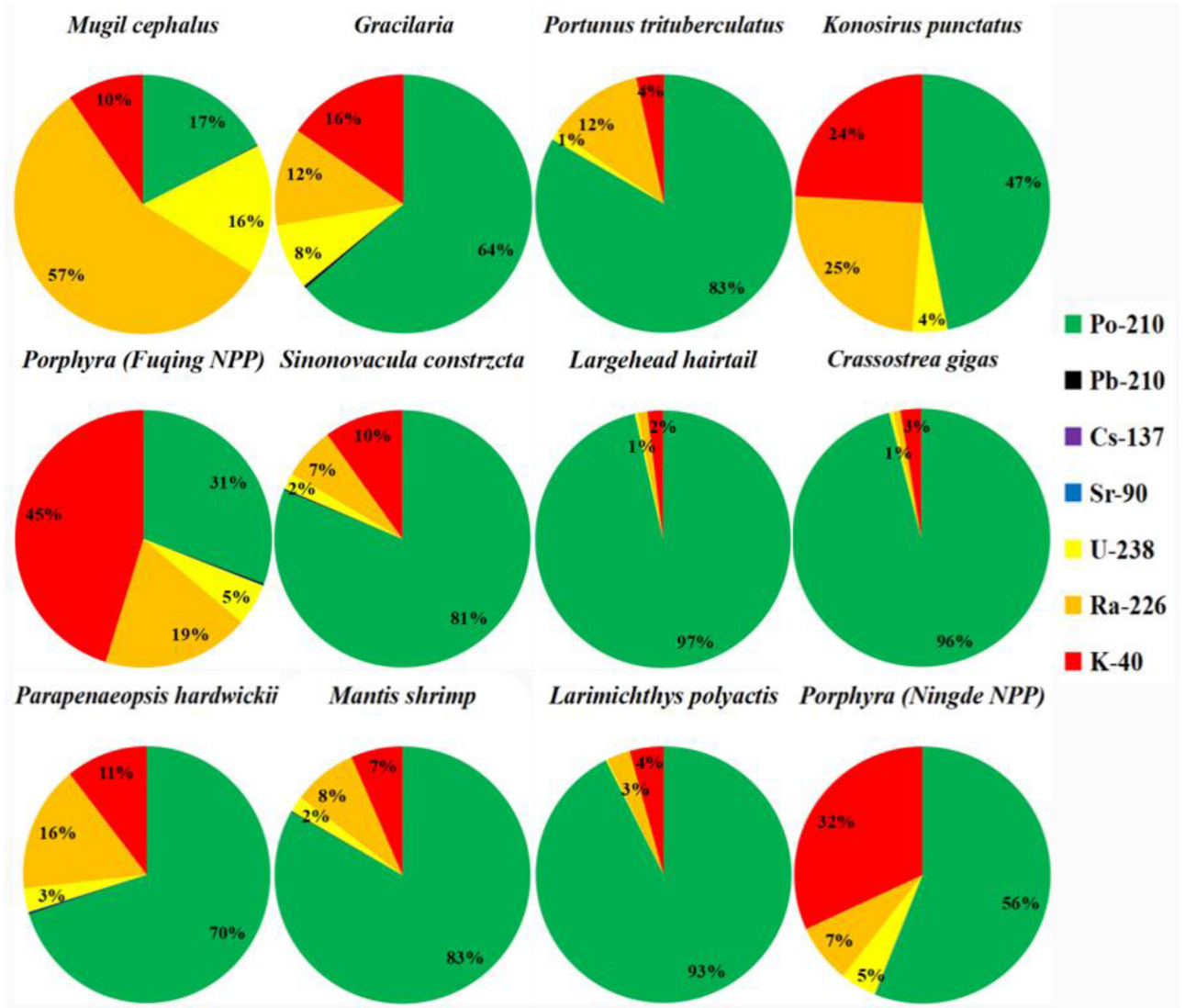


**FIGURE 3 |** Dose contributions of each radionuclide for the different marine organisms sampled in this study.

The dose contributions of different nuclides in different species were plotted in **Figure 3** and show that $^{210}$Po was the dominant dose contributor except for *Mugil cephalus* and *Porphyra* (Fuqing NPP) (47–97%), while $^{226}$Ra and $^{40}$K were the main dose contributors for *Mugil cephalus* and *Porphyra* (Fuqing NPP), respectively. The contribution from external and internal doses for each nuclide (**Table 5**) suggests that the internal doses were much greater than the external doses. In general, the greatest internal dose should be from $^{210}$Po sources because of its alpha emissions. Additional main contributors should be $^{226}$Ra and $^{238}$U, which produced intermediate internal doses because of alpha emissions. Due to high-activity levels in seawater (∼11,500 Bq/m$^3$) and marine organisms (51−174.9 Bq/kg $_{\text{freshweight}}$) as well as emitted high-energy γ-rays (1,460 keV), $^{40}$K generated much higher internal and external dose rates than $^{210}$Pb, $^{137}$Cs, and $^{90}$Sr (EI-Arabi, 2007). Indeed, the dose contribution from $^{137}$Cs and $^{90}$Sr was <0.13%, which was extremely low compared to that of naturally occurring radionuclides.

## Radiation Dose Assessment for Humans

The calculated committed effective dose for humans from ingestion of marine organisms in the area adjacent to Fuqing and Ningde NPPs was 60.74–2,990.41 μSv (**Table 6**). Results show that a maximum committed dose of 2.99 mSv will be received over the following 50 years based on assumed consumption of 50.97 kg of these marine organisms in 1 year. In terms of species, *Porphyra* had the lowest committed effective dose to humans (<100 μSv), while *Portunus trituberculatus*, *Sinonovacula constrzcta*, *Largehead hairtail*, *Crassostrea gigas*, and *Mantis shrimp* had committed effective doses exceeding

**TABLE 6 |** Committed effective dose[a] to humans (in μSv) from the ingestion of various marine organisms (annual consumption).

| Radionuclide | DC[b] | *Mugil cephalus* | *Gracilaria* | *Portunus trituberculatus* | *Konosirus punctatus* | *Porphyra* (Fuqing NPP) | *Sinonovacula constrzcta* | *Largehead hairtail* | *Crassostrea gigas* | *Parapenaeopsis hardwickii* | *Mantis shrimp* | *Larimichthys polyactis* | *Porphyra* (Ningde NPP) |
|---|---|---|---|---|---|---|---|---|---|---|---|---|---|
| | nSv/Bq | | | | | | | | | | | | |
| $^{210}$Po | 1,200 | 137.62 | 187.16 | 2,510.17 | 126.61 | 36.70 | 2,023.92 | 1,972.54 | 2,941.38 | 812.87 | 1,317.47 | 949.88 | 41.59 |
| $^{210}$Pb | 690 | 46.78 | 97.07 | 1.41 | 11.25 | 17.94 | 49.94 | 5.98 | 22.86 | 4.92 | 10.55 | 0.14 | 2.46 |
| $^{137}$Cs | 13 | / | 0.01 | / | / | / | / | 0.05 | 0.02 | 0.02 | 0.02 | / | / |
| $^{90}$Sr | 28 | 0.53 | 0.04 | 0.56 | 0.11 | 0.13 | 0.07 | 0.63 | 0.71 | 1.07 | 0.14 | 0.04 | 0.13 |
| $^{238}$U | 45 | 6.10 | 1.15 | 1.58 | 0.57 | 0.30 | 2.36 | 0.34 | 0.76 | 1.63 | 1.49 | 0.09 | 0.16 |
| $^{226}$Ra | 280 | 22.98 | 1.86 | 17.41 | 3.43 | 1.14 | 5.14 | 1.28 | 0.57 | 7.56 | 5.00 | 1.57 | 0.29 |
| $^{40}$K | 6.2 | 38.27 | 33.69 | 25.88 | 34.03 | 29.52 | 55.27 | 20.13 | 24.11 | 17.98 | 17.51 | 22.91 | 16.12 |
| Sum | | 252.30 | 320.97 | 2,557.01 | 176.01 | 85.72 | 2,136.70 | 2,000.96 | 2,990.41 | 846.06 | 1,352.18 | 974.63 | 60.74 |

*/Indicates that the value was below the MDA. [a]The annual per capita consumption rates of the Chinese population (50.97 kg/year) are for all types of seafood combined, whereas the dose calculations in this study conservatively assumed that the entire consumption consisted solely of a given sample species. The assumed exposure time is 50 years for adults. [b]DC (dose coefficients) radionuclide–specific committed effective dose coefficients for adult human ingestion (ICRP, 2012).*

1,000 μSv. *Crassostrea gigas* produced radiation doses close to 3,000 Sv. The contribution of $^{210}$Po to these committed effective doses was 43–99%. Based on this assumed consumption, the committed effective dose in 1 year (∼0.06 mSv) was far below the 1-m Sv standard (Ministry of Environmental Protection of China, 2002). It is, therefore, safe to consume these marine organisms. The contributions of different nuclides ranked in the order $^{210}$Po > $^{210}$Pb/$^{40}$K > $^{226}$Ra > $^{238}$U > $^{90}$Sr > $^{137}$Cs, where $^{210}$Po was the dominant contributor to the committed effective dose at 43–99%. In contrast, the artificial nuclides $^{90}$Sr and $^{137}$Cs contributed only 0.03–2.2%, and thus made the lowest contribution. This suggests that the committed effective dose from anthropogenic nuclides $^{90}$Sr and $^{137}$Cs is negligible when the NPPs are in operation.

## CONCLUSIONS

The activity levels of $^{210}$Po and $^{210}$Pb in fishes (*Mugil cephalus, Konosirus punctatus, Largehead hairtail, Larimichthys polyactis*), crustaceans (*Mantis shrimp, Parapenaeopsis hardwickii, Portunus trituberculatus*), bivalve mollusks (*Crassostrea gigas, Sinonovacula conzcta*), and macroalgae (*Gracilaria, Porphyra*) collected in coastal waters adjacent to Fuqing and Ningde NPPs were in the range 0.60–48.09 Bq/kg $_{\text{freshweight}}$ and 0.07–2.76 Bq/kg $_{\text{freshweight}}$, respectively. The activity ratios of $^{210}$Po/$^{210}$Pb were in the range 1.1–189.7; calculated BCFs of $^{210}$Po and $^{210}$Pb in marine organisms were 636–44,944 and 3–1,226 L/kg, respectively. The radiation dose rates in the studied marine organisms, ranging from 0.037 to 1.531 μSv/h, were markedly lower than the ERICA ecosystem screening benchmark of 10 μGy/h, suggesting that there were no detectable irradiation effects on the marine organisms studied. The committed effective dose to humans from ingestion of these marine organisms was in the range of 0.06–2.99 mSv. Overall, when the Fuqing and Ningde NPPs are in operation, $^{210}$Po is the dominant radiation dose contributor to both marine organisms and humans, and the dose contributions from artificial nuclides $^{90}$Sr and $^{137}$Cs can be considered negligible.

## DATA AVAILABILITY STATEMENT

The original contributions presented in the study are included in the article/supplementary material, further inquiries can be directed to the corresponding author/s.

## ETHICS STATEMENT

The animal study was reviewed and approved by Third Institute of Oceanography.

## AUTHOR CONTRIBUTIONS

WM designed this work and performed the data analysis. JS performed the sample analysis and radiation assessment. JS and WM wrote the manuscript together. FW and JW edited this manuscript. All authors contributed to the article and approved the submitted version.

## FUNDING

This work was supported by the guided project of the Department of Science and Technology of Fujian Province (2018Y0058), the National Natural Science Foundation of China (41776091, 42076038), Key Special Project for Introduced Talents Team of Southern Marine Science and Engineering Guangdong Laboratory (Guangzhou) (GML2019ZD0606), the Natural Science Foundation of Guangdong Province (2021A1515011886), STU Scientific Research Foundation for Talents (NTF18011), and the Open Fund of the Laboratory for Ocean Dynamics and Climate, the Pilot Qingdao National Laboratory for Marine Science and Technology (No. OCFL-201801).

## REFERENCES

Aba, A., Ismaeel, A., Al-Boloushi, O., Al-Shammari, H., Al-Boloushi, A., and Malak, M. (2020). Atmospheric residence times and excess of unsupported $^{210}$Po in aerosol samples from the Kuwait bay-northern gulf. *Chemosphere* 261:127690. doi: 10.1016/j.chemosphere.2020.127690

Alam, L., and Mohamed, C. A. R. (2011). A mini review on bioaccumulation of $^{210}$Po by marine organisms. *Int. Food Res. J.* 18, 1–10.

Alava, J. J., and Gobas, F. A. (2016). Modeling $^{137}$Cs bioaccumulation in the salmon-resident killer whale food web of the Northeastern Pacific following the Fukushima Nuclear Accident. *Sci. Total Environ.* 544, 56–67. doi: 10.1016/j.scitotenv.2015.11.097

Arnot, J. A., and Gobas, F. A. (2006). A review of bioconcentration factor (BCF) and bioaccumulation factor (BAF) assessments for organic chemicals in aquatic organisms. *Environ. Rev.* 14, 257–297. doi: 10.1139/a06-005

Bam, W., and Maiti, K. (2021). $^{210}$Po-$^{210}$Pb distribution and carbon export in the northern Gulf of Mexico continental slope. *Deep Sea Res Part I* 172:103535. doi: 10.1016/j.dsr.2021.103535

Beresford, N., Brown, J., Copplestone, D., Garnier-Laplace, J., Howard, B., Larsson, C., et al. (2007). *An Integrated Approach to the Assessment and Management of Environmental Risks from Ionizing Radiation. Description of Purpose, Methodology and Application (EC Project Contract No. FI6R-CT-2004-508847)*, June 17, 2005. Available online at: https://www.erica-project.org

Bogdan, S. (1997). Polonium, uranium and plutonium in the southern Baltic Sea. *Ambio* 26, 113.

Carvalho, F. P. (2011). Polonium ($^{210}$Po) and lead ($^{210}$Pb) in marine organisms and their transfer in marine food chains. *J. Environ. Radioact.* 102, 462–472. doi: 10.1016/j.jenvrad.2010.10.011

Carvalho, F. P. (2018). Radionuclide concentration processes in marine organisms: a comprehensive review. *J. Environ. Radioact.* 186, 124–130. doi: 10.1016/j.jenvrad.2017.11.002

Chen, Z. D., Lin, Q., Deng, F., Liu, Y., Song, H. Q., and Li, L. J. (2003). "Radioactivity levels of $^{90}$Sr and $^{137}$Cs in Marine media around the Daya Bay Nuclear Power Plant," in *Compilation of papers from the National Symposium on Monitoring and Evaluation of Radioactive Effluents and the Environment*, Hangzhou, 110–115.

Dong, X. F., Chen, L., Pan, J. S., Wang, J. C., Zhou, S. L.,Cao, Z. G., et al. (2018). $^{210}$Po level in five kinds of typical aquatic products from the yellow sea of China. *J. Nucl. Radiochem.* 40, 67–73. doi: 10.7538/hhx.2018.40.01.0067

EI-Arabi, A. M. (2007). $^{226}$Ra, $^{232}$Th and $^{40}$K concentrations in igneous rocks from eastern desert, Egypt and its radiological implications. *Radiat. Meas.* 42, 94–100. doi: 10.1016/j.radmeas.2006.06.008

FAOSTAT (2018). *Data on Food Balance Sheet of China in 2018*. Available online at: http://www.fao.org/faostat/zh/#data/FBS (accessed December 2018).

Fisher, N. S., Beaugelin-Seiller, K., Hinton, T. G., Baumanna, Z., Madigan, D. J., and GarnierLaplace, J. (2013). Evaluation of radiation doses and associated risk from the Fukushima nuclear accident to marine biota and human consumers of seafood. *Proc. Natl. Acad. Sci. U. S. A.* 110, 10670–10675. doi: 10.1073/pnas.1221834110

Fowler, S. W. (2011). $^{210}$Po in the marine environment with emphasis on its behaviour within the biosphere. *J. Environ. Radioact.* 102, 448–461. doi: 10.1016/j.jenvrad.2010.10.008

Garnier-Laplace, J., Beaugelin-Seiller, K., and Hinton, T. G. (2011). Fukushima wildlife dose reconstruction signals eclolgical consequences. *Environ. Sci. Technol.* 45, 5077–5078. doi: 10.1021/es201637c

Hurtado-Bermudez, S., Valencia, J. M., Rivera-Silva, J., Mas, J. L., Aparicio, I., Santos, J. L., et al. (2019). Levels of radionuclide concentrations in benthic invertebrate species from the Balearic Islands, Western Mediterranean, during 2012-2018. *Mar. Pollut. Bull.* 149:110519. doi: 10.1016/j.marpolbul.2019.110519

IAEA (2004). *IAEA Technical Reports, Series No. 422. ccc. 2004*, 1–95.

IAEA (2005). *Worldwide Marine Radioactivity Studies, Radionuclide Levels in the Oceans and Seas*. IAEA-TECDOC-1429. Vienna: IAEA, 187.

ICRP (2007). The 2007 Recommendations of the International Commission on Radiological Protection. ICRP Publication 103. *Ann. ICRP* 37. doi: 10.1016/j.icrp.2007.10.003

ICRP (2008). Environmental Protection: The Concept and Use of Reference Animals and Plants. ICRP Publication 108. *Ann. ICRP* 3.

ICRP (2012). Compendium of dose coefficients based on ICRP publication 60. ICRP publication 119. *Ann ICRP.* 41(Suppl.):1–130. doi: 10.1016/j.icrp.2012.06.038

Ishii, Y., Matsuzaki, S., and Hayashi, S. (2020). Different factors determine 137Cs concentration factors of freshwater fish and aquatic organisms in lake and river ecosystems. *J. Environ. Radioact.* 213:106102. doi: 10.1016/j.jenvrad.2019.106102

Johansen, M. P., Ruedig, E., Tagami, K., Uchida, S., and Higley, K. (2015). Radiological dose rates to marine fish from the Fukushima Daiichi Accident: the first three years across the North Pacific. *Environ. Sci. Technol.* 49, 1277–1285. doi: 10.1021/es505064d

Khot, M., Chinnaesakki, S., Bara, S. V., Ravi, P. M., and Jaiswar, A. K. (2021). Baseline radionuclide concentration in commercially important brachyuran crabs around Mumbai and Sindhudurg of Maharashtra, India. *J. Radioanal. Nucl. Chem.* 327, 1055–1062. doi: 10.1007/s10967-020-07585-9

Kong, X., Qian, Y., Zheng, Q., and Ji, Y. (2021). Levels and distributions of $^{210}$Pb and $^{210}$Po in selected seafood samples in China and assessment of related dose to population. *Int. J. Environ. Res. Public Health* 18:3036. doi: 10.3390/ijerph18063036

Li, P. X., Li, Z., Zhang, J., Gao, Z. Q., Wang, J. R., Song, Q. N., et al. (2018). Contents of $^{210}$Po in some aquatic organisms and its distribution in different parts of shrimp's bodies. *Radiat. Protect.* 38, 15–18 (in Chinese).

Li, P. X., Li, Z., Zhang, J., Yang, H. L., Gao, Z. Q., Jiang, K., et al. (2016). Determination of $^{210}$Po in food and processed products and estimation of internal dose. *J. Nucl. Radiochem.* 38, 103–106. doi: 10.7538/hhx.2016.38.02.0103

Lin, K. (2018). *The Research of $^{210}$Po and $^{210}$Pb in Marine Environmental Media*. Master Thesis, Nan Hua University, Hengyang.

Lin, Y. Q., Wang, X. Q., Wang, H. J., Cai, J. M., Luo, J. G., and Zhang, Y. (2016). Study on enrichment of $^{210}$Po in shellfish in sea area around nuclear power plant. *Proceedings of the third Academic Exchange conference of Guangdong Occupational Health Association* (Huizhou), 332?334 (in Chinese).

Liu, G. S. (2010). *Isotopic Oceanography*. Zhengzhou: Zhengzhou University Press, 1–298 (in Chinese).

Liu, G. S., and Zhou, C. Y. (2000). Contents and behavior characteristics of $^{137}$Cs and $^{90}$Sr in various mediums of Daya Bay. *J. Oceanogr. Taiwan Strait* 19, 261–268 (in Chinese). doi: 10.3969/j.issn.1000-8160.2000.03.001

Lou, H. L., Lu, Y., Qin, W. C., Liu, T., Shuang, H. Y., Hou, S. G., et al. (2018). Radioactivity levels of $^{137}$Cs and $^{90}$Sr in organisms and estimation of internal dose around Tianwan nuclear power station. *Nucl. Electr. Detect. Technol.* 38, 241–244.

Men, W., Deng, F. F., He, J. H., Yu, W., Wang, F. F., Li, Y. L., et al. (2017). Radioactive impacts on nekton species in the Northwest Pacific and humans more than one year after the Fukushima nuclear accident. *Ecotoxicol. Environ. Saf.* 144, 601–610. doi: 10.1016/j.ecoenv.2017.06.042

Men, W., Wang, F. F., Yu, W., He, J. H., Lin, F., and Deng, F. F. (2020a). Impact of the Fukushima daiichi nuclear power plant accident on the neon flying squids in the Northwest pacific from 2011 to 2018. *Environ. Pollut*. 264:114647. doi: 10.1016/j.envpol.2020.114647

Men, W., Wang, F. F., Yu, W., He, J. H., Lin, F., Deng, F. F., et al. (2020b). Impact of the Fukushima Dai-ichi Nuclear Power Plant Accident on dolphin fishes in the Northwest Pacific. *Chemosphere* 257:127267. doi: 10.1016/j.chemosphere.2020.127267

Ministry of Environmental Protection of China. (2002). *Basic Standards for Protection Against Ionizing Radiation and for the Safety of Radiation Sources, October 8, 2002, GB18871–2002*.

Ministry of Health of the People's Republic of China. (1994). *Limited concentrations of radioactive materials in foods*. 22 February 1994. GB 14882-94.

Seiler, R. L., and Wiemels, J. L. (2012). Occurrence of $^{210}$Po and biological effects of low-level exposure: the need for research. *Environ. Health Perspect*. 120, 1230–1237. doi: 10.1289/ehp.1104607

Sirelkhatim, D. A., Sam, A. K., and Hassona, R. K. (2008). Distribution of $^{226}$Ra-$^{210}$Pb-$^{210}$Po in marine biota and surface sediments of the Red Sea, Sudan. *J. Environ. Radioact*. 99, 1825–1828. doi: 10.1016/j.jenvrad.2008.07.008

Sivakumar, R. (2014). An assessment of the $^{210}$Po ingestion dose due to the consumption of agricultural, marine, fresh water and forest foodstuffs in Gudalore (India). *J. Environ. Radioact*. 137, 96–104. doi: 10.1016/j.jenvrad.2014.06.019

State Oceanic Administration of China (2011). *Technical Specification for Marine Radioactivity Monitoring. No.10. Haihuanzi.*

Stewart, G. M., Fowler, S. W., and Fisher, N. S. (2008). The bioaccumulation of U-series and Th-series radionuclides in marine organisms. *Radioact. Environ*. 13, 269–305. doi: 10.1016/S1569-4860(07)00008-3

Strady, E., Harmelin-Vivien, M., Chiffoleau, J. F., Veron, A., Tronczynski, J., and Radakovitch, O. (2015). $^{210}$Po and $^{210}$Pb trophic transfer within the phytoplankton-zooplankton-anchovy/sardine food web: a case study from the Gulf of Lion (NW Mediterranean Sea). *J. Environ. Radioact*. 143, 141–151. doi: 10.1016/j.jenvrad.2015.02.019

Štrok, M., and Smodiš, B. (2011). Level of $^{210}$Po and $^{210}$Pb in fish and molluscs in Slovenia and the related dose assessment to the population. *Chemosphere* 82, 970–976. doi: 10.1016/j.chemosphere.2010.10.075

UNSCEAR (2000). *UNSCEAR Report 2000, Sources and Effects of Ionizing Radiation*. United Nations Scientific Committee on the Effects of Atomic Radiation.

Yu, W., Johansen, M. P., He, J. H., Men, W., and Lin, L. S. (2018). Artificial radionuclides in neon flying squid from the northwestern Pacific in 2011 following the Fukushima accident. *Biogeosciences* 15, 7235–7242. doi: 10.5194/bg-15-7235-2018

Zhang, L. H., Yang, W. F., Chen, M., Zhu, Y. N., Wang, Z., Fang, Z. M., et al. (2020). Distribution patterns of $^{210}$Po, $^{210}$Pb and the particle export in the Taiwan Strait during the winter. *Acta Oceanol. Sin*. 39, 12–21. doi: 10.1007/s13131-020-1550-z

Zhang, X. L. (2015). *Investigation of Environmental Radiation Background Organisms Strontium-90 and Cesium-137 at Haiyang Nuclear Power Plant in Shandong Province and the Effect of Fukushima Nuclear Accident on Them*. Master Thesis, Soochow University, Suzhou.

**Conflict of Interest:** The authors declare that the research was conducted in the absence of any commercial or financial relationships that could be construed as a potential conflict of interest.

**Publisher's Note:** All claims expressed in this article are solely those of the authors and do not necessarily represent those of their affiliated organizations, or those of the publisher, the editors and the reviewers. Any product that may be evaluated in this article, or claim that may be made by its manufacturer, is not guaranteed or endorsed by the publisher.

*Copyright © 2021 Sun, Men, Wang and Wu. This is an open-access article distributed under the terms of the Creative Commons Attribution License (CC BY). The use, distribution or reproduction in other forums is permitted, provided the original author(s) and the copyright owner(s) are credited and that the original publication in this journal is cited, in accordance with accepted academic practice. No use, distribution or reproduction is permitted which does not comply with these terms.*

frontiers in Marine Science

ORIGINAL RESEARCH
published: 02 November 2021
doi: 10.3389/fmars.2021.716688

# $^{210}$Po/$^{210}$Pb Disequilibria in the Eastern Tropical North Pacific

*Qiang Ma[1,2], Yusheng Qiu[1], Run Zhang[1], E Lv[1], Yipu Huang[1] and Min Chen[1]**

[1] College of Ocean and Earth Sciences, Xiamen University, Xiamen, China, [2] Key Laboratory of Estuarine Ecological Security and Environmental Health, Xiamen University Tan Kah Kee College, Zhangzhou, China

The $^{210}$Po/$^{210}$Pb disequilibrium was attempted to reveal the small-scale particle dynamics in the eastern tropical North Pacific. Seawater samples in the full water column were collected from three sites in the Tehuantepec bowl near the East Pacific Ridge for determination of dissolved and particulate $^{210}$Po and $^{210}$Pb. Our results show that TPo/TPb activity ratios in the full water column at the three sites are less than 1, with an average of 0.56, indicating that the total $^{210}$Po in the oligotrophic sea is significantly deficient. The activity ratios of DPo/DPb in the dissolved phase are less than 1, while those in the particulate phase are greater than 1 (except for the bottom 300 m), indicating fractionation between $^{210}$Po and $^{210}$Pb in the scavenging process. A negative linear relationship between $^{210}$Po deficit and silicate proves that biological activities are responsible for $^{210}$Po deficiency in the upper 200 m. However, the deficit of $^{210}$Po in the bottom 300 m may be caused by the horizontal transport of the hydrothermal plume. After correcting the horizontal contribution, the removal rates of $^{210}$Po for the 200–1,500 m and the bottom 300 m layers increased by 7.5–21 and 26.1–29.5%, respectively. Correspondingly, the variation range of the residence time of a total $^{210}$Po became smaller. Our calculations suggest that horizontal transport is acting as a stabilizer for small-scale variation in the $^{210}$Po deficit in the eastern tropical North Pacific. Our study highlights the need to pay more attention to the small-scale variation of $^{210}$Po deficit when applying $^{210}$Po/$^{210}$Pb disequilibria to trace biogeochemical processes, and the mechanism responsible for this variation deserves further study.

**Keywords: $^{210}$Po, $^{210}$Pb, horizontal transport, eastern tropical North Pacific, particle dynamics**

OPEN ACCESS

***Edited by:***
*Jinzhou Du,*
*East China Normal University, China*

***Reviewed by:***
*Jana Friedrich,*
*Helmholtz Centre for Materials and Coastal Research (HZG), Germany*
*Tsuneo Ono,*
*Japan Fisheries Research and Education Agency (FRA), Japan*

****Correspondence:***
*Min Chen*
*mchen@xmu.edu.cn*

***Specialty section:***
*This article was submitted to Marine Biogeochemistry, a section of the journal Frontiers in Marine Science*

***Received:*** *29 May 2021*
***Accepted:*** *05 October 2021*
***Published:*** *02 November 2021*

***Citation:***
*Ma Q, Qiu Y, Zhang R, Lv E, Huang Y and Chen M (2021) $^{210}$Po/$^{210}$Pb Disequilibria in the Eastern Tropical North Pacific. Front. Mar. Sci. 8:716688. doi: 10.3389/fmars.2021.716688*

## INTRODUCTION

The $^{210}$Pb ($T_{1/2}$ = 22.3 a) in seawater mainly comes from two sources, one is atmospheric deposition, and the other is *in situ* decay of $^{226}$Ra in seawater. The radioactive decay of $^{222}$Rn in the atmosphere produces $^{210}$Pb, which is adsorbed by aerosols and sinks into the ocean. Atmospheric deposition is the main source of $^{210}$Pb in surface seawater. Unlike the upper water that is affected by atmospheric deposition, $^{210}$Pb in deep water is mainly produced by the *in situ* decay of $^{226}$Ra (Cochran, 1992). The source of $^{210}$Po ($T_{1/2}$ = 138.4 days) is mainly produced by the *in situ* decay of its parent $^{210}$Pb in seawater. Atmospheric deposition contributes a little to $^{210}$Po in surface seawater, since the activity ratio of $^{210}$Po/$^{210}$Pb in atmospheric aerosols is as low as about 0.1 (Burton and Stewart, 1960; Lambert and Nezami, 1965; Bacon et al., 1976), which is significantly lower than that in surface water (∼0.5, Shannon et al., 1970; Nozaki et al., 1976).

Although both $^{210}$Po and $^{210}$Pb are particle-reactive nuclides, their biogeochemical pathways are not exactly the same (Chuang et al., 2013; Yang et al., 2013). Previous studies have shown that $^{210}$Pb is more likely adsorbed to the cell wall or scavenged by inorganic particles, while $^{210}$Po is preferentially absorbed by organisms or adsorbed by organic particles (Fisher et al., 1983; Nozaki et al., 1998; Friedrich and Rutgers van der Loeff, 2002). In the process of particle settling, with the remineralization of particulate organic matter, $^{210}$Po is preferentially released back into seawater than $^{210}$Pb (Bacon et al., 1976; Kadko, 1993). It is estimated that at least 50% of the $^{210}$Po exported from the mixed layer is remineralized in the thermocline, while for $^{210}$Pb it is less than 5% (Bacon et al., 1976). In comparison, the biogeochemical behavior of $^{210}$Po is more similar to that of a nutrient (Bacon et al., 1976; Kharkar et al., 1976; Nozaki et al., 1991; Kadko, 1993). The difference in biogeochemical cycles makes it possible to use $^{210}$Po/$^{210}$Pb disequilibrium to track particle dynamics on seasonal or inter-annual time scales in the marine environment.

The disequilibrium between $^{210}$Po and $^{210}$Pb is common in the euphotic zone because of active biological activities. However, because of the scarcity of particles, $^{210}$Po and $^{210}$Pb tend to reach radioactive equilibrium in deep water, such as in the North Atlantic (Bacon et al., 1976, 1988), the Pacific (Turekian and Nozaki, 1980), and the eastern and central Indian Ocean (Cochran et al., 1983). Recently, the deficiency of $^{210}$Po with respect to $^{210}$Pb has been increasingly found in mesopelagic waters, such as in the Sargasso Sea (Kim, 2001), Aleutian Basin (Hu et al., 2014), South China Sea (SCS) (Chung and Wu, 2005; Wei et al., 2014, 2017), and several GEOTRACES stations in the Atlantic Ocean (Church et al., 2012; Rigaud et al., 2015; Tang and Stewart, 2019) and the East Pacific (Niedermiller and Baskaran, 2019). The reason for the deficit of $^{210}$Po in deep water is still unclear, but it may be different in different marine environments. For example, the deficit of $^{210}$Po in the Sargasso Sea was attributed to the biological uptake of $^{210}$Po by bacteria (Kim, 2001). The deficiency of $^{210}$Po in the mesopelagic water of the Aleutian Basin was proposed to be caused by enhanced scavenging due to horizontal transport of shelf sediments (Hu et al., 2014). A similar deficiency in the deep SCS was attributed to the episodic settling of biogenic particles (Wei et al., 2014, 2017). Spatial variability arouses the need to expand study areas with different characteristics to deepen our understanding of $^{210}$Po/$^{210}$Pb disequilibria in deep water.

In this study, seawater samples were collected from three adjacent sites within the Tehuantepec bowl (TB) in the eastern tropical North Pacific during the Oceanic Scientific Expedition of China. Dissolved and particulate $^{210}$Po and $^{210}$Pb were measured to reveal the state of disequilibrium between $^{210}$Po and $^{210}$Pb. We described the variation of the $^{210}$Po deficit on a small spatial scale and discussed the role of oceanic processes, such as horizontal transport and hydrothermal plumes. Several projects, such as GEOSECS and GEOTRACES, have reported disequilibria between $^{210}$Po and $^{210}$Pb in the Pacific, Indian, and Atlantic. However, as far as we know, there has been no report on the eastern equatorial North Pacific. Our study not only supplements $^{210}$Po and $^{210}$Pb data in the global ocean but also helps to understand the small-scale variation in particle dynamics.

# MATERIALS AND METHODS

## Sampling

The seawater samples were collected from the full water column at three sites onboard R/V *DAYANG YI HAO* from November 11–15, 2003. The sites are located in the TB at the southeast corner of the North Pacific Subtropical Gyre (NPSG; **Figure 1**). The TB is an area with high surface dynamic height and centered at 13°N, 105°W. It is a shallow feature that occurs almost entirely above the 12°C isotherms. The anti-cyclonic flow around the TB promotes deepening of the isotherm, where the 20°C isotherm is at least 10 m deeper than its surroundings (Kessler, 2006). In the southeast of TB, the cyclonic Costa Rica Dome (CRD) triggers upwelling, creating a nutrient-rich environment that might support tuna and other fisheries (Ichii et al., 2002). The northwestward flow on the east side of the CRD is known as the Costa Rica Coastal Current (CRCC), which continues along the coast into the Gulf of Tehuantepec, where it turns south to flow around the south side of the TB. The CRCC extends deeply into the water column, with an appreciable flow below the thermocline (Kessler, 2006). Our sampling sites are located in the southern part of the TB, which may be affected by the CRCC (**Figure 1**).

Our sampling sites are confined in a small space, with latitudes between 12.2 and 12.8°N, and longitudes between 103.9 and 104.6°W. The water depths at sites B, D, and F are 3,083, 2,902, and 3,108 m, respectively (**Table 1**). The sampling depth is from surface to bottom. In particular, two or three samples were collected within 300 m from the seafloor to reveal particle dynamics in the bottom boundary layer. The samples were used to determine dissolved and particulate $^{210}$Po and $^{210}$Pb, as well as silicate. Temperature and salinity were recorded by CTD (SBE 911; Seabird, United States) during sampling.

## Determination

### $^{210}$Po and $^{210}$Pb

The seawater sample (5−8 L) used for $^{210}$Po and $^{210}$Pb determination was filtered through a 0.2-μm nitrocellulose membrane to separate the particulate from the dissolved phase. The filtrate was immediately acidified with concentrated HCl to pH $< 2$. The particulate samples were immediately frozen and stored. Back to the onshore laboratory, a known amount of $^{209}$Po and $Pb^{2+}$ spikes, and a $Fe^{3+}$ carrier was added to the acidified filtrate. After 24 h of mixing, ammonium hydroxide was added to form $Fe(OH)_3$ and co-precipitate $^{209}$Po, $^{210}$Po, $^{210}$Pb, and stable Pb (Church et al., 2012; Rigaud et al., 2013). The precipitate was settled overnight, collected by centrifugation, and dissolved in a 0.5-M HCl solution. Ascorbic acid was added to reduce $Fe^{3+}$ until the solution became colorless. Subsequently, 1 ml 20% hydroxylamine hydrochloride and 1 ml 25% sodium citrate was added to complex interfering ions and improve the recovery of Po during the electroplating process. $^{209}$Po and $^{210}$Po were plated on a silver disk at 90°C for 4 h under stirring with a Teflon-coated stirring bar (Yang et al., 2013). For the particulate sample, after adding $^{209}$Po and $Pb^{2+}$ yield tracers, the filter containing particulate matter was digested with a mixed acid

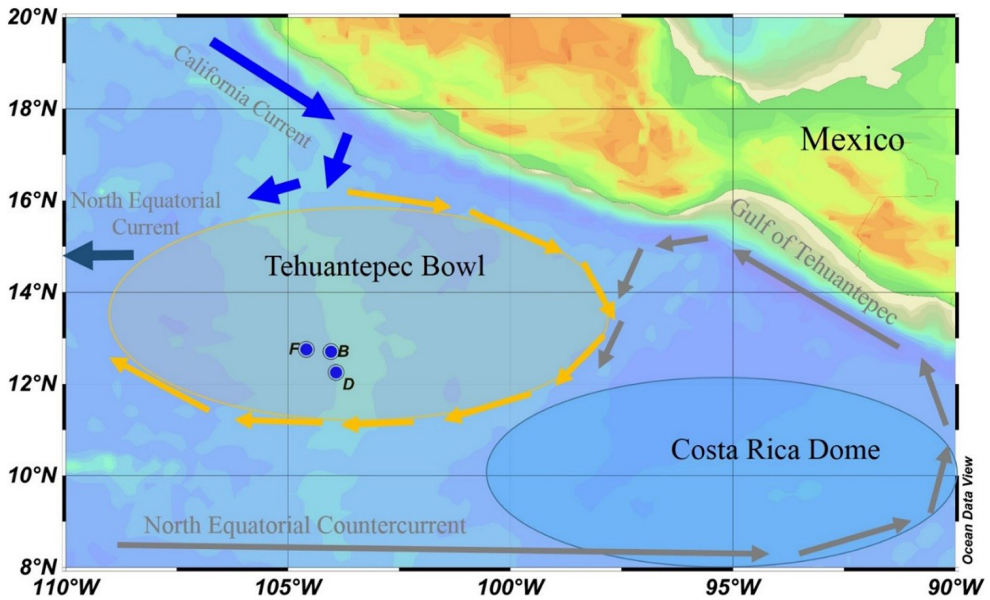


**FIGURE 1 |** Sampling locations in the eastern tropical North Pacific. The Tehuantepec Bowl is a warm core ring, and the Costa Rica Dome is a cold core ring. Currents are represented in gray fonts, and arrows of different colors indicate the general direction of the currents.

solution ($HClO_4$, $HNO_3$, and HF). The subsequent treatment is the same as the dissolved phase. The time from sampling to the separation of $^{210}$Po from $^{210}$Pb was 50–52 days for the dissolved phase and 91–96 days for the particulate phase. The radioactivity of $^{209}$Po and $^{210}$Po was counted by alpha spectrometry (Octête PC, Ortec). The recovery of $^{210}$Po was quantified by the yield of $^{209}$Po. The radioactivity of $^{210}$Pb was calculated by measuring $^{210}$Po radioactivity after approximately 8 months of storage. When calculating $^{210}$Pb activity, a small amount of $^{209}$Po and $^{210}$Po remaining after the first auto-deposition was corrected. The yield of $^{210}$Pb was determined by the added stable Pb, which is measured with an atomic absorption spectrometer. The reported radioactivity of $^{210}$Po and $^{210}$Pb have been corrected for the ingrowth of $^{210}$Po from $^{210}$Pb, instrument background, and reagent blank, and have been decay-corrected to the sampling time (Ma et al., 2017).

The radioactivity of $^{210}$Po is calculated by calibrating the activity of $^{210}$Po measured from the first self-deposition to the sampling time point as follows:

$$A_2^0 = \frac{A_2^1 - A_2^2 e^{\lambda_1 t_1}(e^{-\lambda_1 t_0} - e^{-\lambda_2 t_0})/(e^{-\lambda_1 t_2} - e^{-\lambda_2 t_2})R_1}{e^{-\lambda_2 t_0} R_2} - B \quad (1)$$

**TABLE 1 |** Information for sampling locations in the eastern tropical North Pacific.

| Site | Latitude (°N) | Longitude (°W) | Depth (m) |
|---|---|---|---|
| B | 12.7080 | 104.0336 | 3,083 |
| D | 12.2533 | 103.9203 | 2,902 |
| F | 12.7547 | 104.5886 | 3,108 |

where $A_2^0$is the activity concentration of $^{210}$Po at the time of sampling (dpm/100 L); $A_2^1$ is the activity concentration of $^{210}$Po at the time of first self-deposition (dpm/100 L); $t_0$ represents the time interval from sampling to the first self-deposition; $R_2$ represents the chemical recovery of $^{210}$Po, as determined by $^{209}$Po tracer; $B$ represents the blank in the experimental process.

The radioactivity of $^{210}$Pb was calculated as follows:

$$A_1^0 = \frac{A_2^2(\lambda_2 - \lambda_1)}{\lambda_2 e^{-\lambda_t t_1}(e^{-\lambda_1 t_2} - e^{-\lambda_2 t_2})R_1} - B \quad (2)$$

where $A_1^0$ is the activity of $^{210}$Pb at the time point of co-precipitation (that is, the activity of $^{210}$Pb in the sample, dpm/100 L); $A_2^2$ is the $^{210}$Po activity measured from the second self-deposition sample (dpm/100 L); $\lambda_1$ and $\lambda_2$ are the decay constants of $^{210}$Pb (0.031 $a^{-1}$) and $^{210}$Po (1.828 $a^{-1}$), respectively; $t_1$ and $t_2$ represent the time interval from co-precipitation to the first self-deposition and the time interval from the first to second self-deposition, respectively; $R_1$represents the chemical recovery of $^{210}$Pb, which was determined by stable Pb and the remaining $^{210}$Po after first self-deposition; $B$ represents the blank in the experimental process.

The uncertainty of $^{210}$Po and $^{210}$Pb activity reported here were calculated from the counting error and its propagation. The counting error of dissolved and particulate phases was less than 5 and 10%, respectively.

## Silicate

An aliquot of the seawater sample was collected in a high-density polyethylene bottle, and silicate analysis was performed immediately after sampling. Reactive silicate was determined spectrophotometrically by a method involving a metal-reduced silicomolybdate complex (Parsons et al., 1984). The standard

solution used for silicate determination was GBW 08647. The analytical uncertainty for reactive silicate was 0.2 μmol/L.

## Estimation of $^{226}$Ra Activity

Because of the limitation of sampling volume, the specific activity of $^{226}$Ra at each layer was not measured in this study. However, the surface data measured at 22 sites in the NPSG on the same voyage showed that the specific activity of $^{226}$Ra has a linear positive correlation with silicate (Yang et al., 2007). Taking into account the variation of $^{226}$Ra at different depths, the following relationship was used to estimate the specific activity of $^{226}$Ra in the upper 200 m at our sites to evaluate $^{210}$Pb/$^{226}$Ra disequilibria and $^{210}$Pb atmospheric input: $^{226}$Ra (Bq/m$^3$) = 8.4 + 0.12 * [$SiO_3^{2-}$] (μmol/L) (Ku et al., 1980).

# RESULTS

## Hydro-Chemical Parameters

Profiles of temperature and salinity in the full water column at the three sites show similar pictures, with a thin mixing layer and a thick thermocline (**Figure 2A**). The temperature drops from the bottom of the mixed layer to a depth of 1,500 m, while the salinity increases to a depth of about 200 m, and then drops slightly, resulting in a minimum at a depth of about 1,000 m. This lower salinity is caused by the sinking and transport of Antarctic Intermediate Water (Fiedler and Talley, 2006). The temperature and salinity in the bottom 300 m are very close at the three sites, maintained at 2°C and 34.75, respectively, indicating that the water in the bottom boundary layer is evenly mixed (**Figure 2A**). Although the profiles of temperature and salinity in the full water column are similar, temperature and salinity in the upper 200 m are somewhat different at the three sites. In the mixed layer (above 20 m), the three sites have similar temperatures but slightly different salinity. The salinity in the mixed layer at site F is the highest (∼33.3), while that at site D is the lowest (∼33.18). The main difference appears in the depth interval from 20 to 100 m. The lowest temperature and highest salinity appear at site D, while the highest temperature and lowest salinity appear at site F. The situation at site B is between sites D and F (**Figure 2B**). The difference in temperature and salinity indicates that the subsurface water at the three sites is affected by other water masses. The currents in the study area indicate that the subsurface water at site D may be affected by the upwelling of the CRD, while that at site F may be affected by the coastal water transported by the CRCC (Kessler, 2006).

Silicate at the three sites showed a monotonous increase with depth, reflecting the uptake of silicate by phytoplankton in the euphotic zone and the gradual dissolution of biogenic silica in deep layers (**Figure 2C**). Below 200 m, the silicate concentrations at the three sites are very close, with slightly higher at depths of 200–1,000 m at site B. The silicate concentration in the bottom 300 m is also very consistent among the three sites, stabilizing at 158.1 ± 2 μmol/L (**Figure 2C**). A slight difference in silicate in water above 200 m is observed at the three sites (**Figure 2D**). The silicate concentration above 200 m at site B is higher than that at sites D and F, especially in the mixed layer, which is consistent with low biological productivity in the NPSG. In a depth range of 20–100 m, the silicate concentration at site F is lower than that at site D, which is consistent with the fact that they are affected by coastal water and upwelling water, respectively. The reason why the silicate concentration at site D is lower than that at site B may be that the upwelling silicate from the CRD is consumed by biological uptake during horizontal transport.

## $^{210}$Po

The specific activity of dissolved $^{210}$Po (DPo) ranges from 0.87 ± 0.82 to 18.39 ± 1.27 dpm/100 L, with an average of 7.83 ± 4.29 dpm/100 L. DPo accounts for 58% of total $^{210}$Po (TPo) on average, with the surface and bottom layers being lower (**Table 2**). The DPo profiles at the three sites show that the DPo in the upper 1,500 m water column generally increases with an increase in depth, but decreases significantly in the bottom 300 m (**Figure 3A**). The DPo in the bottom 300 m is close to or even lower than that in the mixed layer. Specifically, the specific activity of DPo in the bottom 300 m at sites B, D, and F are 2.94 ± 1.89, 2.24 ± 0.54, and 4.74 ± 0.34 dpm/100 L, respectively, while those in the mixed layer are 4.85 ± 1.01, 2.12 ± 1.77, and 8.43 ± 3.04 dpm/100 L, respectively. In the upper 200 m water column, the DPo at site B is generally slightly higher than that at sites D and F, which is consistent with low biological productivity in the NPSG (**Figure 3B**).

The average specific activities of particulate $^{210}$Po (PPo) at sites B, D, and F are 4.51 ± 1.55, 4.61 ± 1.79, and 4.52 ± 2.18 dpm/100 L, respectively, with the largest variability at site D (**Table 2**). The PPo in surface water at site F (10.41 ± 1.06 dpm/100 L) is higher than those at site B (6.39 ± 0.61 dpm/100 L) and D (4.42 ± 0.49 dpm/100 L). The PPo at the three sites decreases from the surface to 200 m but differs from 200 to 1,500 m. The PPo at site B remains basically stable, a maximum appears at 500 m at site D, and increases with depth at site F (**Figure 3C**). The specific activities of PPo in the bottom 300 m at the three sites are close to each other and also close to those in the mixed layer (**Figure 3C**). In the upper 200 m, the average specific activity of PPo at site F (5.16 ± 3.14 dpm/100 L) is slightly higher than that at site B (4.06 ± 1.74 dpm/100 L) and site D (4.21 ± 1.08 dpm/100 L) (**Figure 3D**), which supports the possibility of site F being affected by the horizontal transport of coastal water.

The total $^{210}$Po (TPo) varies from 5.29 ± 0.96 to 23.63 ± 1.38 dpm/100 L, with an average of 12.42 ± 4.31 dpm/100 L (**Table 2**). The TPo profiles show a similar pattern among the three sites, generally increasing with depth from the surface, and significantly decreasing in the bottom 300 m (**Figure 3E**). The specific activities of TPo in the bottom 300 m at sites B, D, and F are 9.11 ± 1.53, 7.37 ± 0.16, and 9.98 ± 0.43 dpm/100 L, respectively, and are significantly lower than those at depths of 500–1,500 m (16.3 ± 5.07, 15.84 ± 5.04, and 16.38 ± 2.52 dpm/100L at sites B, D, and F, respectively). In the upper 200 m, except for the surface layer, the specific activities of TPo at the three sites are close to each other, and the average value at site B (11.99 ± 1.15 dpm/100 L) is slightly higher than that at sites D (10.37 ± 2.32 dpm/100L) and F (10.58 ± 0.91 dpm/100 L). The TPo in surface water differs greatly among the three sites, with the

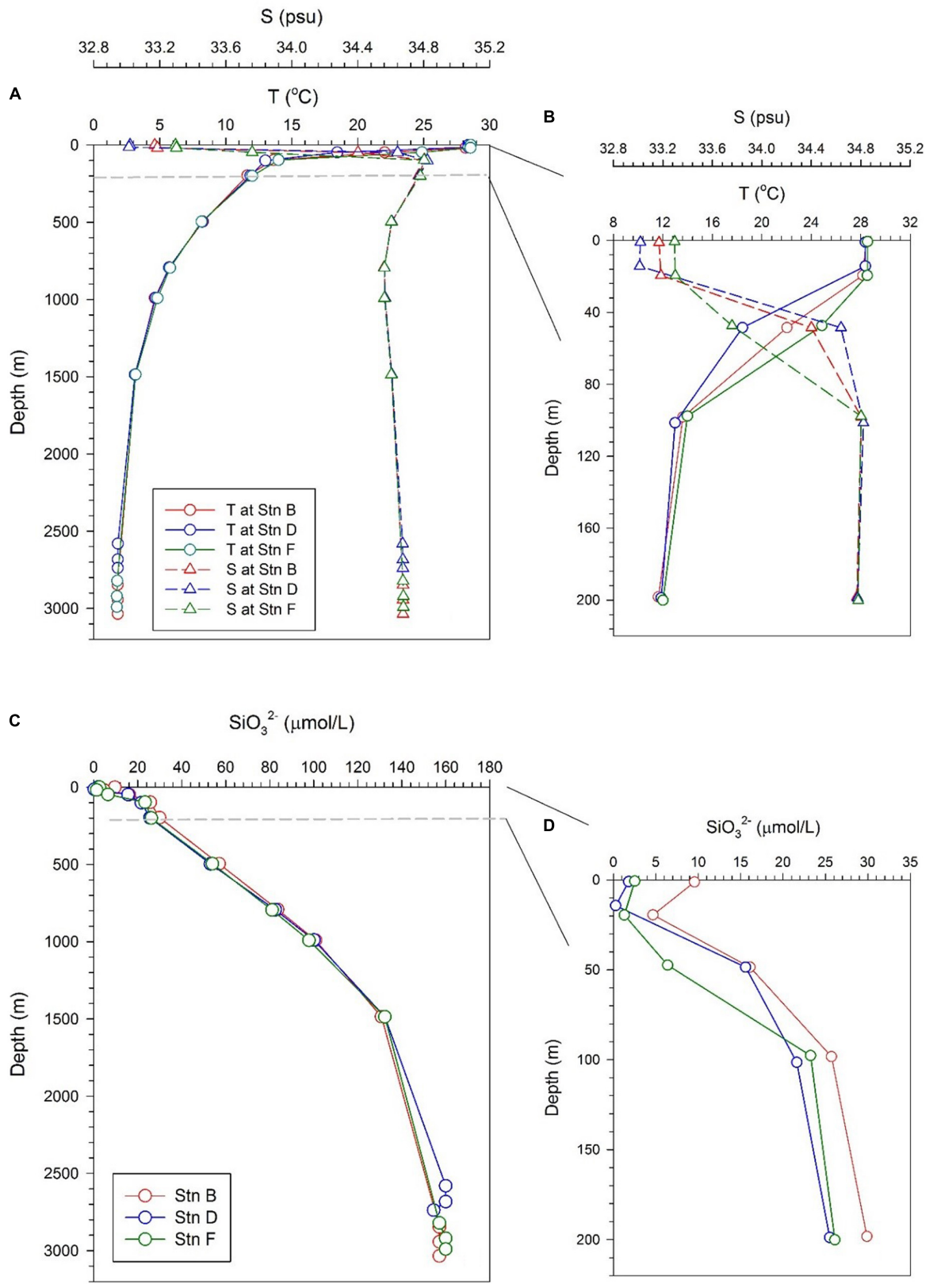


**FIGURE 2 |** Profiles of temperature, salinity, and silicate at the three sites; panels **(A,B)** are profiles of temperature and salinity in the full water column and the upper 200 m, respectively; panels **(C,D)** are the profile of silicate in the full water column and the upper 200 m, respectively.

**TABLE 2 |** The specific activity of $^{210}Po$ and $^{210}Pb$ and activity ratio of $^{210}Po/^{210}Pb$ in the eastern tropical North Pacific.

| Station | Depth (m) | DPo | PPo | TPo | DPb | PPb | TPb | $(Po/Pb)_{A.R.}$ | | |
|---|---|---|---|---|---|---|---|---|---|---|
| | | dpm/100 L | | | | | | D | P | T |
| B | 0 | 4.13 ± 0.98 | 6.39 ± 0.61 | 10.52 ± 1.16 | 25.01 ± 1.93 | 2.79 ± 0.33 | 27.80 ± 1.95 | 0.17 ± 0.04 | 2.29 ± 0.40 | 0.38 ± 0.05 |
| | 20 | 5.56 ± 1.23 | 5.46 ± 0.57 | 11.02 ± 1.35 | 30.80 ± 2.23 | 3.30 ± 0.39 | 34.10 ± 2.26 | 0.18 ± 0.04 | 1.67 ± 0.27 | 0.32 ± 0.05 |
| | 50 | 9.96 ± 1.07 | 3.03 ± 0.37 | 12.99 ± 1.13 | 18.55 ± 1.38 | 2.53 ± 0.26 | 21.08 ± 1.40 | 0.54 ± 0.07 | 1.22 ± 0.20 | 0.62 ± 0.07 |
| | 100 | 10.12 ± 1.14 | 2.86 ± 0.36 | 12.98 ± 1.19 | 15.41 ± 1.12 | 3.35 ± 0.26 | 18.76 ± 1.15 | 0.66 ± 0.09 | 0.85 ± 0.13 | 0.69 ± 0.08 |
| | 200 | 8.39 ± 1.04 | 2.57 ± 0.33 | 10.96 ± 1.09 | 17.66 ± 1.23 | 2.65 ± 0.23 | 20.31 ± 1.26 | 0.48 ± 0.07 | 0.99 ± 0.16 | 0.54 ± 0.06 |
| | 500 | 11.00 ± 1.17 | 4.73 ± 0.49 | 15.73 ± 1.27 | 17.68 ± 1.37 | 2.50 ± 0.27 | 20.18 ± 1.39 | 0.62 ± 0.08 | 1.91 ± 0.29 | 0.78 ± 0.08 |
| | 800 | 9.39 ± 0.95 | 3.12 ± 0.40 | 12.51 ± 1.03 | 21.81 ± 1.81 | 3.10 ± 0.27 | 24.91 ± 1.83 | 0.43 ± 0.06 | 1.02 ± 0.16 | 0.50 ± 0.06 |
| | 1000 | 10.13 ± 0.97 | 3.20 ± 0.38 | 13.33 ± 1.05 | 22.01 ± 1.67 | 2.73 ± 0.23 | 24.74 ± 1.68 | 0.46 ± 0.06 | 1.18 ± 0.17 | 0.54 ± 0.06 |
| | 1500 | 18.39 ± 1.27 | 5.24 ± 0.55 | 23.63 ± 1.38 | 24.92 ± 1.64 | 3.43 ± 0.28 | 28.34 ± 1.66 | 0.74 ± 0.07 | 1.53 ± 0.21 | 0.83 ± 0.07 |
| | 2882 | 5.06 ± 0.72 | 5.08 ± 0.71 | 10.13 ± 1.01 | 12.61 ± 0.98 | 6.24 ± 0.49 | 18.85 ± 1.10 | 0.41 ± 0.07 | 0.81 ± 0.13 | 0.54 ± 0.06 |
| | 2982 | 2.32 ± 0.47 | 5.03 ± 0.71 | 7.35 ± 0.85 | 9.90 ± 0.74 | 5.69 ± 0.61 | 15.60 ± 0.96 | 0.24 ± 0.05 | 0.89 ± 0.16 | 0.47 ± 0.06 |
| | 3068 | 2.43 ± 0.60 | 7.41 ± 0.87 | 9.84 ± 1.06 | 12.01 ± 0.89 | 6.58 ± 0.53 | 18.59 ± 1.03 | 0.20 ± 0.05 | 1.13 ± 0.16 | 0.53 ± 0.06 |
| D | 0 | 0.87 ± 0.82 | 4.42 ± 0.49 | 5.29 ± 0.96 | 30.22 ± 1.80 | 3.62 ± 0.27 | 33.84 ± 1.82 | 0.03 ± 0.03 | 1.22 ± 0.17 | 0.16 ± 0.03 |
| | 20 | 3.37 ± 0.80 | 4.80 ± 0.56 | 8.17 ± 0.98 | 24.65 ± 1.77 | 4.24 ± 0.31 | 28.89 ± 1.80 | 0.14 ± 0.03 | 1.13 ± 0.16 | 0.28 ± 0.04 |
| | 50 | 7.86 ± 0.85 | 3.61 ± 0.45 | 11.46 ± 0.96 | 21.26 ± 1.52 | 3.00 ± 0.25 | 24.25 ± 1.54 | 0.37 ± 0.05 | 1.21 ± 0.18 | 0.47 ± 0.05 |
| | 100 | 6.03 ± 0.69 | 2.71 ± 0.35 | 8.74 ± 0.78 | 16.20 ± 1.26 | 2.73 ± 0.23 | 18.93 ± 1.28 | 0.37 ± 0.05 | 0.99 ± 0.15 | 0.46 ± 0.05 |
| | 200 | 7.60 ± 0.65 | 5.49 ± 0.53 | 13.09 ± 0.84 | 13.64 ± 0.96 | 2.43 ± 0.22 | 16.07 ± 0.98 | 0.56 ± 0.06 | 2.26 ± 0.30 | 0.81 ± 0.07 |
| | 500 | 10.45 ± 1.18 | 9.53 ± 0.79 | 19.98 ± 1.42 | 30.77 ± 2.39 | 2.12 ± 0.25 | 32.89 ± 2.41 | 0.34 ± 0.05 | 4.50 ± 0.67 | 0.61 ± 0.06 |
| | 800 | 5.63 ± 0.89 | 2.91 ± 0.46 | 8.55 ± 1.01 | 22.17 ± 1.75 | 3.25 ± 0.27 | 25.42 ± 1.77 | 0.26 ± 0.05 | 0.92 ± 0.17 | 0.34 ± 0.05 |
| | 1000 | 12.65 ± 1.20 | 4.09 ± 0.47 | 16.75 ± 1.29 | 29.33 ± 2.06 | 2.99 ± 0.27 | 32.32 ± 2.08 | 0.43 ± 0.05 | 1.37 ± 0.20 | 0.52 ± 0.05 |
| | 1500 | 14.52 ± 1.12 | 3.55 ± 0.42 | 18.07 ± 1.19 | 23.57 ± 1.71 | 3.06 ± 0.25 | 26.63 ± 1.73 | 0.62 ± 0.07 | 1.16 ± 0.17 | 0.68 ± 0.06 |
| | 2616 | 2.62 ± 0.49 | 4.86 ± 0.70 | 7.48 ± 0.86 | 10.16 ± 0.76 | 5.94 ± 0.51 | 16.10 ± 0.91 | 0.26 ± 0.05 | 0.82 ± 0.14 | 0.47 ± 0.06 |
| | 2716 | 1.86 ± 0.45 | 5.39 ± 0.73 | 7.25 ± 0.86 | 11.53 ± 0.69 | 6.14 ± 0.52 | 17.67 ± 0.86 | 0.16 ± 0.04 | 0.92 ± 0.15 | 0.42 ± 0.05 |
| | 2773 | nd* | 3.95 ± 0.62 | nd | nd | 6.76 ± 0.47 | nd | nd | nd | nd |
| F | 0 | 10.58 ± 1.62 | 10.41 ± 1.06 | 20.98 ± 1.94 | 32.95 ± 2.73 | 3.51 ± 0.45 | 36.46 ± 2.76 | 0.32 ± 0.06 | 2.97 ± 0.56 | 0.58 ± 0.07 |
| | 20 | 6.28 ± 1.07 | 5.35 ± 0.60 | 11.64 ± 1.22 | 24.47 ± 1.77 | 3.62 ± 0.33 | 28.09 ± 1.80 | 0.26 ± 0.05 | 1.48 ± 0.22 | 0.42 ± 0.05 |
| | 50 | 6.08 ± 0.86 | 4.22 ± 0.42 | 10.30 ± 0.95 | 15.26 ± 1.07 | 2.67 ± 0.22 | 17.93 ± 1.09 | 0.40 ± 0.06 | 1.58 ± 0.20 | 0.57 ± 0.06 |
| | 100 | 8.58 ± 1.10 | 2.31 ± 0.31 | 10.89 ± 1.14 | 19.96 ± 1.36 | 2.40 ± 0.21 | 22.36 ± 1.38 | 0.43 ± 0.06 | 0.96 ± 0.16 | 0.49 ± 0.06 |
| | 200 | 6.02 ± 0.77 | 3.49 ± 0.40 | 9.50 ± 0.87 | 15.48 ± 0.96 | 2.06 ± 0.17 | 17.54 ± 0.98 | 0.39 ± 0.06 | 1.70 ± 0.24 | 0.54 ± 0.06 |
| | 500 | 10.90 ± 1.17 | 3.33 ± 0.37 | 14.23 ± 1.22 | 16.34 ± 1.38 | 2.44 ± 0.20 | 18.78 ± 1.39 | 0.67 ± 0.09 | 1.36 ± 0.19 | 0.76 ± 0.09 |
| | 800 | 13.59 ± 1.45 | 3.02 ± 0.40 | 16.61 ± 1.50 | 19.78 ± 1.66 | 2.85 ± 0.27 | 22.63 ± 1.69 | 0.69 ± 0.09 | 1.06 ± 0.17 | 0.74 ± 0.09 |
| | 1000 | 12.32 ± 1.19 | 2.52 ± 0.40 | 14.84 ± 1.25 | 15.57 ± 1.10 | 2.97 ± 0.24 | 18.54 ± 1.13 | 0.79 ± 0.10 | 0.85 ± 0.15 | 0.80 ± 0.08 |
| | 1500 | 16.00 ± 1.62 | 3.84 ± 0.45 | 19.85 ± 1.69 | 19.87 ± 1.48 | 2.81 ± 0.25 | 22.68 ± 1.50 | 0.81 ± 0.10 | 1.37 ± 0.20 | 0.88 ± 0.10 |
| | 2859 | 4.35 ± 0.58 | 5.97 ± 0.67 | 10.32 ± 0.88 | 9.76 ± 0.66 | 5.44 ± 0.44 | 15.20 ± 0.80 | 0.45 ± 0.07 | 1.10 ± 0.15 | 0.68 ± 0.07 |
| | 2959 | 4.95 ± 0.63 | 5.16 ± 0.68 | 10.11 ± 0.93 | 11.81 ± 0.82 | 6.26 ± 0.45 | 18.07 ± 0.93 | 0.42 ± 0.06 | 0.82 ± 0.13 | 0.56 ± 0.06 |
| | 3028 | 4.93 ± 0.63 | 4.57 ± 0.72 | 9.50 ± 0.96 | 12.65 ± 0.81 | 6.80 ± 0.60 | 19.45 ± 1.01 | 0.39 ± 0.06 | 0.67 ± 0.13 | 0.49 ± 0.06 |

**nd represents no data.*

highest being at site F (20.98 ± 1.94 dpm/100L) and the lowest at site D (5.29 ± 0.96 dpm/100 L) (**Figure 3F**).

## $^{210}Pb$

The specific activity of dissolved $^{210}Pb$ (DPb) ranges from 9.76 ± 0.66 to 32.95 ± 2.73 dpm/100 L, with an average of 19.31 ± 6.58 dpm/100 L (**Table 2**). The profiles of DPb in the full water column at the three sites are similar, and have the following characteristics: (i) a minimum appears at a depth of 100–200 m; (ii) DPb increases from 200 to 1,500 m; (iii) in depths from 200 to 1,500 m, the specific activity of DPb at site D is higher than that at sites B and F; (iv) DPb is lowest at the bottom 300 m (**Figure 4A**). In the upper 200 m water column, the DPb in the mixed layer is higher than those at depths of 20–200 m, and the DPb in the surface water at site B is lower than that at sites D and F (**Figure 4B**).

The specific activity of particulate $^{210}Pb$ (PPb) falls between 2.06 and 6.8 dpm/100 L (**Table 2**), accounting for an average of 20% of the total $^{210}Pb$ (TPb). The PPb decreases from the surface to 200 m, but increases with an increase in depth below 200 m, reflecting the effects of atmospheric deposition and particle scavenging (**Figures 4C,D**). The average specific activities of PPb at the bottom 300 m at sites B, D, and F are 6.17 ± 0.45, 6.28 ± 0.43, and 6.17 ± 0.68 dpm/100 L, respectively, which are significantly higher than those in other layers. In surface water, the PPb at site B (2.79 ± 0.33 dpm/100 L) is lower than those at sites D (3.62 ± 0.27 dpm/100 L) and F (3.51 ± 0.45 dpm/100 L).

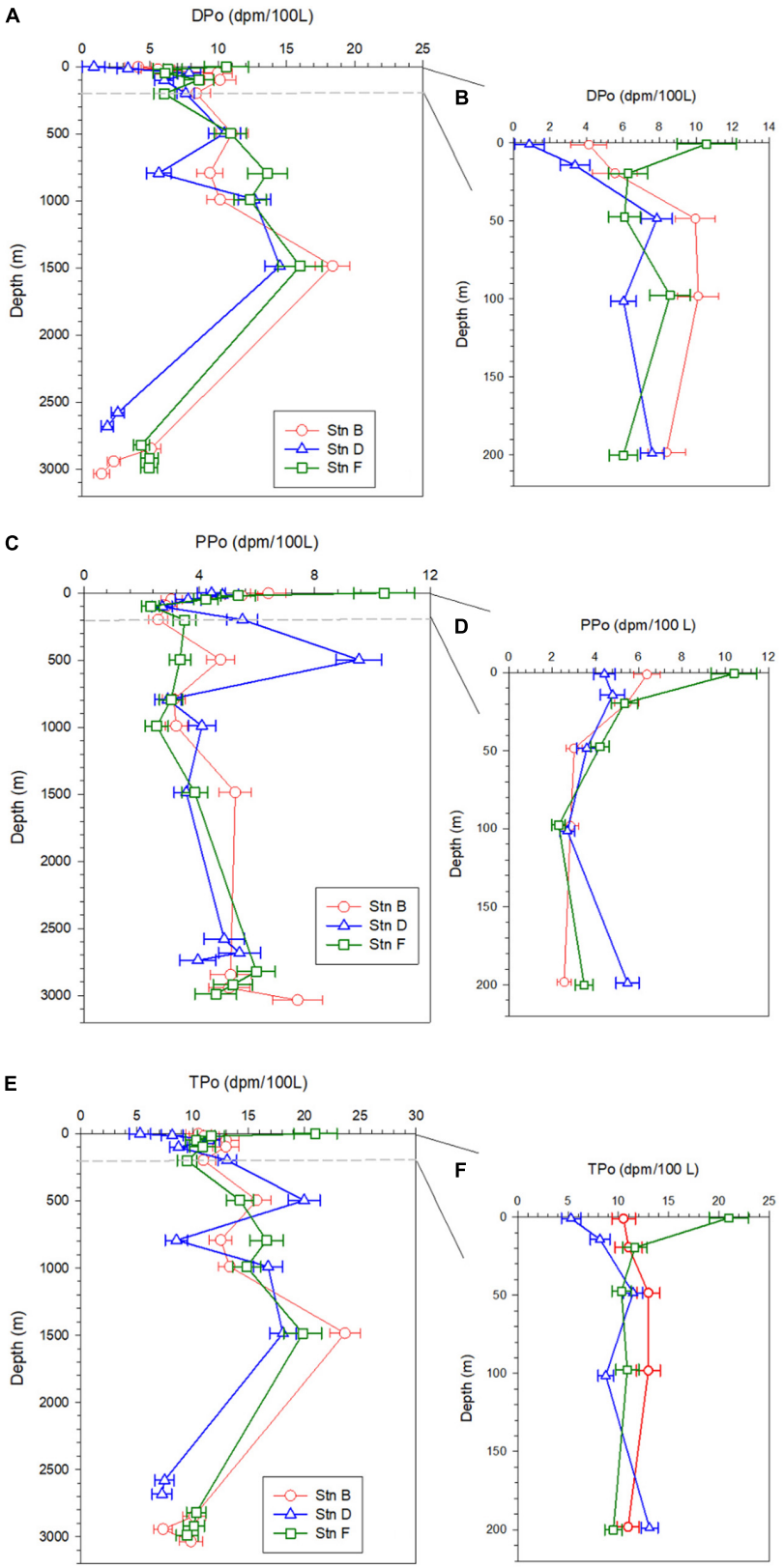


**FIGURE 3 |** Profiles of dissolved $^{210}$Po (DPo), particulate $^{210}$Po (PPo), and total $^{210}$Po (TPo) at the three sites; panels **(A,C,E)** are profiles in the full water column; panels **(B,D,F)** are profiles in the upper 200 m.

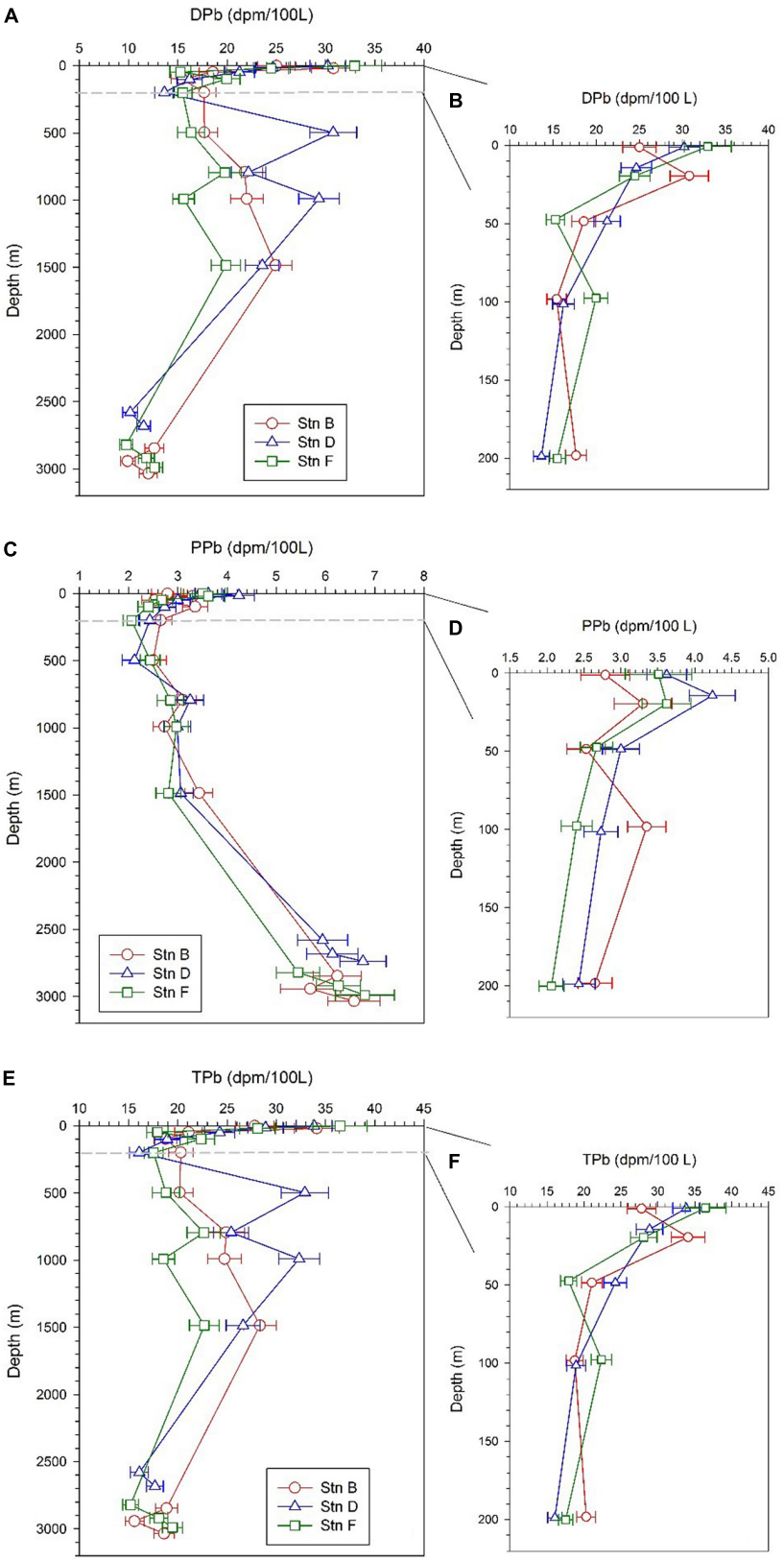


**FIGURE 4 |** Profiles of dissolved $^{210}$Pb (DPb), particulate $^{210}$Pb (PPb), and total $^{210}$Pb (TPb) at the three sites; panels **(A,C,E)** are profiles in the full water column; panels **(B,D,F)** are profiles in the upper 200 m.

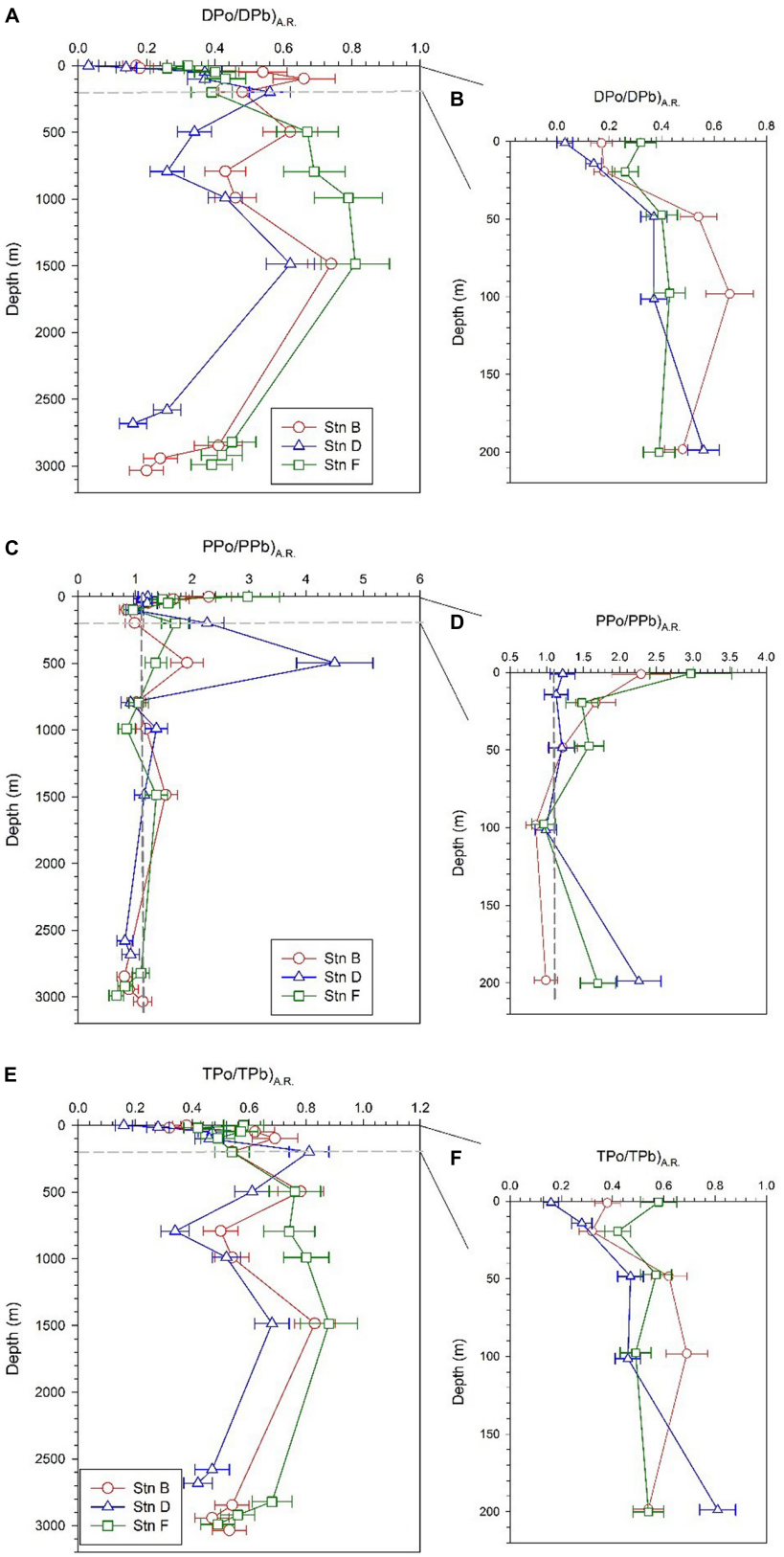


**FIGURE 5 |** Profiles of DPo/DPb activity ratio [$(DPo/DPb)_{A.R.}$] $(PPo/PPb)_{A.R.}$ and $(TPo/TPb)_{A.R.}$ at the three sites; panels **(A,C,E)** are profiles in the full water column; panels **(B,D,F)** are profiles in the upper 200 m.

The TPb ranges from 15.2 to 36.46 dpm/100 L, with an average of 22.97 ± 5.96 dpm/100 L (**Table 2**). The vertical change characteristics of TPb are consistent with DPb, which indicates DPb is the main contributor to TPb (**Figures 4E,F**).

## $^{210}$Po/$^{210}$Pb Activity Ratio

The DPo/DPb activity ratio [$(DPo/DPb)_{A.R.}$] at the three sites varies from 0.03 to 0.81, with an average of 0.42 ± 0.2 (**Table 2**). These values of less than 1 indicate that, compared with DPb, DPo is preferentially adsorbed by particles during the scavenging process. The vertical pattern of $(DPo/DPb)_{A.R.}$ is similar at the three sites, with low values in the surface and bottom (**Figure 5A**). The average $(DPo/DPb)_{A.R.}$ in the mixed layer and the bottom 300 m is 0.18 ± 0.1 and 0.32 ± 0.11, respectively. In the upper 200 m, $(DPo/DPb)_{A.R.}$ increases as the depth increases (**Figure 5B**). In the surface layer and the depths of 200–1,500 m, the order of $DPo/DPb_{A.R.}$ among the three sites is as follows: site F > site B > site D (**Figures 5A,B**).

The PPo/PPb activity ratio [$(PPo/PPb)_{A.R.}$] at our sites varies from 0.67 to 4.5 in the full water column, with an average of 1.37 ± 0.73. Except for the bottom 300 m, the $(PPo/PPb)_{A.R.}$ in other layers is greater than or close to 1, with an average of 1.51 ± 0.77 (**Table 2**). The $(PPo/PPb)_{A.R.}$ profiles show the following characteristics: (i) $(PPo/PPb)_{A.R.}$ in the mixed layer is higher, where site F is as high as 2.97 ± 0.56; (ii) a maximum value appears at a depth of 200 or 500 m, where the $(PPo/PPb)_{A.R.}$ at site F is 1.7 ± 0.24, which appears at 200 m, and the $(PPo/PPb)_{A.R.}$ at sites B and D are 1.91 ± 0.29 and 4.5 ± 0.67, respectively, which appears at 500 m; (iii) The $(PPo/PPb)_{A.R.}$ at the bottom 300 m is close to or less than 1, where the average values at sites B, D, and F are 0.94 ± 0.17, 0.87 ± 0.07, and 0.86 ± 0.22, respectively (**Figures 5C,D**).

The $(TPo/TPb)_{A.R.}$ at all depths of the three sites are less than 1, with an average of 0.56 ± 0.17 (**Table 2**). Since DPo and DPb are the main contributors to TPo and TPb, respectively, the profile of TPo/TPb at each site is very similar to that of DPo/DPb (**Figures 5E,F**).

## TPb/$^{226}$Ra Activity Ratio

The activity ratio in the upper 200 m water column at the three sites ranges from 1.4 to 4.19, showing an overall decrease as the depth increases (**Figure 6**). The $(TPb/^{226}Ra)_{A.R.}$ in the surface water at site B (2.91 ± 0.2) is lower than that at sites D (3.93 ± 0.21) and F (4.19 ± 0.32), indicating that site B is less affected by $^{210}$Pb input from atmospheric deposition. The variation of $(TPb/^{226}Ra)_{A.R.}$ in the upper 200 m water column reflects the net effect between atmospheric input and particle scavenging of $^{210}$Pb.

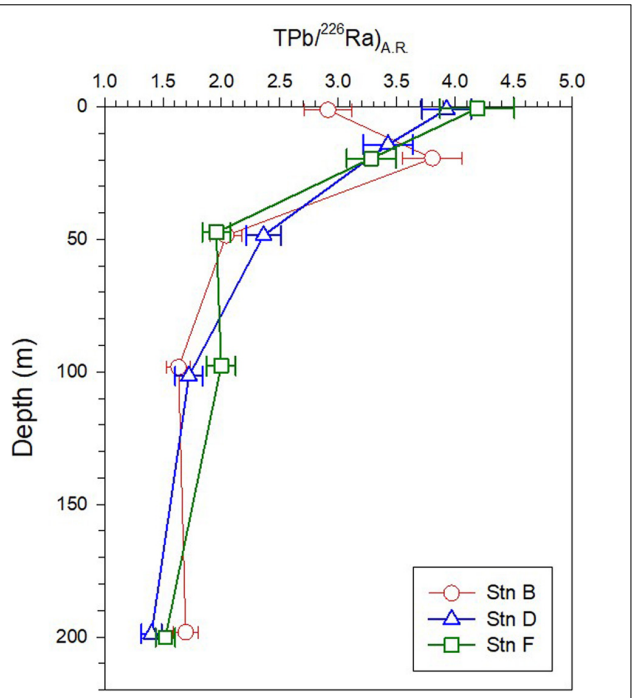


**FIGURE 6 |** Profiles of $(TPb/^{226}Ra)_{A.R.}$ in the upper 200 m at the three sites.

# DISCUSSION

## Small-Scale Variation in $^{210}$Po Deficit

Our study shows that the TPo at the three sites in the equatorial eastern North Pacific is depleted relative to TPb in the full water column, indicating that $^{210}$Po is preferentially scavenged from the waters (**Figure 5**). In order to quantitatively describe the disequilibrium state of $^{210}$Po with respect to $^{210}$Pb, the deficit of $^{210}$Po in each layer is calculated by the following equation: $^{210}$Po deficit = TPb–TPo. Subsequently, the trapezoidal integral is used to calculate the integral deficit of $^{210}$Po in the full water column or a depth interval. Since integral deficit is affected by integral depth, we further divide the integral deficit by the integral depth to obtain the average deficit of $^{210}$Po. Here, the water column is divided into the mixed (above 20 m), subsurface (20–200 m), middle (200–1,500 m), and bottom (bottom 300 m) layers to compare the deficit of $^{210}$Po at the three sites. Our calculations show that the integral deficit of $^{210}$Po in the full water column varies from 14.54 to 28.77 dpm/cm$^2$, with an amplitude of 1.98 times (**Figure 7A**). The deficit of $^{210}$Po in the full water column observed here is similar to that in the Sargasso Sea (Kim, 2001), but different from the observed radioactive equilibrium in deep waters of the North Atlantic (Bacon et al., 1976, 1988), the Pacific (Turekian and Nozaki, 1980), and the eastern and central Indian Ocean (Cochran et al., 1983). Kim (2001) summarized the results reported in the literature at that time, and divided the sea areas into three categories: oligotrophic (the Sargasso Sea, Philippine Sea), mesotrophic (the equatorial and west Southern Atlantic, east southern Pacific, and east northern Pacific) and eutrophic (the Arabian Sea, Bay of New England, and the Indian Ocean), and found that the deficiency of $^{210}$Po in the oligotrophic seas was larger than that in the mesotrophic and eutrophic seas. Recently, Niedermiller and Baskaran (2019) reported $^{210}$Po/$^{210}$Pb disequilibria from near the shore to the oligotrophic ocean along the US GEOTRACES GP16 East Pacific Zonal Transect and found that the $(^{210}Po/^{210}Pb)_{A.R.}$ from 300 m to the sediment/water interface varies among sites, of which

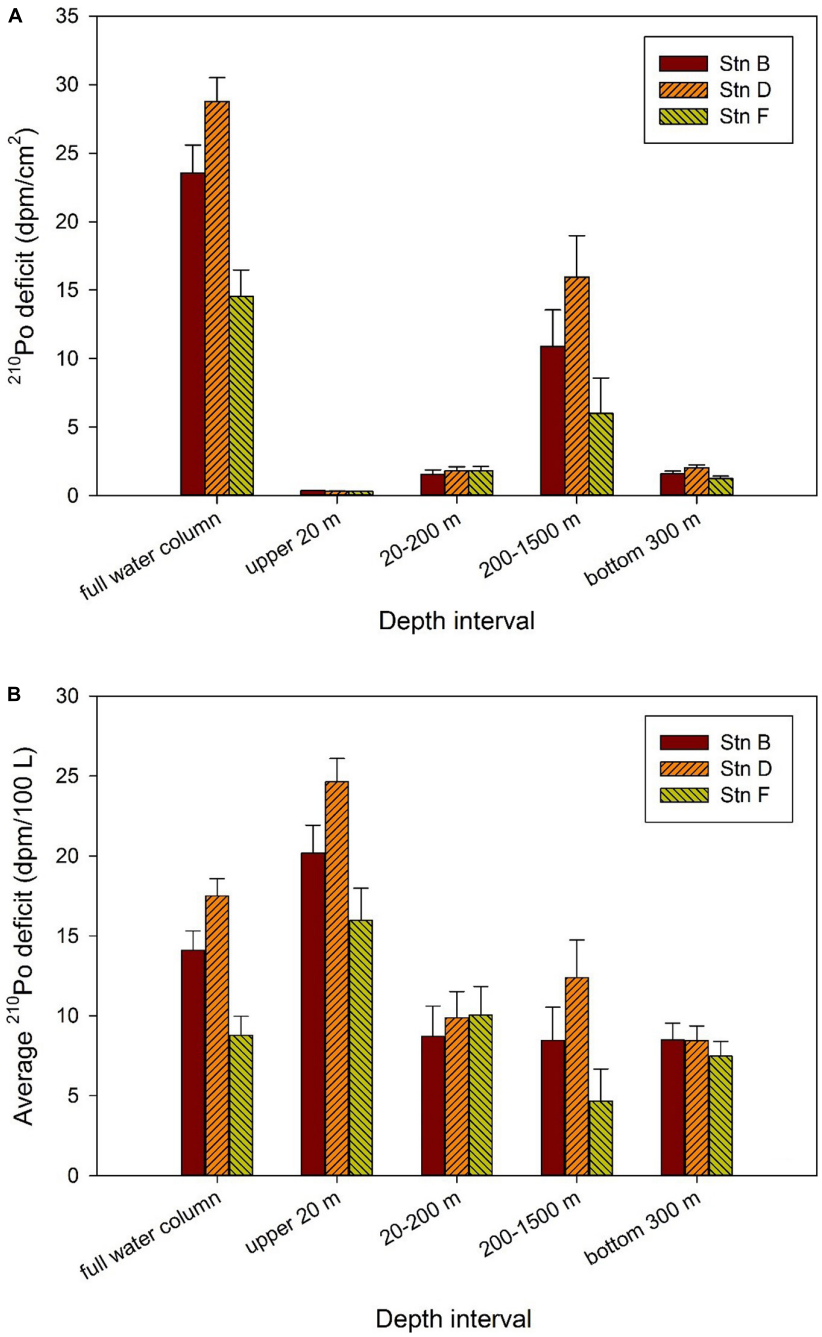


**FIGURE 7 |** Deficit of $^{210}$Po in different depth intervals at the three sites. **(A)** Integral deficit of $^{210}$Po; **(B)** average deficit of $^{210}$Po.

82% is greater than 1.05 or less than 0.95. Our results confirm that $^{210}$Po does not reach equilibrium with $^{210}$Pb in oligotrophic waters in the equatorial eastern North Pacific.

Although our study sites are very close in space, and the variations of temperature, salinity, silicate, and dissolved and particulate $^{210}$Po and $^{210}$Pb are generally similar, the deficit of $^{210}$Po shows changes on a spatial scale. For example, with the exception of 20–200 m depth, the integral and average $^{210}$Po deficits at site F are significantly lower than those at site D. The average $^{210}$Po deficit varies by 1.5, 2.7, 1.1, and 2 times at depths of above 20, 200–1,500, and bottom 300 m, and the full water column, respectively, showing a small-scale variation among the three sites (**Figure 7**).

As far as the waters above 20 m are concerned, the average deficit of $^{210}$Po at the three sites is sorted as follows: site D (24.64 $\pm$ 1.45 dpm/100 L) > site B (20.18 $\pm$ 1.74 dpm/100 L) > site F (15.97 $\pm$ 2.01 dpm/100 L) (**Figure 7**). Interestingly, the order of salinity at these sites is as follows: site D

(33.02 ± 0.01) < site B (33.18 ± 0.01) < site F (33.3 ± 0) (**Figure 2**). This indicates the greater average $^{210}$Po deficit in surface water is significantly affected by low salinity water. The local atmospheric deposition at these three sites should be similar because of their spatial proximity. Therefore, the changes in salinity and $^{210}$Po deficit in waters above 20 m at the three sites may reflect the impact of horizontal input of coastal water. Active particle scavenging and large atmospheric deposition in coastal areas may lead to a large deficit of $^{210}$Po in coastal water. Surface current patterns indicate that the Costa Rica Coastal Current flows along the coast into the Gulf of Tehuantepec, where it turns south to flow around the south side of the TB (Kessler, 2006). This may be the hydrological factor of coastal water affecting our sites. As far as the waters at 200–1,500 and the bottom 300 m are concerned, the average deficit of $^{210}$Po at site D is the largest (12.39 ± 2.35 and 8.44 ± 0.91 dpm/100 L, respectively), while that of site F is the smallest (4.67 ± 2 and 7.47 ± 0.92 dpm/100 L, respectively), which is consistent with the westward flow of hydrothermal plume (Fustec et al., 1987). The situation at depths of 20–200 m seems to be slightly different, with the integral and average deficits among the three sites being similar (**Figure 7**). This may indicate that the plankton at the three sites has a similar ability to scavenge $^{210}$Po, or that the deficit at some sites is submerged by horizontal transport. For example, the subsurface (20–100 m) at site D shows the lowest temperature and highest salinity among the three sites (**Figure 2**), which may be affected by the mixing of CRD upwelling. Because of the strong remineralization of organic matter in deep water in the upwelling zone, the $^{210}$Po in seawater may even exceed $^{210}$Pb (Thomson and Turekian, 1976; Kadko, 1993). The advection of these waters after rising will lead to a reduction in the $^{210}$Po deficit.

Horizontal transport may cause deviations in particle dynamics parameters based on the classical model of $^{210}$Po/$^{210}$Pb disequilibria. In the simplest conceptualization (one-dimensional steady-state model, Bacon et al., 1976), the mass balance equation of TPo ignoring horizontal transport is as follows:

$$P = \lambda_{Po} \cdot (\mathrm{TPb} - \mathrm{TPo}) \tag{3}$$

where $P$ is the removal rate of $^{210}$Po by particle scavenging (dpm/100 L/a), $\lambda_{Po}$ is the decay constant of $^{210}$Po (1.828 $a^{-1}$); TPb and TPo represent the specific activity of total $^{210}$Pb and $^{210}$Po, respectively (dpm/100 L). However, when considering horizontal transport, the mass balance equation of TPo is as follows:

$$P_H = \lambda_{Po} \cdot (\mathrm{TPb} - \mathrm{TPo}) + K_H \cdot \frac{d^2\mathrm{TPo}}{dl^2} \tag{4}$$

where $P_H$ is the removal rate of $^{210}$Po by particle scavenging considering horizontal transport (dpm/100 L/a), $K_H$ is horizontal diffusivity, and $l$ is the scale length. In this study, $K_H$ is derived from the relationship between horizontal diffusivity and scale length: $K_H\left(\frac{cm^2}{s}\right) = 0.0103 \cdot l^{1.15}$ (Okubo, 1971). The value of $l$ is taken as $1 \times 10^5$ m and the resulting $K_H = 3.6 \times 10^9$ $m^2$/a (Kadko, 1993). Under the assumption that the specific activities of TPo and TPb in typical deep seawater are both 20 dpm/100 L, the horizontal transport term can be calculated by $K_H$ * (20 – TPo)/$l^2$ (Kadko, 1993).

In the above two cases, the residence time of total $^{210}$Po with respect to scavenging and removal is calculated by the following equations:

$$\tau = \frac{\mathrm{TPo}}{P} \tag{5}$$

$$\tau_H = \frac{\mathrm{TPo}}{P_H} \tag{6}$$

where $\tau$ and $\tau_H$ represent the residence time of a total $^{210}$Po when horizontal transport is ignored and considered, respectively (a), TPo is the activity concentration of TPo (dpm/100 L).

According to Eqs 3–6, P, $P_H$, $\tau$, and $\tau_H$ in the water column at depths of 200–1,500 m and bottom 300 m at the three sites are calculated. In the calculation, TPb and TPo are respectively substituted with the average specific activities of a total $^{210}$Pb and $^{210}$Po in a certain water column. The calculated values of P, $P_H$, $\tau$, and $\tau_H$ at the three sites are listed in **Table 3**. After considering the contribution of horizontal transport, the removal rates of $^{210}$Po at depths of 200–1,500 m and the bottom 300 m increase by 7.5–21 and 26.1–29.5%, respectively. The greater impact of horizontal transport on the bottom 300 m supports the interference of hydrothermal plumes. After correcting for the effect of horizontal transport, the variation range of the residence time of total $^{210}$Po in the bottom 300 m became smaller and stabilized between 0.77 and 0.79 a (**Table 3**), which is consistent with the reported value (0.7 a) at the bottom 300 m of the southern tropical Pacific Ridge (Niedermiller and Baskaran, 2019). In comparison, the $\tau_H$ values at depths of 200–1,500 m are slightly higher than those at the bottom 300 m (**Table 3**), reflecting that the latter has a more active particle scavenging process. After correcting for the horizontal transport, the removal rate and residence time of the total $^{210}$Po show smaller inter-stational variation, indicating that horizontal transport is acting as a stabilizer of small-scale variation of $^{210}$Po deficit. Note that even after correcting for the effects of horizontal transport, some differences in $P_H$ and $\tau_H$ are observed among the three sites, and they all show the feature that $^{210}$Po is preferentially scavenged. Small-scale differences in bacterial activity and/or chemical composition of particulate organic matter might be the possible reason for this local variation in the $^{210}$Po deficit, which is worthy of further research in the future.

## Possible Reasons for $^{210}$Po Deficiency

The deficit of $^{210}$Po with respect to $^{210}$Pb in the upper 200 m water column may be closely related to phytoplankton activities. A negative relationship between $^{210}$Po deficit and silicate concentration is found in the upper 200 m, indicating that local biological activities enhance the scavenging and removal of $^{210}$Po during the consumption of nutrients (**Figure 8**). According to the fitting equation ($^{210}$Po deficit = 20.18 + 0.5 * [$SiO_3^{2-}$], $n$ = 15, $r^2$ = 0.58, $p$ = 0.001), the $^{210}$Po deficit is estimated to be 20.18 ± 2.1 dpm/100 L when the silicate is completely exhausted. By combining the average activity concentration of TPb in the surface water at the three sites (32.7 ± 4.44 dpm/100

**TABLE 3 |** Removal rate and residence time of a total $^{210}$Po under ignoring and considering horizontal transport.

| Site | Depth interval | P (dpm/100 L/a) | $P_H$ (dpm/100 L/a) | τ (a) | $\tau_H$ (a) |
|---|---|---|---|---|---|
| B | 200–1,500 m | 15.5 ± 3.8 | 17.9 ± 4.0 | 0.86 ± 0.30 | 0.87 ± 0.29 |
| | Bottom 300 m | 15.5 ± 1.9 | 19.6 ± 2.0 | 0.56 ± 0.14 | 0.79 ± 0.13 |
| D | 200–1,500 m | 22.6 ± 4.3 | 24.3 ± 4.4 | 0.68 ± 0.17 | 0.93 ± 0.24 |
| | Bottom 300 m | 15.4 ± 1.7 | 20.0 ± 1.7 | 0.48 ± 0.05 | 0.77 ± 0.11 |
| F | 200–1,500 m | 8.5 ± 3.7 | 10.3 ± 3.9 | 1.76 ± 0.87 | 0.83 ± 0.47 |
| | Bottom 300 m | 13.7 ± 1.7 | 17.3 ± 1.7 | 0.73 ± 0.10 | 0.79 ± 0.12 |

L), the TPo/$TPb_{A.R.}$ corresponding to this deficit is estimated to be 0.38 ± 0.1. This estimate is significantly higher than those reported on aerosols (Burton and Stewart, 1960; Lambert and Nezami, 1965), supporting the effect of biological productivity. Similarly, the TPo inventory was found to show a negative correlation with phosphate and silicate in the upper 60 m water in the GEOTRACES EPZT (the $^{210}$Po deficit may also be correlated with silicate and phosphate, refer to **Figure 6** of the article; Niedermiller and Baskaran, 2019). Nozaki et al. (1997) observed a positive relationship between the removal rate constant of $^{210}$Po and Chl *a* in the surface water in the North Pacific. Therefore, the $^{210}$Po deficit in the upper 200 m at our sites may be due to the uptake by phytoplankton and/or the adsorption onto biogenic particles. The deficit of $^{210}$Po indicates that fractionation between $^{210}$Po and $^{210}$Pb occurs in the scavenging process in the upper 200 m water column. One of the biogeochemical processes leading to this fractionation is the biological uptake of $^{210}$Po by plankton. The uptake of $^{210}$Po by plankton and its subsequent transport along the food chain will result in a $^{210}$Po deficit in ambient seawater (Strady et al., 2015). In this case, changes in planktonic community structure may lead to changes in the deficit of $^{210}$Po (Tang and Stewart, 2019). Another biogeochemical process that causes $^{210}$Po deficit is fractionation during particle adsorption. Both $^{210}$Po and $^{210}$Pb have particle reactivity and can be adsorbed by terrestrial, biogenic, and hydrated particles. The adsorption rate depends on the concentration, physical, and chemical properties of the nuclide, as well as the abundance and chemical composition of particulate matter. Inorganic particles have high efficiency in scavenging $^{210}$Po and $^{210}$Pb, but N-rich organic particles are considered to scavenge $^{210}$Po preferentially (Nozaki et al., 1998; Yang et al., 2013). Therefore, the organic matter produced by photosynthesis of phytoplankton in the euphotic zone may facilitate the removal of $^{210}$Po relative to $^{210}$Pb, leading to the deficit of $^{210}$Po.

The deficit of $^{210}$Po in the deep and bottom water at our sites is puzzling, but this phenomenon has occurred in many deep seas, namely, the East Pacific Rise (Kadko et al., 1987; Kadko, 1993), eastern South Pacific (Niedermiller and Baskaran, 2019), Sargasso Sea (Kim, 2001), and Bering Sea (Hu et al., 2014). Although the average deficit of $^{210}$Po in the deep and bottom waters (below 200 m) at our sites is lower than or comparable to those above 200 m, its integral deficit is much larger (**Figure 7**), showing strong particle scavenging. The relationship between $^{210}$Po deficit and silicate shows that $^{210}$Po deficit did not change significantly with the increase of silicate concentration in the deep water below 200 m (**Figure 8**), indicating that the dissolution of biogenic silica is not a main reason for the fractionation between $^{210}$Po and $^{210}$Pb. Note that our sites are very close to the East Pacific Ridge (**Figure 1**), where there are at least seven hydrothermal vents near 13°N (Fustec et al., 1987). The rise and expansion of effluent plume may be an important reason for the $^{210}$Po deficit. The average TPo/TPb activity ratio at the bottom 300 m of our sites is 0.52 ± 0.08 (**Table 1**), which is close to those at the bottom 600 m of the Southern East Pacific Ridge (average: 0.55 ± 0.16, Niedermiller and Baskaran, 2019) and lower than those at the bottom 200 m of the Endeavor Ridge (average: 0.8 ± 0.06, Kadko, 1993). The low TPo/TPb activity ratio and the large $^{210}$Po deficit in the bottom 300 m indicate that the bottom boundary layer at our sites has active particle dynamics. Although hydrothermal plume affects particle dynamics in the bottom boundary layer, it may not be a major reason for the deficiency of $^{210}$Po in the water at a depth of 200–1,500 m at our sites. The temperature profiles show that the temperature has dropped significantly from 200 to 1,500 m, resulting in strong stratification in the water column (**Figure 2A**). The vertical mixing of the hydrothermal plume is limited by stratification and is unlikely to affect the depth of 200–1,500 m near the ridge. The distribution of $\delta^3$He in the North Pacific indicates that the influence of the $^3$He-rich hydrothermal plume is limited to waters below 1,100 m in our study area (Lupton, 1998). Therefore, the $^{210}$Po depletion at the depth of 200–1,500 m at our three sites may

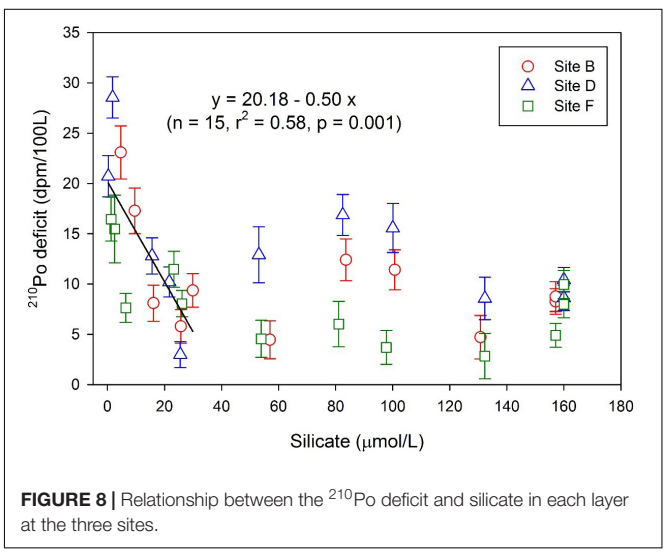


**FIGURE 8 |** Relationship between the $^{210}$Po deficit and silicate in each layer at the three sites.

not be due to particle scavenging enhanced by the hydrothermal plume. We noticed that the integral and average $^{210}$Po deficits at depths of 200–1,500 m at our three sites are close to those in the subsurface of oligotrophic Sargasso Sea (Kim, 2001) and the Philippine Sea (Nozaki et al., 1990). Kim (2001) suggested that the large deficiencies of $^{210}$Po in the Sargasso Sea are likely due to biological removal from the total pool by cyanobacteria and subsequent transfer to nekton *via* grazing. Several studies have shown that $^{210}$Po is effectively taken by bacteria and dispersed between the cell walls, cytoplasm, and high-molecular-weight proteins in a manner similar to sulfur (Fisher et al., 1983; Cherrier et al., 1995; LaRock et al., 1996; Momoshima et al., 2001). The water at the depth of 200–1,500 m at our sites is mainly North Pacific Intermediate Water from the oligotrophic NPSG (Fiedler and Talley, 2006). Similar to the Sargasso Sea, prokaryotes, especially bacteria, dominate the standing stocks and fluxes of carbon and energy, and the physiological diversities of prokaryotic assemblages play an important role in sustaining the cycles of major and trace bio-elements in the NPSG (Karl, 1999). The solid/liquid partitioning of $^{210}$Po at our three sites shows that PPo accounts for 17–48% of TPo in the depth range of 200–1,500 m, with an average of 28% (**Table 2**). The particulate fractions of $^{210}$Po in our study sites are similar to those in the Sargasso Sea (15–75%), which are higher than that in the productive areas of the ocean (Kim, 2001). Therefore, the deficit of $^{210}$Po at the depth of 200–1,500 m at our sites may also be related to the bacterial uptake, just like in the Sargasso Sea.

## CONCLUSION

The $^{210}$Po/$^{210}$Pb pair was used to reveal the particle dynamics at three sites in the Tehuantepec Bowl in the eastern tropical North Pacific. Our results show that the TPo/TPb activity ratios in the full water column at the three sites are all less than 1, with an average of 0.56, confirming a large deficit of a total $^{210}$Po in the oligotrophic sea. A negative linear relationship between $^{210}$Po deficit and silicate was found in the upper 200 m, indicating that biological activities are responsible for this deficiency. The uptake by organisms and adsorption onto biogenic particles trigger the fractionation between $^{210}$Po and $^{210}$Pb, resulting in the deficit of $^{210}$Po in the upper 200 m. In contrast, the deficit of $^{210}$Po in the bottom 300 m may be caused by the horizontal transport of hydrothermal plumes. The $^{210}$Po deficit in our study area shows significant variability on a small spatial scale, showing an effect of horizontal transport. A simple estimate shows that the removal rate of $^{210}$Po in the 200–1,500 m and the bottom 300 m layers increased by 7.5–21 and 26.1–29.5%, respectively, after considering the impact of horizontal transport. The variation range of the residence time of a total $^{210}$Po in deep water becomes smaller after correcting for horizontal contribution, indicating that horizontal transport is acting as a stabilizer of the small-scale variation of $^{210}$Po deficit. Our study confirms that the $^{210}$Po/$^{210}$Pb disequilibria in the eastern tropical North Pacific show a small-scale variation and that the underlying mechanism is worthy of further research in the future.

## DATA AVAILABILITY STATEMENT

The original contributions presented in the study are included in the article/supplementary material, further inquiries can be directed to the corresponding author.

## AUTHOR CONTRIBUTIONS

QM and MC co-designed this study and co-wrote the manuscript. MC sampled onboard. QM and RZ measured $^{210}$Po and $^{210}$Pb. EL determined silicate. YH revised the manuscript. YQ contributed experimental tools. All authors contributed to the article and approved the submitted version.

## FUNDING

This study was supported by the COMRA Program of China (No. DY135-13-E2-03) and the National Natural Science Foundation of China (41721005).

## ACKNOWLEDGMENTS

We thank the captain and crew of R/V *DAYANG YI HAO* for their assistance in sample collection. Thanks to the constructive comments of two reviewers that greatly improved our manuscript.

## REFERENCES

Bacon, M. P., Belastock, R. A., Tecotzky, M., Turekian, K. K., and Spencer, D. W. (1988). Lead-210 and polonium-210 in ocean water profiles of the continental shelf and slope south of New England. *Continent. Shelf Res.* 8, 841–853. doi: 10.1016/0278-4343(88)90079-9

Bacon, M. P., Spencer, D. W., and Brewer, P. G. (1976). $^{210}$Pb/$^{226}$Ra and $^{210}$Po/$^{210}$Pb disequilibria in seawater and suspended particulate matter. *Earth Planetary Sci. Lett.* 32, 277–296. doi: 10.1016/0012-821X(76)90068-6

Burton, W. M., and Stewart, N. G. (1960). Use of long-lived natural radioactivity as an atmospheric tracer. *Nature* 186, 584–589. doi: 10.1038/186584a0

Cherrier, J., Burnett, W. C., and LaRock, P. A. (1995). The uptake of polonium and sulfur by bacteria. *Geomicrobiol. J.* 13, 103–115. doi: 10.1080/01490459509378009

Chuang, C.-Y., Santschi, P. H., Ho, Y. F., Conte, M. H., Guo, L. D., Schumann, D., et al. (2013). Role of biopolymers as major carrier phases of Th, Pa, Pb, Po, and Be radionuclides in settling particles from the Atlantic Ocean. *Mar. Chem.* 157, 131–143. doi: 10.1016/j.marchem.2013.10.002

Chung, Y., and Wu, T. (2005). Large $^{210}$Po deficiency in the northern South China Sea. *Continent. Shelf Res.* 25, 1209–1224. doi: 10.1016/j.csr.2004.12.016

Church, T. M., Rigaud, S., Baskaran, M., Kumar, A., and Stewart, G. (2012). Intercalibration studies of $^{210}$Po and $^{210}$Pb in dissolved and particulate seawater samples. *Limnol. Oceanogr. Methods* 10, 776–789. doi: 10.4319/lom.2012.10.776

Cochran, J. K. (1992). "The oceanic chemistry of the uranium and thorium-series nuclides," in *Uranium-series Disequilibrium Applications to Earth, Marine and Environmental Sciences*, Second Edn, eds M. Ivanovich and R. S. Harmon (Oxford: Clarendon Press), 334–395.

Cochran, J. K., Bacon, M., Krishnaswami, S., and Turekian, K. K. (1983). $^{210}$Po and $^{210}$Pb distribution in the central and eastern Indian Ocean. *Earth Planetary Sci. Lett.* 65, 433–452. doi: 10.1016/0012-821X(83)90180-2

Fiedler, P. C., and Talley, L. D. (2006). Hydrography of the eastern tropical Pacific: A review. *Prog. Oceanogr.* 69, 143–180. doi: 10.1016/j.pocean.2006.03.008

Fisher, N. S., Burns, K. A., Cherry, R. D., and Heyraud, M. (1983). Accumulation and cellular distribution of $^{241}$Am, $^{210}$Pb and $^{210}$Po in two marine algae. *Mar. Ecol. Prog. Ser.* 11, 233–237. doi: 10.3354/meps011233

Friedrich, J., and Rutgers van der Loeff, M. M. (2002). A two-tracer ($^{210}$Po-$^{234}$Th)approach to distinguish organic carbon and biogenic silica export flux in the Antarctic Circumpolar Current. *Deep-Sea Res. I* 49, 101–120. doi: 10.1016/S0967-0637(01)00045-0

Fustec, A., Desbruy, D., and Juniper, S. K. (1987). Deep-sea hydrothermal vent communities at 13°N on the East Pacific Rise: Microdistribution and Temporal variations. *Biol. Oceanogr.* 4, 121–164.

Hu, W. J., Chen, M., Yang, W. F., Zhang, R., Qiu, Y. S., and Zheng, M. F. (2014). Enhanced particle scavenging in deep water of the Aleutian Basin revealed by $^{210}$Po-$^{210}$Pb disequilibria. *J. Geophys. Res. Oceans* 119, 3235–3248. doi: 10.1002/2014JC009819

Ichii, T., Mahapatra, K., Watanbe, T., Yatsu, A., Inagake, D., and Okada, Y. (2002). Occurrence of jumbo flying squid Dosidicus gigas aggregations associated with the countercurrent ridge off the Costa Rica Dome during 1997 El Niño and 1999 La Niña. *Mar. Ecol. Prog. Ser.* 231, 151–166. doi: 10.3354/meps231151

Kadko, D. (1993). Excess $^{210}$Po and nutrient recycling within the California Coastal Transition Zone. *J. Geophys. Res.* 98, 857–864. doi: 10.1029/92JC01932

Kadko, D., Bacon, M. P., and Hudson, A. (1987). Enhanced scavenging of $^{210}$Pb and $^{210}$Po by processes associated with the East Pacific Rise near 8°45′N. *Earth Planetary Sci. Lett.* 81, 349–357. doi: 10.1016/0012-821X(87)90122-1

Karl, D. M. (1999). A sea of change: Biogeochemical variability in the North Pacific Subtropical Gyre. *Ecosystems* 2, 181–214. doi: 10.1007/s100219900068

Kessler, W. S. (2006). The circulation of the eastern tropical Pacific: A review. *Prog. Oceanogr.* 69, 181–217. doi: 10.1016/j.pocean.2006.03.009

Kharkar, D. P., Thomson, J., Turkian, K. K., and Forste, W. O. (1976). Uranium and thorium decay series nuclides in plankton from the Caribbean. *Limnol. Oceanogr.* 21, 294–299. doi: 10.4319/lo.1976.21.2.0294

Kim, G. (2001). Large deficiency of polonium in the oligotrophic ocean's interior. *Earth Planetary Sci. Lett.* 192, 15–21. doi: 10.1016/S0012-821X(01)00431-9

Ku, T. L., Huh, C. A., and Chen, P. S. (1980). Meridional distribution of $^{226}$Ra in the Eastern Pacific along GEOSECS Cruise tracks. *Earth Planetary Sci. Lett.* 49, 293–308. doi: 10.1016/0012-821X(80)90073-4

Lambert, G., and Nezami, M. (1965). Determination of the mean residence time in the troposphere by measurement of the ratio between the concentrations of lead-210 and polonium-210. *Nature* 206, 1343–1344. doi: 10.1038/2061343a0

LaRock, P. L., Hyun, J. H., and Boutelle, S. (1996). Bacterial mobilization of polonium. *Geochim. Cosmochim. Acta* 60, 4321–4328. doi: 10.1016/S0016-7037(96)00255-4

Lupton, J. (1998). Hydrothermal helium plumes in the Pacific Ocean. *J. Geophys. Res.* 103, 15853–15868. doi: 10.1029/98JC00146

Ma, H. Y., Yang, W. F., Zhang, L. H., Zhang, R., Chen, M., Qiu, Y. S., et al. (2017). Utilizing $^{210}$Po deficit to constrain particle dynamics in mesopelagic water, western South China Sea. *Geochem. Geophys. Geosyst.* 18, 1594–1607. doi: 10.1002/2017GC006899

Momoshima, N., Song, L. X., Osaki, S., and Maeda, Y. (2001). Formation and emission of volatile polonium compound by microbial activity and polonium methylation with methylcobalamin. *Environ. Sci. Technol.* 35, 2956–2960.

Niedermiller, J., and Baskaran, M. (2019). Comparison of the scavenging intensity, remineralization and residence time of $^{210}$Po and $^{210}$Pb at key zones (biotic, sediment-water and hydrothermal) along the East Pacific GEOTRACES transect. *J. Environ. Radioact.* 198, 165–188. doi: 10.1016/j.jenvrad.2018.12.016

Nozaki, Y., Dobashi, F., Kato, Y., and Yamamoto, Y. (1998). Distribution of Ra isotopes and the $^{210}$Pb and $^{210}$Po balance in surface seawaters of the mid Northern Hemisphere. *Deep-Sea Res. I* 145, 1263–1284. doi: 10.1016/S0967-0637(98)00016-8

Nozaki, Y., Naoko, I., and Yashima, M. (1990). Unusually large $^{210}$Po deficiencies relative to $^{210}$Pb in the Koroshio Current of the East China and Philippine Sea. *J. Geophys. Res.* 95, 5321–5329. doi: 10.1029/JC095iC04p05321

Nozaki, Y., Thomson, J., and Turekian, K. K. (1976). The distribution of $^{210}$Pb and $^{210}$Po in the surface waters of the Pacific Ocean. *Earth Planetary Sci. Lett.* 32, 304–312. doi: 10.1016/0012-821X(76)90070-4

Nozaki, Y., Tsubota, H., Kasemsupaya, V., Yashima, M., and Ikuta, N. (1991). Residence times of water and particle-reactive $^{210}$Pb and $^{210}$Po in the East China and Yellow Sea. *Geochim. Cosmochim. Acta* 55, 1265–1272. doi: 10.1016/0016-7037(91)90305-O

Nozaki, Y., Zhang, J., and Takeda, A. (1997). $^{210}$Pb and $^{210}$Po in the equatorial Pacific and the Bering Sea: the effects of biological productivity and boundary scavenging. *Deep-Sea Res. II* 44, 2203–2220. doi: 10.1016/S0967-0645(97)00024-6

Okubo, A. (1971). Ocean diffusion diagrams. *Deep-Sea Res.* 18, 789–802. doi: 10.1016/0011-7471(71)90046-5

Parsons, T. R., Maita, Y., and Lalli, C. M. (1984). *A manual of chemical and biological methods for seawater analysis*. Oxford,UK: Pergamon Press.

Rigaud, S., Puigcorbe, V., Camara-Mor, P., Casacuberta, N., Roca-Marti, M., Garcia-Orellana, J., et al. (2013). A methods assessment and recommendations for improving calculations and reducing uncertainties in the determination of $^{210}$Po and $^{210}$Pb activities in seawater. *Limnol. Oceanogr. Methods* 11, 561–571. doi: 10.4319/lom.2013.11.561

Rigaud, S., Stewart, G., Baskaran, M., Marsan, D., and Church, T. (2015). $^{210}$Po and $^{210}$Pb distribution, dissolved-particulate exchange rates, and particulate export along the North Atlantic US GEOTRACES GA03 section. *Deep-Sea Res. II* 116, 60–78. doi: 10.1016/j.dsr2.2014.11.003

Shannon, L. V., Cherry, R. D., and Orren, M. J. (1970). Polonium-210 and lead-210 in the marine environment. *Geochim. Cosmochim. Acta* 34, 701–711. doi: 10.1016/0016-7037(70)90072-4

Strady, E., Harmelin-Vivien, M., Chiffoleau, J. F., Veron, A., Tronczynski, J., and Radakovitch, O. (2015). $^{210}$Po and $^{210}$Pb trophic transfer within the phytoplankton-zooplankton-anchovy/sardine food web: a case study from the Gulf of Lion (NW Mediterranean Sea. *J. Environ. Radioact.* 143, 141–151. doi: 10.1016/j.jenvrad.2015.02.019

Tang, Y., and Stewart, G. (2019). The $^{210}$Po/$^{210}$Pb method to calculate particle export: Lessons learned from the results of three GETRACCES transects. *Mar. Chem.* 217:103692. doi: 10.1016/j.marchem.2019.103692

Thomson, J., and Turekian, K. K. (1976). $^{210}$Po and $^{210}$Pb distribution in ocean water profiles from the eastern South Pacific. *Earth Planetary Sci. Lett.* 32, 297–303. doi: 10.1016/0012-821X(76)90069-8

Turekian, K. K., and Nozaki, Y. (1980). "$^{210}$Po and $^{210}$Pb in the Eastern South Pacific-the role of upwelling on their distributions in the water column," in *Isotope Marine Chemistry*, eds E. D. Goldberg, Y. Horibe, and K. Saruhashi (Tokyo: Uchida Rokkakuho), 157–164.

Wei, C., Chia, C., Chou, W., and Lee, W. (2017). Sinking fluxes of $^{210}$Pb and $^{210}$Po in the deep basin of the northern South China Sea. *J. Environ. Radioact.* 174, 45–53. doi: 10.1016/j.jenvrad.2016.05.026

Wei, C., Yi, M. C., Lin, S. Y., Wen, L., and Lee, W. H. (2014). Seasonal distributions and fluxes of $^{210}$Pb and $^{210}$Po in the northern South China Sea. *Biogeosciences* 11, 6813–6826. doi: 10.5194/bg-11-6813-2014

Yang, J. H., Chen, M., Qiu, Y. S., Li, Y. P., Ma, Q., Lv, E., et al. (2007). $^{226}$Ra evidence for the ecosystem shift over the past 40 years in the North Pacific Subtropical Gyre. *Chinese Sci. Bull.* 52, 832–838. doi: 10.1007/s11434-007-0109-0

Yang, W., Guo, L., Chuang, C. Y., Schumann, D., Ayranov, M., and Santschi, P. H. (2013). Adsorption characteristics of $^{210}$Pb, $^{210}$Po and $^{7}$Be onto micro-particle surfaces and the effects of macromolecular organic compounds. *Geochim. Cosmochim. Acta* 107, 47–64. doi: 10.1016/j.gca.2012.12.039

**Conflict of Interest:** The authors declare that the research was conducted in the absence of any commercial or financial relationships that could be construed as a potential conflict of interest.

**Publisher's Note:** All claims expressed in this article are solely those of the authors and do not necessarily represent those of their affiliated organizations, or those of the publisher, the editors and the reviewers. Any product that may be evaluated in this article, or claim that may be made by its manufacturer, is not guaranteed or endorsed by the publisher.

*Copyright © 2021 Ma, Qiu, Zhang, Lv, Huang and Chen. This is an open-access article distributed under the terms of the Creative Commons Attribution License (CC BY). The use, distribution or reproduction in other forums is permitted, provided the original author(s) and the copyright owner(s) are credited and that the original publication in this journal is cited, in accordance with accepted academic practice. No use, distribution or reproduction is permitted which does not comply with these terms.*

frontiers in Marine Science

HYPOTHESIS AND THEORY
published: 10 November 2021
doi: 10.3389/fmars.2021.694428

# Utilization of Soot and $^{210}$Po-$^{210}$Pb Disequilibria to Constrain Particulate Organic Carbon Fluxes in the Northeastern South China Sea

*Weifeng Yang[1,2]*, Xiufeng Zhao[1,2], Laodong Guo[3], Bangqin Huang[1,4], Min Chen[2], Ziming Fang[5], Xiao Zhang[2] and Yusheng Qiu[2]*

*[1] State Key Laboratory of Marine Environmental Science, Xiamen, China, [2] College of Ocean and Earth Sciences, Xiamen University, Xiamen, China, [3] School of Freshwater Sciences, University of Wisconsin-Milwaukee, Milwaukee, WI, United States, [4] College of the Environment and Ecology, Xiamen University, Xiamen, China, [5] Department of Ocean Science, The Hong Kong University of Science and Technology, Kowloon, Hong Kong SAR, China*

OPEN ACCESS

**Edited by:**
*Pere Masque, International Atomic Energy Agency (IAEA), Monaco*

**Reviewed by:**
*Frédéric André Corentin Le Moigne, UMR 7294 Institut Méditerranéen d'Océanographie (MIO), France*
*Peng Lin, Texas A&M University at Galveston, United States*
*Viena Puigcorbé, Edith Cowan University, Australia*

***Correspondence:**
*Weifeng Yang*
*wyang@xmu.edu.cn*

**Specialty section:**
*This article was submitted to Marine Biogeochemistry, a section of the journal Frontiers in Marine Science*

**Received:** *13 April 2021*
**Accepted:** *04 October 2021*
**Published:** *10 November 2021*

**Citation:**
*Yang W, Zhao X, Guo L, Huang B, Chen M, Fang Z, Zhang X and Qiu Y (2021) Utilization of Soot and $^{210}$Po-$^{210}$Pb Disequilibria to Constrain Particulate Organic Carbon Fluxes in the Northeastern South China Sea. Front. Mar. Sci. 8:694428. doi: 10.3389/fmars.2021.694428*

Black carbon (BC) is believed to be refractory and thus affects the timescale of organic carbon conversion into $CO_2$ and the magnitude of the sink of $CO_2$. However, the fate of BC in the oceans remains poorly understood. Here, $^{210}$Po and $^{210}$Pb were measured to examine the export of soot in the northeastern South China Sea (SCS). Concentrations of soot decreased from 0.141 ± 0.021 μmol-C $L^{-1}$ (mean ± SD) in the mixed layer (0–30 m) to 0.087 μmol-C $L^{-1}$ at the euphotic base (150 m) due to potential photodegradation within the euphotic zone. In the twilight zone, however, the soot showed an increasing pattern along with the total particulate matter and total particulate organic carbon (POC) contents, corresponding to additions from the shelf/slope sediment resuspension through lateral transport. Using the deficits of $^{210}$Po, the export flux of soot from the euphotic zone was calculated to be 0.172 ± 0.016 mmol-C $m^{-2}$ $d^{-1}$ and increased with depth. Assuming that the soot is entirely refractory below the euphotic zone, the sediment-derived soot fluxes were estimated based on the increase in soot fluxes relative to the base of the euphotic zone, with values varying from 0.149 ± 0.030 to 0.96 ± 0.10 μmol-C $L^{-1}$. This indicates that sediment resuspension is an important source of soot to the ocean interior in the SCS. Coupling the sediment-derived soot and $^{210}$Po-derived POC fluxes gave rise to a Martin Curve-like flux attenuation of local euphotic zone-derived POC in the twilight zone with *b* value of 0.70 ± 0.01. These results suggest that soot could be useful for constraining *in situ* POC fluxes and their transport.

**Keywords: soot, polonium, South China Sea, twilight zone, black carbon, biological pump efficiency**

## INTRODUCTION

Black carbon (BC) is the product of incomplete combustion of biomass and fossil fuels (Goldberg, 1985). In the atmosphere, BC has a strong ability to absorb solar radiation (Jacobson, 2001), and thus it has been listed as the second forcing factor in driving the global change following $CO_2$ (Ramanathan and Carmichael, 2008). Owing to its chemical- (except photolysis) and bio-resistant

nature, BC represents the refractory carbon pool on the earth. Previous studies have shown that most of the BC can persist for hundreds to thousands of years either in the soil (Goldberg, 1985; Singh et al., 2012) or in seawater (Ziolkowski and Druffel, 2010; Coppola and Druffel, 2016). Thus, BC is a long-term $CO_2$ sink (Coppola et al., 2014). Understanding the fate of BC would increase our knowledge about the role of BC in the global carbon cycle and climate change.

Over the past years, a line of studies indicated that a large amount of BC gets into the oceans *via* atmospheric deposition (Bao et al., 2017) and river discharge (Wang et al., 2016; Jones et al., 2020). For example, the annual particulate BC (PBC) input from the river discharge was 17–37 Tg (Coppola et al., 2018). Around 34 ± 26% of biomass-generated BC (40–215 Tg $yr^{-1}$, including dissolved BC, i.e., DBC and PBC) gets into the oceans *via* river discharge (Jones et al., 2020). These reports indicate that the ocean is an important reservoir of BC (Masiello and Druffel, 1998; Fang et al., 2018). With an increase in BC emissions from the increase in both fossil fuel combustion and fires emissions, the riverine BC is expected to increase the refractory carbon pool in abyssal oceans (Cheng et al., 2008; Dittmar et al., 2012). However, the cycling of BC in marine environments remains enigmatic with available data.

Based on radiocarbon measurements, BC in deep oceans has a $^{14}C$-age ranging from thousands to tens of thousands of years (Ziolkowski and Druffel, 2010; Coppola et al., 2014; Coppola and Druffel, 2016). However, the global riverine discharge could renew the oceanic BC pool within hundreds of years (Wagner et al., 2018). These results indicate that there must be a large amount of BC being removed after getting into the marine environment. Three recent reports suggested that $\delta^{13}C$ signal, $^{14}C$ age, and DBC spatial pattern support a significant removal of riverine BC in coastal seas (Wagner et al., 2019; Qi et al., 2020; Fang et al., 2021). Available studies have shown that two pathways are responsible for the removal of BC in the ocean. One is photochemical degradation, especially for the condensed aromatic molecular structures (Ziolkowski and Druffel, 2010). This process is proved by *in situ* seawater incubation experiments on DBC (Stubbins et al., 2012; Ward et al., 2014) and the decrease in DBC with depth in the euphotic zone (Fang et al., 2017). The other removal mechanism is the sinking of PBC, which has been reported in different marine environments, such as the Gulf of Maine (Flores-Cervantes et al., 2009), the western Arctic, and Subarctic Ocean (Fang et al., 2016), and Jiaozhou Bay (Feng et al., 2021). Yet, future research is needed to better understand the fate of BC in the ocean, especially regarding the quantification of the magnitude of the removal of BC from the water column.

Since the riverine BC is first discharged into the marginal seas, it is crucial to assess the fate and transport pathways of BC in the marginal seas and thus the cycling of BC in the ocean (Yang and Guo, 2014; Fang et al., 2017). As an important removal process of BC, knowledge about the sinking of PBC would provide insights into the role of BC in transporting carbon from the surface ocean to the deep ocean. As a refractory and photolabile fraction of BC (Stubbins et al., 2012; Fang et al., 2017), the soot was found to distribute widely in shelf sediments (Lohmann et al., 2009; Yang and Guo, 2018). Thus, it is probable that shelf/slope might be of importance for assessing the removal of soot in marine environments. Additionally, soot has been reported as a fraction of particulate organic carbon (POC; Flores-Cervantes et al., 2009; Yang and Guo, 2014; Fang et al., 2016). Investigations on soot, including its abundance and export, should improve our understanding of POC dynamics in the oceans.

The South China Sea (SCS) is the largest marginal sea in the western Pacific Ocean (Chen et al., 2001), which is surrounded by the BC emission hotspots of the world in Southeast Asia countries (Hu et al., 2016). Asia emits more than 1/3 of the global BC (Jurado et al., 2008; Bond et al., 2013). With the prevailing of the Asian monsoons (Wang et al., 2014; Zhang et al., 2016), the SCS is expected to be an important BC reservoir. In this study, the soot was measured along with $^{210}Po$ and $^{210}Pb$ in the northeastern SCS. Our objectives are to (i) examine the abundance and vertical distribution of soot on the slope of the northeastern SCS; (ii) evaluate the export of soot from the euphotic zone to the mesopelagic water and the fate of soot in the SCS; and (iii) explore the potential application of soot to constrain the POC flux in the marginal sea.

# MATERIALS AND METHODS

## Study Area

The main current on the northern SCS shelf flows northeastward and the surface current flows southwestward in the northern basin during summer. Internal solitary waves often introduce the bottom nepheloid layer (BNL) on the northern shelf (Zhang et al., 2014) and the intermediate nepheloid layer (INL) on the slope (Jia et al., 2019). Both the BNLs and INLs result in higher particulate matter concentrations in the mesopelagic layer than the euphotic zone in the SCS (Ma et al., 2017; Zhang et al., 2019) and a large amount of shelf-derived sedimentary matter to the basin (Shih et al., 2019). Particles in the widely extended nepheloid layer over the shelf-slope area of the northern SCS are mainly from sediment resuspension (Zhang et al., 2014; Jia et al., 2019). Owing to the variability in the hydrodynamic conditions, the nepheloid layer also showed significant spatiotemporal variability as observed at different depths during different cruises (Zhang et al., 2019). The C9 station is located on the northeastern SCS slope with a depth of 1,369 m (**Figure 1**). Salinity distributions show complex variability in the upper 100 m (**Figure 1**). The mixed layer of about 30 m (**Figure 1**) is consistent with previous observations during summer in the north SCS (Cai et al., 2015), corresponding to the shallow stratification in summer.

## Sampling

Seawater samples at different depths were collected at station C9 (**Figure 1**) using Niskin bottles attached to a conductivity, temperature and depth (CTD)-rosette system aboard the *R/V Yanping* for the measurements of $^{210}Po$, $^{210}Pb$, soot, and POC on August 8, 2016. In addition, a floating sediment trap having

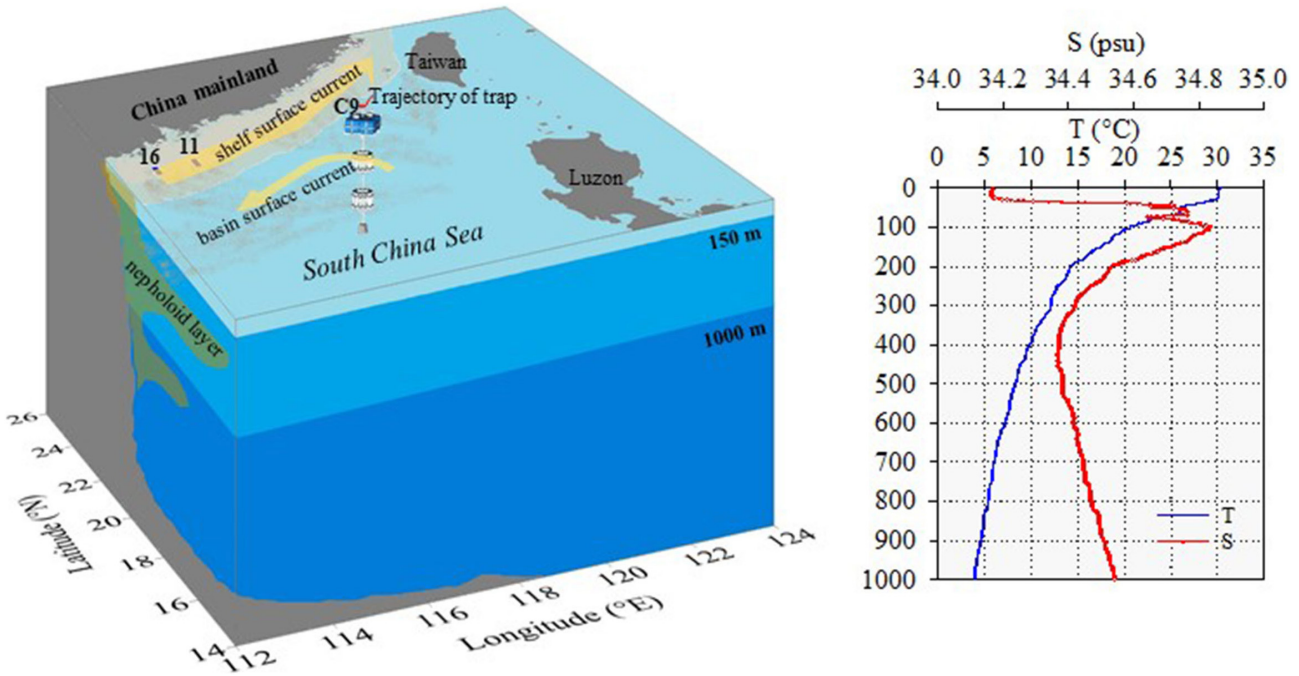


**FIGURE 1 |** Sampling locations for seawater samples (C9), sediment trap samples (C9), and surface sediments (Stations 11 and 16) in the northeastern South China Sea (left) and the distributions of temperature and salinity at station C9 (right). The green shade represents the dispersion of resuspended sediment along the slope below the euphotic zone. The yellow arrows highlight the surface currents in the northern SCS during sampling.

a cylindrical cup with an internal diameter of 95 mm was deployed for 72 h (August 9–12, 2016) to collect sinking particles at 50 and 200 m for $^{210}$Po and POC measurements. The cup was filled with brine with a salinity of 52 psu, prepared by freezing filtered SCS surface water (0.2 μm pore size). Mercury bichloride was added as a biocide. Owing to limited particles from the sediment trap, the soot was not measured. Surface sediments were sampled using a box core sampler at two stations (Stations 11 and 16) on the northern SCS shelf on March 28, 2014 (**Figure 1**) for the measurements of soot and sedimentary organic carbon (SOC).

## $^{210}$Po and $^{210}$Pb Analyses

For the measurements of $^{210}$Po and $^{210}$Pb, 10 L of seawater from each depth was filtered through a polycarbonate membrane (Isopore$^{TM}$) with 0.4 μm pore size to separate >0.4 μm particulate matter from dissolved phases. Analyses of $^{210}$Po and $^{210}$Pb in the <0.4 μm filtrate and >0.4 μm particulate samples were based on the widely used protocols (Church et al., 2012; Rigaud et al., 2013) and elaborated in our previous works (Yang et al., 2013; Ma et al., 2017), which would enable our results to compare with most of the published data. In brief, filtrate samples, after adding accurately known amounts of $^{209}$Po and stable Pb ($PbNO_3$) as the chemical yields of $^{210}$Po and $^{210}$Pb isotopes, respectively, were kept for 24 h to reach the isotopic distribution equilibrium. Then, the samples were adjusted to pH = 8.0 with ammonium hydroxide to form $Fe(OH)_3$ precipitate. The precipitate was allowed to settle overnight and collected *via* centrifugation and decanting the overlying water. Then, the precipitate was redissolved in 0.5 mol $L^{-1}$ HCl solution. After adding ascorbic acid, hydroxylamine hydrochloride, and sodium citrate, Po isotopes including $^{209}$Po and $^{210}$Po were plated on a silver disk at 90°C for 4 h under stirring. The air-dried silver disk was counted using alpha-spectrometry (ORTEC). Particulate samples were digested with mixed $HNO_3$-$HClO_4$-HF after adding $^{209}$Po and stable Pb, evaporated and redissolved in 0.5 mol $L^{-1}$ HCl solution. The plating of Po on the silver disk was the same as that for dissolved samples. $^{210}$Pb was determined *via* $^{210}$Po more than 1.5 years later after the first plating.

The sediment trap collected particles were filtered through a mesh with 1,000 μm pore size to remove swimmers and zooplankton. Then, one aliquot of the small particles was collected on a polycarbonate membrane for $^{210}$Po and $^{210}$Pb measurements, and the treatment was the same as the particulate fractions. The other aliquot was collected on a quartz microfiber filter (QMA) filter for POC measurements. The recoveries of $^{209}$Po and stable Pb for dissolved samples varied from 84 to 94% and from 85 to 93%, respectively. They were more than 95% for particulate samples including trap samples. The counting errors were always <±8%. The uncertainties for all data presented in the study were propagated from the counting errors by incorporating detector backgrounds, reagent blanks,

and membrane blanks. The activities of $^{210}$Po and $^{210}$Pb were corrected back to the sampling time.

## Total Particulate Matter Analysis

For the measurements of total particulate matter (i.e., TPM), along with soot, and POC, 30–48 L of seawater were collected from each depth except the 500 and 1,000 m depths, where only 5 L of seawater were available and were used for POC measurements. Particles were filtered onto a pre-combusted (at 450°C) QMA filter (Whatman$^{TM}$) and de-salted with Milli-Q water. Particulate samples were stored at −18°C. In the land laboratory, these filter samples were dried at 60°C to a constant weight to determine the TPM contents based on the difference in weight between blank filters and filters with TPM.

## Particulate Organic Carbon and Soot Analyses

For the measurements of POC, the samples were fumigated using concentrated HCl to remove inorganic carbon. The total POC content (including soot and autochthonous POC) was measured on an aliquot of the filter sample using an elemental analyzer (Thermo Fisher Scientific, 1112). An aliquot of the filter samples was used to determine soot using the chemoThermal oxidation (CTO)-375 method (Gustafsson et al., 1997, 2001). This method has been proved to effectively quantify soot in sediment (Elmquist et al., 2004; Lohmann et al., 2009) and TPM samples (Yang and Guo, 2014; Fang et al., 2016). In brief, decarbonate filters were combusted at 375°C in the presence of air for 24 h to remove organic carbon except for soot. Then, the soot left on the filters was measured using the same elemental analyzer, as described for POC. The standard material used for POC and soot was international atomic energy agency (IAEA)-C8. The soot and SOC in sediments were measured using procedures described elsewhere (Yang and Guo, 2018). Briefly, the sediment was treated with HCl solution to eliminate carbonate and dried at 60°C. Then, an aliquot of samples was used to measure SOC. The other aliquot of sample was combusted using the same procedures as particulate samples to remove non-soot SOC in sediments. The soot was measured in a manner similar to particulate samples. The National Institute of Standards and Technology (NIST) standard 1941b was measured as samples to ensure data quality. The obtained soot and SOC contents in the standards agree well with previous reports on 1941b (e.g., Gustafsson et al., 2001; Louchouarn et al., 2007; Yang and Guo, 2014).

# RESULTS

The soot concentrations measured along the water column varied from 0.064 to 0.165 μmol-C L$^{-1}$ (**Table 1**) with an average of 0.110 ± 0.036 μmol-C L$^{-1}$ (mean ± SD). Overall, the soot concentrations did not show an increase or decrease trend within the upper euphotic zone (0–75 m), though they had a fluctuation. From 75 m to the euphotic base (150 m), the soot contents showed a quick decline (**Figure 2A**). However, an increasing trend with depth in the soot contents was observed below 200 m, increasing from 0.064 μmol-C L$^{-1}$ at 200 m to 0.090 μmol-C

**TABLE 1** | Temperature, salinity, concentrations of soot and the total particulate organic carbon (POC), activity concentrations of dissolved $^{210}$Po, $^{210}$Pb, and particulate $^{210}$Po, $^{210}$Pb.

| Station | Depth | T | S | POC | Soot | $^{210}Po_D$ | $^{210}Po_P$ | $^{210}Po_T$ | $^{210}Pb_D$ | $^{210}Pb_P$ | $^{210}Pb_T$ | $^{210}Po/^{210}Pb$ | $^{210}Po/^{210}Pb$ | $^{210}Po/^{210}Pb$ |
|---|---|---|---|---|---|---|---|---|---|---|---|---|---|---|
| | (m) | (°C) | (psu) | (μmol-C L$^{-1}$) | | (dpm 100L$^{-1}$) | | | | | | Diss. | Part. | Total |
| C9 | 0 | 30.25 | 34.17 | 2.119 | n.d. | 6.21 ± 0.56 | 1.29 ± 0.12 | 7.5 ± 0.57 | 15.1 ± 1.1 | 1.93 ± 0.20 | 17.0 ± 1.1 | 0.41 ± 0.05 | 0.67 ± 0.09 | 0.44 ± 0.03 |
| 21.67°N | 10 | 30.11 | 34.17 | 0.952 | 0.121 | 5.44 ± 0.48 | 1.12 ± 0.10 | 6.56 ± 0.49 | 15.2 ± 1.1 | 0.98 ± 0.11 | 16.2 ± 1.1 | 0.36 ± 0.04 | 1.14 ± 0.16 | 0.41 ± 0.03 |
| 117.95°E | 30 | 29.76 | 34.21 | 1.492 | 0.151 | 6.19 ± 0.42 | 1.81 ± 0.14 | 8.00 ± 0.44 | 16.7 ± 1.2 | 1.00 ± 0.12 | 17.7 ± 1.2 | 0.37 ± 0.04 | 1.81 ± 0.26 | 0.45 ± 0.03 |
| 2016-8-9 | 50 | 25.95 | 34.67 | 1.019 | 0.124 | 9.22 ± 0.68 | 2.32 ± 0.18 | 11.55 ± 0.70 | 15.6 ± 1.1 | 0.98 ± 0.14 | 16.6 ± 1.1 | 0.59 ± 0.06 | 2.38 ± 0.38 | 0.69 ± 0.05 |
| | 75 | 23.98 | 34.66 | 4.719 | 0.165 | 8.16 ± 0.66 | 2.51 ± 0.19 | 10.67 ± 0.69 | 18.8 ± 1.4 | 0.47 ± 0.10 | 19.3 ± 1.4 | 0.43 ± 0.05 | 5.30 ± 1.16 | 0.55 ± 0.05 |
| | 100 | 20.64 | 34.84 | 3.557 | 0.123 | 7.18 ± 0.61 | 2.57 ± 0.20 | 9.75 ± 0.64 | 16.7 ± 1.3 | 0.90 ± 0.15 | 17.6 ± 1.3 | 0.43 ± 0.05 | 2.85 ± 0.51 | 0.55 ± 0.04 |
| | 150 | 17.59 | 34.72 | 3.090 | 0.087 | 5.81 ± 0.56 | 3.37 ± 0.25 | 9.18 ± 0.62 | 20.4 ± 1.6 | 0.56 ± 0.12 | 21.0 ± 1.6 | 0.28 ± 0.04 | 5.99 ± 1.39 | 0.44 ± 0.04 |
| | 200 | 14.21 | 34.53 | 1.396 | 0.064 | 7.01 ± 0.60 | 2.05 ± 0.16 | 9.06 ± 0.62 | 15.4 ± 1.2 | 0.91 ± 0.13 | 16.4 ± 1.2 | 0.45 ± 0.05 | 2.25 ± 0.36 | 0.55 ± 0.04 |
| | 300 | 12.11 | 34.42 | 1.111 | 0.066 | 5.92 ± 0.48 | 2.56 ± 0.19 | 8.47 ± 0.52 | 13.9 ± 1.0 | 0.98 ± 0.14 | 14.9 ± 1.1 | 0.43 ± 0.05 | 2.62 ± 0.43 | 0.57 ± 0.05 |
| | 500 | 8.31 | 34.38 | 1.095 | n.d. | 6.24 ± 0.54 | 2.05 ± 0.15 | 8.29 ± 0.56 | 16.3 ± 1.1 | 0.68 ± 0.09 | 17.0 ± 1.1 | 0.38 ± 0.04 | 3.02 ± 0.47 | 0.49 ± 0.04 |
| | 800 | 5.40 | 34.47 | 0.930 | 0.090 | 7.01 ± 0.59 | 2.70 ± 0.20 | 9.72 ± 0.62 | 18.5 ± 1.3 | 0.82 ± 0.13 | 19.3 ± 1.3 | 0.38 ± 0.04 | 3.29 ± 0.57 | 0.50 ± 0.04 |
| | 1000 | 3.94 | 34.54 | 1.566 | n.d. | 7.87 ± 0.65 | 2.02 ± 0.15 | 9.89 ± 0.67 | 18.5 ± 1.2 | 0.88 ± 0.11 | 19.3 ± 1.2 | 0.43 ± 0.04 | 2.30 ± 0.33 | 0.51 ± 0.04 |

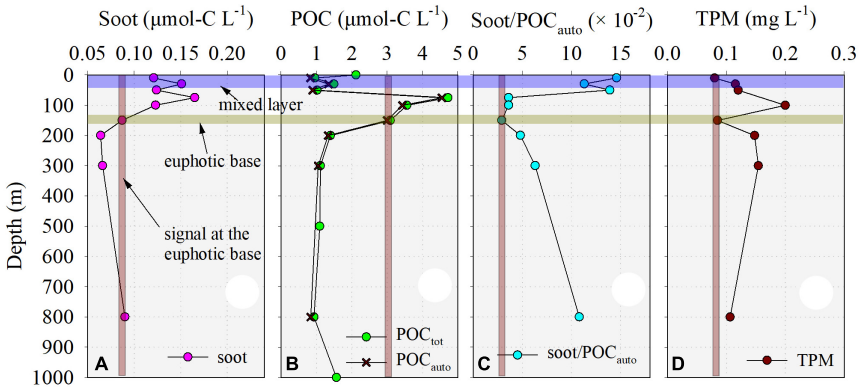


**FIGURE 2 |** Vertical distributions of soot **(A)**, total particulate organic carbon (POC) (i.e., $POC_{tot}$), autochthonous POC excluding soot (i.e., $POC_{auto}$) **(B)**, soot/$POC_{auto}$ ratio **(C)**, and total particulate matter (TPM) **(D)** at station C9 on the slope of the northeastern South China Sea.

$L^{-1}$ at 800 m (**Table 1**). The soot contents were 0.25 mg $g^{-1}$ and 0.17 mg $g^{-1}$ at Stations 11 and 16, respectively.

The total POC ($POC_{tot}$) concentrations in seawater samples varied from 0.93 to 4.72 μmol-C $L^{-1}$, averaging 1.92 ± 1.22 μmol-C $L^{-1}$ (**Table 1**). Similar to soot, $POC_{tot}$ showed little variation in the surface mixing layer (**Figure 2B**). The maximum of $POC_{tot}$ concentration occurred at 75 m, corresponding to summer Chl-*a* maximum in the northern SCS (Cai et al., 2015). Within the lower euphotic zone, $POC_{tot}$ showed a rapid decrease from 4.72 to 3.09 μmol-C $L^{-1}$ (**Figure 2B**). Between 200 and 800 m, nearly constant $POC_{tot}$ concentrations were observed, followed by an increase from 0.930 μmol-C $L^{-1}$ at 800 m to 1.566 μmol-C $L^{-1}$ at 1,000 m. The $POC_{tot}$ contents on the trap-collected particulate matter were 9.12 μmol-C $mg^{-1}$ and 3.66 μmol-C $mg^{-1}$ at 50 and 200 m, respectively. The SOC contents in surface sediment were 2.54 mg $g^{-1}$ and 1.66 mg $g^{-1}$ at Stations 11 and 16, respectively.

The TPM concentrations varied from 0.08 to 0.20 mg $L^{-1}$ with an average of 0.13 ± 0.04 mg $L^{-1}$ (**Figure 2D**). In general, the vertical distribution of TPM followed that of POC in the euphotic zone, showing a dominant biological source of particulate matter. Notably, TPM and soot, both showed increases below the euphotic base (**Figure 2D**), with a TPM concentration of about 50% higher than the average at 150 m (0.09 mg $L^{-1}$).

The total $^{210}$Po and $^{210}$Pb activity concentrations varied from 6.56 to 11.55 dpm $100L^{-1}$ and from 14.89 to 21.00 dpm $100L^{-1}$, respectively (**Table 1**), averaging 9.05 ± 1.39 dpm $100L^{-1}$ and 17.70 ± 1.72 dpm $100L^{-1}$. The total $^{210}$Po/$^{210}$Pb ratio ranged from 0.40 to 0.69, pointing to obvious deficits of $^{210}$Po with respect to $^{210}$Pb in the study area. Our results are consistent with those previously reported deficits of $^{210}$Po for both the euphotic zone (Yang et al., 2009; Wei et al., 2011) and the mesopelagic water in the SCS (Wei et al., 2014; Ma et al., 2017). Although the $Fe(OH)_3$ coprecipitation method may lead to artificially low $^{210}$Po concentrations, hence overestimating $^{210}$Po deficits relative to $^{210}$Pb (i.e., overestimating $^{210}$Po fluxes) (Roca-Martí et al., 2021), the increases with the depth of soot, TPM, and $POC_{tot}$ concentrations (**Figure 2**) indicate that the $^{210}$Po deficits in the study site are clearly impacted by sediment-derived particulate matter in the mesopelagic waters. The $^{210}$Po activities on trap-collected particles were 0.160 dpm $mg^{-1}$ and 0.056 dpm $mg^{-1}$ at 50 and 200 m, respectively. The $^{210}$Pb activities were somewhat lower than $^{210}$Po with the values of 0.035 dpm $mg^{-1}$ and 0.045 dpm $mg^{-1}$, respectively, corresponding to their difference in particle reactivity between $^{210}$Po and $^{210}$Pb.

# DISCUSSION

## Abundance and Distribution of Soot in the Northeastern South China Sea

To date, only limited soot data are available for seawater. As reported in previous studies, the soot concentrations varied from 0.004 to 0.233 μmol-C $L^{-1}$ in the upper 60 m water column in the northern Gulf of Mexico (Yang and Guo, 2014), and from 0.008 to 0.080 μmol-C $L^{-1}$ in surface waters of the Bering Shelf and Chukchi Sea (Fang et al., 2016). On average, the soot concentration in the euphotic zone of the SCS (avg. 0.129 ± 0.027 μmol-C $L^{-1}$, **Table 1**) was higher than both the Gulf of Mexico (avg. 0.050 ± 0.070 μmol-C $L^{-1}$, $n$ = 14) (Yang and Guo, 2014) and the western Arctic and Subarctic Oceans (avg. 0.027 ± 0.020 μmol-C $L^{-1}$, $n$ = 18) (Fang et al., 2016). High soot concentration average of 0.39 ± 0.31 μmol-C $L^{-1}$ ($n$ = 38) was also reported on the shelf of the Gulf of Maine (Flores-Cervantes et al., 2009). These limited studies reflect the significant influence of nearby anthropogenic emissions on the abundance of soot in surface waters. Two studies indicate that soot concentration significantly decreases from the shore within a distance of 100 km (Flores-Cervantes et al., 2009; Yang and Guo, 2014). Thus, fluvial discharged soot would mostly settle into sediments close to the shore. In open water, the atmospheric deposition probably determines the abundance of soot in surface oceans. The soot concentrations varied from 0.064 to 0.090 μmol-C $L^{-1}$ below 200 m in the SCS (**Table 1**), which were much higher than 0.005–0.008 μmol-C $L^{-1}$ observed in the mesopelagic water of the northern Gulf of Mexico (Yang and Guo, 2014). Thus, the northern SCS could be characterized as a region with more abundant soot compared with other

open marine environments. The hotspots of BC emissions are expected to be responsible for the higher soot in the SCS. Indeed, the countries rounding the SCS contributed more than one third of the global BC emissions (Bond et al., 2013). Wet precipitation delivers large amounts of BC to the SCS (Mari et al., 2019). In addition, previous studies have shown that the higher DBC concentrations in the upper 100 m of the SCS (avg. $0.97 \pm 0.22$ μmol-C $L^{-1}$, $n = 79$) (Fang et al., 2017) compared to those observed in Prydz Bay, Antarctica ($0.75 \pm 0.26$ μmol-C $L^{-1}$, $n = 17$, Fang et al., 2018) should largely result from the enhanced emissions around the SCS.

The vertical distribution of soot, to a certain degree, revealed geochemical processes influencing the cycling of soot in the SCS (**Figure 2A**). In the upper water column, fluctuations in the soot concentration were mainly confined in the upper 50 m (**Figure 2**), probably due to water mixing processes mainly within the mixed layer. This view is further supported by the small variations in the $POC_{tot}$ concentration, TSM concentration, and the soot to $POC_{tot}$ ratio (**Figure 2**). By contrast, the soot exhibited a rapid decrease from 75 to 200 m (**Figure 2A**), potentially due to quick removal *via* photochemical degradation and/or sinking (Stubbins et al., 2012; Feng et al., 2021). This layer, characterized by the steep temperature and salinity gradients as shown in **Figure 1**, largely prevented the vertical mixing of seawater with different soot concentrations. Below the euphotic base, soot concentrations increased with depth like the case of TPM (**Figures 2A,D**). An increase in POC concentration was also observed between 800 and 1,000 m (**Figure 2B**). These results implied additional particulate matter sources in addition to those from the overlying water column. Coppola et al. (2014) suggested that resuspended old sediment BC may contribute to the sinking POC in the North Pacific as supported by the $^{14}C$ age of BC, highlighting the redistribution mechanism of BC after sedimentation in the ocean. Our recent study indicated that shelf/slope sediments account for 0.22–9.0 g $m^{-2}$ $d^{-1}$ particle fluxes out of the 700–1,000 m in the SCS (Ma et al., 2017). The occurrence of clay minerals in sediment traps and higher diatom flux in the deeper sediment traps also provided evidence for the dispersion of resuspended sediments into the SCS basin (Ran et al., 2015; Schroeder et al., 2015). Mechanistically, internal solitary waves result in the resuspension of the shelf and slope sediments (Zhang et al., 2014; Jia et al., 2019). Then, the resuspended particles lead to higher TPM content in the water column (Zhang et al., 2014) and extra flux below the euphotic zone in the SCS (Lahajnar et al., 2007; Gaye et al., 2009; Liu et al., 2014; Shih et al., 2019). Thus, shelf/slope sediments are also a source of soot in the mesopelagic waters of the northern SCS.

## $^{210}$Po-Derived Export Flux of Soot

Sinking is an important removal pathway of soot from the water column (Flores-Cervantes et al., 2009; Fang et al., 2016). In this study, the disequilibrium between $^{210}Po$ and $^{210}Pb$ was used to quantify the sinking flux of soot. The widely used mass-balance model for $^{210}Po$ (Bacon et al., 1976) was adopted by incorporating advection and diffusion processes. In general, except for upwelling and mesoscale eddy, vertical advection and horizontal diffusion terms are far smaller than vertical diffusion and horizontal advection (Liang et al., 2014). Thus, we only considered the horizontal advection and vertical diffusion. Briefly, the variation of $^{210}Po$ with time can be expressed as:

$$\frac{dI_{PoT}}{dt} = \lambda_{Po}(I_{PbT} - I_{PoT}) + U\frac{\partial I_{PoT}}{\partial x} + k_z\frac{\partial A_{PoT}}{\partial z} - F_{Po} \quad (1)$$

where $I_{PoT}$ and $I_{PbT}$ are the inventories of the total $^{210}Po$ and $^{210}Pb$ from surface to the export depth (in dpm $m^{-2}$). $\lambda_{Po}$ is the decay constant of $^{210}Po$ (0.0050 $d^{-1}$). $U$ and $k_z$ denote the horizontal advection velocity in cm $s^{-1}$ and vertical diffusive coefficient in $cm^2$ $s^{-1}$. $\partial I_{PoT}/\partial x$ and $\partial A_{PoT}/\partial z$ represent the gradient of inventory and activity of $^{210}Po$, respectively. $F_{Po}$ is the export flux of $^{210}Po$ (in dpm $m^{-2}$ $d^{-1}$). At a steady state, the export flux of $^{210}Po$ becomes:

$$F_{Po} = \lambda_{Po}(I_{PbT} - I_{PoT}) + U\frac{\partial I_{PoT}}{\partial x} + k_z\frac{\partial A_{PoT}}{\partial z} \quad (2)$$

Due to the lack of horizontal gradient of $^{210}Po$ in our study, we could not specifically assess the advection flux at the sampling station. However, we used available data collected during August in the north SCS (Ma et al., 2017) to estimate the influence of advection because these data exhibit a similar deficit of $^{210}Po$ in the mesopelagic SCS. The mean velocities are 15 cm/s in the upper 200 m and 10 cm/s at 500 m during summer in the study area (Gan et al., 2006), where $^{210}Po$ data have been reported (Ma et al., 2017). The calculated advection fluxes of $^{210}Po$ account for $17 \pm 21\%$ and $23 \pm 11\%$ of the fluxes at the euphotic base and the mesopelagic bottom, respectively. The estimates indicate that our results ignoring the advection term would, to a certain extent, lead to higher $^{210}Po$ fluxes at both the euphotic and mesopelagic bases. This overestimate is also propagated to soot flux calculation. In the future, the current-oriented sampling strategy should refine the advection influence. Neglecting advection fluxes will have less of an influence on the application of the soot-$^{210}Po$ coupling to constrain the contribution of soot and POC from the sediments. On the one hand, $^{210}Po$ fluxes were overestimated by comparable magnitude at the euphotic and mesopelagic bases. Subtracting the advection term largely eliminates the overestimates. On the other hand, the $^{210}Po$ flux in the mesopelagic water was much higher than 117% (i.e., flux including the influence of advection of 17%) of its flux at the euphotic base. Thus, neglecting advection fluxes will not influence our conclusions. In our study, the vertical gradients of $^{210}Po$ activity were 0.241 dpm $m^{-4}$ at the euphotic base and 0.009 dpm $m^{-4}$ at the mesopelagic bottom. In the upper SCS, the diffusive coefficient ranges from $10^{-4}$ to $10^{-5}$ $m^2$ $s^{-1}$ even though it could reach $10^{-3}$ $m^2$ $s^{-1}$ in the mid-deep water (Wang et al., 2019). Overall, the estimated diffusive fluxes of $^{210}Po$ account for <3.1% of the results obtained when neglecting advection and diffusion processes. Thus, the diffusivity of $^{210}Po$ should not significantly influence our results.

Using the same export model Eq. (2) and also neglecting the advection and diffusion terms, Wei et al. (2014) found that $^{210}Po$-derived POC fluxes were comparable to those derived from the floating trap during July–October at the South-East Asian Time-series Study (SEATS) station. The same observations were

also applied to carbonate and particulate nitrogen fluxes (Wei et al., 2014). This comparability lent support to the validity of the $^{210}$Po/$^{210}$Pb model in the study area between July and October. In addition, a previous study conducted in our study area that used $^{234}$Th/$^{238}$U tracer showed that when considering vertical and horizontal transport in a 3-D model, the results were unreasonable due to poorly constrained model parameters, whereas when using the 1-D Steady State model, such as the one used in this study, they obtained better results (Cai et al., 2015). Thus, we consider that the 1-D $^{210}$Po/$^{210}$Pb model is currently the best option to constrain particle dynamics in our study.

The export flux of soot ($F$_soot) was calculated using $F_{Po}$ multiplied by the soot to $^{210}$Po$_P$ ratio (in mmol-C dpm$^{-1}$), i.e.,

$$F\_\text{soot} = F_{Po} \times \frac{\text{soot}}{Po_P} \quad (3)$$

where Po$_P$ is the activity concentration of particulate $^{210}$Po.

Since $^{210}$Po showed deficits with respect to $^{210}$Pb from surface to 1,000 m, particles sinking out of the shallow layer are assumed to be responsible for the deficits in deeper layers. Accordingly, the inventories are calculated using trapezoidal integration, with surface and export depths as the upper and lower boundaries. The export flux of soot out of the euphotic zone (at 150 m) was 0.172 ± 0.016 mmol-C m$^{-2}$ d$^{-1}$ (**Table 2**), which is much lower than that of 2.28 mmol-C m$^{-2}$ d$^{-1}$ reported on the shelf of the Gulf of Maine (Flores-Cervantes et al., 2009) and much higher than 0.041–0.097 mmol-C m$^{-2}$ d$^{-1}$ observed on the Chukchi-Bering Shelf (Fang et al., 2016). Due to the contribution of resuspended sediment from the shelf/slope region to the depth below the euphotic zone, the soot export fluxes were indeed higher than that measured within the euphotic zone, varying from 0.282 ± 0.026 mmol-C m$^{-2}$ d$^{-1}$ to 1.13 ± 0.10 mmol-C m$^{-2}$ d$^{-1}$ (**Figure 3A**).

Below the euphotic zone or in the twilight zone, the soot might experience little photolysis, as was supported by the conservative behavior of DBC in the mesopelagic layer of the SCS (Fang et al., 2017). Thus, soot flux would remain constant in the twilight zone if there is no sediment-derived soot or the sinking velocity of soot is constant. The increase in the concentration of both TPM and soot (**Figure 2**) directly supports the contribution of sediment to the elevated soot flux in the mesopelagic zone at the study site. There is no available sinking velocity of particles in the SCS for assessing its influence on soot flux. The increased sinking velocity of particles with depth was observed in several areas (Villa-Alfageme et al., 2016). If this is true in the study area, the flux of soot (estimated using the velocity multiplied by the concentration) would increase even if the soot concentration does not vary. Thus, the increased soot fluxes in this study may include the effect of the sinking velocity, representing the upper limit of the sediment-contributed soot (i.e., $F$_soot$_{sed,i}$), which can be estimated by:

$$F\_\text{soot}_{sed,i} = F\_\text{soot}_i - F\_\text{soot}_{150} \quad (4)$$

where $F$_soot$_i$ denotes the total soot flux at a specific depth below 150 m, and $F$-soot$_{150}$ is the flux at 150 m, i.e., the euphotic base.

The sediment-derived soot fluxes were estimated to be 0.110 ± 0.030 mmol-C m$^{-2}$ d$^{-1}$ at 200 m, 0.149 ± 0.033 mmol-C m$^{-2}$ d$^{-1}$ at 300 m, and 0.96 ± 0.10 mmol-C m$^{-2}$ d$^{-1}$ at 800 m (**Table 2**). Owing to the sediment addition at different depths (Liu et al., 2014; Jia et al., 2019) and the refractory nature of the soot (Yang and Guo, 2018), the soot flux showed an accumulated effect from the euphotic base to the mesopelagic bottom (**Figure 3B**). In the upper twilight zone (200 and 300 m), sediment contribution accounted for 39–46% of the total soot flux, indicating a significant process for the total soot pool in the SCS interior. Near the mesopelagic bottom at 800 m, sediment-sourced soot accounted for as high as 85% of the total flux. It is obvious that, besides the atmospheric deposition, shelf/slope sediment resuspension is the most relevant process influencing the soot budget in the mesopelagic SCS.

## Application of $^{210}$Po-Soot Coupling to Constrain Particulate Organic Carbon Export Flux

Particulate organic carbon flux attenuation in the ocean interior is used to constrain the biological pump efficiency at a depth, i.e., the ratio of POC flux at each specific depth in the mesopelagic zone to that at the euphotic zone base (Martin et al., 1987; Buesseler et al., 2007; Chen et al., 2018). In this study, flux attenuation was used to express the variability of local biogenic POC (excluding soot and sediment-derived autochthonous POC) flux with depth in the study area. Appling Eq. (3) using the POC/Po$_P$ ratios measured on bottle-sampled TPM, the export fluxes of POC$_{tot}$ were estimated (**Figure 3C**). The POC$_{tot}$/$^{210}$Po$_P$ ratio for bottle-sampled TPM was comparable to that of the sediment-trap sample below the euphotic zone (i.e., 200 m), though a little difference was observed at 50 m (**Figure 4**). Due to the lack of trap sample at most depths, the POC/Po$_P$ ratios on bottle-sampled TPM were thus used to calculate the fluxes of POC to facilitate the comparison of POC fluxes at different depths. The POC$_{tot}$ varied from 5.44 ± 0.49 mmol-C m$^{-2}$ d$^{-1}$ to 33.6 ± 2.9 mmol-C m$^{-2}$ d$^{-1}$ (**Table 2**), averaging 12.3 mmol-C m$^{-2}$ d$^{-1}$. Notably, the POC$_{tot}$ flux at 200 m was about four times that at 50 m (**Figure 4**), corresponding to the higher primary productivity in the lower euphotic zone than the upper euphotic zone (Cai et al., 2015).

Since the soot is mostly of terrestrial origin (Gustafsson et al., 2001; Yang and Guo, 2018), the autochthonous POC (POC$_{auto}$) includes POC$_{auto,loc}$ from the local euphotic zone and POC$_{auto,sed}$ from the sediment, but excludes the soot. The calculated POC$_{auto}$ fluxes ranged from 5.12 ± 0.46 mmol-C m$^{-2}$ d$^{-1}$ to 10.49 ± 0.94 mmol-C m$^{-2}$ d$^{-1}$ (**Table 2**). In addition, the POC$_{auto,loc}$ flux out of the euphotic zone (5.97 ± 0.55 mmol-C m$^{-2}$ d$^{-1}$) was comparable to 4.0 ± 1.6 mmol-C m$^{-2}$ d$^{-1}$ ($n$ = 10) previously reported for the adjacent region in the same season (Cai et al., 2015), also supporting the validity of the $^{210}$Po/$^{210}$Pb model.

Below the euphotic base, the POC$_{auto}$ flux showed an increasing trend as observed for the flux of soot (**Figure 3D**). Obviously, the shelf/slope sediment contributed POC$_{auto}$ to the mesopelagic SCS. Based on the fact that POC$_{auto,sed}$ and soot were

**TABLE 2 |** The export fluxes of total POC ($F$_POC$_{tot}$) and soot ($F$-soot), autochthonous POC (i.e., soot-excluded POC, $F$_POC$_{auto}$), sediment contributed soot flux ($F$_soot$_{sed}$) and autochthonous POC ($F$_POC$_{auto,sed}$), and autochthonous POC contributed by local ecosystems in the euphotic zone ($F$_POC$_{auto,loc}$).

| Depth | $F$_soot | $F$_soot$_{sed}$ | $F$_POC$_{tot}$ | $F$_POC$_{auto}$ | $F$_POC$_{auto,sed}$ | $F$_POC$_{auto,loc}$ |
|---|---|---|---|---|---|---|
| (m) | (mmol-C m$^{-2}$ d$^{-1}$) | | | | | |
| 150 | 0.172 ± 0.016 | | 6.14 ± 0.56 | 5.97 ± 0.55 | | 5.97 ± 0.55 |
| 200 | 0.282 ± 0.026 | 0.110 ± 0.030 | 6.20 ± 0.57 | 5.92 ± 0.54 | 0.99 ± 0.27 | 4.93 ± 0.54 |
| 300 | 0.322 ± 0.029 | 0.149 ± 0.033 | 5.44 ± 0.49 | 5.12 ± 0.46 | 1.34 ± 0.30 | 3.78 ± 0.53 |
| 500 | | | 10.7 ± 1.0 | | | |
| 800 | 1.13 ± 0.10 | 0.96 ± 0.10 | 11.6 ± 1.0 | 10.49 ± 0.94 | 8.63 ± 0.93 | 1.87 ± 0.94 |
| 1000 | | | 33.6 ± 2.9 | | | |

*These fluxes were estimated based on the ratios of POC or soot contents to $^{210}$Po activities on total particulate matter (TPM) collected from the water column.*

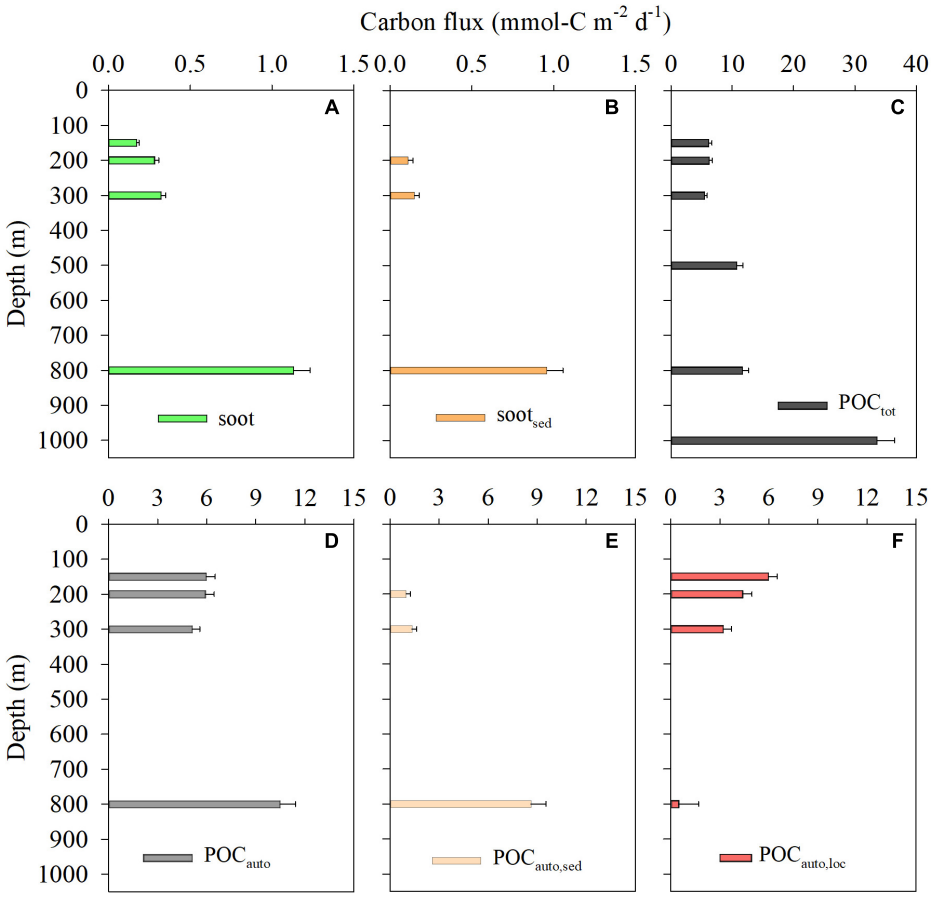


**FIGURE 3 |** Variations of POC and soot fluxes contributed by POC and soot from various pathways: **(A)** $^{210}$Po-derived total soot fluxes, **(B)** sediment-contributed soot fluxes (soot$_{sed}$), **(C)** POC$_{tot}$ fluxes, **(D)** marine biogenic POC (autochthonous POC) (i.e., soot-excluding POC) (POC$_{auto}$), **(E)** sediment-contributed POC$_{auto}$ fluxes (POC$_{auto,sed}$), and **(F)** POC fluxes from local euphotic zone (POC$_{auto,loc}$).

concurrently resuspended, the $^{210}$Po-derived $F$_soot$_{sed}$ and the SOC/soot ratio in surface sediments were used to estimate the POC$_{auto,sed}$ contribution to POC$_{auto}$ flux, i.e.,

$$F\_\mathrm{POC}_{\mathrm{auto,sed,i}} = F\_\mathrm{soot}_{\mathrm{sed,i}} \times \frac{\mathrm{SOC}}{\mathrm{soot}} \quad (5)$$

where $F$_POC$_{auto,sed,i}$ and $F$_soot$_{sed,i}$ denote the fluxes of $F$_POC$_{auto,sed}$ and $F$_soot$_{sed}$ at the specific i depth, respectively. SOC/soot is the ratio of the content of SOC to that of soot in surface sediments. At the two locations where sediment samples were collected (**Figure 1**), the SOC/soot ratio in surface sediments varied from 9.8 to 10.3%. Here, 10% was adopted for estimating the POC$_{auto,sed}$ contribution. It should be noted that the SOC/soot ratio may be different at different shelf/slope sites, and further measurements are needed to confirm this ratio in other regions.

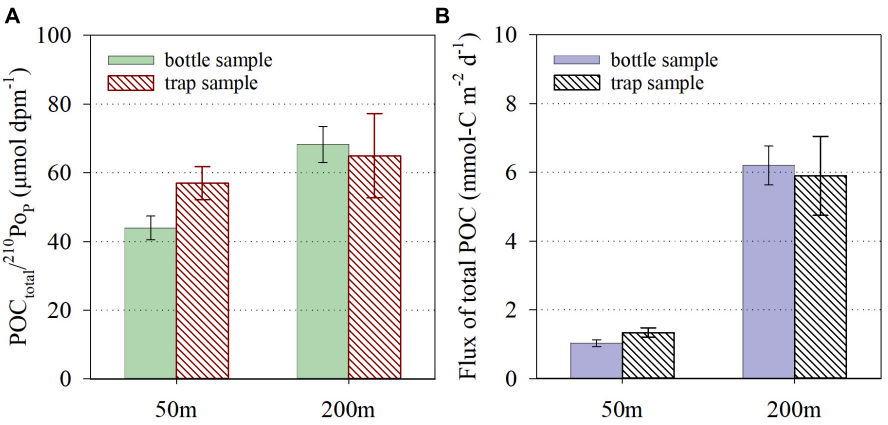


**FIGURE 4 |** Comparisons in the POC/$^{210}$Po ratio **(A)** and estimated total POC flux using $^{210}$Po **(B)** between bottle-sampling TPM and sediment trap-collected particles at 50 and 200 m.

Based on Eq. (5), the $POC_{auto,sed}$ fluxes were estimated to be 0.99 ± 0.27 mmol-C m$^{-2}$ d$^{-1}$ at 200 m, 1.34 ± 0.30 mmol-C m$^{-2}$ d$^{-1}$ at 300 m, and 8.63 ± 0.93 mmol-C m$^{-2}$ d$^{-1}$ at 800 m (**Table 2** and **Figure 3E**). Thus, the $POC_{auto,loc}$ fluxes in the mesopelagic waters can be calculated by subtracting the $POC_{auto,sed}$ fluxes from the $POC_{auto}$ fluxes. The $POC_{auto,loc}$ flux decreased from 4.93 ± 0.54 mmol-C m$^{-2}$ d$^{-1}$ at 200 m to 1.87 ± 0.94 mmol-C m$^{-2}$ d$^{-1}$ at 800 m, showing an attenuation from the euphotic base to 800 m like observations in open oceans (**Figure 3F**).

With the separation of $POC_{auto,loc}$ from $POC_{auto,sed}$, the first vertical distribution of $F\_POC_{auto,loc}$ in the SCS was used to compare the biological pump efficiency between the SCS and other oceanic settings. In the open ocean, the downward flux attenuation of POC is commonly described by the Martin Curve, i.e., $F_z/F_{z0} = (z/z_0)^{-b}$ (Martin et al., 1987), where $b$ describes the flux attenuation rate. The Martin Curve simulates the profiles of POC flux in the water column, and it has been widely used to evaluate the variability of POC fluxes from the euphotic zone to the deep ocean. By normalizing our $^{210}$Po-soot-based $F\_POC_{auto,loc}$ to that at 150 m, $b$ is 0.70 ± 0.01 ($R^2$ = 0.9996, $p < 0.001$) (**Figure 5**). Martin et al. (1987) first reported $b$ values ranging from 0.64 to 0.97 in the Pacific. Later, 1.33 ± 0.15 and 0.51 ± 0.05 were reported for ALOHA and K2 stations (from the VERTIGO project) (**Figure 5**; Buesseler et al., 2007). At station BATS (online data and Lutz et al., 2002), $b$ was 0.83 ± 0.04 (**Figure 5**) and the global mean value was 0.9–1.0 (Kwon et al., 2009). Our result observed in the oligotrophic SCS is comparable to that at station BATS. Globally, the SCS showed a low-moderate attenuation coefficient. Previous studies suggested that particle sinking velocity and temperature mainly influence the transport of POC to mesopelagic water (Buesseler et al., 2007; Henson et al., 2015; Le Moigne et al., 2016). Villa-Alfageme et al. (2016) reported valuable average sinking velocities (ASVs) of TPM at station BATS, showing an increase with depth. Considering the similar oligotrophic environments between the SCS and BATS, it is probable that high temperatures in the euphotic zone in the SCS (e.g., >20°C in the upper 100 m, **Figure 1**) benefits the fast remineralization of slow-sinking particles in shallow water, allowing faster-sinking particles to reach the mesopelagic zone, as observed at BATS (Villa-Alfageme et al., 2016). Owing to limited studies on POC transport in the mesopelagic water in

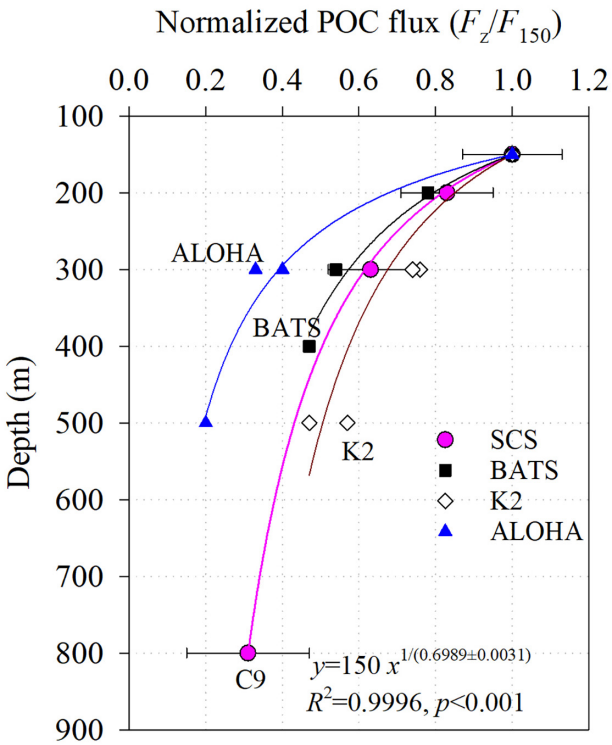


**FIGURE 5 |** Normalized POC flux to 150 m in the northeastern SCS and comparisons with ALOHA, K2 (Buesseler et al., 2007), and BATS (Lutz et al., 2002). Fittings used the Martin Curve, i.e., $F/F_{150} = (z/150)^{-b}$ (Martin et al., 1987), F is the flux of autochthonous and local POC (i.e., $POC_{auto,loc}$) at a depth of z horizon deeper than 150 m, $F_{150}$ is the flux at 150 m, z is the depth of POC flux below 150 m, and b denotes the constant of flux attenuation.

the SCS, extensive studies are needed to elucidate the mechanism controlling the biological pump in the mesopelagic zone of the SCS. Overall, our study indicated that $^{210}$Po-soot coupling could provide insights into the POC flux in the mesopelagic zone.

## CONCLUDING REMARKS

The abundance and export of soot were first evaluated in the northeastern SCS. The results indicated that several processes affected the geochemical cycling of soot in the marine environment. In the surface mixed layer, water mixing played a predominant role in determining the vertical distribution of soot, showing a homogenized soot concentration. In the lower euphotic zone with steep temperature and salinity gradients, photodegradation processes dominated, resulting in a decrease in soot concentrations with depth until the base of the euphotic zone. Below the euphotic zone, sediment resuspension in the shelf/slope region and lateral transport contributed to the increase in soot abundance and fluxes in the mesopelagic layer. The refractory nature of soot lends support for distinguishing the local soot sinking-flux from the sediment-derived soot flux in the twilight zone. By utilizing soot (terrestrial and bio-resistant in nature) and $^{210}$Po-derived POC flux, the local sinking POC flux from the overlying euphotic zone can be separated from the sediment-derived POC. These results revealed the potential application of $^{210}$Po-soot coupling to constrain POC fluxes in marginal seas.

## DATA AVAILABILITY STATEMENT

The original contributions presented in the study are included in the article/supplementary material, further inquiries can be directed to the corresponding author.

## AUTHOR CONTRIBUTIONS

XZhao, ZF, XZhang, and YQ collected and analyzed the samples. WY conceived and wrote the draft of the manuscript. LG, BH, and MC reviewed and edited the draft of the manuscript. All authors approved the submitted version.

## FUNDING

This study was financially supported by the National Key Research and Development Program of China (2016YFA0601201 to BH) and National Natural Science Foundation of China (42076030 and 41476061 to WY).

## ACKNOWLEDGMENTS

We thank YQ for his technical assistance during field trap sampling, crew members of the *R/V Yanping* for their help during sample collection, and three reviewers for their constructive comments that improved the manuscript.

## REFERENCES

Bacon, M. P., Spencer, D. W., and Brewer, P. G. (1976). $^{210}$Pb/$^{226}$Ra and $^{210}$Po/$^{210}$Pb disequilibria in seawater and suspended particulate matter. *Earth Planet. Sci. Lett.* 32, 277–296. doi: 10.1016/0012-821X(76)90068-6

Bao, H., Niggemann, J., Luo, L., Dittmar, T., and Kao, S.-J. (2017). Aerosols as a source of dissolved black carbon to the ocean. *Nat. Commun.* 8:510. doi: 10.1038/s41467-017-00437-3

Bond, T. C., Doherty, S. J., Fahey, D. W., Forster, P. M., Berntsen, T., DeAngelo, B. J., et al. (2013). Bounding the role of black carbon in the climate system: a scientific assessment. *J. Geophys. Res. Atmos.* 118, 5380–5552. doi: 10.1002/jgrd.50171

Buesseler, K. O., Lamborg, C. H., Boyd, P. W., Lam, P. J., Trull, T. W., Bidigare, R. R., et al. (2007). Revisiting carbon flux through the ocean's twilight zone. *Science* 316, 567–570. doi: 10.1126/science.1137959

Cai, P., Zhao, D., Wang, L., Huang, B., and Dai, M. (2015). Role of particle stock and phytoplankton community structure in regulating particulate organic carbon export in a large marginal sea. *J. Geophys. Res. Oceans* 120, 2063–2095. doi: 10.1002/2014JC010432

Chen, C.-T. A., Wang, S.-L., Wang, B.-J., and Pai, S.-C. (2001). Nutrient budgets for the South China Sea basin. *Mar. Chem.* 75, 281–300. doi: 10.1016/S0304-4203(01)00041-X

Chen, Y., Wu, Z., and Li, Q. (2018). Temporal change of export production at Xisha of the Northern South China Sea. *J. Geophys. Res. Oceans* 123, 9305–9319. doi: 10.1029/2017JC013619

Cheng, C.-H., Lehmann, J., and Engelhard, M. H. (2008). Natural oxidation of black carbon in soils: changes in molecular form and surface charge along a climosequence. *Geochim. Cosmochim. Acta* 72, 1598–1610. doi: 10.1016/j.gca.2008.01.010

Church, T. M., Rigaud, S., Baskaran, M., Kumar, A., Friedrich, J., Masqué, P., et al. (2012). Intercalibration studies of $^{210}$Po and $^{210}$Pb in dissolved and particulate seawater samples. *Limnol. Oceanogr. Methods* 10, 776–789. doi: 10.4319/lom.2012.10.776

Coppola, A. I., and Druffel, E. R. M. (2016). Cycling of black carbon in the ocean. *Geophys. Res. Lett.* 43, 4477–4482. doi: 10.1002/2016GL068574

Coppola, A. I., Wiedemeier, D. B., Galy, V., Haghipour, N., Hanke, U. M., Nascimento, G. S., et al. (2018). Global-scale evidence for the refractory nature of riverine black carbon. *Nat. Geosci.* 11, 584–588. doi: 10.1038/s41561-018-0159-8

Coppola, A. I., Ziolkowski, L. A., Masiello, C. A., and Druffel, E. R. M. (2014). Aged black carbon in marine sediments and sinking particles. *Geophys. Res. Lett.* 41, 2427–2433. doi: 10.1002/2013GL059068

Dittmar, T., Eduardo de Rezende, C., Manecki, M., Niggemann, J., Ovalle, A. R. C., Stubbins, A., et al. (2012). Continuous flux of dissolved black carbon from a vanished tropical forest biome. *Nat. Geosci.* 5, 618–622. doi: 10.1038/ngeo1541

Elmquist, M., Gustafsson, Ö, and Andersson, P. (2004). Quantification of sedimentary black carbon using the chemothermal oxidation method: an evaluation of ex situ pre-treatments and standard additions approaches. *Limnol. Oceanogr. Methods* 2, 417–427. doi: 10.4319/lom.2004.2.417

Fang, Z., Yang, W., Chen, M., and Ma, H. (2017). Source and fate of dissolved black carbon in the western South China Sea during the Southwest Monsoon prevailing season. *J. Geophys. Res. Biogeosci.* 122, 2817–2830. doi: 10.1002/2017JG004014

Fang, Z., Yang, W., Chen, M., Stubbins, A., Ma, H., and Jia, R. (2018). Transport of dissolved black carbon from the Prydz Bay Shelf, Antarctica to the deep Southern Ocean. *Limnol. Oceanogr.* 63, 2179–2190. doi: 10.1002/lno.10932

Fang, Z., Yang, W., Chen, M., Zheng, M., and Hu, W. (2016). Abundance and sinking of particulate black carbon in the western Arctic and Subarctic Oceans. *Sci. Rep.* 6:29959. doi: 10.1038/srep29959

Fang, Z., Yang, W., Stubbins, A., Chen, M., Li, J., Jia, R., et al. (2021). Spatial characteristics and removal of dissolved black carbon in the western Arctic Ocean and Bering Sea. *Geochim. Cosmochim. Acta* 304, 178–190. doi: 10.1016/j.gca.2021.04.024

Feng, N., Yang, W., Zhao, X., Chen, M., Qiu, Y., and Zheng, M. (2021). Semi-enclosed bays server as hotspots for black carbon burial: a case study in Jiaozhou Bay, western Yellow Sea. *Sci. Total Environ.* 797:149100. doi: 10.1016/j.scitotenv.2021.149100

Flores-Cervantes, D. X., Plata, D. L., MacFarlane, J. K., Reddy, C. M., and Gschwend, P. M. (2009). Black carbon in marine particulate organic carbon: inputs and cycling of highly recalcitrant organic carbon in the Gulf of Maine. *Mar. Chem.* 113, 172–181. doi: 10.1016/j.marchem.2009.01.012

Gan, J., Li, H., Curchitser, E. N., and Haidvogel, D. B. (2006). Modeling South China Sea circulation: response to seasonal forcing regimes. *J. Geophys. Res.* 111:C06034. doi: 10.1029/2005JC003298

Gaye, B., Wiesner, M. G., and Lahajnar, N. (2009). Nitrogen sources in the South China Sea, as discerned from stable nitrogen isotopic ratios in rivers, sinking particles, and sediments. *Mar. Chem.* 114, 72–85. doi: 10.1016/j.marchem.2009.04.003

Goldberg, E. D. (1985). *Black Carbon In The Environment*. New York: John Wiley.

Gustafsson, Ö, Bucheli, T. D., Kukulska, Z., Andersson, M., Largeau, C., Rouzaud, J.-N., et al. (2001). Evaluation of a protocol for the quantification of black carbon in sediments. *Glob. Biogeochem. Cycles* 15, 881–890. doi: 10.1029/2000GB001380

Gustafsson, Ö, Haghseta, F., Chan, C., Macfarlane, J., and Gschwend, P. M. (1997). Quantification of the dilute sedimentary soot phase: implications for PAH speciation and bioavailability. *Environ. Sci. Technol.* 31, 203–209. doi: 10.1021/es960317s

Henson, S. A., Yool, A., and Sanders, R. J. (2015). Variability in efficiency of particulate organic carbon export: a model study. *Glob. Biogeochem. Cycles* 29, 33–45. doi: 10.1002/2014GB004965

Hu, L., Shi, X., Bai, Y., Fang, Y., Chen, Y., Qiao, S., et al. (2016). Distribution, input pathway and mass inventory of black carbon in sediments of the Gulf of Thailand, SE Asia. *Estuar. Cost. Shlef Sci.* 170, 10–19. doi: 10.1016/j.ecss.2015.12.019

Jacobson, M. Z. (2001). Strong radiative heating due to the mixing state of black carbon in atmospheric aerosols. *Nature* 409, 695–697. doi: 10.1038/35055518

Jia, Y., Tian, Z., Shi, X., Liu, J. P., Chen, J., and Liu, X. (2019). Deep-sea sediment resuspension by internal solitary waves in the Northern South China Sea. *Sci. Rep.* 9:12137. doi: 10.1038/s41598-019-47886-y

Jones, M. W., Coppola, A. I., Santín, C., Dittmar, T., Jaffé, R., Doerr, S. H., et al. (2020). Fires prime terrestrial organic carbon for riverine export to the global oceans. *Nat. Commun.* 11:2791. doi: 10.1038/s41467-020-16576-z

Jurado, E., Dashs, J., Duarte, C. M., and Simó, R. (2008). Atmospheric deposition of organic and black carbon. *Atmos. Environ.* 42, 7931–7939. doi: 10.1016/j.atmosenv.2008.07.029

Kwon, E. Y., Primeau, F., and Sarmiento, J. L. (2009). The impact of remineralization depth on the air-sea carbon balance. *Nat. Geosci.* 2, 630–635. doi: 10.1038/ngeo612

Lahajnar, N., Wiesner, M. G., and Gaye, B. (2007). Fluxes of amino acids and hexosamines to the deep South China Sea. *Deep Sea Res. I* 54, 2120–2144. doi: 10.1016/j.dsr.2007.08.009

Le Moigne, F. A. C., Henson, S. A., Cavan, E., Georges, C., Pabortsava, K., Achterberg, E. P., et al. (2016). What causes the inverse relationship between primary production and export efficiency in the Southern Ocean?. *Geophys. Res. Lett.* 43, 4457–4466. doi: 10.1002/2016GL068480

Liang, H., Zhao, W., Dai, D., and Zhang, J. (2014). Estimation of vertical diffusion coefficient based on a onedimensional temperature diffusion equation with an inverse method. *Acta Oceanol. Sin.* 33, 28–36. doi: 10.1007/s13131-014-0472-z

Liu, J., Clift, P. D., Yan, W., Chen, Z., Chen, H., Xiang, R., et al. (2014). Modern transport and deposition of settling particles in the northern South China Sea: sediment trap evidence adjacent to Xisha Trough. *Deep Sea Res. I* 93, 145–155. doi: 10.1016/j.dsr.2014.08.005

Lohmann, R., Bollinger, K., Cantwell, M., Feichter, J., Fischer-Bruns, I., and Zabel, M. (2009). Fluxes of soot black carbon to South Atlantic sediments. *Glob. Biogeochem. Cycles* 23:GB1015. doi: 10.1029/2008GB003253

Louchouarn, P., Chillrud, R. N., Houel, S., Yan, B., Chaky, D., Rumpel, C., et al. (2007). Elemental and molecular evidence of soot-and char-derived black carbon inputs to New York City's atmosphere during the 20$^{th}$ century. *Environ. Sci. Technol.* 41, 82–87. doi: 10.1021/es061304+

Lutz, M., Dunbar, R., and Caldeira, K. (2002). Regional variability in the vertical flux of particulate organic carbon in the ocean interior. *Glob. Biogeochem. Cycles* 16:1037. doi: 10.1029/2000GB001383

Ma, H., Yang, W., Zhang, L., Zhang, R., Chen, M., Qiu, Y., et al. (2017). Utilizing $^{210}$Po deficit to constrain particle dynamics in mesopelagic water, western South China Sea. *Geochem. Geophys. Geosys.* 18, 1594–1607. doi: 10.1002/2017GC006899

Mari, X., Guinot, B., Thuoc, C. V., Brune, J., Lefebvre, J.-P., Sriram, P. R. A., et al. (2019). Biogeochemical impacts of a black carbon wet deposition event in Halong Bay, Vietnam. *Front. Mar. Sci.* 6:185. doi: 10.3389/fmars.2019.00185

Martin, J. H., Knauer, G. A., Karl, D. M., and Broenkow, W. W. (1987). VERTEX: carbon cycling in the northeast Pacific. *Deep Sea Res. A* 34, 267–285. doi: 10.1016/0198-0149(87)90086-0

Masiello, C. A., and Druffel, E. R. M. (1998). Black carbon in deep-sea sediments. *Science* 280, 1911–1913. doi: 10.1126/science.280.5371.1911

Qi, Y., Fu, W., Tian, J., Luo, C., Shan, S., and Sun, S. (2020). Dissolved black carbon is not likely a significant refractory organic carbon pool in rivers and oceans. *Nat. Commun.* 11:5051. doi: 10.1038/s41467-020-18808-8

Ramanathan, V., and Carmichael, G. (2008). Global and regional climate changes due to black carbon. *Nat. Geosci.* 1, 221–227. doi: 10.1038/ngeo156

Ran, L., Chen, J., Wiesner, M. G., Ling, Z., Lahajnar, N., Yang, Z., et al. (2015). Variability in the abundance and species composition of diatoms in sinking particles in the northern South China Sea: results from time-series moored sediment traps. *Deep Sea Res. II* 122, 15–24. doi: 10.1016/j.dsr2.2015.07.004

Rigaud, S., Puigorbé, V., Camara-Mor, P., Casacuberta, N., Roca-Martí, M., Garcia-Orellana, J., et al. (2013). A methods assessment and recommendations for improving calculations and reducing uncertainties in the determination of $^{210}$Po and $^{210}$Pb activities in seawater. *Limnol. Oceanogr. Methods* 11, 561–571. doi: 10.4319/lom.2013.11.561

Roca-Martí, M., Puigcorbé, V., Castrillejo, M., Casacuberta, N., Garcia-Orellana, J., Cochran, J. K., et al. (2021). Quantifying $^{210}$Po/$^{210}$Pb disequilibrium in seawater: a comparison of two precipitation methods with differing results. *Front. Mar. Sci.* 8:684484. doi: 10.3389/fmars.2021.684484

Schroeder, A., Wiesner, M. G., and Liu, Z. (2015). Fluxes of clay minerals in the South China Sea. *Earth Planet. Sci. Lett.* 430, 30–42. doi: 10.1016/j.epsl.2015.08.001

Shih, Y.-Y., Lin, H.-H., Li, D., Hsieh, H.-H., Hung, C.-C., and Chen, C.-T. A. (2019). Elevated carbon flux in deep waters of the South China Sea. *Sci. Rep.* 9:1496. doi: 10.1038/s41598-018-37726-w

Singh, N., Abiven, S., Torn, M. S., and Schmidt, M. W. I. (2012). Fire-derived organic carbon in soil turns over on a centennial scale. *Biogeosciences* 9, 2847–2857. doi: 10.5194/bg-9-2847-2012

Stubbins, A., Niggemann, J., and Dittmar, T. (2012). Photo-lability of deep ocean dissolved black carbon. *Biogeosciences* 9, 1661–1670. doi: 10.5194/bg-9-1661-2012

Villa-Alfageme, M., de Soto, F. C., Ceballos, E., Giering, S. L. C., Le Moigne, F. A. C., Henson, S., et al. (2016). Geographical, seasonal, and depth variation in sinking particle speeds in the North Atlantic. *Geophys. Res. Lett.* 43, 8609–8616. doi: 10.1002/2016GL069233

Wagner, S., Brandes, J., Spencer, R. G. M., Ma, K., Rosengard, S. Z., Moura, J. M. S., et al. (2019). Isotopic composition of oceanic dissolved black carbon reveals non-riverine source. *Nat. Commun.* 10:5064. doi: 10.1038/s41467-019-13111-7

Wagner, S., Jaffé, R., and Stubbins, A. (2018). Dissolved black carbon in aquatic ecosystems. *Limnol. Oceanogr. Lett.* 3, 168–185. doi: 10.1002/lol2.10076

Wang, D., Wang, Q., Cai, S., Shang, X., Peng, S., Shu, Y., et al. (2019). Advances in research of the mid-deep South China Sea circulation. *Sci. China Earth Sci.* 62, 1992–2004. doi: 10.1007/s11430-019-9546-3

Wang, X., Xu, C., Druffel, E. M., Xue, Y., and Qi, Y. (2016). Two black carbon pools transported by the Changjiang and Huanghe Rivers in China. *Glob. Biogeochem. Cycles* 30, 1778–1790. doi: 10.1002/2016GB005509

Wang, Z., Yang, W., Chen, M., Lin, P., and Qiu, Y. (2014). Intra-annual deposition of atmospheric $^{210}$Pb, $^{210}$Po and the residence times of aerosol in Xiamen, China. *Aerosol Air Qual. Res.* 14, 1402–1410. doi: 10.4209/aaqr.2013.05.0170

Ward, C. P., Sleighter, R. L., Hatcher, P. G., and Cory, R. M. (2014). Insights into the complete and partial photooxidation of black carbon in surface waters. *Environ. Sci. Process. Impacts* 16, 721–731. doi: 10.1039/c3em00597f

Wei, C.-L., Lin, S.-Y., Sheu, D. D., Chou, W.-C., Yi, M.-C., Santschi, P. H., et al. (2011). Particle-reactive radionuclides ($^{234}$Th, $^{210}$Pb, $^{210}$Po) as tracers for the estimation of export production in the South China Sea. *Biogeosciences* 8, 3793–3808. doi: 10.5194/bg-8-3793-2011

Wei, C.-L., Yi, M.-C., Lin, S.-Y., Wen, L.-S., and Lee, W.-H. (2014). Seasonal distributions and fluxes of $^{210}$Pb and $^{210}$Po in the northern South China Sea. *Biogeosciences* 11:6813v6826. doi: 10.5194/bg-11-6813-2014

Yang, W., and Guo, L. (2014). Abundance, distribution and isotopic composition of particulate black carbon in the northern Gulf of Mexico. *Geophys. Res. Lett.* 41, 7619–7625. doi: 10.1002/2014GL061912

Yang, W., and Guo, L. (2018). Sources and burial fluxes of soot black carbon in sediments on the Mackenzie, Chukchi, and Bering Shelves. *Cont. Shelf Res.* 155, 1–10. doi: 10.1016/j.csr.2018.01.008

Yang, W., Guo, L., Chuang, C. Y., Schumann, D., Ayranov, M., and Santschi, P. H. (2013). Adsorption characteristics of $^{210}$Pb, $^{210}$Po and $^{7}$Be onto micro-particle surfaces and the effects of macromolecular organic compounds. *Geochim. Cosmochim. Acta* 107, 47–64. doi: 10.1016/j.gca.2012.12.039

Yang, W., Huang, Y., Chen, M., Qiu, Y., Peng, A., and Zhang, L. (2009). Export and remineralization of POM in the Southern Ocean and the South China Sea estimated from $^{210}$Po/$^{210}$Pb disequilibria. *Chin. Sci. Bull.* 54, 2118–2123. doi: 10.1007/s11434-009-0043-4

Zhang, J., Li, H., Xuan, J., Wu, Z., Yang, Z., Wiesner, M. G., et al. (2019). Enhancement of mesopelagic sinking particle fluxes due to upwelling, aerosol deposition, and monsoonal influences in the northwestern South China Sea. *J. Geophys. Res. Oceans* 124, 99–112. doi: 10.1029/2018JC014704

Zhang, L., Yang, W., Chen, M., Wang, Z., Lin, P., Fang, Z., et al. (2016). Atmospheric deposition of $^{7}$Be in the southeast of China: a case study in Xiamen. *Aerosol Air Qual. Res.* 16, 105–113. doi: 10.4209/aaqr.2015.03.0182

Zhang, X., Chen, J., Xiang, L., Fang, J., Li, Y., Zhu, Y., et al. (2014). A preliminary study on the characteristics of marine nepheloid layers in the northern South China Sea and their influential factors. *Acta Oceanol. Sin.* 36, 51–65.

Ziolkowski, L. A., and Druffel, E. R. M. (2010). Aged black carbon identified in marine dissolved organic carbon. *Geophys. Res. Lett.* 37:L16601. doi: 10.1029/2010GL043963

**Conflict of Interest:** The authors declare that the research was conducted in the absence of any commercial or financial relationships that could be construed as a potential conflict of interest.

**Publisher's Note:** All claims expressed in this article are solely those of the authors and do not necessarily represent those of their affiliated organizations, or those of the publisher, the editors and the reviewers. Any product that may be evaluated in this article, or claim that may be made by its manufacturer, is not guaranteed or endorsed by the publisher.

*Copyright © 2021 Yang, Zhao, Guo, Huang, Chen, Fang, Zhang and Qiu. This is an open-access article distributed under the terms of the Creative Commons Attribution License (CC BY). The use, distribution or reproduction in other forums is permitted, provided the original author(s) and the copyright owner(s) are credited and that the original publication in this journal is cited, in accordance with accepted academic practice. No use, distribution or reproduction is permitted which does not comply with these terms.*

frontiers in Marine Science

ORIGINAL RESEARCH
published: 02 December 2021
doi: 10.3389/fmars.2021.700524

# $^{210}$Po-$^{210}$Pb Disequilibrium in the Western North Pacific Ocean: Particle Cycling and POC Export

*Qiangqiang Zhong[1,2], Tao Yu[1], Hui Lin[1], Jing Lin[1], Jianda Ji[1], Jialin Ni[1], Jinzhou Du[2] and Dekun Huang[1]**

[1] *Third Institute of Oceanography, Ministry of Natural Resource, Xiamen, China,* [2] *State Key Laboratory of Estuarine and Coastal Research, East China Normal University, Shanghai, China*

Estimating the particulate organic carbon (POC) export flux from the upper ocean is fundamental for understanding the efficiency of the biological carbon pump driven by sinking particles in the oceans. The downward POC flux from the surface ocean based on $^{210}$Po-$^{210}$Pb disequilibria in seawater samples from the western North Pacific Ocean (w-NPO) was measured in the early summer (May-June) of 2018. All the profiles showed a large $^{210}$Po deficiency relative to $^{210}$Pb in the euphotic zone (0–150 m), while this $^{210}$Po deficiency vanished below ∼500 m (with $^{210}$Po/$^{210}$Pb ∼1 or > 1). A one-dimensional steady-state irreversible scavenging model was used to quantify the scavenging and removal fluxes of $^{210}$Po and $^{210}$Pb in the euphotic zone of the w-NPO. In the upper ocean (0–150 m), dissolved $^{210}$Po (D-Po) was scavenged into particles with a residence time of 0.6–5.5 year, and the $^{210}$Po export flux out of the euphotic zone was estimated as (0.33–3.49) × $10^4$ dpm/m$^2$/year, resulting in a wide range of particulate $^{210}$Po (P-Po) residence times (83–921 days). However, in the deep ocean (150–1,000 m), $^{210}$Po was transferred from the particulate phase to the dissolved phase. Using an integrated POC inventory and the P-Po residence times (Eppley model) in the w-NPO euphotic zone, the POC export fluxes (mmol C/m$^2$/d) varied from 0.6 ± 0.2 to 8.8 ± 0.4. In comparison, applying the POC/$^{210}$Po ratio of all (>0.45 μm) particles to $^{210}$Po export flux (Buesseler model), the obtained POC export fluxes (mmol C/m$^2$/d) ranged from 0.7 ± 0.1 to 8.6 ± 0.8. Both Buesseler and Eppley methods showed enhanced POC export fluxes at stations near the continental shelf (i.e., Luzon Strait and the Oyashio-Kuroshio mixing region). The Eppley model-based $^{210}$Po-derived POC fluxes agreed well with the Buesseler model-based fluxes, indicating that both models are suitable for assessing POC fluxes in the w-NPO. The POC export efficiency was < 15%, suggesting a moderate biological carbon pump efficiency in the w-NPO. These low export efficiencies may be associated with the dominance of smaller particles and the processes of degradation and subsequent remineralization of these small particles in the euphotic zone of oligotrophic regions in the w-NPO.

**Keywords: $^{210}$Po deficiency, POC export flux, marine biological carbon pump, Western North Pacific Ocean, euphotic zone**

OPEN ACCESS

***Edited by:***
*Pere Masque, IAEA International Atomic Energy Agency, Monaco*

***Reviewed by:***
*María Villa-Alfageme, Seville University, Spain*
*J. Kirk Cochran, Stony Brook University, United States*

****Correspondence:***
*Dekun Huang*
*dkhuang@tio.org.cn*

***Specialty section:***
*This article was submitted to Marine Biogeochemistry, a section of the journal Frontiers in Marine Science*

***Received:*** *26 April 2021*
***Accepted:*** *11 November 2021*
***Published:*** *02 December 2021*

***Citation:***
*Zhong Q, Yu T, Lin H, Lin J, Ji J, Ni J, Du J and Huang D (2021) $^{210}$Po-$^{210}$Pb Disequilibrium in the Western North Pacific Ocean: Particle Cycling and POC Export. Front. Mar. Sci. 8:700524. doi: 10.3389/fmars.2021.700524*

## INTRODUCTION

As the Earth's largest carbon reservoir (IPCC in Climate Change, 2013), the marine ecosystem plays a fundamental role in regulating the atmospheric $CO_2$ concentration and buffering the effects of global climate change (Sabine, 2004) by assimilating carbon from the atmosphere *via* dissolution and photosynthesis in the upper ocean. Even small changes in the magnitude of the downward transport of carbon in the upper ocean can have serious impacts on oceanic carbon sequestration and atmospheric $CO_2$ concentration (Kwon et al., 2009) and thus on global climate change (including global warming). It has been predicted that without the marine biological carbon pump (BCP), the atmospheric $CO_2$ concentration could be approximately 50% higher than its current value (Sanders et al., 2014).

To fully understand how the oceans regulate the atmospheric $CO_2$ concentration, detailed knowledge of the marine carbon cycle is needed. The well-known BCP is one of three major mechanisms by which the ocean takes up atmospheric $CO_2$ (Liu et al., 2018). The BCP is described by these major processes: Phytoplankton convert $CO_2$ into fixed carbon, e.g., carbohydrates or calcium carbonate through photosynthesis in the euphotic zone; Part of the $CO_2$ fixed is transferred to the ocean interior of the ocean, mainly by gravitational sinking of particulate organic carbon (POC); Diffusion, advection and vertical mixing of dissolved organic carbon (DOC) and active bio-transport of organic and inorganic carbon by diel vertical migrating zooplankton are also important carbon removal pathways; Finally very few percentage of fixed carbon will be sequestered in the deep ocean (Buesseler et al., 2007). All these biologically mediated processes constitute the BCP. Thus, sinking particles play an important role in driving the BCP (Falkowski et al., 1998; Ducklow et al., 2001; Wei et al., 2011; Liu et al., 2018).

The ratio of export production (or the POC export flux) to total primary production, known as the "f-ratio" is defined as the export efficiency of the BCP and is used to quantity the strength of the pump (Buesseler and Boyd, 2009). Hence, an investigation of the sinking POC export flux from the upper ocean would provide fundamental parameters for predicting future changes in the marine carbon cycle. To constrain the POC export flux from the upper ocean, two traditional approaches are frequently applied: sediment traps (Honjo et al., 2008; Hayes et al., 2018) and the disequilibrium of the natural radionuclide pair, $^{234}$Th-$^{238}$U (Charette et al., 1999; Benitez-Nelson et al., 2001; Buesseler et al., 2009, 2020; Zhou et al., 2020).

In recent years, another pair of natural radionuclide tracers, $^{210}$Po ($T_{1/2}$ = 138.4 days) and its progenitor $^{210}$Pb ($T_{1/2}$ = 22.4 year), has been shown to be effective at predicting the POC export flux (Murray et al., 2005; Stewart et al., 2007, 2010; Verdeny et al., 2009; Wei et al., 2011; Le Moigne et al., 2013; Roca-Martí et al., 2016; Hayes et al., 2018; Subha Anand et al., 2018; Tang et al., 2019; Horowitz et al., 2020); however, this tracer pair has not been applied frequently. The $^{210}$Po/$^{210}$Pb ratio exhibits different behavior from the $^{234}$Th/$^{238}$U ratio in terms of particle-binding properties in the ocean. $^{234}$Th is particle reactive and is scavenged from surface waters when particles sink into the deep sea, while naturally occurring $^{238}$U is conserved and remains dissolved in well-oxygenated seawater. In contrast, both $^{210}$Po and $^{210}$Pb are particle reactive. In addition, $^{210}$Pb and $^{234}$Th are only adsorbed onto the particle surface, whereas $^{210}$Po is both adsorbed onto surfaces and biologically assimilated into cells by some species of phytoplankton and bacteria (Fisher et al., 1983; Cherrier et al., 1995; LaRock et al., 1996; Stewart and Fisher, 2003a,b). As a result, phytoplankton cells accumulating $^{210}$Po are further ingested by zooplankton, while sinking particles excreted as fecal pellets and biogenic detritus are depleted in $^{210}$Po (Heyraud et al., 1976). This biogeochemical behavior leads to the distribution coefficient of $^{210}$Po being higher than that of $^{210}$Pb (Tang et al., 2017; Zhong et al., 2019). Thus, when particles sink from the upper ocean, the large difference in particle affinity leads to secular disequilibrium between $^{210}$Po and $^{210}$Pb, which can be used to estimate particulate material export in a manner similar to the use of $^{234}$Th-$^{238}$U disequilibrium (Friedrich and Rutgers van der Loeff, 2002; Cochran and Masqué, 2003; Verdeny et al., 2009; Wei et al., 2011; Hayes et al., 2018; Subha Anand et al., 2018; Horowitz et al., 2020). However, relatively few studies have used the $^{210}$Po-$^{210}$Pb disequilibrium method to quantify the POC export flux at a basin wide scale (Ceballos-Romero et al., 2016; Roca-Martí et al., 2016; Tang and Stewart, 2019; Tang et al., 2019).

Oligotrophic open waters compose a major proportion (∼75%) of the surface ocean and account for over 30% of global marine carbon fixation (Shih et al., 2015). The NPO is an important atmospheric carbon sink, it can contribute to ∼25% of the total ocean $CO_2$ uptake per year (Takahashi et al., 2009). By assessing the carbon export in the NPO, the goal of peak carbon dioxide emissions and carbon neutrality for humanity can be achieved more scientifically, and the pace of global climate change can be gradually showed down. As a part of the "Marine Environment Monitoring and Early Warning System Construction in the West Pacific Ocean (MEMEWSC)" project, we took advantage of a unique opportunity to obtain measurements of $^{210}$Po and $^{210}$Pb activity over a large tract of the w-NPO (from 117°E to 146°E and from 20°N to 40°N). In this study, we describe the activity profiles (1,000 m) of $^{210}$Po and $^{210}$Pb at 7 stations spanning different oceanographic regions with different aeolian inputs, distances from the nearest coast and rates of primary production. The goals of this study are listed as follows: (1) To investigate the spatial variability of particle scavenging and removal processes in the water column of each oceanographic region; and (2) to estimate the magnitude and efficiency of the POC export flux derived from the $^{210}$Po-$^{210}$Pb disequilibrium in the euphotic layer of the w-NPO.

## MATERIALS AND METHODS

### Sampling and Preparation

The study area located in the western part of the NPO, covering an area of 20–40°N and 118–153°E. The main surface ocean currents in this region are shown in **Figure 1**. The Kuroshio Current (KC) is the most important western boundary current in the w-NPO, it originates from the North Equatorial Current and subsequently intrudes from the western Philippine Sea into the northern South China Sea (SCS) in the Luzon Strait. The

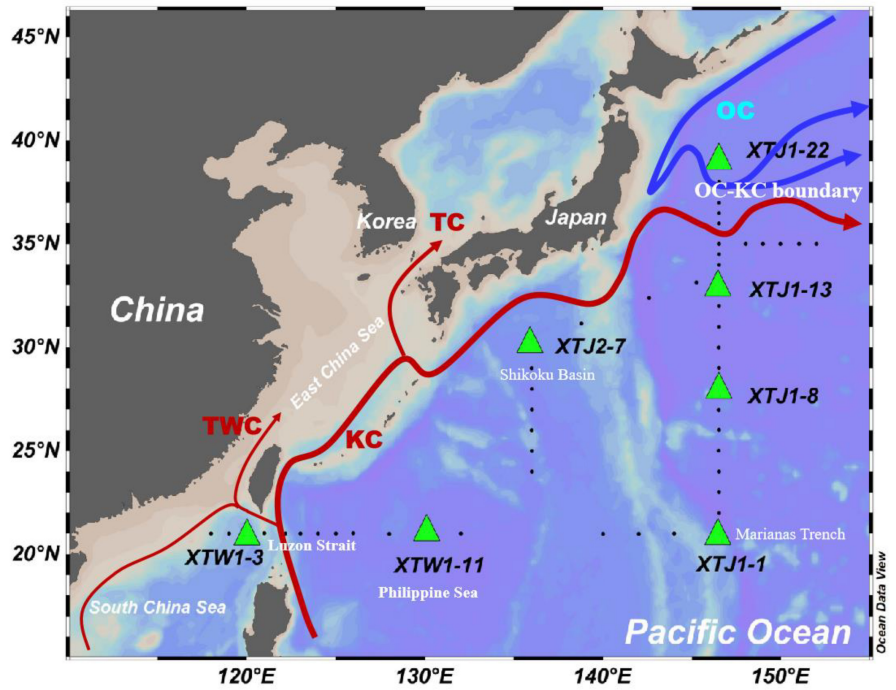


**FIGURE 1 |** Map of the bathymetry and the locations of the sampling stations (black dots) studied during the cruise in the w-NPO. The green triangles indicate the stations where $^{210}$Po and $^{210}$Pb activities were measured. The arrows represent the surface circulation systems of the w-NPO (Yasuda, 2003; Gallagher et al., 2015; Hu et al., 2015). TWC, Taiwan Warm Current; KC, Kuroshio Current; TC, Tsushima Current; OC, Oyashio Current.

main KC enters the East China Sea (ECS) through a channel in east of Taiwan Island and then passes through Tokara Strait at around 30°N. After the current has passed the Shikoku Basin, the northeastward KC merges with the southwestward subarctic Oyashio Current (OC) before leaving the coast of Japan to form the KC Extension in the NPO, resulting in a system known as the Oyashio-Kuroshio boundary region (**Figure 1**).

The MEMEWSC cruise was carried out in May-June 2018 on board RV Xiangyanghong III from the SCS to the Oyashio-Kuroshio mixing region of the western subarctic NPO (**Figure 1**). Dissolved and particulate samples for $^{210}$Po and $^{210}$Pb activity analysis were collected from the water column at 7 stations during the ∼1 month duration of the cruise. Discrete seawater samples were collected using a stainless steel sampling rosette equipped with 24 × 12 L Niskin bottles and a CTD Seabird sensor package. Seawater samples (∼20 L each) were taken from 9 depths from 0 to 1,000 m, with higher resolution in the upper 200 m of the water column. Salinity and temperature were obtained from these sensors (Seabird SBE 9/11plus CTD deployed with two Sea-Bird SBE 3P temperature sensors and two Sea-Bird SBE 4C conductivity sensors). To evaluate the POC export flux, 150 m is chosen as the integration depth according to estimated depth for the base of the euphotic zone on the ship from the Chl-a profiles.

## $^{210}$Po and $^{210}$Pb Determination

Analysis for $^{210}$Pb and $^{210}$Po was described in Zhong et al. (2019). In brief, seawater samples (18–24 L each) were rapidly filtered through 142-mm diameter Nucleopore filters (0.45 μm pore size) to separate the particulate and dissolved $^{210}$Po and $^{210}$Pb. The filtered (dissolved) seawater was then acidified to pH 1–2 with concentrated HCl immediately after collection and spiked with a known amount of $^{209}$Po (No. 7299, Eckert and Ziegler Isotope Products) and stable $Pb^{2+}$ to quantify any subsequent losses of Po and Pb. After equilibration for 6–12 h, 100 mg of $Fe^{3+}$ was added to the solution, the pH was adjusted to approximately 8–9, using concentrated $NH_4OH$ to co-precipitate Po and Pb with $Fe(OH)_3$ precipitate. After settling for 8–12 h, the precipitate was transferred into a 1.5-L polyethylene bottle, and stored on board for processing upon arrival on land. In the laboratory, the precipitate was centrifuged and dissolved in 6 M HCl solution in a clean Teflon beaker, and the pH was neutralized to 1–2. Both $^{210}$Po and $^{209}$Po were auto-plated onto a nickel disc (Zhong et al., 2020) after adding 0.3 g of ascorbic acid, 1 mL of 25% sodium citrate, and 1 mL of 20% hydroxylamine hydrochloride to the solution. The particulate filters were spiked with known quantities of $^{209}$Po and stable $Pb^{2+}$ and totally dissolved in a mixture of HF, $HNO_3$ and $HClO_4$. After evaporating to nearly dryness several times to ensure that all the radionuclides were in dissolved form, the residue was then picked up in dilute HCl (0.1 M) for plating of Po onto a nickel disc. The plating procedure was similar to that utilized for dissolved samples. $^{210}$Po and $^{209}$Po activities were determined by alpha spectrometry (Canberra series 7200-08).

For $^{210}$Pb determination, any remaining Po isotopes in the plating solution was removed by resuspending another nickel disc, and the purified sample solution was re-spiked with

additional $^{209}$Po and stored for ∼12 months to allow ingrowth of $^{210}$Po from $^{210}$Pb, and then polonium isotopes were again auto-deposited, and counted. The recoveries of $^{210}$Pb were determined through the added stable Pb and the measured Pb, using atomic absorption spectrometry (AAS). The in-situ activities of $^{210}$Po and $^{210}$Pb at the sampling date were determined by correcting for decay, ingrowth, chemical recoveries, detector backgrounds, and reagent blanks ($^{210}$Pb and $^{210}$Po present in the stable lead) (Church et al., 2012; Baskaran et al., 2013; Rigaud et al., 2013).

## Particulate Organic Carbon Analysis

POC samples were obtained by filtering 4–6 L seawater through pre-combusted and pre-weighted 25 mm QMA filters (with a pore size of 0.45 μm, Whatman) immediately after sampling, and the filters were then washed 3 times with Milli-Q water to remove salt before frozen storage prior to laboratory analysis. Before the POC content was measured, the sample was oven-dried at 55℃ to a constant weight. Then, the inorganic carbon was removed from the filter by using acid vapor (concentrated HCl) in desiccators for 48 h. The POC was then determined using a Vario ELIII CHNOS Elemental Analyzer. The analytical precision of the method was estimated to be around ± 4%, using triple measurement of the same sample.

# RESULTS

## Hydrographic Characteristics and Particulate Organic Carbon Concentrations During the MEMEWSC Cruise

Vertical profiles of the temperature and salinity in the w-NPO are shown in **Figure 2**. Among the 7 stations, the sea surface temperature (SST) ranged from 15.5 to 28.9℃. The SST was high (27.6–28.9℃) at the low-latitude (21°N) stations (XTW1-3, XTW1-11 and XTJ1-1) but decreased gradually with increasing latitude from station XTJ1-1 (28.4℃) to station XTJ1-22 (15.5℃). Influenced by the OC, station XTJ1-22 showed the lowest SST. Furthermore, the water temperature decreased with increasing depth and did not differ appreciably between stations at 1,000 m (**Figure 2A**).

The salinity profiles spatially differed among the 7 stations (**Figure 2A**). At station XTJ1-22, the salinity decreased rapidly with increasing depth and exhibited a subsurface minimum (33.82) at 150 m, displaying the features of low-salinity subarctic waters (OC), and then the salinity increased gradually to 1,000 m. In contrast to station XTJ1-22, the other six stations exhibited similar salinity distributions, with the maximum values occurring at depths of approximately 150–200 m (**Figure 2A**), indicating the existence of stratification in the water column at each station. However, the salinity in the top 150 m of the water column at station XTW1-3 (located in Luzon Strait) was lower (from 33.80 to 34.66) than that at the station in the NPO basin (from 34.55 to 35.05) (**Figure 2A**). From the temperature-salinity-depth diagram (**Figure 2B**), the water masses can be clearly discriminated for the study area. Station XTJ1-22 showed a signature of OC, and station XTW1-3 might represent the South China Sea water. From the **Figure 2B**, the remaining five stations (XTJ1-1, XTW1-1, XTJ1-8, XTJ2-7, and XTJ1-13) could be divided into two groups with different hydrographic features for the surficial water mass (upper 200 m). One group includes stations XTJ1-1 and XTW1-11, and the other group contains stations XTJ1-8, XTJ1-13, and XTJ2-7, showing a much narrower ranges of salinity and temperature (**Figure 2B**). In 1,000 m, all the stations displayed a similar temperature-salinity feature, with low temperatures of < 5°C and a salinity range of 34.3–34.5. Based on the salinity and temperature profiles, the thermocline was observed between 100 and 200 m. To determine the euphotic zone depth, we use information for the base of the euphotic zone according to the subsurface chlorophyll-a maximums (SCMs) features. The profiles of chlorophyll-a concentrations showed that SCMs could occur between 120 and 150 m for most of the stations (33 out of 43 stations) during the cruise (unpublished data, personal communication with Dr. Jianhua Kang). Hence the euphotic zone could be delimited from 0 to 150 m. Overall, the water column could be divided into two boxes: 0–150 m box (the euphotic zone) and 150–1,000 m box (the mesopelagic zone).

All POC concentration data can be found in **Supplementary Table 1**. In total, the POC concentrations ranged from 1.85 to 14.35 μmol C/L, with an average of 4.15 ± 2.15 μmol C/L in the w-NPO (**Figure 3**). Station XTJ1-22 at the Kuroshio Current-Oyashio Current boundary had the highest POC concentration (mean: 6.23 ± 4.12 μmol C/L) in the upper 150 m, followed by station XTW1-3 (mean: 5.44 ± 1.28 μmol C/L) in the Luzon Strait, while the other five stations had similar POC concentrations with a mean value of 3.12–3.81 μmol C/L (**Table 1**). Almost all POC profiles showed a decrease with increasing water column depth from 0 to 500 m, and remained relatively constant from 500 to 1,000 m except at two stations (XTJ1-8 and XTJ1-13) (**Figure 3**).

## $^{210}$Po and $^{210}$Pb Profiles

Profiles of dissolved $^{210}$Po (D-Po), particulate $^{210}$Po (P-Po), total $^{210}$Po (T-Po), dissolved $^{210}$Pb (D-Pb), particulate $^{210}$Pb (P-Pb) and total $^{210}$Pb (T-Pb) were displayed in **Figures 4**, **5**, respectively. From **Figures 4**, **5**, overall, P-Po and P-Pb showed a similar variation trend, but D-Po showed a little bit of difference comparing with the D-Pb. The activity concentrations of particulate $^{210}$Po (P-Po) ranged from 1.4 to 10.4 dpm/100 L (**Figure 4**), which are comparable to the reported values in the upper Sargasso Sea (>500 m, 0.5–8.2 dpm/100 L) (Kim and Church, 2001), and slightly higher than those in the Aleutian Basin (negligible to 6.0 dpm/100 L) (Hu et al., 2014) and in the North Atlantic Ocean (0.1–7.0 dpm/100 L) (Horowitz et al., 2020). All stations showed a systematic decrease in P-Po activity with depth in the upper 1,000 m, except for station XTW1-3 in the Luzon Strait, which exhibited a subsurface maximum between 200 and 500 m (**Figure 4**).

The activities of dissolved $^{210}$Po (D-Po) varied from 2.87 to 14.57 dpm/100 L (**Figure 4**), which are comparable to other results previously measured in the w-NPO (5.28–14.02 dpm/100 L) (Nozaki and Tsunogai, 1976), the North Atlantic Ocean (0.6–13.1 dpm/100 L) (Horowitz et al., 2020) and the

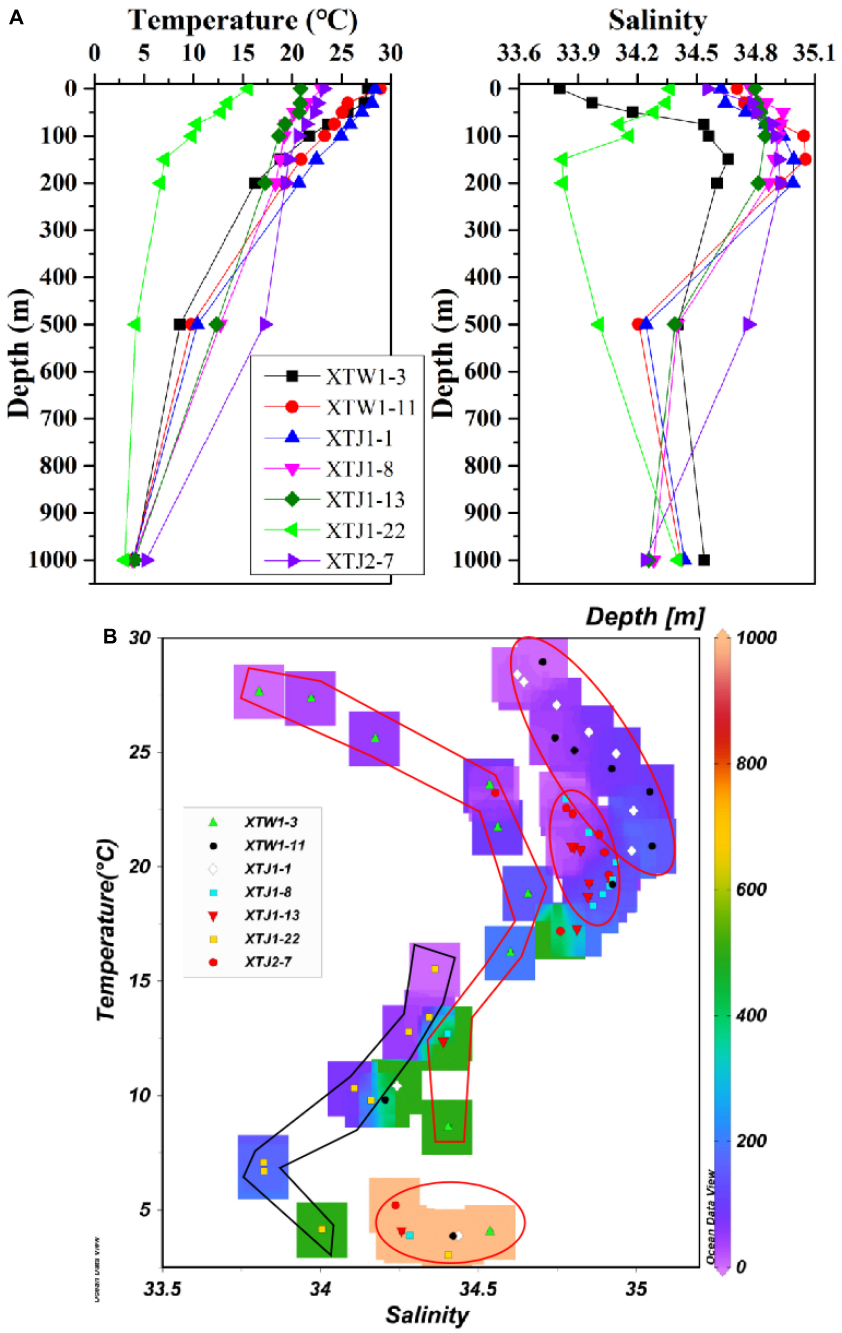


**FIGURE 2 |** Profiles of temperature and salinity **(A)** and temperature-salinity-depth diagram **(B)** for the samples collected in the study area.

western equatorial Pacific Ocean (4.26–14.82 dpm/100 L) (Peck and Smith, 2000), although these regions might correspond to very different biogeochemical conditions. The D-Po concentration was lowest in surface seawater and gradually increased with depth; the subsurface D-Po peak was observed within approximately 50–150 m at all stations (**Figure 4**). This increase in the D-Po concentration with depth is consistent with the rapid scavenging of $^{210}$Po near the surface and the remineralization of particulate $^{210}$Po at depth. The profiles of total $^{210}$Po (T-Po) showed vertical variations similar to those of P-Po, with a range of 4.61–20.69 dpm/100 L.

The activity concentrations of dissolved $^{210}$Pb (D-Pb) and particulate $^{210}$Pb (P-Pb) ranged from 1.86 to 24.45 dpm/100 L and from 1.88 to 31.33 dpm/100 L, respectively (**Figure 5**). The P-Pb activity was highest in the near-surface seawaters at all stations; thus, $^{210}$Pb activity was predominantly in the particulate phase (P-Pb/T-Pb > 50%) in the upper 50 m (**Figure 6**). Below 50 m, P-Pb showed a systematic downward trend with depth.

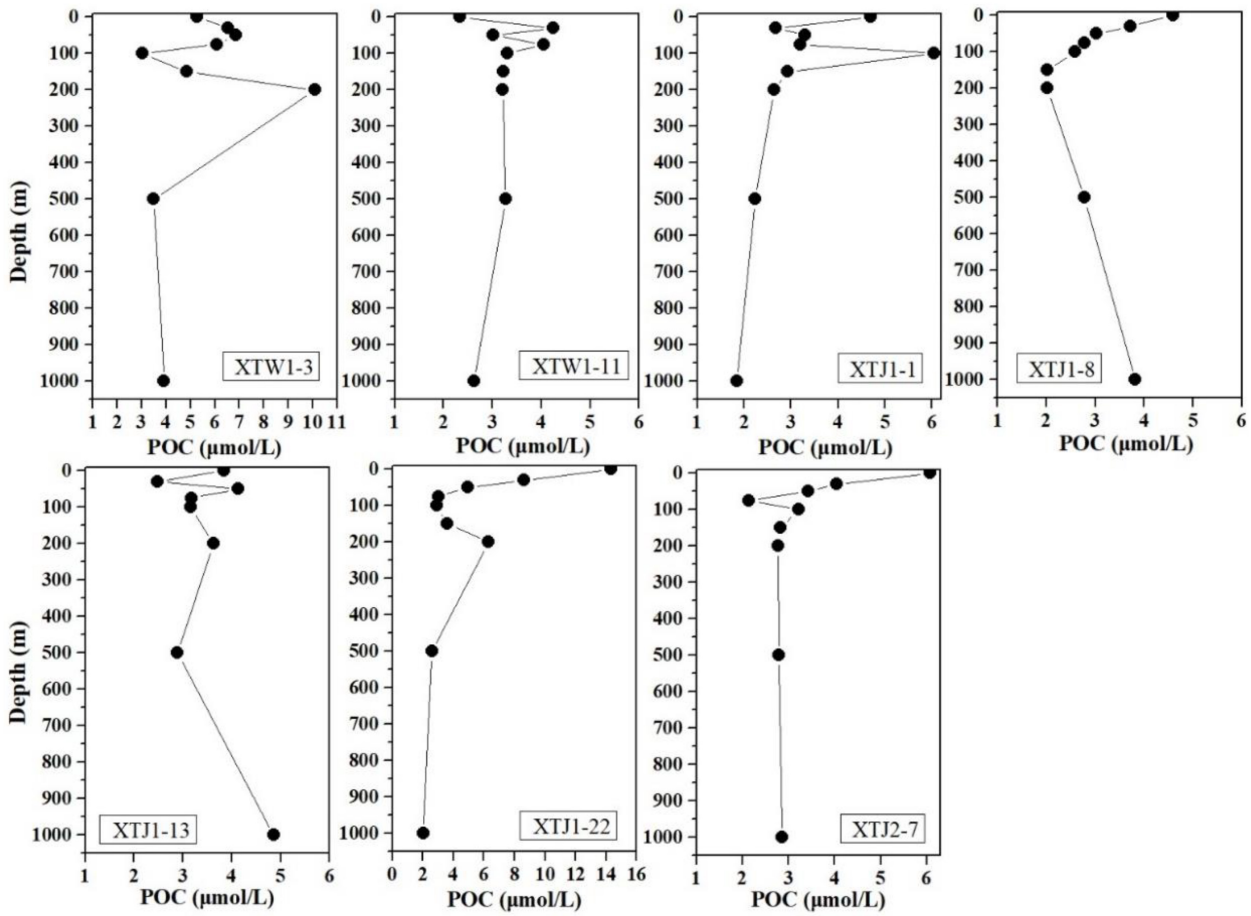


**FIGURE 3 |** Vertical profiles of the POC concentration at 7 stations in the w-NPO during May-June 2018.

**TABLE 1 |** Model calculations of the scavenging rates (J) and removal fluxes (P) for $^{210}$Po and $^{210}$Pb, together with the particulate and dissolved residence times in the surface and deeper layers in the w-NPO.

| Station | Depth layer | Average POC concentration* | Inventory of $^{210}$Po deficit | $J_{Po}$ | $P_{Po}$ | $\tau_{Po-D}$ | $\tau_{Po-P}$ | $J_{Pb}$ | $P_{Pb}$ | $\tau_{Pb-D}$ | $\tau_{Pb-P}$ |
|---|---|---|---|---|---|---|---|---|---|---|---|
| | m | μmol C/L | dpm/m$^2$ | dpm/m$^2$/yr | | yr | d | dpm/m$^2$/yr | | yr | |
| XTW1-3 | 0–150 | 5.44 ± 1.28 | 8,733 ± 694 | 1,693 | 17,242 | 5.5 ± 1.3 | 130 ± 7 | 18,697 | 18,244 | 0.51 ± 0.02 | 0.80 ± 0.03 |
| XTW1-11 | 0–150 | 3.66 ± 0.64 | 6,144 ± 1,058 | 3,464 | 12,509 | 4.2 ± 0.9 | 308 ± 28 | 18,504 | 18,024 | 0.85 ± 0.03 | 0.86 ± 0.04 |
| XTJ1-1 | 0–150 | 3.81 ± 1.29 | 1,121 ± 821 | 7,683 | 3,327 | 1.6 ± 0.2 | 921 ± 229 | 18,504 | 18,317 | 0.85 ± 0.03 | 0.33 ± 0.02 |
| XTJ1-8 | 0–150 | 3.12 ± 0.83 | 4,344 ± 857 | 4,214 | 9,219 | 3.2 ± 0.5 | 275 ± 27 | 18,522 | 18,222 | 0.82 ± 0.03 | 0.53 ± 0.02 |
| XTJ1-13 | 0–150 | 3.36 ± 0.58 | 18,415 ± 1820 | 17,644 | 34,941 | 0.6 ± 0.0 | 83 ± 5 | 18,373 | 17,835 | 1.09 ± 0.05 | 0.98 ± 0.09 |
| XTJ1-22 | 0–150 | 6.23 ± 4.12 | 7,389 ± 457 | 5,921 | 14,785 | 1.1 ± 0.1 | 93 ± 4 | 18,720 | 18,454 | 0.47 ± 0.02 | 0.47 ± 0.01 |
| XTJ2-7 | 0–150 | 3.62 ± 1.24 | 13,507 ± 874 | 9,400 | 25,969 | 1.2 ± 0.1 | 84 ± 4 | 18,517 | 18,053 | 0.83 ± 0.04 | 0.83 ± 0.02 |
| XTW1-3 | 150–1,000 | 5.59 ± 2.65 | 2,5310 ± 7261 | –6,023 | 63,509 | / | 331 ± 40 | 3,132 | 15,575 | 22.9 ± 5.7 | 5.5 ± 0.3 |
| XTW1-11 | 150–1,000 | 3.08 ± 0.27 | –3,910 ± 6,341 | –86,511 | 5,362 | / | / | 3,800 | 15,713 | 13.1 ± 2.6 | 4.8 ± 0.2 |
| XTJ1-1 | 150–1,000 | 2.42 ± 0.41 | –34,615 ± 6270 | –64,036 | –59,950 | / | / | 3,527 | 17,608 | 16.0 ± 3.8 | 1.3 ± 0.1 |
| XTJ1-8 | 150–1,000 | 2.65 ± 0.74 | –16,670 ± 5421 | –26,022 | –21,254 | / | / | 3,297 | 17,649 | 20.3 ± 4.8 | 1.1 ± 0.1 |
| XTJ1-13 | 150–1,000 | 3.63 ± 0.75 | 33,430 ± 4475 | 7,294 | 96,052 | 8.1 ± 4.1 | 85 ± 6 | 3,308 | 16,231 | 18.7 ± 3.2 | 3.2 ± 0.1 |
| XTJ1-22 | 150–1,000 | 3.63 ± 1.64 | 14,370 ± 4187 | –7,166 | 41,054 | / | 155 ± 18 | 3,753 | 17,350 | 13.9 ± 2.2 | 2.1 ± 0.1 |
| XTJ2-7 | 150–1,000 | 2.82 ± 0.03 | 54,550 ± 5731 | 32,338 | 125,688 | / | 103 ± 7 | 3,103 | 15,810 | 22.8 ± 4.8 | 4.6 ± 0.2 |

*"/" denotes an "invalid calculation."*

**Represents the average POC concentration at 0–150 m box and 150–1,000 m box.*

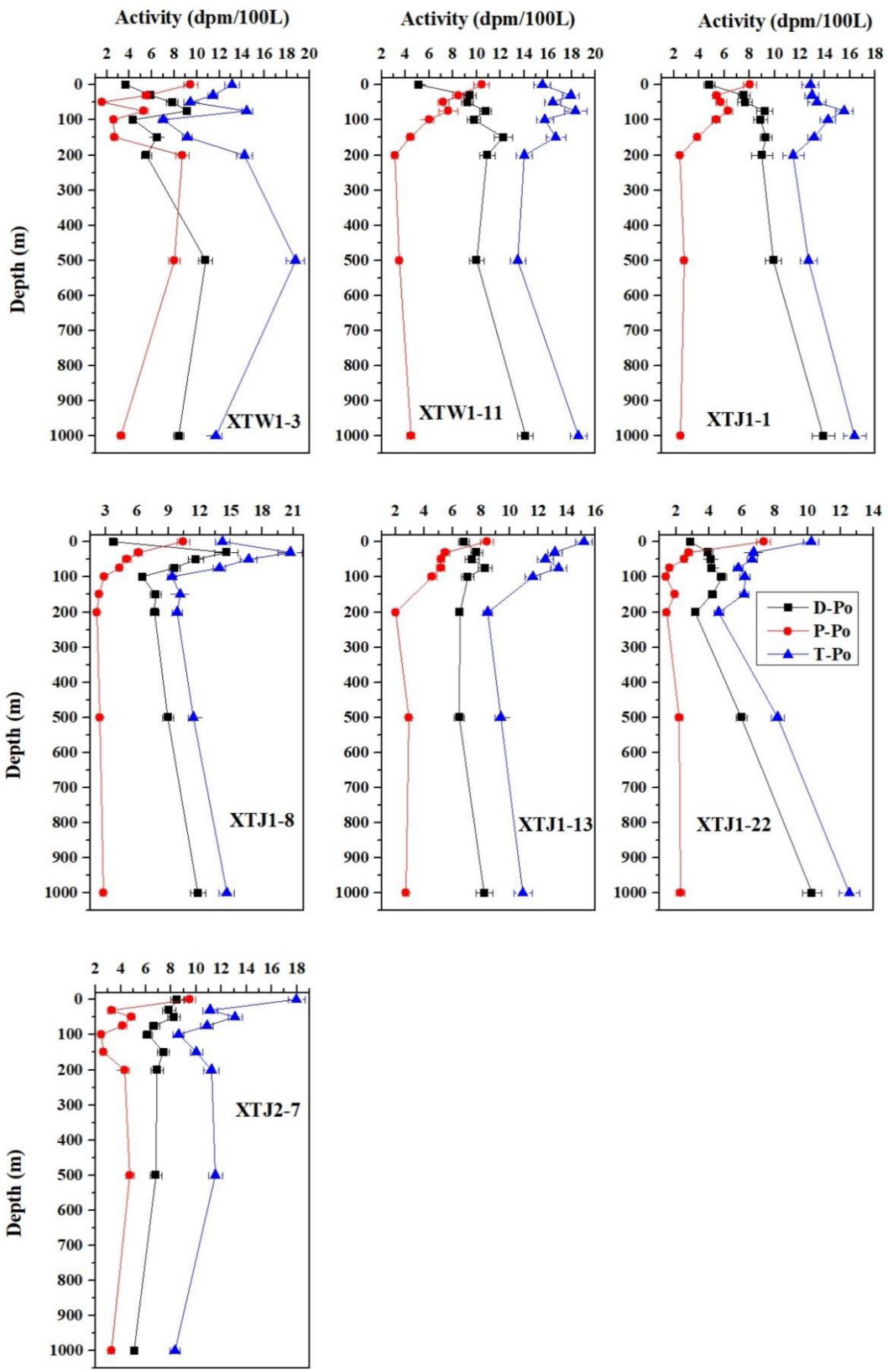


**FIGURE 4 |** Vertical distributions of particulate (P), dissolved (D), and total (T) $^{210}$Po in the water column at each station in the w-NPO.

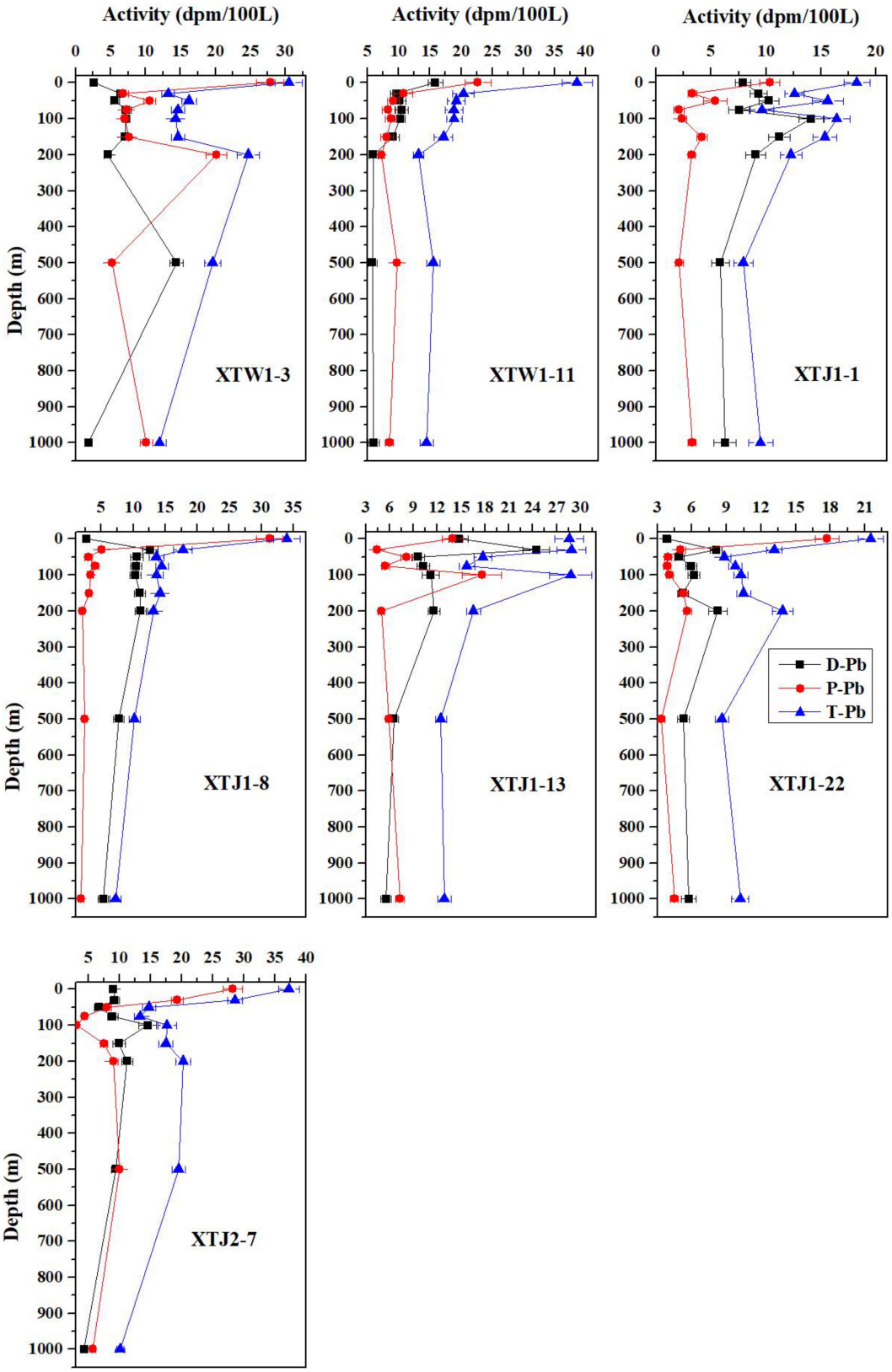


**FIGURE 5 |** Vertical distributions of particulate (P), dissolved (D), and total (T) $^{210}$Pb activities in the water column at each station in the w-NPO.

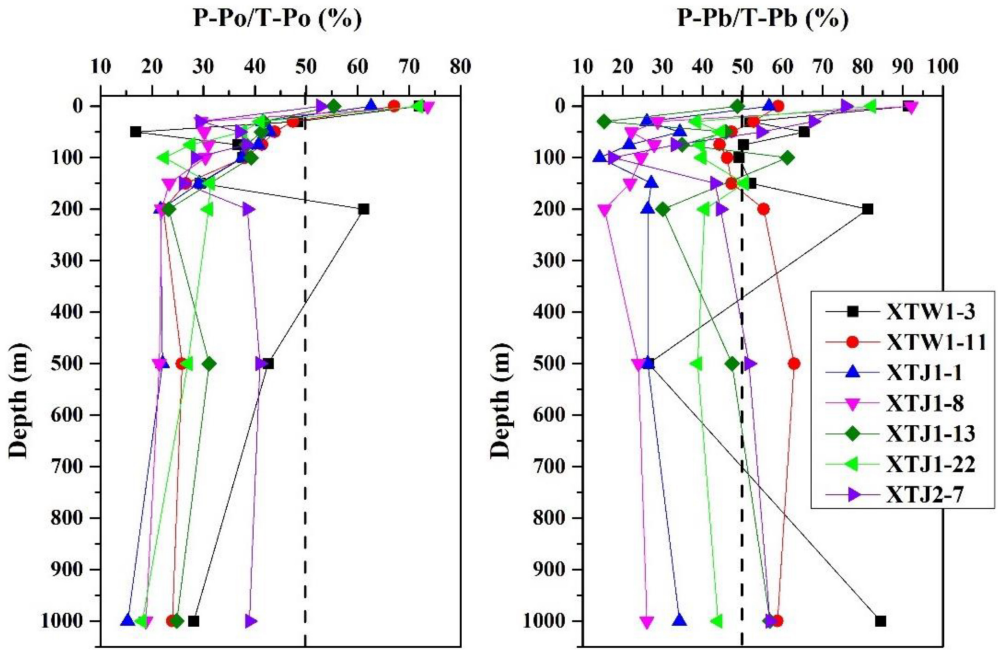


**FIGURE 6 |** Vertical profiles of percentage of particulate $^{210}$Po and $^{210}$Pb in water columns of the w-NPO.

However, the activity of D-Pb was lowest in the surface seawater; then, D-Pb increased with depth from 50 to 200 m and finally decreased below 200 m. All stations had the highest total $^{210}$Pb (T-Pb) concentration at the surface, and T-Pb decreased with depth from the surface to 1,000 m, suggesting a surface source of $^{210}$Pb due to atmospheric input, as indicated by the $^{210}$Pb activity (7.22–38.61 dpm/100 L) being greater than the $^{226}$Ra activity (6.0–14.4 dpm/100 L, Kawakami and Kusakabe, 2008) in the upper water column.

At all stations, the percentages of P-Po in the w-NPO surface seawater (0–50 m) were higher than 50%, showing that P-Po often exceeded D-Po and dominated T-Po. The high fraction of particulate $^{210}$Pb indicated a signature of atmospheric input. Moreover, the P-Po/T-Po percentages decreased slowly to constant values of 20–30% as the water depth increased up to 500 m (**Figure 6**). P-Pb was generally 20–50% of the T-Pb at depths below the mixed layer, demonstrating that T-Pb was dominated by D-Pb in most layers of the water column at all stations in the w-NPO (**Figure 6**). Overall, these findings reveal that both $^{210}$Po and $^{210}$Pb were predominantly present in the dissolved phase below 50 m at all stations (**Figure 6**), as is commonly the case in other oceans.

## $^{210}$Po/$^{210}$Pb Activity Ratio

Vertical profiles of the $^{210}$Po/$^{210}$Pb activity ratios in the particulate, dissolved and total fractions are plotted in **Figure 7**. Particulate matter was enriched in $^{210}$Po (particulate $^{210}$Po/$^{210}$Pb activity ratios $> 1$) at the subsurface (50–100 m) at all stations, especially in the particulate sample from a depth of 75 m at station XTJ1-1, where the P-Po/P-Pb ratio reached $3.04 \pm 0.73$ (**Figure 7**). These data indicates that there was an excess of P-Po relative to P-Pb. The dissolved $^{210}$Po/$^{210}$Pb activity ratios (D-Po/D-Pb) increased with depth, with values $< 1$ at the surface and increasing toward 1 or even $> 1$ below the euphotic zone, which complemented the elevated P-Po/P-Pb ratio. All stations showed similar vertical distributions of T-Po/T-Pb with a significant deficiency of $^{210}$Po relative to $^{210}$Pb from the surface to 200 m. The deficit of $^{210}$Po relative to $^{210}$Pb declined with depth and then approached equilibrium or shifted to an excess ($^{210}$Po/$^{210}$Pb$\approx$1 or $> 1$) at different depths for different stations, except for stations XTJ1-1 and XTJ1-8, which displayed an excess of T-Po relative to T-Pb (T-Po/T-Pb ratio $> 1$) at 50–75 m and at 500–1,000 m. Interestingly, $^{210}$Po excess (T-Po/T-Pb ratios $> 1.2$) was observed in seawater at 500 and 1,000 m of station XTJ1-1 and in seawater at 1,000 m of station XTJ1-8 (**Figure 7**). From **Figure 7**, we can find that this $^{210}$Po excess is caused by the high dissolved $^{210}$Po activity concentration in the deep layers (500–1,000 m), because D-Po/D-Pb ratios at deep layers (500–1,000 m) were much higher than unity (**Figure 7**). And this high dissolved $^{210}$Po activity concentration implied the occurrence of a strong $^{210}$Po dissolution in the deep ocean.

# DISCUSSION

## Enhanced Particle Scavenging of $^{210}$Po and $^{210}$Pb and Deficiency of $^{210}$Po in the Western North Pacific Ocean

Both Pb and Po are particle-reactive elements that can be scavenged effectively from the water column by lithogenic and biogenic particles. **Figure 4** reveals that both the P-Po and the

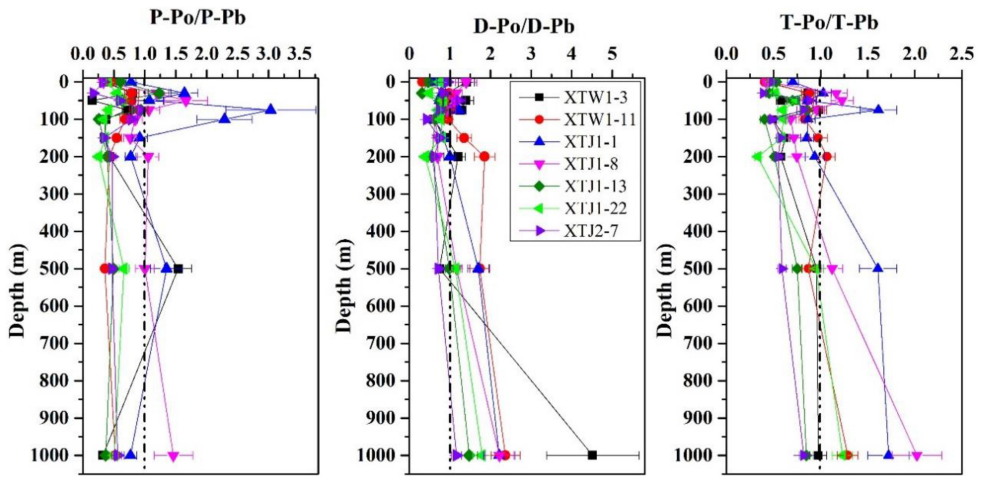


**FIGURE 7 |** Profiles of the activity ratios of $^{210}$Po/$^{210}$Pb in the particulate, dissolved and total fractions in w-NPO.

P-Pb activity concentrations were highest in the near-surface (0–30 m) layers at all stations; additionally, at most stations, the highest POC concentrations were similarly detected in the upper water column (>100 m), as shown in **Figure 3**, which resulted in higher percentages of P-Po/T-Po and P-Pb/T-Pb ratios (>50%) in the near-surface (30–50 m) seawater. The high fraction (30–60%) of particulate $^{210}$Pb for most stations was related to atmospheric deposition of $^{210}$Pb. In the open ocean, the most important input of $^{210}$Pb is the atmospheric deposition, and the $^{210}$Pb is mainly in dissolved phase in the atmospheric deposition samples. $^{210}$Pb is particle-reactive, therefore, in the upper layer with higher primary productivity, some $^{210}$Pb sourced from the atmosphere would be absorbed and enriched by the biogenic particles. In addition, our study area is under the cover of dust deposition from the East Asia (Hayes et al., 2013); during every spring (especially in April-May), the prevailing dust storms from the East Asia would possibly increase the particulate $^{210}$Pb activity.

Furthermore, the P-Po/P-Pb ratios were nearly 1 or higher than 1 within 30–75 m at all stations (**Figure 7**), supporting the previously findings that $^{210}$Po was preferentially scavenged over $^{210}$Pb (Bacon et al., 1976; Murray et al., 2005; Tang and Stewart, 2019). In addition, on all profiles, both P-Po and P-Pb decreased with depth in the upper 100 m, which is consistent with the increases in D-Po and D-Pb (**Figures 4**, **5**). The highest P-Po activity concentrations were presented at the surface for all stations (**Figure 4**), which could be related to particle concentration, since particle concentration is usually higher than in the twilight zone or deeper layers. D-Po increased from the surface to 1,000 m (**Figure 4**), especially at stations XTW1-11 and XTJ1-8, which showed subsurface D-Po maxima at 150 and 50 m, respectively. This phenomenon implies that sinking particulate matter is re-mineralized at depth in the w-NPO, which is supported by an excess of D-Po relative to $^{210}$Pb, with the D-Po/D-Pb activity ratios often > 1 below 200 m (**Figure 7**). Specifically, at station XTW1-11, the feature of D-Po/D-Pb > 1 appeared between 150 and 1,000 m, while at station XTJ1-1, D-Po/D-Pb > 1 only appeared between 500 and 1,000 m. Except for station XTJ2-7, the feature of D-Po/D-Pb > 1 appeared at 1,000 m for all stations (**Figure 7**). Based on the above discussion, it can be concluded that enhanced particle scavenging of both $^{210}$Po and $^{210}$Pb occurred in the upper ocean and that $^{210}$Po adsorbed onto particles from the upper ocean was released in the deeper ocean due to the remineralization of particulate organic matter below the mixed layer.

The minimum activity concentration of $^{210}$Po appeared at the 100 m layer at XTW1-3, XTJ1-8 and XTJ2-7, while the minimum $^{210}$Po activity concentration appeared at the 200 m layer at station XTW1-11, XTJ1-1, XTJ1-13, and XTJ1-22 (**Figure 4**). As shown in **Figure 7**, T-Po was largely deficient relative to T-Pb in the upper 200 m of the w-NPO, with the T-Po/T-Pb ratios as low as 0.4. This phenomenon is similar to the general pattern in which T-Po is usually deficient with respect to T-Pb (T-Po/T-Pb ratio = 0.5) in the euphotic zone due to the rapid removal of Po caused by the sinking of biogenic particles (Bacon et al., 1976; Nozaki et al., 1998; Stewart et al., 2010; Roca-Martí et al., 2016; Subha Anand et al., 2018). In contrast, $^{210}$Po gradually reached secular equilibrium with $^{210}$Pb or even an excess relative to $^{210}$Pb (**Figure 7**) at the bottom of the euphotic zone (∼150 m) or in the mesopelagic waters (500 or 1,000 m) due to the regeneration of $^{210}$Po from sinking particles during particle remineralization. For example, at stations XTJ1-1 and XTJ1-8, T-Po/T-Pb ratios were high up to 1.61–2.02 at 500–1,000 m layers. From **Figures 4**, **5**, we can clearly find that the D-Po activity concentration increased significantly, but at the same layers, both D-Pb and P-Pb activity concentration decreased significantly. The explanation for this increased D-Po activity at the deep layer may be related to strong particle export events. We believe that a strong particle export event occurred in the upper ocean before our sampling, and subsequently sinking particles dissolved at the deep layers. This ultimately increased the activity concentration of dissolved $^{210}$Po in the mesopelagic zone. Similar research cases have also been reported in a review paper published by Verdeny et al. (2009). Such disequilibrium between $^{210}$Po and $^{210}$Pb in the water column could help depict the scavenging rates of $^{210}$Po and

$^{210}$Pb and to estimate the removal flux of particulate matter in the w-NPO.

## Scavenging and Removal Fluxes of $^{210}$Po and $^{210}$Pb in the Western North Pacific Ocean

$^{210}$Pb and $^{210}$Po in the upper ocean come from both atmospheric deposition and *in situ* production *via* parent radionuclide decay. Generally, residence times of $^{210}$Po and $^{210}$Pb in the atmosphere are only several days to several weeks. Hence, $^{210}$Po deposition fluxes to the surface ocean are only approximately 10–20% of those of $^{210}$Pb (Masqué et al., 2002; Baskaran, 2011). Many previous researchers have applied the $^{210}$Po/$^{210}$Pb disequilibrium method to trace the POC export fluxes in the open ocean, polar sea or remote sea areas, but the $^{210}$Po and $^{210}$Pb deposition fluxes have consistently been neglected due to a lack of relevant data (Friedrich and Rutgers van der Loeff, 2002; Murray et al., 2005; Le Moigne et al., 2013; Roca-Martí et al., 2016; Subha Anand et al., 2018; Tang et al., 2019; Horowitz et al., 2020). According to a compilation of global $^{210}$Pb fallout data by Du (2019), among all the observation stations worldwide, Taiwan, Shanghai and Tatsunokuchi recorded the highest annual $^{210}$Pb deposition fluxes, indicating that East Asia exhibits the highest $^{210}$Pb deposition flux in the world. Thus, when applying $^{210}$Po-$^{210}$Pb disequilibrium to study particle dynamics and to estimate the POC export fluxes in the seas of East Asia, the atmospheric inputs of $^{210}$Po and $^{210}$Pb and their impacts on the POC export flux should be considered.

The $^{210}$Po and $^{210}$Pb activities in the ocean are the result of a balance among atmospheric inputs, continuous production from the decay of mother nuclides ($^{210}$Pb or $^{226}$Ra) in seawater, the radioactive decay of $^{210}$Po and $^{210}$Pb, removal onto sinking particles, and transport into or out of the system by advection and diffusion. Generally, the general form of the mass balance equation in the upper ocean for $^{210}$Po and $^{210}$Pb between sources and sinks can be designed as follows:

$$\frac{\partial Pb}{\partial t} = F_{Pb} + \lambda_{Pb} I_{Ra} - \lambda_{Pb} I_{Pb} - k_{Pb} I_{Pb} + V, \quad (1)$$

$$\frac{\partial Po}{\partial t} = F_{Po} + \lambda_{Po} I_{Pb} - \lambda_{Po} I_{Po} - k_{Po} I_{Po} + V, \quad (2)$$

where $\partial Pb/\partial t$ and $\partial Pb/\partial t$ are the changes in the $^{210}$Pb and $^{210}$Po activities with time, respectively; $F_{Pb}$ and $F_{Po}$ (dpm/m$^2$/d) are the atmospheric deposition fluxes of $^{210}$Pb and $^{210}$Po to the sea surface, respectively; $\lambda_{Pb}$ and $\lambda_{Po}$ are the decay constants of $^{210}$Pb and $^{210}$Po (d$^{-1}$), respectively; $I_{Ra}$, $I_{Pb}$ and $I_{Po}$ (dpm/m$^2$/year) are the inventories of $^{226}$Ra, $^{210}$Pb, and $^{210}$Po, respectively; $k_{Pb}$ and $k_{Po}$ are the scavenging (from dissolved to particulate) rate constants of $^{210}$Pb and $^{210}$Po, respectively; and V (dpm/m$^2$/d) is the sum of the advection and diffusion fluxes.

The advection-diffusion term is relatively important only in the case of algal blooms, mesoscale eddies, and upwelling regions (Tang et al., 2019; Horowitz et al., 2020). Generally, a steady-state model can be adopted by ignoring advection and diffusion ($V \approx 0$). **Figure 8** displays the one-dimensional irreversible scavenging conceptual model for $^{210}$Po and $^{210}$Pb in surface and deep waters. Thus, Eqs. (1) and (2) can be rearranged as follows. For the upper ocean (0–150 m), we obtain:

$$\lambda_{Pb} I_{Ra} + F_{Pb} = \lambda_{Pb} I_{Pb-D} + k_{Pb} I_{Pb-D} (= J_{Pb(0-150m)}), \quad (3)$$

$$J_{Pb(0-150m)} = \lambda_{Pb} I_{Pb-D} + P_{Pb(0-150m)}, \quad (4)$$

$$\lambda_{Po} I_{Pb-D} + F_{Po} = \lambda_{Po} I_{Po-D} + k_{Po} I_{Po-D} (= J_{Po(0-150m)}), \quad (5)$$

$$\lambda_{Po} I_{Pb-P} + J_{Po(0-150m)} = \lambda_{Po} I_{Po-P} + P_{Po(0-150m)}, \quad (6)$$

where Eqs. (3) and (4) are mass-balance equations for D-Pb and P-Pb, and Eqs (5) and (6) are mass-balance equations for D-Po and P-Po.

The residence times of $^{210}$Po and $^{210}$Pb in the upper ocean can therefore be written as:

$$\tau_{Po-D(0-150m)} = I_{Po-D} \Big/ J_{Po(0-150m)}, \quad (7)$$

$$\tau_{Po-P(0-150m)} = I_{Po-P} \Big/ P_{Po(0-150m)}, \quad (8)$$

$$\tau_{Pb-D(0-150m)} = I_{Pb-D} \Big/ J_{Pb(0-150m)}, \quad (9)$$

$$\tau_{Pb-P(0-150m)} = I_{Pb-P} \Big/ P_{Pb(0-150m)}. \quad (10)$$

Similarly, for the deeper ocean (150–1,000 m), we obtain:

$$\lambda_{Pb} I_{Ra} = \lambda_{Pb} I_{Pb-D} + k_{Pb} I_{Pb-D} (= J_{Pb(150-1000m)}), \quad (11)$$

$$P_{Pb(0-150m)} = \lambda_{Pb} I_{Pb-P} + P_{Pb(150-1000m)}, \quad (12)$$

$$\lambda_{Po} I_{Pb-D} = \lambda_{Po} I_{Po-D} + k_{Po} I_{Po-D} (= J_{Po(150-1000m)}), \quad (13)$$

$$P_{Po(0-150m)} + \lambda_{Po} I_{Pb-P} + J_{Po(150-1000m)} = \lambda_{Po} I_{Po-P} + P_{Po(150-1000m)}. \quad (14)$$

The residence times of $^{210}$Po and $^{210}$Pb in the deeper ocean can therefore be written as:

$$\tau_{Po-D(150-1000m)} = I_{Po-D} \Big/ J_{Po(150-1000m)}, \quad (15)$$

$$\tau_{Po-P(150-1000m)} = I_{Po-P} \Big/ P_{Po(150-1000m)}, \quad (16)$$

$$\tau_{Pb-D(150-1000m)} = I_{Pb-D} \Big/ J_{Pb(150-1000m)}, \quad (17)$$

$$\tau_{Pb-P(150-1000m)} = I_{Pb-P} \Big/ P_{Pb(150-1000m)}. \quad (18)$$

In the above equations, $I_{Pb}$ and $I_{Po}$ are the inventories of $^{210}$Pb and $^{210}$Po, respectively, in the different boxes; $P_{Pb}$ and $P_{Po}$ are the removal fluxes of P-Pb and P-Po, respectively, by particles

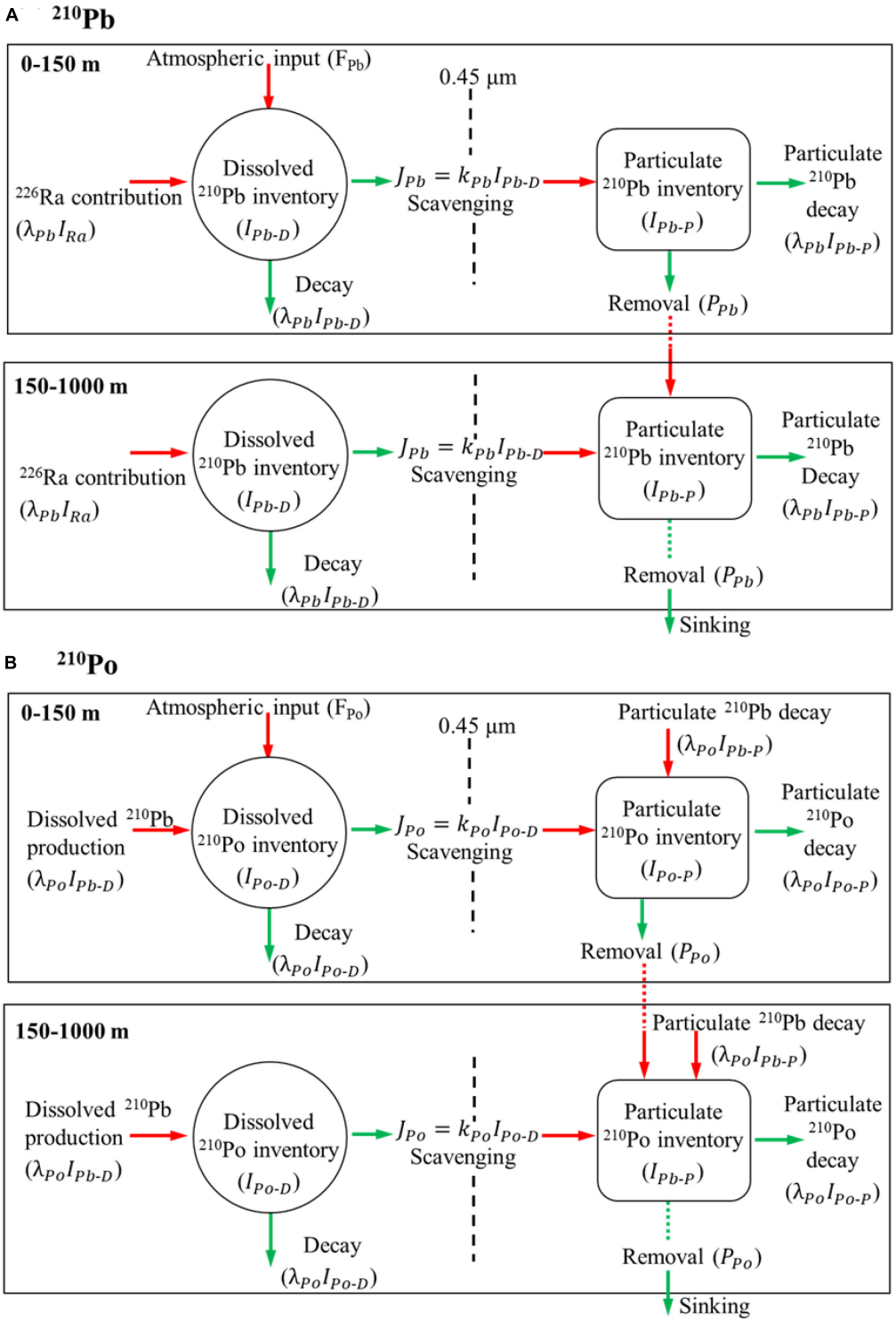


**FIGURE 8 |** Conceptual diagram describing the one-dimensional steady-state irreversible scavenging model for $^{210}$Pb **(A)** and $^{210}$Po **(B)** in the upper ocean and the deeper ocean (modified from Bacon et al., 1976; Shimmield et al., 1995).

sinking out of the box; $J_{Pb}$ and $J_{Po}$ are the rates of scavenging of $^{210}$Pb and $^{210}$Po, respectively (if a radionuclide is transferred from solution to the particulate phase by particle scavenging, then J is positive, while J is negative for opposite); and $\tau_P$ and $\tau_D$ are the residence times of the radionuclides in the particulate and dissolved phases, respectively.

The average annual atmospheric $^{210}$Pb deposition flux ($F_{Pb}$) in East Asian is 18540 dpm/m$^2$/yr ($n$ = 25, Zhong, 2020), while the atmospheric flux of $^{210}$Po ($F_{Po}$) is usually assumed to be only 10% of $F_{Pb}$ (Turekian et al., 1977; Masqué et al., 2002; Baskaran, 2011). **Table 1** shows the scavenging rates, removal fluxes and residence times of $^{210}$Po and $^{210}$Pb in the near-surface and deeper ocean. Inventories of $^{226}$Ra were calculated based on published data from station KH-71-3-S (which is very close to station XTJ1-8) in the w-NPO (Nozaki and Tsunogai, 1976), the $^{226}$Ra inventories in the 0–150 m and 150-1,000 m boxes were calculated to be 14,625 dpm/m$^2$ and 172,530 dpm/m$^2$, respectively (see **Table 2**).

Within the 0–150 m surface layer, $J_{Po}$ ranged from 1,693 to 17,644 dpm/m$^2$/yr; these positive values confirm that $^{210}$Po was transferred from the dissolved phase to the particulate phase due to the scavenging of sinking particles in the upper ocean. Correspondingly, the removal flux of $^{210}$Po ranged from 3,327 to 34,941 dpm/m$^2$/year, showing a large spatial variation in the w-NPO. The residence times of D-Po ($\tau_{Po-D}$) and P-Po ($\tau_{Po-P}$) in the upper 0–150 m layer ranged from 0.6 to 5.5 year and from 83 to 921 days, respectively. Interestingly, the values of $\tau_{Po-D}$ (0.6–1.2 year) and $\tau_{Po-P}$ (83–93 days) at the three more northerly stations (XTJ1-13, XTJ1-22, and XTJ2-7) were much lower than the values of $\tau_{Po-D}$ (1.6–5.5 year) and $\tau_{Po-P}$ (130–921 days) of the more southerly stations (XTW1-3, XTW1-11, XTJ1-1, and XTJ1-8). Generally, the residence time of 0.6 years was common for dissolved $^{210}$Po under more biologically productive conditions in the ocean (Shimmield et al., 1995). The $\tau_{Po-D}$ at stations XTJ1-13, XTJ1-22, and XTJ2-7 were much shorter than the other four stations, and correspondently, the average POC concentration at 0–150 m box were higher than the other four stations (**Table 1**), which supports that the residence time of dissolved $^{210}$Po was shorter when the biological activity was higher. In addition, longer particulate residence times are related to inefficient vertical removal processes (low export fluxes), which can be confirmed from the removal flux of $^{210}$Po ($P_{Po}$). As seen from **Table 1**, the $P_{Po}$ values of the three more northerly stations (3,327–17,242 dpm/m$^2$/year) were much lower than those of the four more southerly stations (14,785–34,941 dpm/m$^2$/year). The above phenomena suggest that the upper waters of the southern part of the w-NPO are characterized by inefficient vertical removal processes and high turnover rates, while strong particle export occurred in the northern part of the w-NPO.

At greater depths (150–1,000 m), the $J_{Po}$ values were negative at all stations except stations XTJ1-13 and XTJ2-7 (**Table 1**), further demonstrating the occurrence of $^{210}$Po remineralization in the deeper ocean. However, due to the release of $^{210}$Po, $\tau_{Po-D}$ could not be calculated at almost all stations in the deeper layer (150–1,000 m) except at station XTJ1-13. The $P_{Po}$ values were negative at stations XTJ1-1 and XTJ1-8, implying that $^{210}$Po could not be removed from the 150–1,000 m layer to the much deeper (>1,000 m) ocean at these two sampling sites. In addition, the $\tau_{Po-P}$ in the 150–1,000 m layer ranged from 85 to 331 d at the remaining four stations (XTW1-3, XTJ1-13, XTJ 1-22, and XTJ2-7).

In the upper 0–150 m, the scavenging rates of $^{210}$Pb ($J_{Pb}$) varied between 18,373 and 18,720 dpm/m$^2$/yr and the removal fluxes of $^{210}$Pb ($P_{Pb}$) ranged from 17,835 to 18,454 dpm/m$^2$/year (**Table 1**). As atmospheric input is the dominant source term for $^{210}$Pb in the upper ocean, the removal flux of $^{210}$Pb was close to the constant atmospheric $^{210}$Pb deposition flux of 18,540 dpm/m$^2$/year. The values of $\tau_{Pb-D}$ and $\tau_{Pb-P}$ in the upper ocean (0–150 m) were nearly on the same level, ranging from 0.47 to 1.09 year and from 0.33 to 0.98 year, respectively. However, in the deeper ocean (150–1,000 m), the scavenging rate of $^{210}$Pb decreased significantly to a low level of 3,103–3,800 dpm/m$^2$/year, whereas the removal flux of $^{210}$Pb remained at a high level (15,575–17,649 dpm/m$^2$/year). Moreover, the residence times of D-Pb and P-Pb below 150 m were calculated to be 13.1–22.9 and 1.1–5.5 year, respectively.

## Particulate Organic Carbon Export Flux Estimated From $^{210}$Po Deficiency

The scavenging of particle-reactive nuclides produces a deficiency of the daughter nuclides with respect to their parents in the water column. From these daughter deficiencies, Buesseler et al. (1992) developed a method to estimate the POC export flux ($F_{POC}$) from the upper ocean by using $^{234}$Th-$^{238}$U disequilibrium, and this method has been applied extensively. $F_{POC}$ can be derived by multiplying the daughter nuclide removal flux from the euphotic zone by the ratio of the POC concentration to the daughter nuclide activity of the total particulate material. Similarly, based on the $^{210}$Po deficiency, the POC export flux is expressed as follows:

$$F_{POC}(Buesseler) = \frac{POC}{A^P_{Po}} \times P_{Po}, \quad (19)$$

where $POC/A^P_{Po}$ denotes the measured POC/$^{210}$Po ratio in particulate matter, and $P_{Po}$ denotes the removal flux of $^{210}$Po at the output interface of 150 m.

Similarly, Coale and Bruland (1987) showed that the profile of $^{234}$Th was closely linked to the profiles of nutrients and chlorophyll, implying that the cycling of $^{234}$Th was linked to the cycling of organic matter. This led Eppley (1989) to assume that, if the residence times of POC and $^{234}$Th in surface waters are similar, the $^{234}$Th flux can be used to calculate $F_{POC}$. Because

**TABLE 2 |** $^{226}$Ra inventories integrated from 0 to 150 m and from 150 to 1,000 m in the w-NPO.

| Station | Longitude | Latitude | Date | Integrated depth (m) | $^{226}$Ra inventory (dpm/m$^2$) | Reference |
|---|---|---|---|---|---|---|
| KH-71-3-S | 28°29'N | 145°06'E | 29-Jun | 0–150 | 14,625 | Nozaki and Tsunogai, 1976 |
| | | | | 150–1,000 | 172,530 | |

*Dissolved $^{226}$Ra data is cited from Nozaki and Tsunogai (1976).*

$^{210}$Po has stronger particle affinity in organic matter than $^{234}$Th, $^{210}$Po could be superior to $^{234}$Th as a tracer for POC; hence, based on Eppley's assumption, the $^{210}$Po-based POC flux can also be derived as follows:

$$I_{POC} = \int_0^z (POC)\, dz, \quad (20)$$

$$F_{POC}(Eppley) = \frac{I_{POC}}{\tau_{Po-P}}, \quad (21)$$

where $I_{POC}$ stands for the integral inventory of POC in the upper ocean and $\tau_{Po-P}$ is the residence time of $^{210}$Po in the particulate phase.

The POC fluxes estimated by the Eppley and Buesseler models in the upper layer of the w-NPO (0–150 m) are displayed in **Table 3** and **Figure 9**. From **Figure 9A**, we can divide these seven stations into two groups. One group (Group I) includes the station XTW1-3 in the Luzon Strait, station XTJ2-7 in the northern Shikoku Basin, and station XTJ1-22 located in the Oyashio Current -Kuroshio Current boundary near the main island of Japan, which showed a higher estimated $F_{POC}$ level of 6–9 mmol C/m$^2$/d (see **Table 3** and **Figure 9A**). The common characteristic of Group I was that all of them were located near the continental shelf of East Asia. However, station XTJ1-22 was also affected by the cold and nutrient-rich Oyashio Current, which appears to promote high primary production and subsequently high POC export flux. Therefore, the FPOC of station XTJ1-22 was the highest among all stations (**Figure 9A**).

By contrast, the other four stations (XTJ1-1, XTW1-11, XTJ1-8, and XTJ1-13 station) can form another group (Group II), which denoted a lower POC export flux level in the w-NPO (**Figure 9A**). Concretely, the lowest POC export (<1 mmol C/m$^2$/day) was found at station XTJ1-1 in the Marianas Trench, at which the negligible sinking flux of $^{210}$Po (3,327 dpm/m$^2$/year, **Table 1**) was the most obvious feature. The relatively lower POC export fluxes (1–2 mmol C/m$^2$/day) at stations XTW1-11 and XTJ1-8 were derived from the relatively low sinking fluxes of $^{210}$Po (**Table 1**) and relatively low particulate POC/$^{210}$Po ratios (**Table 3**). Geographically, these four stations of Group II (XTW1-11, XTJ1-1, XTJ1-8, and XTJ1-13) were located in the central gyre of the w-NPO, which had the lower particulate POC/$^{210}$Po ratios in total suspended matters comparing with values of the stations (XTW1-3, XTJ1-22, and XTJ2-7) in Group I close to the East Asian continent (**Table 3**). $F_{POC}$ of stations in Group II were much lower than those of Group I, which may be related to the dominated phytoplankton. The central gyre of the w-NPO (stations of Group II) is an oligotrophic area where the phytoplankton community is dominated by picoplankton (such as smaller diatoms or coccolithophores), and these small size phytoplankton produce a low POC flux due to the oligotrophic living conditions in this region. Interestingly, in these areas, stations in Group II had much higher particulate POC/$^{210}$Po ratios than those of stations in the central gyre of the w-NPO (Group I). For example, the stations XTW1-3, XTJ1-22, and XTJ2-7, located at the margins of the Chinese mainland and the main island of Japan, have higher particulate POC/$^{210}$Po ratios of 181 ± 16, 184 ± 16, and 108 ± 10 μmol/dpm, respectively. And the other four stations XTW1-11, XTJ1-1, XTJ1-8, and XTJ1-13, located in the central gyre of the w-NPO, have much lower particulate POC/$^{210}$Po ratios of 73 ± 5, 76 ± 6, 84 ± 7, and 69 ± 5 μmol/dpm, respectively (**Table 2**). Generally, smaller phytoplankton cells can scavenge more $^{210}$Po (smaller particles dominate higher particulate $^{210}$Po activity relative to larger particles in the non-oligotrophic area) due to their larger surface area per unit of volume, lowering their particulate POC/$^{210}$Po ratios (Tang et al., 2019).

Overall, the POC fluxes calculated by the Eppley method and Buesseler method ranged from 0.6 to 8.8 mmol C/m$^2$/d and from 0.7 to 8.6 mmol C/m$^2$/d, respectively (**Figure 9A**). These values are in good agreement with the estimated POC fluxes derived *via* the steady-state $^{210}$Po-$^{210}$Pb method in other open oceans with similar latitudes (negligible to 8.5 mmol C/m$^2$/day) (Kim and Church, 2001; Stewart et al., 2007; Verdeny et al., 2009; Roca-Martí et al., 2016; Tang et al., 2019; Horowitz et al., 2020). From **Figure 9A**, although there are some differences, Eppley model and Buesseler model-derived $F_{POC}$, are very similar within uncertainties. Buesseler model estimated $F_{POC}$ were 24 and 43% higher than that of Eppley model for stations XTW1-3 and XTJ2-7, respectively. However, Eppley model-derived $F_{POC}$ was 17% higher than that of Buesseler model

**TABLE 3 |** POC fluxes and *e-ratios* derived from $^{210}$Po tracer by the Eppley and Buesseler models.

| Station | Integrated depth | $^{210}$Po-derived $F_{POC}$ (Eppley model) | *e-ratio**(Eppley model) | Particulate POC/$^{210}$Po at 150 m | $^{210}$Po-derived $F_{POC}$ (Buesseler model) | *e-ratio** (Buesseler model) |
|---|---|---|---|---|---|---|
| | m | mmol C/m$^2$/d | % | μmol/dpm | mmol C/m$^2$/d | % |
| XTW1-3 | 0–150 | 6.0 ± 0.3 | 9.7 | 181 ± 16 | 8.6 ± 0.8 | 13.9 |
| XTW1-11 | 0–150 | 1.7 ± 0.2 | 2.7 | 73 ± 5 | 2.5 ± 0.2 | 4.0 |
| XTJ1-1 | 0–150 | 0.6 ± 0.2 | 1.0 | 76 ± 6 | 0.7 ± 0.1 | 1.1 |
| XTJ1-8 | 0–150 | 1.6 ± 0.2 | 2.6 | 84 ± 7 | 2.1 ± 0.2 | 3.4 |
| XTJ1-13 | 0–150 | 5.9 ± 0.4 | 9.5 | 69 ± 5 | 6.6 ± 0.5 | 10.6 |
| XTJ1-22 | 0–150 | 8.8 ± 0.4 | 14.2 | 184 ± 16 | 7.5 ± 0.6 | 12.1 |
| XTJ2-7 | 0–150 | 6.2 ± 0.3 | 10.0 | 108 ± 10 | 7.7 ± 0.7 | 12.4 |

*The uncertainties in the $^{210}$Po-derived POC flux were estimated based on the propagation of error. The export interface is defined at 150 m. *The primary production for calculating the e-ratio values was 62 ± 19 mmol C/m$^2$/d (cited from Palevsky et al., 2016).*

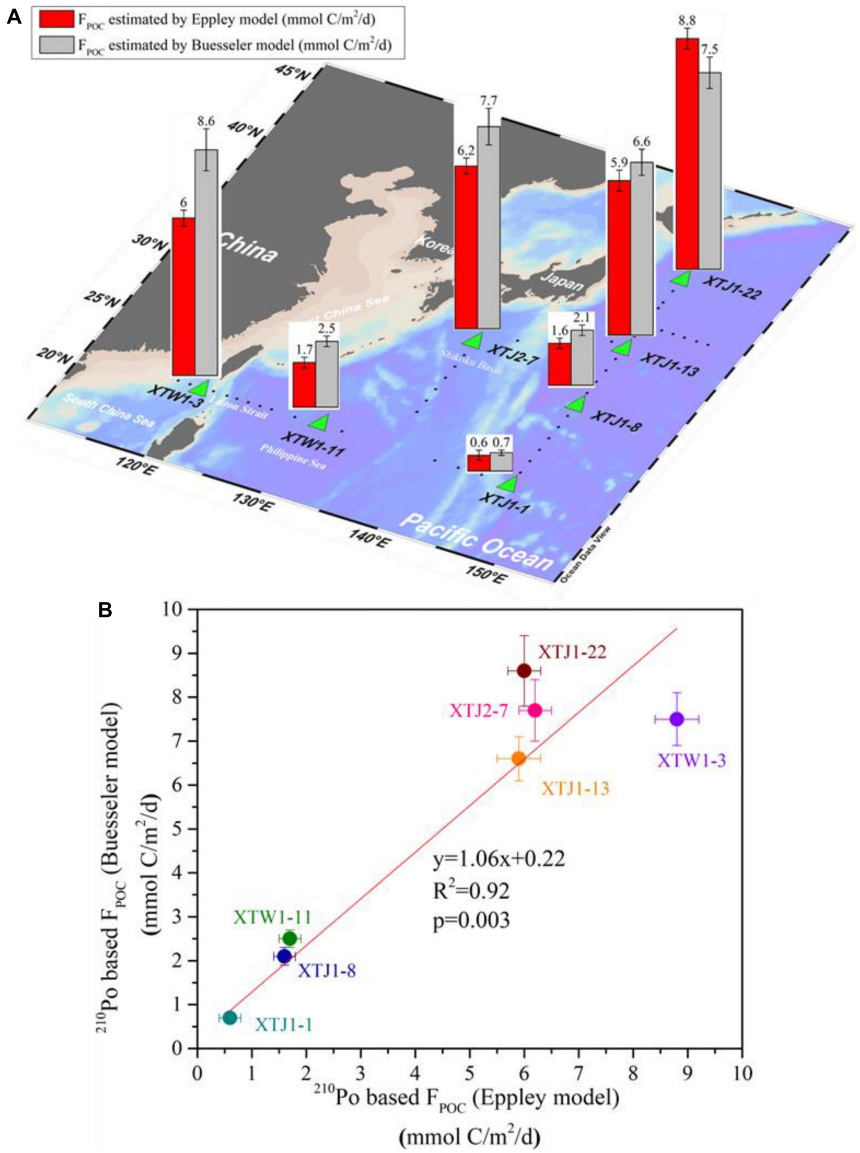


**FIGURE 9 | (A)** Spatial distribution of POC export fluxes derived from $^{210}$Po for the upper w-NPO. **(B)** Relation between the Eppley and Buesseler model-calculated POC export fluxes.

for station XTJ1-22. The difference of $F_{POC}$ results given by different models may be related to the assumptions of the models. For example, the Eppley model's assumption that the residence times of POC and particulate daughter radionuclides ($^{234}$Th or $^{210}$Po) should be the same within the upper ocean is possibly too demanding in the real ocean and therefore is often difficult to achieve. Murray et al. (1989) compared the residence times of $^{234}$Th and POC in the euphotic zone of the eastern equatorial Pacific and found that the residence time of $^{234}$Th was approximately three times less than that of POC. In contrast, the Buesseler model needs to assume only that the same particulate matter serves as the carrier of POC and $^{234}$Th (or $^{210}$Po), which is relatively easy to achieve in the actual sea. For some specific stations, the difference between two models may be significant, hence, more care should be taken when selecting the model. But on a larger spatial scale in our study area, Eppley model can also provide reasonable estimation results. For example, **Figure 9B** shows that Eppley model-derived $F_{POC}$ was well correlated with the Buesseler model-derived $F_{POC}$ in the w-NPO ($n$ = 7, slope = 1.06, $R^2$ = 0.92, $p$ = 0.003); additionally, the $^{210}$Po-POC export fluxes based on the Eppley and Buesseler models had very similar spatial distribution features (**Figure 9A**). These evidences suggest that the hypothesis of the Eppley model is also valid in the w-NPO and this agreement of Eppley model-derived $F_{POC}$ and Buesseler model-derived $F_{POC}$ in the w-NPO probably suggest the residence times of $^{210}$Po and POC were similar in the upper ocean.

## Comparison of Particulate Organic Carbon Export Fluxes Among Different Regions of the Western North Pacific Ocean and Its Surrounding Marginal Seas

The $^{210}$Po-derived POC export fluxes from the upper ocean (5.9–8.8 mmol C/m$^2$/day) at the stations along the edges of the w-NPO (close to the East Asian land masses) were significantly higher (by a factor of 2∼14) than the fluxes determined from the interior (oligotrophic) seawater in the w-NPO (i.e., XTW1-11, XTJ1-1, and XTJ1-8: 0.6–2.5 mmol C/m$^2$/d) (**Table 3** and **Figure 9**). Comparing our POC fluxes with other fluxes in different regions of the Pacific Ocean and its surrounding marginal seas (**Table 4**, in which the POC fluxes were estimated either by sediment traps or by the $^{234}$Th-$^{238}$U and $^{210}$Po-$^{210}$Pb disequilibrium methods), reveals systematic higher POC fluxes occurring in the marginal seas surrounding the w-NPO (**Figure 10**). For example, the POC export fluxes in the Pacific Ocean were much smaller than those reported for the SCS (2.0–16.7 mmol C/m$^2$/day, $^{234}$Th-$^{238}$U disequilibrium, Zhou et al., 2020), inner shelf of the ECS (4.8–65.4 mmol C/m$^2$/day, trap, Hung et al., 2013), and the Sea of Japan (3.2–26.3 mmol C/m$^2$/day, $^{234}$Th-$^{238}$U disequilibrium, Kawakami et al., 2015).

The NPO is a region of particular interest for quantifying the rate and efficiency of the BCP, as this region is a major sink for atmospheric $CO_2$, absorbing 0.5 Pg C/year, ∼25% of the total ocean $CO_2$ uptake (Takahashi et al., 2009). As an important part of the NPO, the subtropical oligotrophic w-NPO is a typical nitrate-deficient water region and is characterized by low chlorophyll-a (Chl a) concentrations (Chen et al., 2013), and this region occurs a band of strong $CO_2$ uptake between 30 and 40°N, overlapping with the transition zone between the subtropical and subarctic gyres (Shih et al., 2015). Researchers stated the importance of the contributions of biological carbon export to the NPO sink (Ayers and Lozier, 2012). However, the characteristics of the POC export flux in the w-NPO region are not well understood (Kawakami et al., 2015; Shih et al., 2015). Using the information available, based on the summary of the published POC export fluxes in the North Pacific Ocean (**Table 4** and **Figure 10**), we can obtain a preliminary general view for the distribution feature of POC export flux. Although there were spatial differences, the overall mean level of POC export flux was below 10 mmol C/m$^{2/}$day. Specifically, the POC fluxes in our study area of the w-NPO (0.6–8.8 mmol C/m$^2$/day) are comparable to the results of other published studies obtained with the $^{234}$Th-$^{238}$U method in other Pacific Ocean regions under general production condition (**Figure 10A**), such as the subarctic northeastern Pacific Ocean (2.8–7.6 mmol C/m$^2$/d, from February 1996 to February 1997, Charette et al., 1999; 2.01 ± 0.56 ($n$ = 61) mmol C/m$^2$/d in August/September 2018 with no bloom, Buesseler et al., 2020), station ALOHA in the North Pacific Subtropical Gyre (0.4–4.0 mmol C/m$^2$/d, from April 1999 to March 2000, Benitez-Nelson et al., 2001; neiligible-7.0 mmol C/m$^2$/day, in June/July 2004 with no bloom, Buesseler et al., 2009), station K2 in the western subarctic North Pacific (1.9–10.1 mmol C/m$^2$/day, in July/August 2005 with no bloom, Buesseler et al., 2009) and the North Pacific tropical and subtropical gyre (0.1–6.3 mmol C/m$^2$/day, in August/September 2015 with no bloom, Umhau et al., 2019).

**TABLE 4 |** Comparison of the POC export fluxes estimated in different regions throughout the w-NPO and its surrounding marginal seas.

| Number | Locations | Export layer (m) | POC flux (mmol C/m$^2$/d) | | e-ratio (%) | Method | References |
|---|---|---|---|---|---|---|---|
| | | | Range | Average | | | |
| 1 | NE Pacific | 25–100 | 2.8–7.6 | 5.8 ± 2.6 ($n$ = 3) | 6–13 | $^{234}$Th-$^{238}$U | Charette et al., 1999 |
| 2 | NE Pacific | 120 | 1.0–3.3 | 2.0 ± 0.6 ($n$ = 61) | 13 ± 5 | $^{234}$Th-$^{238}$U | Buesseler et al., 2020 |
| 3 | North Pacific (ALOHA) | 150 | 1.2–10.4 | 4.0 ± 2.3 ($n$ = 9) | 8.8 | $^{234}$Th-$^{238}$U | Benitez-Nelson et al., 2001 |
| 4 | North Pacific (ALOHA) | 150 | 0–6.9 | 2.1 ± 2.0 ($n$ = 19) | 12 | $^{234}$Th-$^{238}$U | Buesseler et al., 2009 |
| 5 | Western subarctic North Pacific (K2) | 150 | 1.9–10.1 | 6.3 ± 2.5 ($n$ = 26) | 14 | $^{234}$Th-$^{238}$U | |
| 6 | North Pacific tropical and subtropical gyre | 150 | 0.1–6.3 | 2.3 ± 2.5 ($n$ = 5) | NA | Trap and $^{234}$Th-$^{238}$U | Umhau et al., 2019 |
| 7 | Western subarctic North Pacific (K2) | 100 | 1.2–23.7 | 8.0 ± 7.9 ($n$ = 6) | 3–46 | $^{234}$Th-$^{238}$U | Kawakami et al., 2015 |
| 8 | SCS (SEATS) | 100 | 2.0–16.7 | 5.2 ± 4.2 ($n$ = 11) | 9–34 | $^{234}$Th-$^{238}$U | Zhou et al., 2020 |
| 9 | Sea of Japan | 100 | 3.2–26.3 | 12.0 ± 8.3 ($n$ = 12) | 7–56 | $^{234}$Th-$^{238}$U | Kim et al., 2011 |
| 10 | Central ECS | 55–80 | 1.4–2.7 | 2.1 ± 0.6 ($n$ = 5) | NA | $^{210}$Po-$^{210}$Pb | Su et al., 2017 |
| 11 | Southern ECS | 70 | 18.7–46.0 | 26.8 ± 13.0 ($n$ = 4) | 13–28 | Trap | Shih et al., 2013 |
| 12 | ECS (inner shelf) | 20–30 | 5.7–65.4 | 32.4 ± 22.2 ($n$ = 5) | 9–91 | Trap | Hung et al., 2013 |
| 13 | ECS (outer shelf) | 100–120 | 4.8–5.3 | 5.0 ± 0.3 ($n$ = 2) | 5–14 | Trap | |
| 14 | ECS (Kuroshio) | 120 | 2.3 | 2.3 ± 0.3 ($n$ = 1) | 6 | Trap and $^{234}$Th-$^{238}$U | Hung and Gong, 2007 |
| 15 | w-NPO | 150 | 0.6–8.8* | 4.4 ± 3.1 ($n$ = 7)* | 1.0–14.2 | $^{210}$Po-$^{210}$Pb | This study |
| | | | 0.7–8.6# | 5.1 ± 3.2 ($n$ = 7)# | | | |

*SEATS (18°N 116°E): the South-East Asian Time-series Study site; ALOHA (22.75°N, 158°W): the Hawaii Ocean Time-series (HOT) station; K2 (47°N 160°E): A key time-series mooring station operated by the Japan Agency for Marine Earth Science Technology.*

**POC fluxes estimated by the Eppley model.*

*#POC fluxes estimated by the Buesseler model.*

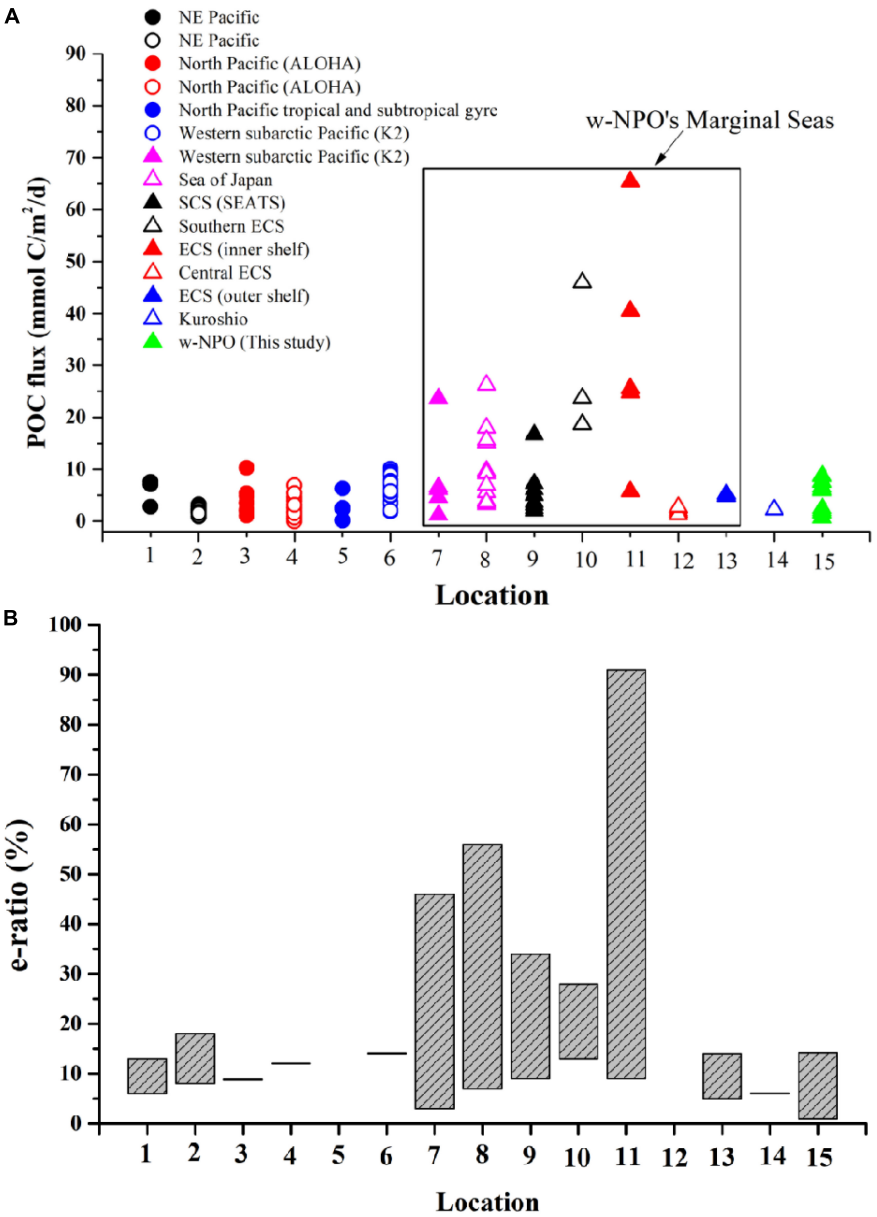


**FIGURE 10 |** Comparison of the POC export fluxes **(A)** and export efficiency **(B)** in different sea areas of the Pacific Ocean and its marginal seas. Data are derived from the references in **Table 4** and this study.

Export efficiency can be defined as the ratio of POC export to primary production (the *e-ratio*, Buesseler, 1998). Although primary productivity levels were not available for the studied sampling stations, Palevsky et al. (2016) summarized the annual and seasonal net primary productivity (NPP) estimates for the western North Pacific. Since our sampling activities took place from late May to late June 2018, we preliminarily evaluated the *e-ratio*s of the BCP in the w-NPO by using the summer NPP estimates for the regions of the North Pacific (62 ± 19 mmol C/m$^2$/day), hence, the *e-ratio* values were calculated to be in the range of 1.0–14.2% (**Table 3**), which are similar to the previously reported values in the North Pacific (**Table 4** and **Figure 10B**; Charette et al., 1999; Benitez-Nelson et al., 2001; Buesseler et al., 2009, 2020). As can be seen from **Figure 10B**, the e-ratios of biological carbon pump were more variable in the marginal seas than that in the Pacific Ocean. For example, the e-ratios were very consistent (in a level of < 20%) in the NE Pacific, North Pacific, and w-NPO. However, in the marginal seas, the POC fluxes and e-ratios changed over a very wide range (**Figure 10B**). One extreme case reported in the inner shelf of ECS showed that the e-ratios ranged from 10 to 90% (Hung et al., 2013). The *e-ratios* in our study were below 15%, suggesting a moderate BCP efficiency in the w-NPO. By comparison, it can be found that the BCP strengths in some marginal seas of the Pacific Ocean [for

example, *e-ratio* = 9–91% in the inner shelf of ECS (Hung et al., 2013), 13–28% in the Southern ECS (Shih et al., 2013), and 7–56% in the Sea of Japan (Kim et al., 2011)] is stronger than that in the interior of the Pacific Ocean (for example, *e-ratio* = ∼10% at station XTJ2-7 in the Shikoku Basin, 3–4% at station XTW1-11 in the Philippine Basin, and ∼1% at station XTJ1-1 in the Mariana Trench).

We compiled a table for comparing the export efficiencies of BCP in other open seas, as shown in the **Table 5**. It is worth noting that the *e-ratios* are similar in such different areas. For example, the *e-ratios* < 15% observed in our study are similar to those found in the North Atlantic (Iberian Basin, 0.5–2.5%; Irminger Basin, 3 ± 3%; western European Basin, 5 ± 5%; Iceland Basin, 6 ± 6%; and Labrador Basin, 10 ± 3%, see Tang et al., 2019). The similarity between our study and Tang et al. (2019) is that both sampling activities were carried out in May-June, however, the difference is that our study area was in an oligotrophic subtropical region (medium-low latitudes) and the study area of Tang et al. (2019) was in a temperate system (medium-high latitudes). In addition, Tang et al. (2019) started sampling when the bloom was starting, hence, the POC fluxes and *e-ratios* were still low. Ceballos-Romero et al. (2016) pointed that export efficiency was significantly discrepant in different stages of the bloom and the export efficiency also showed a strong seasonal variability in the North Atlantic. By comparison with study case of Ceballos-Romero et al. (2016) in the North Atlantic Ocean, we can find that algal blooming has a significant influence on BCP efficiency. Ceballos-Romero et al. (2016) reported two sampling campaigns: one sampling was carried out in the pre-bloom stage (April-May 2010), and the export efficiency was high at that moment (∼50%); another sampling was carried out in the decline of the bloom and post-bloom stage (July–August 2010), and the export efficiency was very low (3%). Obviously, our study displayed results from medium-low latitudes with no bloom, therefore, the low e-ratios of 1.0–14.2% were reasonable.

In addition, the *e-ratios* in the w-NPO (1.0–14.2%, this study) are close to or slightly higher than that in the low-latitude tropical seas and oceans, for example, the equatorial Pacific (1–10%, Buesseler, 1998) and the Arabian Sea (1–10%, Buesseler, 1998; 0.2–11.7%, Subha Anand et al., 2017). This low e-ratios of < 10% might represent the values of BCP efficiency under general condition for tropical ocean, considering the weak seasonal variation of tropical oceans and the oligotrophic features. However, the *e-ratios* in the w-NPO are much lower than those reported at high-latitude sites (>25%), such as the Eurasian Basin of the Arctic Ocean (60 ± 40%, Roca-Martí et al., 2016), the Bellingshausen Sea (37% at station K, Shimmield et al., 1995) and the Weddell Sea and the Antarctic Polar Front (16–100%, Rutgers van der Loeff et al., 1997), since most of these study cases in the high-latitude seas were related to the bloom situation or the increase of chlorophyll-a, POC and plankton biomass concentrations (Shimmield et al., 1995; Rutgers van der Loeff et al., 1997). The lower export efficiencies observed in the w-NPO may be consistent with the predominance of smaller phytoplankton in the oligotrophic seawater. The oligotrophic feature might weaken the export strength of the BCP in the w-NPO. Indeed, small particles are usually slow-sinking particles that are more likely to be degraded during their descent (Villa-Alfageme et al., 2016), leading to lower export efficiencies. In our study, we also observed negative scavenging rates (J) of $^{210}$Po (negative J values mean that radionuclides are transferred from particles to the dissolved phase) below 150 m in the w-NPO (**Table 1**), which supports the occurrence of particle degradation, leading to a low export efficiency. For example, the lowest $J_{Po}$ values in the 150–1,000 m segment were observed at stations XTW1-11 ($J_{Po}$ = –86,511 dpm/m$^2$/year), XTJ1-1 ($J_{Po}$ = –64,036 dpm/m$^2$/year) and XTJ1-8 ($J_{Po}$ = –26,022 dpm/m$^2$/year), and correspondingly, these three stations have the lowest e-ratios (based on Eppley model: 1.0–2.7%; based on Buesseler model: 1.1–4.0% **Table 3**).

**TABLE 5 |** Summary of carbon export efficiencies (*e-ratios*) based upon $^{210}$Po or $^{234}$Th approach in global open oceans.

| Ocean | Site | Longitude | Latitude | Observation time | Method | e-ratio | References |
|---|---|---|---|---|---|---|---|
| Atlantic Ocean | Iberian basin | 15°W-9°W | 39–42°N | May–June 2014 | $^{210}$Po-$^{210}$Pb method | 0.5–2.5% (*n* = 2) | Tang et al., 2019 |
| | Irminger basin | 43–35°W | 59–61°N | | | 3 ± 3% (*n* = 2) | |
| | Western European basin | 24–19°W | 46–51°N | | | 5 ± 5% (*n* = 3) | |
| | Iceland basin | 32–25°W | 55–60°N | | | 6 ± 6% (*n* = 2) | |
| | Labrador basin | 52–45°W | 52–59°N | | | 10 ± 3% (*N* = 3) | |
| Pacific Ocean | Equatorial Pacific | 95–170°W | 12–12°S | Spring and fall 1992 | $^{234}$Th-$^{238}$U method | 1–10% (*n* = 14) | Buesseler, 1998 |
| Indian Ocean | Arabian Sea | 57–65°E | 10–18°N | Aug.–Sept. 1995 | | 1–10% (*n* = 19) | |
| Indian Ocean | Arabian Sea | 70–87°E | 25°S-19°N | March–April 2014 | | 0.2–11.7% (*n* = 13) | Subha Anand et al., 2017 |
| Pacific Ocean | w-NPO | 118–153°E | 20–40°N | May–June 2018 | $^{210}$Po-$^{210}$Pb method | 1.0–14.2% (*n* = 7) | This study |
| Arctic Ocean | Eurasian Basin | 17 –131°E | 81–88.8°N | Aug.–Sept. 2012 | $^{210}$Po-$^{210}$Pb and $^{234}$Th-$^{238}$U method | 60 ± 40% (*n* = 7) | Roca-Martí et al., 2016 |
| Southern Ocean | Bellingshausen Sea | 84°56'W | 67°36'S | Nov.–Dec. 1992 | $^{210}$Po-$^{210}$Pb and $^{234}$Th-$^{238}$U method | 37% (*n* = 1) | Shimmield et al., 1995 |
| Southern Ocean | Weddell Sea/Polar Front | 49°35'W | 47–57°S | Oct.–Dec. 1992 | $^{234}$Th-$^{238}$U method | 16–100% (*n* = 20) | Rutgers van der Loeff et al., 1997; Buesseler, 1998 |

## CONCLUSION

In this study, we reported the vertical distributions of D-Po, P-Po, D-Pb, and P-Pb activities in the w-NPO during late spring and early summer to constrain the particle dynamics (scavenging rates and removal fluxes of $^{210}$Po and $^{210}$Pb), and to estimate the carbon export production (POC export flux). More than 50% of the radionuclides were found in the dissolved phase below a depth of 50 m, while a small proportion was associated with the particulate phase. However, the percentages of P-Po and P-Pb were higher than 50% (even up to 90%) in the surface seawater (0–50 m). $^{210}$Po deficits relative to $^{210}$Pb were observed in the upper 150 m at all the stations, however such $^{210}$Po deficiencies can even extend to deeper ocean (such as 500 m) at some stations. In the interior of the w-NPO, the excess $^{210}$Po (total $^{210}$Po/$^{210}$Pb $> 1$) activities in the deeper ocean (500–1,000 m) at stations XTJ1-1 and XTJ1-8 were attributed to the release of $^{210}$Po due to biogenic particle release during sinking. Based on a conceptual one-dimensional irreversible scavenging model, the residence times of $^{210}$Po and $^{210}$Pb in the w-NPO were obtained. In the upper ocean (0–150 m), the residence times of D-Po ($\tau_{Po-D}$, 0.6–5.5 year) were much higher than those of P-Po ($\tau_{Po-P}$, 83–921 days), while in the deep ocean (below 150 m), the residence times of D-Pb were calculated to be 13.1–22.9 year, 2–10 times longer than those of P-Pb (1.1–5.5 year).

Based on $^{210}$Po-$^{210}$Pb disequilibrium, we found that the Eppley model-derived POC export fluxes agreed well with those derived from the Buesseler model in the upper ocean of the w-NPO, suggesting that particulate $^{210}$Po and POC may have similar residence time in the water column. Overall, the $^{210}$Po-derived POC fluxes varied spatially, ranging from 0.6 to $< 9$ mmol C/m$^2$/day, with the highest export fluxes at stations close to the East Asian continental shelf and the lowest export fluxes at stations in the ocean basin. We concluded that POC export fluxes tended to increase with decreasing distance from the continental margins. The POC export efficiencies also showed regional differences even within the same basin, with *e-ratio* values ranging from 1.0 to 14.2%, suggesting a moderate BCP efficiency in the w-NPO. The low export efficiencies may be associated with the dominance of smaller particles and particle release below the euphotic zone. The negative scavenging rates of $^{210}$Po ($-J_{Po}$) below 150 m at stations in the central basin of the w-NPO supports the occurrence of particle dissolution. Comparing with the reported *e-ratios* in other open seas, relatively higher carbon export efficiencies occurred at high-latitude sites.

## DATA AVAILABILITY STATEMENT

The original contributions presented in the study are included in the article/**Supplementary Material**, further inquiries can be directed to the corresponding author/s.

## AUTHOR CONTRIBUTIONS

QZ was responsible for conceptualization, methodology, sample analysis, data processing, writing original draft, writing–review, and revising. DH, TY, and JD provided a financial support and helped in article reviewing. JL, JJ, and JN contributed to the review of the manuscript. All authors contributed to the article and approved the submitted version.

## FUNDING

This study was funded by the China Postdoctoral Science Foundation (2021M693780), the Scientific Research Foundation of Third Institute of Oceanography, MNR (2019004), the Science and Technology Plan Projects of Guangxi Zhuang Autonomous Region (2017AB30024) and the Science Foundation of the Fujian Province (2018Y0059 and 2019Y0073).

## ACKNOWLEDGMENTS

We are grateful to the captain and crew of the R/V Xiangyanghong III for their support at sea. Many thanks to members of RIC group in ECNU (especially Lady Langlin) for their assistance with expedition preparation.

## SUPPLEMENTARY MATERIAL

The Supplementary Material for this article can be found online at: https://www.frontiersin.org/articles/10.3389/fmars.2021.700524/full#supplementary-material

## REFERENCES

Ayers, J. M., and Lozier, M. S. (2012). Unraveling dynamical controls on the North Pacific carbon sink. *J. Geophys. Res. Oceans* 117:C01017. doi: 10.1029/2011JC007368

Bacon, M. P., Spencer, D. W., and Brewer, P. G. (1976). $^{210}$Pb/226Ra and $^{210}$Po/$^{210}$Pb disequilibria in seawater and suspended particulate matter. *Earth Planet. Sci. Lett.* 32, 277–296. doi: 10.1016/0012-821x(76)90068-6

Baskaran, M. (2011). Po-210 and Pb-210 as atmospheric tracers and global atmospheric Pb-210 fallout: a review. *J. Environ. Radioact.* 102, 500–513. doi: 10.1016/j.jenvrad.2010.10.007

Baskaran, M., Church, T., Hong, G., Kumar, A., Ma, Q., Choi, H., et al. (2013). Effects of flow rates and composition of the filter, and decay/ingrowth correction factors involved with the determination of *in situ* particulate $^{210}$Po and $^{210}$Pb in seawater. *Limnol. Oceanogr. Methods* 11, 126–138. doi: 10.4319/lom.2013.11.126

Benitez-Nelson, C. R., Buesseler, K. O., Karl, D. M., and Andrews, J. (2001). A time-series study of particulate matter export in the north pacific subtropical gyre based on $^{234}$Th:$^{238}$U disequilibrium. *Deep Sea Res. Part I Oceanogr. Res. Pap.* 48, 2595–2611. doi: 10.1016/s0967-0637(01)00032-2

Buesseler, K. O. (1998). The decoupling of production and particulate export in the surface ocean. *Glob. Biogeochem. Cycles* 12, 297–310. doi: 10.1038/nature02631

Buesseler, K. O., and Boyd, P. (2009). Shedding light on processes that control particle export and flux attenuation in the twilight zone of the open ocean. *Limnol. Oceanogr.* 54, 1210–1232. doi: 10.4319/lo.2009.54.4.1210

Buesseler, K. O., Antia, A. N., Chen, M., Fowler, S. W., Gardner, W. D., Gustafsson, O., et al. (2007). An assessment of the use of sediment traps for estimating upper ocean particle fluxes. *J. Mar. Res.* 65, 345–416.

Buesseler, K. O., Bacon, M. P., Cochran, J. K., and Livingston, H. D. (1992). Carbon and nitrogen export during the JGOFS North Atlantic Bloom experiment estimated from $^{234}$Th:$^{238}$U disequilibria. *Deep Sea Res. Part A Oceanogr. Res. Pap.* 39, 1115–1137. doi: 10.1016/0198-0149(92)90060-7

Buesseler, K. O., Benitez-Nelson, C. R., Roca-Marti, M., Wyatt, A. M., Resplandy, L., Clevenger, S. J., et al. (2020). High-resolution spatial and temporal measurements of particulate organic carbon flux using thorium-234 in the northeast Pacific Ocean during the EXport processes in the ocean from remote sensing field campaign. *Elem. Sci. Anth.* 8, 30. doi: 10.1525/elementa.030

Buesseler, K. O., Pike, S., Maiti, K., Lamborg, C. H., Siegel, D. A., and Trull, T. W. (2009). Thorium-234 as a tracer of spatial, temporal and vertical variability in particle flux in the north pacific. *Deep Sea Res. Part I Oceanogr. Res. Pap.* 56, 1143–1167. doi: 10.1016/j.dsr.2009.04.001

Ceballos-Romero, E., Le Moigne, F. A. C., Henson, S., Marsay, C. M., Sanders, R. J., García-Tenorio, R., et al. (2016). Influence of bloom dynamics on particle export efficiency in the North Atlantic: a comparative study of radioanalytical techniques and sediment traps. *Mar. Chem.* 186, 198–210. doi: 10.1016/j.marchem.2016.10.001

Charette, M. A., Moran, S. B., and Bishop, J. K. B. (1999). $^{234}$Th as a tracer of particulate organic carbon export in the subarctic northeast Pacific Ocean. *Deep Sea Res. Part II Top. Stud. Oceanogr.* 46, 2833–2861. doi: 10.1016/s0967-0645(99)00085-5

Chen, K. S., Hung, C. C., Gong, G. C., Chou, W. C., Chung, C. C., Shih, Y. Y., et al. (2013). Enhanced POC export in the oligotrophic northwest Pacific Ocean after extreme weather events. *Geophys. Res. Lett.* 40, 5728–5734. doi: 10.1002/2013gl058300

Cherrier, J., Burnett, W. C., and LaRock, P. A. (1995). Uptake of polonium and sulfur by bacteria. *Geomicrobiol. J.* 13, 103–115.

Church, T., Rigaud, S., Baskran, M., Kumar, A., Friedrich, J., Masqué, P., et al. (2012). Intercalibration studies of $^{210}$Po and $^{210}$Pb in dissolved and particulate seawater samples. *Limnol. Oceanogr. Methods* 10, 776–789. doi: 10.4319/lom.2012.10.776

Coale, K. H., and Bruland, K. W. (1987). Oceanic stratified euphotic zone as elucidated by $^{234}$Th:$^{238}$U disequilibria. *Limnol. Oceanogr.* 32, 189–200. doi: 10.4319/lo.1987.32.1.0189

Cochran, J. K., and Masqué, P. (2003). Short-lived U/Th series radionuclides in the ocean: tracers for scavenging rates, export fluxes and particle dynamics. *Rev. Mineral. Geochem.* 52, 461–492. doi: 10.2113/0520461

Du, J. (2019). *Study on the Depositional Processes of the Atmospheric Fallout Radionuclides and their Application on Tracing Modern Sedimentation Processes at the East China Sea.* Ph.D thesis. Shanghai: East China Normal University.

Ducklow, H., Steinberg, D., and Buesseler, K. (2001). Upper ocean carbon export and the biological pump. *Oceanography* 14, 50–58. doi: 10.5670/oceanog.2001.06

Eppley, R. W. (1989). "New production: history, methods, problems," in *Productivity of the Ocean: Present and Past*, eds W. Berger, V. Smetacek, and G. Wefer (New York, NY: John Wiley), 85–97.

Falkowski, P. G., Barber, R. T., and Smetacek, V. (1998). Biogeochemical controls and feedbacks on ocean primary production. *Science* 281, 200–206.

Fisher, N. S., Burns, K. A., Cherry, R. D., and Heyraud, M. (1983). Accumulation and cellular distribution of 241Am, $^{210}$Po, and $^{210}$Pb in two marine algae. *Mar. Ecol. Prog. Ser.* 11, 233–237.

Friedrich, J., and Rutgers van der Loeff, M. (2002). A two-tracer ($^{210}$Po-$^{234}$Th) approach to distinguish organic carbon and biogenic silica export flux in the Antarctic Circumpolar Current. *Deep Sea Res. Part I Oceanogr. Res. Pap.* 49, 101–120. doi: 10.1016/s0967-0637(01)00045-0

Gallagher, S. J., Kitamura, A., Iryu, Y., Itaki, T., and Hoiles, P. W. (2015). The Pliocene to recent history of the Kuroshio and Tsushima Currents: a multi-proxy approach. *Prog. Earth Planet. Sci.* 2, 1–23.

Hayes, C. T., Anderson, R. F., Fleisher, M. Q., Serno, S., Winckler, G., and Gersonde, R. (2013). Quantifying lithogenic inputs to the North Pacific Ocean using the long-lived thorium isotopes. *Earth Planet. Sci. Lett.* 383, 16–25. doi: 10.1016/j.epsl.2013.09.025

Hayes, C. T., Black, E. E., Anderson, R. F., Baskaran, M., Buesseler, K. O., Charette, M. A., et al. (2018). Flux of particulate elements in the North Atlantic Ocean constrained by multiple radionuclides. *Glob. Biogeochem. Cycles* 32, 1738–1758. doi: 10.1029/2018GB005994

Heyraud, M., Fowler, S. W., Beasley, T. M., and Cherry, R. D. (1976). Polonium-210 in euphausiids: a detailed study. *Mar. Biol.* 34, 127–136. doi: 10.1007/bf00390754

Honjo, S., Manganini, S. J., Krishfield, R. A., and Francois, R. (2008). Particulate organic carbon fluxes to the ocean interior and factors controlling the biological pump: a synthesis of global sediment trap programs since 1983. *Prog. Oceanogr.* 76, 217–285.

Horowitz, E. J., Cochran, J. K., Bacon, M. P., and Hirschberg, D. J. (2020). $^{210}$Po and $^{210}$Pb distributions during a phytoplankton bloom in the North Atlantic: implications for POC export. *Deep See Res. Part I Oceanogr. Res. Pap.* 164:103339. doi: 10.1016/j.dsr.2020.103339

Hu, D., Wu, L., Cai, W., Gupta, A. S., Ganachaud, A., Qiu, B., et al. (2015). Pacific western boundary currents and their roles in climate. *Nature* 522, 299–308.

Hu, W., Chen, M., Yang, W., Zhang, R., Qiu, Y., and Zheng, M. (2014). Enhanced particle scavenging in deep water of the Aleutian Basin revealed by $^{210}$Po-$^{210}$Pb disequilibria. *J. Geophys. Res. Oceans* 119, 3235–3248. doi: 10.1002/2014JC009819

Hung, C. C., and Gong, G. C. (2007). Export flux of POC in the main stream of the Kuroshio. *Geophys. Res. Lett.* 34:L18606. doi: 10.1029/2007GL030236

Hung, C.-C., Tseng, C.-W., Gong, G. C., Chen, K. S., Chen, M. H., and Hsu, S.-C. (2013). Fluxes of particulate organic carbon in the East China Sea in summer. *Biogeosciences* 10, 6469–6484. doi: 10.1016/j.envpol.2018.11.059

IPCC in Climate Change (2013). "Chapter 6: Carbon and other biogeochemical cycle," in *The Physical Science Basis. Contribution of Working Group I to the Fifth Assessment Report of the Intergovernmental Panel on Climate Change*, Vol. 2013, eds T. F. Stocker, D. Qin, G.-K. Plattner, M. Tignor, S. K. Allen, J. Boschung, et al. (Cambridge: Cambridge University Press), 471.

Kawakami, H., and Kusakabe, M. (2008). Surface water mixing estimated from 228Ra and 226Ra in the northwestern North Pacific. *J. Environ. Radioact.* 99, 1335–1340. doi: 10.1016/j.jenvrad.2008.04.011

Kawakami, H., Honda, M. C., Matsumoto, K., Wakita, M., Kitamura, M., Fujiki, T., et al. (2015). POC fluxes estimated from $^{234}$Th in late spring-early summer in the western subarctic North Pacific. *J. Oceanogr.* 71, 311–324.

Kim, D., Choi, M. S., Oh, H. Y., Song, Y. H., Noh, J. H., and Kim, K. H. (2011). Seasonal export fluxes of particulate organic carbon from $^{234}$Th/$^{238}$U disequilibrium measurements in the Ulleung basin (Tsushima Basin) of the East Sea (Sea of Japan). *J. Oceanogr.* 67, 577–588. doi: 10.1007/s10872-011-0058-8

Kim, G., and Church, T. M. (2001). Seasonal biogeochemical fluxes of $^{234}$Th and $^{210}$Po in the upper Sargasso Sea: influence from atmospheric iron deposition. *Glob. Biogeochem. Cycles* 15, 651–661. doi: 10.1029/2000gb001313

Kwon, E. Y., Primeau, F., and Sarmiento, J. L. (2009). The impact of remineralization depth on the air-sea carbon balance. *Nat. Geosci.* 2, 630–635. doi: 10.1029/2020GL091746

LaRock, P., Hyun, J. H., Boutelle, S., Burnett, W. C., and Hull, C. D. (1996). Bacterial mobilization of polonium. *Geochim. Cosmochim. Acta* 60, 4321–4328. doi: 10.1016/s0016-7037(96)00255-4

Le Moigne, F. A. C., Villa-Alfageme, M., Sanders, R. J., Marsay, C., Henson, S., and García-Tenorio, R. (2013). Export of organic carbon and biominerals derived from $^{234}$Th and $^{210}$Po at the Porcupine Abyssal Plain. *Deep Sea Res. Part I Oceanogr. Res. Pap.* 72, 88–101.

Liu, Q., Guo, X., Yin, Z., Zhou, K., Roberts, E. G., and Dai, M. (2018). Carbon fluxes in the China Seas: an overview and perspective. *Sci. China Earth Sci.* 61, 1564–1582. doi: 10.1007/s11430-017-9267-4

Masqué, P., Sanchez-Cabeza, J. A., Bruach, J. M., Palacios, E., and Canals, M. (2002). Balance and residence times of $^{210}$Pb and $^{210}$Po in surface waters of the northwestern Mediterranean Sea. *Cont. Shelf Res.* 22, 2127–2146. doi: 10.1016/s0278-4343(02)00074-2

Murray, J. W., Downs, J. N., Strom, S., Wei, C.-L., and Jannasch, H. W. (1989). Nutrient assimilation, export production and $^{234}$Th scavenging in the eastern equatorial Pacific. *Deep Sea Res. Part I Oceanogr. Res. Pap.* 36, 1471–1489.

Murray, J. W., Paul, B., Dunne, J. P., and Chapin, T. (2005). $^{234}$Th, $^{210}$Pb, $^{210}$Po and stable Pb in the central equatorial Pacific: tracers for particle cycling. *Deep Sea Res. Part I Oceanogr. Res. Pap.* 52, 2109–2139. doi: 10.1016/j.dsr.2005.06.016

Nozaki, Y., and Tsunogai, S. (1976). 226Ra, $^{210}$Pb and $^{210}$Po disequilibria in the western North Pacific. *Earth Planet. Sci. Lett.* 32, 313–321.

Nozaki, Y., Dobashi, F., Kato, Y., and Yamamoto, Y. (1998). Distribution of Ra isotopes and the $^{210}$Pb and $^{210}$Po balance in surface seawaters of the mid

Northern Hemisphere. *Deep Sea Res. Part I Oceanogr. Res. Pap.* 45, 1263–1284. doi: 10.1016/s0967-0637(98)00016-8

Palevsky, H. I., Quay, P. D., Lockwood, D. E., and Nicholson, D. P. (2016). The annual cycle of gross primary production, net community production, and export efficiency across the North Pacific Ocean. *Glob. Biogeochem. Cycles* 30, 361–380.

Peck, G. A., and Smith, J. D. (2000). Distribution of dissolved and particulate 226Ra, $^{210}$Pb and $^{210}$Po in the Bismarck Sea and western equatorial Pacific Ocean. *Mar. Freshwater Res.* 51, 647–658.

Rigaud, S., Puigcorbé, V., Cámara-Mor, P., Casacuberta, N., Roca-Martí, M., Garcia-Orellana, J., et al. (2013). A methods assessment and recommendations for improving calculations and reducing uncertainties in the determination of $^{210}$Po and $^{210}$Pb activities in seawater. *Limnol. Oceanogr. Methods* 11, 561–571. doi: 10.4319/lom.2013.11.561

Roca-Martí, M., Puigcorbé, V., Rutgers van der Loeff, M. M., Katlein, C., Fernández-Méndez, M., Peeken, I., et al. (2016). Carbon export fluxes and export efficiency in the central Arctic during the record sea-ice minimum in 2012: a joint $^{234}$Th/$^{238}$U and $^{210}$Po/$^{210}$Pb study. *J. Geophys. Res. Oceans* 121, 5030–5049. doi: 10.1002/2016jc011816

Rutgers van der Loeff, M. M., Friedrich, J., and Bathmann, U. V. (1997). Carbon export during the Spring Bloom at the Antarctic Polar Front, determined with the natural tracer $^{234}$Th. *Deep Sea Res. Part II Top. Stud. Oceanogr.* 44, 457–478.

Sabine, C. L. (2004). The oceanic sink for anthropogenic CO2. *Science* 305, 367–371. doi: 10.1126/science.1097403

Sanders, R., Henson, S. A., Koski, M., De La Rocha, C. L., Painter, S. C., Poulton, A. J., et al. (2014). The biological carbon pump in the North Atlantic. *Prog. Oceanogr.* 129, 200–218. doi: 10.1016/j.pocean.2014.05.005

Shih, Y. Y., Hsieh, J. S., Gong, G. C., Hung, C. C., Chou, W. C., Lee, M. A., et al. (2013). Field observations of changes in SST, chlorophyll and POC flux in the southern East China Sea before and after the passage of Typhoon Jangmi. *Terr. Atmos. Ocean. Sci.* 24, 899–910. doi: 10.3319/tao.2013.05.23.01(oc)

Shih, Y. Y., Hung, C. C., Gong, G. C., Chung, W. C., Wang, Y. H., Lee, I. H., et al. (2015). Enhanced particulate organic carbon export at eddy edges in the oligotrophic Western North Pacific Ocean. *PLoS One* 10:e0131538. doi: 10.1371/journal.pone.0131538

Shimmield, G. B., Ritchie, G. D., and Fileman, T. W. (1995). The impact of marginal ice zone processes on the distribution of $^{210}$Pb, $^{210}$Po and $^{234}$Th and implications for new production in the Bellingshausen Sea, Antarctica. *Deep Sea Res. Part II Top. Stud. Oceanogr.* 42, 1313–1335. doi: 10.1016/0967-0645(95)00071-w

Stewart, G. M., and Fisher, N. S. (2003a). Experimental studies on the accumulation of polonium-210 by marine phytoplankton. *Limnol. Oceanogr.* 48, 1193–1201. doi: 10.4319/lo.2003.48.3.1193

Stewart, G. M., and Fisher, N. S. (2003b). Bioaccumulation of polonium-210 in marine copepods. *Limnol. Oceanogr.* 48, 2011–2019.

Stewart, G. M., Moran, S. B., and Lomas, M. W. (2010). Seasonal POC fluxes at BATS estimated from $^{210}$Po deficits. *Deep Sea Res. Part I Oceanogr. Res. Pap.* 57, 113–124. doi: 10.1016/j.dsr.2009.09.007

Stewart, G., Cochran, J. K., Miquel, J. C., Masqué, P., Szlosek, J., Rodriguez y Baena, A. M., et al. (2007). Comparing POC export from $^{234}$Th/$^{238}$U and $^{210}$Po/$^{210}$Pb disequilibria with estimates from sediment traps in the northwest Mediterranean. *Deep Sea Res. Part I Oceanogr. Res. Pap.* 54, 1549–1570. doi: 10.1016/j.dsr.2007.06.005

Su, K., Du, J., Baskaran, M., and Zhang, J. (2017). $^{210}$Po and $^{210}$Pb disequilibrium at the PN section in the East China Sea. *J. Environ. Radioact.* 174, 54–65. doi: 10.1016/j.jenvrad.2016.07.031

Subha Anand, S. S., Rengarajan, R., Shenoy, D., Gauns, M., and Naqvi, S. W. A. (2018). POC export fluxes in the Arabian Sea and the Bay of Bengal: a simultaneous $^{234}$Th/$^{238}$U and $^{210}$Po/$^{210}$Pb study. *Mar. Chem.* 198, 70–87.

Subha Anand, S., Rengarajan, R., Sarma, V. V. S. S., Sudheer, A. K., Bhushan, R., and Singh, S. K. (2017). Spatial variability of upper ocean POC export in the Bay of Bengal and the Indian Ocean determined using particle-reactive $^{234}$Th. *J. Geophys. Res. Oceans* 122, 3753–3770. doi: 10.1002/2016JC012639

Takahashi, T., Sutherland, S. C., Wanninkhof, R., Sweeney, C., Feely, R. A., Chipman, D. W., et al. (2009). Climatological mean and decadal change in surface ocean pCO2, and net sea-air CO2 flux over the global oceans. *Deep Sea Res. Part II Top. Stud. Oceanogr.* 56, 554–577. doi: 10.1016/j.dsr2.2008.12.009

Tang, Y., and Stewart, G. (2019). The $^{210}$Po/$^{210}$Pb method to calculate particle export: lessons learned from the results of three GEOTRACES transects. *Mar. Chem.* 217:103692. doi: 10.1016/j.marchem.2019.103692

Tang, Y., Lemaitre, N., Castrillejo, M., Roca-Martí, M., Masqué, P., and Stewart, G. (2019). The export flux of particulate organic carbon derived from $^{210}$Po/$^{210}$Pb disequilibria along the North Atlantic GEOTRACES GA01 transect: GEOVIDE cruise. *Biogeosciences* 16, 309–327. doi: 10.5194/bg-16-309-2019

Tang, Y., Stewart, G., Lam, P. J., Riguad, S., and Church, T. (2017). The influence of particle concentration and composition on the fractionation of $^{210}$Po and $^{210}$Pb along the North Atlantic GEOTRACES transect GA03. *Deep Sea Res. Part I Oceanogr. Res. Pap.* 128, 42–54. doi: 10.1016/j.dsr.2017.09.001

Turekian, K. K., Nozaki, Y., and Benninger, L. K. (1977). Geochemistry of atmospheric radon and radon products. *Annu. Rev. Earth Planet. Sci.* 5, 227–255. doi: 10.1146/annurev.ea.05.050177.001303

Umhau, B. P., Benitez-Nelson, C. R., Close, H. G., Hannides, C., Motta, L., Popp, B. N., et al. (2019). Seasonal and spatial changes in carbon and nitrogen fluxes estimated using $^{234}$Th:$^{238}$U disequilibria in the North Pacific tropical and subtropical gyre. *Mar. Chem.* 217:103705. doi: 10.1016/j.marchem.2019.103705

Verdeny, E., Masqué, P., Garcia-Orellana, J., Hanfland, C., Cochran, J. K., and Stewart, G. (2009). POC export from ocean surface waters by means of $^{234}$Th/$^{238}$U and $^{210}$Po/$^{210}$Pb disequilibria: a review of the use of two radiotracer pairs. *Deep Sea Res. Part II Top. Stud. Oceanogr.* 56, 1502–1518. doi: 10.1016/j.dsr2.2008.12.018

Villa-Alfageme, M., de Soto, F. C., Ceballos, E., Giering, S. L. C., Le Moigne, F. A. C., Henson, S., et al. (2016). Geographical, seasonal, and depth variation in sinking particle speeds in the North Atlantic. *Geophys. Res. Lett.* 43, 8609–8616. doi: 10.1002/2016GL069233

Wei, C. L., Lin, S. Y., Sheu, D. D., Chou, W. C., Yi, M. C., Santschi, P. H., et al. (2011). Particle-reactive radionuclides ($^{234}$Th, $^{210}$Pb, $^{210}$Po) as tracers for the estimation of export production in the South China Sea. *Biogeosciences* 8, 3793–3808.

Yasuda, I. (2003). Hydrographic structure and variability in the Kuroshio-Oyashio transition area. *J. Oceanogr.* 59, 389–402.

Zhong, Q. (2020). *Atmospheric Deposition of Radionuclides and its Application in POC Export Fluxes of the Upper Sea.* Ph.D thesis. Shanghai: East China Normal University. (In Chinese with English Abstract).

Zhong, Q., Puigcorbé, V., Sanders, C., and Du, J. (2020). Analysis of $^{210}$Po, $^{210}$Bi, and $^{210}$Pb in atmospheric and oceanic samples by simultaneously auto-plating $^{210}$Po and $^{210}$Bi onto a nickel disc. *J. Environ. Radioact.* 220–221:106301. doi: 10.1016/j.jenvrad.2020.106301

Zhong, Q., Wang, J., Du, J., Bi, Q., and Zhao, F. (2019). The $^{210}$Po/$^{210}$Pb disequilibrium in a spring-blooming marginal sea, the Southern Yellow Sea. *J. Environ. Radioact.* 207, 15–26. doi: 10.1016/j.jenvrad.2019.05.017

Zhou, K., Dai, M., Maiti, K., Chen, W., and Xie, Y. (2020). Impact of physical and biogeochemical forcing on particle export in the South China Sea. *Prog. Oceanog.* 187:102403. doi: 10.1016/j.pocean.2020.102403

**Conflict of Interest:** The authors declare that the research was conducted in the absence of any commercial or financial relationships that could be construed as a potential conflict of interest.

**Publisher's Note:** All claims expressed in this article are solely those of the authors and do not necessarily represent those of their affiliated organizations, or those of the publisher, the editors and the reviewers. Any product that may be evaluated in this article, or claim that may be made by its manufacturer, is not guaranteed or endorsed by the publisher.

*Copyright © 2021 Zhong, Yu, Lin, Lin, Ji, Ni, Du and Huang. This is an open-access article distributed under the terms of the Creative Commons Attribution License (CC BY). The use, distribution or reproduction in other forums is permitted, provided the original author(s) and the copyright owner(s) are credited and that the original publication in this journal is cited, in accordance with accepted academic practice. No use, distribution or reproduction is permitted which does not comply with these terms.*

frontiers in Marine Science

ORIGINAL RESEARCH
published: 22 December 2021
doi: 10.3389/fmars.2021.701897

# $^{210}$Pb-Derived Bioturbation Rates in Sediments Around Seamounts in the Tropical Northwest Pacific

*Feng Lin*, Cai Lin*, Hui Lin*, Xiuwu Sun* and Li Lin**

*Third Institute of Oceanography, Ministry of Natural Resources, Xiamen, China*

To evaluate bioturbation coefficients ($D_B$) and mixing depths (L), $^{210}$Pb and $^{226}$Ra activity was measured in two sediments cores (from water depths of 5,398 m and 4,428 m), which were collected from seamount areas in the Northwest Pacific. Using a steady-state diffusion mode, we estimated $D_B$ values of 16.8 and 24.1 cm$^2$/a, higher than those in abyssal sediments and those predicted by traditional empirical equations. Corresponding *L* values varied between 19.3 and 23.1 cm. These high values indicate that seamounts are the area of active bioturbation. A one-dimensional model for the transport of total organic carbon (TOC) from the surface layer of sediments to the deep layer was developed using the distribution pattern of the specific activity of excess $^{210}$Pb ($^{210}Pb_{ex}$) and its relationship with TOC. The model showed that the TOC flux transmitted downward by bioturbation was 0.09 mmol/(cm$^2$·a) and 0.12 mmol/(cm$^2$·a).

**Keywords: seamount, $^{210}$Pb, $^{226}$Ra, bioturbation, Northwest Pacific, TOC**

OPEN ACCESS

***Edited by:***
*Weifeng Yang,*
*Xiamen University, China*

***Reviewed by:***
*Leonardo Langone,*
*Institute of Polar Sciences, National Research Council (CNR), Italy*
*Junwen Wu,*
*Shantou University, China*

****Correspondence:***
*Feng Lin*
*linfeng@tio.org.cn*
*Cai Lin*
*lincai@tio.org.cn*
*Hui Lin*
*linhui@tio.org.cn*
*Xiuwu Sun*
*sunxiuwu@tio.org.cn*
*Li Lin*
*linli@tio.org.cn*

***Specialty section:***
*This article was submitted to Marine Biogeochemistry, a section of the journal Frontiers in Marine Science*

***Received:*** *28 April 2021*
***Accepted:*** *29 November 2021*
***Published:*** *22 December 2021*

***Citation:***
*Lin F, Lin C, Lin H, Sun X and Lin L (2021) $^{210}$Pb-Derived Bioturbation Rates in Sediments Around Seamounts in the Tropical Northwest Pacific. Front. Mar. Sci. 8:701897. doi: 10.3389/fmars.2021.701897*

## INTRODUCTION

Biological mixing of marine sediments (bioturbation) can substantially modify the physical, chemical, and biological properties of the sediment record (Trauth et al., 1997). These alterations are reflected in any high-resolution sedimentary record as an attenuation of the short-term variability and major phase shifts between various paleoclimatic tracers (Rodríguez-Tovar and Uchman, 2008). Bioturbation by benthic organisms can affect early diagenesis in surface sediments and the sedimentary record. For example, bioturbation can transport newly deposited material to deep sediment. Bioturbation can also affect the structure and evolution of seafloor communities (Aller, 1994). The importance of bioturbation in mediating biogeochemical processes in the upper centimeters of oceanic sediments provides a compelling reason for wanting to quantify *in situ* rates of bioturbation (Teal et al., 2008). The process of bioturbation, which involves both the dispersal of sediment particles (i.e., sediment reworking) and the transport of interstitial porewater (i.e., bioirrigation) by benthic organisms, occurs in the most oxic sediments and is therefore of global importance.

The bioturbation coefficient is one of the key parameters for the numerical simulation of sediment diagenesis. It is a measure of the transport of organic carbon into the sediment, which places constraints on the redox system of the sediment (Thiel and Tiefsee-Umweltschutz, 2001). Quantification of the bioturbation, therefore, is a prerequisite for the numerical modeling of geochemical processes induced by anthropogenic activities within deep-sea sediment (Suckow et al., 2001).

Seamounts are a unique ecosystem in oceanic environments and are hotspots for pelagic and benthic organisms (Yang et al., 2019). Limited by sampling conditions and other factors, bioturbation in marine sediments around seamounts has been rarely studied until now. Anthropogenic activities, such as the exploitation of polymetallic nodules, can disturb the deep-sea floor and have negative impacts on benthic ecology (Thiel and Tiefsee-Umweltschutz, 2001; Jones et al., 2017). For example, the biogeochemical environment of the seabed along and around seabed mining routes can be altered significantly due to the resuspension of sediments, the release of chemically active substances into the water column, and the subsequent resettlement of the aforementioned materials.

Radioactive disequilibria between radionuclides of the natural uranium and thorium series are used extensively to establish timescales of sedimentation and diagenetic processes within the sediment. $^{210}$Pb is a natural radionuclide with a half-life of 22.3 years that has been used extensively to estimate sedimentation rates and biological mixing. $^{210}$Pb, produced in the atmosphere and water column by the decay of $^{226}$Ra and $^{222}$Rn, is exported to the seabed by sinking particles. The $^{210}$Pb incorporated into the sediment from this process is called "excess $^{210}$Pb" ($^{210}Pb_{ex}$) in that it is of more than $^{210}$Pb that is produced *in situ* from the decay of $^{226}$Ra and $^{222}$Rn within the sediment column (supported $^{210}$Pb). The $^{210}Pb_{ex}$ signal decreases over time and approaches zero after about 100 years. If sediment accumulation alone controls the distribution of $^{210}Pb_{ex}$, then $^{210}Pb_{ex}$ activity should not be detectable in parts of the sediment column deposited 100 years ago. However, the $^{210}Pb_{ex}$ signal commonly extends downward, below the expected depth for zero activity in deep-sea sediments, owing to sediment mixing by bioturbation (Legeleux et al., 1994; Yang et al., 2019). In this study, we use $^{210}$Pb and $^{226}$Ra as radiotracers to quantify the bioturbation mixing depth and diffusion coefficient based on a steady-state diffusion model.

# MATERIALS AND METHODS

## Study Areas

A large area in the Western Pacific Basin is remarkable for its many large and small seamounts formed during the Cretaceous. Two sediment cores were collected from the MP4 seamount (McDonnell Guyot) of the Marcus-Wake Seamount Cluster in the subtropical Western Pacific Ocean (**Figure 1**). The heights of these seamounts range from 3,656 to 4,022 m, and the base depth is about 5,500 m.

Core MP4-S05-MC08 is from the seamount and MP4-S01-MC07 is from the foothill of mount MP4 in the Western Pacific Ocean. In the sea basin on the north and south sides of the MP4 seamount, the coverage of polymetallic nodules is more than 90%. The nodules on the north side are mainly medium sized, while those on the south side are mainly small (<3 cm).

## Sampling

Two sediment cores were collected from the area around MP4 using multiple corers with an inner diameter of 9.5 cm during the R/V XIANGYANGHONG03 Monitoring and Protection of Ecology and Environment Cruise, which was at sea during July–August 2017 (**Table 1**). The multiple corers used in our sampling is able to collect sediments without disturbance. Once aboard the ship, multiple-core tubes were extruded and sectioned at 1 cm intervals for the upper 2-cm depth and then at 2-cm intervals to the end. Each subsample was sealed in a clean polyethylene bag and stored frozen at −18°C.

## Assessment of Environmental Background Data

Before analysis, the sediment samples were freeze-dried and homogenized. Water content was determined gravimetrically during freeze-drying.

For the total organic carbon (TOC), 2-g samples were first acidified for 24 h with 4 mol/L HCl and rinsed at least three times with deionized water to remove carbonate carbon. The residues were dried at 50°C, ground, and homogenized. Carbon and nitrogen contents were determined using a Fisons CHN analyzer following the procedure described by Froelich (1980) and modified by Hedges and Stern (1984). Every sample was analyzed in duplicate and the results averaged.

## Analysis of $^{210}$Pb and $^{226}$Ra

The radioactivity of $^{210}$Pb was determined using a 46.5 keV gamma-ray with a branching ratio of 4.25% and high-purity germanium (HPGe) detectors (ORTEC 8030, AMETEK, Berwyn, PA, United States). The detection efficiency was calibrated using marine sediment reference standard IAEA-385 (International Atomic Energy Agency, Austria). The specific activity of $^{210}$Pb was calculated by the following equation:

$$A = \sum_{i=1}^{n} \left( \frac{N_i}{t} - \frac{N_{bi}}{t_b} \right) \times \frac{1}{\varepsilon_i Y_i m},$$

where A is the specific activity of $^{210}$Pb (Bq/kg), Ni and Nbi are peak areas at 46.5 keV of the sample and the blank respectively, t and tb are counting times for sample and blank respectively, $\varepsilon_i$ is detection efficiency of $^{210}$Pb, Y is branch ratio (4.25%), and m is the weight of the sample (kg).

All the values of excess $^{210}$Pb were decay corrected (22.3-year half-life) to the date of the core collection. A correction for self-absorption of the low-energy $^{210}$Pb gamma rays was made using the method of Cutshall et al. (1983).

The post-homogenized sediments were sealed in a polyethylene box for at least 20 days. The radioactivity of $^{226}$Ra was determined by detection of its decay products $^{214}$Pb and $^{214}$Bi using gamma spectrometry with HPGe detector (ORTEC 8030). The energy transitions are 295.2 keV (18.4%) and 351.9 keV (35.6%) of $^{214}$Pb, and 609.3 keV (45.495) and 1,120.3 keV (14.91%) of $^{214}$Bi. Our results showed that the specific activities of $^{226}$Ra calculated from peak areas under the 295.2 keV were consistent with those under 609.3 keV, but the activities *via* 351.9 and 1,120.3 keV were inconsistent. The specific activity of $^{226}$Ra from 351.9 keV gamma ray was overestimated due to interference of $^{211}$Bi, which emits a gamma

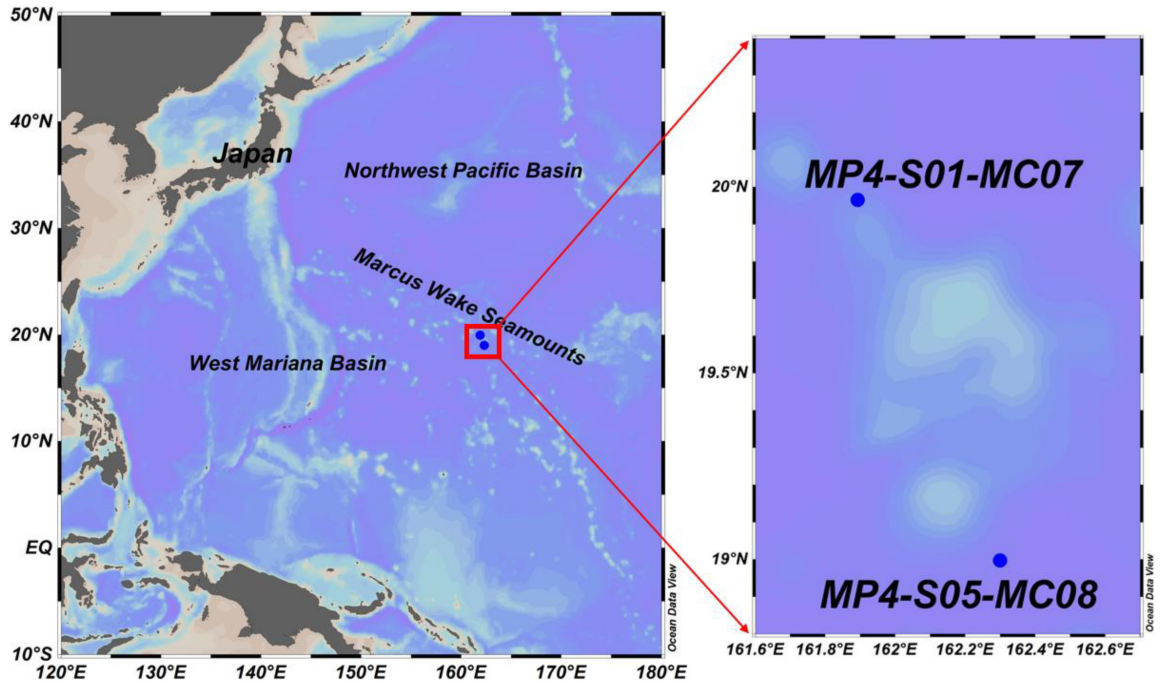


**FIGURE 1 |** Sampling locations.

**TABLE 1 |** Sampling locations, water depth, organic carbon content ($C_{org}$), bioturbation ($D_B$), and mixing depth (L).

| Area | Station | Latitude (°N) | Longitude (°E) | Depth (m) | $C_{org}$ (%) | $D_B$ ($cm^2/a$) | L (cm) |
|---|---|---|---|---|---|---|---|
| Seamounts | MP04-S05-MC08 | 18.9975 | 162.2994 | 5398 | 0.28 | 16.8 | 19.3 |
| | MP04-S01-MC07 | 19.9660 | 161.8922 | 4428 | 0.24 | 24.1 | 23.1 |

ray at 351.1 keV (12.91%). The specific activity of $^{226}$Ra from the 1,120.3 keV gamma ray fluctuated substantially due to its low branch ratio (14.91%). Thus, only the peak areas under 295.2 and 609.3 keV were used to calculate the specific activity of $^{226}$Ra in this study. The detection efficiency of $^{226}$Ra was calibrated using marine sediment standard IAEA-385.

The excess $^{210}$Pb ($^{210}Pb_{ex}$), i.e., the fraction exceeding parent-isotope activity, was determined by subtracting $^{226}$Ra activity from the total $^{210}$Pb activity.

# RESULTS

## Distribution of $^{210}$Pb, $^{226}$Ra, and $^{210}Pb_{ex}$ in the Sediment Cores

The $^{210}$Pb, $^{226}$Ra, and $^{210}Pb_{ex}$ profiles are shown in **Figure 2**. The $^{226}$Ra values ranged from 42.75 to 298.87 Bq/kg, with an average of 138.14 ± 67.02 Bq/kg. In the two cores, the highest values were at the subsurface. All profiles show an approximately exponential decrease with depth.

The $^{210}$Pb values ranged from 130.74 to 1659.62 Bq/kg, with an average of 487.73 ± 261.91 Bq/kg. The specific activity of $^{210}$Pb in sediments increased with depth within a few centimeters of the surface layer and then decreased exponentially with the depth after reaching the maximum value. The specific activity of $^{210}Pb_{ex}$ decreases exponentially with depth and shows the same tread as $^{210}$Pb.

Two stations are located near the Zhanlun seamounts. The highest value (848.02 Bq/kg) at station MP4-S05-MC08 appeared at 1–2 cm in the subsurface layer, while the highest value (759.51 Bq/kg) at station MP4-S01-MC07 appeared at 4–6 cm. These values are comparable to the $^{210}$Pb values measured by Suckow et al. (2001) in abyssal sediments in the Peru Basin.

Back mixing, in which benthic animal activity such as feeding carries subsurface sediment to the surface, also occurs in many deep sediments. This activity makes the radionuclides at the surface decline rapidly with depth. However, in the subsurface "wide shoulder" (that is, the nuclide specific activity within a certain depth with the increase of the depth remains unchanged) or a great value.

Examples of this pattern include $^{210}Pb_{ex}$ and $^{234}Th_{ex}$ in abyssal sediments (140°W, 0°−5°N) in the equatorial Pacific (Smith et al., 1996) and $^{210}Pb_{ex}$ and $^{137}$Cs in abyssal sediments from the northeastern tropical Atlantic (Pope et al., 1996). A three-dimensional distribution of $^{210}$Pb of sediments from the continental slope of Newfoundland showed that the mixing of sediments is uneven and the inclined burrowing movement of benthic animals transports a large amount of surface sediments into the interior. As a result, the maximum value of $^{210}$Pb

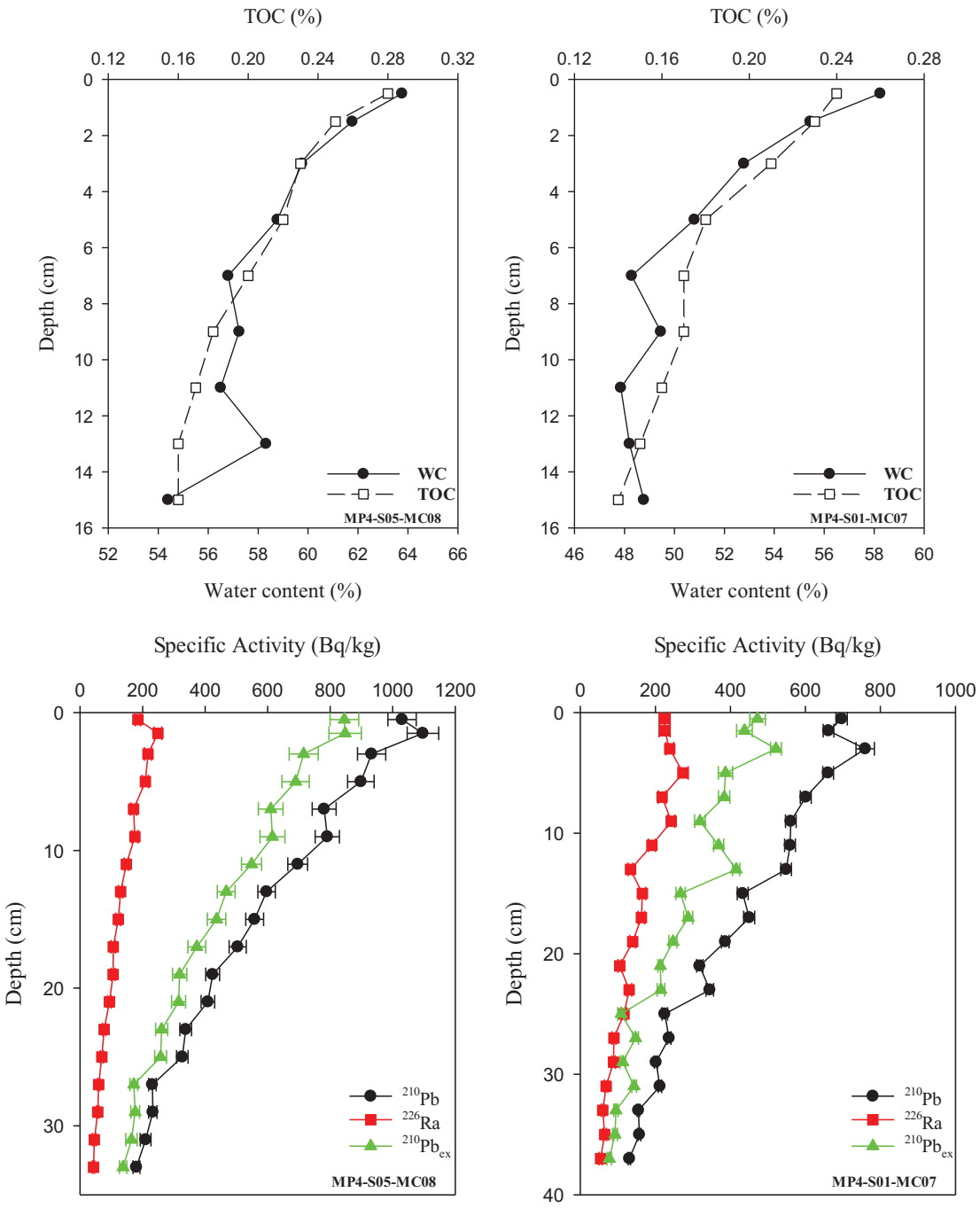


**FIGURE 2 |** Profiles of total organic carbon, water content, and activity of $^{210}$Pb, $^{226}$Ra, and $^{210}$Pb$_{ex}$ in sediment cores.

is at a certain depth under the sediment–water interface (Smith and Schafer, 1984).

## Distribution of Total Organic Carbon, Water Content, and Total Nitrogen

Total organic carbon varied between 0.14 and 0.28%, with an average of 0.19 ± 0.04%. The pattern shows an exponential decline with depth. The TOC in our study is lower than the central North Pacific (0.21–0.40%) (Müller and Suess, 1979) and the central equatorial Pacific (0.26–0.68%) (Smith et al., 1996).

Water content varied between 47 and 89%. The overall trend is a gradual decrease with depth, which is similar to the change in TOC.

Total nitrogen content at the sediment surface fluctuated between 0.06 and 0.07%, with values at the northern station

lower than the southern station. The surface C/N ratios were 4.9 at both stations.

## Bioturbation ($D_B$ and L)

The relevance of biological mixing in the inventory estimates was inferred from the bioturbation coefficient ($D_B$). $D_B$ and bioturbation mixing depth (L) were estimated from the specific activity of the vertical distribution of $^{210}Pb_{ex}$ in the sediment.

Owing to the half-life of $^{210}Pb$, the $^{210}Pb_{ex}$ signal is detectable for only about 100 years. Since sedimentation rates in the deep-sea area are less than 1 millimeter per thousand years (Nozaki et al., 1977; Yang et al., 2019), $^{210}Pb_{ex}$ should be detectable only within the top 1 mm of the sediment column. All the earlier studies have found $^{210}Pb$ in the deep-sea sediments down to a depth of several centimeters, which was interpreted to be a result of bioturbation (Nozaki et al., 1977; Smith and Schafer, 1984; Muñoz et al., 2007).

Goldberg and Koide (1962) and Guinasso and Schink (1975) described the process of bioturbation in a first approximation steady-state diffusion model that included radioactive decay.

This model was improved by Nozaki et al. (1977). When a biological diffusion model is applied, the biological mixing process of tracer material in sediments must meet two conditions: (1) the frequency of biological mixing must be much greater than the disappearance rate of the tracer and (2) the size of the particle exchange must be smaller than the size of the tracer profile and the thickness of the mixing layer.

$$\frac{\partial}{\partial t}(\rho A) = \frac{\partial}{\partial z}\left(\rho D_B \frac{\partial A}{\partial z}\right) - \frac{\partial}{\partial z}(\rho S A) - \lambda \rho A, \quad (1)$$

where $z$ is the depth within the sediment column (cm), A is the tracer-specific activity of $^{210}Pb_{ex}$ (Bq/kg) in the depth of $z$, $\rho$ is the bulk sediment density (g/cm$^3$), $D_B$ is the bioturbation coefficient (cm$^2$/a), S is the sedimentation rate (cm/a), $\lambda$ is the decay constant of $^{210}Pb$ (0.031 a$^{-1}$), and t is the time (a).

In this model, the bioturbation process is considered to be a vortices-like diffusion mixing process. It is assumed that in the mixing layer, the biological disturbance coefficient $D_B$, deposition rate S, and $\rho$ of sediment density are in a constant state, such that $\frac{\partial}{\partial t}(\rho A) = 0$.

The solution with the boundary conditions, $A = A_0$ at $z = 0$ and $A \to 0$ at $z \to \infty$ (Equation 1) is given by:

$$A = A_0 exp\left[\frac{S - \sqrt{S^2 + 4\lambda D_B}}{2D_B} z\right]. \quad (2)$$

Since the deposition rate of oceanic sediments is generally in the order of mm/ka, and the timescale of the action of $^{210}Pb$ tracer bioturbation is only about 100 a, the deposition of sediments can be ignored within the timescale of the tracer, and the aforementioned equation is simplified to:

$$A = A_0 exp\left[-z\sqrt{\lambda / D_B}\right]. \quad (3)$$

An exponential fit to a measured depth profile of $^{210}Pb_{ex}$, therefore, gives a quantitative measure of the bioturbation. In this model, the mixing depth L is the depth in the sediment at which the fitted tracer concentration has decreased to 1/e and can be computed by:

$$L = \sqrt{D_B / \lambda}. \quad (4)$$

According to **Figure 3**, $D_B$ and L in MP4-S01-MC07 are 24.1 cm$^2$/a and 23.1 cm, and are 16.8 cm$^2$/a and 19.3 cm in MP4-S05-MC08, respectively.

The average is $20.5 \pm 5.2$ cm$^2$/a, which is the same as the global average of 19.98 $\pm$ 42.64 cm$^2$/a (Teal et al., 2008) but higher than the bioturbation coefficients of the deep-sea sediments in the Western Pacific and high-productivity areas such as the Peru Basin (Suckow et al., 2001), Washington shelf edge (Yan and Zhou, 2004), Puget Bay (Carpenter et al., 1985), and the southwest polar shelf (Maire et al., 2008). Both stations were sampled in the summer, which, according to the statistics of Teal et al. (2008), is the time when the bioturbation rate is the highest. The aforementioned differences reveal the possible relationship between the intensity of the biological disturbance and sea productivity. Some studies also show that POC output flux in the water column regulates the depth of sediment mixing layer and the intensity of bioturbation (Smith et al., 1997; Boudreau, 1998).

# DISCUSSION

There are many factors influencing the bioturbation of sediments, such as deposition rate, organic carbon deposition flux at the sediment–water interface, abundance of benthic organisms, community structure, living habits and disturbance mode, water depth, oxygen solubility in bottom water or penetration of dissolved oxygen in sediments, sediment type, and hydrodynamic conditions. These factors interact with each other to affect biological disturbance, but the relative importance of each factor varies in different marine environments. However, the intensity of biological disturbance in specific sea areas is usually regulated by major influencing factors.

## Influence of Water Depth

It can be seen from **Table 1** that there is a higher bioturbation coefficient at the station with the shallower water depth. This is consistent with the law discovered by Middelburg et al. (1997) that global marine sediment bioturbation decreases with increasing water depth. An empirical is proposed to describe the relationship between $D_B$ and water depth based on data from the Eastern Pacific and the North Atlantic ($D_B = 5.2 \times 10^{0.762 - 0.0004 \times Z}$). According to this equation, the values of $D_B$ (0.51 and 0.21 cm$^2$/a) in our study are two orders of magnitude lower than those derived by $^{210}Pb_{ex}$.

Although statistics of Middelburg are based on the global sediment bioturbation data, there are only two deep water stations in this study. More data will be needed to confirm and support this theory in the future.

## Relationship Between Bioturbation and Organic Carbon and Nitrogen Contents in Sediments

Animals that forage for sediments in the deep ocean far outnumber those that feed on the suspended matter. Because the

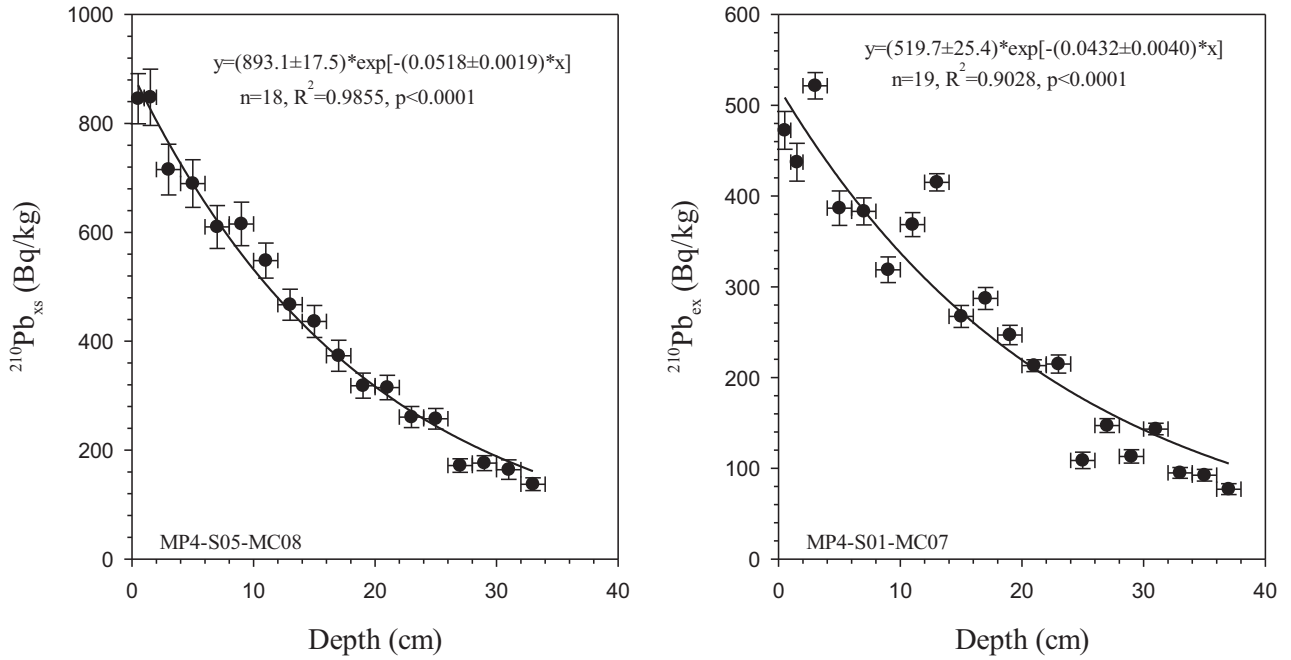


**FIGURE 3 |** The relationship between specific activity of $^{210}Pb_{ex}$ and depth in sediment cores. The fitting curve and equation are shown in each panel.

amount of nutrients in the form of bacteria and other particles is so small, sediment-eating animals have to eat large amounts of sediment to get enough organic carbon to survive. It is estimated that 100 g of sediment may pass through the digestive tract of sea cucumbers every day (Gage and Tyler, 1991). Therefore, the content of organic matter in sediments directly affects the ability of animals to process sediment particles. Boudreau (1998) believed that biological mixing strength increased with the increase of food quantity. They defined the biological diffusion coefficient as a function of the unstable concentration of active organic matter. That is, unstable organic matter degrades as it is mixed downward, and all available unstable organic matter degrades to a certain depth, so the biological diffusion coefficient as a function of organic matter disappears.

Bioturbation in this study area may be controlled by TOC content in sediments. It can be seen from **Figure 4**. In both cores, there is a good positive correlation between the specific activity of $^{210}Pb_{ex}$ and the content of TOC. This result is consistent with the positive correlation between food sources and bioturbation intensity observed in the northeast Atlantic (Legeleux et al., 1994) and the central equatorial Pacific (Pope et al., 1996; Smith et al., 2000).

Studies have shown that the POC output flux in the water column of the tropical Pacific controls the rate of benthic biological and chemical processes (Pope et al., 1996; Alperin et al., 2002). The research results in the polymetallic nodule area of the Eastern Pacific Ocean also show that the higher the organic carbon content, the stronger the biological disturbance effect (Yan and Zhou, 2004). Unfortunately, in this study, we did not estimate the accumulation flux of organic carbon in the surface sediments.

## Transport of Total Organic Carbon by Bioturbation

In bioturbation mixed sediments, organic matter is transported to deep sediments to provide organic carbon for deep organisms. Using the distribution pattern of specific activity of $^{210}Pb_{ex}$ in **Figure 4** and the relationship between $^{210}Pb_{ex}$ and TOC, one-dimensional model for the transport of TOC from the surface layer of sediments to the deep layer can be established:

$$F_b = -D_b \frac{dC_{TOC}}{dz}, \tag{5}$$

where $F_b$ represents the flux of TOC [mmol/(cm$^2$*a)], $dC_{TOC}/dz$ represents the vertical density gradient of $C_{TOC}$, and the negative sign indicates the downward direction of the flux. The distribution of TOC content in the sediments of MP4-S05-MC08 and MP4-S01-MC07 stations was fitted, and the following equation was obtained:

$$C_{TOC} = 0.263 - 0.008z \left(R^2 = 0.93,\ P < 0.001\right), \tag{6}$$

$$C_{TOC} = 0.231 - 0.007z \left(R^2 = 0.91,\ P < 0.001\right). \tag{7}$$

It can be seen from the equations aforementioned that there is a good linear correlation in the two stations and the depth, which conforms to the following equation:

$$C_{TOC} = b + a \times z. \tag{8}$$

Differential of $C_{TOC}$ with respect to depth $z$, we can get:

$$\frac{dC_{TOC}}{dz} = a. \tag{9}$$

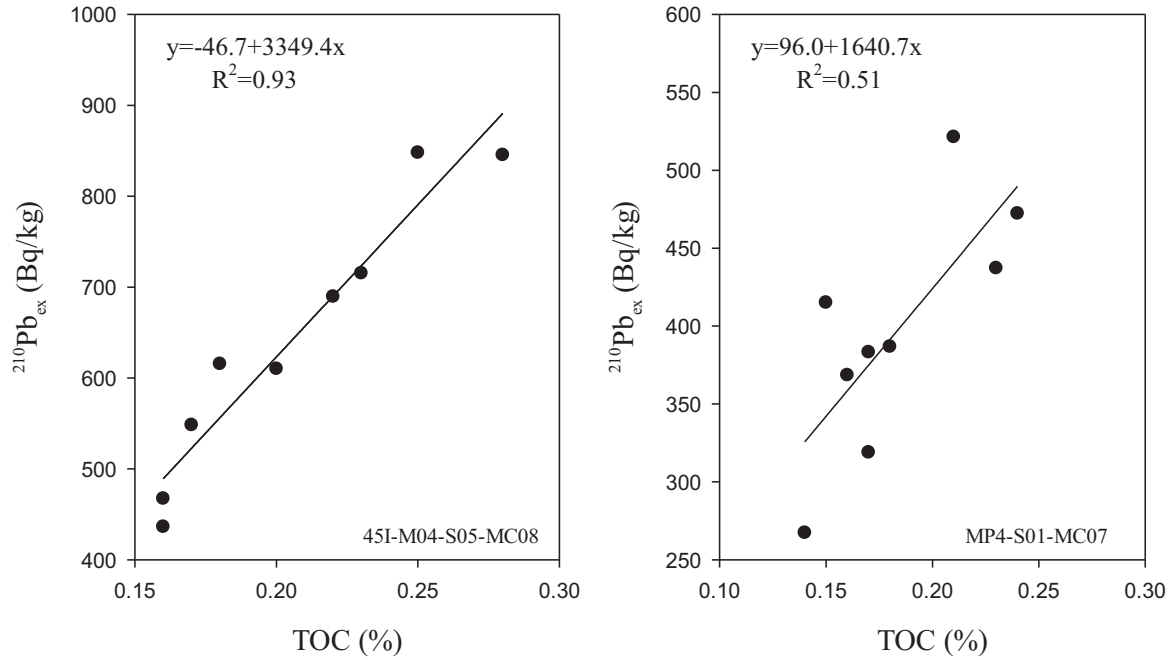


**FIGURE 4 |** The relationship between $^{210}Pb_{ex}$ and TOC.

The fitted a and the obtained bioturbation coefficient $D_B$ were substituted, and the TOC flux transmitted downward by bioturbation at stations MP4-S05-MC08 and MP4-S01-MC07 were calculated to be 0.09 and 0.12 mmol/($cm^2$·a), respectively.

It should be noted that this model is based mainly on the biological disturbance caused by deep $^{210}Pb_{ex}$ and TOC concentration in sediments and the direct relationship between the disturbance process of TOC to calculate the transmission, while getting the coefficient of the $D_B$ has been considered in biological disturbance model $^{210}Pb$ downward mixing in the process of decay. However, this model does not take into account the degradation of downward transmission in the process of TOC; therefore, the results obtained with the model represent the upper limit of the TOC conveying.

## CONCLUSION

Based on the distribution of $^{210}Pb_{ex}$ in sediment cores and one-dimensional steady-state vortex diffusion model, the bioturbation coefficient of marine sediments was found to range from 16.8 to 24.1 $cm^2$/a with an average of 20.5 ± 5.2 $cm^2$/a. The bioturbation mixing depth ranged between 19.3 and 23.1 cm with an average of 21.2 ± 2.7 cm, which is above the global average. This indicates that the region is experiencing a strong bioturbation effect. Bioturbation is influenced mainly by the TOC content in sediments, the composition of controlled biological communities, and water depth. The relationship between $^{210}Pb_{ex}$ and TOC was used to quantify the organic carbon transported from surface sediments to deep layers by core biological activity. We estimated the TOC flux transmitted downward by bioturbation was 0.09 and 0.12 mmol/($cm^2$·a).

## DATA AVAILABILITY STATEMENT

The original contributions presented in the study are included in the article/supplementary material, further inquiries can be directed to the corresponding authors.

## AUTHOR CONTRIBUTIONS

FL, CL, and HL contributed to conception and design of the study. LL organized the database. XS performed the statistical analysis. All authors contributed to manuscript revision, read, and approved the submitted version.

## FUNDING

This work was supported by the Scientific Research Foundation of Third Institute of Oceanography, MNR (2020012), the Monitoring and Protection of Ecology and Environment in the eastern Pacific Ocean (No. DY-135-E2-5-02), and Global Change and Air-Sea Interaction II (GASI-01-NPC-STsum).

## ACKNOWLEDGMENTS

We sincerely appreciate the Monitoring and Protection of Ecology and Environment Cruise in 2017 and the crew of the R/V XIANGYANGHONG03 for their assistance in sample collection.

## REFERENCES


Aller, R. C. (1994). Bioturbation and remineralization of sedimentary organic matter: effects of redox oscillation. *Chem. Geol.* 114, 331–345. doi: 10.1016/0009-2541(94)90062-0

Alperin, M. J., Suayah, I. B., Benninger, L. K., and Martens, C. S. (2002). Modern organic carbon burial fluxes, recent sedimentation rates, and particle mixing rates from the upper continental slope near Cape Hatteras, North Carolina (USA). *Deep Sea Res. II Top. Stud. Oceanogr.* 49, 4645–4665. doi: 10.1016/S0967-0645(02)00133-9

Boudreau, B. P. (1998). Mean mixed depth of sediments: the wherefore and the why. *Limnol. Oceanogr.* 43, 524–526. doi: 10.4319/lo.1998.43.3.0524

Carpenter, R., Peterson, M., and Bennett, J. (1985). 210Pb-derived sediment accumulation and mixing rates for the greater Puget Sound region. *Mar. Geol.* 64, 291–312. doi: 10.1016/0025-3227(85)90109-4

Cutshall, N. H., Larsen, I. L., and Olsen, C. R. (1983). Direct analysis of 210Pb in sediment samples: self-absorption corrections. *Nucl. Instrum. Methods Phys. Res.* 206, 309–312. doi: 10.1016/0167-5087(83)91273-5

Froelich, P. (1980). Analysis of organic carbon in marine sediments. *Limnol. Oceanogr.* 25, 564–572.

Gage, J. D., and Tyler, P. A. (1991). *Deep-Sea Biology: A Natural History of Organisms at the Deep-Sea Floor*. Cambridge: Cambridge University Press.

Goldberg, E. D., and Koide, M. (1962). Geochronological studies of deep sea sediments by the ionium/thorium method. *Geochim. Cosmochim. Acta.* 26, 417–450. doi: 10.1016/0016-7037(62)90112-6

Guinasso, N. Jr., and Schink, D. (1975). Quantitative estimates of biological mixing rates in abyssal sediments. *J. Geophys. Res.* 80, 3032–3043. doi: 10.1029/JC080i021p03032

Hedges, J. I., and Stern, J. H. (1984). Carbon and nitrogen determinations of carbonate-containing solids1. *Limnol. Oceanogr.* 29, 657–663. doi: 10.4319/lo.1984.29.3.0657

Jones, D. O., Kaiser, S., Sweetman, A. K., Smith, C. R., Menot, L., Vink, A., et al. (2017). Biological responses to disturbance from simulated deep-sea polymetallic nodule mining. *PLoS One* 12:e0171750. doi: 10.1371/journal.pone.0171750

Legeleux, F., Reyss, J.-L., and Schmidt, S. (1994). Particle mixing rates in sediments of the northeast tropical Atlantic: evidence from 210Pbxs, 137Cs, 228Thxs and 234Thxs downcore distributions. *Earth Planet. Sci. Lett.* 128, 545–562. doi: 10.1016/0012-821X(94)90169-4

Maire, O., Lecroart, P., Meysman, F., Rosenberg, R., Duchêne, J.-C., and Grémare, A. (2008). Quantification of sediment reworking rates in bioturbation research: a review. *Aquat. Biol.* 2, 219–238. doi: 10.3354/ab00053

Middelburg, J. J., Soetaert, K., and Herman, P. M. (1997). Empirical relationships for use in global diagenetic models. *Deep Sea Res. I Oceanogr. Res. Pap.* 44, 327–344. doi: 10.1016/S0967-0637(96)00101-X

Müller, P. J., and Suess, E. (1979). Productivity, sedimentation rate, and sedimentary organic matter in the oceans—I. Organic carbon preservation. *Deep Sea Res. Part A Oceanogr. Res. Pap.* 26, 1347–1362. doi: 10.1016/0198-0149(79)90003-7

Muñoz, P., Sellanes, J., Lange, C., Palma, M., and Salamanca, M. A. (2007). Temporal variability of 210Pb fluxes and bioturbation in shelf sediments beneath the high primary production area off concepción, central-southern Chile (36°S). *Prog. Oceanogr.* 75, 586–602. doi: 10.1016/j.pocean.2007.08.015

Nozaki, Y., Cochran, J. K., Turekian, K. K., and Keller, G. (1977). Radiocarbon and 210Pb distribution in submersible-taken deep-sea cores from Project FAMOUS. *Earth Planet. Sci. Lett.* 34, 167–173. doi: 10.1016/0012-821X(77)90001-2

Pope, R., DeMaster, D., Smith, C., and Seltmann, H. Jr. (1996). Rapid bioturbation in equatorial Pacific sediments: evidence from excess 234Th measurements. *Deep Sea Res. II Top. Stud. Oceanogr.* 43, 1339–1364. doi: 10.1016/0967-0645(96)00009-4

Rodríguez-Tovar, F. J., and Uchman, A. (2008). Bioturbational disturbance of the cretaceous-palaeogene (K-Pg) boundary layer: implications for the interpretation of the K-Pg boundary impact event. *Geobios* 41, 661–667. doi: 10.1016/j.geobios.2008.01.003

Smith, C. R., Berelson, W., Demaster, D. J., Dobbs, F. C., Hammond, D., Hoover, D. J., et al. (1997). Latitudinal variations in benthic processes in the abyssal equatorial Pacific: control by biogenic particle flux. *Deep Sea Res. II Top. Stud. Oceanogr.* 44, 2295–2317. doi: 10.1016/S0967-0645(97)00022-2

Smith, C. R., Hoover, D. J., Doan, S. E., Pope, R. H., Demaster, D. J., Dobbs, F. C., et al. (1996). Phytodetritus at the abyssal seafloor across 10° of latitude in the central equatorial Pacific. *Deep Sea Res. II Top. Stud. Oceanogr.* 43, 1309–1338. doi: 10.1016/0967-0645(96)00015-X

Smith, C. R., Levin, L. A., Hoover, D. J., McMurtry, G., and Gage, J. D. (2000). Variations in bioturbation across the oxygen minimum zone in the northwest Arabian Sea. *Deep Sea Res. Part II Top. Stud. Oceanogr.* 47, 227–257. doi: 10.1016/S0967-0645(99)00108-3

Smith, J., and Schafer, C. (1984). Bioturbation processes in continental slope and rise sediments delineated by Pb–210, microfossil and textural indicators. *J. Mar. Res.* 42, 1117–1145. doi: 10.1357/002224084788520738

Suckow, A., Treppke, U., Wiedicke, M. H., and Weber, M. E. (2001). Bioturbation coefficients of deep-sea sediments from the Peru Basin determined by gamma spectrometry of 210Pbexc. *Deep Sea Res. II Top. Stud. Oceanogr.* 48, 3569–3592. doi: 10.1016/S0967-0645(01)00057-1

Teal, L., Bulling, M. T., Parker, E., and Solan, M. (2008). Global patterns of bioturbation intensity and mixed depth of marine soft sediments. *Aquat. Biol.* 2, 207–218. doi: 10.3354/ab00052

Thiel, H., and Tiefsee-Umweltschutz, F. (2001). Evaluation of the environmental consequences of polymetallic nodule mining based on the results of the TUSCH Research Association. *Deep Sea Res. II Top. Stud. Oceanogr.* 48, 3433–3452. doi: 10.1016/S0967-0645(01)00051-0

Trauth, M. H., Sarnthein, M., and Arnold, M. (1997). Bioturbational mixing depth and carbon flux at the seafloor. *Paleoceanography* 12, 517–526. doi: 10.1029/97PA00722

Yan, Q., and Zhou, H. (2004). Bioturbation in near-surface sediments from the COMRA polymetallic nodule area: evidence from excess 210Pb measurements. *Chinese Sci. Bull.* 49, 2538–2542.

Yang, Z., Qian, Q., Chen, M., Zhang, R., Yang, W., Zheng, M., et al. (2019). Enhanced but highly variable bioturbation around seamounts in the northwest Pacific. *Deep Sea Res. I Oceanogr. Res. Pap.* 156:103190. doi: 10.1016/j.dsr.2019.103190


**Conflict of Interest:** The authors declare that the research was conducted in the absence of any commercial or financial relationships that could be construed as a potential conflict of interest.

**Publisher's Note:** All claims expressed in this article are solely those of the authors and do not necessarily represent those of their affiliated organizations, or those of the publisher, the editors and the reviewers. Any product that may be evaluated in this article, or claim that may be made by its manufacturer, is not guaranteed or endorsed by the publisher.

*Copyright © 2021 Lin, Lin, Lin, Sun and Lin. This is an open-access article distributed under the terms of the Creative Commons Attribution License (CC BY). The use, distribution or reproduction in other forums is permitted, provided the original author(s) and the copyright owner(s) are credited and that the original publication in this journal is cited, in accordance with accepted academic practice. No use, distribution or reproduction is permitted which does not comply with these terms.*

# Advantages of publishing in Frontiers

**OPEN ACCESS**
Articles are free to read for greatest visibility and readership

**FAST PUBLICATION**
Around 90 days from submission to decision

**HIGH QUALITY PEER-REVIEW**
Rigorous, collaborative, and constructive peer-review

**TRANSPARENT PEER-REVIEW**
Editors and reviewers acknowledged by name on published articles

**Frontiers**
Avenue du Tribunal-Fédéral 34
1005 Lausanne | Switzerland

**Visit us:** www.frontiersin.org
**Contact us:** frontiersin.org/about/contact

**REPRODUCIBILITY OF RESEARCH**
Support open data and methods to enhance research reproducibility

**DIGITAL PUBLISHING**
Articles designed for optimal readership across devices

**FOLLOW US**
@frontiersin

**IMPACT METRICS**
Advanced article metrics track visibility across digital media

**EXTENSIVE PROMOTION**
Marketing and promotion of impactful research

**LOOP RESEARCH NETWORK**
Our network increases your article's readership